

CONTENTS

#142	Measurement of X-ray CTR Signals from GaN/GaInN/GaN a High Temperatures Using Newly Developed Measurement System	585
	Y. Takeda, T. Mizuno, H. Kamiya, K. Ninoi, and M. Tabuchi	
#143	Development of New X-ray CTR Scattering Measurement System Using Johansson Monochromator	589
	Masao Tabuchi, Hiroshi Tameoka, Tatsuya Kawase, and Yoshikazu Takeda	
#144	Study on accumulation process of As atoms in InP/GaInAs/InP hetero-structures	593
	Masao Tabuchi, Akiko Mori, Hiroshi Tameoka, Katsunori Fujii, and Yoshikazu Takeda	
#145	Quantitative Analysis of the Strain Field beneath the Si₃N₄/Si(001) Interface Formed by the Xe/NH₃ Plasma Nitridation using a Multiple-Wave X-ray Diffraction Phenomenon	597
	Wataru Yashiro, Yoshitaka Yoda, Takashi Aratani, Akinobu Teramoto, Takeo Hattori and Kazushi Miki	
#146	X-ray Optics with Small Vertical Divergence and Horizontal Focusing For an X-ray Standing-wave Measurement	601
	Osami Sakata, Togo Kudo, Hiroaki Yamanaka, and Yasuhiko Imai	
#147	Development of novel oxide multilayer mirrors at "water-window" wavelengths by atomic layer deposition / atomic layer epitaxy	605
	Hiroshi Kumagai, Yuji Tanaka, Yusuke Masuda, Tsutomu Shinagawa and Ataru Kobayashi	
#148	Design of novel titanium oxide/nickel oxide multilayer mirror for attosecond soft x rays	609
	Hiroshi Kumagai and Yusuke Masudai	
#149	Study of thin-film thickness and density by high-resolution Rutherford backscattering spectrometry and X-ray reflectivity	613
	Amane Kitahara, Satoshi Yasuno and Kazuhisa Fujikawa	
#150	Non-destructive analysis on oxidation states of Ti atoms in the passivation film formed on SUS321 using hard X-ray photoelectron spectroscopy	617
	Shin Takahashi, Mitsutoshi Yokomizo, Masugu Sato, Masatake Machida and Son Jin-Young	
#151	Development of femtosecond X-ray source in helium atmosphere with millijoule high-repetition-rate femtosecond laser ...	621
	Masaki Hada and Jiro Matsuo	
#152	Measurement of crystallization temperature of Pd-based amorphous alloy thin film by energy dispersive X-ray reflectometry	627
	Tokujiro Yamamoto, Kouichi Hayashi, Kosuke Suzuki, Masahisa Ito, Hisamichi Kimura and Akihisa Inoue	
#153	X-ray specular and off-specular reflection from a protein adsorbed at a liquid surface	631
	Yohko F. Yano, Tomoya Uruga, Hajime Tanida, Hidenori Toyokawa, Yasuko Terada, Masafumi Takagaki, and Hironari Yamada	
#154	X-ray Reflectivity Evaluation of the Thermal Cycling Effects in Methylcellulose Thin Films	639
	Vallerie Ann Innis-SAMSON and Kenji SAKURAI	
#155	Spall Fracture of Metallic Aluminum Induced by Penetration of Liquid Gallium-Indium Alloy and Moisture at Room Temperature	643
	Mari Mizusawa and Kenji Sakurai	
#156	Orientation Characteristics of a Slit Carbon Plate used as an RF Electric Shielding	647
	Tokoh Nishikubo, Hiroki Endo and Mineo Itoh	
#157	Electromagnetic Wave Absorption by Rice Hull Carbon	651
	Mitsuhiro Kaneta, Takeshi Takahashi, Tomoyuki Kanaya and Hiroshi Iizuka	
#158	Production of Titanium Oxide Layers on Woodceramics by Plasma Thermal Spraying	655
	Akira Hashimoto, Akito Takasaki, Susumu Uematsu and Toshihiro Okabe	
#159	Study on Utilization of Cutting Chips of Wood Ceramics	659
	Kazuhiko Ogawa and Toshihiro Okabe	
#160	Carbon Electrode from Carbonized Wood for Polymer Electrolyte Fuel Cell	663
	Masashi Fujisawa, Yasuji Kurimoto, Yuji Imamura and Hirai Kikuchi	
#161	Electromagnetic Shielding in Rubber Composite Materials with Soy Hull Carbon Particles	667
	Michiaki Shishido, Taku Ogawa, Hiroyuki Goto, Takeshi Takahashi and Hiroshi Iizuka	
#162	Change of Elastic-Plastic Behavior on Compressive Deformation by Densification of Wood	671
	Ohtani Tadashi	
#163	Hydrogen Desorption Properties of Woodceramics	675
	H;28;Hydrogen Desorption Properties of Woodceramics;Akito Takasaki and Toshihiro Okabe	
#164	Functionality Control of Lignophenol by Demethylation of Methoxyl group -Successive Structural Conversion of Syringyl Type Lignophenol-	679
	Keigo Mikame and Masamitsu Funaoka	
#165	Influences of Lignophenol-Derivatives on Performances of Photo-Chemical Cells	683
	Mitsuru Aoyagi, Nao Umetani and Masamitsu Funaoka	

#166 Separation by Molecular Weight during Purification Process of Lignophenol	687
Mitsuru Aoyagi and Masamitsu Funaoka	
#167 Preparation of Novel Lignophenol-based Polymers using Cellulose Fibers as Vanishing Reaction-Supports	691
Mitsuru Aoyagi, Satoko Yonekura, Chika Miyasaka and Masamitsu Funaoka	
#168 Pre-processing by Shock Loading for Freeze-drying	695
Toshiaki Watanabe, Ayumi Takemoto, Daisuke Sawamura, Yusuke Yamashita, Hironori Maehara and Shigeru Itoh	
#169 Properties of Humidity-Controlling Charcoal Produced from Wood Waste	699
Takahisa Nakai, Kentaro Abe, Tadashi Ohtani and Yuuji Ishitobi	
#170 Development of Smokeless Carbonization and Combustion Technique Aiming at Versatile Use of Woody Biomass	703
Kiyotoshi Ogami, Ginji Sugiura, Takemichi Tsurumi and Osamu Kobayashi	
#171 Bending Creep of Sugi Glulam with Low Young's Modulus Laminae for the Inner Layer	707
Shiro Aratake, Akihiro Matsumoto, Hideki Morita and Takanori Arima	
#172 Analysis of Allergy from The Standpoint of Ecology - Safety and Clinical Use of Hinokithiol Derived from Aomori Hiba ...	711
Fumiko Juji, Shigetoshi Kobayashi, Tsutomu Iwata, Yutaka Morita, Hidemi Nakagawa, Tooru Fukui, Yoshihiko Inamori and Toshihiro Okabe	
#173 New Utilization Method of Essential Oils from Woody Biomass	715
Yoshito Ohtani, Pornpun Siramon, Rini Pujjiarti and Hideaki Ichiura	
#174 Cellulose / Copper Blend and Porous Copper Prepared by Mechano-Chemical Treatments	719
Hitomi Miyamoto, Chisato Ueda, Chihiro Yamane, Mariko Ago, Kunihiko Okajima, Takashi Endo and Makiko Hattori	
#175 Potential of Bamboo Forest as Molecule Forming Field	723
H;75;Potential of Bamboo Forest as Molecule Forming Field;Hao Ren and Masamitsu Funaoka	
#176 Potential of Herbaceous Lignocellulosics as Industrial Raw Materials	727
H;79;Potential of Herbaceous Lignocellulosics as Industrial Raw Materials;Hao Ren and Masamitsu Funaoka	
#177 New EFB Refining System Using Structural Units of EFB Lignin	731
Takanori Shinano, Masamitsu Funaoka, Yoshihito Shirai and Mohd Ali Hassan	
#178 Response of Lignophenols for Oxidation and Reduction Systems	735
Shimpei Horii and Masamitsu Funaoka	
#179 Rearrangement of Lignin Polymer Network with Lignin Precursors	739
Maiko Okura and Masamitsu Funaoka	
#180 CO₂ adsorption/desorption on mesoporous silica at various pressures	743
Ryosuke Nakanishi, Masaya Suzuki I, Keiichi Inukai, Masaki Maeda	
#181 Hydrogen Generating Gel Systems Induced by Visible Light and Application to Artificial Photosynthesis	747
Kosuke Okeyoshi and Ryo Yoshida	
#182 Low Driven Voltage Electrochromic Devices Using Aqueous Polyaniline/poly(4-styrenesulfonic acid)	751
Atsushi Aoki and Maiko Yoshida	
#183 The Hall effect measurement in the high resistance In₂O₃-ZnO polycrystalline films	755
K. Yamada, T. Yamaguchi, N. Kokubo, B. Shinokazi, K. Yano, H. Nakamura	
#184 Dependence of Size of Liquid Phase Pulsed Laser Ablated ZnO Nanoparticles on pH of the Medium	759
P.M. Aneesh, Arun Aravind, R. Reshmi, R.S. Ajimsha and M.K.Jayaraj	
#185 Hydrophilicity Switching of Silica Surface Incorporated with Thermoresponsive Polymer	765
Takeshi Higuchi, Wataru Tanji, Tadairo Aita and Shimio Sato	
#186 Electrochemical Properties and Microstructure of C/LiFePO₄ Powders Prepared by Spray Pyrolysis	769
Motofumi Yamada, Koji Egawa, Takashi Ogihara and Takayuki Kodera	
#187 Synthesis and Properties of Nitrogen Atom Encapsulated Fullerene	773
Jamal Uddin Ahamed, Sunao Miyanaga, Toshiro Kaneko and Rikizo Hatakeyama	
#188 Polar Coincident Site Lattice Figure - Multiple Domain Growth of Bismuth Cuprate Superconducting Film	777
S. Kaneko, K. Akiyama, Y. Hirabayashi, T. Ito, Y. Motoizumi, K. Yoshida, T. Horiuchi, M. Soga, M. Yasui, M. Kano, M. Kumagai, H. Funakubo and M. Yoshimoto	
#189 Magneto-Resistance Effect in γ'-Fe₄N/CrO₂ Granular System	781
Ryota Taninoki, Yuya Konishi, Masatomo Uehara and Yoshihide Kimishima	
#190 Texture and Formability of Heat-treatable Magnesium Alloy Sheets Processed by Differential Speed Rolling	785
Xinsheng Huang, Kazutaka Suzuki, Akira Watazu, Ichinori Shigematsu and Naobumi Saito	
#191 Low Temperature Preparation of TiO₂ Films by RF Magnetron Sputtering Method	789
Masaaki ISAI, Tatsuya ENDO, Yuichi MIZUCHI	
#192 Characterization of Si₃N₄-TiN Composites Prepared by Spark Plasma Sintering	793
Norhayati Ahmad, Kozo Obara, Soichiro Sameshima, Hidekazu Sueyoshi	

Measurement of X-ray CTR Signals from GaN/GaInN/GaN at High Temperatures Using Newly Developed Measurement System

Y. Takeda, T. Mizuno, H. Kamiya, K. Ninoi, and M. Tabuchi*

Department of Crystalline Materials Science, Nagoya University,

Fax: 81-52-789-3239, e-mail: takeda@numse.nagoya-u.ac.jp

*Venture Business Laboratory, Nagoya University

Fax: 81-52-789-5448, e-mail: tabuchi@vbl.nagoya-u.ac.jp

Furo-cho, Chikusa-ku, Nagoya 464-8603, Japan

A combined system of laboratory X-ray CTR scattering measurement and MOVPE growth facility was set up and CTR measurement on GaN/GaInN/GaN heterostructure was conducted at room temperature and high temperatures up to 1000 °C. Clear CTR signals and composition profiles were obtained even at 1000 °C.

Key words: CTR, MOVPE, Laboratory X-ray, GaN/GaInN/GaN, High temperature

1. INTRODUCTION

In our previous papers, we reported the design and setup of the laboratory level X-ray CTR (crystal truncation rod) scattering measurement system and successful measurement of the CTR signals from InP/GaInAs/InP and GaN/GaInN/GaN heterostructures at room temperature within 100 min. The improvements made were to use a multi-layered focusing mirror and an asymmetry-cut double-crystal to collect and squeeze the X-rays from the rotating target X-ray source and to use slits between the sample and the detector to avoid stray X-rays [1-2].

Our intention is to investigate the growth process of, for example GaN/GaInN/GaN, using the monolayer-

sensitive X-ray CTR scattering. The MOVPE (metalorganic vapor phase epitaxy) reactor with two Be windows was installed to the laboratory X-ray system [1].

In this paper, we report the proper operation of the measurement system with the reactor installed and the X-ray CTR scattering measurements on the GaN/GaInN/GaN heterostructure at as high as 1000°C.

2. REACTOR AND STAGE

Though a picture of the X-ray system and installed reactor was shown in our previous paper [1], some details of the reactor structure and the XYZ-stage are described here. Fig. 1 shows the side view and front view

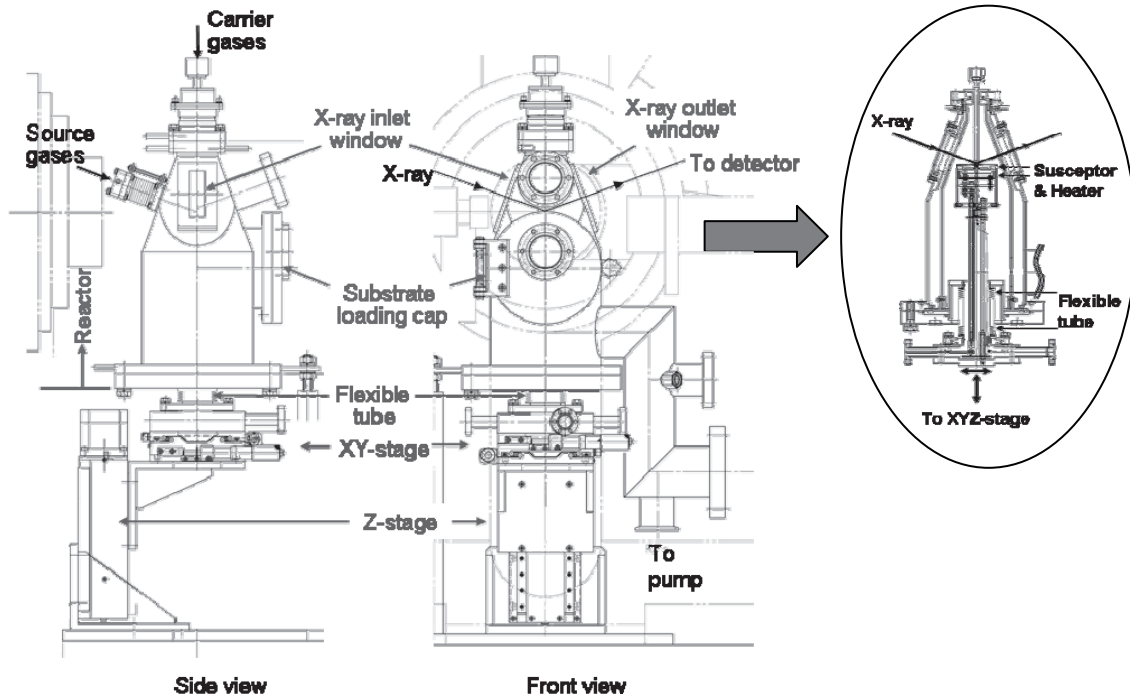


Fig. 1 Side view and front view of reactor and XYZ-stage for positioning the susceptor surface to the X-rays, while the reactor is fixed. Be windows are used for the X-ray path through the reactor. The inset is to show the susceptor and heater inside the reactor.

view of the reactor and stage. The reactor part is fixed at a proper position to the X-ray source and detector and there is no freedom for the reactor to be adjusted because pipes for gas introduction and tubes for pumping are fixed to reactor.

To adjust the sample position against the incoming and outgoing X-rays, an XYZ-stage was set to move the susceptor and heater part through a flange connected by a flexible tube to the reactor as shown in the inset of Fig. 1. The Z-stage is essential for sample positioning and is tough enough to support the XY-stage from the pulling-up force when the reactor was pumped to vacuum. The thickness of the Be window was 0.3mm. The intensity lowered to 85% of the original one due to the two Be windows.

3. HIGH TEMPERATURE MEASUREMENTS

3.1 S/B ratio

First of all, it is well anticipated that the thermal diffuse-scattering (B: background) increases and the CTR scattering intensity (S: signal) decreases at higher temperatures. To find whether the S/B ratio is high enough to measure the CTR scattering profile at higher temperatures, we measured the temperature dependence of the CTR peak intensity (at around 1.95 in Fig. 4) and thermal diffuse-scattering intensity using the GaN/GaInN/GaN wafer on sapphire substrate as shown in Fig. 2. In the temperature-change process it was necessary to wait for about 50 min until the susceptor and heater expansions were stabilized. The sample height was adjusted by the Z-stage.

The temperature dependence of the S/B ratio is shown in Fig. 3. The experimental data are shown by (●). The calculation of S was made using a standard diffraction intensity where the Debye-Waller factor

$$S \propto \exp(-2M) \tag{1}$$

is the most temperature-dependent. M is a function of Θ_D/T where Θ_D is the Debye temperature. The thermal diffuse-scattering intensity (B) is proportional to the temperature T and the Debye-Waller factor as

$$B \propto T \cdot \exp(-2M) \tag{2}$$

when $T > \Theta_D$. Then, $S/B \propto 1/T$ when $T > \Theta_D$ and $S/B = \text{Constant}$ when $T < \Theta_D$ ($\Theta_D = 600\text{K}$ was used.). In the comparison, the S/B values by experiments and by calculation were normalized at RT(300K). Considering those temperature dependent factors and using the intensity at RT as the initial value, the temperature dependence of S/B (●) was calculated.

At 1000°C (1273K) the ratio decreased to half at RT. The decrease of the S/B ratio is mostly caused by the increase of B that is the thermal diffuse-scattering.

Fig. 4 shows the CTR spectra measured at RT for 100min, at 1000°C for 100min, and at 1000°C for 200min. The backgrounds (mostly due to the thermal diffuse-scattering) are subtracted. To increase the S/B ratio at 1000°C the CTR scattering was measured for 200min. The spectrum quality looks better than that at

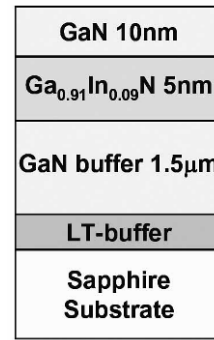


Fig. 2 Sample structure to measure the temperature dependence of S/B ratio.

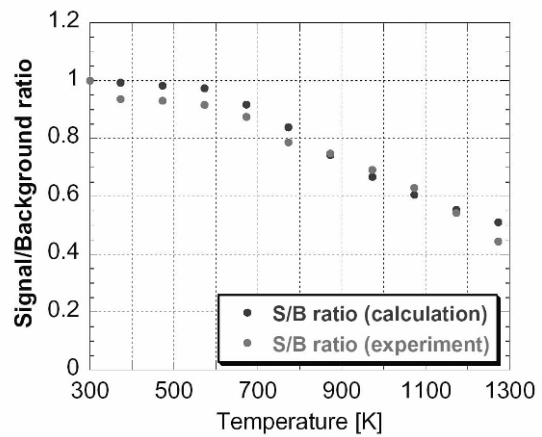


Fig. 3 The temperature dependence of S/B ratio from the sample (●) shown in Fig. 2. (●) is a calculation changing the temperature dependent parameters in the CTR scattering and the thermal diffuse-scattering. The intensities at RT (300K) were used as initial values.

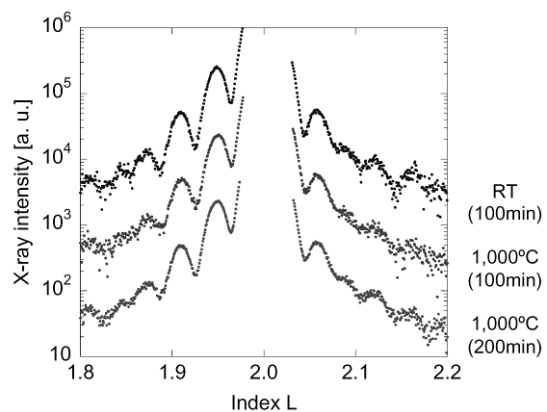


Fig. 4 CTR spectra at RT measured for 100min, at 1000°C for 100min, and at 1000°C for 200min. Background (thermal diffuse-scattering) is subtracted.

RT for 100min.

3.2 Spectra at high temperatures and curve-fitting

Two different wafers, as shown in Fig. 5, were used to measure the temperature dependence of the CTR spectra. Measured CTR spectra at several temperatures and at RT before and after the heating are shown in Fig. 6 in the case of GaN/GaInN/GaN on sapphire substrate. Fig. 7 is the similar spectra from GaInN/GaInN/GaInN on GaN substrate. Gray lines in both figures are the best-fit curves.

The fitting results were better in the case of GaInN/GaInN/GaInN on GaN substrate. It is visually clear and also indicated by the R-factor values in both figures. There was curving of the wafer of GaN/GaInN/GaN on sapphire substrate probably due to the difference in the thermal expansion coefficients between GaN and sapphire, even at RT, and should change with temperature. In the calculation those effects were not included (curving should be

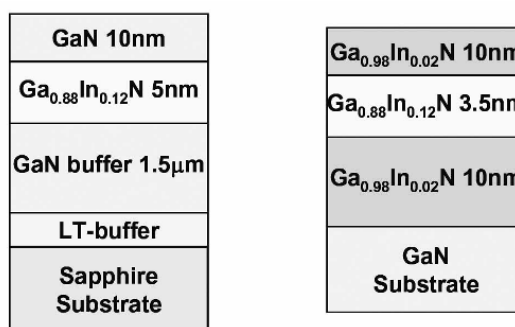


Fig. 5 Two different wafers (left; GaN/GaInN/GaN on sapphire substrate and right; GaInN/GaInN/GaInN on GaN substrate), used for temperature dependence measurements of the CTR spectra.

Fig. 6 CTR spectra from GaN/GaInN/GaN on sapphire substrate at several temperatures and at RT before and after heating. Gray curves are best-fit curves to each spectrum. R-factor indicates the fitting quality.

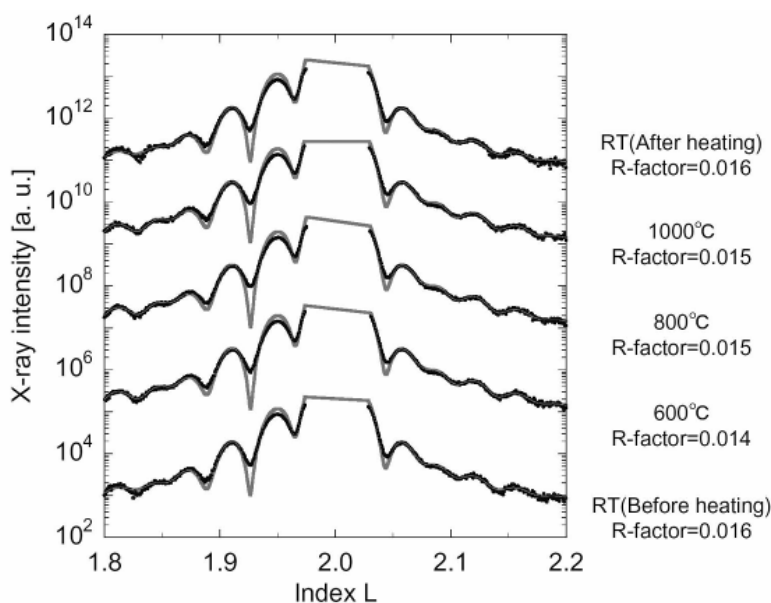
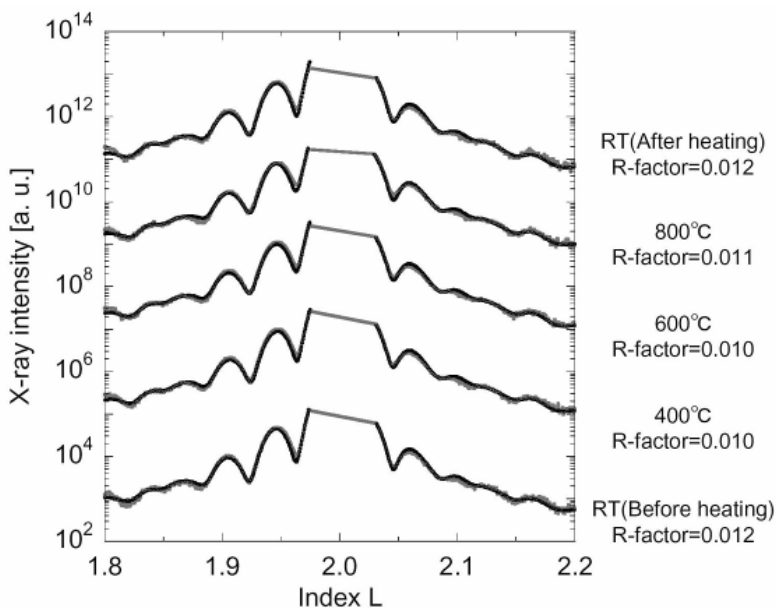


Fig. 7 CTR spectra from GaInN/GaInN/GaInN on GaN substrate at several temperatures and at RT before and after heating. Gray curves are best-fit curves to each spectrum. R-factor indicates the fitting quality.



temperature-dependent since the velocity of the misfit dislocations is also temperature-dependent) and they may affect the fitting quality.

3.3 Composition profiles

Indium (In) composition profiles are shown in Figs. 8 and 9. Fig. 8 shows In composition profiles in GaN/GaInN/GaN on sapphire substrate at RT before heating and at 1000°C obtained from Fig. 6. Fig. 9 shows In composition profiles in GaInN/GaInN/GaInN on GaN substrate at RT before heating and at 800°C obtained from Fig. 7.

In both cases, there looks no significant difference between profiles at RT and at high temperatures. In compositions at peak are much lower, in both cases, than those designed (In compositions in Fig. 5 are those

values designed.). This difference has been our experience in other many samples. Our understanding is that the In composition is determined from X-ray diffraction, XPS, and/or AES on *thick layers*. However, in a thin (several nm) layers, In is not fully incorporated from gas phase to solid phase. There observed, as in Fig. 7 and 8, a tendency that In increases to the growth direction.

This effect is our first target to investigate using the measurement system described in this paper.

The safety facilities are being designed and installed just in case the Be windows abruptly break at a raised susceptor temperature in a hydrogen and metalorganic source gases.

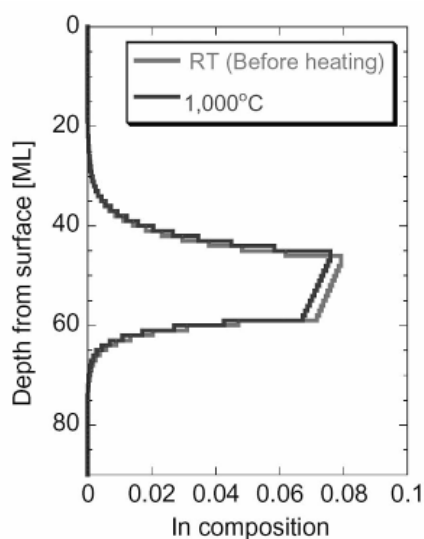


Fig. 8 In composition profiles in GaN/GaInN/GaN on sapphire substrate at RT before heating and at 1000°C obtained from Fig. 6.

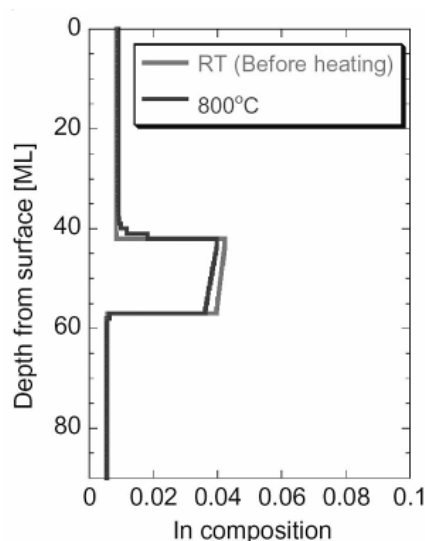


Fig. 9 In composition profiles in GaInN/GaInN/GaInN on GaN substrate at RT before heating and at 800°C obtained from Fig. 7.

4. SUMMARY

A detailed structure of the reactor and the XYZ-stage installed in the X-ray diffraction measurement system was described, and the proper operation of the whole measurement system on the Ga(In)N/GaInN/Ga(In)N heterostructure at as high as 1000°C was reported. Though there are several ambiguities in the analysis due to strain in the wafer, very different In profiles were obtained for the case of Ga(In)N/GaInN/Ga(In)N on sapphire and that on GaN.

ACKNOWLEDGEMENTS

This work was supported in part by the Grant-in-Aid for Scientific Research (S) #18106001 and (B) #19360006 from the Japan Society for the Promotion of Science.

REFERENCES

- [1] Y. Takeda, Y. Maeda, T. Mizuno, and M. Tabuchi, *Trans. Mat. Res. Soc. Jpn.*, **33**, 547-550 (2008).
- [2] Y. Maeda, T. Mizuno, A. Mori, M. Tabuchi, and Y. Takeda, *Trans. Mat. Res. Soc. Jpn.*, **33**, 591-594 (2008).

(Received July 14, 2009; Accepted August 31, 2009)

Development of New X-ray CTR Scattering Measurement System Using Johansson Monochromator

Masao Tabuchi, Hiroshi Tameoka*, Tatsuya Kawase*, and Yoshikazu Takeda*

Venture Business Laboratory, Nagoya University, Furo-cho, Chikusa-ku, Nagoya 464-8603, Japan

Fax: 81-52-789-5430, e-mail: tabuchi@vbl.nagoya-u.ac.jp

*Graduate School of Engineering, Nagoya University, Furo-cho, Chikusa-ku, Nagoya 464-8603, Japan

A new X-ray CTR scattering measurement system was reported that was equipped with a Johansson monochromator to focus X-rays at a sample position. Using the focused X-rays and a two-dimensional detector, X-ray CTR scattering measurement was able to be carried out without moving any component of the measurement system. The results of the X-ray CTR scattering measurement using the new system successfully demonstrated that the CTR scattering profiles were comparable to that measured at PF using synchrotron radiation even when the measurement time was 10 minutes or longer. The results suggested that the new measurement system is useful for quick and in-situ X-ray CTR scattering measurements.

Key words: X-ray CTR scattering, Johansson monochromator, focused X-ray, quick/in-situ measurement

1. INTRODUCTION

When a distribution of an X-ray intensity scattered by a crystal is measured carefully in reciprocal space, a rod-like distribution, which is normal to a surface of the crystal, could be observed around each Bragg point. The rod-like distribution of the X-ray intensity is called X-ray crystal truncation rod scattering (X-ray CTR scattering).[1-3] Since the origin of the X-ray CTR scattering is an abrupt truncation of a crystalline periodicity at a surface, and the intensity is sensitively modulated by non-periodic structures in the crystal, we could obtain much information on the surface and on the non-periodic structure from the X-ray CTR scattering profiles.[4-8] We have shown that interface structures, i.e., distributions of atoms across the interfaces, of hetero-epitaxially grown semiconductor crystals can be discussed at an atomic scale from the analysis of the measured X-ray CTR scattering profiles.[9-13]

Although, the X-ray CTR scattering measurement is so powerful to investigate an interface at an atomic scale, it has not been a popular measurement, since it is usually considered that a very brilliant X-ray source like a synchrotron is necessary for the X-ray CTR scattering measurement.

In this work, we report on the development of a new X-ray diffractometer equipped with a Johansson monochromator that is used to obtain focused X-rays at a sample position.[14,15] Using the focused X-rays, we could successfully reduce the X-ray CTR scattering measurement time even when an usual rotating-anode X-ray tube operated at 50kV and 300mA was used for the X-ray source. The system could be applicable to the in-situ X-ray diffraction and X-ray CTR scattering measurement when the measurement system is well established.

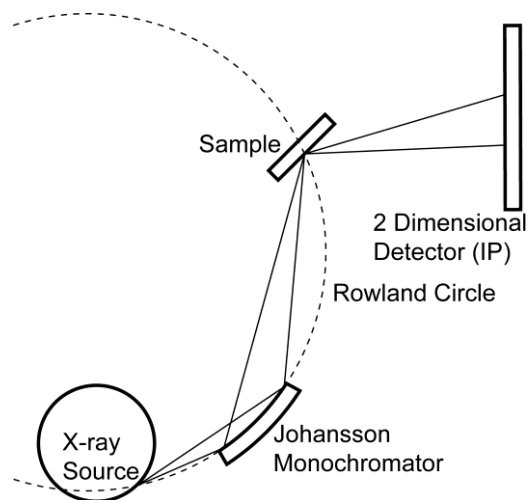


Fig. 1: Schematically drawn new measurement system equipped with a Johansson monochromator to focus X-ray at a sample position.

2. X-RAY CTR SCATTERING MEASUREMENT SYSTEM EQUIPPED WITH JOHANSSON MONOCHROMATOR

A new X-ray CTR scattering measurement system equipped with a Johansson monochromator was designed and constructed. Figure 1 shows the construction of the system schematically. The X-ray source was a line-focused rotating-anode X-ray tube operated at 50kV and 300mA (maximum operation power was 60 kV and 300 mA). The target was Cu. An asymmetrically cut Ge (111) Johansson crystal of which Rowland circle radius was 361mm was placed just after the X-ray source. Cu-K α line was monochromatized by the Johansson crystal. The X-rays were focused at 220 mm away from the crystal and the maximum convergence angle of the X-rays

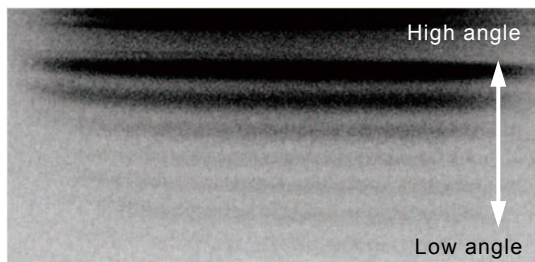


Fig. 2: Recorded X-ray scattering intensity on an Imaging Plate, using the new measurement system. Lower-angle-side region of InP 002 Bragg point was measured for an InP/GaInAs/InP structure sample for 10 minutes.

focused by the Johansson crystal was about 3.2 degrees, although, it was restricted to 2.85 degrees to eliminate the effect of the edge of the crystal. A goniometer was placed at the focusing point to hold a sample at a proper angle to the incident X-rays. An imaging plate (IP) was used as a detector to record the scattered X-rays two-dimensionally. It was important that there was no need to rotate X-ray source, sample, nor IP by utilizing the focused X-rays and the 2D detector. We could obtain a map of scattered X-ray intensities in a certain angle region at once without moving anything.

3. X-RAY CTR SCATTERING MEASUREMENT USING THE NEW SYSTEM

In order to discuss the potential of the new X-ray CTR scattering measurement system, an InP(30ML)/GaInAs(5ML)/InP structure crystal grown on InP substrate by OMVPE (organometallic vapor phase epitaxy) method was used. Figure 2 shows the scattered X-ray intensity distributions in the lower-angle-side region of InP 002 Bragg point for the sample recorded on the IP. The pattern was elongated in horizontal direction, since a line focused X-ray source was used. The focused image of the X-rays at the sample position was a line. The stripe pattern was observed in Fig. 2, since the CTR scattering intensity was modulated by the interference between the X-rays reflected by the InP and GaInAs layers. The Bragg peak, which should locate above the image, was not recorded intentionally, since the Bragg peak and diffuse scattering near the Bragg peak were too strong to observe the relatively weak CTR scattering profiles. As shown in Fig. 2, the X-ray CTR scattering and the modulation on the profile were clearly observed by using the proposed measurement system.

Figure 3 shows the measured X-ray CTR scattering profiles obtained from the distributions of scattered X-ray intensity as shown in Fig. 2 for the same sample. The measurement time was changed from 1 to 60 minutes and the measurement was conducted in the lower-angle-side region of the InP 002 Bragg point. The range of the index l , from 1.6 to 1.8, was corresponded to the convergence angle of the focused X-rays, 2.8 degrees. A profile measured at BL6A of Photon Factory at KEK in Tsukuba, Japan is also shown in Fig. 3, which had been already analyzed and given a good quantitative result on the interface structure at an atomic scale. Wavelength of the X-rays was set at

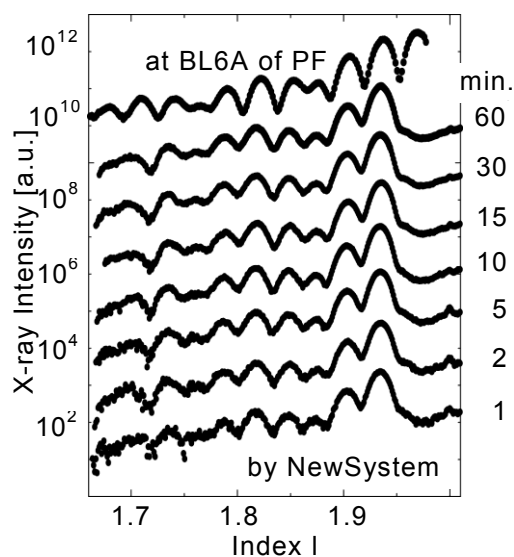


Fig. 3: X-ray CTR scattering profiles measured by the new measurement system and measured at PF. Even when the measurement time was so short as 1 minutes, the feature of the profile was well observed, though the background was relatively strong. The background level, S/N , decreased with the increase of measurement time, t , like as $S/N \propto \sqrt{1/t}$, as usual measurements using X-ray. Therefore, the background level at 60min was roughly about 1/10th of that at 1min. When the measurement time was 60 min the profile is comparable to that measured at PF.

0.1nm and the measurement time was 15min, for the measurement at PF.

As shown in Fig. 3, when the measurement time was 10 minutes or longer, the quality of the profiles was comparable to that measured at BL6A. We can understand that the profiles measured by using the new system showed identical features, i.e., positions of the peaks and valleys observed on the profiles and the relative difference of the heights and depths of them, to that measured at BL6A. The results indicated that the new system is available to analyze the layer structures.

Moreover, even when the measurement time was so short as 1 minutes, the quality of the profile was not so bad. It suggested that the new measurement system is potentially applicable for a quick measurement.

Further, we should point out that it is not necessary to move any components of the new measurement system including the sample, essentially. Therefore, the new measurement system should be very suitable for the in-situ measurement system combining with other experimental systems, i.e., crystal growth system, heat treatment system, optical measurement system, and so on.

4. CONCLUSIONS

A new X-ray CTR scattering measurement system was reported that was equipped with a Johansson monochromator to focus X-rays at a sample position. Using the focused X-rays and two-dimensional detector, the X-ray CTR scattering measurement could be carried out without moving any component of the measurement

system. The results of the X-ray CTR scattering measurement using the new system successfully demonstrated that the CTR scattering profiles were comparable to that measured at PF using synchrotron radiation when the measurement time was 10 minutes or longer. The results suggested that the new measurement system is useful for quick and in-situ X-ray CTR scattering measurements.

5. ACKNOWLEDGEMENTS

This work was supported in part by the Grant-in-Aid for Scientific Research (S) #18106001 and (B)#19360006 from the Japan Society for the Promotion of Science.

REFERENCES

- [1] I. K. Robinson, *Rev. B*, **33**, 3830-3836(1986).
- [2] I. K. Robinson, D. J. Tweet, *Rep. Prog. Phys.*, **55**, 599-651(1992).
- [3] T. Shimura, and J. Harada, *J. Appl. Cryst.*, **26**, 151-158(1993).
- [4] D. W. Kisker, G. B. Stephenson, P. H. Fuoss, F. J. Lamelas, S. Bewnann, P. Imperatori, *J. Cryst. Growth*, **124**, 1-9(1992).
- [5] F. J. Lamelas, P. H. Fuoss, D. W. Kisker, G. B. Stephenson, P. Imperatori, S. Bewnann, *Phys. Rev. B*, **49** 1957-1965(1994).
- [6] I. K. Robinson, R. T. Tung, R. Feidenhans, *Phys. Rev. B*, **38**, 3632-3635(1988).
- [7] E. D. Specht, G. E. Ice, C. J. Peters, C. J. Sparks, N. Lucas, X.-M. Zhu, R. Moret, and H. Morkoc, *Phys. Rev. B*, **43**, 12425-12430(1991).
- [8] H. Hashizume, M. Sugiyama, T. Niwa, O. Sakata, and P. L. Cowan, *Rev. Sci. Instrum.*, **63**, 1142-1145(1992).
- [9] Y. Takeda, Y. Sakuraba, K. Fujibayashi, M. Tabuchi, T. Kumamoto, I. Takahashi, J. Harada, and H. Kamei, *Appl. Phys. Lett.*, **66**, 332-334(1995).
- [10] M. Tabuchi, R. Takahashi, M. Araki, K. Hirayama, N. Futakuchi, Y. Shimogaki, Y. Nakano, and Y. Takeda, *Appl. Surf. Sci.*, **159**, 250-255(2000).
- [11] M. Tabuchi, H. Kyouzu, M. Takemi, and Y. Takeda, *Appl. Surf. Sci.*, **216**, 526-531(2003).
- [12] I. Yamakawa, R. Oga, Y. Fujiwara, Y. Takeda, and A. Nakamura, *Appl. Phys. Lett.*, **84**, 4436-4438(2004).
- [13] A. Mori, Y. Ohtake, T. Ujihara, M. Tabuchi, and Y. Takeda, 19th. Inter. Conf. On Indium Phosphide and Related Materials (IPRM'07).
- [14] T. Johansson, *Über ein neuartiges, genau fokussierendes Röntgenspektrometer. Z. Phys.*, **82**, 507-528(1933).
- [15] J. Cermak, *Czech. J. Phys. B*, **17**, 1073-1085(1967).

(Received July 14, 2009; Accepted September 18, 2009)

Study on accumulation process of As atoms in InP/GaInAs/InP hetero-structures

Masao Tabuchi, Akiko Mori*, Hiroshi Tameoka*, Katsunori Fujii*, and Yoshikazu Takeda*

Venture Business Laboratory, Nagoya University, Furo-cho, Chikusa-ku, Nagoya 464-8603, Japan

Fax: 81-52-789-5430, e-mail: tabuchi@vbl.nagoya-u.ac.jp

*Graduate School of Engineering, Nagoya University, Furo-cho, Chikusa-ku, Nagoya 464-8603, Japan

The distributions of As atoms at InP/GaInAs interfaces were investigated by analyzing the X-ray CTR scattering spectra for the samples grown at different growth temperatures and with different H₂-flushing times. From the results of the investigation, the adsorption and desorption processes of As atom on the GaInAs surface during the growth were discussed. Although the desorption of As from a surface progressed at all the investigated temperatures, 590, 620, and 650°C, a part of the As atoms, about 1.2[ML], remained on the surface even when the H₂-flushing time was long. On the other hand, when the H₂-flushing time was short, the amounts of As atoms were larger at higher growth temperatures, which suggested the decomposition of As precursor was enhanced at higher growth temperatures. All the results strongly indicated that the amount of As atoms incorporated in InP layer sensitively depends on the balance between the desorption and adsorption of As and that it is difficult to predict the degree of distribution of the As without a high resolution interface analysis like the X-ray CTR scattering measurement.

Key words: X-ray CTR scattering, buried interfaces of semiconductors, adsorption, desorption

1. INTRODUCTION

Hetero-structures of III-V compound semiconductors have been utilized widely for high performance devices such as HEMTs (high electron mobility transistors), lasers, and HBTs (heterojunction-bipolar transistors). For the high performance devices, highly defined hetero-structures, such as quantum well structures of which layer thicknesses are designed at a monolayer range, are epitaxially grown using advanced crystal growth technique. However, it is recognized that a compositional grading arises unexpectedly at the hetero-interfaces even when the hetero-structures are grown by OMVPE (organometallic vapor phase epitaxy) that is one of the most advanced semiconductor growth technique.

We have investigated the degree of the compositional grading at the hetero-interfaces using X-ray crystal truncation rod (CTR) scattering measurement. The X-ray CTR scattering measurement is a powerful technique to investigate the buried interfaces and determine the distributions of atoms quantitatively at an atomic-scale[1-7]. In these works, investigating InP/GaInAs hetero-interfaces, we had shown that the compositional grading of group-V elements can be suppressed by controlling a H₂-flushing time before the growth of InP on the GaInAs layer when the growth temperature was 620°C.[8] The result suggested that As adsorption is an significant origin that causes the compositional grading at the InP/GaInAs interface.

In this work, the adsorption of the As atoms on the GaInAs surface depending on the growth temperature is discussed via the study on the compositional grading at the upper InP/GaInAs interfaces in InP/Ga_{0.47}In_{0.53}As/InP structures using the X-ray CTR scattering method.

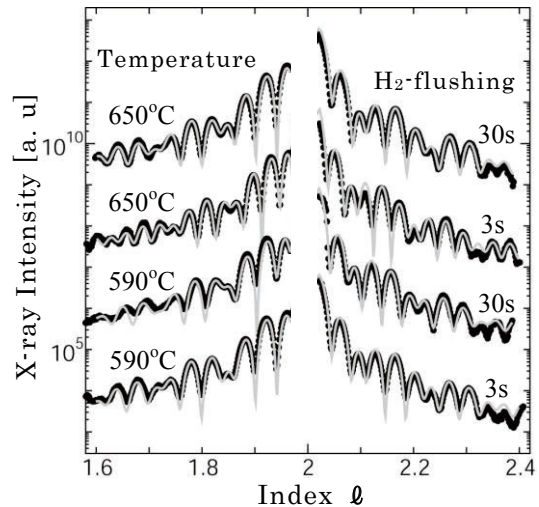


Fig.1: Measured and theoretically calculated X-ray CTR scattering spectra of the samples grown at 590 and 650°C. 002 Bragg peaks of InP locate at $l=2.0$ although they were truncated in the figure.

2. EXPERIMENTAL

InP(50ML)/Ga_{0.47}In_{0.53}As(15ML)/InP structure samples were grown on InP (001) just oriented substrates by OMVPE at 590, 620, and 650°C. At the upper InP/GaInAs interface, H₂-flushing time was changed from 3 to 30 sec, for which only H₂ gas was flowed in order to flush out excess source gases from the OMVPE reactor. By analyzing the difference among the As distributions at the interfaces depending on the H₂-flushing time, we can discuss the degree of As

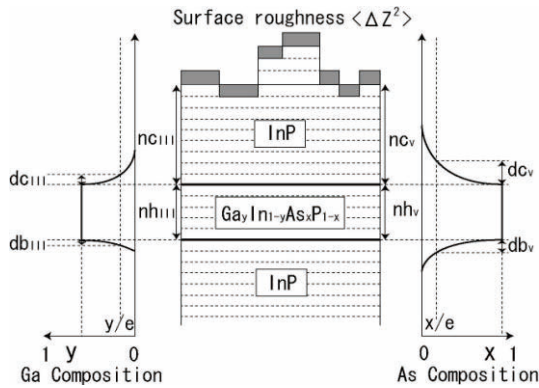


Fig. 2: A model structure to calculate a CTR scattering spectrum. The measured X-ray CTR scattering spectra were analyzed by comparing them with the theoretically calculated spectra based on this model. The model structure contains 10 parameters to describe the distributions of Ga and As in the InP/GaInAs/InP hetero-structure.

adsorption on the growing surface at a growth temperature.

TBAs, TBP, TMIn, and TEGa were used as source gases. Growth rate was 1.0 ML(molecular layer)/s and V/III ratio was fixed at 20 for all the samples.

The distributions of As atoms at the InP/GaInAs interfaces were analyzed from the results of the X-ray CTR scattering measurement. The X-ray CTR scattering measurement was carried out at the BL6A of the Photon Factory at the High Energy Accelerator Research Organization in Tsukuba, Japan. Wavelength of the X-ray was set at 0.1nm. A CCD camera was used to record the distribution of the scattered X-ray intensity around InP 002 Bragg peak.

In Figure 1, measured X-ray CTR scattering spectra of the InP/Ga_{0.47}In_{0.53}As/InP structure samples grown at 590°C and 650°C are shown as examples. The spectra were measured along [00 ℓ] direction, which was normal to the surface, in the reciprocal space. The peaks appeared at $\ell=2$ are 002 Bragg peak of InP, although they were not plotted near the Bragg point since the peaks were too high. As shown in Fig. 1, clear oscillations were observed in the range of $1.6 < \ell < 2.4$ for all the samples. The oscillation was caused by the interferences between reflected X-ray by InP and GaInAs layers. The difference of the amplitude of the oscillations reflected the degree of the distributions of atoms.

3. RESULTS AND DISCUSSIONS

The measured X-ray CTR scattering spectra were analyzed by comparing them with theoretically calculated spectra based on a model structure as shown in Fig. 2. Parameters that describe the distributions of atoms and roughness of the surface were contained in the model. The distributions of Ga and As atoms into the InP layers from GaInAs layer were assumed to be given by the simple form:

$$x = x_0 \exp\left(-\frac{d}{d_0}\right)$$

where x was Ga or As composition at d [ML] away

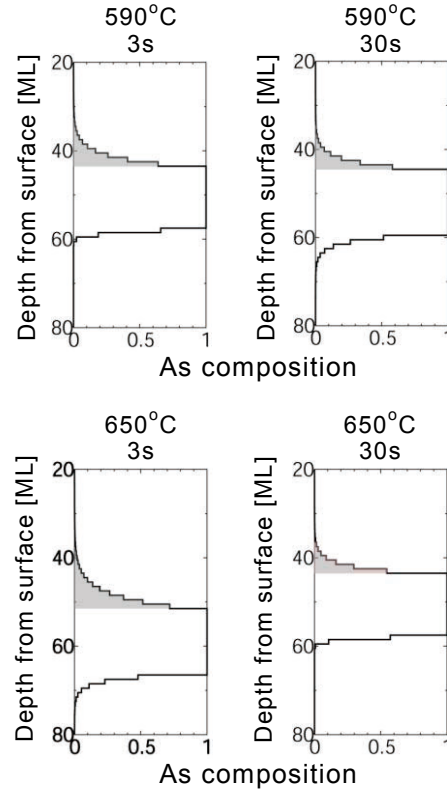


Fig.3: Composition profiles of As in the samples grown at 590 and 650°C obtained from the analysis of the X-ray CTR scattering spectra. The change of the degree of the compositional grading was small at 590°C with the change of the H₂-flushing time. On the other hand, at higher growth temperature, 650°C, the degree of compositional grading decreased when H₂-flushing time was long. The amount of As in InP cap layer was calculated by summing up the As composition in the hatched region.

from an interface. x_0 was a Ga or As composition in the GaInAs layer, and d_0 was the parameter that represented the degree of the distribution. The theoretically calculated best-fitted spectra are also shown in Fig. 1 as grey lines.

Figure 3 shows examples of the distributions of As obtained from the analysis of the X-ray CTR scattering spectra. The hatched areas in Fig. 3, observed at the upper InP/GaInAs interface, represented the distributions of As in the InP cap layers. Amounts of the As incorporated in the InP cap layers were calculated and plotted in Fig. 4.

The distributions of As were also observed at the bottom GaInAs/InP interfaces. The amounts of As incorporated in the lower InP layers were from 0.7 to 1.2MLs. Since, the difference was within a standard error range and the change of the amount of As was not consistent between at 590 and 650°C, it was difficult to discuss on the change of the lower interface structures. The distributions of As at lower interface were considered to be mainly caused by the exchange between P and As on top of InP before the growth of the GaInAs layer. Therefore, if a part of the distribution was caused by the roughness of the interface, the effect

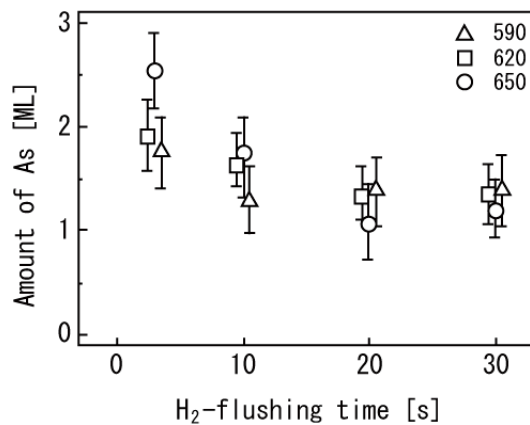


Fig.4: Relationships between the H₂-flushing time and the amount of As incorporated in the InP cap layer. The amount of As decreased with the increase of the H₂-flushing time at all the growth temperatures

was probably not so big on the amount of As incorporated in the InP layer at the upper interfaces.

Figure 4 shows the relationships between the amount of As incorporated in the InP cap layer and the H₂-flushing time. The error bars were defined as regions where R-factor increase by 20% at the border. As shown in Fig. 4, the amount of As decreased with the increase of the H₂-flushing time at all the growth temperatures, i.e., 590, 620, and 650°C. It indicated that a part of As atoms adsorbing on the GaInAs surface desorbed during the H₂-flushing.

When the H₂-flushing time was long, the decrease of the amount of As was observed to saturate at about 1.2 ML. The result suggested that there should be other effects, such as, roughness of GaInAs surface and/or formation of stable surface reconstruction structure that determine minimal As concentration on a surface.

On the other hand, when the H₂-flushing time was short, the amount of As was larger at higher growth temperatures. It is considered to be caused by the enhancement of the decomposition of As precursor at higher growth temperature resulting more adsorption of As[9].

All the results strongly indicated that the amount of the As atoms incorporated in the InP layer sensitively depends on the balance between the desorption and adsorption of As and that it is difficult to predict the degree of distribution of the As without a high resolution interface analysis like the X-ray CTR scattering measurement.

4. CONCLUSIONS

The distributions of As atoms at the InP/GaInAs interfaces were investigated by analyzing the X-ray CTR scattering spectra for the samples grown at different growth temperatures and with different H₂-flushing times. From the results of the investigation, the adsorption and desorption processes of As atoms on the GaInAs surface during the growth were discussed. Although the desorption of As from a surface progressed at all the investigated temperatures, 590, 620, and 650°C, a part of the As atoms, about 1.2[ML] at all the

temperatures, remained on the surface even when the H₂-flushing time was long. On the other hand, when the H₂-flushing time was short, the amount of As atoms were larger at higher growth temperature, which suggested the decomposition of As precursor was enhanced at higher growth temperatures. All the results strongly indicated that the amount of As atoms incorporated in InP layer sensitively depends on the balance between the desorption and adsorption of As and that it is difficult to predict the degree of distribution of the As without a high resolution interface analysis like the X-ray CTR scattering measurement.

ACKNOWLEDGEMENTS

This work was performed as a part of the projects 2007G557 and 2006G247 accepted by the Photon Factory Program Advisory Committee. This work was supported in part by the Grant-in-Aid for Scientific Research (S) #18106001 and (B) #19360006 from the Japan Society for the Promotion of Science.

REFERENCES

- [1] I. K. Robinson, *Rev. B*, **33**, 3830-3836(1986).
- [2] I. K. Robinson, D. J. Tweet, *Rep. Prog. Phys.*, **55**, 599-651(1992).
- [3] T. Shimura, and J. Harada, *J. Appl. Cryst.*, **26**, 151-158(1993).
- [4] Y. Takeda, Y. Sakuraba, K. Fujibayashi, M. Tabuchi, T. Kumamoto, I. Takahashi, J. Harada, and H. Kamei, *Appl. Phys. Lett.*, **66**, 332-334(1995).
- [5] M. Tabuchi, R. Takahashi, M. Araki, K. Hirayama, N. Futakuchi, Y. Shimogaki, Y. Nakano, and Y. Takeda, *Appl. Surf. Sci.*, **159**, 250-255(2000).
- [6] M. Tabuchi, H. Kyozu, M. Takemi, and Y. Takeda, *Appl. Surf. Sci.*, **216**, 526-531(2003).
- [7] I. Yamakawa, R. Oga, Y. Fujiwara, Y. Takeda, and A. Nakamura, *Appl. Phys. Lett.*, **84**, 4436-4438(2004).
- [8] A. Mori, Y. Ohtake, T. Ujihara, M. Tabuchi, and Y. Takeda, 19th. Inter. Conf. On Indium Phosphide and Related Materials (IPRM'07).
- [9] M. Sugiyama, K. Kusunoki, Y. Shimogaki, S. Sudo, Y. Nakano, H. Nagamoto, K. Sugawara, K. Tada, and H. Komiya, *Appl. Surf. Sci.*, **117/118**, 746-752(1997).

(Received July 14, 2009; Accepted September 18, 2009)

Quantitative Analysis of the Strain Field beneath the Si₃N₄/Si(001) Interface Formed by the Xe/NH₃ Plasma Nitridation using a Multiple-Wave X-ray Diffraction Phenomenon

Wataru Yashiro, Yoshitaka Yoda*, Takashi Aratani**,
Akinobu Teramoto**, Takeo Hattori** and Kazushi Miki***

Department of Advanced Materials Science, Graduate School of Frontier Sciences, the University of Tokyo,
5-1-5 Kashiwanoha, Kashiwa, Chiba 277-8561, Japan

Fax: 81-4-7136-3997, e-mail: yashiro@mml.k.u-tokyo.ac.jp

*Japan Synchrotron Radiation Research Institute (JASRI),

1-1-1 Kouto, Sayo-gun, Sayo-cho, Hyogo 679-5198, Japan

**New Industry Creation Hatchery Center (NICHe), Tohoku University,

6-6-10, Aoba, Aramaki, Aoba-ku, Sendai 980-8579, Japan

***Nanomaterials Laboratory (NML), National Research Institute of Materials Science (NIMS),
1-2-1 Sengen, Tsukuba, Ibaraki 305-0047, Japan

We show a quantitative analysis of the strain field beneath the Si₃N₄/Si(001) interface formed by nitrogen-hydrogen (NH) radicals (the Xe/NH₃ plasma nitridation). The strain field was investigated by using a multiple-wave X-ray diffraction phenomenon, *i.e.*, interaction between the Bragg reflection and crystal-truncation-rod (CTR) scattering. We present a master formula for the amplitude of CTR scattering from a crystal with strain. We constructed model functions for the strain field and determined several parameters using the least-squares fitting. The result suggests that inversion of the sign of the strain occurs near the interface.

Key words: X-ray diffraction, Silicon, Silicon nitrides, Nitridation, Strain

1. INTRODUCTION

Strain induced by an interface affects its electronic structure, but a full understanding of such strains is still lacking. This is true even in the case of the silicon dioxide-silicon interface, which has been applied to electronic devices since the 1960s. In previous papers [1-5], we have investigated strain fields beneath the SiO₂/Si interfaces using a multiple X-ray diffraction phenomenon, which is *modulation of the crystal-truncation-rod (CTR) scattering intensity under a Bragg reflection* [6-11]. Using this technique has revealed that there is a very small strain field beneath the SiO₂/Si interface whose depth extends up to several tens of nanometers and has a static fluctuation in the lateral direction. Information on the depth profile of the strain has been also qualitatively obtained using this technique [2,3,5]. In this paper we present a master formula for the CTR scattering from a crystal with strain, and attempt to quantitatively analyze the strain field beneath the Si₃N₄/Si(001) interface formed by the high-density Xe/NH₃ plasma using this technique. The Si₃N₄ film formed by the Xe/NH₃ plasma (NH radicals) is attracting increasing attention as a high-κ gate because of its high relative dielectric constant and low interface state density in the case of Si(001), Si(111), and Si(110) [12].

2. EXPERIMENT

We investigated the strain fields beneath the Si₃N₄/Si(001) interface by measuring the modulation profiles of the CTR scattering on the 50 rod under the 004 Bragg reflection (see Fig. 1) [1-4]. We define the surface unit cell vectors **a**_{s1}, **a**_{s2}, and **a**_{s3} by **a**_{s1} = **a**₁/√2 +

a₂/√2, -**a**₁/√2 + **a**₂/√2, and **a**₃, where **a**₁, **a**₂, and **a**₃ are the unit cell vectors of the diamond cubic structure of Si. From the modulation profile, we can determine the phase difference between two CTR scatterings: one is the CTR scattering from the incident X-rays and the other is that from the Bragg reflection. Here, we consider the strain field illustrated in Fig. 2, where Δ**d**_j is the deviation of the lattice spacing between the (j-1)th and jth atomic planes from the lattice spacing in bulk **d** and Δ**D**_j is the sum of displacements beneath the jth plane. The amplitude A^{CTR}(**q**) of the CTR scattering near a Bragg reflection can be related to the depth profile Δ**D**(z) (defined as it satisfies Δ**D**_j = Δ**D**(j**d**)) as follows:

$$A^{\text{CTR}}(\mathbf{q}) \approx \frac{F(\mathbf{q})e^{2\pi i \mathbf{q} \cdot (nd)} [e^{2\pi i \mathbf{q} \cdot \Delta \mathbf{D}_n} + \xi(\mathbf{q}; \Delta q_z)]}{2\pi \Delta q_z d} \quad (1)$$

where **q** is the scattering vector, F(**q**) is the structure factor, Δq_z is the deviation of the z component of the scattering vector from the Bragg reflection (the z coordinate is defined perpendicular to the interface as shown in Fig. 2), and ξ(**q**; Δq_z) is defined by

$$\xi(\mathbf{q}; \Delta q_z) \equiv - \int_{-\infty}^0 2\pi i e^{2\pi i \mathbf{q} \cdot \Delta \mathbf{D}(z)} \frac{d(\mathbf{q} \cdot \Delta \mathbf{D}(z + nd))}{dz} e^{2\pi i \Delta q_z z} dz \quad (2)$$

Note that **q** is almost constant around a Bragg point. ξ(**q**; Δq_z) can then be regarded as the Fourier transform of -2πie^{2πiq · Δ**D**} d(**q**·Δ**D**)/dz. Thus, we can obtain information about Δ**D**(z) from the modulation profile.

Particularly when $|\mathbf{q} \cdot \Delta \mathbf{D}(z)|$ is sufficiently small and the band width of $\zeta(\mathbf{q}; \Delta q_z)$ is much smaller than Δq_z , $\zeta(\mathbf{q}; \Delta q_z)$ is negligible. We can then obtain $\mathbf{h}_B \cdot \Delta \mathbf{D}_n$ from the modulation profile, where \mathbf{h}_B is the scattering vector of the Bragg reflection.

The experiment was performed at BL09XU in SPring-8, where a high-brilliance horizontally polarized X-ray beam from the undulator is available [14]. The premonochromatized SR beam was shaped by slits into a size of 1 mm (vertical) \times 1 mm (horizontal), and then highly monochromatized using two 444 Bragg reflections from two Si(111) channel-cut crystals arranged in the (+ +) geometry. The wavelength of X-rays was fixed around 1.24 Å. The sample was placed on a very flat plate on a high-precision goniometer. A glancing-angle (θ) scan was performed around the 004 Bragg point, and at each angle, the CTR scattering was analyzed using a Ge(111) crystal. The intensities measured by the NaI scintillation counter were integrated after subtraction of the backgrounds and then normalized by the counts of the beam flux monitor placed in front of the sample.

As the sample n-type Si(001) substrates were prepared. First, wet oxidation of these substrates was performed at 1100 °C in order to form oxide films. After etching the oxide films in an HCl/HF mixture solution, nitridation of these substrates using NH radicals produced in a microwave-excited, high-density Xe/NH₃ mixture plasma was performed at a pressure of 20 Pa and substrate temperature of 600 °C. The microwave frequency and power density were 2.45 GHz and 1.67 W/cm², respectively. Using spectroscopic ellipsometry, the thickness of the Si₃N₄ film was estimated to be 1.36 nm.

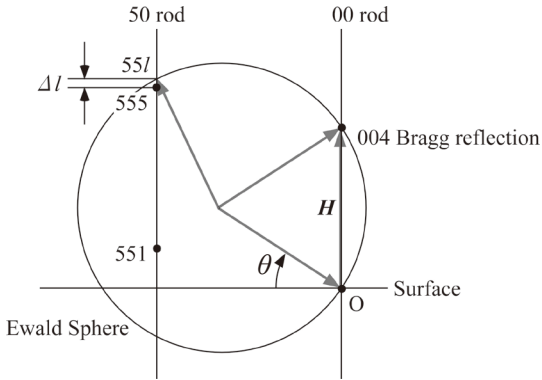


Fig. 1. Illustration of the diffraction condition where the intensity of CTR scattering is modulated by the 004 Bragg reflection. The parameter l is the momentum transfer perpendicular to the surface, and Δl is the deviation of l from the 555 Bragg point.

3. RESULT AND DISCUSSION

The experimental results of the phase difference are shown in Fig. 3. The abscissa of Fig. 3 is Δl , which is defined by $\Delta q_z d$ (see Fig. 1). The parameter Δl was changed by changing the wavelength of the X-rays,

which moves the intersection point between the Ewald sphere and 50 rod.

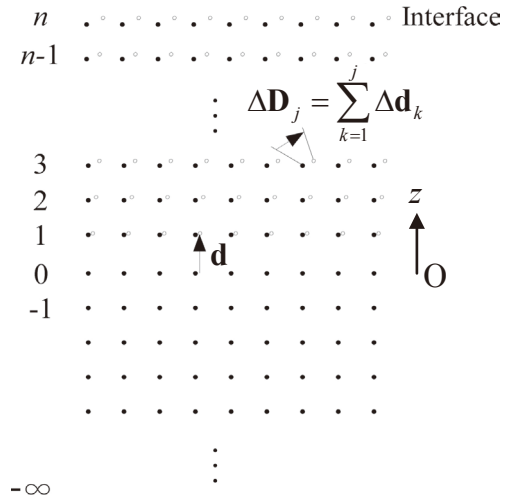


Fig. 2. Illustration of a strain field model beneath the Si₃N₄/Si(001) interface. A strained layer containing n atomic planes is formed on an ideal semi-infinite perfect crystal. The filled circles represent the positions of atoms or unit cells in bulk crystal, and the open circles represents those in the strained layer beneath the interface. The parameter $\Delta \mathbf{D}_j$ is defined by the sum of displacements beneath the j th atomic plane, and $\Delta \mathbf{d}_j$ is the deviation of the lattice spacing between the $(j-1)$ th and j th atomic planes from the lattice spacing in bulk, \mathbf{d} . The direction of the z axis is defined as perpendicular to the interface, and its origin is at the 0th layer.

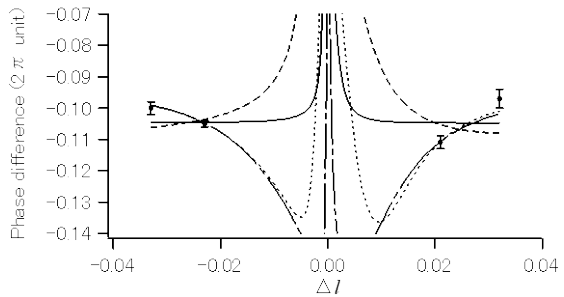


Fig. 3. The experimental results of the phase difference between the CTR scattering arising from the incident X-rays and that from the Bragg reflection (The experimental situation is presented in Fig. 1). The abscissa is Δl , which is defined by $\Delta q_z d$ (see also Fig. 1). The solid line corresponds to $A = -0.108$ and $a = 0.001$, while the broken line corresponds to $A = -0.127$ and $a = 0.005$ (model 1). The dotted line is the best-fitting curve when $A = -0.134$, $a = 0.004$, $B = 0.130$, and $b = 0.012$, and the dashed-dotted line is the curve when $A = -0.099$, $B = 0.072$, and $b = 0.014$ (model 2).

The phase differences were not zero, a fact that is not explained by a perfect crystal even when surface roughness is taken into account. Note that the rocking curves of the 004 Bragg reflection were explained by a perfect crystal. These facts support the idea that a very small and long-range strain field is induced by the NH radical nitridation, the depth of which is sufficiently small compared with the extinction depth of the 004 Bragg reflection [2]. The phase difference's dependence on Δl suggests that the lattice spacing in the strain field is not constant.

First, we consider an exponentially decaying function model (model 1) for $\Delta\mathbf{D}(z)$ in order to explain the experimental result; that is, we assume that $\mathbf{h}_B \cdot \Delta\mathbf{D}(z+nd)$ is given by:

$$\mathbf{h}_B \cdot \Delta\mathbf{D}(z+nd) = Ae^{az} \quad (3)$$

Here, A corresponds to the total displacement of the atomic plane beneath the interface. The solid line in Fig. 3 is the calculated curve for $A = -0.108$ and $a = 0.001$. This case corresponds to $\zeta \approx 0$ in Eq. (1), where the band width of ζ defined by Eq. (2) is sufficiently small. The broken line corresponds to $A = -0.127$ and $a = 0.005$. The inclinations of the curve on both sides become large as a increases, and their signs are contrary to the experimental data. This suggests that this model is not sufficient to describe the strain field.

Next, we consider a model function that is expressed by a sum of two exponential functions (model 2). That is, we assumed that

$$\mathbf{h}_B \cdot \Delta\mathbf{D}(z+nd) = Ae^{az} + Be^{bz} \quad (4)$$

and performed the least-squares fitting. The dotted line in Fig. 3 is the best-fitting curve, where $A = -0.134$, $a = 0.004$, $B = 0.130$, and $b = 0.012$ ($\chi^2 = 1.93$). It should be noted that, in this case, the number of data points is the same as the number of parameters; thus, the obtained parameters have large errors. In addition, parameter b and the signs of A and B obtained by the fitting were not sensitive to a ; for example, when a is fixed at 0.0005, the fitting is also good ($\chi^2 = 2.89$) when $A = -0.099$, $B = 0.072$, and $b = 0.014$ (dashed-dotted line in Fig. 3).

The depth profiles of the strain (ε_{zz}) obtained above are illustrated in Fig. 4. The solid and dashed lines are the depth profiles corresponding to the cases of $a = 0.004$ and 0.0005, respectively. The inversion of the sign of the strain is seen near the interface. This inversion is due to positive $d(\mathbf{h}_B \cdot \Delta\mathbf{D})/dz$ at the interface, which is given by $Aa + Bb$. We also performed the least-squares fitting under the condition of $Aa + Bb < 0$, but no good fit was obtained. Similar strain distribution has been reported under thick SiO_2 strips [14] fabricated on a Si substrate, although the strain field was deeper due to the thick strips and their edges. Although it is necessary to use more experimental data for a better fitting, the sign and order of B and b should be correctly given by the above fitting, which suggests that the inversion of sign actually occurs near the interface.

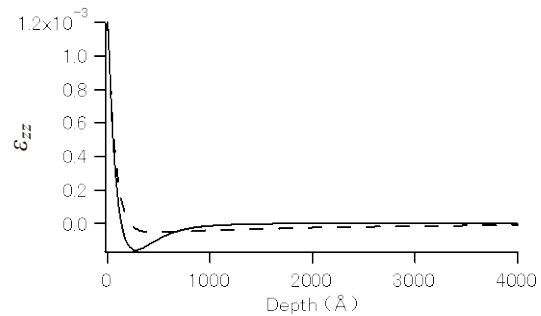


Fig. 4. Quantitatively obtained depth profiles of strain (ε_{zz}) beneath the $\text{Si}_3\text{N}_4/\text{Si}(001)$ interface.

4. CONCLUSION

A multiple-wave X-ray diffraction technique was applied to quantitatively investigate the depth profile of the strain beneath the $\text{Si}_3\text{N}_4/\text{Si}(001)$ interface formed by NH radicals. The experimentally obtained modulation profiles of the intensity of the CTR scattering showed that there is a very small and long-range strain field beneath the $\text{Si}_3\text{N}_4/\text{Si}(001)$ interface formed by the Xe/ NH_3 plasma nitridation (NH radical nitridation). We constructed two models for the strain field, and performed the least-squares fitting to the experimentally obtained phase difference of CTR scattering amplitudes. The result suggested that inversion of the sign of the strain occurs near the interface.

ACKNOWLEDGEMENTS

The experiment was performed at SPring-8 (2007B1076). This research was partially supported by the Ministry of Education, Science, Sports and Culture, Grant-in-Aid for Young Scientists (B), 19760020, 2007, and carried out under the Visiting Researcher's Program of the Institute for Solid State Physics, the University of Tokyo.

REFERENCES

- [1] W. Yashiro, K. Sumitani, T. Takahashi, Y. Yoda, and K. Miki, *Surf. Sci.* **550**, 93-105 (2004).
- [2] W. Yashiro, K. Sumitani, T. Takahashi, Y. Yoda, K. Takahashi, T. Hattori, and K. Miki, *International Workshop on Dielectric Thin Films for Future ULSI Devices — Science and Technology (IWDTF2004)*, 109-110 (2004).
- [3] W. Yashiro, S. Kusano, K. Miki, Y. Yoda, K. Takahashi, M. Yamamoto, and T. Hattori, *Trans. Mat. Res. Soc. Jpn.* **32**, 227-229 (2007).
- [4] W. Yashiro, Y. Yoda, K. Takahashi, M. Yamamoto, T. Hattori, and K. Miki, *J. Phys.: Conf. Ser.* **83**, 012009 (2007).
- [5] W. Yashiro, Y. Yoda, Y. Matsushita, T. Aratani, A. Teramoto, T. Hattori, and K. Miki, *Trans. Mat. Res. Soc. Jpn.* **33**, 607-611 (2008).
- [6] T. Takahashi and S. Nakatani, *Surf. Sci.*, **326**, 347-360 (1995).
- [7] V. M. Kaganer, M. Albrecht, A. Hirnet, M. Gierer, W. Moritz, B. Jenichen, and K. H. Ploog, *Phys. Rev. B*

61, R16355-R16358 (2000).

[8] T. Takahashi, W. Yashiro, M. Takahashi, S. Kusano, X.W. Zhang and M. Ando, *Phys. Rev. B* **62**, 3630-3638 (2000).

[9] W. Yashiro, K. Shimizu, K. Hirano, and T. Takahashi, *Jpn. J. Appl. Phys.*, **41**, L592-L594 (2002).

[10] W. Yashiro, K. Sumitani, Y. Yoda, and T. Takahashi, *Jpn. J. Appl. Phys.*, **42**, 6658-6662 (2003).

[11] O. Litzman and Mikulik, *J. Phys.: Condens. Matter*, **11**, 5767-5779 (1999).

[12] M. Higuchi, S. Sugawa, E. Ikinaga, J. Ushio, H. Nohira, T. Maruizumi, A. Teramoto, T. Ohimi, and T. Hattori, *Appl. Phys. Lett.* **90**, 123114 (2007).

[13] Y. Yoda, M. Yabashi, K. Izumi, X.W. Zhang, S. Kishimoto, S. Kitao, M. Seto, T. Mitsui, T. Harami, Y. Imai, and S. Kikuta, *Nucl. Instrum. Meth. A* **467**, 715-718 (2001).

[14] S. Di Fonzo, W. Jark, S. Lagomarsino, C. Giannini, L. De Caro, A. Cedola, and M. Müller, *Nature*, **403** 638-640 (2000).

(Received July 14, 2009; Accepted September 17, 2009)

X-ray Optics with Small Vertical Divergence and Horizontal Focusing For an X-ray Standing-wave Measurement

Osami Sakata^{1,2}, Togo Kudo¹, Hiroaki Yamanaka^{1,2}, and Yasuhiko Imai¹

¹Japan Synchrotron Radiation Research Institute / SPring-8, Kouto 1-1-1, Sayo, Sayo-gun, Hyogo 679-5198, Japan

²JST-CREST, Sanbancho Bldg., 5, Sanbancho, Chiyoda-ku, Tokyo 102-0075, Japan

Fax: 81-791-58-0830, e-mail: o-sakata@spring8.or.jp

An x-ray optics was proposed for dynamical diffraction measurements of a non-ideal crystal. It was composed of a pair of channel-cut Si (004) crystals and a one-dimensional focusing lens system. Vertical angular divergence values were measured as FWHM's of ca. 1.3 arc secs for an incident photon energy of 12.4 keV during a rocking scan around the analyzer sapphire 0006 reflection when the second channel-cut crystal was fixed at five deviation angles. The experimental angular resolution deconvoluted is about 1.3 arc secs at the deviation angle of ca. 0.7 arc sec. A typical photon flux was around 10^9 photons/s as a peak value of the rocking scan for an incident slit of 0.2 x 0.1 mm. The horizontal beam size measured at the focal distance of ca. 200 mm was 4.3 μm .

Key words: optics, dynamical x-ray diffraction, channel-cut crystal, horizontal focusing

1. INTRODUCTION

A feedback control system for stabilizing an incident x-ray intensity from a beamline monochromator was designed by Krolzig et al.[1, 2]. A dynamic combination of a micrometer positioner driven by a piezoelectric element and monitoring the diffracted x-ray intensity enabled an angular control of the monochromator with sub-arcsec precision. This was a key instrument for conducting a synchrotron measurement; consequently, many beam lines at synchrotron facilities adopted the system. Further, recent improvement of the system has added a new function of stabilizing the beam position of the incident x-rays[3] and was useful for extended x-ray absorption fine structure spectroscopy measurements[4].

The x-ray standing wave (XSW) technique allows us to perform element-specific and structural analysis of surface adsorbed atoms as well as buried hetero-interfaces with high spatial resolution. A yield profile of secondary emissions like fluorescence x-rays, here called an XSW profile, is recorded during a rocking scan of a sample in case of using hard x-rays. The angular width of the rocking curve is intrinsically several arc secs when calculated for a perfect crystal on the basis of dynamical diffraction theory. Bedzyk et al. have introduced a postmonochromator optics[5], which is an upgrade feedback control system, to prepare the incident beam in a way that avoids angle and photon energy averaging effects that would smear the XSW profile. Here we report on a combined system of a one-dimensional focusing lens plus the postmonochromator optics for performing measurements of dynamical diffraction of a non-ideal single crystal like an oxide material.

2. REQUIREMENTS FOR XSW MEASUREMENTS

XSW measurements of a non-ideal crystal require the followings:

1) a beam of a small angular divergence should be incident

because of the narrow angular width abovementioned of the intrinsic rocking curve for hard x-rays and

2) a small area on a sample should be irradiated as much as possible because its crystalline domain is small. In addition, recording the yield profile of weak secondary emissions takes long time; hence,

3) the optics necessitates stabilizing the intensity and angle of the incident beam.

In the following section, we discuss advantages and disadvantages of three setups that have already used and propose our optics.

3. DESIGN CONSIDERATIONS

The non-dispersive parallel setting, which usually employs an identical reflection of the same material for the two crystals of a monochromator and sample, meets requirement 1). We inconveniently need to change the arrangement of the monochromator when a different reflection of the sample is investigated. The postmonochromator optics uses a non-dispersive pair of channel-cut crystals and can substitute for the non-dispersive parallel setting to generate quasi-plane waves even if the optics is not changed.

A different solution is to use a combined setup[6] which is composed of a one-bounce capillary and a miniature Si (400) channel-cut crystal as Kazimirov et al. proposed. The setup fills the three requirements mentioned above. Example parameters written in ref.[6] for 12.5 keV x-rays were a) beam sizes of 10 μm after the capillary and 6 μm for Si(400) collimating crystals, b) the (004) rocking curve width of 14 μrad from the standard Si(001) wafer, and c) intensities from 0.9×10^6 to 3×10^6 photons / s.

The small divergence and small size of the beam consisted; however, the setup was considerably at the cost reducing the x-ray intensity in the scattering plane.

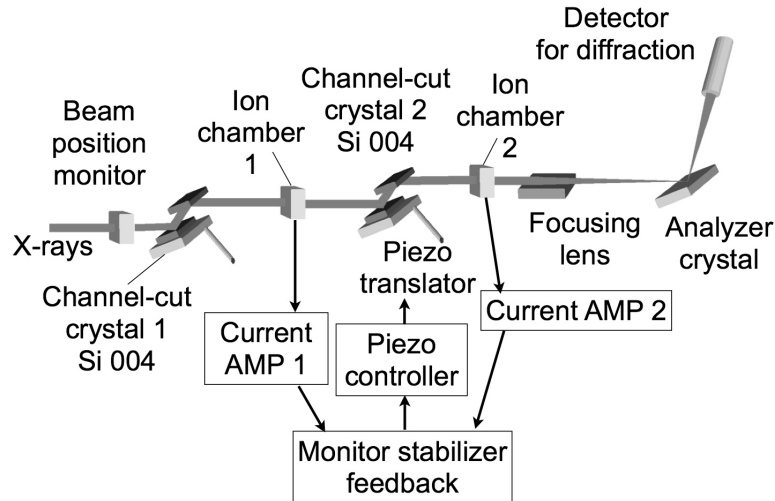


Fig. 1: Schematic of experimental setup and feedback loop of an electric stabilizer unit.

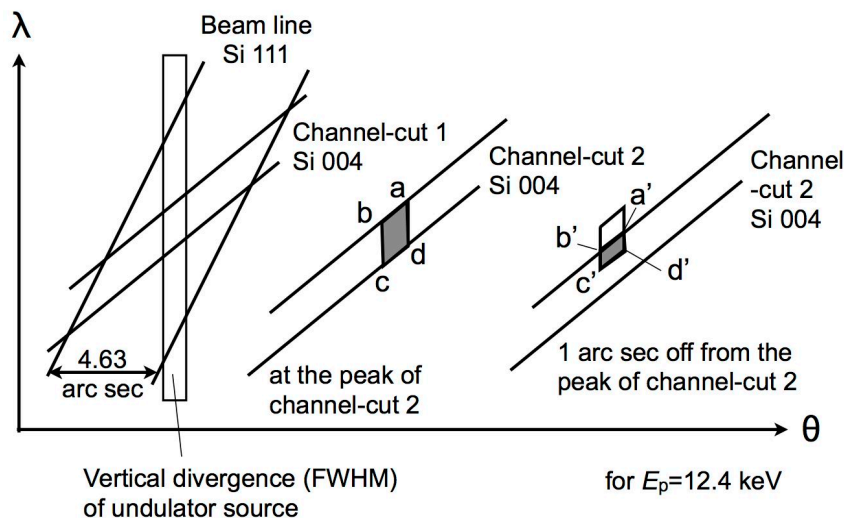


Fig. 2: DuMond diagrams of the optics. The optics admits x-rays represented by parallelograms $abcd$ and $a'b'c'd'$.

We here propose a modified optics (Fig. 1) that provides us with a small divergence in the scattering plane and a small beam in the horizontal direction. In other words, the 1D focusing element is added to the postmonochromator optics. Figure 2 shows the DuMond diagram for the undulator source, the beam line Si (111) monochromator, and the pair of Si (004) postmonochromator reflections at $E_p = 12.4$ keV. The FWHM vertical divergence of the undulator source is estimated using the vertical beam size 1.02 arc secs of $\sigma = 6 \mu\text{m}$ and vertical divergence of $\sigma = 1 \mu\text{rad}$. The parallelogram $abcd$ or $a'b'c'd'$ shows x-ray divergences of angle and wavelength that the optics generates. The divergences will smear a dynamical rocking curve and XSW profile. We can detune the second channel-cut crystal to change the range of the wavelength dispersion.

4. EXPERIMENTAL

We prepared the setup (Fig. 1) at BL13XU, SPring-8. The channel-cut crystal was fine-tuned using a piezo-

driven rotary stage with a leaf spring (Fig. 3(a)). The piezo-translator controller received a signal from a monitor stabilizer. X-ray intensities in front of / in the rear of the channel-cut crystal were monitored with ion chambers and converted to voltages from currents through current amplifiers; successively the voltages proportional to the x-ray intensities came in the stabilizer. A voltage to stable a ratio of the voltages was applied to the piezo translator through a division amp. To achieve performance to fill requirement 1) and 2), a strain-free mount of the crystal is crucial. Accordingly, the channel-cut crystals had two grooves at the bottoms (Fig. 3(b)).

The 1D focusing lens system used was made from an SU-8 resist on a Si wafer substrate fabricated by Forschungszentrum Karlsruhe. The system consists of 26 micrometer-size lenses of which aperture was $320 \mu\text{m}$. The focal distance calculated was 200 mm. We used the lens to focus x-rays in the horizontal direction.

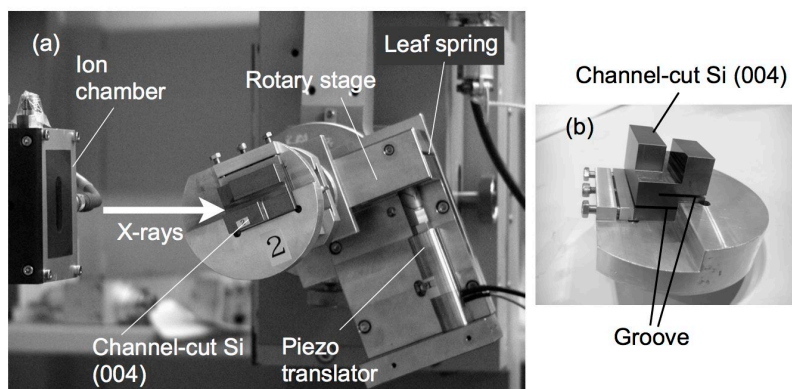


Fig. 3: Photos of channel-cut crystal. Part of optics (a). The holder for the strain-free mount of the crystal (b).

5. RESULTS

We measured divergences and intensities that the optics generated. Fig. 4 plots observed vertical divergence angles. The FWHM divergence angles were measured when an analyzer crystal was rocked at a fixed deviation angle of the second channel-cut crystal. On the other hand, a photon flux (the right axis in Fig. 4) was a peak value of the rocking scan.

We intentionally chose a sapphire crystal (0001) grown by the heat-exchange method (HEM) as the analyzer crystal. The 0006 reflection was used. The incident slit was located between ion chamber 1 and channel-cut crystal 2. The slit aperture used was 0.2 (horizontal) x 0.1 (vertical) mm. The intrinsic FWHM calculated is 0.4 arc secs; simply, the experimental angular resolution deconvoluted is about 1.3 arc secs at the deviation angle of ca. 0.7 arc sec. Other intrinsic widths calculated are, for example, 3.32, 2.46, and 2.54 arc secs for the 1 0 -1 4, 2 -1 -1 3, and 0 1 -1 2 reflection, respectively. By comparison with these values, the resolution obtained is enough small for performing a dynamical diffraction measurement. While Fig. 2 implies the angular divergence is independent of any deviation angle of the second channel-cut crystal, observed FWHM values were as a function of the deviation angle. This might be

ascribed to the dispersion effect of wavelength. We will use the deviation angle of ca. 0.7 arc secs which gives an enough small divergence angle as well as a reasonable intensity to perform XSW measurements.

The lateral beam size measured at the analyzer position was 4.3 μm using a knife-edge scan (shown in Fig. 5). The knife was made of a Au foil. The reduction ratio was 0.002.

6. SUMMARY

We made a setup of the optics composed of a pair of channel-cut Si (004) crystals and a 1D focusing lens system. The vertical divergence and photon flux were evaluated using the 0006 reflection of the sapphire crystal. The horizontal beam size was also measured at the focal distance.

ACKNOWLEDGMENTS

The measurements were supported by Japan Synchrotron Radiation Research Institute under proposals Nos. 2008A1602 and 2008B1540/BL13XU. This work was also partly supported by Ministry of Education, Culture, Sports, Science and Technology of Japan.

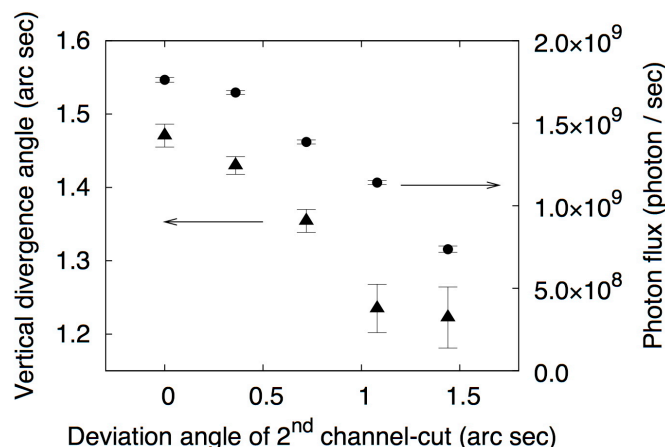


Fig. 4. Vertical angular divergence (▲) and intensity (●) as a function of the deviation angle of the second channel-cut crystal. An analyzer crystal used was a HEM sapphire single crystal.

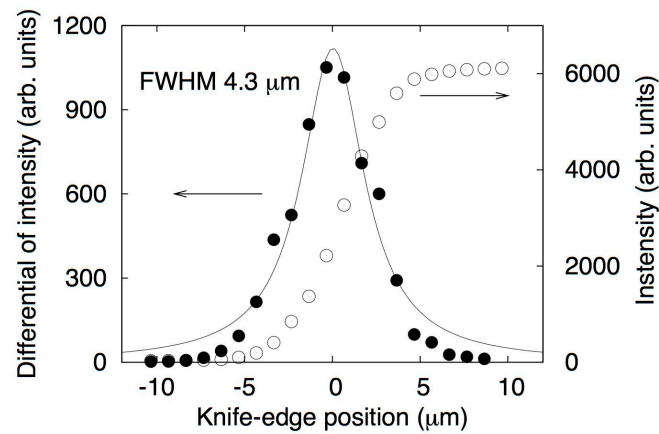


Fig. 5: Knife-edge scan and lateral beam size.

REFERENCES

- [1] A. Krolzig, G. Materlik, and J. Zegenhagen, Nucl. Instr. Meth. **208**, 613-619 (1983).
- [2] A. Krolzig, G. Materlik, M. Swars, and J. Zegenhagen, Nucl. Instr. Meth. **219**, 430-434 (1984).
- [3] T. Kudo, H. Tanida, S. Inoue, T. Hirono, Y. Furukawa, Y. Nishino, M. Suzuki, and T. Ishikawa, AIP conference proceedings, **CP879**, 954-958 (2007).
- [4] T. Kudo and H. Tanida, Rev. Sci. Instrum. **78**, 033104-1~033104-4 (2007).
- [5] M. J. Bedzyk and L. Cheng, Reviews in Mineralogy and Geochemistry, **49**, 221-266 (2002).
- [6] A. Kazimirov, D.H. Bilderback, R. Huang, A. Sirenko, and A. Ougazzaden, J.Phys. D: Appl. Phys. **37**, L9-L12 (2004).

(Received July 14, 2009; Accepted August 31, 2009)

Development of novel oxide multilayer mirrors at "water-window" wavelengths by atomic layer deposition / atomic layer epitaxy

Hiroshi Kumagai, Yuji Tanaka, Yusuke Masuda, Tsutomu Shinagawa*
and Ataru Kobayashi

Faculty of Engineering, Osaka City University, 3-3-138 Sugimoto, Sumiyoshiku, Osakashi, Osaka 558-8585, Japan

Fax: 81-06-6605-2846, e-mail: kumagai@a-phys.eng.osaka-cu.ac.jp

*Osaka Municipal Technical Research Institute, 1-6-50 Morinomiya, Joto-ku, Osakasi, Osaka 536-8553, Japan

The authors proposed that novel oxide superlattice structures of crystalline TiO₂/ZnO on sapphire substrates could be fabricated for high-reflection multilayer mirrors at 2.734 nm. In the experimental study, both rutile TiO₂ (200) and wurtzite ZnO (0001) thin films were grown epitaxially on the same sapphire (0001) substrates by atomic layer epitaxy (ALE) at 450°C. The authors also demonstrated for the first time that the novel oxide superlattice structure of 10-bilayer TiO₂/ZnO on a sapphire substrate gave high reflectance at 2.734 nm.

Key words: soft x ray, water window, multilayer, ALD, ALE

1. INTRODUCTION

Since Barbee et al. successfully demonstrated near-normal-incidence ($\theta=15.5^\circ$) soft-x-ray reflectors with high reflectances of 67% at 17.0 nm using 20-bilayer Mo/Si multilayers deposited by magnetron sputtering [1], there have been various studies on the fabrication of soft-x-ray multilayer reflectors using electron beam evaporation and ion beam, rf and dc magnetron sputtering deposition. In particular, development of high-performance normal-incidence multilayer optics for the water-window wavelength region between the oxygen and carbon K absorption edges at 2.33 and 4.36 nm, respectively, where water is relatively transmissive and organic materials are absorptive, has been a technical challenge of great interest. The extremely small periods (1.2-2.2 nm) of soft-x-ray reflectors require very rigorous specifications to be met with respect to interface roughness and interlayer mixing, because interface roughness on an atomic scale has a substantial effect on soft-x-ray reflectance.

Although the Fresnel coefficients of materials are so small at these wavelengths that a large number of bilayers must be used, which means that the problems of interface roughness and imperfect interfaces due to interlayer mixing become serious, the highest reflectance achieved at water-window wavelengths (3.11 nm) and near normal incidence ($\theta=9.2^\circ$) has been reported to be 32% [2], owing to the various efforts which have been made in this field.

The authors have proposed the use of a novel metal oxide multilayer for soft-x-ray reflectors at water-window wavelengths [3], because an oxide multilayer can prevent the formation of an alloy at the interface, and the absorption of oxygen in oxides is negligible at the water-window

wavelengths; moreover, the metal oxide multilayer can be fabricated by the atomic layer deposition or atomic layer epitaxy technique. These techniques can be used to control surfaces on an atomic scale by sequentially dosing the surface with appropriate chemical precursors and then promoting surface chemical reactions which are inherently self-limiting. We have found that the self-limiting adsorption mechanism works in the fabrication of oxide thin films such as aluminum oxide and titanium oxide [4-7]. And we reported that we have experimentally demonstrated high reflectance of over 30% at a wavelength of 2.734 nm and an incident angle of 71.8° from the normal incidence using novel metal oxide multilayers of titanium oxide and aluminum oxide fabricated by the atomic layer deposition method of controlled growth with sequential surface chemical reactions. For x-ray processing, crystalline multilayer mirrors might be rather useful than amorphous ones. Therefore, the authors demonstrated that novel oxide superlattice structures of crystalline TiO₂/ZnO on sapphire substrates were fabricated for high-reflection multilayer mirrors at 2.734 nm recently.

2. EXPERIMENTAL SETUP

The schematic diagram of the experimental set-up is presented in Fig. 1. It is comprised of a stainless-steel vacuum chamber, three computer-controlled leak valves, a turbo molecular pump (TMP), a capacitor manometer, a cold cathode gauge, and an infrared-ray heater.

The vacuum chamber was evacuated by a TMP and the pressure in the chamber during the deposition was maintained below 10^{-6} Torr. The substrate temperature was 450 °C. Reactant vapors were introduced alternately through three computer-controlled leak valves.

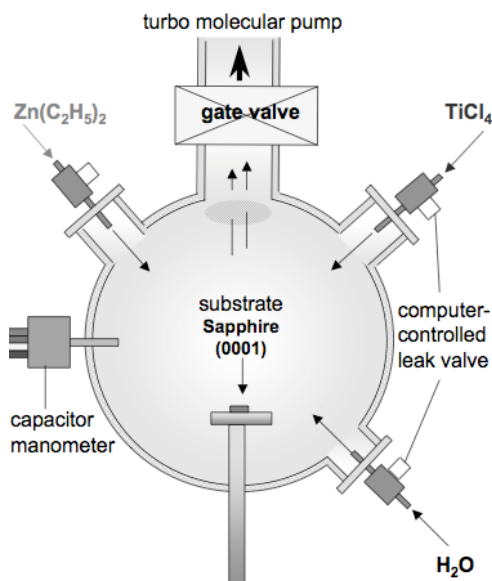


Fig. 1 Schematic diagram of apparatus.

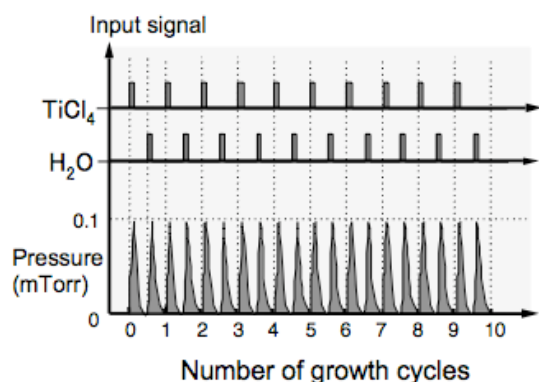


Fig. 2 Schematic diagram of input signals applied on the computer controlled leak valves.

As a substrate, sapphire (0001) was used. To obtain clean surface, the substrate was ultrasonically cleaned in acetone. ZnO films were deposited using diethylzinc (DEZ) as a source of Zn, water (H_2O) as a source of oxygen, while TiO_2 films were deposited using tetrachlorotitanium (TCT) as a source of Ti, water (H_2O) as a source of oxygen. The deposition cycle process consisted of repeated cycles, which contained 1 s dosing of DEZ (TCT), 2 s evacuation, 1 s dosing of H_2O , and 2 s evacuation. One growth cycle takes 6 s. Figure 2 shows DEZ and H_2O input signals applied to computer-controlled leak valves and they supply the pressure pulses of reactant vapor in the growth chamber.

The film thickness and refractive index of the ZnO and TiO_2 single layer films were determined using a variable angle spectroscopic ellipsometer. The crystallinity was measured using x-ray

diffraction analysis (XRD) ($\text{Cu-K}\alpha$), and the multilayer periodicity was examined by using low-angle XRD. The reflectivity for soft x-rays was measured using monochromatized synchrotron radiation (SR) located Ultraviolet Synchrotron Radiation Facility (UVSOR), Institute for Molecular Science, Okazaki, Japan.

3. ATOMIC LAYER EPITAXY OF ZnO AND TiO_2 FILMS ON SAPPHIRE SUBSTRATE

First of all, we investigated the self-limiting condition with varying reactant vapor pressures. Figure 3 shows plots of the growth rate of ZnO films on sapphire (0001) as a function of the vapor pressures of DEZ and H_2O . Growth rates were determined from the thickness of the film divided by the number of growth cycles. Here, the number of growth cycle was 90 and deposition temperature was 450°C . As shown in Fig. 3, the growth rate of ZnO was found to be near 0.26 nm/cycle when the vapor pressures of DEZ and H_2O are between 3×10^{-4} Torr and 7×10^{-4} Torr. It is noteworthy the length of ZnO (0001) monolayer. Moreover, the refractive indices ($\lambda = 632.8$ nm) of ZnO films were about 1.92 from 3×10^{-4} Torr to 7×10^{-4} Torr. This value of 1.92 is close to the index of refraction of a ZnO bulk crystal [8]. These results indicate that self-limiting window is observed in the vapor pressure ranging from 3×10^{-4} Torr to 7×10^{-4} Torr. The film thickness of ZnO on sapphire (0001) increased with increasing the cycle number, when the deposition temperature was 450°C and the vapor pressures of DEZ and H_2O were 4×10^{-4} Torr. The growth rate was constant as 0.26 nm/cycle. This result indicates that ZnO film thickness can be controlled by the number of cycle. Figure 4 shows the results of XRD measurements of ZnO film prepared 90 cycles at 450°C . Both the wurtzite (0002) reflection peak is observed.

Figure 5 also shows plots of the growth rate of TiO_2 films on sapphire (0001) as a function of the vapor pressures of TCT and H_2O . Here, the number of growth cycle was 180 and deposition temperature was 450°C . As shown in Fig. 5, the growth rate of TiO_2 was found to be near 0.076 nm/cycle, when the vapor pressures of TCT and H_2O are between 3×10^{-4} Torr and 6×10^{-4} Torr. The growth rate of 0.076 is nearly one-third the length of rutile (200) monolayer [9]. This indicates that self-limiting window is observed in the vapor pressure range from 3×10^{-4} Torr to 6×10^{-4} Torr.

The film thickness of TiO_2 on sapphire (0001) increased with increasing the cycle number, when the deposition temperature was 450°C and the vapor pressures of TCT and H_2O were 5×10^{-4} Torr. The growth rate was constant as 0.076 nm/cycle, indicating that TiO_2 film thickness can also be controlled by the number of cycle.

Figure 6 shows the results of XRD measurements of TiO_2 film prepared 180 cycles at 450°C . An intense rutile (200) peak is observed. This result indicates that TiO_2 film is grown on sapphire (0001) substrate epitaxially.

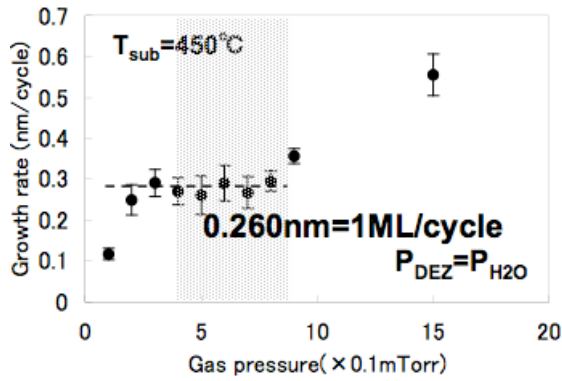


Fig. 3 Growth rate of ZnO films as a function of reactant vapor pressure.

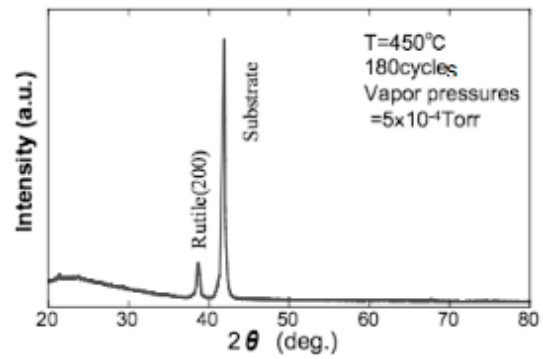


Fig. 6. XRD spectrum of TiO₂ film.

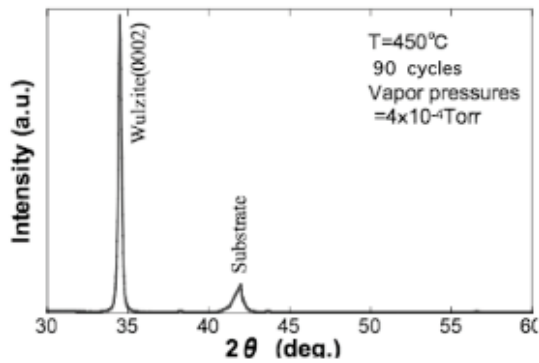


Fig. 4 XRD spectrum of ZnO film.

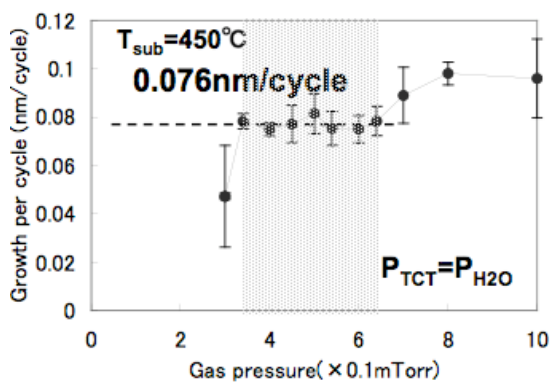


Fig. 5 Growth rate of TiO₂ films as a function of reactant vapor pressure.

4. FABRICATION OF 10-BILAYER TiO₂/ZnO MULTILAYER

We prepared a 10-bilayer TiO₂/ZnO multilayer at a substrate temperature of 450 °C. This multilayer consists of 10 pairs of 30 cycles TiO₂ layer and 20 cycles ZnO layer, so target layer-pair thickness is 7.48 nm (30 cycles x 0.076 nm/cycle for TiO₂ + 20 cycles x 0.26 nm/cycle for ZnO).

Figure 7 shows the result of low-angle XRD measurement of this multilayer. The thickness of layer-pair can be determined from low-angle XRD measurement using the Bragg relationship ($n\lambda = 2d\sin\theta$), where n is the diffraction order, λ is the wavelength, d is the thickness of layer-pair, θ is peak position of the Bragg reflection. The first Bragg peak is observed at a grazing angle of $2\theta = 0.606^\circ$, which corresponds to the layer-pair thickness of 14.58 nm. The reason why the measured layer-pair thickness is larger than that of calculated is not understood, but the growth rate may depend on the surface [10]. Figure 8 shows the result of measured reflectivity of this fabricated multilayer. The peak reflectivity is 9.6% at the wavelength of around 2.73 nm and a grazing angle of $2\theta = 9.5^\circ$. The reason why the peak reflectivity is observed at the wavelength of around 2.73 nm is because this multilayer mirror uses anomalous dispersion around Ti absorption edge (2.73 nm).

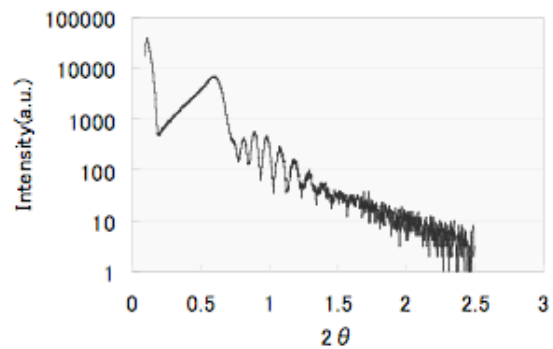


Fig. 7. Low-angle XRD spectrum of fabricated 10-bilayer TiO₂/ZnO multilayer.

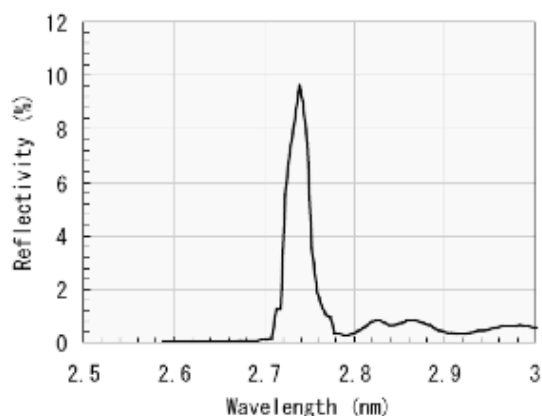


Fig. 8 Experimental reflectivity of fabricated 10-bilayer TiO₂/ZnO multilayer.

5. CONCLUSION

ZnO and TiO₂ films were grown on sapphire (0001) substrate using ALE technique at a substrate temperature of 450°C. These films were observed self-limiting growth. The ZnO films were deposited using DEZ and H₂O and it displayed a growth rate of nearly 0.26 nm/cycle. The TiO₂ films were deposited using TCT and H₂O and it displayed a growth rate of nearly 0.076 nm/cycle.

We proposed and then fabricated 10-bilayer TiO₂/ZnO multilayer mirror using ALE technique at a substrate temperature of 450°C. This multilayer achieved reflectivity of 9.6% at the wavelength of around 2.73 nm and a grazing angle of $2\theta = 9.5^\circ$. The growth rates of ZnO and TiO₂ in the multilayer were different from those in single layer films because the growth rate depends on used substrate. The TiO₂/ZnO multilayer will be useful for soft X-ray mirror if further studies are conducted in terms of growth rate, interface, surface roughness, and reactant vapors.

References

- [1] A.-S. Morlens, P. Balcou, P. Zeitoun, C. Valentin, V. Laude and S. kazamias, *Opt. Lett.*, **30**, 1554-1556 (2005).
- [2] F. Salmassi and E. M. Gullikson, *Abstracts of the 8th International Conference on the Physics of X-ray Multilayer Structures*, 39 (2006).
- [3] D. M. Hausmann, P. de Rouffignac, A. Smith, R. Gordon and D. Monsma, *Thin Solid Films*, **443**, 1-4 (2003).
- [4] S. M. George, A. W. Ott and J. W. Klaus, *J. Phys. Chem.*, **100**, 13121-13131 (1996).
- [5] S. J. Kwon, *Jpn. J. Appl. Phys.*, **44**, 1062-1066 (2005).
- [6] J. W. Elam, Z. A. Sechrist and S. M. George, *Thin Solid Films*, **414**, 43-55 (2002).
- [7] H. Kumagai, K. Toyoda, K. Kobayashi, M. Obara and Y. Iimura, *Appl. Phys. Lett.*, **70**, 2338-2340 (2003).

- [8] E. M. Wong, J. E. Bonevich and P. C. Searson, *J. Phys. Chem.*, **B102**, 7770-7775 (1998).
- [9] K. Fukushima, G. H. Takaoka and I. Yamada, *Jpn. J. Appl. Phys.*, **32**, 3561-3565 (1993).
- [10] J. Aarik, A. Aidla, H. Mänder, T. Uustare, M. Schuisky and A. Härsta, *J. Crystal Growth*, **242**, 189-198 (2002).

(Received July 14, 2009; Accepted August 22, 2009)

Design of novel titanium oxide/nickel oxide multilayer mirror for attosecond soft x rays

Hiroshi Kumagai and Yusuke Masuda

Faculty of Engineering, Osaka City University, 3-3-138 Sugimoto, Sumiyoshiku, Osakashi, Osaka 558-8585, Japan

Fax: 81-06-6605-2846, e-mail: kumagai@a-phys.eng.osaka-cu.ac.jp

A novel attosecond multilayer mirror was designed at “water-window” wavelengths with a combination of TiO and NiO, which were the same NaCl-type crystal structures of nearly equal lattice constants (TiO = 0.41766 nm, NiO = 0.41684 nm). The theoretical calculation of the TiO/NiO multilayer mirror indicated that the high reflectivity over 50% was attainable at 2.73 nm and at an incident angle of 18.9° from the normal incidence. Moreover, it also indicated that stacking of some multilayer blocks with different periods became effective in reflecting attosecond soft x rays.

Key words: soft x-rays, multilayer, attosecond, titanium oxide, nickel oxide, chirped mirror

1. INTRODUCTION

Development of high-performance normal-incidence multilayer optics for the water-window wavelength region between the oxygen and carbon K absorption edges at 2.33 and 4.36 nm, respectively, where water is relatively transmissive and organic materials are absorptive, has been a technical challenge of great interest. The extremely small periods ~1.2–2.2 nm of soft-x-ray mirrors require very rigorous specifications to be met with respect to interface roughness and interlayer mixing, because interface roughness on an atomic scale has a substantial effect on soft-x-ray reflectance.

Although the Fresnel coefficients of materials are so small at these wavelengths that a large number of bilayers must be used, which means that the problems of interface roughness and imperfect interfaces due to interlayer mixing become serious, the highest reflectance achieved at water-window wavelengths (3.11 nm) and near normal incidence ($\theta=9.2^\circ$) has been reported to be 32% [1], owing to the various efforts which have been made in this field.

One of the authors have proposed the use of a novel metal oxide multilayer for soft-x-ray mirrors at water-window wavelengths [2], because an oxide multilayer can prevent the formation of an alloy at the interface, and the absorption of oxygen in oxides is negligible at the water-window wavelengths; moreover, the metal oxide multilayer can be fabricated by the atomic layer deposition or atomic layer epitaxy (ALE) technique. These techniques can be used to control surfaces on an atomic scale by sequentially dosing the surface with appropriate chemical precursors and then promoting surface chemical reactions which are inherently self-limiting, unlike the conventional fabrication methods of soft-x-ray multilayer mirrors using e-beam evaporation, ion beam sputtering, rf and dc magnetron sputtering and so on. We have found that the self-limiting adsorption mechanism works in the fabrication of oxide thin films such as aluminum oxide and titanium oxide[3-6].

One of the authors also demonstrated experimentally high reflectances over 30% at the water-window wavelengths with 20 bilayers of amorphous titanium oxide and aluminum oxide fabricated by the atomic layer deposition method of controlled growth with sequential surface chemical reactions [7].

Metal oxide multilayers can be fabricated also by ALE technique. With the layer-by-layer growth nature of ALE, the periodicity in multilayer mirrors is able to be controlled with the higher precision [8]. This advantage is also valuable for the fabrication of other functional multilayer structures, such as chirped mirrors, which are useful for compensating for temporal broadening of the x-ray pulse [9].

In this paper, we proposed novel titanium oxide / nickel oxide multilayer mirrors for attosecond soft x rays, and then reported their high reflectances and strong possibility of being attosecond mirrors.

2. TiO/NiO MIRROR STRUCTURE

In order to obtain higher reflectivity, a combination of binary materials whose refractive indices are as different as possible and whose absorption coefficients are as small as possible, should be selected. Especially, the titanium L absorption edge, which is located at 2.733 nm, is important to obtain higher reflectivity at the water-window wavelengths. The real part of the Fresnel's coefficient for nickel is relatively high at the wavelength, generating a large difference between the real parts of the binary Fresnel coefficients. Moreover, the imaginary parts of both the Fresnel's coefficients are relatively small. The difference between the real parts of the Fresnel coefficients of the binary oxides is almost the same as that between titanium and nickel. Thus, a combination of TiO/NiO becomes a promising candidate for the wavelengths around 2.733 nm.

In addition, both TiO and NiO are the same NaCl-type crystal structures [10]. Therefore, it is possible to make a multilayer of the artificial superlattice between TiO and NiO on MgO(111) substrates, as MgO also has the NaCl-type crystal structure. Especially, the (111)-oriented reflection planes in the NaCl lattice model indicates that metal layers and oxygen layers are separate. This separation is suited for ALE methods where the adsorption of vapor precursors should be stopped at one monolayer (ML) automatically through the self-limiting mechanism. Moreover, TiO, NiO, and MgO have almost the same lattice constants and therefore there is little lattice mismatch between these oxides (TiO = 0.41766 nm, NiO = 0.41684 nm, MgO = 0.42112 nm) [10]. Consequently, the combination of TiO/NiO has potential enough to be a very attractive water-window multilayer mirror.

3. THEORETICAL CALCULATIONS AND DISCUSSION

Reflectivities of multilayer mirrors were calculated through the Fresnel's equation with the complex refractive indices. Figure 1 shows the theoretical calculations of the reflectivity (s polarization) of the $(\text{TiO})_3(\text{NiO})_3$ periodic multilayer mirror, where x and y of $(\text{TiO})_x(\text{NiO})_y$ denote layer numbers in one period for TiO and NiO, respectively. The high reflectivity over 50% at the wavelength of 2.73 nm as shown in Fig. 1(a) and an incident angle of 18.9° from the normal incidence as shown in Fig. 1(b) is obtainable. Fig. 1(c) shows the theoretical reflectivity as a function of numbers of binary layers. With 400 bilayers, 99% of the highest reflectivity is attainable.

Recently, coherent soft-x-ray source based on the high-order harmonic generation which enables to generate attosecond (as) pulses have received considerable attention. High harmonics generated by the nonlinear interaction of ultrashort pulses from a 800-nm high-intensity Ti:sapphire laser with rare gas is currently the most promising way to generate attosecond pulses. The high harmonic spectrum has the very characteristic shape; it falls off for the first few harmonics, then shows the "plateau" where all the harmonics have the same intensity strength, and finally ends up with the "cutoff" [11]. The cutoff value depends on the IR laser intensity and it is said that the cutoff will extend the water-window region. The ultrashort pulses are the result of the spectral interference of many high-order harmonics. The phase relation between harmonics is not linear but there exists inherent group delay dispersion between harmonics that broadens the pulse duration [12]. Chirped mirrors are one of the solutions proposed to overcome this fundamental limitation. Those mirrors must have both a bandwidth to make interfere as much as possible high-order harmonics and the opposite phase of high-order harmonics that we can control [9]. This induces the particular specification with the multi-block spectral structure based on the multi-periodic

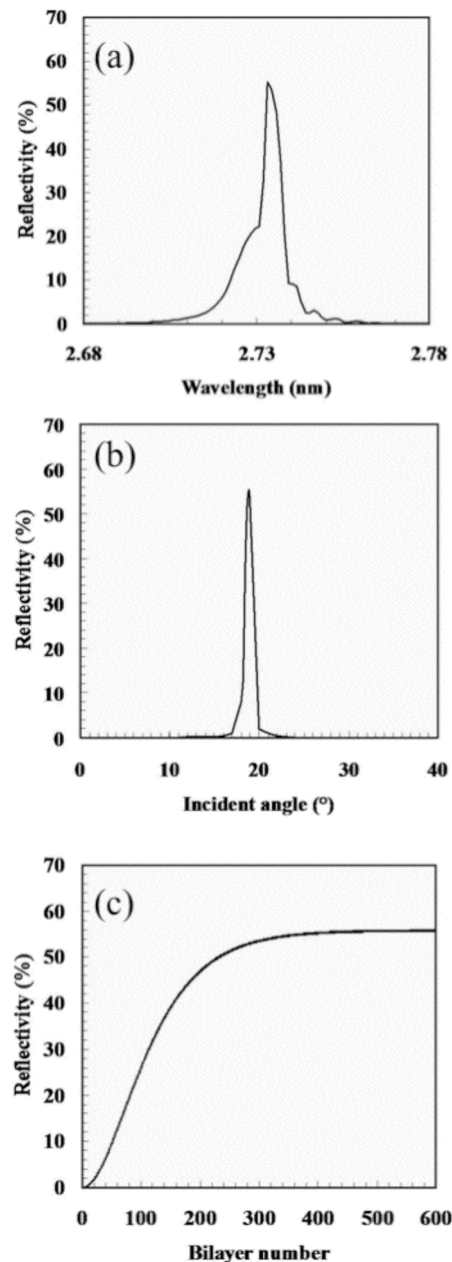


Fig.1: Calculated reflectivities (s-polarization) of the $(\text{TiO})_3(\text{NiO})_3$ -period multilayer mirror as functions of wavelength (a), incident angle (b), and number of bilayers (c).

mirrors. In order to design the attosecond mirror in the water-window wavelengths, we performed the following theoretical calculations.

Figure 2 shows theoretical calculations of the reflectivity of $[(\text{TiO})_3(\text{NiO})_3]_{100}$ and $[(\text{TiO})_4(\text{NiO})_3]_{100}$ multilayer mirrors in the 2.6-3.3 nm region and the corresponding single-periodic structures. In Fig. 2, $[(\text{TiO})_3(\text{NiO})_3]_{100} = (3,3)_{100}$ represents 100 bilayers of the $(\text{TiO})_3(\text{NiO})_3$ single-periodic multilayer mirror; $\lambda_{3,3}$ and $\lambda_{4,3}$ indicate the reflection wavelength of $(3,3)_{100}$ and that of $(4,3)_{100}$, respectively. As shown in Fig. 2,

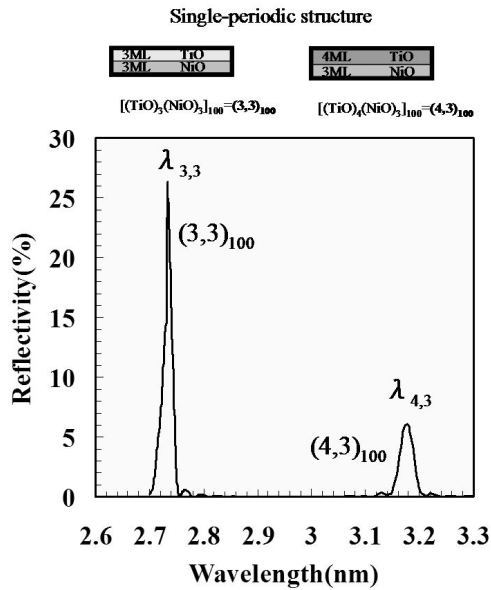


Fig.2: Calculated reflectivities of single-period multilayer mirrors.

each theoretical reflection peak has a narrow bandwidth, and there is a wide gap between neighbors. This property is, indeed, undesirable for a broadband mirror. This disadvantage is caused by the discrete thickness of ML, from the layer-by-layer growth of ALE. However, adoption of the multi-periodic structure can solve the above problem.

In order to control the reflection wavelength precisely, the multi-periodic structure should be proposed [8]. The reflection wavelength of the multi-periodic mirror is determined by the combined ratio of the periodic layers. With the use of this simple combination rule, multi-periodic mirrors at the selected wavelength are designed. Figure 3 indicates two examples of the calculated reflectivity of multi-period mirrors. In Fig. 3, a reflection peak midway of $\lambda_{3,3}$ and $\lambda_{4,3}$, $(\lambda_{3,3} + \lambda_{4,3})/2 = 2.956$ nm is produced by a combination of $(\text{TiO})_3(\text{NiO})_3$ and $(\text{TiO})_4(\text{NiO})_3$ in the ratio of 1:1. Correspondingly, $(8\lambda_{3,3} + \lambda_{4,3})/9 = 2.780$ nm mirror is obtained from $(\text{TiO})_3(\text{NiO})_3:(\text{TiO})_4(\text{NiO})_3 = 8:1$. It is important that one period of $(\text{TiO})_4(\text{NiO})_3$, should be inserted uniformly into the major period, $(\text{TiO})_3(\text{NiO})_3$ to obtain a higher reflectivity at 2.78 nm. With the use of this method, the wavelength for the reflection peak is controllable fractionally.

Next, a multi-period structure like the so-called “supermirror” is useful for broadband reflection in the water-window. This structure is based on the depth-graded stacking of some blocks which have different wavelengths where reflections peak. Figure 4 shows the calculated reflection peaks of various single-period mirrors with the same number of bilayers in the wavelength region from 2.7 nm to 2.9 nm. In this figure, each calculated reflection peak is controlled to be near neighbors. The reason that the reflection peaks around 2.733

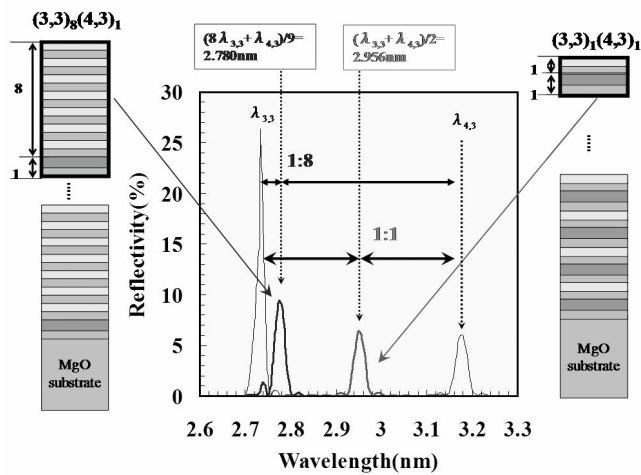


Fig.3: Calculated reflectivities of the multi-period structure mirror.

nm are outstanding is due to the anomalous dispersion around the titanium L absorption edge.

Figure 5 shows the results of these theoretical calculations. Fig. 5(a) shows the calculated reflectivity (black line) and the phase relation (gray line) of the chirped mirror. It is note that the chirped mirror can give the reflectivity of about 1-5 % over the large bandwidth covering from 2.73 nm to 2.89 nm in the water-window. As shown in Fig. 5 (b), the shortest pulse of 150 as is obtainable theoretically when it can interfere with each other over the spectral range in this mirror in phase. By varying the number of blocks and the thickness of the multilayers, phase variations and reflectances can be designed for your request.

$[(\text{TiO})_3(\text{NiO})_3]_x[(\text{TiO})_4(\text{NiO})_3]_y = [x:y]$	(3,3) ^{single}	[19:1]	[10:1]	[8:1]	[6:1]	[4:1]	[3:1]	[2:1]
reflection wavelength peak (nm)	2.733	2.751	2.770	2.779	2.795	2.819	2.844	2.879

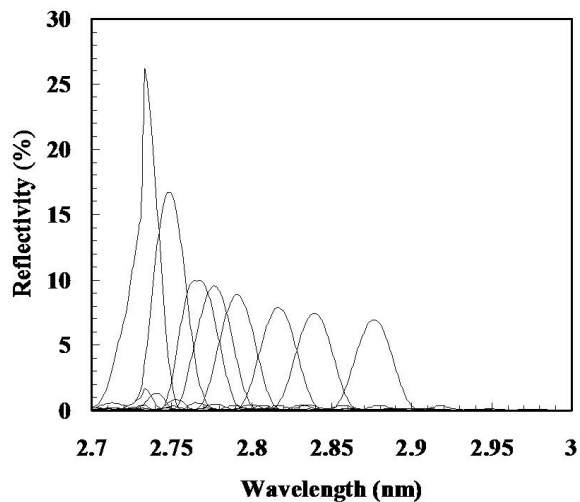


Fig. 4 Calculated reflectivities of various single-period mirrors in the wavelength region from 2.7 nm to 2.9 nm.

4. CONCLUSION

We have proposed the novel TiO/NiO multilayer mirror based on an atomic layer epitaxy technique to fabricate high-reflection robust mirrors for attosecond soft x rays at the water-window wavelengths. The layer thickness of the multilayer mirror is controllable exactly by ALE of controlled growth with sequential surface chemical reactions. This is advantageous for the artificial superlattice multilayer of TiO/NiO on MgO(111), which has NaCl-type (111)-reflection planes where metal layers or oxygen layers are alternative. The theoretical calculation of the periodic TiO/NiO multilayer mirror indicated high reflectance over 50 % at a wavelength of 2.73 nm and an incident angle of 18.9° from the normal incidence. Moreover, it also indicated that the multi-block structure could control the reflectivity and the phase of a 150-attosecond pulse.

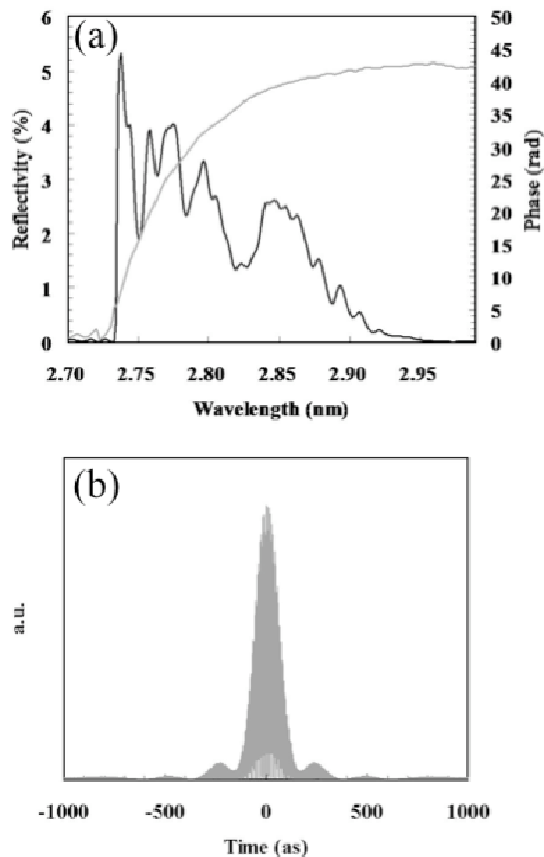


Fig.5: Calculated reflectivity (black line) and phase relation (gray line) of the attosecond mirror (a) and Fourier transformation of the reflectivity (b).

REFERENCES

- [1] F. Salmassi and E. M. Gullikson, *Abstracts of the 8th International Conference on the Physics of X-ray Multilayer Structures*, 39 (2006).
- [2] H. Kumagai, M. Matsumoto, Y. Kawamura, K. Toyoda, and M. Obara, *Jpn. J. Appl. Phys.* **32**, 7086-7089 (1994).
- [3] H. Kumagai, K. Toyoda, M. Matsumoto, and M. Obara, *Jpn. J. Appl. Phys.* **32**, 6137-6140 (1993).
- [4] H. Kumagai and K. Toyoda, *Appl. Surf. Sci.* **82/83**, 481-486 (1994).
- [5] H. Kumagai, M. Matsumoto, K. Toyoda, M. Obara, and M. Suzuki, *Thin Solid Films* **263**, 47-53 (1995).
- [6] H. Kumagai, M. Matsumoto, K. Toyoda, and M. Obara, *J. Mater. Sci. Lett.* **15**, 1081-1083 (1996).
- [7] H. Kumagai, K. Toyoda, K. Kobayashi, M. Obara, and Y. Iimura, *Appl. Phys. Lett.*, **70**, 2338-2340 (1997).
- [8] M. Ishii, S. Iwai, H. Kawata, T. Ueki, and Y. Aoyagi, *J. Cryst. Growth*. **180**, 15-21 (1997)
- [9] A.-S. Morlens, M.-F. Ravet, V. Laude, R. López-Martens, M. Roulliay, A. Jérôme, F. Delmotte, F. Bridou, S. Kazamias, P. Balcou, and P. Zeitoun, *Proc. of SPIE* **5963**, 59630W (2005)
- [10] A. A. Valeeva, A. A. Rempel, W. Sprengel and H.-E. Schaefera, *Phys. Chem. Chem. Phys.* **5**, 2304-2307 (2003).
- [11] K. Midorikawa, *Springer Handbook of Lasers and Optics*, Springer, 819-827 (2007).
- [12] Y. Mairesse, A. de Bohan, L. Franzinski, H. Merdji, P. Monchicourt, P. Breger, M. Kovacev, B. Carré, H. Muller, P. Agostini, and P. Salières, *Science* **302**, 1540-1543 (2003)

(Received July 14, 2009; Accepted September 17, 2009)

Study of thin-film thickness and density by high-resolution Rutherford backscattering spectrometry and X-ray reflectivity

Amane Kitahara, Satoshi Yasuno and Kazuhisa Fujikawa
 Electronics Technology Department, KOBELCO RESEARCH INSTITUTE, INC.,
 1-5-5 Takatsukadai, Nishiku, Kobe, 651-2271, Japan
 Fax: 81-78-992-6143, e-mail: kitahara.amane@kki.kobelco.com

High-resolution Rutherford backscattering spectrometry (HR-RBS) and X-ray reflectivity (XRR) are both powerful tools that can be used to investigate thin film structures with the same depth resolution. HR-RBS can be used to analyze low-density contrast films since it reveals the chemical composition in films. The elemental information aids the XRR analysis of films containing localized hydrogen atoms and low-electron-density contrast layers.

Key words: high-resolution RBS, X-ray reflectivity, high- k , diamond-like carbon

1. INTRODUCTION

X-ray reflectivity (XRR) and Rutherford backscattering spectrometry (RBS) have already been used successfully to study thin film structures and characterize their film thickness, composition, roughness and density. XRR can be used to quantify electron density distribution and film thickness, but not the elemental compositions. On the other hand, RBS can be used to quantify chemical composition and areal density (atoms/cm²), but not the absolute thickness without a known volume density (g/cm³) [1]. The two methods thus provide complementary information that can be used for thin film analysis. We present XRR and high-resolution RBS (HR-RBS) analyses of two systems: (1) HfO₂ (0.5-6nm thick) on SiO₂/Si and (2) diamond-like carbon (DLC) film on a bare Si wafer. We then discuss the advantages of each method.

2. EXPERIMENTAL

XRR measurements were performed using a Rigaku SmartLab system with Cu-K α radiation. HR-RBS measurements were carried out with 450keV He⁺ ions using a Kobe Steel HRBS500 system equipped with a high-stability Cockcroft-Walton-type high-voltage generator and a high-resolution energy analyzer (~0.15%) [2-4].

We prepared two types of thin films. For the first type, HfO₂ and SiO₂ were deposited on Si(001) substrates by atomic layer deposition. Nominal thicknesses of 0.5, 1, 2, 4 and 6 nm were deposited for the HfO₂ on a 1-nm-thick SiO₂ layer on the Si substrate. These are labeled HfO₂~0.5 nm, ~1 nm, ~2 nm, ~4 nm, and ~6 nm, respectively. For the second type, a DLC film was deposited on a bare Si wafer by electron cyclotron resonance CVD.

3. RESULTS AND DISCUSSION

3.1 HfO₂/SiO₂/Si

Figure 1 shows the HR-RBS spectra of the HfO₂/SiO₂/Si series. The peaks of three elements (Hf, Si, and O) were observed individually in the spectra. The width of the peaks indicated the relative thickness. We obtained the thickness of each HfO₂ and SiO₂ layer

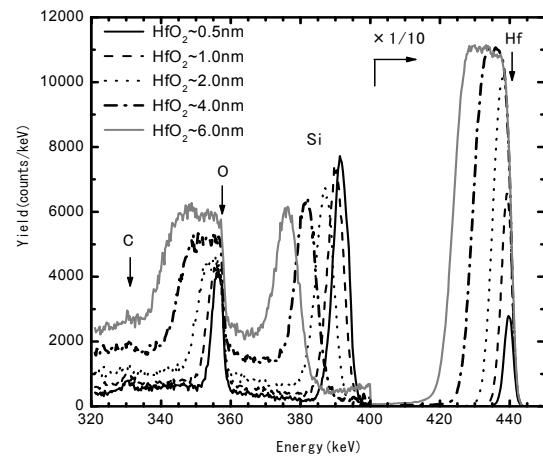


Fig. 1. HR-RBS results of HfO₂/SiO₂/Si systems. Widths of Hf and O peaks correspond to their thickness under the surface.

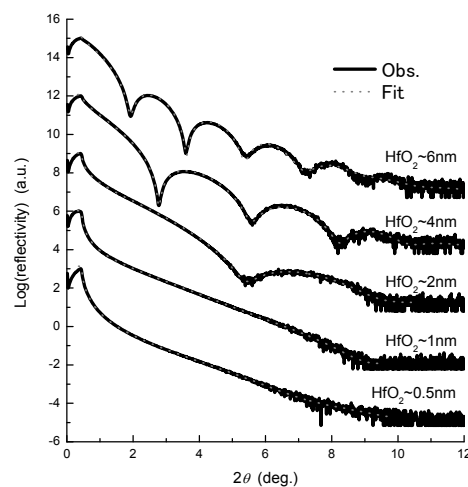


Fig. 2. Measured and fitted XRR of HfO₂/SiO₂/Si systems.

Table I

Obtained thicknesses of HfO₂ layer and SiO₂ layer on a Si substrate by HR-RBS and XRR methods.

Sample: HfO ₂ ~	HR-RBS		XRR	
	HfO ₂ thickness (nm)	SiO ₂ thickness (nm)	HfO ₂ thickness (nm)	SiO ₂ thickness (nm)
~0.5 nm	0.21	1.39	1.20	1.16
~1.0 nm	0.60	1.47	0.78	1.08
~2.0 nm	1.53	1.33	1.72	1.00
~4.0 nm	3.16	1.42	3.27	0.96
~6.0 nm	4.77	1.19	4.92	2.00

from curve fitting procedure and replacing the estimated areal densities (atoms/cm²) with the bulk volume densities (9.68 g/cm³ and 2.20 g/cm³, respectively). Width of the Hf peaks indicated the HfO₂ thicknesses. The O peak in SiO₂ was determined by subtracting the O peak in HfO₂ from the total O peak, since the O peak was composed of the two oxide layers. Then, the SiO₂ thickness was calculated.

Figure 2 shows XRR data corresponding to the HR-RBS spectra given in Fig. 1. The density contrast between HfO₂ and Si affected the visible XRR oscillations, whereas SiO₂ layer did not feature remarkable oscillations because of the low-density contrast and very thin film. However, the oscillation periodicity changes did not indicate only HfO₂ film thickness changes, but also the SiO₂ film thickness. We calculated thicknesses of the top of the HfO₂ film and the interfacial SiO₂ film using XRR simulations. Then, we imposed the existence of the HfO₂ and the SiO₂ layers on the simulation models. The thicknesses calculated by HR-RBS and XRR are shown in Table I.

XRR can be used to evaluate the HfO₂ thicknesses with high accuracy due to high-density contrast. The thicknesses of HfO₂ layer obtained by HR-RBS were almost equal to the thicknesses obtained by XRR, except for HfO₂~ 0.5nm. However, it is not as sensitive when measuring the thin and low-density contrast between the SiO₂ layer and the Si substrate with laboratory X-ray equipment. The SiO₂ thicknesses obtained by XRR did not converge on a stable value when least-squares fitting procedure was carried out. On the other hand, HR-RBS could detect a very thin film such as a low-density contrast. Hence, we could confirm the thicknesses of SiO₂ on the XRR simulations.

3.2. Diamond-like carbon film on Si

Figure 3 shows the elemental depth profile of a DLC film on a Si wafer obtained from HR-RBS analysis and elastic recoil detection analysis (HR-ERDA) for hydrogen atoms. There existed localized Fe and Ar atoms at the interface between carbon and Si. The Fe atoms remained as contaminants in the chamber since DLC films were usually prepared by deposition on a steel plate as a hard coating. XRR also detected a high-density layer at the interface of the sample, as shown in Fig. 4. The depth (nm) - density (g/cm³) profile of the DLC film was obtained by fitting the measured XRR using a multiple carbon layer model. However, we could not determine the existence of Fe and Ar at the interface using only the XRR method. In Fig. 4, we recalculated the depth-density profile replacing the chemical

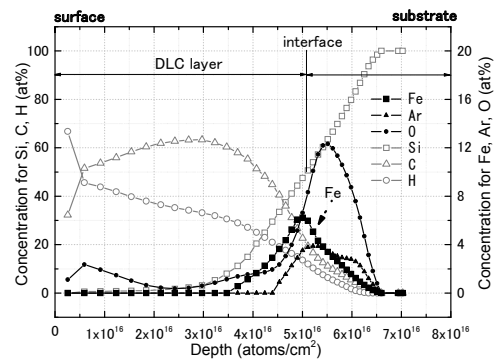


Fig. 3 Elemental depth profiles of H, C, O, Si, Ar, and Fe near DLC surface and interface estimated by HR-RBS.

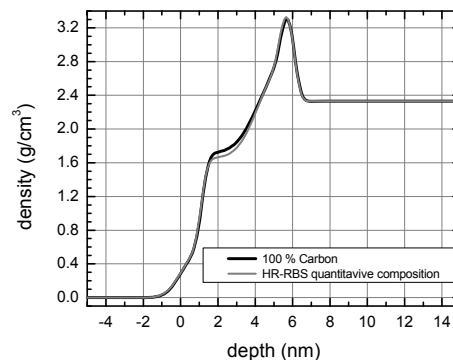


Fig. 4 Depth vs. density profile of DLC film on Si determined by XRR.

composition estimated by HR-RBS and HR-ERDA with carbon. The recalculated profile had a low density near the surface due to concentration of hydrogen.

The electron density obtained by XRR can be converted to the volume density using chemical components in the DLC films obtained by HR-RBS. Furthermore, the converted volume density converts the thickness of layers described in units of 'atoms/cm²' into units of 'nm' for the HR-RBS results. Then, we can verify the film thickness using both methods.

4. SUMMARY

We demonstrated two examples of thin film analyses through XRR and HR-RBS measurements. The two methods can be used to non-destructively measure film thicknesses on a substrate with sub-nanometer resolution. When conducting XRR using laboratory equipment, it is advantageous to independently quantify the film thickness and electron density, except for systems with low-density contrast of less than ca. 5%. HR-RBS analyzes the localization and interdiffusion of elements in thin film layers even if the system consists of low-density contrast and includes hydrogen.

REFERENCES

- [1] W. K. Chu, J. W. Mayer, M.-A. Nicolet, "Backscattering Spectrometry," Academic Press, New York (1978).
- [2] K. Kimura, M. Kimura, Y. Mori, M. Maehara, H. Fukuyama, AIP Conf. Proc., **475**, 500-503 (1999).
- [3] C. Ichihara, N. Kawakami, S. Yasuno, A. Hino, K. Fujikawa, A. Kobayashi, M. Ochi, H. Gotoh, T. Kugimiya, *Micron.*, **40**, 66-69 (2009).
- [4]http://www.kobelco.co.jp/technobook/p238_e.htm.

(Received July 14, 2009; Accepted September 24, 2009)

Non-destructive analysis on oxidation states of Ti atoms in the passivation film formed on SUS321 using hard X-ray photoelectron spectroscopy

Shin Takahashi^{1*}, Mitsutoshi Yokomizo¹, Masugu Sato², Masatake Machida² and Son Jin-Young²

¹ Kobelco Research Institute, Hyogo 651-2271, Japan

Fax: 81-78-992-6314, e-mail: takahashi.shin@kki.kobelco.com

² Japan Synchrotron Radiation Research Institute, Hyogo 679-5198, Japan

An oxidation state of a small amount of Ti in the naturally formed passivation film on stainless steel (Fe-Cr alloy, SUS321) was non-destructively evaluated using angle resolved hard X-ray photoelectron spectroscopy (HX-PES) at BL46XU in SPring-8. The synchrotron radiation with photon energy of 7942.5 eV was used as an excitation source. The intensity of Cr 1s peak assigned to metallic state gradually increased with increasing of take-off angle θ from 15° to 30°. It drastically increased at larger take-off angle region (30~80°). The results clearly suggest a formation of passivation film on SUS321 and enough large probing depth of HX-PES to evaluate the chemical states of elements placed below the passivation film. Ti 1s spectra collected at take-off angles from 15 to 80° revealed only Ti in tetravalent state. Taking an inelastic mean free path length of Ti 1s photoelectrons into account, it suggests that only Ti in tetravalent state exists in and below the passivation film.

Key words: Hard X-ray photoelectron spectroscopy, Passivation film, Stainless steel

1. INTRODUCTION

A conventional soft X-ray photoelectron spectroscopy (SX-PES) is widely applied to evaluate the oxidation states of elements in the materials. Al $K\alpha$ and Mg $K\alpha$ lines are generally used as an excitation source to emit photoelectrons. With these excitation sources, only photoelectrons emitted around shallow area can escape from materials into vacuum due to small kinetic energy. For this reason, it is known as a surface sensitive technique. It is, however, also desirable to the evaluation of elements placed in the buried interface or bulk. In some cases, Ar⁺ sputter or chemical etching method has been used to removal of surface layers to make bare buried interface as a pretreatment technique, which is sure to give chemical alternation around the interface. Utilizing a photon in the hard X-ray region is the simple way to emit photoelectrons with enough high kinetic energy to escape from bulk or buried interface without destructive pretreatment, if some essential problems are solved. One of the most serious problems is rapid reduction of subshell photo-ionization cross-section as increasing of photon energy [1]. G. Beamsom et al. developed photoelectron spectrometer equipped with Cu $K\alpha$ sealed tube and LiF(110) Johansson type monochromator [2]. According to them, several hours are required to obtain clear photoelectron spectrum. High brilliance synchrotron radiation beam is essential to use as an excitation source in order to achieve high throughput measurements or to evaluate a small amount of elements.

Recently, the hard X-ray photoelectron spectroscopy (HX-PES) using synchrotron radiation has been developed [3] and started to share for the industrial

usage at SPring-8 [4]. We applied it to evaluate the oxidation states of small amount of additional elements in stainless steel (Fe-Cr alloy) at BL46XU in SPring-8. Stainless steel is commonly used materials for industrial products due to its good property in corrosion resistance. Cr oxide film plays a role as the protective film to interrupt a progression of rust formation into the bulk. The small amount of additional elements such as Ti, Nb, Cu, Ni and so on are known to improve corrosion resistance property of passivation film [5, 6]. It is not, however, precisely known how such elements play a role in improvement of corrosion resistance yet. An estimation of chemical states of additional elements in the oxide film or at around buried interface between oxide film and substrate will help to understand a corrosion resistance mechanism. Thus, HX-PES is expected as a useful tool for evaluation of oxide film formed on steel.

2. EXPERIMENTAL

Naturally formed passivation film on SUS321 (Nilaco corporation) was used as a sample for the present study. SX-PES combined with Ar⁺ sputter method was carried out by Quantera SXM photoelectron spectrometer (Ulvac-Phi, Inc.) in order to obtain depth profile of elemental composition of passivation film. Ar⁺ beam with the energy of 1.0 keV was irradiated onto sample surface at an incidence angle of 45°. The sputter rate obtained by standard SiO₂ sample is 1.13 nm min⁻¹ under present condition. The photoelectrons emitted by monochromated Al $K\alpha$ line (1486.7

eV) were detected at take-off angle θ of 45° with respect to sample surface. The probing depth is roughly deduced to be less than 5 nm, in the present experimental condition.

For the non-destructive analysis on oxidation state of elements in passivation film, HX-PES was performed using synchrotron radiation with the photon energy of 7942.5 eV at an undulator beamline BL46XU in SPring-8. The synchrotron radiation was monochromated by Si(111) double crystal monochromator. Two Rh-coated curved mirrors were placed at the most downstream of optics hutch for the elimination of higher harmonics and horizontal focusing. A Si(111) channel cut monochromator mounted between Si(111) double crystal monochromator and Rh-coated mirrors was used to reduce photon bandwidth for achievement of high resolution HX-PES. A vertical focusing mirror was mounted outside of optics hutch. The Gammadata-Sienta R-4000 electron energy analyzer was used with the input lens axis directed in the parallel direction to the polarization plane of synchrotron radiation beam. The photon energy and energy resolution were checked by Au $4f_{7/2}$ core level spectrum and Fermi edge spectrum with analyzer pass energy of 200 eV. The full width at half maximum of Au $4f_{7/2}$ was 470 meV. In order to changing probing depth, take-off angle θ of emitted photoelectrons was varied from 15° to 80° with respect to sample surface by rotating sample.

The spectra were analyzed using standard least-squares-fitting with Voigt line shape after subtraction of background by Shirley method [7].

3. RESULTS AND DISCUSSION

3-1 SX-PES combined with Ar^+ sputter

Fig. 1 shows depth profile of O, Fe, Cr, Ti, Ni of SUS321 as a function of Ar^+ sputter time (min). The vertical axis represents atomic concentration (%) of elemental composition calculated from relative sensitivity factor, transmission function of spectrometer and peak area intensities of O 1s, Fe 2p, Cr 2p, Ti 2p, Ni 2p core level spectra. The depth profile shows formation of oxide layer (passivation film) on SUS321 surface. Ti atoms with the atomic concentration of less than 5.0% are uniformly distributed in depth direction. Here, we should note that core level spectra of each element were measured after destruction of surface by Ar^+ sputter. Figs. 2 (a) and (b) show Cr 2p and Ti 2p spectra at each Ar^+ sputter time, respectively. The Cr $2p_{3/2}$ peaks suggest the existence of Cr^0 and Cr^{3+} , which are placed at binding energy of 574.5 eV and 576.9 eV, respectively. The peak components originated from Cr^0 grows at longer sputter time than 2.0 min. Ti 2p spectra suggest the existence of Ti^{4+} . The full width at half maximum (FWHM) of Ti $2p_{3/2}$ become broader with increasing of Ar^+ sputter time as shown in Fig 2(c), suggesting an appearance of Ti in lower oxidation states (Ti^{3+} or Ti^{2+}). One may consider that it reflects

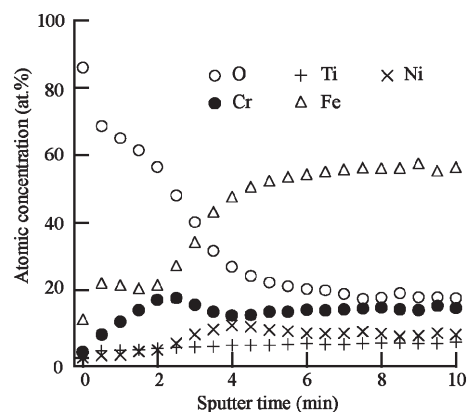


Fig. 1, Depth profile of O, Ti, Ni, Cr and Fe in SUS321 as a function of Ar^+ sputter time (min)

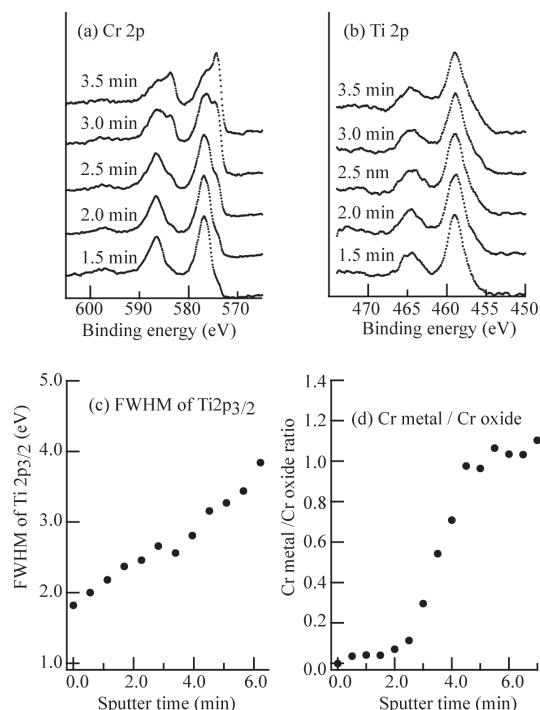


Fig.2, Cr 2p (a) and Ti 2p (b) spectra taken at each sputter time. FWHM of Ti $2p_{3/2}$ (c) and Cr metal / Cr oxide ratio (d) as a function of sputter time, respectively.

realistic distribution of various oxidation states of Ti in depth direction. On the other hand, however, it is possible to speculate that the appearance of various oxidation states is result of reduction by Ar^+ sputter.

Assuming that oxidation state of Cr oxide does not change by Ar^+ sputter according to ref. [8], we obtain depth profile of peak area intensity ratio of $\text{Cr}^0/\text{Cr}^{3+}$ by analysis of Cr $2p_{3/2}$ peak as shown in Fig. 2 (d). The profile suggests constant distribution of Cr atoms in metallic state at sputter time region between 0.5 and 2.0 min. Here, we define an interface between passivation film

and substrate at sputter time of 3.5 min, where the $\text{Cr}^0/\text{Cr}^{3+}$ ratio increases by a middle of maximum and minimum values.

3-2 Angle resolved HX-PES

Figs. 3 (a) and (b) show Cr 1s and Ti 1s spectra obtained using synchrotron radiation with the photon energy of 7942.5 eV at θ of 15°, 30°, 55° and 80°, respectively. The horizontal axis of spectra represents in kinetic energy scale. We must pay attention that probing depth strongly depends on the kinetic energy of photoelectrons even at same θ . The probing depth d is expressed by $3\lambda\sin\theta$, where λ is inelastic mean free path (IMFP) of photoelectrons. Approximately, kinetic energies of Cr 1s and Ti 1s photoelectrons are 1951 and 2974 eV, respectively. Assuming that passivation film consists of Cr_2O_3 and Fe_2O_3 , the calculated IMFPs of Cr 1s and Ti 1s using TPP-2M formula [9] are about 3.4 and 4.7 nm, respectively. The probing depth of Ti 1s is about 1.4 times larger than that of Cr 1s in the passivation film.

The Cr 1s spectra consist of two components at each θ . The peak located at lower kinetic energy side is assigned to Cr^{3+} , while the other peak at higher kinetic energy side is assigned to Cr in metallic state. By analysis of line shape of Cr 1s spectra, we obtained relative peak area intensity ratio of Cr^0 against Cr^{3+} ($\text{Cr}^0/\text{Cr}^{3+}$) as a function of $\sin\theta$ as shown in Fig. 3(c). The curve of intensity ratio shows slight increasing at small $\sin\theta$ region and drastic increasing at larger $\sin\theta$ region. The intensity ratio is expected to increase when a probing depth reaches around oxide/metal interface. Thus, the interface defined in Fig. 2 (d) may be placed at the region between $\sin\theta = 0.50$ and 0.82 (calculated probing depth: $3\lambda\sin\theta = 5.1$ nm and 8.2 nm) in the profile shown in Fig. 3(c). Although, it is difficult to determine definitely the oxide/metal interface due to less measurement points of θ , the probing depth is enough large to reach interface. Here, we remind difficulty in obtaining depth profile accurately by analysis of angle resolved measurement due to heavy dependence on assumed structural model and the effects of surface roughness. Despite SX-PES combined with Ar^+ sputter is destructive technique, it is useful to obtain an atomic concentration depth profile.

Ti 1s spectra show single core level peak at kinetic energy of 2973.6 eV and satellite structure at lower kinetic energy side. The difference in kinetic energy between Ti 1s peak and satellite structure is 13.4 eV. This is identical to the previous work on TiO_2 powder using HX-PES by N. Moslemzader et al [10]. The satellite structure results from monopole charge transfer excitation. For this reason, we assigned that the Ti 1s peaks were originated from Ti^{4+} . Interestingly, the shape of spectra is independent to θ , meaning a uniform distribution of Ti^{4+} in depth direction contrary to the result shown in Fig. 2. Thus, we concluded that the appearance of Ti in lower

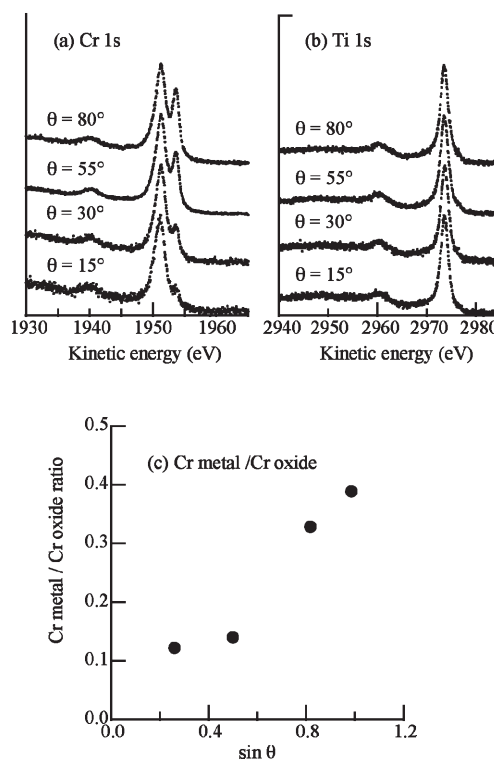


Fig. 3, Cr 1s (a) and Ti 1s (b) spectra taken at various take-off angle θ , respectively. Relative peak area intensity ratio (c) of Cr metal against Cr oxide as a function of $\sin\theta$.

oxidation states found in the Ti 2p spectra obtained by SX-PES is results of the reduction of Ti^{4+} caused by Ar^+ sputter. As mentioned above, the IMFP of Ti 1s photoelectrons is about 1.4 times larger than that of Cr 1s photoelectrons even at same take-off angles, i.e., the probing depth of Ti 1s photoelectrons collected at θ of 55° or 80° crosses well over the $\text{Cr}^0/\text{Cr}^{3+}$ interface. It means that Ti atoms placed even at below the interface are in the tetravalent state.

Previous studies on structural analysis of FeOOH particle, which is corrosion product of steel, precipitated from aqueous solution containing Ti^{4+} suggested that Ti^{4+} promotes the formation of α - FeOOH fine particles and inhibits the formation of unstable β - FeOOH [5, 6]. It may produce similar effects on stainless steel surface. As a result, a dense passivation film consisting of Cr oxide and α - FeOOH fine particles forms on stainless steel surface, which prevents penetration of harmful elements into the steel substrate.

Our present result, that Ti is in tetravalent state even at below the passivation film, possibly suggests that oxidation of Ti occurs prior to form passivation film at surface. In that case, oxidation state of Ti is important in formation of dense passivation film on stainless steel.

4. CONCLUSION

Oxidation states of Cr and Ti in the passivation film formed on SUS321 were non-destructively evaluated by HX-PES. The angle resolved Cr 1s spectra suggest that HX-PES provides enough large probing depth to evaluate oxidation states of elements around or under the interface between passivation film and stainless steel substrate without etching surface layer. As a result, we found that Ti atoms were in oxidized state (Ti^{4+}) even at the deeper point than the interface. However, it is difficult to obtain depth profile accurately by angle resolved measurement. HX-PES with the assistance of SX-PES combined with Ar^+ sputter method is realistic way to evaluate materials in depth direction.

ACKNOWLEDGEMENTS

This work (Proposal No. 2009A1841) was performed at BL46XU in the SPring-8 with approval of industrial application project of Japan Synchrotron Radiation Research Institute.

REFERENCES

- [1] J.J. Yeh, I. Lindau, *At. Data Nucl. Data Tables* 32, 1 (1985).
- [2] G. Beamson, S.R. Haines, N. Moslemzadeh, P. Tsakiropoulos, J.F. Watts, P. Weightman, K. Williams, *J. Electron Spectrosc. Relat. Phenom.*, 142, 151-162 (2005).
- [3] Y. Takata, M. Yabashi, K. Tamasaku, Y. Nishino, D. Miwa, T. Ishikawa, E. Ikenaga, K. Horiba, S. Shin, M. Arita, K. Shimada, H. Namatame, M. Taniguchi, H. Nohira, T. Hattori, S. Sodergren, B. Wannberg, K. Kobayashi, *Nucl. Instr. and Meth. A* 547, 50-55 (2005).
- [4] www.spring8.or.jp/
- [5] T. Ishikawa, K. Katoh, A. Yasukawa, K. Kandori, T. Nakayama, F. Yuse, *Corrosion Sci.*, 43, 1727-1738 (2001).
- [6] T. Ishikawa, K. Katoh, A. Yasukawa, K. Kandori, T. Nakayama, F. Yuse, *J. Mater. Chem.*, 10, 543-547 (2000).
- [7] D.A. Shirley, *Phys. Rev. B*, 5, 4709-4714 (1972).
- [8] S. Hashimoto, *Hyomen Kagaku*, 25, 198-204, (2004).
- [9] S. Tamura, C.J. Powell, D.R. Penn, *Surf. Interface Anal.*, 29, 77-89, (1993); 21 165-176 (1994).
- [10] N. Moslemzadeh, G. Beamson, P. Tsakiropoulos, J.F. Watts, S.R. Haines, P. Weightman, *J. Electron Spectrosc. Relat. Phenom.*, 152, 148-151 (2006).

(Received July 14, 2009; Accepted August 22, 2009)

Development of femtosecond X-ray source in helium atmosphere with millijoule high-repetition-rate femtosecond laser

Masaki Hada¹ and Jiro Matsuo²

¹Department of Nuclear Engineering, Kyoto University, Sakyo, Kyoto, Japan 606-8501
Fax: 81-774-38-3978, e-mail: hadamasaki@nucleng.kyoto-u.ac.jp

²Quantum Science and Engineering Center, Kyoto University, Gokasho, Uji, Kyoto, Japan 611-0011
Fax: 81-774-38-3978, e-mail: matsuo@nucleng.kyoto-u.ac.jp

High intensity Cu K α X-ray was generated in helium at atmospheric pressure (760 torr) using a commercial millijoule high-repetition rate Ti: sapphire laser. The characteristic K α X-ray was generated by focusing the 0.06 mJ–1.46 mJ, 100 fs and 1 kHz repetition femtosecond laser onto a solid Cu target to a spot with a 5 μ m diameter. We obtained the characteristic K α X-ray of 5.4×10^9 photos/s into 2π sr at a 1 kHz repetition rate with 5.0×10^{-6} conversion efficiency. K α X-ray intensity can be enhanced with 4–8% prepulse plasma into 7.7×10^9 photos/s/sr with 6.8×10^{-6} conversion efficiency. The X-ray intensity and conversion efficiency in helium achieved the almost the same level as in vacuum. Such vacuum-free femtosecond X-ray source with a tabletop laser can be a promising and easy accessible tool for time-resolved X-ray diffraction and other radiographic applications. The time-resolved X-ray diffraction experiment would reveal the ultrafast dynamics in crystalline materials, such as coherent phonon vibrations and ultrafast phase transitions.

Key words: laser-induced plasma, X-ray, ultrafast science, femtosecond laser

1. INTRODUCTION

Hard X-ray from femtosecond laser-produced plasma has gained much interest, as unique time resolved X-ray diffraction (XRD) experiments demonstrate and reveal the atomic dynamics of chemical reactions, phase transitions and coherent phonon vibrations.[1-4] Those X-ray diffraction and other X-ray radiographic applications such as the time-resolved X-ray absorption fine structure experiment would reveal the ultrafast dynamics of coherent phonon vibrations and ultrafast phase transitions, but also the structural dynamics of light-sensitive organic materials. A variety of femtosecond X-ray sources has been developed, such as laser-produced plasma X-ray source, ultrafast hard X-ray produced by synchrotron and XFEL.[3,5-6] The intensity or coherency of X-ray in synchrotrons or XFEL is quite high, however, the instruments are very expensive and it is required huge and complex facilities; moreover, the availability of those huge facilities is limited. Laser-produced plasma X-ray source are required to be comparatively small, lab-scale facility. Laser-produced plasma X-ray sources have consisted of high-power (above 100 millijoule) and low-repetition-rate (about 10 Hz) lasers and the K α -X-ray intensity using this large size laser was reported to be 10^8 – 10^{11} cps/sr with conversion efficiency of 10^{-4} – 10^{-5} . [7-10] Generally an X-ray intensity of more than several 10^8 cps/sr is required for time-resolved XRD experiments, and a laser-plasma X-ray of 10^9 – 10^{11} cps/sr is desirable.[11] This intensity is sufficiently high for the X-ray radiographic applications. Nevertheless, the utilization of such

ultrafast pulsed X-ray has been limited because of the complexity of the huge vacuum system and difficulty in managing a high-power laser. To date, a huge laboratory-top laser and a large size vacuum chamber are requisites to generate ultrafast pulsed X-ray radiation. In this laboratory-scale ultrafast X-ray source, there are also some problems with target forms and debris from the target caused by laser ablation. Regarding the target form, thin tape or wire typed targets have been used because the space in the vacuum chamber is limited. The small tape or wire target can be put in a vacuum chamber; however target lifetime is quite short at about several hours or at most a few days. It is difficult to control the surface of the thin tape or wire within a few micrometers. There is also the problem of debris from the target. When the high-power laser is focused onto the target, target materials are blown off and deposited on the focusing lens, windows, and other optics. Thin polymer tape covers have been employed to avoid the debris problem. Thus, such ultrafast pulsed X-ray sources were required to be more compact, easier to access, and have higher conversion efficiency into characteristic X-ray.

Recently, the compact designed tabletop submillijoule to several millijoule femtosecond laser has been reported to be available for generating hard X-ray with an intensity of about 10^8 – 10^{10} cps/sr with the K α X-ray conversion efficiency of 10^{-5} – 10^{-6} . [12-14] Although the experimental scale of a femtosecond laser could be successfully reduced with a tabletop femtosecond laser, difficulties remain when using

	synchrotron X-ray	laser-induced plasma X-ray		
		High Power (>100mJ)	Low Power (~1mJ)	
size of the facility	facility-top	laboratory-top	table-top	
Laser forcing condition		in vacuum condition		in atmospheric condition
X-ray intensity	$10^{15} \sim 10^{17}$ cps/mm ² ·(mrad) ² ·0.1%	$10^8 \sim 10^{11}$ cps/sr	$10^8 \sim 10^{10}$ cps/sr	$10^8 \sim 10^9$ cps/sr
X-ray conversion efficiency (K _α X-ray)		$10^{-4} \sim 10^{-5}$ [7-10]	$10^{-5} \sim 10^{-6}$ [12-14]	$\sim 10^{-6}$ [16,17,this work]
available pulse duration (estimation)	100 fs – 100 ps [3]	200 fs – 2 ps [18]	100 fs – 2 ps [18]	100 fs – 2 ps [18]
cost	extremely high	high	low	low
user-convenience	huge facility limitation of utilities	huge laser system complexity in utility of vacuum	compact laser system complexity in utility of vacuum	compact laser system no vacuum system

Table 1: General comparison of the laser-induced plasma X-ray with low-power femtosecond laser with X-ray from synchrotron and high-power femtosecond laser.

a huge and complex vacuum chamber system; such as target manipulation, target lifetime, and debris emissions. Therefore, a high-intensity X-ray source that can operate in atmospheric pressure (760 torr) with a tabletop laser could be a desirable tool for ultrafast time-resolved measurements. Laser-induced plasma X-ray sources in helium atmospheric condition have been reported, however the X-ray intensity from these sources was quite low.[15] Very recently, J. A. Nees *et al.* has been developed a high intensity X-ray source ($\sim 5 \times 10^9$ cps) in helium atmospheric condition at the high plasma intensity of above 1.0×10^{18} W/cm². [16,17] Nevertheless, the high intensity plasma above 1.0×10^{18} W/cm² would extend the pulse duration of X-ray up to picosecond order.

The plasma intensity generated on the laser focusing spot, is the key parameter for the pulse duration of the laser-induced plasma X-ray. The plasma intensity is calculated with the laser power of a single pulse, its pulse duration and the diameter of focusing spot. As for the pulse duration of pulsed X-ray, computer simulated study has been demonstrated that the pulse duration of X-ray was extended with increase of the laser plasma intensity.[18] At the plasma intensity of 1.0×10^{16} W/cm² and 1.0×10^{18} W/cm², the extension of pulse duration was ~ 100 fs and ~ 1 ps respectively. Therefore, laser-induced plasma source with lower (at most 5.0×10^{16} W/cm²) plasma intensity is required for the time-resolved X-ray diffraction applications. Experimental methods for the pulse duration measurement are the ultrafast streak camera measurement and the pump-probe measurement of ultrafast dynamics. The pulse duration of ultrafast X-ray is directly measured with the streak camera. In the streak camera lights are changed into electrons and the electrons are accelerated and detected with the detector. In this process, the generated electrons have wide-range energy and it makes the pulse duration resolution of streak camera more than a few picoseconds. Thus until now, in order to measure the pulse duration of ultrafast X-ray precisely, it is required to observe the ultrafast change of X-ray diffraction patterns. In Table 1, we summarized the general comparison among the X-ray

from synchrotron and laser-induced plasma X-ray with high power and low power femtosecond laser.

When a high-intensity laser pulse is focused onto a target, at first the pulse changes the surface of the target into near-solid-density plasma by ionization of surface constituents. The absorption process of the laser pulse into the surface materials varies with the intensity of the laser pulse. For plasma intensities in the range $1\lambda^2 < 4 \times 10^{16}$ W $\mu\text{m}^2/\text{cm}^2$, laser-produced plasmas are reported to be absorbed into the target via collisionless processes such as resonant absorption.[19-23] Hot electrons in the produced laser plasma are interacted with the incident laser pulse and are accelerated into the solid target. As the high energy electrons are penetrate into the target material, X-rays are generated via ionization of target material by the high energy electrons or bremsstrahlung. This X-rays are generated when hot electron are on the surface of the target; thus, the pulse duration of the laser-produced X-ray is similar to the incident laser pulse, i.e., several hundred fs. This laser-produced plasma has the potential of a unique, wide range of energy electron and sub-keV to 100 keV range of hard X-ray source.

The generated X-ray intensity is enhanced with prepulse, which produces very weak plasma on the target surface prior to the main pulse.[12,24-27] The mechanism of X-ray intensity enhancement with prepulse is explained by the strong interaction between electrons in the preplasma and the main laser pulse. The prepulse produces weak plasma on the surface of the target and electrons in the plasma are gradually expand from the surface within a distance of more than a few micrometers in the time scale of 10–100 ps. Then, the main pulse enters the plasma and the dispersed electrons are accelerated into the target surface. It has been reported that the X-ray intensity with prepulse enhancement is three to ten times higher than with only a main pulse, and the time separation between prepulse and main pulse is on the order of 10–100 ps.[12,27]

Regarding prepulse, there is an advantage and disadvantage; the advantage is improving the X-ray yield and the disadvantage is the extension of the X-ray pulse duration. The electrons in plasma can expand from the surface to distance of more than 30 μm even in low vacuum pressure of 10 torr. A traveling distance of more than 30 μm from the surface at the speed of light indicates that the pulse duration extension was more than 100fs.

In this study, we demonstrated a compact and high-intensity ultrafast pulsed X-ray source constructed in a helium atmosphere at plasma intensity (effective) of $1.0\text{--}4.0 \times 10^{16} \text{ W}\mu\text{m}^2/\text{cm}^2$. It is possible to reduce the overall size of the X-ray source system without the complexity of a vacuum system. It is also feasible to set a long-lived and large-sized target regardless of the vacuum chamber in air. The samples measured with time-resolved XRD are placed close to the X-ray generating spot without a vacuum system, enabling the efficiently use of the generated X-ray. This vacuum-free X-ray system allows us to avoid the debris problem. At atmospheric pressure, the debris cannot reach the focusing lens or other optics, which are placed some ten millimeters away from the focusing spot. With helium or other gas jet, the debris can be easily collected with a filter.

2. EXPERIMENTAL

Fig. 1 shows the experimental setup for ultrafast pulsed X-ray generation with various prepulse time separations. The mode-locked Ti:sapphire laser generated femtosecond optical pulses of about 100 fs duration with wavelength at 800 nm, and the optical pulses were amplified at about 3.5 mJ/pulse through a regenerative amplifier (Spectra Physics / Model Spitfire Pro XP) with repetition rate of 1 kHz. The laser pulse profile was TEM₀₀ and it was *p*-polarized. The optical pulse had a prepulse which was generated in the regenerative amplifier laser system itself, as leakage through the Pockels cell before the final pulse of the pulse train was switched off. The prepulse contrast to the main pulse was measured to be 8×10^{-4} , and the time separation between the prepulse and main pulse was 20 ns. The influence of the prepulse plasma on X-ray generation is negligible in this time regime of ten nanoseconds prepulse even if the prepulse generates preplasma on the target surface.[12]

The optical pulse generated through the regenerative amplifier was separated by the 1:9 beam splitter. The stronger pulse was changed its polarization by the first $\lambda/2$ waveplate and was reflected in the part of the *s*-polarized pulse by the polarized mirror. The intensity of the main pulse can be varied with this polarized mirror. The main pulse changed its polarization to *p* by the second $\lambda/2$ waveplate and penetrated a polarized beam splitter that reflected the *s*-polarized beam 30% and let the *p*-polarized beam go through. The weaker pulse for inducing

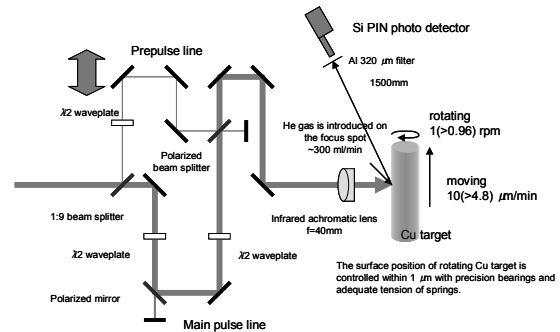


Fig.1: The experimental setup for ultrafast pulsed X-ray generation with various prepulse time separations.

preplasma changed its polarization into *s*, went through an optical delay line, and was reflected by the polarized beam splitter. The main pulse and prepulse were brought in the same line and focused into a rotating copper target with an infrared achromatic lens ($f = 40 \text{ mm}$, N.A. = 0.2). The focusing spot size was 5 μm , which was measured by the crater size of the focusing spot. This spot size was well corresponded to the diffraction limit of this infrared achromatic lens (4.8 μm). The pulse duration of the laser pulse on the surface of copper target was 100 fs. The power of the optical main pulse was 0.06 mJ – 1.46 mJ and the power of prepulse was fixed 0.06 mJ. The copper target was a circular cylinder of 100 mm diameter and 300 mm length. The surface position of rotating copper target was controlled within $\pm 1 \mu\text{m}$ with precision bearings and adequate tension of springs, and was measured with a micrometer during rotation. The copper target rotates at a rate of 1 (> 0.96) rpm, which could be varied in the range 0.24–1 rpm and moves in the axial direction at the rate of 10 (> 5) $\mu\text{m}/\text{min}$, which gives a fresh copper surface with each laser shot. An X-ray generating operation of more than 20 days can be available with this long-life copper target. Near the focus point atmosphere in the Cu target system can be changed between air and helium. The helium gas was introducing with 1/4 inches gas nozzle and the flow rate of helium gas was 500 ml/min. In air, the debris from the target was not deposited on the focusing lens or other optics. We also made same X-ray generation system with Cu target in a vacuum chamber to compare with the X-ray intensity at atmospheric pressure in air and under vacuum (20 mtorr).

The X-ray generated from focusing the laser pulse onto a copper target was measured with a PIN-Si photo detector (Amptek / XR-100CR) which has a 300 μm thick, 7 mm² square silicon sensor. The detection efficiency of this PIN-Si photo detector is approximately 100% for an 8 keV X-ray. The detector was sealed with 25 μm thickness Be window through which 8 keV X-ray passes without any losses. A spectroscopy amplifier (CANBERRA / 2022 Spectroscopy Amplifier) was used to amplify the signal, which

was tallied up with a multichannel analyzer (SEIKO EG&G / TRUMP-MCA-2k). The detector was placed 1500 mm away from the focusing spot at an angle of 60° . In a vacuum condition, the X-ray went through 3 mm in vacuum and 1497mm in air. In helium atmosphere or in vacuum conditions, a thin aluminum filter of $320 \mu\text{m}$ was placed before the detector. This filter reduces the X-ray intensity to 1.72% for a Cu $K\alpha$ X-ray. The long distance between the X-ray focusing spot and the detector and the Al filter allowed us to measure the X-ray photons as a Poisson distribution single photon counting. Two different photons cannot be detected at once in the order of 1 millisecond using a Si photo detector and multichannel analyzer. If more than one photon is in the same detecting time, the total energy of the photons will be measured with the Si photo detector. In any conditions, it took 40 s to obtain each X-ray spectrum.

3. RESULTS AND DISCUSSION

The typical X-ray spectrum obtained with the Si-PIN photo detector is shown in Figure 2. The dashed line with square symbols is the X-ray spectrum measured with the Si-PIN photo detector. The X-ray generated on the focusing spot went through 1500 mm air and $320 \mu\text{m}$ Al filter (in He atmosphere or in vacuum condition), thus the X-ray intensity were reduced depending on their energy to obtain the single photon counting. The solid line with circle symbols was calculated X-ray spectrum. X-ray radiation from p -polarized laser is regarded as isotropic radiation.[28] As shown by the solid line of Figure 2, the strong Cu $K\alpha$ X-ray line (8.05 keV), $K\beta$ X-ray line (8.91 keV) and a small part of the bremsstrahlung X-ray were found in the energy range of several keV.

In Figure 3, the $K\alpha$ intensity was plotted as a function of the plasma intensity in various atmospheric conditions. The plasma intensity was varied from 1.5×10^{15} – $4.0 \times 10^{16} \text{ W}\mu\text{m}^2/\text{cm}^2$ to change the incident laser pulse energy in the range 0.06–1.46 mJ/pulse by rotating the first $\lambda/2$ waveplate of the main pulse line in Figure 1. At this plasma energy, the laser absorption process into the target is collisionless. The polarized mirror in the main pulse line lets p -polarized light pass through and s -polarized light be reflected. In this condition, the prepulse line was blocked and the influence of the preplasma was negligible. We obtained high intensity Cu $K\alpha$ X-rays with 2.6 – 5.4×10^9 photons/sr/s above the plasma intensity of $2.0 \times 10^{16} \text{ W}\mu\text{m}^2/\text{cm}^2$ in He atmosphere. This intensity was more than 60 times that in air, and close to the intensity of 1.2 – 1.8×10^{10} photons/sr/s obtained in vacuum. Generally, a value of at least several 10^8 cps/sr characteristic X-ray is required for time-resolved XRD or other applications. In Figure 3, the horizontal dashed line shows the X-ray intensity of 1.0×10^9 cps/sr. We obtained an intensity of 5.4×10^9 cps/sr in helium atmosphere, which is

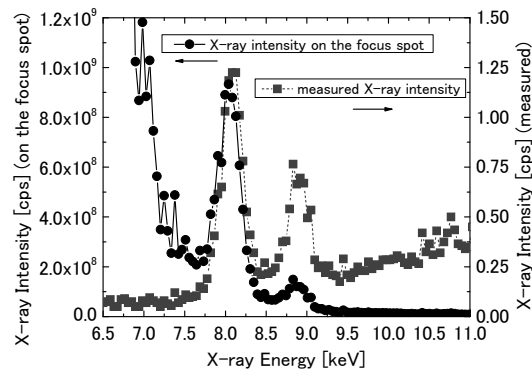


Fig.2: Typical X-ray spectrum. The dashed line with square symbols is measured X-ray spectrum with Si-PIN photo detector, and the solid line with circle symbols is the X-ray spectrum calculated from the X-ray intensity reduction by the air layer and Al filter.

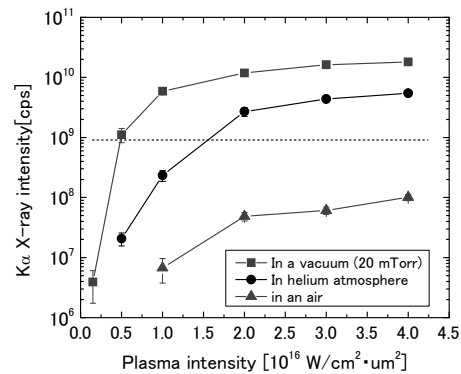


Fig.3: $K\alpha$ X-ray intensity in various atmospheres; solid line with square: vacuum (20 mtorr), solid line with circles: in helium, solid line with triangle: in air

sufficiently high for time-resolved X-ray measurements.

The relationship between X-ray intensity and the condition of the atmosphere can be approximately explained with the mean free path of electrons according to the collision model of diatomic molecules.[29] The electrons in the plasma produced by the incident laser pulse expand several micrometers. If the electrons collide with the atoms/molecules of the atmosphere gas and lose their energy before or during acceleration with the incident pulse, the electrons can not reach the surface of the target and also cannot produce X-rays. In this collision model of diatomic molecules, the number of electrons decreases exponentially as the electrons move in the atmosphere. Thus, the X-ray intensity can be expressed by the equation $I = I_0 \exp(-A/\lambda)$. Here, I_0 is the intensity of the X-ray generated on the target, I is the intensity of the measured X-ray in the atmosphere, and A and λ are the traveling

length and electron mean free path in the atmosphere, respectively. In this focusing condition, electrons travel with the velocity of the light about $1.47 \mu\text{m}$ in atmosphere gases; A is $1.47 \mu\text{m}$. [29] The electron mean free path in vacuum conditions (20 mtorr) is 13 mm and I/I_0 is 100% without any loss of diatomic molecules in this collision model, while the electron mean free path in helium is $1.01 \mu\text{m}$ and $0.34 \mu\text{m}$ in air. Therefore, the intensity ratio I/I_0 is about 30% in helium and 1% in air. The X-ray intensity that can be obtained in air is only 1% of that in vacuum, i.e., $1.2\text{--}1.8 \times 10^{10}$ cps/sr. This means that $K\alpha$ X-ray intensity of at most 1.8×10^8 cps/sr can be obtained in air which is smaller than several 10^8 cps/sr and quite difficult to use for the time-resolved X-ray measurements. The $K\alpha$ X-ray intensity observed in a helium atmosphere was $2.6\text{--}5.4 \times 10^9$ cps/sr, which is about 30% of $1.2\text{--}1.8 \times 10^{10}$ cps/sr measured in a vacuum. This intensity is sufficiently high for the required intensity of several 10^8 cps/sr. Thus, it is possible to utilize the $K\alpha$ X-ray generated at atmospheric pressure in helium for the time-resolved XRD or other applications.

X-ray intensity can be enhanced with prepulse plasma because of the strong coupling between the laser pulse and preplasma generated with prepulse. The intensity of preplasma was $1.6 \times 10^{15} \text{W}\mu\text{m}^2/\text{cm}^2$ which was 4-8% of the main plasma power between $2.0 \times 10^{16} \text{W}\mu\text{m}^2/\text{cm}^2$ and $4.0 \times 10^{16} \text{W}\mu\text{m}^2/\text{cm}^2$, and the separation time between the prepulse and the main pulse was 5 ps. Above the plasma intensity of $2.0 \times 10^{16} \text{W}\mu\text{m}^2/\text{cm}^2$, the obtained X-ray intensities with prepulse were 1.3 times higher in helium and 2.0 times higher in air. The $K\alpha$ X-ray intensity obtained in helium with prepulse was 7.7×10^9 cps/sr, which was 40% of the yield in a vacuum without prepulse. In a vacuum, the $K\alpha$ X-ray intensity with prepulse enhancement has been reported to be three to ten times higher than with the main pulse only. [12,27] The prepulse enhancement effect of $K\alpha$ X-ray intensity in a helium atmosphere was smaller than that in a vacuum. At plasma intensity of $3.0 \times 10^{16} \text{W}\mu\text{m}^2/\text{cm}^2$ in helium at atmospheric pressure, the X-ray intensity with prepulse in helium was almost constant for any separation time during 1-50 ps. However, the prepulse enhancement in vacuum was reported to be higher and to have a peak in the function of the pulse separation time in the range of 30-50 ps. [12,27]

This result can be also explained with collision of diatomic molecules. In vacuum conditions, electrons generated by preplasma can expand from a few to several micrometers from the target surface because of the electron mean free path of below 1 mm to 100 mm. Then, the electrons in preplasma can be accelerated by the main pulse and produce X-rays. However, in helium at atmosphere pressure, the electrons in preplasma can travel only 1-2 μm from the surface because the electron mean free path is $1.01 \mu\text{m}$. Almost

all electrons in the preplasma interact with helium atoms and lose their energy. A small amount of electrons with very slow velocity remain in the near-surface region of the target and can be accelerated with the main pulse. These electrons produce the X-ray with a prepulse enhancement value of 1.3. Even though a prepulse enhancement of 1.3 times was observed in helium at atmospheric pressure, it is better to construct the X-ray generation systems without prepulse line. As shown in Figure 1, there are some optical loss for building the prepulse line: 10% loss by the 1:9 beam splitter, 10% loss by the polarized beam splitter, and a few percents loss by the additional mirrors required to let the main pulse and prepulse pass through the same line. The total loss from constructing such a complex main pulse and prepulse line amounts to more than 30%. Thus, by removing the prepulse line and increasing the main laser power, an X-ray intensity 1.3 times higher than without prepulse with plasma power of $4.0 \times 10^{16} \text{W}\mu\text{m}^2/\text{cm}^2$ can be obtained in helium at atmospheric pressure.

Above the plasma intensity of $2.0 \times 10^{16} \text{W}\mu\text{m}^2/\text{cm}^2$, the $K\alpha$ X-ray conversion efficiency calculated from the X-ray intensity and incident pulse energy in helium at atmospheric pressure was $5.0 (\pm 0.2) \times 10^{-6}$, a value 60 times higher than that in air (8.2×10^{-8}) and close to the value in a vacuum ($1.8\text{--}2.1 \times 10^{-5}$). A $K\alpha$ conversion efficiency of 10^{-6} to 10^{-5} is also need to obtain X-ray intensity of more than several 10^8 cps required for time-resolved XRD. However, in air the $K\alpha$ X-ray intensity or conversion efficiency was quite low; in helium at atmospheric pressure, the $K\alpha$ X-ray intensity and conversion efficiency achieved the value of 5.4×10^9 cps and 5.0×10^{-6} , which are sufficiently high for time-resolved XRD or other X-ray applications. This vacuum-free, compact and easy-to-access X-ray generation system can be operated in helium at atmospheric pressure. The conversion efficiency obtained by other groups using high repetition millijoule or submillijoule laser has been reported to be about $4.6 \times 10^{-6}\text{--}3.2 \times 10^{-5}$. [12-14] in vacuum conditions and $\sim 5.0 \times 10^{-6}$ in helium atmospheric conditions. The $K\alpha$ X-ray intensity obtained in helium at atmospheric pressure was also of the same order as the other works using high repetition millijoule or submillijoule laser in vacuum conditions. Thus this compactly designed high-intensity $K\alpha$ X-ray source that can operate at atmospheric pressure without using a large and complex vacuum chamber can be a useful and promising tool for the time-resolved XRD or other radiographic applications.

4. CONCLUSION

High intensity $K\alpha$ X-ray generation at a high repetition was demonstrated with tabletop commercial ultrafast laser system in helium at atmospheric pressure. Millijoule, 100 fs laser pulses were focused onto a well-controlled Cu

surface at intensities of 5×10^{15} to 4×10^{16} $W\mu m^2/cm^2$. The intensity of the generated $K\alpha$ X-ray in helium at atmospheric pressure was 5.4×10^9 cps/sr with 1 kHz repetition rate and conversion efficiency of 5.0×10^{-6} . This X-ray intensity is close to that obtained in vacuum condition and is high enough for the time-resolved XRD or other X-ray applications. The $K\alpha$ X-ray intensity was enhanced with 4–8% prepulse plasma into 7.7×10^9 cps/sr and 6.8×10^{-6} conversion efficiency. Regarding the prepulse, it would be better to construct a simpler X-ray generation system without the prepulse line because of the optical losses in the system. Such a high-intensity, vacuum-free femtosecond X-ray source with a tabletop laser could be a promising tool for the time-resolved XRD or other radiographic applications.

ACKNOWLEDGEMENTS

This work is partially supported by the JST, CREST. We would like to thank Dr. T. Aoki, Dr. T. Seki, Dr. S. Ninomiya, Mr. K. Ichiki, Mr. H. Yamada, Mr. Y. Yamamoto, Mr. T. Yamanobe, Mr. Y. Wakamatsu and Ms S. Ibuki from Kyoto University for discussing X-ray generation systems.

REFERENCES

- [1] C. Rose-Petruck, R. Jimenez, T. Guo, A. Cavalleri, C. W. Siders, F. Raksi, J. A. Squier, B. C. Walker, K. R. Wilson, C. P. J. Barty, *Nature (London)* **398**, 310-312 (1999).
- [2] K. Sokolowski-Tinten, C. Blome, J. Blums, A. Cavalleri, C. Dietrich, A. Tarasevitch, I. Uschmann, E. Forster, M. Kammler, M. Horn-von-Hoegen, D. von der Linde, *Nature (London)* **422**, 287-289 (2003).
- [3] A. M. Lindenberg, J. Larsson, K. Sokolowski-Tinten, K. J. Gaffney, C. Blome, O. Synnergren, J. Sheppard, C. Caleman, A. G. MacPhee, D. Weinstein, D. P. Lowney, T. K. Allison, T. Matthews, R. W. Falcone, A. L. Cavalieri, D. M. Fritz, S. H. Lee, P. H. Bucksbaum, D. A. Reis, J. Rudati, P. H. Fuoss, C. C. Kao, D. P. Siddons, R. Pahl, J. Als-Nielsen, S. Duesterer, R. Ischebeck, H. Schlarb, H. Schulte-Schrepping, Th. Tschentscher, J. Schneider, D. von der Linde, O. Hignette, F. Sette, H. N. Chapman, R. W. Lee, T. N. Hansen, S. Techert, J. S. Wark, M. Bergh, G. Huldt, D. van der Spoel, N. Timneanu, J. Hajdu, R. A. Akre, E. Bong, P. Krejcik, J. Arthur, S. Brennan, K. Luening, J. B. Hastings, *Science* **308**, 392-395 (2005).
- [4] D. M. Fritz, D. A. Reis, B. Adams, R. A. Akre, J. Arthur, C. Blome, P. H. Bucksbaum, A. L. Cavalieri, S. Engemann, S. Fahy, R. W. Falcone, P. H. Fuoss, K. J. Gaffney, M. J. George, J. Hajdu, M. P. Hertlein, P. B. Hillyard, M. Horn-von-Hoegen, M. Kammler, J. Kaspar, R. Kienberger, P. Krejcik, S. H. Lee, A. M. Lindenberg, B. McFarland, D. Meyer, T. Montagne, É. D. Murray, A. J. Nelson, M. Nicoul, R. Pahl, J. Rudati, H. Schlarb, D. P. Siddons, K. Sokolowski-Tinten, Th. Tschentscher, D. von der Linde, J. B. Hastings, *Science* **315**, 633-636 (2007).
- [5] P. Lucas, S. Webber, Eds. (IEEE, Piscataway, NJ, 2003), p. 423-425.
- [6] R. Service, *Science* **298**, 1356-1368 (2002).
- [7] M. Yoshida, Y. Fujimoto, Y. Hironaka, K.G. Nakamura, K. Kondo, M. Ohtani, H. Tsunemi: *Appl. Phys. Lett.* **73**, 2393-2395 (1998).
- [8] E.C. Eder, G. Pretzler, E. Fill, K. Eidmann, A. Saemann: *Appl. Phys. B70*, 211-217 (2000).
- [9] E. Fill, J. Bayerl, R. Tommasini: *Rev. Sci. Instrum.* **73**, 2190-2192 (2002).
- [10] C.W. Siders, A. Cavalleri, K. Sokolowski-Tinten, T. Guo, C. Töth, R. Jimenez, C. Rose-Petruck, M. Kammler, M. Horn von Hoegen, D. von der Linde, K.R. Wilson, C.P.J. Barty: *SPIE Proc.* **3776**, 302-311 (1999).
- [11] K. Sokolowski-Tinten, D. von der Linde, *J. Phys.: Condens. Matter* **16** R1517-1536 (2004)
- [12] C.L. Rettig, W.M. Roquemore, J.R. Gord, *Appl. Phys. B93* 365-372 (2008).
- [13] M. Hagedorn, J. Kutzner, G. Tsilimis, H. Zacharias, *Appl. Phys. B77* 49-57 (2003).
- [14] C. G. Serbanescu, J. A. Chakera, and R. Fedosejevs, *Rev. Sci. Instruments* **78**, 103502 (2007).
- [15] Y. Jiang, T. Lee, W. Li, G. Ketwaroo, and C. G. Rose-Petruck, *J. Opt. Soc. Am. B* **20**, 229-237 (2003).
- [16] B. Hou, J. Easter, K. Krushelnick, and J. A. Nees, *Appl. Phys. Lett.* **92**, 161501 (2008).
- [17] B. Hou, J. Easter, A. Mordovanakis, K. Krushelnick, and J. A. Nees, *Opt. Express* **16**, 17695 (2008).
- [18] Ch. Reich, P. Gibbon, I. Uschmann, and E. Förster, *Phys. Rev. Lett.* **84**, 4846-4849 (2000).
- [19] K. Eidmann, J. Meyer-ter-Vehn, T. Schlegel, and S. Hüller, *Phys. Rev. E* **62**, 1202-1214 (2000).
- [20] R. Fedosejevs, R. Ottmann, R. Sigel, G. Kühnle, S. Szatmari, and F. P. Schäfer, *Phys. Rev. Lett.* **64**, 1250-1253 (1990).
- [21] D. F. Price, R. M. More, R. S. Walling, G. Guethlein, R. L. Shepherd, R.E. Stewart, and W. E. White, *Phys. Rev. Lett.* **75**, 252-255 (1995).
- [22] D. W. Forslund, J. M. Kindel, and K. Lee, *Phys. Rev. Lett.* **39**, 284-288 (1977).
- [23] P. Gibbon and E. Förster, *Plasma Phys. Controlled Fusion* **38**, 769-793 (1996).
- [24] D. Kuhike, U. Herpers, D. von der Linde, *Appl. Phys. Lett.* **50**, 1785-1787 (1987).
- [25] O. R. Wood, W. T. Silfvast, H. W. K. Tom, W. H. Knox, R. L. Fork, C. H. Brito-Cruz, M. C. Downer, P. J. Maloney, *Appl Phys. Lett.* **53**, 654-656 (1988).
- [26] H. Nakano, T. Nishikawa, H. Ahn, and N. Uesugi, *Appl. Phys. Lett.* **69**, 2992-2994 (1996).
- [27] J. Kutzner, M. Sillies, T. Witting, G. Tsilimis, H. Zacharias, *Appl. Phys. B78*, 949-955 (2004).
- [28] Y. Hironaka, K.G. Nakamura, K. Kondo, *Appl. Phys. Lett.* **77** 4110-4111 (2000).
- [29] M. Hada, J. Matsuo, submitting to *Appl. Phys. B*

(Received July 14, 2009; Accepted August 22, 2009)

Measurement of crystallization temperature of Pd-based amorphous alloy thin film by energy dispersive X-ray reflectometry

Tokujiro Yamamoto, Kouichi Hayashi, Kosuke Suzuki*, Masahisa Ito**, Hisamichi Kimura and Akihisa Inoue***

Institute for Materials Research, Tohoku University, Sendai 980-8577, Japan

Fax: 81-22-215-2159, e-mail: toku@imr.tohoku.ac.jp

*Graduate student, Department of Engineering, Gunma University, Kiryu 376-8515, Japan

**Department of Engineering, Gunma University, Kiryu 376-8515, Japan

***Tohoku University, Sendai 980-8577, Japan

X-ray reflectivity of a Pd-based amorphous alloy thin film was measured by an energy dispersive method in the vicinity of crystallization temperature upon heating. A large number of oscillations of X-ray reflectivity were clearly observed, because the surface of the amorphous alloy thin film is extraordinary smooth. The oscillations of X-ray reflection became smaller after crystallization of the film, as the surface roughness of the film is increased by grain boundaries. Thickness of the film estimated from the distance between the peaks of the oscillations was decreased when the film was heated to higher temperature than 140 °C. It is considered that the crystallization temperature of the Pd-based amorphous alloy thin film is about 140 °C.

Key words: amorphous alloy thin film, X-ray reflectivity, crystallization

1. INTRODUCTION

Amorphous alloys possess various attractive properties for structural materials, such as high strength, soft magnetism and corrosion resistance. Because of those excellent properties, amorphous alloy thin films are promising for micro/nano-electro mechanical systems (MEMS/NEMS). In order to use amorphous alloy thin films for MEMS/NEMS devices, measuring crystallization temperature (T_x) of the films is important. For amorphous thick films, whose thickness is larger than several micron-meter, it is able to measure T_x by using the conventional thermal analysis, e.g. differential scanning calorimetry (DSC) or thermal mechanical analysis (TMA), as same as bulky amorphous specimens. However, it is difficult to measure T_x by those thermal analytical methods for thin films. It is considered that measuring resistance of the film upon heating is one of the traditional methods to determine T_x of amorphous thin films. But electronic current flows only on the surface of the thin films, thus it is necessary to develop a new method to measure T_x of amorphous alloy thin films. In the present study, the thickness of a Pd-based amorphous alloy thin film was examined upon heating by means of energy dispersive X-ray reflectivity measurement.

2. EXPERIMENTAL PROCEDURES

Pd-based amorphous alloy ribbons were prepared by melt-spinning using a Cu single roll, and T_x of the ribbons was measured by means of DSC, which is one of the conventional thermal analytical methods, at a heating rate of 40 K/min. An amorphous alloy thin film was deposited on glass substrate in vacuum by heating alloy ingots. The thickness of the film was measured by using a surface profilometer using a stylus. The

as-prepared ribbons and thin film are amorphous, as no sharp diffraction peaks are found in their X-ray diffraction (XRD) patterns. In-situ measurement of energy dispersive X-ray reflectivity of the film on heating in a N_2 gas flow was performed by using white X-ray and a pure Ge type solid state detector (SSD) at BL-3C in Photon Factory, KEK. The grazing incidence angle and reflection angle were fixed at 0.2° and 0.4°, respectively. The cross sections of the incident and reflected X-ray are $50 \times 120 \mu m^2$ and $25 \times 50 \mu m^2$, respectively. X-ray reflectivity was measured for 8 s every 10 s. The film was crystallized during the in-situ X-ray reflectivity measurement, because diffraction peaks from crystalline phases are found in an XRD pattern recorded after the reflectivity measurement.

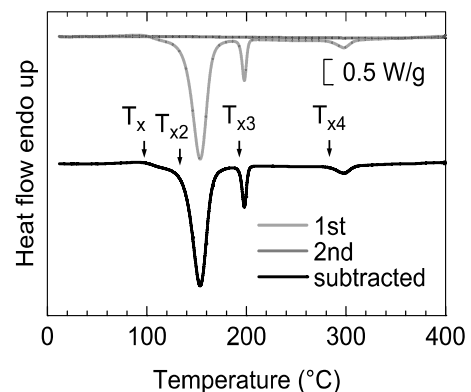


Fig. 1 DSC traces of the Pd-based amorphous melt-spun ribbons measured at a heating rate of 40 K/min.

3. RESULTS AND DISCUSSION

Fig. 1 shows the DSC traces of the Pd-based amorphous alloy ribbons. Exothermic peaks were observed at different four temperatures. Among them, the first exothermic peak is associated with crystallization. Thus, T_x is 99 °C. The peak temperature of the largest exothermic heat flow is 154 °C. It was revealed by EPMA that the difference of the composition between the Pd-based amorphous ribbons and thin film is within about 5 atomic percent. The thickness of the thin film measured by the surface profilometer is about 120 nm.

Fig. 2 shows the X-ray reflectivity measured in the present study. The white X-ray spectrum for BL-3C was measured with Al attenuator whose thickness is 10 mm and is also shown in Fig. 3. The specimen was heated up at a heating rate of 10 – 20 K/min. The profile of oscillations of the reflectivity changes at about 25 keV, corresponding to Pd L-edge absorption. The oscillations are clearly observed even though the photon energy is high at lower temperature than about 140 °C. However, they become faint for higher photon energy region, with increasing temperature. As Albertini et al. [1] mentioned, the thickness of the thin film can be estimated from the distance of scattering parameter between the peaks of the oscillations, Δq . Scattering parameter, q , is defined as

$$q = \frac{4\pi \sin \theta}{\lambda}$$

where θ is the grazing incidence angle and λ is the wavelength of X-ray photons having energy E . The relationship between E and λ is

$$E = h \frac{c}{\lambda}$$

where h is Planck's constant and c is the speed of light. The thickness, d , of the thin film is obtained as

$$d = \frac{2\pi}{\Delta q}$$

In the present study, the energy resolution of the SSD used is 48 eV. When the energy distance of the peak of the oscillations is 1500 eV or 1548 eV, the film thickness is 118.4 nm or 114.7 nm. Thus, spatial resolution is 3.7 nm.

Fig. 4 shows the calculated film thickness as a function of temperature for the oscillations whose photon energy is higher than Pd L-edge. The film thickness was 130 nm approximately when the temperature was lower than 140 °C, while it was about 127 nm for higher temperature than 140 °C. It seems that this change in the film thickness is discrete. The decrease in the film thickness upon heating means increase in the density of the film. Therefore, it is considered that the discrete change in the film thickness was caused by crystallization and that the crystallization temperature is about 140 °C.

As shown in Fig. 1, T_x of the Pd-based amorphous alloys used in the present study is 99 °C and is 40 K lower than the crystallization temperature measured by X-ray reflectivity. However, this difference is reasonable, because the temperature of the film was not monitored at the same place where the incident white X-ray is irradiated and because the composition of the film is not exactly the same with that of the ribbons. For more precise analysis of the reflectivity, calculation of the profiles of energy dispersive X-ray reflectivity should be

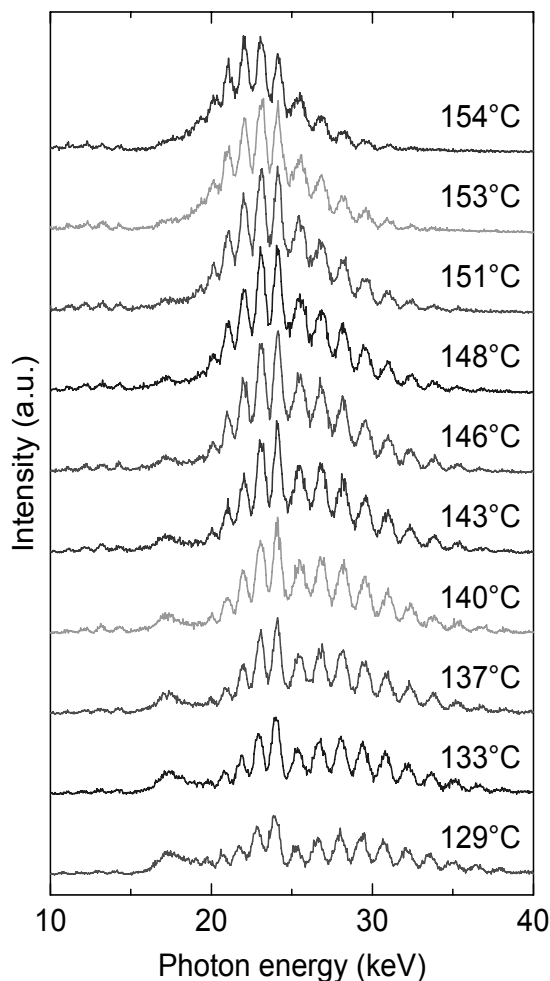


Fig. 2 Energy dispersive X-ray reflectivity of the Pd-based amorphous alloy thin film upon heating. The profiles were measured every 10 s. The grazing incident angle was fixed to 0.2°.

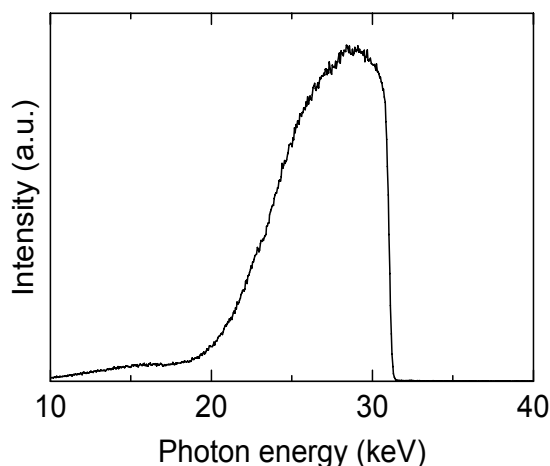


Fig. 3 White X-ray spectrum measured using Al plate which is 10 mm in thickness.

carried out by using a model proposed by Albertini et al. [1] in order to determine the film thickness.

4. CONCLUSIONS

Measurement of crystallization temperature of the Pd-based amorphous alloy thin film was demonstrated by energy dispersive X-ray reflectivity upon heating using white X-ray and SSD. The thickness of the Pd-based amorphous alloy thin film was decreased with increasing temperature. The crystallization temperature of the Pd-based amorphous alloy thin film was about 140 °C.

5. ACKNOWLEDGMENTS

The authors also thank Mr. Saito and Mr. Murakami for their surface profilometer and EPMA operation, respectively. Part of this work was carried out at COE Laboratory, IMR, TU. Part of this work was also carried out by using several equipments supported by Research and Development Project on Advanced Metallic Glasses, Inorganic Materials and Joining Technology, IMR, TU. Part of this work was carried out at BL-3C in Photon Factory, KEK (Proposal No. 2006G278 and 2008G569).

REFERENCE

[1] V. Rossi Albertini, B. Paci and A. Generosi, *J. Phys. D: Appl. Phys.*, **39**, R461-R486 (2006).

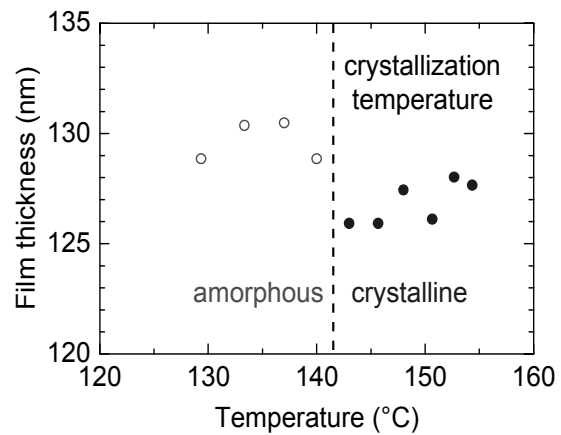


Fig. 4 The film thickness as a function of temperature.

(Received July 14, 2009; Accepted August 31, 2009)

X-ray specular and off-specular reflection from a protein adsorbed at a liquid surface

Yohko F. Yano¹, Tomoya Uruga², Hajime Tanida², Hidenori Toyokawa²,
Yasuko Terada², Masafumi Takagaki², and Hironari Yamada³

¹Research organization of Science & Engineering, Ritsumeikan University,
1-1-1 Noji-Higashi, Kusatsu-shi, Shiga, 525-8577 Japan
Fax: 81-77-561-2680, e-mail: y-yano@fc.ritsumei.ac.jp

²Japan Synchrotron Radiation Research Institute, 1-1-1 Kouto, Sayo, Hyogo 679-5198 Japan

³Department of Photonics, Ritsumeikan University

X-ray specular and off-specular reflection was investigated to analyze the out-of-plane and in-plane structures of a globular protein adsorbed at an air/water interface in the presence of a salt. The x-ray reflectivity was used to obtain the electron density profile normal to the surface. The electron density profile indicates the presence of a double layer consisting of a lower-density lysozyme layer below a densely packed top layer. From the off-specular diffuse scattering, the protein layer could be well described by a simple exponentially decaying height–height correlation function with a correlation length of 500 Å. This suggests that the protein molecules aggregate and form islands on the water surface. A simple formula for describing the off-specular excess scattering above the capillary wave fluctuation was proposed to explain the lateral fluctuation of an inhomogeneous layer above a liquid surface.

Key words: x-ray reflectivity, off-specular diffuse scattering, PILATUS, air/water interface, lysozyme

1. INTRODUCTION

X-ray reflection is a powerful tool for investigating the structure of buried interfaces. It can be used to obtain the density profile normal to the surface with a subnanometer spatial resolution. By carefully examining diffuse scattering in the vicinity of specular reflection peaks, structural information parallel to the surface, namely the height–height correlation function, can also be obtained [1].

The surface morphology of liquid surfaces is governed by thermally excited capillary waves with molecular-size amplitudes and micrometer-order wavelengths [2]. Sinha *et al.* have theoretically demonstrated that diffuse scattering from liquid surfaces diverges algebraically at the specular reflection angle, creating large tails that extend into the surrounding off-specular region [3]. This theoretical prediction has been verified experimentally for simple molecular liquids [4–8] and liquid metals [7–10]. In contrast, scattering that exceeds the predicted capillary contribution has been observed for Langmuir monolayers on a water surface [11–14]. Fukuto *et al.* proposed a sum rule for scattering from an inhomogeneous layer on a liquid surface [12]. They used a simple exponentially decaying correlation function to describe the height–height correlation function of a Langmuir monolayer and they derived the correlation length and the surface roughness.

However, x-ray off-specular diffuse scattering measurements have been less popular than x-ray reflectivity measurements for the following reasons:

1. A system with a high angular resolution is necessary to detect the diffuse scattering intensity.
2. The scattered intensity is much weaker than the

x-ray reflection.

3. The structural information is derived using a complicated fitting procedure and is rather ambiguous.

We recently developed a liquid interface reflectometer at SPring-8 [15, 16]. This reflectometer is equipped with a two-dimensional single x-ray photon counting pixel array detector (PILATUS) and can achieve an x-ray reflectivity of nearly 10^{-9} with an integration time of only 1 s at each angle, exhibiting enormous potential for rapid measurements. Previously, time-resolved measurements with a time resolution of 3 min were performed for the adsorption of a globular protein on an air/water interface [17].

In the present study, we exploit the advantages of the two-dimensional PILATUS detector to investigate both the x-ray specular reflection and the off-specular diffuse scattering intensities to analyze the out-of-plane and in-plane structures of a globular protein (lysozyme) adsorbed at an air/water interface. We also propose a simple formula for describing the diffuse scattering from an inhomogeneous protein layer on a water surface.

2. GRAZING INCIDENCE X-RAY SCATTERING TECHNIQUES

2.1 Liquid interface reflectometer

X-ray reflectivity measurements were performed using a liquid interface reflectometer developed at the BL37XU beamline of SPring-8 [15, 16]. Brilliant undulator radiation at 15 keV ($\lambda = 0.826$ Å) was used as the x-ray source; it had horizontal beam width of 50 μm . A single x-ray photon counting pixel detector, PILATUS [18, 19], with an area of 487×195 pixels (172 $\mu\text{m}/\text{pixel}$) was located 538 mm from the center of the sample. The

integration time at each incident angle was 1 s. Each pixel of PILATUS contains a charge-sensitive amplifier, a shaper amplifier, a single level discriminator and a 20 bit counter. The counting rate capability depends on the time constant of shaper amplifier, which is about 100 nsec in this experimental setup. This condition allows to detect up to 10^5 counts/pixel/s within the dead time of 1%. A set of aluminum sheets with a thickness in the range 1–6 mm was employed as an attenuator at the incident angle $\alpha < 0.9^\circ$ to prevent the counting rate exceeding 10^5 counts/pixel/s. The scattering geometry is illustrated in Fig. 1. The incident wave vector \mathbf{k}_{in} strikes the liquid surface at an incident angle α . The scattered x-rays are characterized by the output wave vector \mathbf{k}_{out} , which makes an angle β to the surface and an angle 2θ to the plane of incidence. The Cartesian components of the wave vector transfer $\mathbf{q} = \mathbf{k}_{\text{out}} - \mathbf{k}_{\text{in}}$ are defined as:

$$\begin{aligned} q_z &= k[\sin(\alpha) + \sin(\beta)] \\ q_x &= k \cos(\beta) \sin(2\theta) \\ q_y &= k[\cos(\beta) \cos(2\theta) - \cos(\alpha)] \end{aligned} \quad (1)$$

where $k = 2\pi/\lambda$. The typical FWHMs of the reflection profile at the incident angle α of 0.01° projected on the detector are 1.5 pixels horizontally (i.e., parallel to the x-axis) and 2.0 pixels vertically (i.e., parallel to the z-axis), which are related to reciprocal-space resolutions through $\Delta q_x \sim k \Delta(2\theta)$ and $\Delta q_z \sim k \sin(\beta) \Delta\beta$.

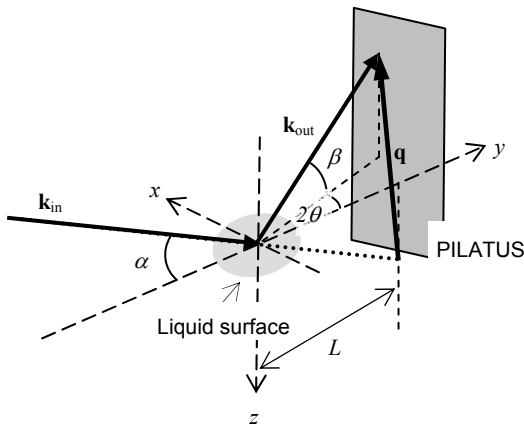


Fig. 1 X-ray scattering geometry. Incident wave vector \mathbf{k}_{in} strikes the liquid surface at an incident angle α . The scattered x-rays are characterized by the output wave vector \mathbf{k}_{out} , which makes an angle β to the surface and an angle 2θ to the plane of incidence. The scattering intensity is detected by PILATUS, which is located $L = 538$ mm from the center of the liquid surface.

2.2 X-ray specular reflectivity

In the specular reflection condition, the reflectivity is measured as a function of q_z when $q_x = q_y = 0$, or equivalently $\beta = \alpha$ and $2\theta = 0$. Figure 2 shows a typical image around a reflection peak detected by PILATUS. Since this reflection peak was detected over five pixels horizontally, we considered the intensity measured five pixels from the center of the peak to be background. A reflection profile $I(z)$ was obtained by summing the signal intensities and subtracting the background as:

$$\frac{I(z)}{I_0} = \frac{1}{I_0} \left\{ \sum_{|x| \leq 3} I(z, x) - \frac{1}{2} [I(z, x = -5) + I(z, x = +5)] \right\} \quad (2)$$

The total signal intensity corresponding to the first term in Eq. (2) and the background corresponding to the second and third terms are shown in Fig. 3. The reflection profile over a range of four orders of magnitudes was obtained after the background subtraction.

The reflectivity is calculated by summing the reflection profiles around the peak region of 13 pixels and normalizing this value with the intensity of the incident beam, which was monitored using an ionization chamber [15].

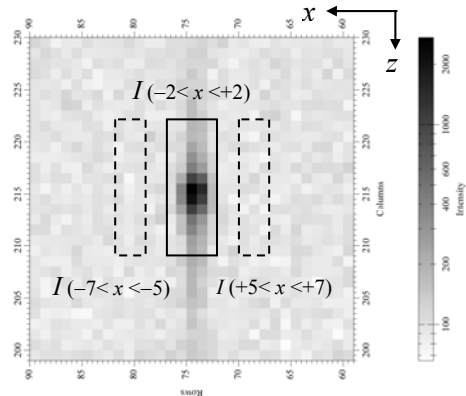


Fig. 2 Enlarge picture of an x-ray specular reflection image on PILATUS. Each square corresponds to a pixel with dimensions of $172 \mu\text{m} \times 172 \mu\text{m}$.

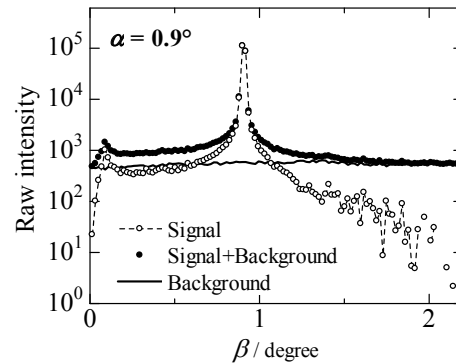


Fig. 3 Integrated signal, integrated background and integrated signal plus background for a reflection profile at $\alpha = 0.9^\circ$.

The x-ray specular reflectivity for liquid surfaces is described by the Born approximation [7, 20]:

$$R(q_z) = R_F |\Phi(q_z)|^2 CW(q_z, T, \gamma) \quad (3)$$

where R_F is the Fresnel reflectivity for an ideally flat interface and $|\Phi(q_z)|^2$ is the intrinsic structure factor normal to the surface, which is expressed as:

$$|\Phi(q_z)|^2 = \left| \frac{1}{\rho^{\text{Bulk}}} \int dz \frac{\partial \langle \rho(z) \rangle_{xy}}{\partial z} e^{iq_z z} \right|^2 \quad (4)$$

where $\langle \rho(z) \rangle_{xy}$ is the lateral average electron density profile. $CW(q_z, T, \gamma)$ is the surface roughness term due to capillary waves and is given by:

$$CW(q_z, T, \gamma) = \exp(-\sigma_{cw}^2 q_z^2), \quad (5)$$

with

$$\sigma_{cw}^2 = \left(\frac{k_B T}{2\pi\gamma} \right) \ln \left(\frac{q_{\max}}{\Delta q_y} \right),$$

where γ is the surface tension, q_{\max} is the upper cutoff for capillary contributions, which is determined by the condition that the number of capillary wave modes is of the order of the number of molecules per unit surface area; this is equivalent to fixing $q_{\max} \sim 2\pi/d$, where d is on the order of the intermolecular distance. Δq_y is the instrumental resolution of $\Delta q_y \sim k \sin(\beta) \Delta\beta$, where $\Delta\beta$ is related to the number of pixels summed to calculate the reflectivity as $13 \text{ pixels} \times 0.172 \text{ mm/pixel} / 538 \text{ mm}$.

2.3 X-ray off-specular diffuse scattering

In off-specular diffuse scattering, the scattering intensity is measured at non-specular conditions: $\alpha \neq \beta$, or equivalently $q_x, q_y \neq 0$. A β -scan method, in which the scattered intensity is measured as a function of β at constant α has typically been conducted independently of x-ray reflectivity measurements. In the present study, we used the reflection profile normalizing with the peak intensity of the reflection profile at the incident angle α of 0.01° , which was assumed to be equivalent of the incident beam intensity I_0 , as the off-specular diffuse scattering intensity.

The normalized intensity I/I_0 is generally equal to the convolution of the differential cross section $d\sigma/d\Omega$ with an appropriate instrumental resolution function Ξ :

$$\frac{I(q)}{I_0} = \int \frac{d^2 q'_{xy}}{k^2 \sin(\beta)} \Xi_q(q_{xy} - q'_{xy}) \frac{1}{A_0} \frac{d\sigma}{d\Omega}(q'_{xy}) \quad (6)$$

$$\Xi_q(\delta q_x, \delta q_y) = \begin{cases} 1 & \text{if } |\delta q_x| \leq \Delta q_x / 2, |\delta q_y| \leq \Delta q_y / 2. \\ 0 & \text{otherwise} \end{cases}$$

The differential cross section for a homogeneous liquid surface is described by the capillary wave model [2,7] and can be written as:

$$\frac{1}{A_0} \left(\frac{d\sigma}{d\Omega} \right)_{hmg} \approx \frac{1}{16\pi^2} \left(\frac{q_c}{2} \right)^4 \frac{T_F(\alpha) T_F(\beta)}{q_z^2 \sin(\alpha)} \times |\Phi_0(q_z)|^2 \frac{2\pi\eta}{q_{xy}^2} \left(\frac{q_{xy}}{q_{\max}} \right)^\eta, \quad (7)$$

for $\eta = (k_B T / 2\pi\gamma) q_z^2 < 2$, where A_0 is the cross-sectional area of the incident beam, q_c is the critical vector, and $T_F(\alpha)$ is the Fresnel transmission factor [1]. The scattering from a homogeneous liquid surface is described by the characteristic power law $1/q_{xy}^{2-\eta}$ of capillary-wave thermal diffuse scattering.

Fukuto *et al.* established a sum rule for scattering from capillary fluctuations on liquid surfaces [12]. If an

inhomogeneous film (in which the local electron density deviates from the lateral average electron density profile $\langle \rho(z) \rangle_{xy}$) is formed on a liquid surface, additional scattering is superimposed on the diffuse scattering:

$$\frac{1}{A_0} \left(\frac{d\sigma}{d\Omega} \right)_{inhmg} \approx \frac{1}{16\pi^2} \left(\frac{q_c}{2} \right)^4 \frac{\phi_2^2 e^{-\sigma_2^2 q_z^2}}{\sin(\alpha)} \times \frac{1}{(2\pi)^2} \int_{q'_{xy} \leq q_{\max}} d^2 \mathbf{q}'_{xy} \frac{2\pi\eta}{q_{xy}'^2} \left(\frac{q'_{xy}}{q_{\max}} \right)^\eta C_2(\mathbf{q}_{xy} - \mathbf{q}'_{xy}) \quad (8)$$

where ϕ_2 is the average electron density ratio of the film to the bulk phase, σ_2 is the root-mean-square roughness of the film/gas interface, and C_2 is the Fourier transform of a simple exponentially decaying height-height correlation function $c_2(r_{xy}) = \sigma_2^2 \exp(-r_{xy}/\xi)$:

$$C_2(q) = \frac{2\pi\sigma_2^2 \xi^2}{(1 + \xi^2 q^2)^3}, \quad (9)$$

with a correlation length ξ .

3. MATERIALS

The globular protein, lysozyme (LSZ), is elliptical in shape with approximate dimensions $30 \times 30 \times 45 \text{ \AA}^3$. It is regarded as a rigid molecule due to the presence of four disulphide bridges. LSZ was selected because its three-dimensional conformation is very stable in solution and its adsorption behavior has been extensively studied [21–25]. Previously, time-resolved x-ray reflectivity measurements were performed for LSZ adsorbed at a air/water interface to investigate the mechanism of adsorption-induced protein unfolding [17]. The time dependence of the density profile at the air/water interface revealed that the molecular conformation changed significantly during adsorption. In the present study, we focus on the adsorption process in the presence of a salt.

3 \times crystallized and lyophilized hen egg lysozyme was purchased from Sigma (Prod. No. L6876) and used as supplied. Protein solutions were made using a phosphate buffer solution (0.02 M $\text{NaH}_2\text{PO}_4/\text{Na}_2\text{HPO}_4$) of pH 7 (ionic strength: 0.02 M) using UHQ-grade water. Protein solutions were made to concentrations of 43 mg/mL, from which 1 cm³ portions were added to a 42 cm³ buffer solution with 2 M NaCl in a Langmuir trough to give final concentrations of 1 mg/mL.

4. RESULTS AND DISCUSSION

4.1 X-ray specular reflectivity

The reflectivity data were divided by the Fresnel reflectivity of the buffer solution and the capillary wave contribution $CW(q_z, T, \gamma)$ given by Eq. (5). The intrinsic structure factors for the buffer solution and LSZ in the buffer were measured two hours after injection and are shown in Fig. 4(a). They were fitted using a three-box model using the Parratt32 software package [26] by taking the thicknesses d , the electron densities ρ , and the roughnesses σ of the three slabs as parameters. Table 1 lists the obtained parameters for LSZ in the buffer solution. The electron density profile shown in Fig. 4(b)

differs slightly from that obtained previously at the same LSZ concentration in the absence of a salt [17]. Subtracting the electron density of the buffer solution, the areas of slabs 0–2 (where the air is considered to be slab 0) and 2–3 are almost equivalent, suggesting that the adsorbed LSZ forms a double layer consisting of a densely packed first layer (slabs 0–2) above a thicker LSZ layer with a lower density (slabs 2–3).

Table 1 Structural parameters for LSZ in the buffer solution obtained by refining Fig. 4(a)

Slab number	Slab thickness d [Å]	Electron density ρ [$e^-/\text{Å}^3$]	Interface roughness σ [Å]
1	5.06	0.48	1.83
2	11.34	0.465	2.77
3	49.71	0.43	2.42
bulk		0.39	23.18

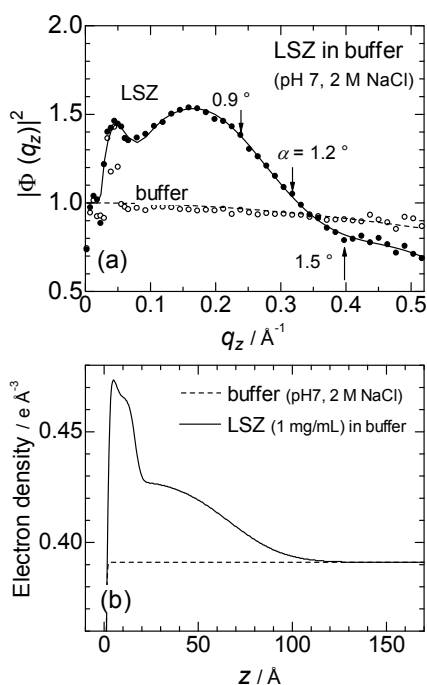


Fig. 4 (a) X-ray reflectivity profiles measured 2 hours after LSZ injection. The data were divided by the Fresnel reflectivity of the air/buffer interface. The continuous lines are the fits to the data. (b) Electron density profiles correspond to the fits to the data.

The density profiles obtained by nonlinear least-squares fitting of reflectivity curves is generally not unique. Therefore, we examined the underlying origin of the obtained x-ray reflectivity profiles to evaluate their accuracy.

The structure factor of an N -box model with sharp interfaces and uniform electron densities ρ_j and ρ_k becomes:

$$|\Phi(q_z)|^2 = \frac{1}{\rho_{\text{Bulk}}^2} \times \sum_{j=0}^N \sum_{k=0}^N (\rho_{j+1} - \rho_j)(\rho_{k+1} - \rho_k) \cos\{q_z(z_k - z_j)\} \quad (10)$$

where z_j is the depth at which the j th interface is located. The x-ray reflectivity profiles are mainly generated by the interference between the x-ray beams reflected from the interfaces having large electron density differences, $(\rho_{j+1} - \rho_j)$. Since the electron densities of the air and slab 1 differ the most in the present case, we calculated the terms with $j = 0$ and $k = 1-3$ in Eq. (10) and plotted them in Fig. 5. If the interface roughness is taken into account, the amplitudes of the cosine curves diminish at high q_z , and they fit the x-ray reflectivity profiles. The broad peak around $q_z = 0.2 \text{ Å}^{-1}$ is attributed to slabs 0–2, which correspond to the first layer of the adsorbed LSZ. The second layer (slabs 0–3) causes an additional peak in $q_z < 0.1 \text{ Å}^{-1}$, whose amplitude is proportional to the amount adsorbed.

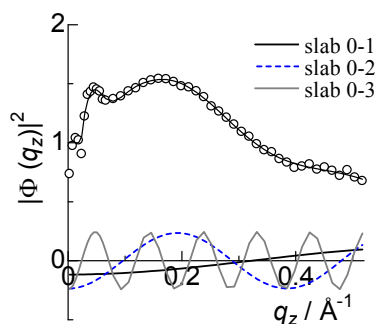


Fig. 5 Decomposition of the structure factor for x-ray reflectivity profiles measured 2 hours after LSZ injection. The data were divided by the Fresnel reflectivity of the air/buffer interface.

4.2 X-ray off-specular diffuse scattering in q_z direction

Figure 6 shows two-dimensional images of x-ray reflection peaks for x-rays incident at $\alpha = 1.5^\circ$. The intensity of off-specular diffuse scattering increased drastically after LSZ injection. A small peak, known as a Yoneda wing [27], is clearly visible at $\beta = \alpha_c$ in Fig. 6(b).

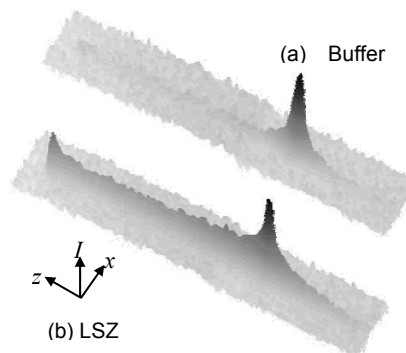


Fig. 6 Two-dimensional images of x-ray reflection peaks. (a) Buffer solution. (b) LSZ in the buffer solution measured 2 hours after injection. A small peak called the Yoneda wing at $\beta = \alpha_c$ is clearly visible.

Figure 7 shows the normalized reflection profiles of three different x-rays incident angles, which were detected without the Al attenuator. The open symbols correspond to those for the buffer solution, while the filled symbols correspond to those for LSZ in the buffer

solution measured two hours after injection. The central peaks correspond to specular reflections.

The solid and dashed curves in Fig. 7 correspond to the theoretically predicted intensities for the capillary wave (CW) model calculated using Eqs. (6) and (7) with parameters $\gamma = 76.05$ mN/m and $q_{\max} \sim 2\pi/d = 2\pi/2.8$ \AA^{-1} for the buffer solution, $\gamma = 66.1$ mN/m and $q_{\max} = 2\pi/30$ \AA^{-1} for the LSZ in the buffer solution. The intrinsic structure factor $|\Phi_0(q_z)|^2$ in Eq. (7) is calculated by a polynomial fit of the observed data shown in Fig. 4(a) in the region $q_z > 0.1$ \AA^{-1} . Since the differential cross section in Eq. (7) diverges at $q_{xy} = 0$, we calculated the diffuse scattering intensities in the region $q_{xy} > 10^{-5}$ \AA^{-1} . The calculated diffuse scattering intensities with the instrumental resolutions of $\Delta q_x \sim k \Delta(2\theta)$ and $\Delta q_y \sim k \sin(\beta)\Delta\beta$, with $\Delta(2\theta) \sim 2.3$ pixels $\times 0.172$ mm/pixel / 538 mm and $\Delta\beta \sim 3.0$ pixels $\times 0.172$ mm/pixel / 538 mm, which are 1.5 times larger than the FWHMs of the reflection profile at the incident angle α of 0.01° , exhibit good agreement with the observed intensities for the buffer solutions at the three different incident angles α . In contrast, the observed intensities for the LSZ in the buffer solution are much larger than the theoretically predicted intensities. This excess scattering arises from the inhomogeneity of the surface.

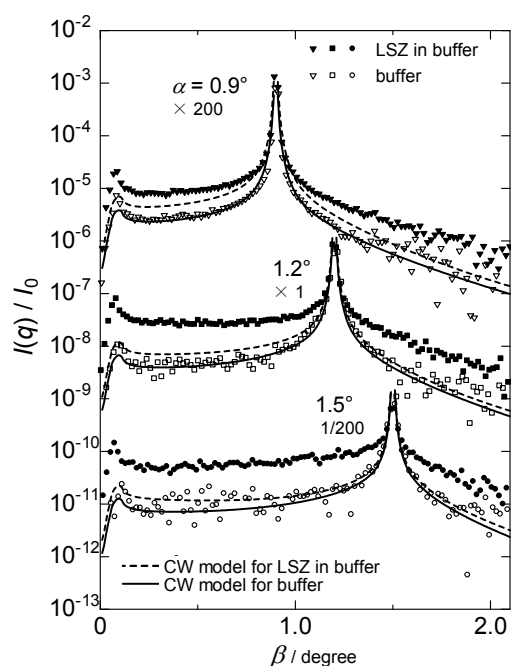


Fig. 7 Reflection profiles at $\alpha = 0.9^\circ$, 1.2° , and 1.5° . The solid curves represent the theoretical predictions based on the capillary wave model and are calculated using Eqs. (6) and (7). The observed intensities for the buffer solution (the open symbols) exhibit good agreement with those for the CW model (the solid curves), while the observed intensities for the LSZ in the buffer solution (the filled symbols) are much larger than those for the CW model (the dashed curves).

To obtain the structural parameters (i.e., the correlation length ξ and the root-mean-square roughness of the film/gas interface σ_2) of an inhomogeneous film

formed on a liquid surface, Fukuto *et al.* performed the q_{xy} -integration in Eq. (8) numerically to fit the whole pattern of the excess scattering [12,13]:

$$\left[\frac{I(q)}{I_0} \right]_{inhmg} = \frac{I(q)}{I_0} - \left[\frac{I(q)}{I_0} \right]_{hmg} \quad (11)$$

To avoid such a complicated integration, we fitted the observed excess scattering intensities away from the specular condition with the following expression (see Appendix A1):

$$\left[\frac{I(q)}{I_0} \right]_{inhmg} \approx N \frac{e^{-\sigma_2^2 q^2}}{(1 + \xi^2 q^2)^{3/2}} \quad (12)$$

The fitting parameters are the arbitrary constant N , the correlation length ξ , and the root-mean-square roughness of the film/gas interface σ_2 . Since the profile width is related to ξ , while the asymmetry of the profile is related to σ_2 , these parameters can be obtained almost independently of each other.

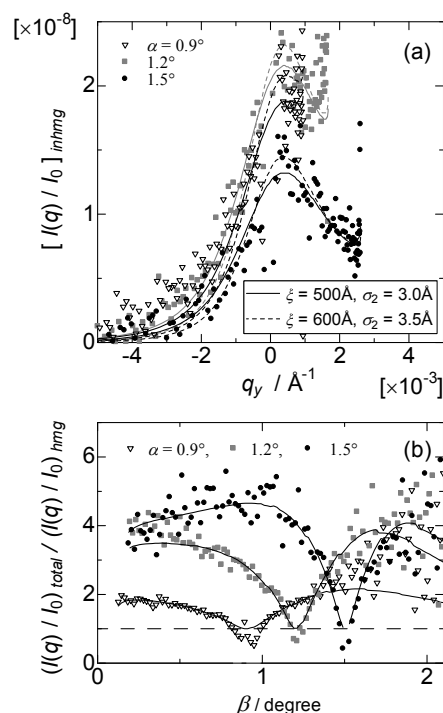


Fig. 8 (a) Excess scattering from the inhomogeneous LSZ film adsorbed by the buffer surface. The solid curves are the best fits obtained using the inhomogeneous model expressed by Eq. (12) with $\xi = 500$ \AA and $\sigma_2 = 3.0$ \AA . (b) The ratio of measured intensity to the homogeneous (or CW) contribution.

The excess scattering intensities denoted by the symbols in Fig. 8(a) are obtained by subtracting the calculated intensity for the CW model from the observed intensity. The best fit with Eq. (12) is obtained when $\xi = 500$ \AA and $\sigma_2 = 3.0$ \AA (the solid curves in Fig. 8) for three different x-rays incident angles α . The calculated profile with $\xi = 600$ \AA and $\sigma_2 = 3.5$ \AA (denoted by the dashed curves) are also shown in Fig. 8(a) to indicate the

differences. The fit is more clearly evident in Fig. 8(b) showing the ratio of measured intensity to the homogeneous (or CW) contribution.

The estimated correlation length of $\xi = 500 \text{ \AA}$ is approximately 10 times larger than the LSZ molecule, suggesting that the inhomogeneity originates from an island above the buffer surface. It is reasonable to conjecture that the LSZ molecules aggregate and form islands in the manner shown in Fig. 9. As discussed in Sec. 4.1, the x-ray reflectivity indicates that the adsorbed LSZ molecules form a double layer. It is not certain whether the whole or only the topmost double layer forms the island. However, the electron density profile shown in Fig. 4(b) differs from that obtained when no salt was present [17]. To clarify this, we need to estimate the arbitrary constant N in Eq. (12), which includes the structure factor of the inhomogeneous layer, to correlate the intrinsic structure factor derived from x-ray reflectivity measurements. This will be discussed elsewhere [28].

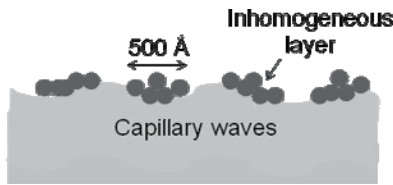


Fig. 9 Schematic model of inhomogeneous LSZ layer adsorbed at a buffer surface. The LSZ molecules aggregate to form islands above the buffer surface.

4.3 X-ray off-specular diffuse scattering in q_x direction

If the inhomogeneous layer has a particular structure in a particular direction, the scattered intensities are expected to differ in the q_x and q_y directions. Figure 10 shows the projection in the x direction of the x-ray reflection peaks shown in Fig. 6. The profiles for the buffer solution and for LSZ in the buffer solution appear to be quite similar to each other, in contrast with that in the q_y direction. The diffuse scattering produced by the surface inhomogeneity cannot be detected in the q_x direction, since the estimated effective coherence length along the surface of $1/\Delta q_x \sim 200 \text{ \AA}$ is much smaller than that in the q_y direction of $1/\Delta q_y \sim 6300 \text{ \AA}$ at $\alpha = 1.5^\circ$. In addition, there is no excess scattering produced by the smaller lateral fluctuations.

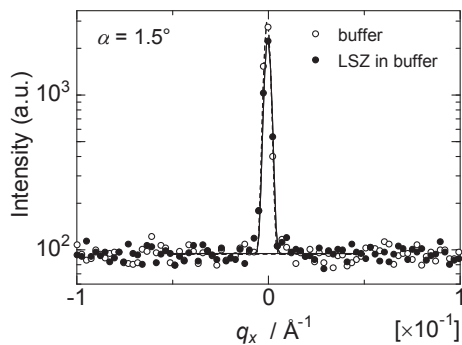


Fig. 10 x -projection of x-ray reflection peaks shown in Fig. 6. The profiles for the buffer solution and for LSZ in the buffer solution appear to be quite similar to each other.

5. CONCLUSION

We have analyzed the specular and off-specular reflection from a globular protein, LSZ, adsorbed at an air/buffer interface in the presence of a salt. The electron density profile, which differs slightly from a previous obtained result at the same LSZ concentration in the absence of a salt [17], indicates the formation of a double layer consisting of a lower-density LSZ layer beneath a densely packed top layer. The off-specular diffuse scattering from the buffer solution exhibits good agreement with the CW model. By contrast, that from LSZ in the buffer solution measured two hours after injection is higher than predicted. We proposed a simple formula to describe the excess scattering intensity. The formula fitted the excess scattering at different incident angles with a correlation length ξ of 500 \AA and the root-mean-square roughness of the film/gas interface σ_2 of 3.0 \AA , suggesting that the LSZ molecules aggregate to form islands with diameters of about 500 \AA above the buffer surface. The excess scattering produced by the surface inhomogeneity was not observed in the q_x direction, since the estimated effective coherence length along the surface of $1/\Delta q_x \sim 200 \text{ \AA}$ is much shorter than the correlation length of the inhomogeneous layer.

The PILATUS detector accurately obtains the full range of x-ray specular and off-specular reflections in an extremely short time (1 s), allowing the out-of-plane and in-plane structures of a biological system at an interface to be determined for the first time.

ACKNOWLEDGEMENTS

The authors are grateful for helpful discussions with Professor Peter Pershan of Harvard University (see Appendix A2) and Emeritus Professor Takao Iijima of Gakushuin University. The synchrotron radiation experiments were performed at the BL37XU in the SPring-8 facility with the approval of the Japan Synchrotron Radiation Research Institute (JASRI) (Proposal No. 2009A1686).

APPENDIX

A1 Derivation of Eq. (12)

In a previous study, Fukuto *et al.* performed the q_{xy} -integration in Eq. (8) numerically to fit the whole pattern of the excess scattering to obtain the parameters ξ and σ_2 [12,13]. To avoid such a complicated integration, we propose a simple formula to describe the excess scattering intensity.

In the previous study, the electron density normal to the surface for the inhomogeneous film $\phi_2 \cdot \rho_{\text{Bulk}}$ was assumed to be constant [12,13]. In contrast, in the present study, the electron density varies with z (see Sec. 4.1). Therefore, we used Eq. (8)' instead of Eq. (8)

$$\frac{1}{A_0} \left(\frac{d\sigma}{d\Omega} \right)_{\text{inhmg}} \approx \frac{1}{16\pi^2} \left(\frac{q_c}{2} \right)^4 \frac{e^{-\sigma_2^2 q_z^2}}{q_z^2 \sin(\alpha)} |\Phi_2(q_z)|^2 \times \frac{1}{(2\pi)^2} \int_{q'_{xy} \leq q_{\text{max}}} d^2 \mathbf{q}'_{xy} \frac{2\pi\eta}{q'^2_{xy}} \left(\frac{q'_{xy}}{q_{\text{max}}} \right)^\eta C_2(\mathbf{q}_{xy} - \mathbf{q}'_{xy})$$

with

$$|\Phi_2(q_z)|^2 = \left| \frac{1}{\rho_{\text{Bulk}}} \int dz \frac{\partial \langle \rho(z) \rangle_{xy}}{\partial z} e^{iq_z z} \right|^2. \quad (8')$$

Furthermore, the asymptotic decay $1/q_{xy}'^{2-\eta}$ in the q_{xy}' -integration can be roughly approximated with a delta function $\delta(q_{xy}')$ to give:

$$\frac{1}{A_0} \left(\frac{d\sigma}{d\Omega} \right)_{inhmg} \approx \frac{1}{16\pi^2} \left(\frac{q_c}{2} \right)^4 \frac{e^{-\sigma^2 q_z^2}}{q_z^2 \sin(\alpha)} |\Phi_2(q_z)|^2 \times \frac{N'}{(2\pi)^2} \int_{q_{xy} \leq q_{max}} d^2 \mathbf{q}'_{xy} 2\pi\eta \delta(\mathbf{q}'_{xy}) C_2(\mathbf{q}_{xy} - \mathbf{q}'_{xy}) \quad (8)''$$

where N' is a factor generated by this approximation.

Except for the region close to the specular condition, the scattering intensity profile is not greatly affected by the instrumental resolution function. Thus, the instrumental resolution function Ξ can be replaced by a delta function $\delta(q_{xy} - q_{xy}')$:

$$\Xi_q(q_{xy} - q_{xy}') = \delta(q_{xy} - q_{xy}') \quad \text{if } |q_{xy}| \gg 0 \quad (13)$$

Using Eqs. (6), (8)'', (9), and (13), we obtain the excess scattering intensity:

$$\left[\frac{I(q)}{I_0} \right]_{inhmg} \approx N \frac{e^{-\sigma^2 q_z^2}}{(1 + \xi^2 q^2)^{\frac{3}{2}}} \quad (12)$$

In spite of the rough approximations used, Eq. (12) describes the excess scattering very well, as shown in Fig. 8.

A2 Reply to Prof. Pershan's comments

Below are several helpful comments given by Professor Peter Pershan who has conducted a lot of pioneering work on liquid surfaces and our responses to them.

(1) Importance of defining the instrumental resolution when estimating the correlation length of inhomogeneities

“There is a fundamental problem in trying to separate the effects of surface inhomogeneities from capillary roughness that I would like to try to explain.

In principle if one had infinitely fine resolution the capillary wave scattering for your model of the surface would lead to an intense/sharp peak at $q_{xy} = 0$ that would dominate any of the excess scattering due to surface inhomogeneities. This occurs because if gravity is neglected the amplitude of the capillary peak is an infinitely high singularity while the surface inhomogeneities have a finite width/finite amplitude. As the resolution becomes coarser the singular capillary peak broadens and the intensity of the scattering due to the inhomogeneities increases. At the point that the resolution becomes comparable to the correlation length of the inhomogeneities it becomes hard to distinguish between these two signals. One way this can sometimes be done is to compare the FWHM of the diffuse profile (your Fig. 6) with the FWHM of the direct beam. For a flat surface in which the capillary waves dominate the diffuse scattering the FWHM width of the profile should be comparable to the resolution determined width of the direct beam. Is this true for your measurement?

On the other hand, if $1/\xi$ is comparable to, or smaller

than, the resolution the two signals can not easily be separated. One possible way for large η (i.e. for large $(k_B T / 2\pi\gamma) q_z^2$) is that for large q_{xy} the tails of the diffuse scattering do become larger than the correlation determined tails of the inhomogeneities (i.e. your Eq. 9 or 12) and that might be a good signature if you really know the shape of the inhomogeneity induced scattering and can show that the measured diffuse scattering is dominated by the capillary form. This leads me to comparing your Fig. 6 to Fig. 4 in Masa's 1998 PRL [12]. Note that for Masa's figure the diffuse scattering at $\beta = \alpha$ is the same for the homogeneous/inhomogeneous surfaces. This means that that the specular condition the scattering for the inhomogeneous surface is dominated by the singular peak in the capillary spectrum. Masa could be certain of this because he reports measurements of the difference $\Delta I = I(\theta = 0) - I(\delta\theta)$ that is defined in the second column of Masa's 1998 PRL So long as $1/\xi >$ the resolution the excess scattering at $\beta = \alpha$ makes no contribution to ΔI and his Fig. 4 is just the excess. I don't know if you can do this with your data.”

– Unfortunately, we don't have the direct beam profile to compare with the diffuse scattering profile. However, as Fig. 7 shows, the shape of the diffuse scattering profile close to the specular region exhibits very good agreement with that predicted by the capillary wave (CW) model with an instrumental resolution estimated from the FWHMs of the reflection profile at the incident angle α of 0.01° . Furthermore, the effective coherence length along the surface of $1/\Delta q_y \sim 6300 \text{ \AA}$ at $\alpha = 1.5^\circ$ is much larger than the correlation length ξ of 500 \AA for the inhomogeneous layer, allowing the excess scattering to be separated from the CW contribution in the present case. Figure 8(b) shows the ratio of our measured intensity to the homogeneous (or CW) contribution in accordance with Masa's Fig. 4 in 1998 PRL [12]. The intensities at $\beta = \alpha$ deviate slightly from unity, which might be caused by an error in the estimated instrumental resolution or intrinsic structure factor $|\Phi_0(q_z)|^2$. However, in contrast with Masa's case, our $1/\xi$ is much larger than the resolution described above. Furthermore, the diffuse scattering intensity from our inhomogeneous layer is much larger than the CW contribution out of the specular region, as shown in Fig. 7 and 8(b). We consider, therefore, that we do not have to treat our data in the strict manner that Masa did and that we can estimate the correlation length ξ outside the specular region using the simple formula proposed in this paper.

(2) Background subtraction

“When you subtract the background this way (See 2.2) you can also be subtracting a contribution from the capillary waves at small q_y . When we do something like this the theoretical model that we use is the difference between the capillary theory for the two signals.”

– We think we do not have to consider the CW contribution in the background subtraction even though we took a point very close to the specular region ($q_x \sim 0.012 \text{ \AA}^{-1}$) as the background. As shown in Fig. 10, the intensity outside of the specular region is almost constant because of the scattering from the x-ray windows, the bulk liquid, etc., which become much

larger than the CW contribution when no receiving slit is present.

(3) Formula describing the capillary wave model

"I don't use the Sanyal formula [6]. But, as I wrote in the article in P. S. Pershan, "X-ray Scattering From Liquid Surfaces: Effect of Resolution", *Journal of Physical Chemistry B* 113, 3639 (2009) [20], the Sanyal formula is OK for reflectivity if η is less than one. On the other hand, you can not use it if you want to subtract the out of the plane diffuse scattering since it assumes an infinitely wide resolution. You say that you do subtract background but the theory that you compare the background subtracted data with does not include this effect."

– We used Sanyal's formula in the first draft and a previous paper [15], because this formula can describe both the specular and off-specular reflection profiles using a single equation. As you pointed out, however, this formula which has a $q_y^{\eta-1}$ shape instead of $q_{xy}^{\eta-2}$ as a result integrating in the q_x direction, which does not fit the present case very well in which the resolution in the q_x direction is only several tens of times coarser than that in the q_y direction. In the revised paper, we recalculated the diffuse scattering using Eqs. (6) and (7) instead of using Sanyal's formula.

Figure A1 shows an example of the theoretical prediction for the CW model calculated using Eqs. (6) and (7), compared with that calculated using Sanyal's formula. In the specular region and the large β region, Eqs. (6) and (7) fit the observed intensity much better than Sanyal's formula.

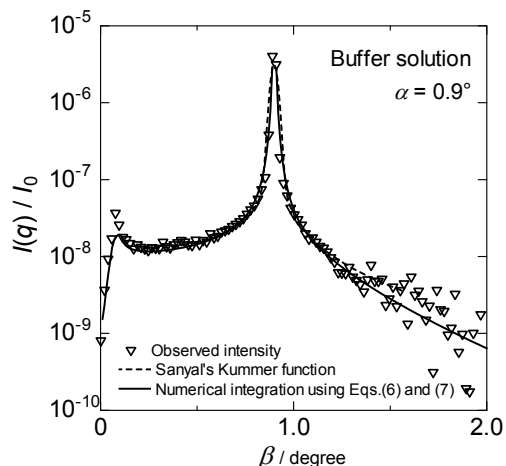


Fig. A1 Reflection profiles for the buffer solution at $\alpha = 0.9^\circ$. The theoretical predictions for the CW model are calculated using Eqs. (6) and (7) (the solid curve is the same curve shown in Fig. 7), and Sanyal's formula (dashed curve).

REFERENCES

[1] M. Tolan: "X-Ray Scattering from Soft-Matter Thin Films", Springer (1999), pp113-149.
 [2] F. P. Buff, R. A. Lovett and F. H. Stillinger, *Phys. Rev. Lett.* **15**, 621-623 (1965).
 [3] S. K. Sinha, E. B. Sirota, S. Gasoff, and E. B. Stanley, *Phys. Rev.* **B38**, 2297-2311 (1988).
 [4] A. Braslau, M. Deutsch, P. S. Pershan, A. H. Weiss, J. Als-Nielsen and J. Bohr, *Phys. Rev. Lett.* **54**, 114-117

(1985).

[5] D. K. Schwartz, M. L. Schlossman, E. H. Kawamoto, G. J. Kellogg, P. S. Pershan and B. M. Ocko, *Phys. Rev.* **A41**, 5687-5690 (1990).
 [6] M. K. Sanyal, S. K. Sinha, K. G. Huang, and B. M. Ocko, *Phys. Rev. Lett.* **66**, 628-631 (1991).
 [7] P. S. Pershan, *Colloids Surface A171*, 149-157 (2000).
 [8] O. Shpyrko, M. Fukuto, P. S. Pershan, B. Ocko, I. Kuzmenko, T. Gog, and M. Deutsch, *Phys. Rev.* **B69**, 245423 (2004).
 [9] H. Tostmann, E. DiMasi, P. S. Pershan, B. M. Ocko, O. G. Shpyrko, and M. Deutsch, *Phys. Rev.* **B59**, 783-791 (1999).
 [10] O. Shpyrko, P. Huber, A. Grigoriev, P. S. Pershan, B. Ocko, H. Tostmann and M. Deutsch, *Phys. Rev.* **B67**, 115405 (2003).
 [11] Z. Li. Zhao, J. Quinn, M. H. Rafailovich, J. Sokolov, R. B. Lennox, A. Eisenberg, X. Z. Wu, M. W. Kim, S. K. Sinha, and M. Tolan, *Langmuir*, **11**, 4785-4792 (1995).
 [12] M. Fukuto, R. K. Heilmann, P. S. Pershan, J. A. Griffiths, S. M. Yu, and D. A. Tirrell, *Phys. Rev. Lett.* **81**, 3455-3458 (1998).
 [13] M. Fukuto, R. K. Heilmann, P. S. Pershan, S. M. Yu, J. A. Griffiths, and D. A. Tirrell, *J. Chem. Phys.* **111**, 9761-9777 (1999).
 [14] M. Fukuto, R. K. Heilmann, P. S. Pershan, A. Badia, and R. B. Lennox, *J. Chem. Phys.* **120**, 3446-3459 (2004).
 [15] Y. F. Yano, T. Uruga, H. Tanida, H. Toyokawa, Y. Terada, and M. Takagaki, *J. Phys. Conf. Ser.* **83**, 012024 (2007).
 [16] Y. F. Yano, T. Uruga, H. Tanida, H. Toyokawa, Y. Terada, M. Takagaki, and H. Yamada, *Eur. Phys. Special Topics*, **167**, 101-105 (2009).
 [17] Y. F. Yano, T. Uruga, H. Tanida, H. Toyokawa, Y. Terada, M. Takagaki, and H. Yamada, *Langmuir*, **25**, 32-35 (2009).
 [18] <http://pilatus.web.psi.ch/pilatus.htm>
 [19] P. Kraft, A. Bergamaschi, Ch. Broennimann, R. Dinapoli, E. F. Eikenberry, B. Henrich, I. Johnson, A. Mozzanica, C. M. Schlepütz, P. R. Willmott and B. Schmitt, *J. Synchrotron Rad.* **16**, 368-375 (2009).
 [20] P. S. Pershan, *J. Phys. Chem.* **B113**, 3639-3646 (2009).
 [21] D. E. Graham, and M. C. Phillips, *J. Colloid Interface Sci.* **70**, 403-414 (1979).
 [22] B. C. Tripp, J. J. Magda, and J. D. Andrade, *J. Colloid Interface Sci.* **173**, 16-27 (1995).
 [23] M. D. Lad, F. J. Birembaut, M. Matthew, R. A. Frazier, and R. J. Green, *Phys. Chem. Chem. Phys.* **8**, 2179-2186 (2006).
 [24] J. R. Lu, T. J. Su, R. K. Thomas, and J. Penfold, J. Webster, *J. Chem. Soc. Faraday Trans.* **94**, 3279-3287 (1998).
 [25] C. Postel, O. Abillon, and B. Desbat, *J. Colloid Interface Sci.* **266**, 74-81 (2003).
 [26] This Reflectivity software is available from: <http://www.hmi.de/bensc/instrumentation/instrumente/v6/refl/parratt_en.htm>.
 [27] Y. Yoneda, *Phys. Rev.* **131**, 2010-2013 (1963).
 [28] Y. F. Yano, T. Uruga, H. Tanida, H. Toyokawa, Y. Terada, M. Takagaki, and H. Yamada, in preparation.

(Received July 14, 2009; Accepted September 17, 2009)

X-ray Reflectivity Evaluation of the Thermal Cycling Effects in Methylcellulose Thin Films

Vallerie Ann Innis-SAMSON¹ and Kenji SAKURAI*^{1,2}

¹University of Tsukuba, Tsukuba, Ibaraki, JAPAN

²National Institute of Materials Science (NIMS), Sengen, Tsukuba, Ibaraki, JAPAN

Fax: 81-029-859-2821, e-mail: sakurai@yuhgiri.nims.go.jp

Changes in the layer thickness and roughness of as-prepared methylcellulose (MC) films with thermal cycling were studied using the X-ray reflectivity technique. It was found that thermal stress induced by rapid and slow thermal cycling brings no apparent changes in the surface and interface roughness after thermal cycling. On the other hand, some reduction of layer thickness was observed. With rapid thermal cycling, the relative shrinkage of the films is much higher at a maximum of 5% change at 15 cycles. With slow thermal cycling, it remains at a maximum of 3.6% even after 20 thermal cycles. Such film shrinkage is highly dependent on the initial film thickness and the amount of absorbed water molecules in the film.

Key words: thermal stability, thermal cycling

1. INTRODUCTION

Methylcellulose (MC) is a chemical compound derived from cellulose and exhibits temperature-related inverse solubility and gelation behavior in aqueous solution. It is also known to exhibit thermoreversible volume phase separation in water at a lower critical solution temperature (LCST) of $\sim 70^\circ\text{C}$ [1]. At the LCST, polymer chains undergo a coil to globule transition in solution due to increased hydrophobic dehydration. In thin film geometry, some previous reports [2,3] have pointed out that water molecules are still trapped/absorbed in an MC thin film at room temperature because of the hydrophilic nature of the polymer and its low moisture vapor transmission rate. The amount of such water remaining in the film is extremely important, because it can affect the property of the MC thin film, particularly with regard to the temperature dependence of the surface and the interface.

On the other hand, the thermal stability of the film structure is of great importance, because thermal stress can be induced due to the difference in thermal expansion coefficient between the polymer layer and the substrate. It is also possible to modify or enhance certain properties such as alignment of polymer chains along a certain direction and electrical conductivity [4,5]. We have previously reported the thermal stability of MC thin films heated at the supposed phase transition temperature for volume phase separation in solution, 70°C , then quenched to room temperature [6]. X-ray reflectivity (XRR) measurements before and after the heating process showed no significant change, indicating that the MC thin film is quite stable in terms of the parameter obtained from XRR, i.e., the density, the layer thickness, the roughness of the surface and the interface between the polymer layer and the substrate. However, the next question is what happens when heating and cooling are repeated.

In the present study, we applied thermal cycling to the MC thin films to investigate further the thermal stability

of the films if subjected to thermal stress brought about by thermal cycling and also to ascertain if thermal cycling can contribute to desorption of the water molecules in the film. Thermal cycling of MC films was done at both slow and rapid heating/cooling rates for different numbers of cycles and the films were measured by XRR.

2. EXPERIMENTAL

Analytical grade MC polymer powder (with degree of substitution (DS): ca. 1.6-1.9 and molecular weight (MW): $4 \times 10^4 \text{ gmol}^{-1}$) from Sigma-Aldrich Inc. was used without further purification. An MC solution with a concentration of 0.5% w/v was prepared in distilled water via hot water dispersion and cold water dissolution. 60 μl of the solution (with a temperature of $\sim 10^\circ\text{C}$) was pipetted onto a clean Si substrate and spin-coated at a final speed of 5000rpm for 30 seconds. The prepared MC thin films were stored in a desiccator for 24 hours prior to measurement by XRR to obtain data before thermal cycling. Thermal cycling was done by heating the films to 80°C at a specified ramp rate, kept at 80°C for 10 minutes, then cooled down to 25°C and kept at 25°C also for 10 minutes before starting the next cycle. Thermal cycling was done continuously for each film between 25°C - 80°C . Slow thermal cycling was done in a vacuum oven (AS ONE AV0-250N), without a vacuum, at a heating rate of $\sim 1^\circ\text{C}/\text{min}$ while the cooling rate was $\sim 1^\circ\text{C}/3\text{min}$. Vacuum heating was not done in order to facilitate comparison with rapid thermal cycling, which was done in open air with the use of a home-built Peltier-controlled heating stage. The heating and cooling rate was $\sim 10^\circ\text{C}/\text{min}$.

XRR measurements of the films were done after thermal cycling (that is back to 25°C) using a home-built X-ray reflectometer with a θ - 2θ geometry and Cu as the target. The incident X-ray energy used was Cu- $K\alpha_1$ monochromatic X-rays 8.048keV ($\lambda=1.541\text{\AA}$). The data analysis was done based on least-squares fitting [7,8] to

Parratt's theoretical reflectivity. Further details of the procedure are described elsewhere [6].

3. RESULTS AND DISCUSSION

Shown in Figure 1 are the XRR profiles of MC thin films subjected to slow heating/cooling cycles for 5, 10, 15, 20 and 25 cycles. Thermal cycling for the specified number of cycles was done on a different film and not continuously on the same film because of the hygroscopic nature of the polymer. In the data fitting of all the XRR profiles, a simple single-layer model on top of the substrate was used. The thin native oxide layer, SiO_2 , and some possibly contaminated layers on top of the substrate were neglected, because it was found that finally obtained results are not affected by such layers. The critical angle of MC was observed at around 2.2 mrad, and it agrees well with that calculated from the reported density value of the MC, 1.31 g/cm^3 . As the angular spread of the present reflectometer is nearly 0.1 mrad (this is mainly limited by the energy resolution of the monochromator), the precision in determining the critical angle at 2.2 mrad will be around 5%. In our case, detailed simulation to see the shape of the curve in addition to the position of the critical angle indicates that a density value of $1.31 \pm 0.06 \text{ g/cm}^3$ is reasonable in order to explain all the experimental data obtained in this study. In other words, the density change during thermal cycling at the 25°C - 80°C range is not significant, being within 5%.

The summarized thickness and interface roughness parameters derived from the curve fitting are shown in Table 1 for the slow heating/cooling cycle before and after thermal cycling. In the model fit of the XRR profiles, as previously mentioned, a single-layer model was used and the native SiO_2 layer was entirely neglected. We can assume that the SiO_2 layer does not change with heating at 80°C , which is too low for silicon oxide to grow in an ordinary environment. Polymer films prepared by spin-coating are described as being in a metastable state owing to the fast evaporation of the solvent during spin-coating which leads to frozen-in non-equilibrated chain conformations of the polymer [9]. Thickness changes associated with solvent loss can occur at room temperature over time and ultra-slow structural relaxation is expected [9, 10]. As seen from Table 1, the decrease in the layer thickness of the polymer after 5-10 thermal cycles for MC films is so small that we can just interpret this as no change in layer thickness with this number of thermal cycles. Actually, layer thickness changes of less than 5 \AA are likely in polymer systems because of the constant absorption/desorption of water molecules or other gas over time.

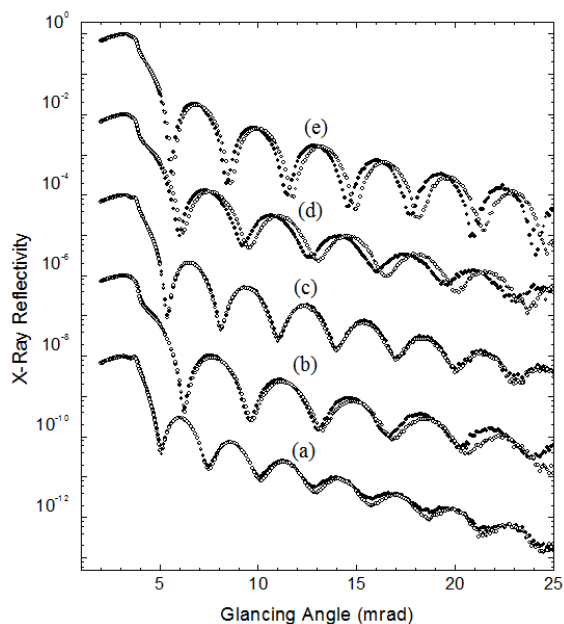


Fig.1 XRR profiles of MC thin films before (closed shapes) and after slow thermal cycling (open shapes): (a) 5 cycles (b) 10 cycles (c) 15 cycles (d) 20 cycles (e) 25 cycles. For clarity, all curves are shifted in the intensity scale.

Significant film thickness change begins only from 20 and 25 thermal cycles which have 3.6% and 2.5% film contraction respectively. The change in thickness of the MC films can be due to desorption of absorbed water molecules in the thin film with heating and structural relaxation of the non-equilibrated polymer chain conformations. The amount of film shrinkage in the slow thermal cycling does not show a systematic dependence on the number of thermal cycles in our study because of the variability of the initial film thickness. The thin films were all spin-coated at the same spin speed and spin time but the final film thickness value varies around $250 \text{ \AA} \pm 15\%$. Film shrinkage appears to be easily observed in thinner films. This phenomenon has also been described in other polymer thin film systems which can be due to the early onset of structural relaxation in thinner films [11, 12]. The variability of film thickness shrinkage may also be due to the amount of water molecules actually absorbed in the thin film such that the amount desorbed during heating also varies. It is important to note though that MC films do not show significant film contraction

Table 1: Layer thickness d and interface roughness σ_{int} parameters for the XRR profiles of the MC thin films before and after slow thermal cycling.

Number of thermal cycles	Before heating		After thermal cycling		Absolute shrinkage ($\Delta d = d_i - d_f$) (\AA)	Relative shrinkage ($\Delta d_{rel} = (d_i - d_f) \times 100 / d_i$) (%)
	d_i (\AA)	σ_{int} (\AA)	d_f (\AA)	σ_{int} (\AA)		
5	280	17	278	15	2	0.7%
10	229	15	226	12	3	1.3%
15	254	10	254	10	0	0%
20	221	14	213	12	8	3.6%
25	243	5	237	5	6	2.5%

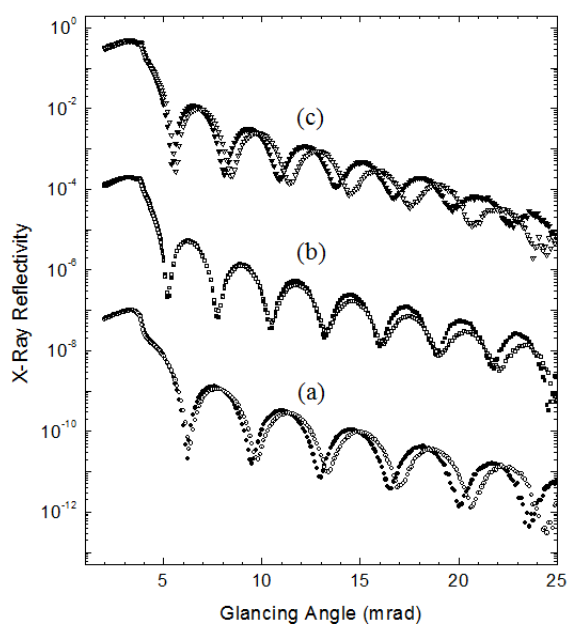


Fig. 2 XRR profiles of MC thin films before (closed shapes) and after rapid thermal cycling (open shapes): (a) 5 cycles (b) 10 cycles (c) 15 cycles. For clarity, the curves are shifted in the intensity scale.

for 5-15 thermal cycles which means that they retain the solvent (water) and the bound water is not easily removed from the polymer structure. In Table 1, we have included the values for absolute shrinkage and relative shrinkage of the thin films. Absolute shrinkage relates to the solvent loss of the film while relative shrinkage relates to the solvent loss per unit of thickness. Relative shrinkage for the slow thermal cycling even after 20 and 25 thermal cycles is less than 5%. Such thermal stability and very slow solvent loss in the MC thin film is ideal for applications that require moisture retention but slow desorption of the absorbed water molecules.

Surface roughness for all the as-prepared films was between 2 Å - 5 Å. This surface roughness corresponds to a smooth film surface and subsequent evaporation of the solvent with the heating/cooling cycle did not roughen the surface. Surface roughness is dependent on the evaporation of the solvent on the film [13]. Interface roughness is expected to change more with thermal cycling because of the thermal stress generated. However, there appears to be no marked difference in the interface roughness of the film before and after thermal cycling as shown in Table 1. Even with films that have higher interface roughness mainly due to film preparation differences, interface roughness does not become any greater after thermal cycling. This suggests that there is no formation of holes or dewetting centers that will lead to film rupture. This can be interpreted as good thermal stability between the interface of the polymer and the substrate even with accumulated thermal stress due to temperature rise and the difference in thermal expansion between the oxide layer of the Si substrate and the polymer.

In the case of rapid heating/cooling cycles, the change in film thickness is more rapid as shown in Figure 2. The

values for thickness parameter, absolute and relative shrinkage are summarized in Table 2. Change in thickness is more apparent at the 5 and 15 cycle films which have thinner initial film thickness. For the 5 and 15 cycle thin films, relative thickness change is 2.8% and 5% respectively. The slow thermal cycle only showed a maximum relative thickness change of 3.6% at 20 cycles. This means that rapid thermal cycles decrease film thickness earlier than slow thermal cycles. This is because of rapid solvent loss and minimal reabsorption of water molecules in air because of the fast heating and cooling rate. Since measurement after thermal cycling was done at $T=25^{\circ}\text{C}$, we can say that the contraction with heating is irreversible, which means that the contraction is mostly due to solvent loss. In the study of Orts et. al [14], which reported similar contraction of polystyrene (PS) films upon heating below the glass transition temperature, T_g , the contraction was reversible, that is the films returned to their original thickness at room temperature. The PS films studied were annealed at 90°C to remove all the solvent prior to thermal cycling. Such contraction was attributed mainly to the weakening of the polymer network with moderate heating, which contracts the film. After cooling, the network strengthens again and the original film thickness is regained [9]. In our case, the MC films were not heated to remove all the solvent prior to thermal cycling. This step was omitted in the MC film preparation because prior experiments showed that drying at 80°C for 12 hours or 100°C for one hour did not significantly decrease the film thickness. Only with thermal cycling was significant change in layer thickness observed, especially rapid thermal cycling. The increased thermal stress in the film due to the higher heating rate and the sequential heating and cooling may have dissociated the intermolecular and intramolecular H-bonds within water molecules and/or between water/MC interactions, which resulted in the faster desorption of the bound water molecules in the film.

For the thicker 10-cycle film, relative thickness change is only 1.1%. As previously mentioned, this non-uniform response to thermal cycling might be due to the initial film thickness and the actual absorbed water molecules in the thin film. The 10-cycle thin film was the thickest among the three samples used and thus film response with temperature might be different from the thinner films. For other polymer systems, as-prepared thicker films expand when heated below the glass transition temperature, similar to bulk properties [12]. This might also be the case for thicker MC films for which film expansion can occur instead of film contraction with heating at temperatures below T_g .

Comparing relative shrinkage values for slow and rapid thermal cycling, values for rapid cycling are higher than those for slow cycling. With slow thermal cycling, the time elapsed during the cooling process may have allowed the films to reabsorb water molecules in the surrounding air and thus film shrinkage proceeds at a slower rate. With rapid thermal cycling, films contract easily with rapid evaporation and minimal reabsorption of water molecules in air.

Because of variability in the initial thickness of film used in this study, further investigations into the correlation of film thickness with thermal cycling needs to be done.

Table 2: Layer thickness d and interface roughness σ_{int} parameters for the XRR profiles of the MC films before and after rapid thermal cycling

Number of thermal cycles	Before heating		After thermal cycling		Absolute shrinkage	Relative shrinkage
	d_i (Å)	σ_{int} (Å)	d_f (Å)	σ_{int} (Å)	$(\Delta d = d_i - d_f)$ (Å)	$(\Delta d_{rel} = (d_i - d_f) \times 100 / d_i)$ (%)
5	214	6	208	5	6	2.8%
10	270	7	267	9	3	1.1%
15	257	10	244	9	13	5.0%

4. CONCLUSION

The influence of rapid and slow thermal cycling of MC thin films was studied in order to investigate further thermal stability and possible atomic-scale changes due to thermal stress. It was found that MC thin films exhibit only small changes in surface and interface roughness after thermal cycling. On the other hand, due to solvent evaporation and structural relaxation, some clear thickness changes were observed after 20 thermal cycles. In addition, with rapid thermal cycling, relative shrinkage of the films is higher than with slow thermal cycling. A 5% relative thickness change was observed after only 15 thermal cycles. This is because of rapid solvent loss in the film and minimal reabsorption of surrounding water molecules in air. The increased thermal stress in the film due to the higher heating rate and sequential heating and cooling may have dissociated the intermolecular and intramolecular H-bonds within water molecules and/or between water/MC interactions, which resulted in the faster desorption of the bound water molecules in the film. Film shrinkage is highly dependent on the initial film thickness and the actual absorbed water molecules in the film such that there is no clear trend observed with the number of thermal cycles and the magnitude of film shrinkage.

Acknowledgements

The authors would like to thank Dr. M. Shoji and Dr. M. Mizusawa for their valuable discussion during the research. One of the authors (V.I-S) has been supported by a Ministry of Education, Culture, Sports, Science and Technology (MEXT) Japanese Government Scholarship.

References:

- [1] M. Takahashi, M. Shimazaki, J. Yamamoto. *J. Polym. Sci. B* **39**, 91-100 (2001).
- [2] A. Gomez, G. Cruz, M.O. Polo, *J. Appl. Phys.* **89** (10), 5431-5437 (2001).
- [3] S. Lin, S. Wang, Y. Wei, M. Li, *Surface Science* **601**, 781-785 (2007).
- [4] H. Nomura, M. Asano, *Jpn. J. Appl. Phys.* **34**, 6143-6148 (1995).
- [5] S. Lopez, E. Santiago, M. Rojas, D. Contreras, *J. Phys. Conference Series* **167**, 012059 (2009).
- [6] V.A.I. Samson and K. Sakurai. *X-ray. Spec.* **38** (5), 376-381 (2009).
- [7] K. Sakurai, A. Iida. *Jpn. J. Appl. Phys.*, **31**, L113-L115 (1992)
- [8] K. Sakurai and A. Iida, *Adv. in X-ray Anal.* **35**, 813-818 (1992).
- [9] G. Reiter, P.G. de Gennes. *Eur. Phys. J. E* **6**, 25-28 (2001).

[10] H. Richardson, C. Carelli, J.L. Keddie, M. Sferrazza. *Eur. Phys. J. E* **12**, 437-441 (2003).

[11] T. Kanaya, T. Miyazaki, R. Inoue, K. Nishida. *Phys. Stat. Sol. (b)* **242** (3), 595-606 (2005).

[12] T. Miyazaki, K. Nishida, T. Kanaya. *Phys. Rev. E* **69**, 022801 (2004).

[13] K. Strawhecker, S. Kumar. *Macromolecules* **34**, 4669-4672 (2001).

[14] W. Orts, J. van Zanten, W. Wu, S. Satija. *Phys. Rev. Lett.* **71**, 867-870 (1993).

(Received July 14, 2009; Accepted September 24, 2009)

Spall Fracture of Metallic Aluminum Induced by Penetration of Liquid Gallium-Indium Alloy and Moisture at Room Temperature

Mari Mizusawa and Kenji Sakurai*

National Institute of Materials Science (NIMS), Sengen, Tsukuba, Ibaraki, JAPAN

Fax: 81-029-859-2821, e-mail: sakurai@yuhgiri.nims.go.jp

The present paper reports on brittle spall fracture of aluminum foil and sheet at room temperature. It was found that fairly rapid fracture takes place upon contact with liquid $\text{Ga}_{83}\text{In}_{17}$ alloy in the presence of moisture. A rapid increase in temperature was observed during the reaction. Observation in a different atmosphere clarified that moisture has a strong influence on the present fracture process, although the phenomena are basically correlated to embrittlement by liquid $\text{Ga}_{83}\text{In}_{17}$ alloy penetrating into the grain boundaries of aluminum polycrystals. The fine debris obtained through the spall fracture was identified as metallic aluminum, neither bulk oxides nor hydroxides.

Key words: grain boundary, liquid metal embrittlement, fracture; moisture effects

1. INTRODUCTION

As is well known, when liquid gallium penetrates the surface of metallic aluminum, it degrades the latter's mechanical properties [1, 2]. Recently, the interfacial penetration of liquid gallium into the aluminum grain boundaries was demonstrated by synchrotron X-ray microscopy, including micro-tomography [3-9], transmission electron microscopy [10] and atomic-force microscopy [11]. Such penetration can be sometimes even used to illuminate the grain boundaries of aluminum alloys in scanning electron microscopy observation. [12]. Although the reaction proceeds in normal atmosphere, it does not take place at room temperature, because the melting point of gallium is 29.8°C. It would be interesting, therefore, if it were possible to lower the reaction temperature so that no heating was necessary in order to maintain a fluid liquid state. Indium-doped-gallium alloy, which is promising as a contact material [13], forms eutectic at 15.7°C for In:Ga=17:83. That is, the material is liquid at room temperature. In the present research, the penetration of indium-doped-gallium alloy rather than simple gallium metals was investigated, with particular consideration given to the influence of normal air and moisture. Extraordinary effects, such as spall fracture of the aluminum surface and rapid exotherm, are discussed later.

2. EXPERIMENTAL

The samples studied in this research are metallic aluminum foil (~15µm t) and sheet (~0.3mm t), which were cut into 10×10~30×30 mm samples. The surface was rinsed with acetone before the experiments. Commercially available liquid $\text{Ga}_{83}\text{In}_{17}$ alloy (melting point 15.7°C, Ultra-Pure Chemical Laboratory, Japan) was dropped on to the center of a glass substrate. The drop size was ca. 2~3mm in diameter. Then, aluminum foil was placed on the drop and sandwiched with another glass plate. The penetration of liquid alloy into the foil was observed in different atmospheres: (i) vacuum

(~10⁻³ Torr), (ii) Ar (1 atm), (iii) dried N₂ gas (1 atm) and (iv) in air. For sheet samples, the alloy was simply dropped on to the sample. Heating tests were carried out in air. The samples were kept at 30, 50, and 70°C for 30 min, respectively. For observation during the experiments, a normal optical microscope (Type SCZ, Carton), a metallurgical microscope (Olympus BX600), a scanning electron microscope (S-3100ST, JEOL, acceleration voltage 10 kV), and an X-ray powder diffractometer (RINT2500, Rigaku Corp., Cu Kα radiation, 40kV-300mA) were employed. A thermocouple (type K) and digital multimeter (Keithley 2000) were used for measuring the temperature increase caused by the spall fracture of aluminum.

3. RESULTS AND DISCUSSION

Fig. 1 shows the changes observed in the surface of aluminum foil that had been in contact with liquid $\text{Ga}_{83}\text{In}_{17}$ in a vacuum for 1 h and then exposed to air. While no significant changes were apparent while in the vacuum, exposure to air caused an abrupt change. In most cases, the alloy penetrated from the back and the color of the aluminum surface became non-metallic, i.e., gray, in a few minutes after exposure to air. The changes proceeded in the following way: first, the center became gray, then the outer region started to change, and finally, the intervening region, i.e., between the center and outer region, gradually changed. These distorted regions did not recover and did not exhibit additional changes even after a considerable time had elapsed. The results were quite similar in an Ar or N₂ environment. The color of the aluminum surface did not change, but some roughening was visible around the region where the $\text{Ga}_{83}\text{In}_{17}$ alloy was dropped. As soon as the sample was exposed to air, the surface changed dramatically. The gradual changes continued for a number of hours, and finished after ca. 7 h. As shown in Fig. 2, the area that underwent a color transformation is formed around the small residue of $\text{Ga}_{83}\text{In}_{17}$ alloy, which was located almost at the center of the aluminum

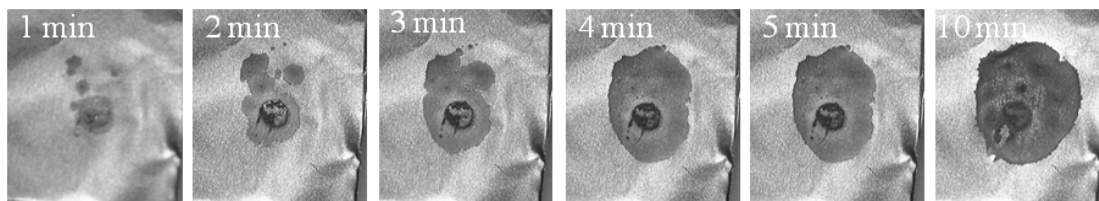


Fig. 1 Optical microscope observation of embrittlement in aluminum. Liquid Ga₈₃In₁₇ alloy was dropped onto an aluminum surface in a vacuum (~10⁻³ Torr) and kept for 1 h. Then, the sample was exposed to the air. The series of photos was taken immediately after such exposure.

foil. One can see a dark-gray angled belt, which corresponds to the outer edge of the initial rapid invasion of Ga₈₃In₁₇ alloy. The diffused border is caused by subsequent slow changes.

In contrast, some differences in the final states were observed when contact was made in air. In particular, much depends on the humidity. For the 25×25 mm aluminum foil, a complete color change was observed for almost the whole surface (not shown here), but the dark-gray belt shown in Fig. 2 did not appear.

Fig. 3 shows the observation of the effect of heating in air on the surface of the aluminum foil in contact with liquid Ga₈₃In₁₇. During heating, the color was almost the same, even in air, but changed rapidly once heating stopped. The extension of the gray area was dependent on the temperature. The size for the sample kept at 70°C was much larger than that for 30°C. This indicates that heating facilitates the diffusion of liquid Ga₈₃In₁₇ in aluminum, while fracturing does not occur in this case. Cessation of heating and then cooling to room temperature causes similar effects to removing the sample after keeping it in a vacuum or in Ar or N₂ gases. In the early stage of this research, some oxidation of the surface was considered as the origin of the color changes,

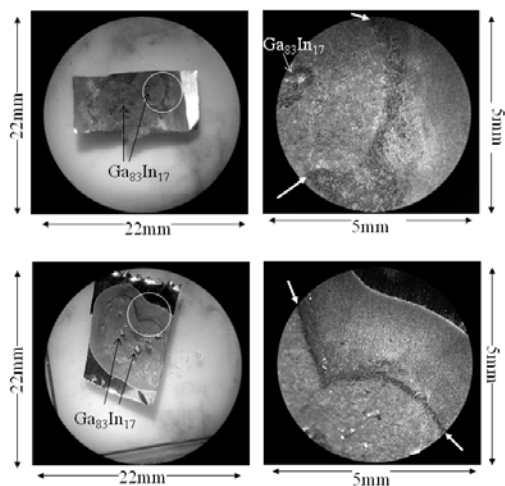


Fig. 2 The effect of atmosphere in embrittlement of aluminum. Liquid Ga₈₃In₁₇ alloy was dropped onto an aluminum surface in an Ar (a) or N₂ (b) atmosphere and kept for 1 h. Then, the sample was exposed to air. The photos were taken after 7 h under an optical microscope in air. The right-hand photos are enlargements of the circled areas in the left-hand photos. The dark gray belt was formed in the initial abrupt reaction just after exposure to air. As indicated by the arrows, one can see that the borders of the belt are quite diffused, which correlates to the reaction slowing down.

but the results indicate that this is not true.

Therefore, in the present research, the influence of moisture in air was examined. First, it was found that keeping the sample in a drier was effective in suppressing the reaction. The color of the aluminum foil did not change even in air, in a manner similar to an atmosphere of Ar or N₂ gases. Second, generally, the sample becomes brittle simply by lowering the temperature to the solidification point of Ga₈₃In₁₇ alloy. However, we did not find any apparent quick changes when the sample was put into liquid nitrogen. This is due to the absence of moisture. Third, water was directly instilled on to the sample in order to thoroughly ensure the impact of moisture. Fig. 4 shows the drastic fracture of aluminum sheet metal following the instillation of water. The residue of Ga₈₃In₁₇ alloy was removed before instillation. Within 30 sec after dropping on the water, bubbles were seen, and the sample was inflated, and fractured. The gray area, which is caused by the erosion of Ga₈₃In₁₇ alloy, spread during contact, but the border was not blurred. Absorbing water induces rapid spall fracture and the aluminum foil or sheet can be broken into fine powders. Such a change can be observed several seconds after instillation. Even in an Ar atmosphere, almost the same results were obtained. We attribute this to the penetration of water into the grain boundaries that were expanded with Ga₈₃In₁₇ alloys. Almost the same phenomena were confirmed when methanol was applied. However, hexanes did not have any affect at all. Probably, the polarity of the solvent affects the

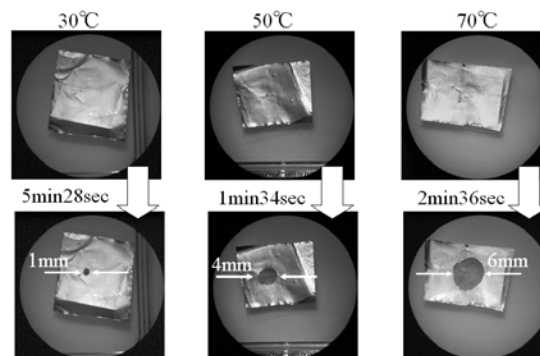


Fig. 3 Effect of heating in embrittlement of aluminum. Liquid Ga₈₃In₁₇ alloy was dropped onto an aluminum surface in air at various temperatures (30°C, 50°C and 70°C). The sample was placed on the hot plate, and kept for 30 min. Cooling then started by switching off the heater, and the upper photos were taken immediately after that, and after some delay, the lower photos were captured.

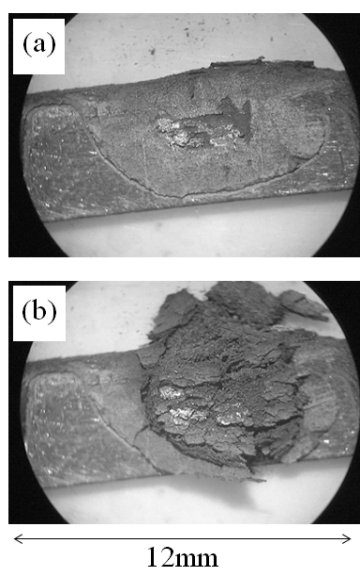


Fig. 4 (a) Brittle texture of aluminum formed by contact with $\text{Ga}_{83}\text{In}_{17}$ alloy and by exposure to air. The surface color of the area invaded by $\text{Ga}_{83}\text{In}_{17}$ alloy changed. (b) Spall fracture of aluminum by dropping water onto the brittle texture shown in (a).

penetration of the grain boundaries. Fourth, surface modification could affect the reaction with moisture in air. One possible way of averting such erosion of the $\text{Ga}_{83}\text{In}_{17}$ alloy would be to prepare an oxide layer on the upper surface. It was confirmed that an anode oxidation film made in 0.1M H_2SO_4 at 10V for 10 min is effective, and no special change was observed even when the sample was placed in contact with liquid $\text{Ga}_{83}\text{In}_{17}$ alloy in air.

In order to further investigate the influence of water on embrittlement, an aluminum foil in contact with $\text{Ga}_{83}\text{In}_{17}$ alloy for 22 h was placed in water. Fine fractions were sampled from the precipitated materials, and dried in air. Fig. 5 (a) shows a SEM image of typical fragments that fractured rapidly from aluminum foil through the addition of water. One can see strip-like fragments of around $1 \times 10 \mu\text{m}^2$, which are covered with small triangular flakes up to $12 \mu\text{m}$. In contrast, when aluminum sheet was used instead of foil, the size distribution of the fractured fragments ranged widely from 0.1-100 μm , and the fragments were typically flake-like. This is because the aluminum was broken only along the direction of rolling and was not torn into isolated grains. In addition, as shown in Fig. 5 (b), the fragments exhibit an X-ray powder pattern corresponding to metallic aluminum. This indicates that, because of the reaction, aluminum oxides and hydroxides are only on the surface, not inside the grains. In addition, the peaks from gallium, indium and their oxide were not observed in this case. The amount of $\text{Ga}_{83}\text{In}_{17}$ alloy absorbed at the boundaries was not so significant.

Another important fact is that the spall fracture of aluminum is exothermal. Fig. 6 shows the results of temperature measurements of the water held in a vial with a piece of aluminum metal. The vial is held in a thermal insulator, and the initial temperature was kept at 20 °C. $\text{Ga}_{83}\text{In}_{17}$ alloy was placed on the aluminum

sheet for two hours before instilling the water. As shown in Fig.6, the water temperature can be typically raised higher than 25 °C, although this obviously depends on the given amount of water, when the aluminum metal is added. We observed that the given amount of water could even become steam when the amount is reduced to 1 ml or less. The rise in temperature is due to the energy release of the chemical bonding at the grain boundaries as solid bulk during its drastic breakdown into micrometer-sized fractions.

It has been suggested that water has a crucial influence on spall fracture. Such a drastic reaction was not observed in experiments using pure metallic gallium. One should note the differences in the wetting nature of liquid gallium and $\text{Ga}_{83}\text{In}_{17}$ alloy with respect to a solid aluminum surface. While liquid gallium is likely to be aggregated, liquid $\text{Ga}_{83}\text{In}_{17}$ alloy has a much smaller angle of contact and therefore spreads over the surface very easily [14,15]. The penetration into the grain boundaries of aluminum is easier for liquid $\text{Ga}_{83}\text{In}_{17}$ alloy than for liquid gallium. The existence of a large amount of water can cause the formation of some oxides and/or hydroxides at the grain boundaries, which are filled with liquid $\text{Ga}_{83}\text{In}_{17}$ alloy spreading along the interfaces. Because of volume expansion through solidification and/or formation of oxides/hydroxides (although the total amount would be very small to detect by X-ray diffraction), spall fracture of aluminum can

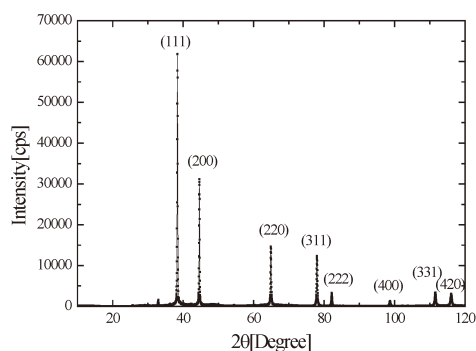
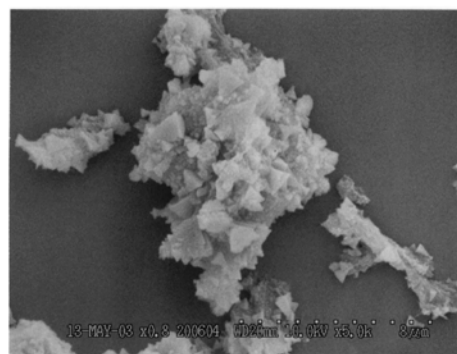


Fig. 5 (a) SEM image of the aluminum fraction obtained by adding water to foil that has been in contact with $\text{Ga}_{83}\text{In}_{17}$ alloy for 22 h in air. The white dotted line shows the scale as $8 \mu\text{m}$. (b) X-ray diffraction pattern of the aluminum fraction. Indexes of metallic aluminum are shown. A small peak at 32.9 deg ($d=2.719 \text{ \AA}$) is not from aluminum, and is close to (-202) reflection of Al_2O_3 ($d=2.7295 \text{ \AA}$).

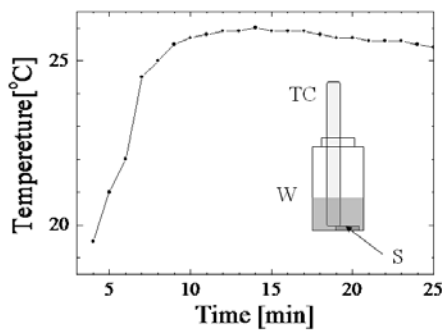


Fig. 6 Measurement of temperature increase during the spall fracture of aluminum. TC: thermo-couple gauge, W: water and S: sample (aluminum sheet or foil embrittled by $\text{Ga}_{83}\text{In}_{17}$ alloy).

take place. The phenomena found in the present research are unique for a combination of $\text{Ga}_{83}\text{In}_{17}$ alloy and metallic aluminum. This is simply due to penetration being much more rapid compared with liquid gallium.

As for the much slower reaction with normal levels of moisture that are present in air, instead of the intentional addition of water, it is worthwhile mentioning the change in morphology. Metallurgical microscopic observation in air revealed that there are two successive steps in the change to the gray area; (i) it extends along the grain boundaries, polishing scratches, and direction of rolling, and then becomes dark but remains flat, and (ii) it is raised up like a scale, and the surface becomes rough. Since the second step takes place right after the first step, the gray area remains flat around the borders. The mechanical and electrical properties also changed substantially. The sample appeared to lose both strength and good conductivity, indicating that the aluminum foil became brittle and that the surface was split into micro particles. The moisture can induce a remarkable spall fracture just because of such a brittle texture.

In summary, spall fracture of metallic aluminum foil and sheet were studied. Liquid $\text{Ga}_{83}\text{In}_{17}$ alloy can penetrate into the grain boundaries of aluminum, and break the texture into fine fragments rapidly in the presence of water. The reaction is exothermal and can heat its ambience.

ACKNOWLEDGMENTS

This work was partly supported by the Active Nano-Characterization and Technology Project, Special Coordination Funds of the MEXT, Japanese Government.

REFERENCES

- [1] W. Rostoker, J. M. McCaughey and H. Markus, "Embrittlement by Liquid Metals", New York, Rheinhold Pub (1960).
- [2] M. G. Nicholas and C. F. Old, *J. Mater. Sci.*, **14**, 1-18 (1979).
- [3] W. Ludwig and D. Bellet, *Mater. Sci. and Eng.*, **A281**, 198-203 (2000).
- [4] W. L. Tsai, Y. Hwu, C. H. Chen, L. W. Chang, J. H.

Je, H. M. Lin and G. Margaritondo, *Nucl. Instrum. & Meth.*, **B199**, 457-463 (2003).

[5] E. Pereiro-Lopez, W. Ludwig and D. Bellet, *Acta Mater.*, **52**, 321-332 (2004).

[6] W. Ludwig, E. Pereiro-Lopez and D. Bellet, *Acta Mater.*, **53**, 151-162 (2005).

[7] T. Ohgaki, H. Toda, I. Sinclair, J.-Y. Buffiere, W. Ludwig, T. Kobayashi, M. Niinomi, and T. Akahori, *Materials Sci. & Eng.* **A406**, 261-267 (2005).

[8] E. Pereiro-Lopez, W. Ludwig, D. Bellet, P. Cloetens, and C. Lemaignan, *Phys. Rev. Lett.*, **95**, 215501 (2005).

[9] M. Kobayashi, H. Toda, K. Uesugi, T. Ohgaki, T. Kobayashi, Y. Takayama, and B.-G. Ahn, *Philos. Mag.*, **86**, 4351-4366 (2006).

[10] R. C. Hugo and R. G. Hoagland, *Acta Mater.*, **48**, 1949-1957 (2000).

[11] R. Tanaka, P.-K. Choi, H. Koizumi and S. Hyodo, *Mater. Trans. JIM*, **41**, 138-140 (2001).

[12] J. Hagstrom, O. V. Mishin and B. Hutchinson, *Scripta Mater.*, **49**, 1035-1040 (2003).

[13] E. Gmelin, M. Asen-Palmer, M. Reuther and R. Villar, *J. Phys. D: Appl. Phys.*, **32**, R19-R43 (1999).

[14] T. Tanaka, M. Matsuda, K. Nakao, Y. Katayama, D. Kaneko, S. Hara, X. Xing and Z. Qiao, *Z. Metallkd.*, **92**, 1242-1246 (2001).

[15] M. V. Trenikhin, A. V. Bubnov, A. I. Nizovskii, and V. K. Duplyakin, *Inorg. Mater.*, **42**, 256-260 (2006).

(Received July 14, 2009; Accepted September 24, 2009)

Orientation Characteristics of a Slit Carbon Plate Used as an RF Electric Shield

Tokoh Nishikubo, Hiroki Endo, and Mineo Itoh

Interdisci. Grad. School of Sci. and Engi., Grad. School of Kinki Univ., 3-4-1, Kowakae, Higashi-Osaka, Osaka, 577-8502, Tel: +81-6-5782-2332, Fax: +81-6-5782-4301, e-mail: t-nishikubo@hotmail.co.jp

Recently, the contamination of electromagnetic environment has become more serious due to the widespread use of electronic devices, namely those used for communication, computation, and automation, among others. Therefore, with the rapid development in these technologies, there has been an increased need for electromagnetic shielding in the radio frequency (RF) region. As one of the basic areas of research for improving the electromagnetic environment, the present authors have developed a slit carbon plate as an RF electric shield that displays orientation characteristics in the shielding results. Little is known, however, about the orientation characteristics found in the RF electric shielding degree SD_E of the slit carbon plate. The present authors examine and clarify the orientation characteristics found in the RF electric shielding effects of the slit carbon plate. Experimental results show the dependencies of the orientation characteristics on the length and width of the slit. For reference, the orientation characteristics found in the RF magnetic shielding are also shown.

Key words: RF electric shielding, orientation characteristics, natural resource, carbon

1. INTRODUCTION

Recently, the contamination of electromagnetic environment has increased with the rapid development in the industrial field [1, 2]. Furthermore, the use of natural resources is required in many applications, such as those in robots, medical instruments, automobiles, and aerospace, among others [3, 4]. Therefore, it is convenient if a natural resource can be applied to the problem of the reduction of electromagnetic environmental pollution. As a natural resource, the present authors have developed a carbon plate that displays orientation characteristics in the RF magnetic shielding effects of a plane wave [5, 6], as one of the basic areas of research for the improvement of electromagnetic environment [7–9].

Little is known, however, about the orientation characteristics found in RF electric shielding effects of a carbon plate. To examine these characteristics, a slit was cut in the center of a carbon plate; termed the slit carbon plate. The RF electric shielding degrees SD_{EH} and SD_{EP} are measured when holding the slits horizontal and perpendicular to the ground, respectively. The shielding degrees decreased with an increase of frequency in the region from 1 MHz (70 dB) to 400 MHz (36 dB), and displayed similar characteristics. Furthermore, the value of SD_{EH} , in the frequency region of 400 MHz (36 dB) to 3 GHz (77 dB), increased with radio frequency. The value of SD_{EP} indicated an average value of 38 dB in this frequency region. That is, the difference in the RF electric shielding degree ($SD_{EH} - SD_{EP}$) as related to the orientation of the slit represents the orientation characteristics. These orientation characteristics can be used in the application of a switch for a microwave guide, for the greater directivity of a low noise antenna, and as a filter for a radio frequency band, among others.

Experimental results revealed several characteristics of the slit carbon plate that include the dependencies of the orientation characteristics on the slit length and slit width. Also discussed are the orientation characteristics

found in the RF magnetic shielding of the slit carbon plate.

2. EXPERIMENTAL PROCEDURE

2.1 Fabrication of the slit carbon plate

In the present research, use was made of a commercial carbon plate (TOYO TANSO, IG-110, 50 mm square, thickness of 2 mm). A slit (width w of 1 mm, length L of 42 mm) was cut on the surface of the carbon plate with the use of a diamond saw at a low cutting rate to prevent any influence of heat and cracking [6]. In order to facilitate the systematic investigation of the orientation characteristics as related to the slit length L of the carbon plate, a series of carbon plates with different slits (L of 7 mm to 42 mm, w of 1 mm) were manufactured. In addition, slit carbon plates (L of 42 mm) having slit widths w from 1 mm to 11 mm were constructed.

2.2 Experimental system for measuring the RF electromagnetic shielding effects

Figure 1 illustrates the geometry of the metal cells and the carbon plate with the slit oriented horizontally to the ground. The experimental system for measuring the RF electromagnetic shielding effects, the electric shielding degree SD_E and the magnetic shielding degree SD_H , was arranged as reported in Ref. [5]. The RF output of the tracking generator (HP, 8594E), which includes a spectrum analyzer, in the frequency region from 1 MHz to 3 GHz, is amplified by 50 dB by the use of broadband amplifier (Kalmus, 210LC-CE), and then guided to the transmitting antenna in the metal cell. The output of the receiving antenna is amplified by 38 dB using a preamplifier (Sonoma, 317), and guided to the spectrum analyzer. The results from the spectrum analyzer are then transferred through a GPIB cable to a laptop computer. In the present research, the input power of the transmitting antenna and the distance between both metal cells were held constant at 10 dBm and 17 mm, respectively. In addition, two metal cells were used to

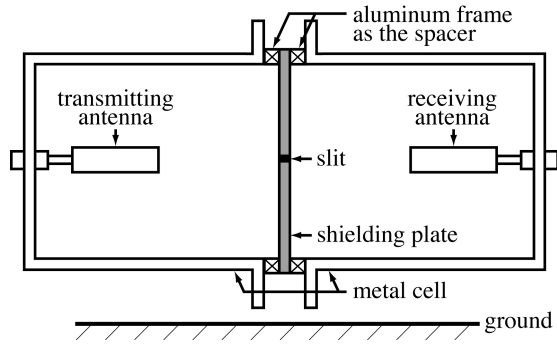


Fig. 1. Schematic diagram illustrating the metal cells and apparatus used to measure the RF electromagnetic shielding effects for the horizontal-oriented slit carbon plate.

form a plane wave, such as reported in Ref. [7]. The coaxial cable employed as the receiving line was threaded through ferrite rings, in order to reduce any interference between the transmitting and receiving lines. Probe and loop antennae were used for measuring the RF electric and magnetic shielding effects.

The RF electric shielding degree SD_E was calculated as follows, being defined in terms of the reduction in the electric field that occurs due to the shielding material [10]. In the present research, the value of SD_E is defined as $SD_E = 10 \log_{10}(P_{E0}/P_{E1})$. Here, P_{E0} and P_{E1} are the strength of the incident electric field and that of the transmitted wave as it emerges from the shielding plate, respectively. On the other hand, the value of the RF magnetic shielding degree SD_H is determined by $SD_H = 10 \log_{10}(P_{H0}/P_{H1})$. In this case, P_{H1} and P_{H0} are the output of the magnetic field power of the receiving antenna, with and without the carbon plate, respectively. The values of SD_E for the horizontal- and perpendicular-oriented slit plates are termed SD_{EH} and SD_{EP} , respectively. The values of SD_H when holding the slit horizontally and perpendicularly are termed SD_{HH} and SD_{HP} , respectively.

3. RESULTS AND DISCUSSION

3.1 RF electric and magnetic shielding characteristics of the slit carbon plates

Figure 2 shows the RF electric shielding degree SD_E for the non-slit and slit (slit length L of 42 mm, slit width w of 1 mm) carbon plates as a function of frequency f , under a constant RF electric output power P_E of 10 dBm of the transmitting antenna. In this figure, the values of RF electric shielding degree SD_{EN} (open squares), SD_{EH} (open circles), and SD_{EP} (solid circles) represent the results for the non-, horizontal-, and perpendicular-oriented (to the ground) slit carbon plates, respectively. It can be seen that the values of SD_{EN} , SD_{EH} , and SD_{EP} decrease as the frequency f increases in the region from 1 MHz (70 dB) to 400 MHz (36 dB), and display similar shielding characteristics. In addition, the values of SD_{EH} increase as frequency f increases in the region from 400 MHz (36 dB) to 3 GHz (77 dB), while the values of SD_{EP} indicate an average of 38 dB in this frequency region. The difference in the values of shielding degree of the carbon plates as related to the orientation of the slit indicates the orientation

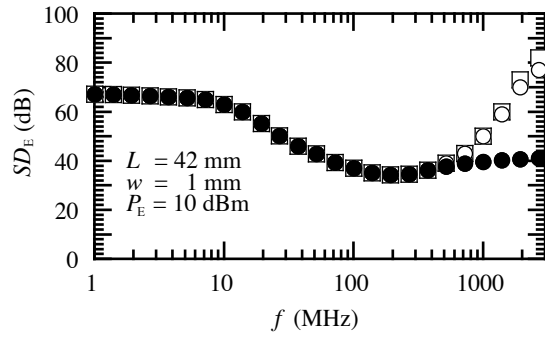


Fig. 2. The RF electric shielding degree SD_E of the carbon plates as functions of frequency f , under a constant RF output power P_E of 10 dBm. Here, the open squares (SD_{EN}), open circles (SD_{EH}), and solid circles (SD_{EP}) represent the shielding characteristics for the non-slit, horizontal-oriented slit, and perpendicular-oriented slit plates, respectively.

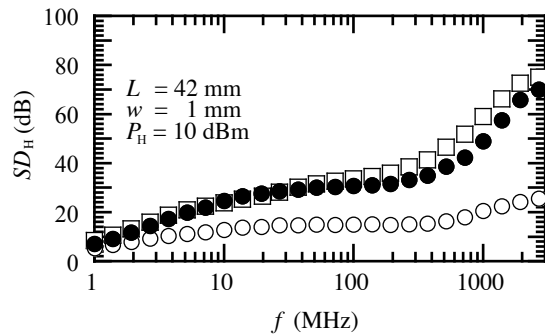


Fig. 3. Characteristics of the RF magnetic shielding degree SD_H for the carbon plates as functions of frequency f [6]. Here, The open squares (SD_{HN}), open circles (SD_{HH}), and solid circles (SD_{HP}) represent the values of SD_H for the non-, horizontal-oriented slit, and perpendicular-oriented slit plates, respectively.

characteristics. The orientation characteristics display a more remarkable effect as the value of f increases. For example, the difference in RF electric shielding degree ($SD_{EH} - SD_{EP}$) is approximately 37 dB at 3 GHz.

Figure 3 [6] shows the characteristics of the RF magnetic shielding degree, for the same plates as shown in Fig. 2, as functions of frequency f , under a constant RF magnetic output power P_H of 10 dBm. In this figure, the values of RF magnetic shielding degree of SD_{HN} (open squares), SD_{HH} (open circles), and SD_{HP} (solid circles) represent the results for the non-, horizontal-, and perpendicular-oriented slit carbon plates. It can be seen that the values of SD_{HN} , SD_{HH} , and SD_{HP} for the carbon plates increase with increasing frequency in the region from 1 MHz to 3 GHz. In this frequency region, the values of SD_{HH} are low compared with those of SD_{HP} . That is, the orientation characteristics in the RF magnetic shielding of the slit carbon plates are completely opposite to those found in the RF electric shielding. In addition, orientation characteristics in the RF magnetic shielding are obtained over a broader frequency region than those found in the RF electric shielding.

3.2 Slit length dependence of orientation characteristics for the slit carbon plate

In order to facilitate a systematic investigation of the orientation characteristics for the slit carbon plate, the present research has modified the slit length L over the region of 0 mm (non-slit) to 42 mm. Figure 4 shows the characteristics of the RF electric shielding degree SD_E as a function of slit length L . The open and solid circles represent the values of SD_{EH} and SD_{EP} for the horizontal- and perpendicular-oriented slit plates at 3 GHz, respectively, under a constant P_E of 10 dBm. It is found that values of SD_{EH} remain constant at approximately 80 dB in the length region from 0 mm to 42 mm. However, the values of SD_{EP} decrease as the slit length L increases in this region. It can be seen that the values of SD_E for the slit carbon plates display orientation characteristics related to the values of L in the length region from 14 mm to 42 mm. That is, the difference in the RF electric shielding degree ($SD_{EH} - SD_{EP}$) increases in the region from 14 mm (15 dB) to 42 mm (37 dB) under the frequency condition of 3 GHz. It is found that the orientation characteristics are more remarkable as the values of L increase.

The dependence of RF magnetic shielding degree SD_H on the slit length L for the same plates as shown in Fig. 4 is displayed in Fig. 5 [6]. In this figure, the characteris-

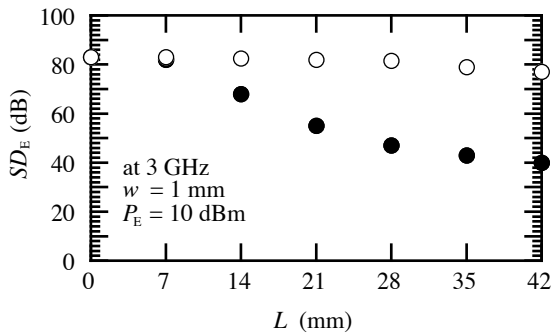


Fig. 4. The characteristics of SD_E for the slit carbon plates as functions of slit length L . Here, the open (SD_{EH}) and solid (SD_{EP}) circles show the results for the horizontal- and perpendicular-oriented slit plates, respectively, for the radio frequency of 3 GHz.

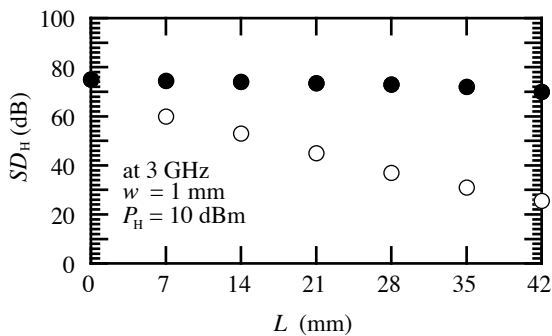


Fig. 5. The characteristics of SD_H for the slit carbon plates as functions of slit length L [6]. Here, the open (SD_{HH}) and solid (SD_{HP}) circles show the results for the horizontal- and perpendicular-oriented slit plates, respectively, at an RF of 3 GHz.

tics shown by the open and solid circles are the results of SD_{HH} and SD_{HP} for the horizontal- and perpendicular-oriented slit plates, respectively, under the constant conditions of f of 3 GHz and P_H of 10 dBm. From these results, it is again seen that the orientation characteristics in RF magnetic shielding of the slit carbon plates are opposite to those found in the RF electric shielding. It is, however, found that these RF magnetic shielding characteristics exhibited similar tendencies as those shown in Fig. 4.

3.3 Slit width dependence of orientation characteristics for the slit carbon plate

The orientation characteristics of the slit carbon plates (slit length L of 42 mm) were then examined for various slit widths of 1 mm to 11 mm. Figure 6 shows the dependence of RF electric shielding degree SD_E for the slit carbon plates on the slit width w , under a constant P_E of 10 dBm. In this figure, the open and solid circles represent the values of SD_{EH} and SD_{EP} at 3 GHz, respectively. It is found that both the values of SD_{EH} and of SD_{EP} decrease as the slit width w increases for widths from 1 mm to 11 mm. In addition, the slit carbon plates tend to exhibit weaker orientation characteristics when the slit width w increases in the region from 1 mm (37 dB) to 11 mm (4 dB). Also, similar tendencies for

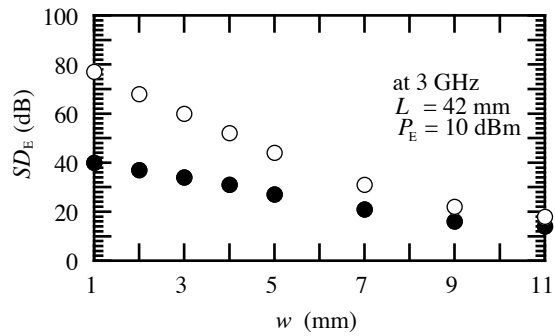


Fig. 6. The characteristics of SD_E for the slit carbon plates as functions of slit width w . Here, open (SD_{EH}) and solid (SD_{EP}) circles represent the values of SD_E for the horizontal- and perpendicular-oriented slit plates, respectively, at 3 GHz.

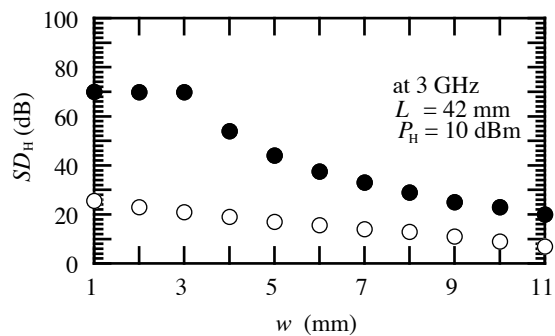


Fig. 7. The characteristics of SD_H for the slit carbon plates as functions of slit width w [6]. Here, open (SD_{HH}) and solid (SD_{HP}) circles represent the values of SD_H for the horizontal- and perpendicular-oriented slit plates, respectively, at 3 GHz.

frequencies in the range from 400 MHz to 3 GHz were obtained for these widths (not shown).

Figure 7 [6] displays the distributions of RF magnetic shielding degree SD_H for slit carbon plates (slit lengths L of 42 mm) as functions of the slit width w , under a constant P_H of 10 dBm. The open and solid circles represent the characteristics of SD_{HH} and SD_{HP} for the horizontal- and perpendicular-oriented slit plates at 3 GHz, respectively. As reported in Ref. [6], it can be seen that the value of SD_{HH} for the horizontal-oriented slit carbon plate slightly decrease as slit width w increases in the region from 1 mm (25 dB) to 11 mm (8 dB). On the other hand, the values of SD_{HP} for the perpendicular-oriented slit plate remain constant in the width region from 1 mm to 3 mm, and then exhibit a sharp decrease as the slit width w increase in the range from 3 mm (70 dB) to 11 mm (20 dB). That is, over the slit width region from 1 mm to 3 mm, the plates maintain high orientation characteristics.

It was further determined that for values of both SD_E and SD_H [6] for all carbon plates, such as shown in Figs. 2–7, exhibited similar shielding characteristics in the thickness region from 2 mm to 10 mm (not shown).

The orientation characteristics of the RF electric and magnetic shieldings for the slit carbon plates as a function of RF output power were also determined. Both the characteristics of SD_E and those of SD_H [6] displayed no evidence of dependence on the values of RF output power P_E and P_H in the region from 5 dBm to 30 dBm (not shown).

4. CONCLUSIONS

With the rapid development in many technologies, such as robots, medical instruments, automobiles, and aerospace, among others, attention has been focused on the electromagnetic environment and associated problems. As one of the basic areas of research for the improvement of electromagnetic environment by employing a natural resource as a shield, the present authors have developed a carbon plate that displays orientation characteristics for a plane wave. Previously, the orientation characteristics of RF electric shielding of the slit carbon plate have been unknown. The present research, therefore, examined and clarified the orientation characteristics found in the RF electric shielding of slit carbon plates. The results of present research can be summarized as follows:

(1) The values of RF electric shielding degree SD_{EP} for the slit carbon plate perpendicular-oriented to the ground were less than those of the shielding degree SD_{EH} for the horizontal-oriented slit plate in the frequency region from 400 MHz to 3 GHz, such as was shown in Fig. 2. That is, the difference in the shielding degrees of the plates as related to the orientation of the slit indicated the orientation characteristics.

(2) The orientation characteristics with regard to the direction of the slit in the RF magnetic shielding of the carbon plates were opposite to those found in the RF electric shielding in the frequency region from 400 MHz

to 3 GHz, such as was shown in Figs. 2 and 3. In addition, the orientation characteristics of the RF magnetic shielding were obtained over a broader frequency region than those found in the RF electric shielding.

(3) The dependence of the orientation characteristics in RF electric and magnetic shieldings on the slit length were opposite of each other with regard to the slit direction, such as was shown in Figs. 4 and 5. It was, however, found that these RF electric and RF magnetic shielding characteristics exhibited similar tendencies. Furthermore, the RF electric and magnetic shieldings of the slit carbon plate (w of 1 mm) displayed more remarkable orientation characteristics as the values of L increased.

(4) The differences, $SD_{EH} - SD_{EP}$ and $SD_{HP} - SD_{HH}$, decreased as the slit width w increased from 1 mm to 11 mm, such as was shown in Figs. 6 and 7. That is, the most suitable condition for better orientation characteristics in RF electric and RF magnetic shieldings was to fabricate the carbon plate with a narrower slit width.

These results indicate important criteria fundamental to the design of practical RF shielding systems that display orientation characteristics. The present authors are now investigating the physical meanings related to the orientation characteristics of the slit carbon plates.

REFERENCES

- [1] H. W. Ott, "Noise Reduction Techniques in Electronics Systems", John Wiley & Sons, Inc., Canada (1988) pp. 1-27.
- [2] U. S. Inan and A. S. Inan, "Electromagnetic Waves", Ed. by M. Horton, Prentice Hall Inc., New Jersey (2000) pp. 35-37.
- [3] M. Inagaki, "New Carbons: Control of Structure and Functions", Elsevier Science Ltd., UK (2000) pp. 1-13, 177-211.
- [4] L. E. Anderson et al, "Biological and Medical Aspects of Electromagnetic Fields", Ed. by F. S. Barnes and B. Greenebaum, CRC Press, New York (2007) pp. 413-25.
- [5] T. Nishikubo, H. Endo, K. Itoh, and M. Itoh, *IEEE Transactions on Applied Superconductivity*, **18**, 1382-86 (2007).
- [6] T. Nishikubo, H. Endo, and M. Itoh, *IEEE Transactions on Instrumentation and Measurement Technology*, **58**, in printing.
- [7] H. Norikane, T. Nishikubo, S. Gokyu, K. Itoh, and M. Itoh, *IEEE Transactions on Applied Superconductivity*, **16**, 1765-68 (2006).
- [8] T. Nishikubo, H. Norikane, H. Endo, K. Itoh, F. Tojo, and M. Itoh, *Transactions of the Materials Research Society of Japan*, **32**, 1063-66 (2007).
- [9] T. Nishikubo, H. Endo, H. Norikane, K. Itoh, F. Tojo, and M. Itoh, *Transactions of the Materials Research Society of Japan*, **32**, 1067-70 (2007).
- [10] S. A. Schelkunoff, "Electromagnetic Waves", Van Nostrand, Princeton (1943) pp. 303-11.

(Received December 12, 2008; Accepted September 16, 2009)

Electromagnetic Wave Absorption by Rice Hull Carbon

Mitsuhiro Kaneta*, Takeshi Takahashi**, Tomoyuki Kanaya*** and Hiroshi Iizuka****

* Graduate School of Science and Engineering,
Yamagata University, 4-3-16 Jonan, Yonezawa 992-8510, Japan
Fax: +81-238-26-3212, e-mail: dws21711@dip.yz.yamagata-u.ac.jp

**Sanwa Yushi Co.Ltd., Tendo 994-0044, Japan

***Miyasaka Polymer Co.Ltd., Yonezawa 992-0083, Japan

****Faculty of Engineering, Yamagata University, 4-3-16 Jonan, Yonezawa 992-8510, Japan

We have carried out the project for the useful utilization of the remaining rice hull as an industrial carbon material. The rice hull carbon (RHC) powder is manufactured by carbonizing in a nitrogen gas atmosphere at high temperature, then crushing and sieving. The rice hull has a natural porous structure. The diameter of the unit cell is about 10 μ m. The porous structure retained even after the carbonizing and crushing. The composite material comprised of the RHC and Ethylene Propylene Diene Methylene linkage rubbers is manufactured by molding and vulcanizing. In this study, the characteristic of electromagnetic wave absorption (reflectivity) was measured in frequency band between 50MHz and 8GHz for the composite material. The composite material possessed a high characteristic of electromagnetic wave absorption for 2GHz-8GHz. The characteristics were further affected by the test piece thickness and the RHC powder content.

Key words: Rice-Hull, Porous carbon material, Rubber composite material, Electromagnetic wave absorption, Reflectivity.

1. INTRODUCTION

Rice is a staple food, and its amount is about 10 million tons per year in Japan. The rice hull is the by-product of the rice and the amount is about 2.6 million tons per year [1]. About 1.7 million tons of the rice hull is reused as a fertilizer, a carbonizing chaff and a soil conditioner, etc. The rice hull contains about 80 mass% of the organic constituent and 20 mass% of the inorganic constituent. The main inorganic constituent is silica, whose amount is more than 95mass% [2]. The authors have carried out the project for the useful utilization of the remaining rice hull as an industrial carbon material [3,4].

The rice hull carbon (RHC) powder is manufactured by carbonizing the rice hull in a nitrogen gas atmosphere at high temperature, then crushing and sieving the carbonized particles. The RHC powder contains about 56 mass% of the carbon, about 32 mass% of the oxygen and about 9 mass% of the silicon. The RHC powder is expected to use as a functional filler for the plastics and rubbers, since it provides new functions for the composite material [5].

In this study, the characteristic of electromagnetic wave absorption (reflectivity) was measured in frequency band between 50MHz and 8GHz for the composite material comprised of RHC/Ethylene Propylene Diene Methylene linkage (EPDM). More over, the influence of RHC

powder contents and test piece thickness on the electromagnetic wave absorption was evaluated.

2. EXPERIMENTAL PROCEDURE

2.1 Manufacturing process

Fig.1 shows the manufacturing process of the RHC powder and the RHC/EPDM composite. At first, the rice hull was carbonized in nitrogen gas atmosphere at 900 $^{\circ}$ C for 3 hours. The carbonized rice hull was then pulverized by a mill to obtain the RHC powder. The RHC powder was sieved by 106 μ m meshed filter to obtain the powder of 20 μ m median diameter. The composite material of the RHC powder and EPDM is manufactured by molding and vulcanizing.

Fig.2 shows the natural porous structure of the rice hull. The diameter of the unit cell is about 10 μ m. Fig.3 shows the macrostructure of the RHC powder. The porous structure retains even after the carbonizing and crushing.

2.2 Test pieces

The electromagnetic wave absorption characteristic was evaluated dividing the measuring bands into 50MHz-3GHz and 2GHz-8GHz.

Fig.4 (a) shows the test piece of S parameter method for 50MHz-3GHz. The shape of the test piece is toroidal. Fig.4 (b) shows the test pieces of arch method for 2GHz-8GHz. The geometry of the test piece is 300(w) \times 300(h) \times t(thickness).

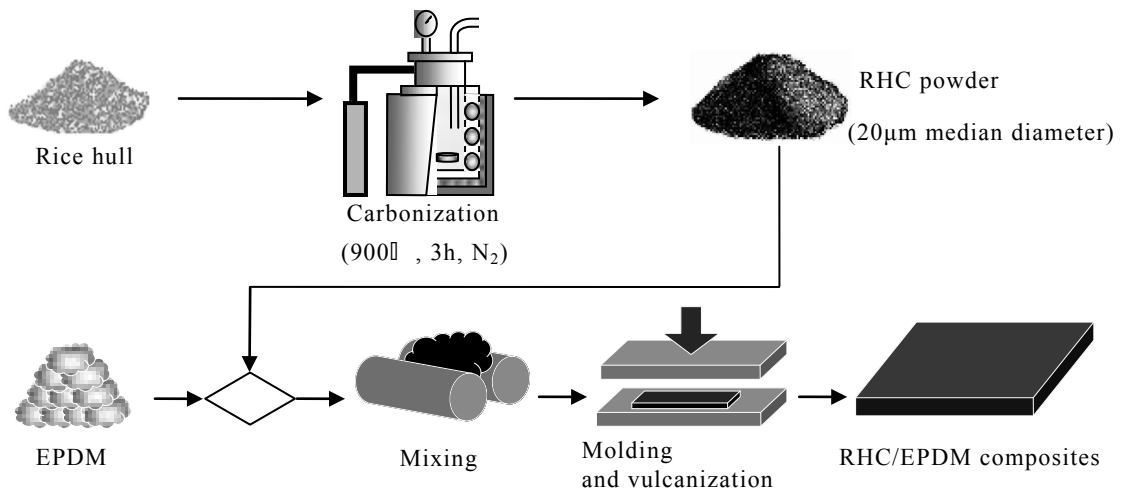


Fig.1 Manufacturing process of RHC powder and rubber composite material.

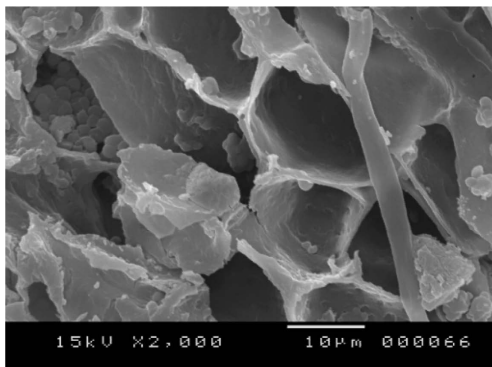


Fig.2 Macrostructures of rice hull.

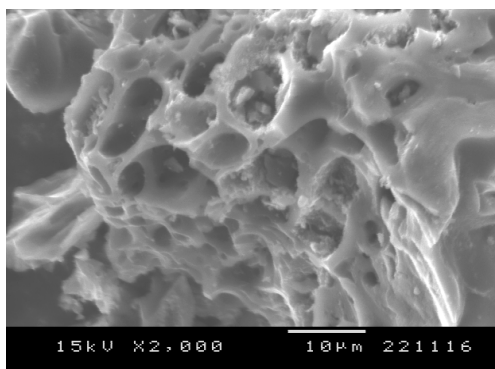
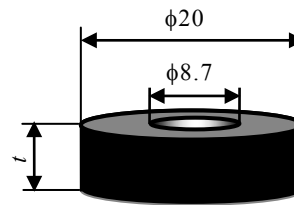
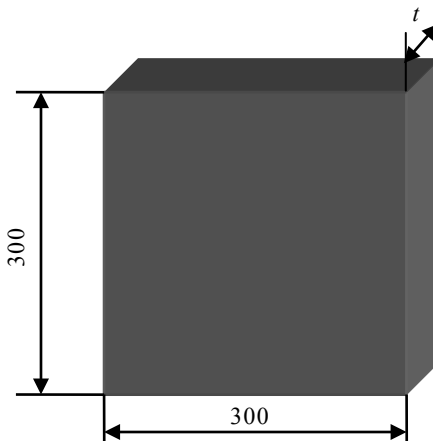


Fig.3 Macrostructures of RHC powder that was carbonized at 900°C.

Table 1 lists the RHC powder contents of the test pieces. The test piece thickness was 2.5mm for the test pieces to evaluate the effect of the RHC powder content. The powder content was 300 per hundred rubber (phr) when the effect of the test piece thickness was evaluated.



(a) Test piece for 50MHz-3GHz.



(b) Test piece for 2GHz-8GHz.

Fig.4 Geometry of test pieces for electromagnetic wave absorption. (a) is used for S parameter method, (b) is used for arch method.

2.3 Electromagnetic wave absorption tests

The electromagnetic wave absorption in the 50MHz-3GHz was measured by the S parameter method. Fig.5 shows the measuring system of the S parameter method. The test piece was put into a jig and the measurement, applied the incident wave perpendicularly to the test piece.

Table 1 Thickness and RHC powder contents of test piece.

No.	Thickness [mm]	Content [phr]
1	2.5	100
2		200
3		300
4		400
5	0.5	300
6	1	
7	1.5	
8	2	
9	2.5	
10	5	

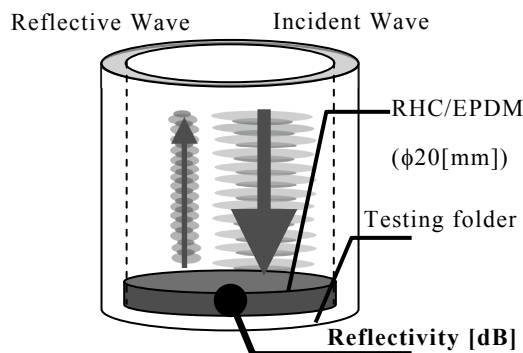


Fig.5 Measuring system by S parameter method for 50MHz-3GHz.

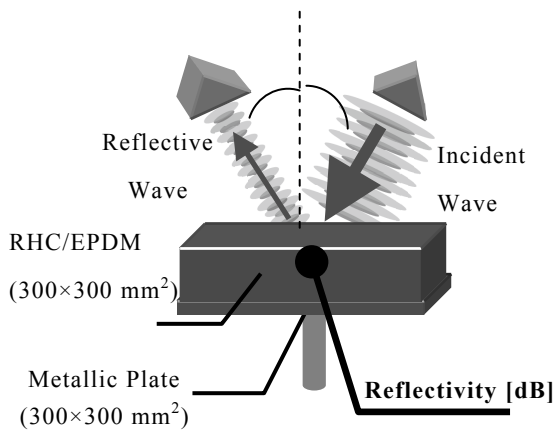
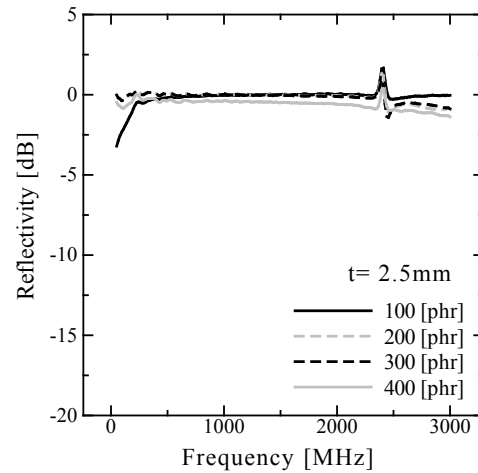
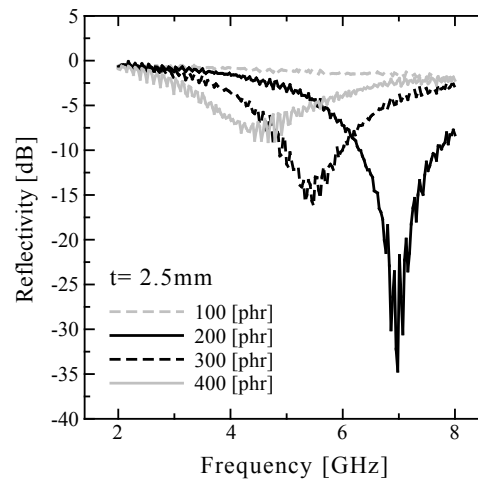


Fig.6 Measuring system by arch method for 2GHz-8GHz.

The electromagnetic wave absorption characteristic under 2GHz-8GHz was evaluated by using the arch testing method. Fig.6 shows the measuring system of the arch testing method. The incident wave was applied from the transmitter to the test piece. The amount of electromagnetic wave absorption (reflectivity) was evaluated using the power loss between the incident wave and the reflective wave in each frequency.



(a) 50MHz-3GHz.



(b) 2GHz-8GHz.

Fig.7 Effect of RHC powder content in RHC/EPDM on electromagnetic wave absorption (reflectivity).

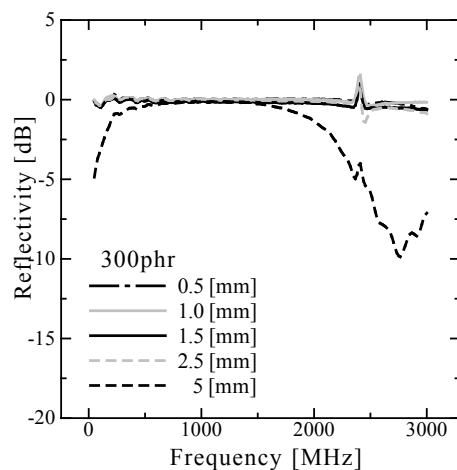
3. EXPERIMENTAL RESULTS AND DISCUSSION

3.1 Effect of powder content on reflectivity

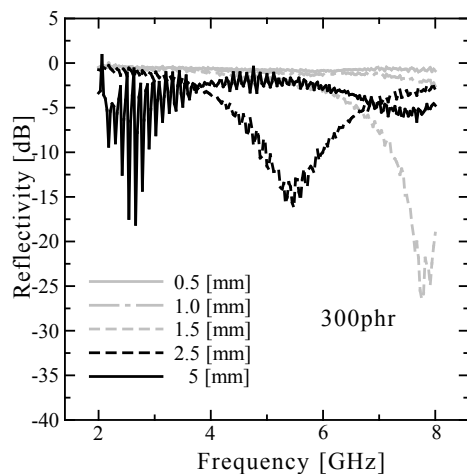
Fig.7 (a) shows the effect of the amount of RHC powder on the characteristic of electromagnetic wave absorption for 50MHz-3GHz. The electromagnetic wave absorption was low, and about -3dB or less.

Fig.7 (b) shows the effect of the RHC powder on the characteristic of electromagnetic reflectivity for 2GHz-8GHz. The test piece with 200 phr has considerably high electromagnetic wave absorption of about -35dB at about 7GHz. The test piece with 300 phr has about -15dB peak value at about 5.3GHz absorption frequency.

The distance between the RHC powders is considered to be narrow in the RHC/EPDM in which a lot of RHC powders were included. We have confirmed that the high powder composite of the RHC/EPDM had a



(a) 50MHz-3GHz.



(b) 2GHz-8GHz

Fig. 8 Effect of Board thickness on electromagnetic wave absorption (reflectivity).

high electromagnetic wave shielding under low frequency band of 1-1000MHz, although the wave penetrated in the low powder content of RHC/EPDM. The results of Fig. 7 (a) implies that the electromagnetic wave is almost reflected on the test piece surface under low frequency bands. Therefore, it is considered that there is a reasonable amount of RHC powder content for the wave absorption.

Moreover, the peak absorption values and the absorption frequency are changed with amount of the filler content as shown in Fig. 7 (b).

3.2 Effect of test piece thickness

Fig. 8 (a) shows the effect of test piece thickness on the reflectivity for 50MHz-3GHz. The test piece with thickness 5mm has the peak value of about -5dB at about 50MHz, and about -10dB at about 2.7GHz.

Fig. 8 (b) shows the effect of test piece thickness on the

reflectivity for 2GHz-8GHz. The test piece thickness 1.5mm obtained the high electromagnetic wave absorption of about -25dB at about 8GHz. Moreover, the test piece with thickness 2.5mm obtained about -15dB at about 5.5GHz, and the test piece with thickness 5mm was obtained about -10dB at about 2.6GHz. The peak values and the absorption frequency are changed with the test piece thickness.

These results show that there is an optimum combination of the RHC powder content and the test piece thickness to obtain a high electromagnetic wave absorption for a given frequency band.

4. CONCLUSION

The characteristic of electromagnetic wave absorption was measured in frequency band of 50MHz-8GHz for the composite material of RHC/EPDM. The authors evaluated the influence of RHC powder contents and test piece thickness. The summary of the obtained results was described as follows.

- (1) The considerably high electromagnetic wave absorption of about -35dB at about 7GHz was obtained for test piece with 200 phr.
- (2) The peak values and the absorption frequency are changed with the powder contents and test piece thickness.
- (3) There is an optimum combination of the RHC powder contents and the test piece thickness to obtain a high electromagnetic wave absorption for a given frequency band.

ACKNOWLEDGMENTS

The authors wish to express their gratitude to Associate Professor Hiroki Anzai, Tsuruoka National College of Technology, for his experimental support.

The authors wish to express their gratitude to the Ministry of Agriculture, Forestry and Fisheries of Japan for their financial support on "New technology development for activation of food industry by academic, industry, and governmental cooperation"

REFERENCES

- [1] T.Ishitani, K.Ohtsubo, "The Science of Rice (in Japanese)", Asakura Shoten, Tokyo (1995) p.172.
- [2] S.Chandrasekhar, K.G.Styanarayana, P.N.Pramada, P.Raghavan, "Processing Properties and Applications of Reactive Silica from Rice Husk", J. Mater. Sci., 38, 3159-68 (2003).
- [3] H.Iizuka, G.Kato, K.Igarashi, S.Shikano and T.Takahashi, "Mechanical Properties of Porous Carbon Materials made from Rice Bran", J. Soc. Mater. Sci. Jpn. 49, 625-630 (2000).
- [4] M.Shishido, S.Kubo, T.Takahashi and H.Iizuka, "Mechanical Properties of Porous Carbon Materials made from Rice Hull", Trans. Mater. Res. Soc. Jpn. 31, 993-996 (2006).
- [5] M.Shishido, Y.Kurita, M.Ishikawa and H.Iizuka, Trans. Mater. Res. Soc. Jpn. 32, No.4, 1039-1042. (2007).

(Received December 12, 2008; Accepted September 16, 2009)

Production of Titanium Oxide Layers on Woodceramics by Plasma Thermal Spraying

Akira Hashimoto, Akito Takasaki, Susumu Uematsu*, and Toshihiro Okabe**

Department of Engineering Science and Mechanics, Shibaura Institute of Technology, Koto-ku, Tokyo 135-8548

*Structure & Materials Department, National Maritime Research Institute, Mitaka, Tokyo 181-0004

**Material Technology Division, Aomori Industrial Research Center, Aomori 030-0113

The anatase titanium oxide (TiO₂) powders were coated on the woodceramics, which were made from radiata pine wood fiberboards carbonized at 923 K, by means of three electrodes type-plasma thermal spraying in air, in which plasma was ejected from each electrode. Water-resistant and photocatalytic performances of TiO₂ coated woodceramics were investigated. Both the rutile and the anatase TiO₂ were produced after thermal spraying. A lower power thermal spraying produced much amount of anatase TiO₂. The water-resistant performance for the woodceramics was improved by thermal spraying and thermal spraying with a lower power much improved this performance. The photocatalytic performance determined from concentration variations of ethanol in a vessel during an ultra violet light exposure to the woodceramics indicated that the concentration decreased much faster (about 85 % decrease in 4 h) for the woodceramics after thermal spraying. It is indicated that photocatalytic performance was improved by thermal spraying.

Keywords: Woodceramics, thermal spraying, TiO₂, photocatalytic effect, water-resistance

1. INTRODUCTION

Woodceramics [1], which are carbonized at elevated temperatures in a vacuum after impregnating phenol resin, are new kinds of porous carbonaceous materials and composites that can be made from biomass like wood wastes. They are expected to be used in a wide range of industrial fields. Their mechanical properties are dependent upon the amount of phenol resin and carbonized temperature [2]. They are thought to be very much attractive as one of the advanced building materials because of high compressive strength [2] and excellent electromagnetic shielding characteristics [3].

On the other hand, since the discovery of a photosensitive anatase titanium oxide (TiO₂) electrode by Fujishima et al. [4, 5], photocatalytic TiO₂ has received much attention because of their strong photo-oxidizing ability when exposed to light. The anatase TiO₂ degrades harmful organic contaminants and provides antimicrobial function. More recently, photocatalytic TiO₂ was synthesized in the form of thin films, to take advantage of its functional properties over a wide range of substrate materials. As a result, commercialized products such as self-cleaning glass, air cleaning lamp, wiperless windshield etc. have been demonstrated [6]. In this study, to expand the fields of industrial application and to functionalize the total performances of woodceramics, we attempted to produce anatase TiO₂ layers on woodceramics by means of plasma thermal spraying. The organic contaminants on the TiO₂ are generally decomposed into CO₂ and H₂O by absorbing the light, so that antifouling, antibacterial or deodorant effects can be expected if TiO₂ layers are produced on the woodceramics.

2. EXPERIMENTAL PROCEDURES

The starting woody material used in this study was medium-density radiata pine fiberboards. These

materials were impregnated with phenol resin, and then they were carbonized at 923 K in a vacuum. The final products are porous carbonaceous materials called "woodceramics".

Three electrodes type-thermal spraying, in which the plasma is ejected from each electrode to the woodceramics surface, was carried out with an Ar-He plasma in air. This thermal spraying reduces the temperature increase in the powder, compared with that by normal single electrode type-thermal spraying technique. The arc voltage was kept to 34 V. The arc currents and the spraying distances between gun torch and the woodceramics were varied. Table 1 summarizes the experimental conditions for thermal spraying. In this table, no powder means spraying without powders to be supplied. The anatase TiO₂ powders were automatically supplied from a glass container to the gun torch and sprayed onto the woodceramics board with about 100 x 100 mm² (thickness was 10 mm). The Powder feeding rate was approximately 10 g/min. The woodceramics surface was thermally sprayed from top to bottom and number of the transverse per one spraying scan was two for sample C, and for other samples it was just one. The

Table 1 Experimental conditions for thermal spraying.

Sample	Spraying Distance (mm)	Current (A)	Number of transverse
No powder	80	230	1
Sample A	80	230	1
Sample B	80	200	1
Sample C	120	260	2

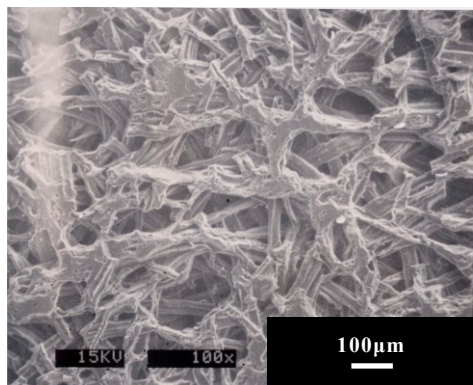


Fig. 1 Surface of the woodceramics carbonized at 923 K.

scanning velocity was about 7.2 m/min on average for all samples. X-ray diffraction (XRD) measurements were made using a JEOL JDX-11PA with Cu-K α radiation at 30 kV and 20 mA to identify the deposited products on the woodceramics. Scanning electron microscopy (SEM) observation with energy dispersive X-ray (EDX) detector was also performed before and after thermal spraying.

The small sized woodceramics samples were immersed in pure water in a vessel for several times and the water-resistant properties were investigated. The photocatalytic performances were also measured. The small sized woodceramics sample was put in a vessel with volume of 4.7 l, and ethanol with initial concentration of 1400 ppm was injected into the vessel. An ultra violet (UV) light with intensity of 614 $\mu\text{W}/\text{cm}^2$ was exposed to the woodceramics surface through the quartz glass upper of the vessel. The concentration of ethanol in the vessel was measured every one hour by gas detecting tubes at a room temperature (298 K).

3. RESULTS AND DISCUSSION

Fig. 1 shows the surface of the woodceramics carbonized at 923 K. Because the starting materials

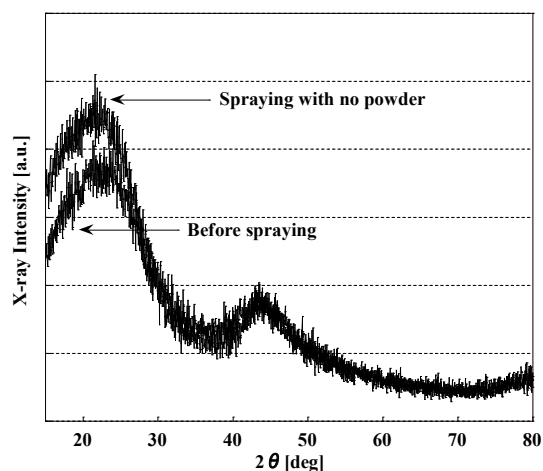


Fig. 2 X-ray diffraction patterns for the woodceramics before and after thermal spraying without powders.

were medium-density radiata pine fiberboards, the woodceramics still possess fiber-like structure showing porous materials.

Fig. 2 shows XRD patterns for the woodceramics before and after thermal spraying without powders. Different from the graphite, one can observe only two broad XRD peaks for both woodceramics indicating that the structure of the woodceramics is turbostratic one (long range ordering of the graphite structure almost disappears but rough alignment of graphite interlayer (graphene sheets) still remains). The carbonization seems to be enhanced after thermal spraying without powders, because the XRD intensity of the (002) plane for the graphite slightly increases after thermal spraying.

Fig. 3 shows XRD patterns of the woodceramics thermally sprayed with anatase TiO₂ powders at three experimental conditions shown in Table 1. Two types of titanium oxides, that are anatase and rutile, are observed on all the samples indicating that the rutile may be formed after partial melting of the anatase or the anatase directly transforms into the rutile because the rutile structure is the most thermally stable. XRD intensities of the anatase TiO₂ for sample B, whose spraying current is lower than that for sample A, become stronger suppressing the formation of the rutile TiO₂. To increase the number of the transverse per one spraying scan is also effective to suppress the transformation of the anatase TiO₂ (sample C) because the corresponding XRD peaks become stronger. We had attempted to produce the anatase TiO₂ on the woodceramics by a single electrode type-thermal spraying at comparatively low power. However, in any cases, the deposited products were the rutile after thermal spraying, indicating that the single electrode type-thermal spraying increased the powder temperature, and enhanced the transformation to the rutile TiO₂ from the anatase one.

Fig. 4 shows the surface of the woodceramics after thermal spraying and corresponding EDX analyses (Ti and O). Although the woodceramics is porous materials, the woodceramics surface is relatively covered well with TiO₂.

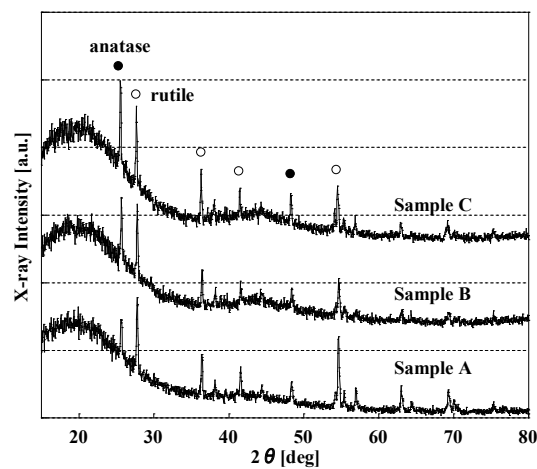


Fig. 3 X-ray diffraction patterns for the woodceramics after thermal spraying.

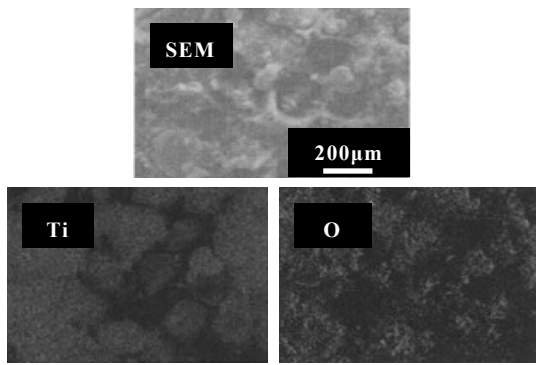


Fig. 4 Surface of the woodceramics after thermal spraying (sample C) and corresponding energy dispersive X-ray analyses results for Ti and O.

Fig. 5 shows water-resistant performances for the woodceramics with and without thermal spraying at three experimental conditions. The performance for the woodceramics without thermal spraying is also included in Fig. 5. The water-resistant performance for the woodceramics is improved by thermal spraying so that the TiO₂ powders seem to deposit and seal the pores of the woodceramics. Thermal spraying with comparatively low power (sample B) much improves the water-resistant performance, because of denser coating. Further improvement is needed to functionalize the woodceramics. Multiple number of spraying at the present experimental conditions seems to damage the surface since the performance of sample C is lowest among them.

The photocatalytic performances of the woodceramics before and after thermal spraying were determined by variations of ethanol concentrations during an exposure of UV light. The results are shown in Fig. 6. The concentration variation in the vessel without sample is also included in Fig. 6. The concentration decreases with increasing the exposure time of the UV light for both samples (with and without thermal spraying). The

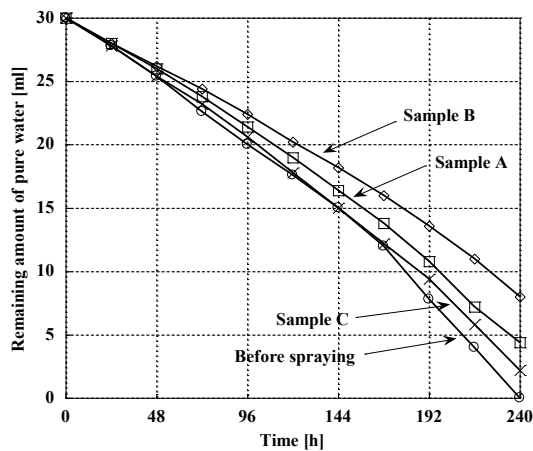


Fig. 5 Pure water immersing test results for the woodceramics after thermal spraying at three spraying conditions shown in Table 1.

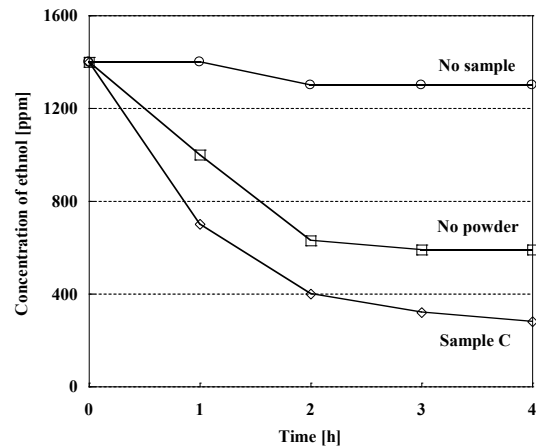


Fig. 6 Photocatalytic test results, determined from ethanol concentration variations during an exposure of ultra violet light, for the woodceramics before and after thermal spraying. The result without sample is also included.

woodceramics itself may absorb some amount of ethanol, however, the concentration for the sample with thermal spraying (sample C) is much lower (about 200 ppm in 4 h, which is about 85 % decrease from the beginning) than that without thermal spraying, indicating existence of photocatalytic effect for the woodceramics with thermal spraying of the anatase TiO₂ powders.

4. CONCLUSIONS

We attempted to produce TiO₂ layers on the woodceramics carbonized at 923 K by means of three electrode type-thermal spraying technique with anatase TiO₂ powders, and their water-resistant and photocatalytic performances of the products were investigated. The results obtained are summarized as follows.

1. Thermal spraying with anatase TiO₂ produced two kinds of TiO₂, rutile and anatase, on the surface of woodceramics. A lower power thermal spraying suppressed the transformation of the anatase TiO₂.
2. The water-resistant performance for the woodceramics was improved by thermal spraying. A low power thermal spraying enhanced denser TiO₂ deposition even in pores of the woodceramics.
3. The decomposition of ethanol during an ultra violet light exposure was enhanced for the woodceramics with thermal spraying, showing the photocatalytic effect of TiO₂.

Acknowledgements

The authors would like to thank Mr. Yuh Ebihara, a graduate student of Shibaura Institute of Technology (now, Kanto Auto Works, Ltd.) at that time, for his experimental works.

REFERENCES

- [1] T. Okabe, K. Saito, K. Hokkirigawa, J. Porous Mater., **2**, 207 (1996).
- [2] H. Iizuka, M. Fushitani, T. Okabe, and K. Saito, J.

Porous Mater., **6**, 175 (1999).

[3] K. Shibata, T. Okabe, K. Saito, J. Porous Mater., **4**, 269 (1997).

[4] A. Fujishima, K. Honda, Nature, **238**, 37 (1972).

[5] A. Fujishima, K. Kohayakawa, K. Honda, J. Electrochemi. Soc., **122**, 1487 (1975).

[6] C.-J. Chung, P.-Y. Hsieh, C.-H. Hsiao, H.-I. Lin, A. Leyland, Surface & Coatings Tech., **203**, 1689 (2009).

(Received December 12, 2008; Accepted September 16, 2009)

Study on Utilization of Cutting Chips of Wood Ceramics

Kazuhiko Ogawa,¹⁾ Toshihiro Okabe²⁾

¹⁾Tokyo Inst. Polytechnic Univ., 2-32-1 Ogawanishi-machi Kodaira, Tokyo 187-0035, Japan
 FAX: 81-42-346-7125, e-mail: ogawa@tokyo-pc.ac.jp

²⁾Aomori Ind. Res. Center, 4-1 1-6, Daini - Toyamachi, Aomori 030-0113, Japan,
 FAX: 81-172-35-5093, e-mail: okabe@aomori-tech.go.jp

Recently, the generation of poisonous substances, such as formaldehyde, from adhesives or paints used for interior finishing projects has become a serious problem. Dust and cutting chips produced while working with woodceramics (WCS) are currently put into disposal. This study aimed to determine a way to recycle dust and cutting chips. The authors focused on the excellent gas adsorptivity of WCS, and attempted to use these materials in construction. Several paints were prepared to adsorb poisonous substances in the air to prevent sick house syndrome. A large amount of wooden building materials, from which WCS are produced, is discharged from construction sites every day. Therefore, if they can be reused as construction materials, one of ideal recycles can be achieved. Thus, WCS have great potential to be used as eco-friendly materials.

Key words: woodceramics

1. Introduction

Wood ceramics (WCS) are a family of porous carbon materials that are obtained from wooden construction waste, sawdust, etc. by the following steps: (1) compression molding is performed on a raw material (wooden construction waste, sawdust, etc.), (2) vacant spaces in the obtained material are impregnated with phenol resin, and (3) the impregnated material is carbonized between 200°C and 2000°C in an oxygen-free atmosphere. WCS are light and hard, and are now finding uses as materials for electromagnetic shielding^{1), 2)}, heating media^{3), 4)}, and moisture and ammonia sensors^{5), 6)}, based on their excellent characteristics of thermal resistance, conductivity, and cost performance. Moreover, their outstanding adsorption performance has attracted attention in many fields.

When the carbonization is performed at 800°C, the obtained WCS shrink by approximately 20% in the plane direction and 26% in the thickness direction after the carbonization. This is because the shrinkage percentage differs according to the fiber direction of the wooden material, and consequently, deformation occurs during carbonization⁷⁾. Therefore, a secondary fabrication, such as cutting and grinding, is performed

after the carbonization, when producing components that require accuracy⁸⁾. During this secondary fabrication, large amounts of cutting chips and dust are produced, and the majority of these are currently put into disposal.

Volatile organic compounds (VOCs) such as formaldehyde in residences and buildings have become a health issue, and countermeasures to eliminate them are urgently required. As shown in Figure 1, WCS have a porous structure, which we recognized as possibly having good adsorption performance. We therefore proposed to mix cutting chips from WCS secondary fabrication with a water-based emulsion type paint used for interior finishing projects. Our hypothesis was that the film of this mixed paint could have formaldehyde-adsorbing properties. This would also allow us to recycle the dust and cutting chips produced while working with WCS, and to use these again as a building material. The end result would be production with close to zero emission (no waste would now be generated in the process of manufacturing WCS products from construction waste), as shown in Figure 2.

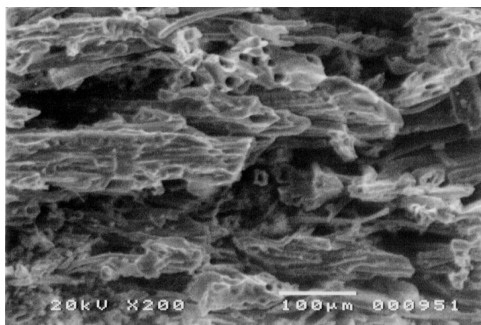


Fig. 1 Porous structure in WCS

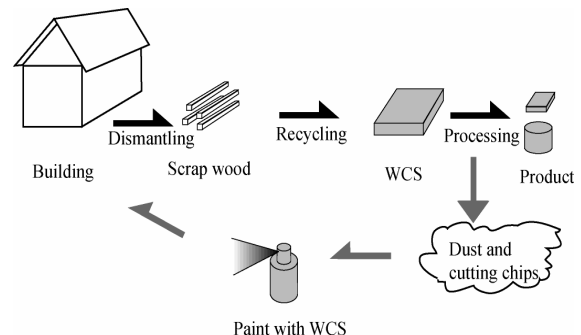


Fig. 2 Recycling of WCS in the building production

2. Methods

This experiment primarily used a medium density fiberboard (MDF) carbonized at 650°C as the WCS. This type of WCS is currently employed in heating elements of heaters etc., and it is expected to be the form used in the most applications. Cutting chips with 0.05–0.1 mm particle diameters, which were produced while working with WCS using a cutting grinder, were used as the WCS powder in this experiment, on the assumption of actual use. As a paint, F☆☆☆☆ water-based emulsion paint (Viny-Deluxe; Kansai Paint Co., Ltd., Japan) was used. Generation of formaldehyde from this paint itself was considered to have been minimized. An emulsion-type gray paint (lusterless) was used for the undercoating.

A desiccator with a 5.4-L capacity was used in the adsorption test, and formaldehyde adsorption performance of the paint mixed with WCS was investigated under a temperature of 20°C ± 1°C. In addition, the standard mixing ratio of WCS to the paint was determined to be 5%, based on the intensity of the paint film⁹⁾. The viscosity of the paint when mixed with WCS was fixed (L.H.S viscosity: 13–15 s) to minimize the error in each test caused by the differences in the mixing ratio. A plasterboard (60 × 60 × 12 mm) for building use was used for all of the specimens, and the emulsion-type gray paint was applied to the undercoating.

3. Particle diameter, carbonization temperature, and adsorption performance of WCS

The quality and adsorption performance are reported to differ according to the carbonization temperature. Therefore, the effects of carbonization temperature and WCS particle diameter on formaldehyde adsorption performance by the paint film were first investigated. In the temperature comparison test, cutting chips produced carbonized at 500°C–1200°C were used. In the comparison test of the particle diameter, cutting chips at 650°C were classified into 7 sizes using sieves of different meshes (#40–#230).

The sieved chips were mixed with the paint to prepare the specimens. After mixing 5 wt% of the sieved chips with the water-based emulsion paint, the mixed paint was applied to the plasterboard using a spray gun. Since the diameter of the nozzle of the spray gun was 1 mm, the paints mixed with WCS consisting of particles larger than 0.56 mm were difficult to apply using the spray gun. Therefore, these paints were applied using a brush to form the films. After painting, the surface of the specimen was ground using a #240 emery paper, and the adsorption performance was investigated (adsorption test).

For the adsorption test, approximately 5–6 ppm formaldehyde gas was generated in the desiccator by burning 0.001 mg paraformaldehyde. The formaldehyde concentration was measured using a formaldehyde meter (Formaldemeter htv; JMS Inc., Papan) for 20 h (20°C ± 1°C) at intervals of 30 min. The formaldehyde adsorption amount was compared among the painted specimens.

Figure 3 shows the changes in the formaldehyde concentration according to the particle diameter of WCS. No difference in formaldehyde adsorption was

seen in response to changes in the particle diameters. Therefore, particle diameter was eliminated as a factor

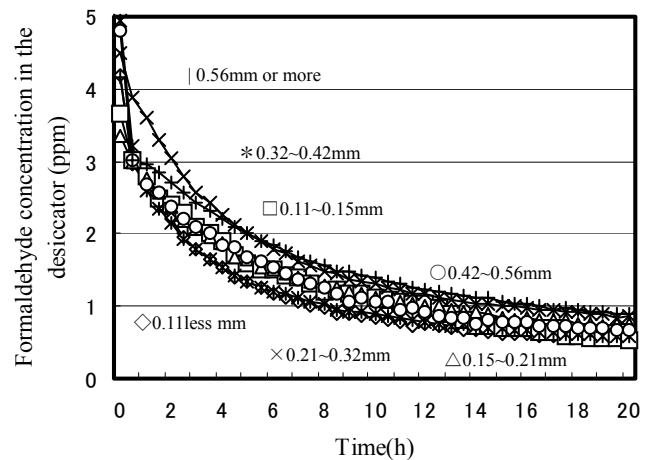


Fig.3 Changes in the formaldehyde concentration according to the particle diameter of WCS

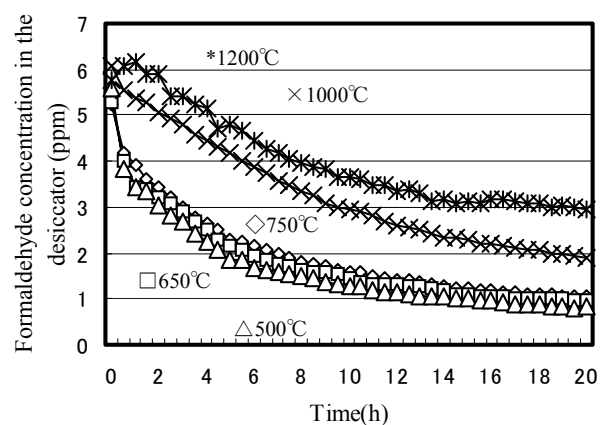
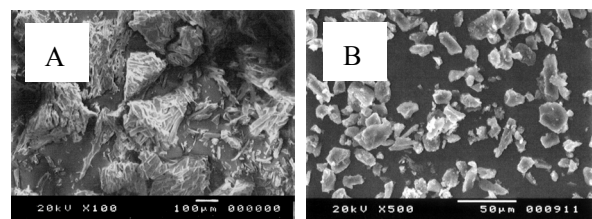


Fig.4 Changes in the formaldehyde concentration according to carbonization temperature of WCS



(A) Production temperature of 650°C and sieve mesh #50
(B) Production temperature of 1000°C and sieve mesh #300

Fig.5 Difference in the porous area between carbonization temperatures

affecting the formaldehyde adsorption performance of the paint film.

Figure 4 shows the changes in the formaldehyde concentration according to the carbonization temperature of the WCS. Formaldehyde adsorption performance was greatly affected by the carbonization temperature. Paint films mixed with WCS chips carbonized at 500°C and 600°C were excellent in their formaldehyde adsorption performance. As shown in the scanning electron microscope (SEM) photographs in Figure 5, the porous area of carbonized WCS was reduced as the carbonization temperature was increased. The adsorption capacity of WCS fired at a lower temperature was therefore greater than that carbonized at a higher temperature.

5. Comparison with other adsorbents

Activated carbon and bincho char both have excellent adsorption performance, and they are often used for interior work such as damp-proofing materials or adsorbing VOCs. In this experiment, specimens were prepared by applying a water-based emulsion paint mixed with either WCS, activated carbon, or bincho char at a ratio of 5 wt%. The difference in the formaldehyde adsorption performance among these specimens was then investigated. The experimental conditions were the same as described above; i.e., approximately 5–6 ppm formaldehyde gas was generated in the desiccator before the measurement. Figure 6 shows the comparison of formaldehyde adsorption performance among the three specimens. Formaldehyde adsorption performance of WCS was inferior to that of either activated carbon or bincho char, particularly during the first 3 h. However, 20 h after the initiation of the test, the formaldehyde concentration in the desiccator was approximately 0.5 ppm when activated carbon or bincho was used, and had been reduced to approximately 0.6 ppm by WCS. Therefore, if any of these adsorbents are used for longer than 20 h, the formaldehyde concentration in the desiccator will be reduced to almost the same level.

6. Application of WCS to organic-solvent-based paint (lacquer)

When a paint itself is a source of formaldehyde generation, this can be inhibited by mixing WCS with the paint. By mixing WCS with an organic-solvent-based paint, we thought that the release of formaldehyde immediately after paint application would be inhibited. For this test, WCS, activated carbon, or bincho were mixed with a lacquer-based paint, and the formaldehyde concentration in the desiccator after paint application was compared. As shown in Figure 7, the effect of WCS was lower than that of activated carbon or bincho on inhibition of formaldehyde release. However, the difference in the effect among the three adsorbents became smaller with time, with no significant difference observed at slightly less than 20 h after the initiation of the test. In total, the formaldehyde concentration was reduced by half. Therefore, mixing WCS into a lacquer-based paint could reduce generation of formaldehyde from the paint after its application.

7. Effect of the mixing ratio of WCS on paint lightness

The paint lightness was decreased after mixing with WCS. Using the $L^*a^*b^*$ colorimetric system (JIS Z8729), the effect of the different mixing rate of WCS cutting chips on the decrease in lightness was investigated. The mixing rate was set to be 0%, 5%, 10%, or 15%. In addition, a grey color paint with lightness 59 (L^*) was used for the undercoating. A spectrophotometer (CM-600d; Konica Minolta Holdings, Inc., Japan) was used to measure the lightness. As shown in Figure 8, the lightness decreased by approximately 12, 21, and 25 (L^*) when 5%, 10%, and 15% WCS were mixed, respectively. Since a general gray paint was used for the undercoating in this experiment, the lightness was lower when the paint with the mixing ratio of only 5% was used than when a general gray paint for top-coating was used. If a paint mixed with WCS is used for interior work, the mixing ratio should be below 5% in order to minimize the decrease in lightness.

When WCS was mixed with paint, not only lightness but also the gloss of the paint film was decreased. Figure 9 shows the relationship between gloss of the

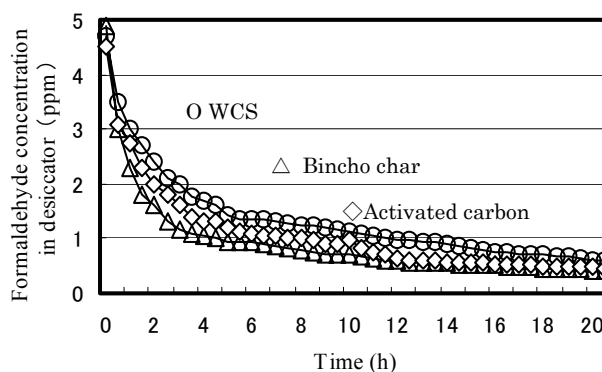


Fig.6 Comparison of the adsorption performance of the coating film

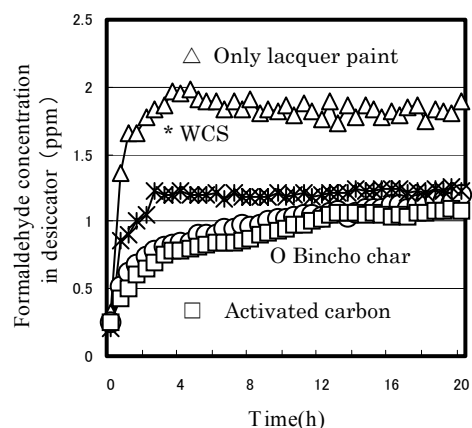


Fig.7 Formaldehyde adsorption characteristics of coating with WCS, bincho char and activated carbon

paint film and the mixing ratio of WCS obtained in accordance with JIS Z8741. As shown in this figure, gloss was reduced by half in all of the measurement angles when 10% of WCS was mixed. The highest concentration (5%) of WCS to be used as an interior material decreased gloss by 30%–40%.

8. Conclusion

This study demonstrated that by taking advantage of its porous property and by mixing it with paint, WCS could be effectively used as a material having a formaldehyde adsorption function. The carbonization temperature of WCS affected formaldehyde adsorption performance, and paint films containing WCS carbonized at 500°C and 600°C (the porous area was larger) were excellent in formaldehyde adsorption performance. Formaldehyde adsorption performance of WCS was inferior to that of activated carbon or bincho char within 5 h after the initiation of the test. However,

organic-solvent-based paint, WCS could inhibit formaldehyde generation at the initial stage. Although the lightness of a paint film decreased when WCS was mixed with paint, its range was allowable when WCS was used as an interior material. By mixing with paint, WCS powder and cutting chips produced in secondary fabrication could be utilized effectively. Based on the results presented here, we are convinced that the production of WCS with almost no discharging waste can be achieved.

References

- [1] T. Okabe: "Wood Ceramics," Uchidarokakuho Co., LTD, (1996) pp. 42–109
- [2] K. Yamamoto, T. Matsuura, M. Mondo, S. Tsukawaki, M. Miki and J. Takada: *Mat. Res. Soc. Jp.*, Vol. 26, No. 3, pp. 863–866 (2001)
- [3] M. Miki, T. Kikuchi, M. Nakamura, K. Hatakeyama and J. Takada: *Trans. Mat. Res. Soc. Jp.*, Vol. 26, No. 3, pp. 867–870 (2001)
- [4] T. Okabe, T. Hirose, R. Ozao, M. Otsuka, M. Mayuzumi, J. Tuzi, H. Chiba and S. Shibata: *Trans. Mat. Res. Soc. Japan.*, Vol.29, No. 5, pp. 2431–2434 (2004)
- [5] K. Kakishita and T. Suda: *Trans. Mat. Res. Soc. Jp.*, Vol. 26, No. 3, pp. 875–877 (2001)
- [6] K. Kakishita and T. Suda: *Trans. Mat. Res. Soc. Jp.*, Vol. 29, No. 5, pp 2427–2430 (2004)
- [7] T. Okabe "Wood Ceramics," Uchidarokakuho Co., Ltd., (1996), pp. 133–134
- [8] K. Hata: Doctoral thesis "Research on the processing characteristics of Wood Ceramics," Shibaura Institute of Technology (1999)
- [9] Ogawa Kazuhiko, Nagata Akihide, Okabe Toshihiro, and Ogawa Makoto: *Transactions of Japan Society for Interior Studies*, Vol. 7, pp. 27–30 (2007)

(Received December 12, 2008; Accepted September 16, 2009)

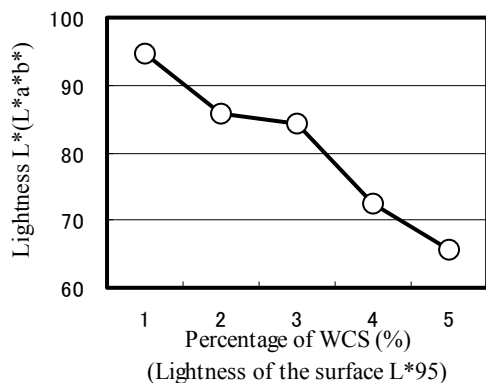


Fig.8 Decrease in the lightness of paint by mixing with WCS

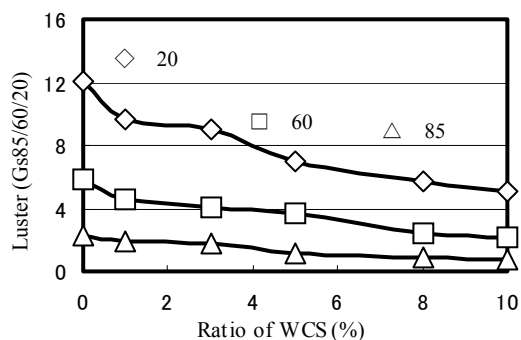


Fig.9 Ratio of wcs and luster of the painting

the performance of WCS was expected to be similar to that of activated carbon and bincho char when they were used for longer than 20 h. When mixed with

Carbon Electrode From Carbonized Wood For Polymer Electrolyte Fuel Cell

Masashi Fujisawa^{1*}, Yasuji Kurimoto¹, Yuji Imamura², Hikari Kikuchi³

¹ Institute of Wood Technology, Akita Prefectural University, 11-1 Kaiezaka Nosiro, Akita, 016-0876, Japan

² Research Institute for Sustainable Humanosphere, Kyoto University, Gokasho, Uji, Kyoto, 611-0011, Japan

³ SSALLOY CO., LTD., 3-13-26 Kagamiyama, Higashi-hiroshima, Hiroshima, 739-0046, Japan

*Corresponding author. Tel: +81-185-52-6985, Fax: +81-185-52-6976, E-mail: fujirish@yahoo.co.jp

In this research, we studied the characteristics of the carbon electrode from carbonized wood and its influence on the performance of Polymer Electrolyte Fuel Cell (PEFC). The carbon electrodes were made by pulse current sintering 32-45 μm wood charcoal powder at 800, 1000 and 1200°C under vacuum. The microstructures of carbon electrodes were observed by scanning electron microscopy (SEM), and the electrical conductivity of carbon electrodes was measured at room temperature by a four-probe-method. The evaluation of the performance of current-voltage was conducted in a single cell of PEFC with carbon electrodes. The electric conductivity increased slightly with the sintering temperature. The current-voltage measurement provided an overall quantitative evaluation of the fuel cell power density. A maximum power density of 0.0079 W/cm² was obtained in the carbon electrode sintered at 800°C. It can be considered that the porous structure of carbon electrode affects the power density.

Key words: carbon electrode, wood charcoal, polymer electrolyte fuel cell

1. Introduction

Research on the development of new energy sources has recently been receiving considerable attentions due to the increasing concerns on the environmental problems. Traditional energy production based on fossil fuels such as oil and coal is on the verge of exhaustion. Currently, we are paying attentions to the fuel cell as an innovative clean power generation.

Polymer electrolyte fuel cell (PEFC) is a device to convert chemical energy to electrical energy. In PEFC, current is generated by a simple electrochemical reaction involving the transfer of charge (electrons) between an electrode and chemical specie. The electrode performs a significant role in the function of PEFC and flow of electrons and gases [1-3].

In this research, we studied the characteristics of the carbon electrode from carbonized wood and its influence on the performance of PEFC.

2. Experimental Procedure

Japanese cedar (*Cryptomeria japonica*) was chopped into 30-mm-sized pieces. These pieces were heated in a laboratory-scale electric furnace at a heating rate of 4°C/min up to a temperature of 700°C under an Ar gas flow (100 ml/min) and maintained at that temperature for 1 h. Wood charcoal powder with particle sizes in the range 32-45 μm was prepared using sieves and vibration mill. The powder was put into a 20-mm-diameter graphite die, which was sintered at 800, 1000 and

1200°C under vacuum using a pulse current sintering device (S S Alloy Co. Ltd., VCSP-II). The temperature was raised at a rate of 500°C/min and maintained for 30 min. The pulse current sintering method is a novel process where metals, ceramics and composites can be sintered in short time [4-6]. As the current passes through the graphite dies as well as the sample, the sample is heated from both the inside and the outside at the same time. In this technique the phenomenon of microscopic electric discharge between particles is generated under pressure. After the reaction, it was naturally cooled to room temperature. A pressure of 40 MPa was applied as soon as sintering was commenced and was released immediately after the reaction had been completed. The reaction temperature was monitored by measuring the temperature of the front surface of the graphite die using an optical pyrometer. Finally, the carbon electrode made by pulse current sintering from wood charcoal powder was 20-mm-diameter and 2-mm-thickness. The carbon electrode was used as the gas diffusion layer and current collector.

The Pt/C catalyst ink was sprayed onto both sides of the Nafion 115 membrane. The amount of Pt/C catalyst used in the spraying technique was 2 mg/cm². The carbon electrodes were hot-pressed onto both sides of the Nafion membrane at 140°C for 30 min to form a MEA. The carbon electrode had a round shape and the diameter was 20 mm. The MEA was installed into a single cell of PEFC.

The microstructures of carbon electrodes were observed by scanning electron microscopy (SEM), and the electrical conductivity of carbon electrodes was measured at room temperature by a four-probe-method (Loresta HP MCP-T410). The evaluation of the performance of current-voltage was conducted in a single cell of PEFC with carbon electrodes. Humidified hydrogen and air gases flowed into the anode and the cathode at 0.01 MPa and open condition, respectively. The fuel cell was operated at room temperature.

3. Results and discussion

Figure 1 shows SEM images of cross sections of carbon electrodes sintered at 800 and 1200°C. In the carbon electrodes sintered at 800°C, the particles were closely packed (Fig. 1 (a)), while in the carbon electrodes that had been treated at the higher sintering temperature, the particles were even more closely packed (Fig. 1 (b)).

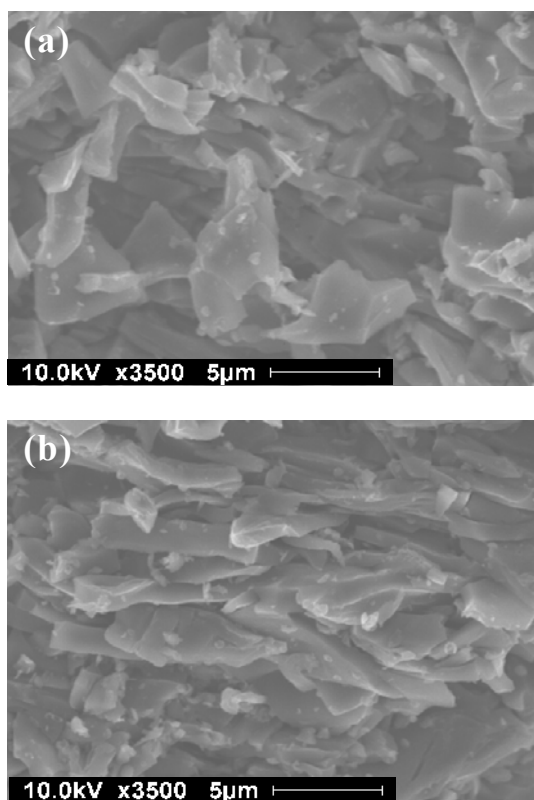


Fig. 1. SEM images of cross sections of carbon electrodes sintered at (a) 800°C and (b) 1200°C.

The bulk densities of carbon electrodes are shown in Fig. 2. The bulk densities showed a tendency to increase with sintering temperature. A maximum in the bulk density of 1.09 g/cm^3 was reached in the carbon electrodes sintered at 1200°C. It is considered that the condition of particles shown in Fig. 1 affects the bulk densities.

The electrical conductivity (σ) at room temperature of

carbon electrodes sintered at 800, 1000 and 1200°C are shown in Fig. 3. The electrical conductivity increased with an increase in sintering temperature. A maximum in the electrical conductivity of $1.11 \times 10^2 \text{ S/cm}$ was reached in the carbon electrodes sintered at 1200°C. It seems that the condition of particles shown in Fig. 1 affects the electrical conductivity.

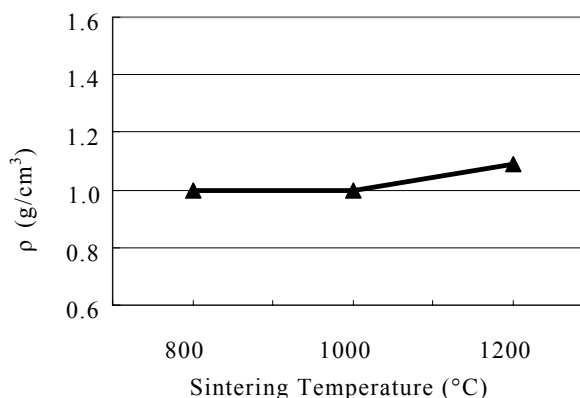


Fig. 2. The bulk densities (ρ) of carbon electrodes sintered at 800, 1000 and 1200°C.

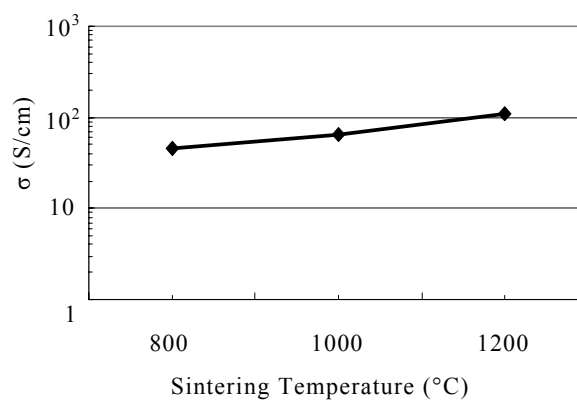


Fig. 3. The electrical conductivity (σ) at room temperature of carbon electrodes sintered at 800, 1000 and 1200°C.

Fig. 4 shows the current-voltage performance of the fuel cell with carbon electrodes sintered at 800, 1000 and 1200°C. All fuel cells showed an open voltage of 0.8 V. The output voltage decreased with an increase in the current density [1, 7]. The voltage slowly decreased with the increase of current density in the fuel cell with carbon electrodes sintered at low temperature. The best performance was obtained at the fuel cell with carbon electrodes sintered at 800°C.

Fig. 5 shows the dependence of the current density on the power density generated by the fuel cells with

carbon electrodes sintered at 800, 1000 and 1200°C. The large power density was obtained in the fuel cell with carbon electrodes sintered at low temperature. A maximum power density of 0.0079 W/cm² was obtained in the fuel cell with carbon electrode sintered at 800°C. It is considered that the condition of particles and the difference of gases diffusion affect the current-voltage performance.

As a matter of fact the general fuel cell performance measures two orders of magnitude higher than a present result on fuel cell with carbon electrode from carbonized wood. However, it is to be expected that the addition of catalyst can improve the performance of the fuel cell.

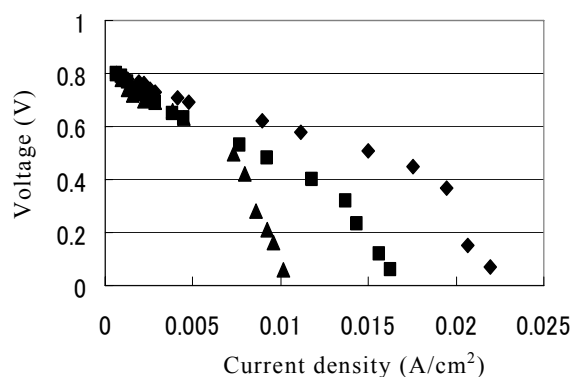


Fig. 4. The current-voltage performance of the fuel cell with carbon electrodes sintered at 800°C (◆), 1000°C (■) and 1200°C(▲).

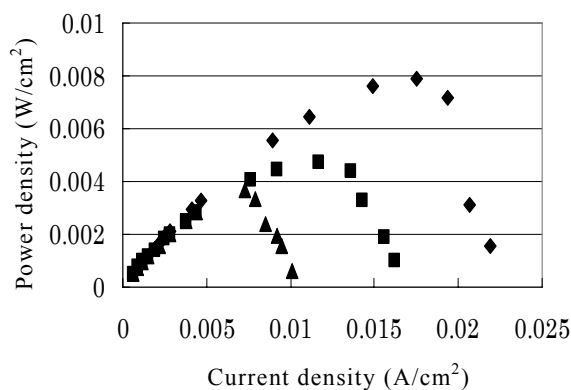


Fig. 5. The dependence of the current density on the power density generated by the fuel cells with carbon electrodes sintered at 800°C (◆), 1000°C (■) and 1200°C(▲).

4. Conclusion

We studied the characteristics of the carbon electrode from carbonized wood and its influence on the performance of PEFC. The carbon electrodes were made by pulse current sintering 32-45 μm wood charcoal powder at 800, 1000 and 1200°C under vacuum. The

micro-structural change of carbon electrodes were revealed by SEM as a function of the sintering temperature. The electric conductivity of carbon electrodes increased slightly with the sintering temperature. The current-voltage measurement provided an overall quantitative evaluation of the fuel cell power density. A maximum power density of 0.0079 W/cm² was obtained in the carbon electrode sintered at 800°C.

Acknowledgement

The authors acknowledge the cooperative studies using collaborative research facilities of wood composite hall, Research Institute for Sustainable Humanosphere, Kyoto University

References

- [1] R.B. Mathur, Priyanka H. Maheshwari, T.L. Dharmi and R.P. Tandon, *Electrochimica Acta.*, **52**, 4809-4817 (2007).
- [2] M.F. Mathias, J. Roth, J. Fleming, W. Lehnert, in: W. Vielstich, A. Lamm, H.A. Gasteiger (Eds.), *Hand Book of Fuel Cells-Fundamentals, Technology and Applications*, vol. 3, John Wiley and Sons Ltd., NY, 2003, Part 3, Chapter 42, p. 518.
- [3] M. Kheirmand, H. Gharibi, R.A. Mirzaie, M. Faraji and M. Zhiani, *Journal of Power Sources.*, **169**, 327-333 (2007)
- [4] L. Gao, H. Z. Wang, J. S. Hong, H. Miyamoto, K. Miyamoto, Y. Nishikawa and S. D. D. L. Torre. *J. Eur. Ceram. Soc.*, **19**, 609-613 (1999).
- [5] L. Gao, H. Wang, H. Kawaoka, T. Sekino and K. Niihara. *J. Eur. Ceram. Soc.*, **22**, 785-789 (2002).
- [6] L. Gao, H. Z. Wang, J. S. Hong, H. Miyamoto, K. Miyamoto, Y. Nishikawa and S. D. D. L. Torre. *Nanostruct. Mater.*, **11**, 43-49 (1999).
- [7] Y. Show. *Surf. Coat.*, **202**, 1252-1255 (2007)

(Received December 12, 2008; Accepted September 16, 2009)

Electromagnetic Shielding in Rubber Composite Materials with Soy Hull Carbon Particles

Michiaki SHISHIDO*, Taku OGAWA**, Hiroyuki GOTO***, Takeshi TAKAHASHI**** and Hiroshi IIZUKA**

* Department of Control and Information Systems Engineering, Tsuruoka National College of Technology, 104 Inookasawada, Tsuruoka 997-8511, Japan
 Fax: +81-235-25-9078, e-mail: m-shishido@tsuruoka-nct.ac.jp

**Faculty of Engineering, Yamagata University, 4-3-16 Jonan, Yonezawa 992-8510, Japan

***The Nisshin Oillio Group, Ltd., Tokyo 104-8285, Japan

****Sanwa Yushi Co.Ltd., Tendo 994-0044, Japan

Soy hull is an agricultural by-product, and has been almost always recycled as an animal fodder for many years. Therefore, a new effective function has been studied for an industrial material. For example, the authors have investigated the soy-hull carbon (SHC) particles as a functional filler for rubbers and plastics. The SHC particle is manufactured by carbonizing the dehydrated soy hull in nitrogen gas atmosphere at high temperature. The SHC particle, consequently the porous carbon particle in which the natural porous structure retains. In this study, the characteristic of the electromagnetic shielding was investigated for the SHC/EPDM composite, which was prepared by kneading the SHC particle with the ethylene propylene diene methylene (EPDM) rubber. The degree of the electromagnetic shielding (SE) of this composite with SHC particle of 400 mass% was found to show a relatively-high value in the frequency region from 50 (SE:40dB) to 150 (SE:30dB). The degree of the absorption (RD) for electromagnetic wave was furthermore, depended on the amount of the SHC particle content, and was shown the high value (RD:-18dB) under the high frequency of 6.5 GHz.

Key words: Soy Hull, Carbonization, Electromagnetic Shielding, Electromagnetic absorption, Conductivity

1. INTRODUCTION

Soy hull is an agricultural by-product which is produced during the manufacturing process of the cooking oil. The most of the soy hull is recycled as an animal fodder and so on. Therefore, the soy hull has been attempted to use effectively as a function added industrial material. For example, the present authors have investigated the porous carbon material that was made from the soy hull [1]. The soy-hull carbon (SHC) particle is manufactured by carbonizing the dehydrated soy hull in nitrogen gas atmosphere at high temperature.

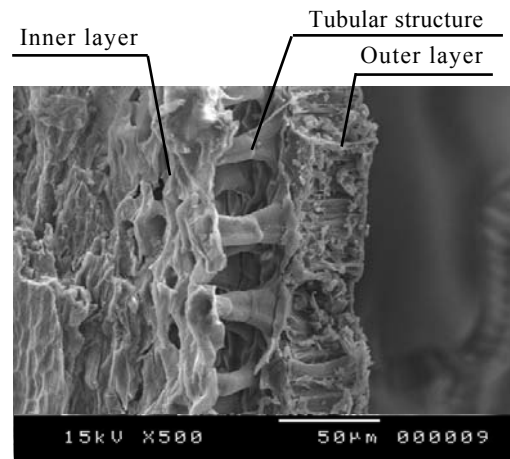
Some new porous carbon materials have been developed utilizing the natural porous structures of some plant matters, for example, the wood [2], the bamboo [3], the rice bran [4], the rice hull [5], and so on. Especially, the woodceramics [2] is a pioneer work to use the natural plants for the industrial functional materials, as a view point of the recycling. The production technology of the woodceramics has been applied to the bamboo, rice bran, rice hull and so on. The porous carbon materials are expected as sliding materials and electric devices, because the materials retain many beneficial properties of the carbon. The electromagnetic shielding property was reported for the woodceramics [6], bincho-charcoal [7] and so on.

In this study, the characteristics of the conductivity and the electromagnetic shielding of the SHC particle was investigated for the SHC rubber composite material, which was prepared by kneading the SHC particle with ethylene propylene diene methylene linkage (EPDM).

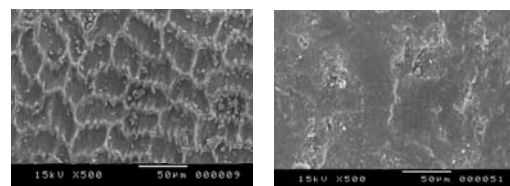
2. EXPERIMENTAL PROCEDURE

2.1 Soy hull

Fig.1(a) shows the cross section of the raw soy hull.



(a) Cross section



(b) Inner layer

(c) Outer layer

Fig.1 Macrostructure of raw soy hull

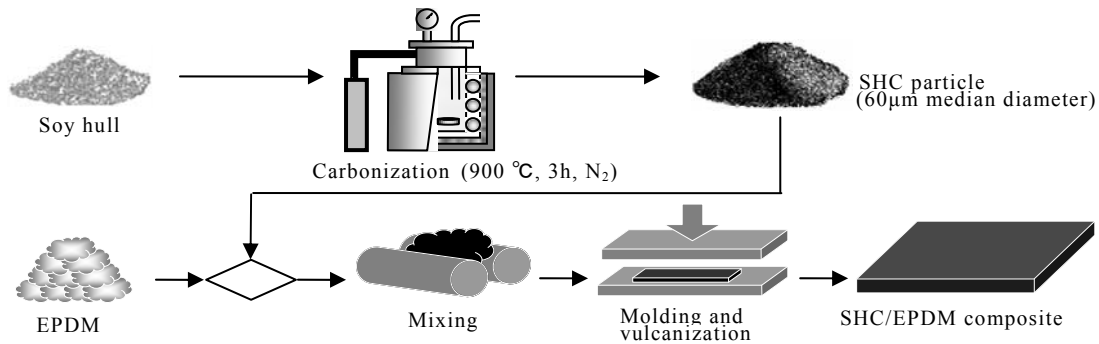


Fig.2 Manufacturing process of SHC particle and SHC rubber composite material

The outer and inner surface layers are connected with a tubular structure (about 30µm thickness). The tubular structure is a unique porous structure, and is different from the other porous structures of the natural plants. Fig.1(b) shows the macrostructure of the inner surface layer of the soy hull, which has a hydrophilic areolas structure. Fig.1(c) shows the macrostructure of the outer surface layer. The outer surface layer is hard with the hydrophobic property for protecting the seed from external charge.

2.2 Manufacturing process

Fig.2 shows the manufacturing process of the SHC particle and the rubber composite material. At first, the soy hull is drying and then carbonizing in the nitrogen gas atmosphere at 900 °C. The carbonized soy hull was pulverized by a mill to obtain the SHC particle. The SHC particle was sieved using 106 µm meshed filter to obtain the powder with 60 µm median diameter. In addition, the SHC powder of 2 µm median diameter was obtained by milling the SHC particle for 10 hrs by a vibrating mill. The EPDM was used as the matrix of the rubber composite material. The EPDM is widely used as the industrial materials for its low cost and high weather resistance.

Fig.3(a) shows the components of the raw soy hull. The soy hull contains about 2 mass% of inorganic constituent, about 48 mass% of organic constituent and the others are water and oil. Fig.3(b) shows the components of the SHC particle. The percentage of the inorganic constituent is about 2 mass%. The content of the organic constituent is about 87 mass% and the others are about 12 mass%. During the carbonization process, many parts of the others were evaporated.

The SHC/EPDM composite material was prepared by mixing the SHC particle, the EPDM and some additives in a roll kneading machine. The amount of the SHC particle was increased every 100 mass% from 100 mass% to 400 mass%. After kneading, the material was vulcanized, and then molded at 170±5 °C in vacuum of -80 kPa. The width (w), depth (d), and thickness (t) of the SHC/EPDM for measuring the volume resistivity and electromagnetic shielding degree were 150, 150, and 2.5mm respectively. In present research, the values of w, d of test piece with the values for t of 0.5, 1, 1.5, 2 and 5mm for measuring the electromagnetic absorption degree were each value of 300 mm.

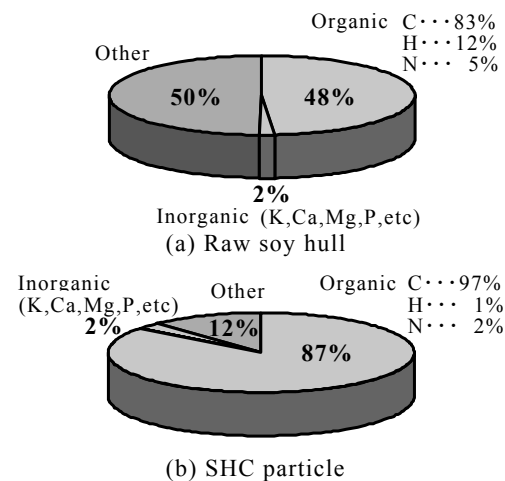


Fig.3 Components of raw soy hull and SHC particle

2.3 Experimental procedure

Fig.4 shows the measuring sites for the volume resistivity. The volume resistivity was measured referring to the Japanese Industrial Standards of JIS-K7194 with nine measuring sites.

Fig.5 shows the schematic illustration of the electromagnetic shielding tests. The test was carried out using the Advantest-method with a spectrum analyzer. The surface of the test piece was arrayed with vertical incident wave angle. This test evaluated electric field using dipole antenna. The degree of the electromagnetic shielding (SE) was evaluated as the power loss between the incident wave and the transmitted wave. The SE was measured using the following formula (1).

$$SE = -10 \log \frac{P_t}{P_i} \quad (\text{dB}) \quad (1)$$

where P_t is the power of transmitted wave (W), P_i is the power of incident wave (W). The measuring frequency range was from 1 to 500 MHz.

Fig.6 shows the schematic illustration of electromagnetic absorption test. The measurements were carried out with the Arch-test method. An incident wave reflects completely with the metal plate. The degree of the electromagnetic absorption (reflectivity) was evaluated as the power loss

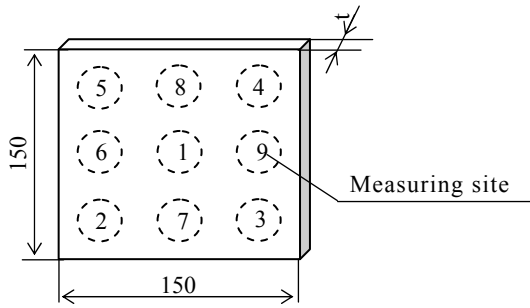


Fig.4 Measuring sites for volume resistivity

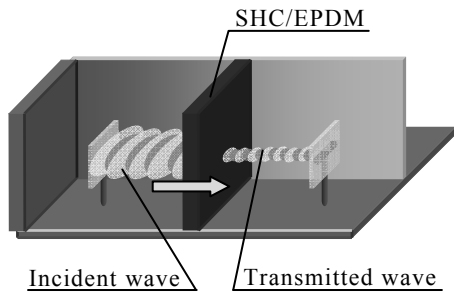


Fig.5 Schematic Illustration of electromagnetic shielding tests

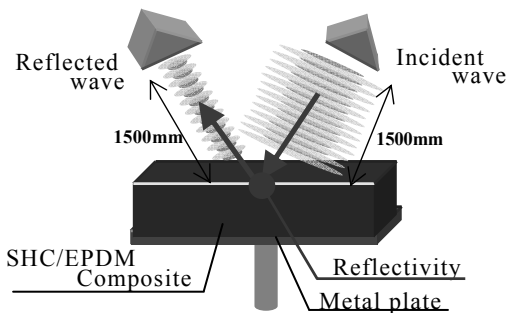


Fig.6 Schematic illustration of electromagnetic absorption tests

between the incident wave and the reflected wave. The reflectivity was measured using the following formula (2).

$$R = 10 \log \frac{P_r}{P_i} \text{ (dB)} \quad (2)$$

where R is the reflectivity, P_r is the power of reflected wave (W), P_i is the incident wave (W). The measuring frequency range was from 2 to 8 GHz.

3. EXPERIMENTAL RESULTS AND DISCUSSION

3.1 Volume resistivity

Fig.7 shows the resistivity ρ of SHC/EPDM on the measuring site such as shown in Fig.4. In this figure, the open diamonds, closes, open squares, open triangles, and open circles are the measured results of ρ for the amount of SHC particle with 0, 100, 200, 300, and 400 mass%, respectively. The resistivity depends on the content of the SHC particle. All the volume resistances are almost even at the nine measuring sites. The SHC particle was considered to be uniformly dispersed.

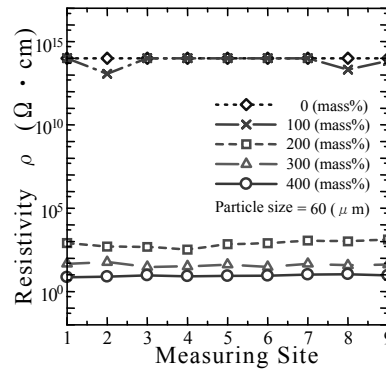


Fig.7 Resistivity ρ of SHC/EPDM on the measuring site

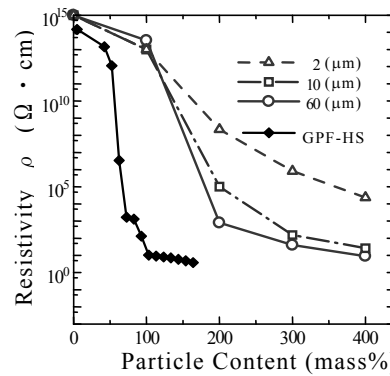


Fig.8 Effect of SHC particle diameter on value of ρ of the SHC/EPDM

Fig.8 shows the effect of the SHC particle diameter on the value of ρ of the SHC/EPDM. In this figure, open triangles, open squares, open circles, and solid diamonds are the results of ρ for SHC particle sizes of 20, 10, and 60 μm , respectively. It is found that the resistivity gradually decreases with increasing the content of the SHC particles. The percolation phenomenon, in which the value of ρ suddenly decreases with increasing the particle content. The percolation phenomenon is an unfavorable property for the manufacturing of the conductive composite materials. The ordinary fillers, such as Carbonblack (GPF-HS) induce the percolation phenomenon. By contrast, percolation phenomenon the SHC/EPDM does not occur as shown in Fig.8.

Moreover, the resistivity (ρ) is higher in the test piece with the small particles than that with the large particles. It is hard to make a conductive path in the composites with decreasing the particle diameter. These result shows that the value of ρ can be controlled by adjusting the additive rate and the particle diameter.

3.2 Electromagnetic shielding

Fig.9 shows the electromagnetic shielding of the SHC/EPDM under the low frequency conditions. In this figure, the open circles, open diamonds, inverted open triangles, open triangles, and open squares are the measured results of SE for the amount of SHC particle with 0, 100, 200, 300, and 400 mass%, respectively. The

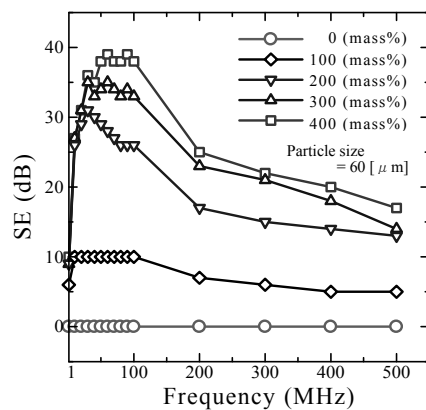


Fig.9 Electromagnetic shielding of SHC/EPDM under low frequency conditions

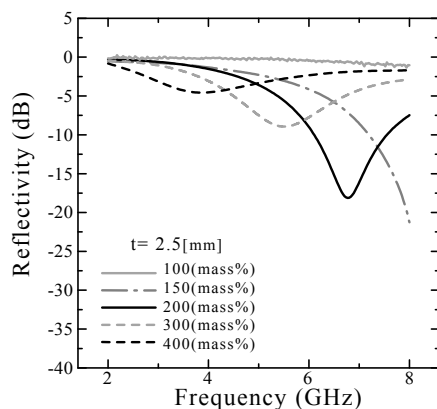


Fig.10 Electromagnetic absorption of SHC/EPDM under high frequency conditions

degree of the SE is increase with increasing the content of the SHC particle, and exceeds 30 dB under 50-100 MHz in the test piece with 400 mass%.

In addition, the shield effect is still high even in the test piece with 200 mass%. The shielding effect was considered to be contributed by the reflecting effect on the test piece surface.

3.3 Electromagnetic absorption

Fig.10 shows the electromagnetic absorption of the SHC/EPDM under the high frequency conditions. In this figure, the light solid line, light dashed line, dark solid line, light broken line, and dark broken line are the measured results of reflectivity for the amount of SHC particle with 100, 150, 200, 300, and 400 mass%, respectively. The peak absorption values and the absorption frequency are changed with amount of the filler content. The degree of the electromagnetic absorption (RD) exceeds -18dB under 7.5-8GHz in the test piece with 150 mass%. The peak of the RD shifts to the low frequency area with increase of the additive rate, and the attenuation decreases.

As mentioned above, the large amount of SHC particle is able to mix with EPDM rubber. The manufacturing cost is another important factor for the industrial application. The soy hull is an agricultural by-product and the cost is lower than

the ordinary fillers. The soy hull is able to use as a natural-origin material to the industrial filler.

4. CONCLUSION

The electromagnetic shielding were investigated for the rubber composite materials with the SHC particle. The summary of the obtained results was described as follows.

- (1) The resistivity of the SHC/EPDM is controllable by adjusting the particle size and additive rate.
- (2) The degree of the electromagnetic shielding (SE) exceeds 30dB under 50-150 MHz in the test piece with 400 mass%.
- (3) The degree of the electromagnetic absorption (RD) exceeds -18 dB under 7.5-8 GHz in the test piece with 150 mass%.
- (4) The soy hull is able to use as a natural -origin material to the industrial filler.

ACKNOWLEDGEMENTS

The authors wish sincerely to express their gratitude to Miyasaka Polymer Co. Ltd. for the preparation of the test pieces and to Associate Professor Hiroki Anzai, Tsuruoka National College of Technology for his experimental support.

REFERENCES

- [1] T.Ogawa, M.Shishido, T.Takahashi, H.Goto and H.Iizuka, "Mechanical Properties of Porous Carbon Materials made from Agricultural Wastes", The 18th Symposium of the Materials Research Society of Japan Program and Abstract, p.293 (2007).
- [2] T.Okabe, K.Saito and K.Hokkirigawa, "New Porous Carbon Materials, Woodceramics: Development and Fundamental Properties", Journal of Porous Materials, Vol.2, No.3, pp.207-213 (1995).
- [3] T.Shinmura, K.Matsunaga, K.Nishi, T.Kokusyo, "Study on the Electric Characteristics and the Shielding Effect for Electromagnetic Waves of Bamboo Charcoal", Reports of Kagoshima Prefectural Institute of Industrial Technology, No.12, pp.47-52(1999).
- [4] H.Iizuka, T.Noguchi and S.Shikano, "A New Porous Carbon Material made from Rice Bran", J. Mater. Engng. Resources, Vol.11, pp.10-15 (2003).
- [5] M.Shishido, S.Kubo, T.Takahashi and H.Iizuka, "Mechanical Properties of Porous Carbon Materials made from Rice Hull", Trans. Mater. Res. Soc. Jpn., Vol.31, pp.993-996 (2006).
- [6] K. Shibata, T. Okabe, K. Saito, T. Okayama, M. Shimada, A. Yamamura and R. Yamamoto, "Electromagnetic Wave Shielding Properties of the Woodceramics made from Wastepaper", Proceedings of The Third International Conference on Ecomaterials, Tsukuba, Japan, pp.210-213(1997).
- [7] H.Norikane, T.Nishikubo, S.Gokyu, K.Itoh and M.Itoh, "RF Magnetic Shielding Effects of a Compound Plate Constructed from Bincho-Chaocoal and Ferrite Plates", IEEE Transactions on Applied Superconductivity, Vol.16, No.2, pp.1765-1768(2006).

(Received December 12, 2008; Accepted September 16, 2009)

CHANGE OF ELASTIC-PLASTIC BEHAVIOR ON COMPRESSIVE DEFORMATION BY DENSIFICATION OF WOOD

Tadashi Ohtani *

*College of education, Ibaraki University, Bunkyo 2-1-1, Mito, Japan
Fax:81-29-228-8272, e-mail: t-ohtani @mx.ibaraki.ac.jp

Compressed wood is the material densified by the heat-treated condition with high temperature. The mechanical compression property was examined by using the Japanese cedar (*Cryptomeria japonica* D.Don) compressed into different density, and the change of elastic-plastic behavior on the compressive deformation was investigated. The results are summarized that the plastic region before reaching to the maximum stress of the stress-strain curves in the compression test decreased with the larger compression ratio. The other compression property was also obtained from the surface hardness test, and the index of the elastic-plastic behavior changed from plasticity to elasticity in condition of larger compression ratio. From these results, it was suggested that the plastic behavior with yielding in the mechanical property of the compressed wood was affected by densification of wooden porous tissue, and that the compressed wood could obtain the higher strength and hardness.

Key words: Compressed wood, Stress, Strain, Elastic-plastic behavior, Compression property

1. INTRODUCTION

Compressed wood is the material densified by the heat-treated condition with high temperature, and the material property shows the higher strength and hardness than that of non densified softwood. The research of the compressed wood has been watched with interest because the use of softwood such as Japanese cedar might be promoted in the domestic forest product. Therefore the manufactured methodology of compressed wood has been developed and the research of the cellular compressive mechanics has been done since 1990's in Japan [1-2]. Recently the compressed wood has been used in various applications such as the flooring, interior and construction materials [2]. The other useful application has also been proposed that the hardened charcoal of the compressed wood might be manufactured from softwood [3].

In above useful application of the compressed wood, the information of mechanical property such as the strength and hardness should be important. Therefore the research on the mechanical property of compressed wood has been reported [4-5], however the detail research has been reported a few on the densified effect of cellular structure. If the effect of cellular structure on the mechanical property of wood itself could also be clarified, it might be possible that the examination on the densified effect of compressed wood become an important cue.

From above reason, the compressive behavior of the compression test and surface hardness test was examined by using the Japanese cedar compressed into different density. The densified effect of the compressed wood was also investigated in change of the elastic-plastic behavior.

2. MATERIAL AND METHOD

2.1. Material

The heartwood of Japanese cedar (*Cryptomeria*

japonica D.Don) was used for the experimental sample material. The average density of the sample material was 0.35 g/cm³, and the moisture content was 11.0 %. After the sample material was pre-heated between the upper and lower press board, it was compressed in the radial direction at the pressed speed with 0.16 mm/s.

Table 1 shows the property of compressed wood used for the experiment. The heat-treated temperature during the compression was 180°C and the heat-treatment after the compression was continued for five hours to fix the compressed dimension. The compression ratio *CR* was calculated from change of the dimensional length when the sample was compressed to the radial direction, and the *CR* was set in condition of 30, 50 and 70%. The density of the compressed wood as shown in Table 1 was ranged from 0.41 to 0.92 g/cm³ and the moisture content was from 5.7 to 6.4 %. The control material of uncompressed and non heat-treated wood was also used in comparison with the compressed wood.

2.2. Compression test

The compression test in parallel to the fiber grain was conducted by using sample material as listed in Table 1. The test specimens were prepared in the cross section with 15 mm × 15 mm to tangential and radial direction and in the height with 30mm to longitudinal direction. The compression test was conducted in environment of the room temperature with 20°C and relative humidity with 60%. The test specimen was compressed at the cross-head speed with 1 mm/min in the testing machine. The compression test was measured for ten times in each testing condition. After the compression test, the stress and strain were calculated from the compression load and the movement of cross-head, respectively.

2.3. Bending test

In order to compare the compressive deformation of

Table 1 Properties of sample specimen used for the experiment

Sample specimen	Heat-treated Temperature: T [°C]	Compression ratio CR [%]	Density [g/cm ³]	Moisture content [%]
Compressed wood	180	30	0.41	5.8
		50	0.60	6.4
		70	0.92	5.7
Control	—	0	0.35	11.0

the compression test and the bending test, the four-point bending test was investigated. The bending test specimen was prepared in the square section of 15 mm with the length of 240 mm to longitudinal direction. The bending test was measured for ten times in each testing condition. In the bending test, the strain gauge was stuck on the center part where the compression and tension force acts to the surface of test specimen. The amount of strain was measured by the strain gauge on both surfaces. From the strain data, the information of compressive deformation was investigated as following.

The stress σ_c where the compression force acts can be estimated as shown in the equation (1) of bending moment M by theory of Nadai [6].

$$\sigma_c = \frac{\sigma_t \frac{d}{d\theta} (M\theta^2)}{bh^2 \sigma_t \theta - \frac{d}{d\theta} (M\theta^2)} \quad (1)$$

Here σ_t is the stress where the tension force acts, and the width (b) and the height (h) are the parameters of cross section, respectively. Considering the tensile stress σ_t as shown in equation (1), the plastic region of the stress-strain behavior is known to be well little in the tension behavior of wood [7]. Therefore the value of σ_t can be estimated as shown in the equation (2) when assumed that Hooke's law can be applied.

$$\sigma_t = E_t \varepsilon_t \quad (2)$$

E is the young's modulus, and ε_t is the strain where the tension force acts. When it is assumed that the natural axis is in the center part of cross section, the bending moment M is represented as shown in the equation (3).

$$M = \frac{Ebh^2 \varepsilon_t}{6} \quad (3)$$

When the strain generated in the neutral axis is defined as \hat{GH} as shown in Fig.1, it can be expected that the

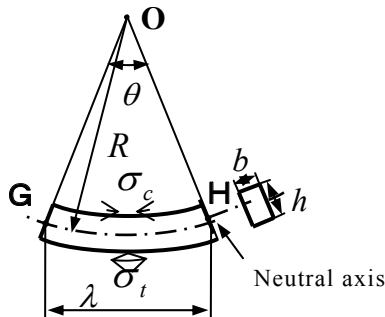


Fig.1 Stress of the compression and tension in bending.

range of \hat{GH} is very small. Thus, When \hat{GH} is considered as λ , θ can be expressed as shown in the equation (4).

$$\theta = \frac{2\lambda\varepsilon_t}{h} \quad (4)$$

From above equations of (2)- (4), the compression stress σ_c was estimated by the bending test.

2.3. Hardness test

In order to examine the surface hardness of the compressed wood, the Brinell hardness test was conducted on the practical utilized surface of tangential section. In the Brinell hardness test, the steel ball with the diameter of 10mm was intended in depth of $1/\pi$ (0.32mm). From the intended force P (N), the Brinell hardness HB was calculated as shown in equation (5).

$$HB = \frac{P}{10} \quad (5)$$

The steel ball in the hardness test was intended between the intervals with 10mm on the sample specimen, and the average value of HB was obtained from the data of nine points.

The hardness test in different tip shape of the ball indenter was also investigated, and the Vickers hardness test such as adapted in metal was conducted in this experiment. In the Vickers hardness test, the quadratic pyramid in faced sections with $\alpha = 136^\circ$ was intended. The length of double diagonal lines was measured on the experimented material surface. The value of Vickers hardness HV was calculated from the average length d as shown in equation (6).

$$HV = \frac{2P \sin(\alpha/2)}{d^2} \quad (6)$$

2.4. Evaluation of elastic-plastic behavior

In order to investigate the elastic-plastic behavior in the hardness property, the average pressure P_m in contact between the steel ball and the hardness test specimen was calculated from the equation (7), which was proposed by Hertz [8].

$$P_m = \frac{P}{1.1\pi \left(\frac{P \cdot r}{2} \left(\frac{1}{E_1} + \frac{1}{E_2} \right) \right)^{2/3}} \quad (7)$$

E_1 and E_2 are the elastic modulus of the hardness test specimen and steel ball, respectively. The elastic modulus of the test specimen was obtained from the result of compression test, and that of the steel ball was used from the steel material (210GPa).

From the average pressure of P_m , the index c was obtained in relationship with the yield stress σ_y as shown

in equation (8) due to evaluation of the elastic-plastic behavior. The value of σ_y was estimated from the maximum stress of compression stress-strain curves in parallel to the fiber grain.

$$Pm = c \cdot \sigma_y \quad (8)$$

3. RESULTS AND DISCUSSION

3.1 Elastic-plastic behavior in compression test

Fig.2 shows the relationship between the stress σ and strain ϵ when the compression test was conducted in parallel to the fiber grain of the compressed wood and the control material. In the σ - ϵ curves of the test specimen on different compression ratio, the stress of control material increases nonlinearly after increasing linearly, and decreases gradually after reached to the maximum. In contrast with the control material, the region of nonlinearity in the compressed wood tends to be less than that region of the control material until reached to the maximum, and the stress is rapidly lower. From this result, it might be possible that the plastic behavior in σ - ϵ curves changes in boundary of before and after the maximum by effect of densification. Therefore the ratio of plastic strain was estimated from the σ - ϵ curves.

Fig.3 shows the relationship between the ratio of plastic strain ($\epsilon_p / (\epsilon_p + \epsilon_e)$) and the compression ratio CR . The result of bending test as shown in Fig.3 means the value which obtained from the primary bending theory of the equation (1)-(4). In ratio of plastic strain as shown in Fig.3, the ratio estimated by the compression test is larger than that of the bending test as the compression ratio CR is lower. However, the ratio decreases with increasing the compression ratio, and the value tends to be close to that of the bending test. The result indicates that, by the effect of densification, the ratio of plastic region decreases in the stress-strain curves of the compressed wood.

From above result, it is found that the densified effect decreased the plastic region in the stress-strain.

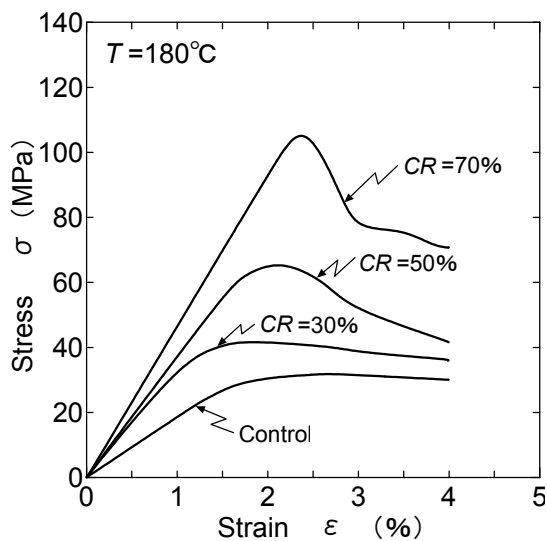


Fig.2 Relationship between the stress σ and the strain ϵ of the compressed wood in heated with $T=180^\circ\text{C}$.

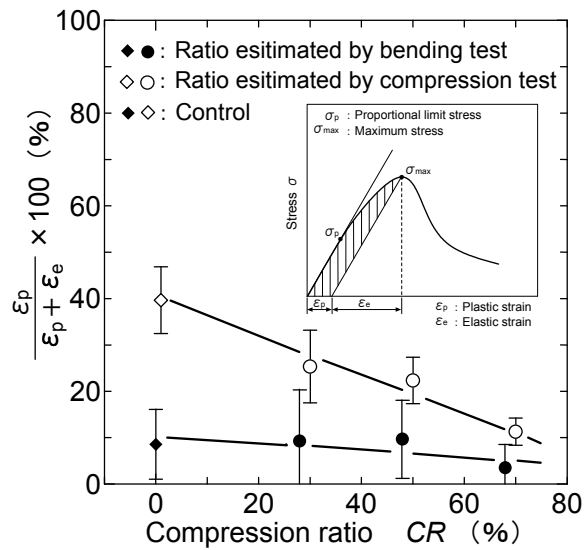


Fig.3 Relationship between the ratio of plastic strain($\epsilon_p / (\epsilon_p + \epsilon_e)$) and the compression ratio CR before reached to the maximum stress.

3.2 Elastic-plastic behavior in hardness property

Fig.4 shows the relationship between the Brinell hardness HB and the compression ratio CR in the tangential section of the compressed wood and the control material. The value HB shown in Fig.4 increases exponentially with increasing the compression ratio CR . The result indicates that the compressed wood become extremely harder in the compression ratio, more than $CR = 50\%$, and the hardness value is about three times harder than that of control material.

Fig.5 shows the relationship between the index c and the compression ratio CR when the index c was obtained from the average pressure P_m due to evaluation of the elastic-plastic behavior. In comparison of the index c shown in Fig.5, the index of quadratic pyramid also

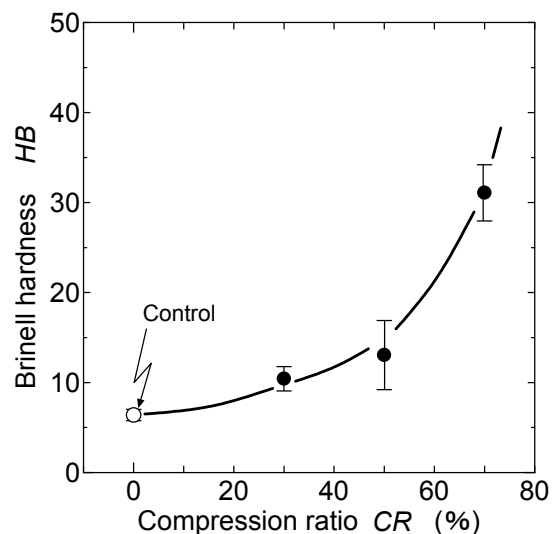


Fig.4 Relationship between the Brinell hardness HB and the compression ratio CR .

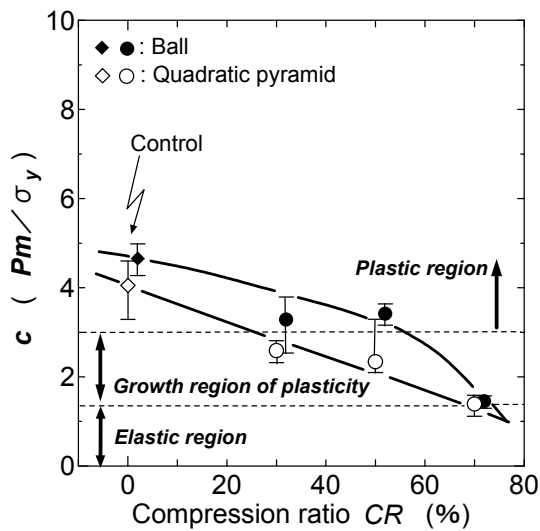


Fig.5 Relationship between the value of c (P_m/σ_y) and the compression ratio CR .

shows the result obtained from the Vicker's hardness test. The both hardness tests show the result of the indenter depth with $h = 0.08$ mm. As shown in Fig.5, the index c of the ball and quadratic pyramid indenters decreases with CR , and the value reaches to approximately $c = 1.3$ in condition of $CR = 70\%$.

Here the previous research has been reported that the index with $0 < c < 1.3$ means in range of the elastic region, the range of $1.3 \leq c < 3$ in the growth region of plasticity, and the range of $c > 3$ in the plastic region in contact with much harder material rather than wood [8]. From the previous report, the result can be thought that the hardness property on the practical utilized surface of tangential section changes to elasticity by the densified effect.

4. CONCLUSION

The compressive behavior of the compression test and surface hardness test were examined by using the Japanese cedar compressed on the different density. The effect obtained by densified wood was shown as follows.

- (1) The information of the stress-strain curves in the compression test provided that the strength of the compressed wood increased with the larger compression ratio, however the ratio of plastic region decreased.
- (2) The hardness value of the compressed wood was larger with larger compression ratio, and the property showed elasticity when the elastic-plastic behavior on the material surface was evaluated from the hardness tests of the ball and quadratic pyramid indenters.
- (3) From above results of the compression and hardness tests, it was suggested that the disappearance of the cellular structure with porous tissue affect to the elastic-plastic behavior with yielding.

5. REFERENCE

- [1] M. Norimoto, "Larger compressive deformation in wood", Mokuza Gakkaishi, Vol.39, pp.867-874 (1993)
- [2] M. Inoue, "The present state and view of compressed wood", Wood Industry, Vol.56, pp.245-249(1991)
- [3] T. Ohtani, Y. Suginoara, T.Kitamura, "Control of hardness and flammability property in carbonized condition of compressed sugi wood", Wood Industry, Vol.59, pp.585-590(2004)
- [4] M. Asai, H. Nishimura, "Effect of manufacturing conditions on bending strength of compressed wood", Transactions of the Japan society of mechanical engineering, Series A, Vol.67, pp.267-272(2001)
- [5] T. Ohtani, Y. Kubojima, K. Matsushita, "Fracture morphology and effect of compression volume on tensile strength of compressed wood", Mokuza Gakkaishi, Vol.51, pp.189-195(2005)
- [6] A.Nadai, "Theory of flow bridge and fracture of solids", p.358(1950) McGraw-Hill.
- [7] I. Asano, "On the compressive fiber stress in the plastic bending of wood beams", Mokuza Gakkaishi, Vol.12, pp.155-160(1966)
- [8] F.Bowden, D.Tabor, "The friction and lubrication of solids", p.10(1986) Clarendon press • Oxford
- [9] Y. Murase, M. Ota, "On the contacting deformation of wood by intending steel ball", Mokuza Gakkaishi, Vol.17, pp.271-276(1971)

(Received December 12, 2008; Accepted September 16, 2009)

Hydrogen Desorption Properties of Woodceramics

Akito Takasaki, and Toshihiro Okabe*

Department of Engineering Science and Mechanics, Shibaura Institute of Technology, Koto-ku, Tokyo 135-8548

*Material Technology Division, Aomori Industrial Research Center, Aomori 030-0113

Hydrogen desorption properties of woodceramics, made from radiata pine wood fiberboards carbonized at 923 K and 1473 K, hydrogenated at a temperature of 303 K at an initial hydrogen pressure of 4 MPa, were investigated by means of thermal desorption spectroscopy. Hydrogen desorption initiated at temperatures of more than 750 K, and the accelerated hydrogen desorption occurred at about 1200 K for woodceramics carbonized at 923 K, but almost no hydrogen desorption was observed for those carbonized at 1473 K. Deposition of magnesium (Mg) enhanced the hydrogen absorption and desorption for woodceramics carbonized at 923 K. The activation energy of hydrogen desorption for woodceramics carbonized at 923 K with and without optimal amount of Mg was about 176 and 130 kJ/mol, respectively. No hydride (MgH_2) formation was observed for the woodceramics deposited with Mg after hydrogenation.

Keywords: Woodceramics, hydrogen desorption, carbonization, magnesium, catalysis

1. INTRODUCTION

Woodceramics [1] have been developed as new kinds of porous carbonaceous materials that can be made from biomass like wood wastes. They possess quite good properties for electrical resistance, electromagnetic shielding and infrared radiation, and are being expected to be used in a wide range of industrial fields, such as wear-resistant materials, heat insulator and infrared radiators, etc [2, 3].

There are still some arguments whether carbonaceous materials, such as carbon nanotubes, absorb hydrogen or not because literature data on the storage capacities of hydrogen in carbonaceous materials, like carbon nanostructures, show a scatter over several orders of magnitude which cannot be solely explained by the limited quantity or purity of these materials [4]. In our previous study, aiming to expand the industrial applications of woodceramics, we have reported that woodceramics carbonized at 923 K absorbed about 0.64 wt.% hydrogen at a temperature of 303 K and at an initial hydrogen pressure of 3 MPa, whereas those carbonized at 1473 K absorbed almost no hydrogen, suggesting that carbonizing temperature was important for hydrogen capacity [5]. In this study, as a continuation from the previous study, hydrogen desorption performances of the woodceramics, which were made by carbonizing radiata pine wood fiberboards at temperatures of 923 K and 1473 K, were investigated mainly by means of thermal desorption spectroscopy (TDS), and the effect of carbonizing temperature on the hydrogen desorption performances was investigated.

2. EXPERIMENTAL PROCEDURE

The starting woody material used in this study was medium-density radiata pine fiberboards. These materials were impregnated with phenolic resin, and then were carbonized at 923 K and 1473 K. The final products are porous carbonaceous materials called "woodceramics".

The boards were cut into small samples, and hydrogen

absorption experiment for the samples was carried out in a high-pressure vessel, which was made of stainless steel. The vessel containing the sample was evacuated by a rotary pump and then back-filled with pure (99.99999%) hydrogen gas several times, and the final hydrogen pressure was kept to 3 MPa. The vessel was heated by an electric heater surrounding the vessel and was kept to a temperature of 303 K. After hydrogenation, hydrogen desorption properties were analyzed by means of thermal desorption spectroscopy (TDS) equipped with a quadrupole mass analyzer, ULVAC-QMS 200. After mounting the sample in a sample holder, the holder was evacuated by a turbo-molecular pump to a vacuum level of 10^{-6} Pa, and then hydrogen ion (H_2^+) current, which corresponds to hydrogen evolution rate, was monitored by the quadrupole mass analyzer during heating the sample by an infrared gold image furnace at a constant heating rate. Magnesium (Mg) was also deposited in a vacuum to catalyze the surface of the woodceramics. The microstructural change of the woodceramics before and after deposition was investigated by X-ray diffraction (XRD) measurement, which was performed by a JEOL JDX-11PA, using $\text{Cu-K}\alpha$ radiation at 30 kV and 20 mA.

3. RESULTS AND DISCUSSION

Fig.1 (a) and (b) show the TDS spectra for woodceramics carbonized at 923 K and 1473 K, respectively, before and after hydrogenation measured at heating rate of 20 K/min. The TDS spectrum without sample (blank run) measured at a heating rate of 20 K/min, which determine back grounds of the experiments, are also included in Fig. 1. No prominent TDS peaks were found for blank run and for woodceramics carbonized at both temperatures before hydrogenation. However, for woodceramics carbonized at a low temperature (Fig. 1(a)) after hydrogenation, a weak and a strong TDS peaks are observed at about 900 K and 1200 K, respectively, whereas no prominent peaks for the woodceramics

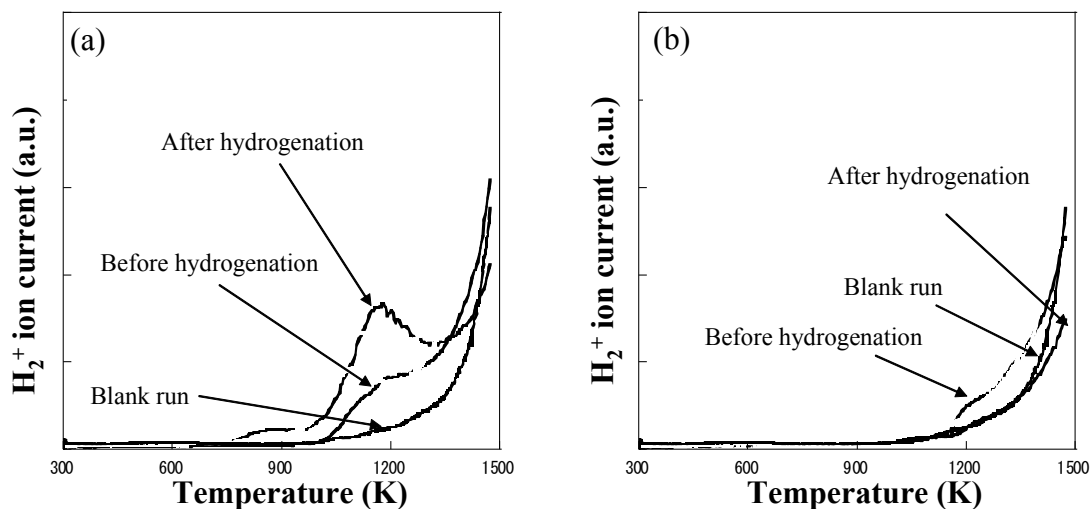


Fig. 1 Thermal desorption spectra of hydrogen for woodceramics carbonized at (a) 923 K and (b) 1473 K, respectively, before and after hydrogenation (heating rate: 20 K/min). The spectrum measured without sample (blank run) are also included.

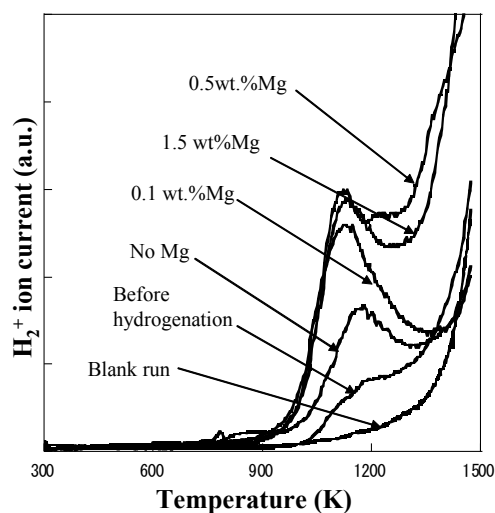


Fig.2 Thermal desorption spectra for the hydrogenated woodceramics carbonized at 923 K before and after deposition of some amounts of Mg. The Mg concentrations are the deposited Mg amount in wt.% derived from change in the total mass before and after Mg deposition. The TDS spectra before hydrogenation and for blank run are also included.

carbonized at 1473 K. These indicate that woodceramics carbonized at lower temperatures occlude some amount of hydrogen, which agrees well with our previous hydrogen absorption experiment [5]. Two TDS peaks (at about 700 K and 1000 K (heating rate was not reported although the peaks depend on it)) were also reported for a nanostructured graphite mechanically milled for 80 h under hydrogen pressures [6], in which the low temperature peak (700 K) was assigned to the desorption of hydrogen atoms trapped at some defects between the graphite planes and the high temperature peak (1000 K) to that of those trapped at the edges of graphene sheets. The mechanical milling, which is a kind of dynamic processing in powder

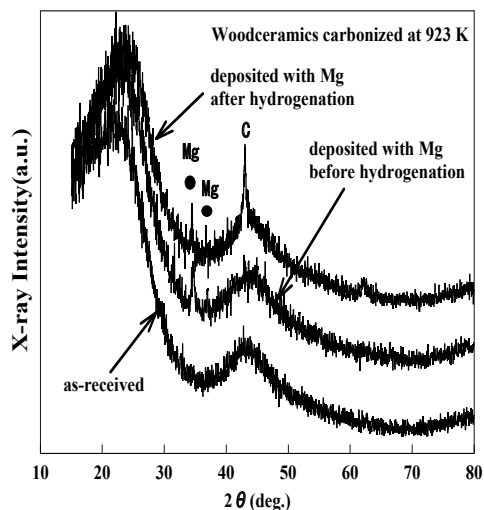


Fig. 3 X-ray diffraction patterns for the Mg-deposited woodceramics carbonized at 923 K before and after hydrogenation. The pattern for as-received woodceramics is also included.

technology, generally results in the formation of dangling carbon bonds in graphite [7], and the relative ratio of CH_x covalent bonds is reported to increase if the milling is performed under hydrogen atmosphere [8]. Although the woodceramics used in this study were not processed (by mechanical milling), those carbonized at lower temperatures are thought to possess comparative number of dangling bonds at the edge of graphene sheets.

To modify the hydrogen absorption property for the woodceramics carbonized at 923 K, Mg was deposited to the woodceramics in vacuum, because Mg has relatively good chemical affinity with hydrogen. Fig. 2 shows TDS spectra (measured at a heating rate of 20 K/min) for the hydrogenated woodceramics carbonized at 923 K after deposition of some amounts of Mg. The

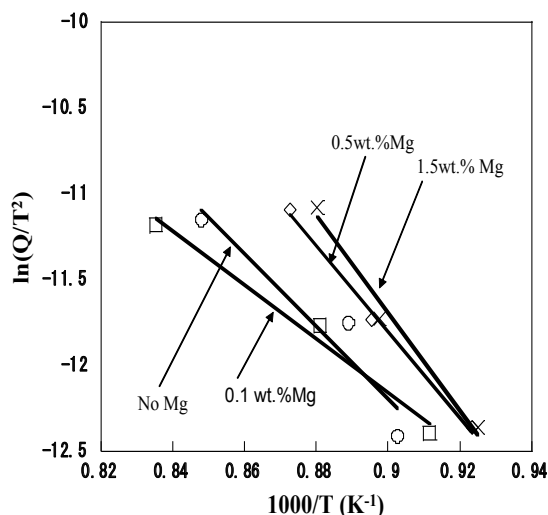


Fig.4 Kissinger plot for the hydrogenated woodceramics carbonized at 923 K before and after depositions of some amounts of Mg.

Mg concentrations shown in Fig. 2 are the deposited Mg amount in wt.% derived from change in the total mass before and after Mg deposition. The TDS spectra for the woodceramics without Mg deposition and for blank run are also included in Fig. 2. When one compares with the TDS spectra without Mg deposition, the peak at about 1200 K becomes more prominent with increasing the amount of deposited Mg, indicating that much hydrogen was occluded after Mg deposition. However, no improvement of hydrogen absorption was found for the woodceramics carbonized at 1473 K after Mg deposition. Fig. 3 shows XRD patterns for the Mg-deposited woodceramics carbonized at 923 K before and after hydrogenation. The XRD pattern for as-received woodceramics is also included in Fig. 3. Different from the graphite, one can observe only two broad XRD peaks for as-received woodceramics, indicating that the structure of the woodceramics is a turbostratic one (long range ordering of the graphite structure almost disappears but rough alignment of graphite interlayer (graphene sheets) still remains). The weak XRD peaks can be found after Mg deposition even after hydrogenation, suggesting that Mg does not transform into hydride (MgH_2) at the present experimental temperature (303 K), acting as a catalyst for hydrogen absorption. The strong XRD peak observed at about $2\theta=42^\circ$ after hydrogenation is due to the diffraction from the (100) crystal plane of the graphite structure.

The activation energy for hydrogen desorption can be estimated from the shift in the peak temperature for TDS measurements made at different heating rates [9], using,

$$\ln\left(\frac{Q}{T^2}\right) = -\left(\frac{E}{RT}\right) + A, \quad (1)$$

where Q is the heating rate (K/min), T the peak temperature (K), R the molar gas constant (J/mol K) and E the activation energy for hydrogen desorption (J/mol).

Fig. 4 shows Kissinger plot of equation (1) for the woodceramics carbonized at 923 K before and after depositions of some amounts of Mg. Table 1 summarizes the activation energies obtained from the slope of the Kissinger plot shown in Fig.4. The activation energy for hydrogen desorption for the woodceramics carbonized at 923 K without Mg deposition is 177 kJ/mol. Although the deposition of small amount of Mg decreases the activation energy, comparatively large amount deposition of Mg increases the energy. In this experiment, deposition of 0.1 wt.% Mg gives the lowest activation energy for hydrogen desorption.

Table 1 Activation energies for the woodceramics carbonized at 923 K before and after deposition of some amounts of Mg.

Sample condition	Activation energy (kJ/mol)
No deposition	177
0.1 wt.% Mg deposition	130
0.5 wt.% Mg deposition	208
1.5 wt.% Mg deposition	235

4. CONCLUSIONS

Hydrogen desorption properties for woodceramics carbonized at temperatures of 923 K and 1473 K were investigated by means of thermal desorption spectroscopy equipped with a quadrupole mass analyzer. The results obtained were summarized as follows.

1. Hydrogen desorption initiated at temperatures of more than 750 K, and the accelerated hydrogen desorption occurred at about 1200 K for woodceramics carbonized at 923 K, but almost no hydrogen desorption was observed for those carbonized at 1473 K.
2. Mg deposition improved the hydrogen absorption capacities only for woodceramics carbonized at 923 K. The activation energy of hydrogen desorption for the woodceramics carbonized at 923 K was about 177 kJ/mol before Mg deposition, but it was lowered if an optimal amount of Mg was deposited on the woodceramics.
3. No hydride (MgH_2) formation was observed for the woodceramics after Mg deposition, indicating that Mg is just acting as a catalyst for hydrogen absorption.

ACKNOWLEDGEMENTS

The authors are grateful to Messrs. Kohei Tsukada and Muhammad Yusuf Bin Musa, a graduate and an undergraduate students, respectively, of Shibaura Institute of Technology at that time, for their help of the experiments. A part of this research was supported by the European Commission (project Dev-BIOSOFC, FP6-042436, MTKD-CT-2006-042436).

REFERENCES

- [1] T. Okabe, K. Saito, K. Hokkirigawa, J. Porous Mater., **2**, 207 (1996).

- [2] M. Kano, M. Momota, T. Okabe, K. Saito, *Thermochim. Acta*, **292**, 17 (1997).
- [3] K. Shibata, T. Okabe, K. Saito, *J. Porous Mater.*, **4**, 269 (1997).
- [4] M. Hirscher, M. Becher, M. Haluska, F. von Zeppelin, X. Chen, U. Dettlaff-Weglikowska, S. Roth, *J. Alloys Comps.*, **356-357**, 433 (2003)
- [5] A. Takasaki, M. Otsuka, T. Okabe, *Trans. Mater. Res. Soc. Japan*, **30**, 1151 (2005)
- [6] D.M. Chen, T. Ichikawa, H. Fujii, N. Ogita, M. Udagawa, Y. Kitano, E. Tanabe, *J. Alloys Comps.*, **354**, L5 (2003)
- [7] T. Fukunaga, K. Nagano, U. Mizutani, H. Wakayama, Y. Fukushima, *J. Non-Cryst. Solids*, **232-234**, 416 (1998)
- [8] S. Orimo, G. Majer, T. Fukunaga, A. Züttel, L. Schlapbach, H. Fujii, *Appl. Phys. Lett.*, **75**, 3093 (1999)
- [9] H.E. Kissinger, *Anal. Chem.*, **27**, 1702 (1957)

(Received December 12, 2008; Accepted September 16, 2009)

Functionality control of lignophenol by demethylation of methoxyl group -Successive structural conversion of syringyl type lignophenol-

Keigo Mikame and Masamitsu Funaoka

Graduate School of Bioresources, Mie University, SORST JST, 1577, Kurima-machiya, Tsu, Mie 514-8507, Japan

Fax: +81-59-231-9517,

E-mail: mikame@bio.mie-u.ac.jp

Although lignin is the most abundant natural phenolic polymer, its phenol activity is extremely low. Because most phenolic hydroxyl groups of lignin precursors were etherified in the biosynthetic process. In the present work, successive cleavage of ether linkages of lignin was carried out

Lignophenols synthesized from native lignins through the phase-separation process were depolymerized under the mild alkaline condition. The guaiacyl and syringyl aryl coumaran dimmers were isolated from the hardwood lignocresol treated with 1.0 N NaOH in 21% and 7.4%, respectively. Demethylation of methoxyl group in the syringyl aryl coumaran dimer was carried out using boron tribromide. The pyrogallol type and 3-methoxy catechol type aryl coumaran were detected with LC/MS analysis. The pattern of demethylation of methoxyl group in the syringyl aryl coumaran dimer was controlled by lewis acid treatment condition.

Key words: lignin, lignophenol, phase-separation system, methoxyl group, demethylation

1. INTRODUCTION

Recently the utilization of plant biomaterials for petroleum substitute has already been partially commercialized. For example, polylactic acid as a biodegradable plastic from corn or sugarcane molasses and biodiesel oil from soybean oil or palm oil have already been produce in large volume. Thus the aliphatic compounds as petroleum substitute will be able to get from plant materials, if increased production efficiency is proceeded by research and development.

On the other hands, the aromatic compounds as petroleum substitute from plant biomaterials are hardly produced.

Lignin is the most abundant natural aromatic polymer and exists in plant cell walls as one of the major constituents. It serves as cement between wood fibers, a stiffening agent within fibers, and a barrier to the enzymatic degradation of the cell wall.

However, in contrast to the importance and potential of lignin in nature, lignin-based products have scarcely been in human life, because complicated structure and although lignin is the

most abundant natural phenolic polymer, its phenol activity is extremely low. Native lignin have only 0.1 to 0.2 mol/C₉ of phenolic hydroxyl groups.^{1,2} Because most phenolic hydroxyl groups of lignin precursors are etherified in the three steps biosynthetic process.^{3,4}

The first step is formation of methoxyl group. Lignin monomer is formed from phenylalanine or tyrosine via cinnamate pathway. In this pathway although *p*-coumaric acid is hydroxylated by P-450 type hydroxylase, the hydroxylated compounds (caffeic acid and 5-hydroxyferulic acid) is immediately methylated by *O*-methyl transferase. As a result one or two lignin-specific methoxyl groups are formed and phenolic hydroxyl groups are etherified.

The second step is polymerization of lignin precursors (coniferyl alcohol, sinapyl alcohol and *p*-coumaryl alcohol) via aryl ether linkage by radical coupling from enzymatic dehydrogenation.

The third step is formation benzyl aryl ether. Because a part of oligomeric products formed through radical coupling has quinonemethid structure, benzyl aryl ether linkage is formed by

addition of adjacent phenolic hydroxyl groups or carbohydrates.

Therefore many of phenolic hydroxyl groups are blocked by ether linkage. In other words, lignin has many latent phenolic hydroxyl groups.

In this study, we carried out successive cleavage of these ether linkages of lignin through the reverse pathway of lignin biosynthetic mechanism.

The first step is cleavage of benzyl aryl ether through the phase-separation system. In the process composed of phenols and concentrated acid, native lignin was modified by phenol derivatives to selectively grafted benzyl position, the most reactive sites, to give 1,1-Bis(aryl) propane type lignin-based recyclable polymer (lignophenol).⁵⁻⁸

The second step is cleavage of C β aryl ether linkages by switching functions of lignophenol under the mild alkaline condition.⁸

The third step is demethylation of the aromatic methoxyl groups.⁹

In this paper, we controlled the pattern of demethylation of methoxyl group in the syringyl aryl coumaran dimmer which had two methoxyl groups by lewis acid treatment condition.

2. EXPERIMENTAL

2.1 Preparation of lignocresol through the phase-separation system

For solvation of lignin with phenol derivatives, 3 mol/C9 (phenyl propane unit of lignin) of *p*-cresol dissolved in acetone was added to defatted birch wood meal and acetone was evaporated with stirring. Sulfuric acid (72%, 10 ml/g wood) was added to the mixture and the vigorous stirring was continued at 30°C for 60 min. The reaction mixture was rapidly poured to excess distilled water. The insoluble fraction was collected by centrifugation, washed with distilled water until neutral and lyophilized. The dried insoluble fraction was extracted with acetone. The acetone solution was then concentrated under reduced pressure and added dropwise to an excess amount of diethyl ether with stirring. The precipitated lignin derivative (lignocresol) was collected by centrifugation. Yields of lignocresol from birch were 22.2% of wood.

2.2 Separation of low molecular weight fraction from birch lignocresol 2nd derivatives.

The dissolved lignocresol in 1.0 N NaOH solution was heating at 170°C for 1.0 hr. After cooling, reaction mixture was acidified by the 1.0 N HCl. The precipitant was washed by de-ionized water and then dried. The molecular weight distribution of 2nd derivatives from

this lignocresol analyzed with size exclusion chromatography (SEC).

(SEC condition)

Column; Shodex GPC KF-801,802,803,804, Eluent; THF, Flow rate; 1.0 ml/min, Temp.; 40°C, Detect; 280nm, Standard: polystyrene standard

Second derivatives of lignocresol was fractionated by preparative SEC on Shimadzu LC-8A recycle preparative system equipped with Shimadzu SPD-10AUV/VIS detector. Shodex GPC KF-5002.5 (50 mm ID x 300 mm) was connected and THF was used as an eluent (flow rate; 10 ml/min).

2.4 Demethylation of methoxyl group of 2nd derivatives low molecular weight fraction from birch lignocresol.

Two ml of 1M boron tribromide dichloromethane solution was slowly added to a solution of 67mg of the low molecular weight fraction of 2nd derivatives in dichloromethane. In this reaction, demethylation was controlled by reaction temperature and time.

1) The reaction mixture was stirred at -78°C for 1hr under nitrogen gas and gradually warmed up to room temperature and stirred for 60 min.

2) The reaction mixture was stirred at -78°C for 1hr under nitrogen gas and gradually warmed up to room temperature for 1hr and stopped.

3) The reaction mixture was stirred at -78°C for 1hr under nitrogen gas and gradually warmed up to -40°C and stopped.

4) The reaction mixture was stirred at -78°C for 3hr under nitrogen gas.

After these reaction, water was added to quench the reaction, and the mixture was extracted with ethyl acetate. The ethyl acetate extract was dried with Na₂SO₄, and the solvent was evaporated. The reaction mixture was analyzed by LC/MS.

<LC/MS condition>

MS mode: APCI negative, Column: Imtakt Cadenza CD-C18, 3.0mm ID x 100mm, Eluent: 50% methanol, 0.3ml/min, Column temp: 40°C

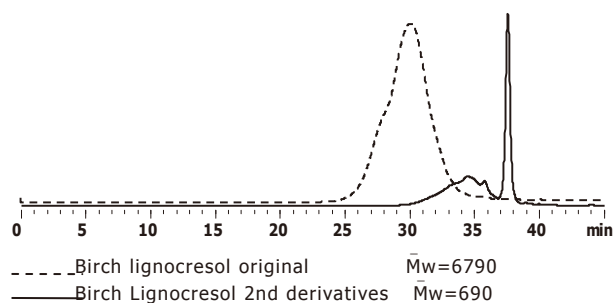


Fig. 1 SEC profiles of birch lignocresol and the 2nd derivatives

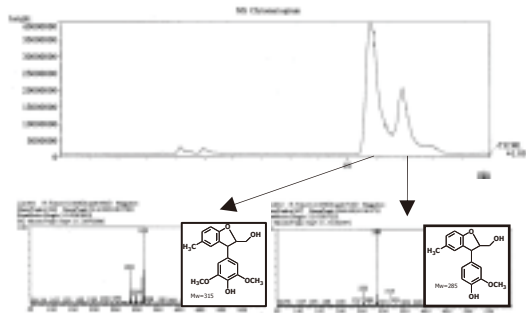


Fig. 2 LC/MS analysis of birch lignocresol 2nd derivatives low molecular weight fraction

3. RESULTS AND DISCUSSION

3.1 Separation of low molecular weight fraction from birch lignocresol 2nd derivatives..

In the phase-separation system, native lignin was modified by selectively grafting *p*-cresol to benzyl position to give lignocresol composed mainly of 1,1-bis(aryl)propane-type units.

As shown Fig. 1, lignocresol from birch was significantly depolymerized under alkaline treatment, indicated major peak at 37min (about $M_w=300$). This peak was fractionated by preparative SEC. As a results of LC/MS analysis, two compounds ($M_w=315$ and 285) were detected from birch lignocresol 2nd derivatives (Fig.2).

The structure of $M_w=285$ compound was determined by $^1\text{H-NMR}$ and $^{13}\text{C-NMR}$. This compound was guaiacyl aryl coumaran.⁹ The structure of $M_w=315$ compound was determined as syringyl aryl coumaran (Fig.3).⁹ It was suggested that these aryl coumarans were formed by neighboring group participation reaction: the phenoxide ion grafted phenols readily attacked the electron deficient β position nucleophilically, resulting in the cleavage of β -aryl ether linkage.⁸

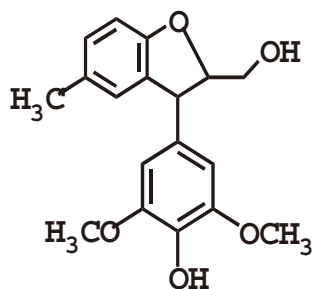


Fig. 3 The structure of syringyl aryl coumaran from lignocresol 2nd derivatives.

3.2 Demethylation of methoxyl group of 2nd derivatives low molecular weight fraction from birch lignocresol.

Demethylation of methoxyl group in the syringyl

aryl coumaran dimer which had two methoxyl groups was carried out using boron tribromide (BBr_3) under the four conditions.

1) at -78°C for 1hr and at room temperature for 60 min.

In LC/MS analysis, the ethyl acetate extractive of reaction mixture contained peak having $m/z=285$ (Fig.4). This peak was presumed pyrogallol type aryl coumaran which was demethylated two methoxyl groups from syringyl aryl coumaran. The 3-methoxy catechol type aryl coumaran which was demethylated one methoxyl groups from syringyl aryl coumaran was not detected.

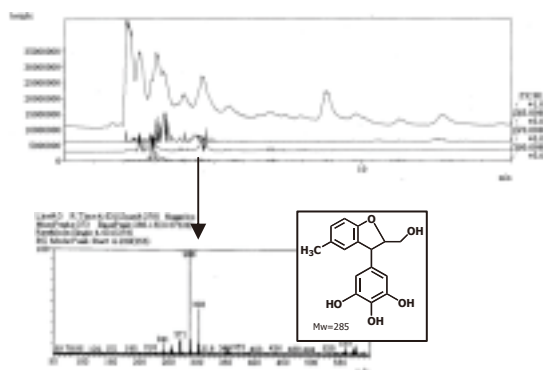


Fig. 4 LC/MS analysis of birch lignocresol 2nd derivatives low molecular weight fraction treated with BBr_3 at -78°C for 1hr and room temperature for 1hr

2) at -78°C for 1hr and gradually warmed up to room temperature for 1hr and stopped.

In this condition, the ethyl acetate extractive of reaction mixture contained peaks having $m/z=285$ and $m/z=300$. The peak of $m/z=300$ was 3-methoxy catechol type aryl coumaran (Fig.5).

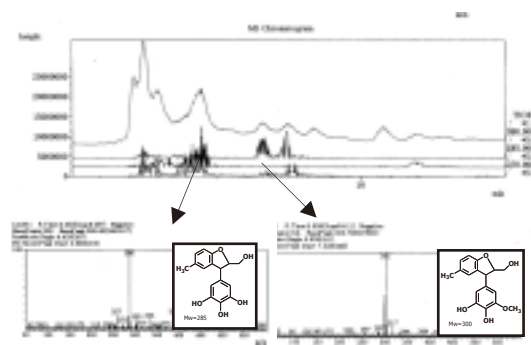


Fig. 5 LC/MS analysis of birch lignocresol 2nd derivatives low molecular weight fraction treated with BBr_3 at -78°C for 1hr and room temperature for 0min

3) at -78°C for 1hr and -40°C for 1hr.

In this condition, although two peaks having $m/z=285$ and $m/z=300$ were detected, the contents of these peaks

were increased compared to condition 2). But substrate (syringyl aryl coumaran) was more remaining than condition 2) (Fig. 6). Thus it was thought that secondary modification of demethylated compounds araised in condition 2).

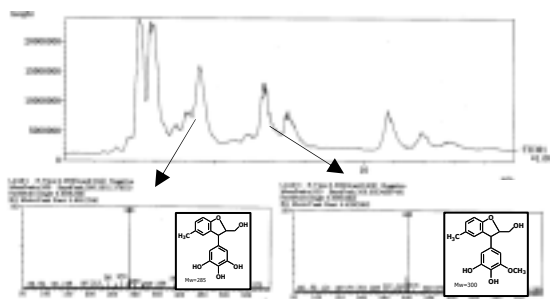


Fig. 6 LC/MS analysis of birch lignocresol 2nd derivatives low molecular weight fraction treated with BBr₃ at -78°C for 1hr and -40°C for 1hr

4) at -78°C for 3hr

In this most mild condition, the ethyl acetate extractive of reaction mixture contained peak having m/z=300. The 3-methoxy pyrogallol type aryl coumaran was not detected (Fig. 7).

These results show that the patterns of demethylation of methoxyl group in the syringyl aryl coumaran dimer are able to control by lewis acid treatment condition.

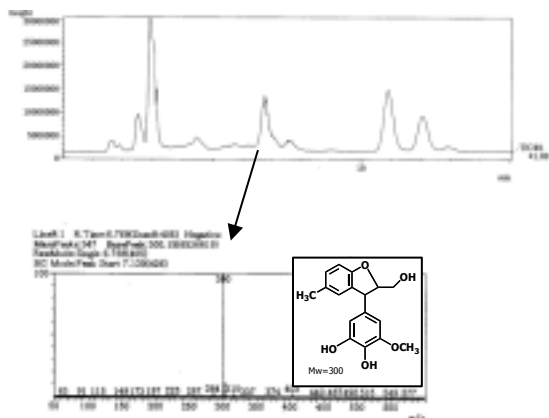


Fig. 7 LC/MS analysis of birch lignocresol 2nd derivatives low molecular weight fraction treated with BBr₃ at -78°C for 3hr

4. CONCLUSION

It is important to utilize lignin for oil substitution aromatic compounds because lignin is most abundant native aromatic compounds. However its phenol activity is extremely low. Because most phenolic hydroxyl groups of lignin precursors were

etherified in the biosynthetic process. We carried out successive cleavage of these ether linkages of lignin and phenolic activation through the reverse pathway of lignin biosynthetic mechanism.

The native lignin was converted highly phenolic functional polymer (lignophenol) controlled molecular weight through the phase-separation treatment. The lignophenols was depolymerized to dimer level with alkaline treatment. And the methoxyl group of the dimer compound was demethylated with lewis acid treatment (Fig. 8). The patterns of demethylation of methoxyl group in the syringyl aryl coumaran dimer are able to control by lewis acid treatment condition.

These successive cleavages of ether linkages of lignin is similar to decomposition mechanism of lignin in ecosystem. The decomposed lignin has several functions. Therefore the decomposed compounds from lignophenol also have high potentiality of aromatic compounds.

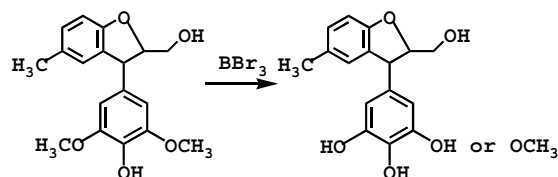


Fig. 8 Demethylation of the methoxyl group of syringyl aryl coumaran with BBr₃

5. References

- [1] Y.-Z. Lai and M. Funaoka, *J. Wood chem. Technol.*, **13**, 43-54 (1993).
- [2] Y.-Z. Lai and M. Funaoka, *Holzforchung* **47**, 333-338 (1993).
- [3] K. Freudenberg, *Science*, **148**, 595-600 (1965).
- [4] T. Higuchi, *J. Biochem*, **45**, 515-528 (1958).
- [5] M. Funaoka and I. Abe, *Tappi Journal* **72**, 145-149(1989).
- [6] M. Funaoka, M. Matsubara, N. Seki and S. Fukatsu, *Biotechnol. Bioeng.*, **46**, 545-552 (1995).
- [7] M. Funaoka and S. Fukatsu, *Holzforchung* **50**, 245-252 (1996).
- [8] M. Funaoka, *Polymer Internati onal*, **47**, 277-290 (1998)
- [9] K. Mikame, M. Funaoka, *Trans. Materials Res. Soc. Japan*, **33**, 1149-1152 (2008)

(Received December 12, 2008; Accepted September 16, 2009)

Influences of Lignophenol-Derivatives on Performances of Photo-Chemical Cells

Mitsuru Aoyagi, Nao Umetani and Masamitsu Funaoka

Graduate School of Bioresources, Mie University, Japan Science and Technology Agency (JST)-Solution Oriented Research for Science and Technology (SORST), 1577 Kurimamachiya-Cho, Tsu, 514-8507, Japan
Fax: +81-59-231-9591, e-mail: aoyagi@bio.mie-u.ac.jp

Hinoki Cypress (*Chamaecyparis obtusa*)-lignophenol (*p*-cresol type, HCLC), which is directly and quantitatively synthesized from wood through the phase-separation system, hydroxymethylated HCLC (HCLC-HM) and polymerized HCLC-HM by heat-set (HCLC-HM-P) were used as materials for photo-sensitizers for nano-porous TiO₂ electrodes. In order to investigate influences of structural features of lignophenol derivatives, HCLC, HCLC-HM and HCLC-HM-P were reacted under alkaline conditions at 140 °C (neighbouring group participation) and 170°C (aryl migration). After these derivatives were investigated by ionization difference spectra using UV-Vis, FT-IR, ¹H-NMR and GPC, all derivatives were used as photo-sensitizers. There were different tendencies of HCLC from both HCLC-HM and HCLC-HM-P derivatives. As both HCLC-HM and HCLC-HM-P derivatives kept their polymeric structures, not only arylcoumaran or stilbene but also quinoid type structures acted as good photo absorbers. Based on these results, HCLC-HM-P-TiO₂ electrodes polymerized directly demonstrated $V_{oc} = 0.48$ V, $I_{sc} = 4.00$ mAcm⁻², $FF = 0.61$ and $\eta = 1.06$ % under 100.0 mWcm⁻² of visible light irradiation. Especially I_{sc} was drastically improved. Moreover hardwood lignophenol showed same tendency.

Key words: lignin, lignophenol, solar cell, sensitizer, phenolic resin

1. INTRODUCTION

Recently both global environmental crisis and exhaustion of fossil carbon resources have been attracted. For example, global warming phenomena by green-house effect gases such as CO₂, methane and chlorofluorocarbons are paid a lot of attentions in the world. In order to overcome these problems, supply of both sustainable energy and carbon resources have to replaces from fossil carbons to natural resources such as solar energy and biomass.

Making a lot of efforts, wide variety of solar cell technology has been developed. Recently dye-sensitized solar cells (DSSCs) have been attracted after Gratzel developed with nano-crystalline TiO₂ electrodes [1]. Up to 11 % of efficiencies with Ruthenium sensitizers have been reported [2]. Moreover natural pigments such as anthocyanin, anthocyanidin, porphyrine, tannin and polyphenols [3-8] have also been paid a lot of attentions. It is good combination between natural dyes and DSSCs, however natural dyes extracted easily but only small amounts. For example, anthocyanine was extracted only

75 mg / 100 g materials [9-13]. In order to solve this problem, lignophenol (LP) and its derivatives have been applied for DSSCs [14-18], because LP was derived directly from lignocellulosics quantitatively through the phase-separation system [19-20]. For example, 220 g of LP was obtained from 1000 g of Hinoki Cypress (*Chamaecyparis obtusa*) [21]. The best photo-electricity conversion performance of LP-cell with second derivative-II of HCLC showed $V_{oc} = 0.51$ V, $I_{sc} = 10.23$ mAcm⁻², $FF = 0.59$ and $\eta = 3.61$ % under 85.0 mWcm⁻² of visible light irradiation [16]. Recently, hydroxymethylated LP showed good results due to rich hydroxyl groups and quinoid groups [18]. In this study, investigations of both relationships between structural features of LP derivatives and of performances on photo-electricity conversion of the solar cells were carried out. Moreover, new-type electrodes with direct polymerization on TiO₂ films were tried for the cells.

2. EXPERIMENTAL

2.1 Synthesis of Lignophenols

Both Hinoki cypress (HC, *Chamaecyparis obtusa*) and Birch (BI, *Betula platyphylla*) were used as softwood and hardwood materials for the phase-separation system, respectively. The woody materials were milled for 80 mesh passed. Extractives in the materials were removed by benzene/ethanol (2/1, v./v.) in a Soxhlet reflux system for 96 hrs. LPs have been synthesized following the phase-separation system [19-20]. Two-step method (process II) of the phase-separation system was also carried out for HC as follows. The material (500 g) was mixed with *p*-cresol in acetone. Amounts of *p*-cresol were 3 mol / phenylpropane units (C₉ units), which were subunits of

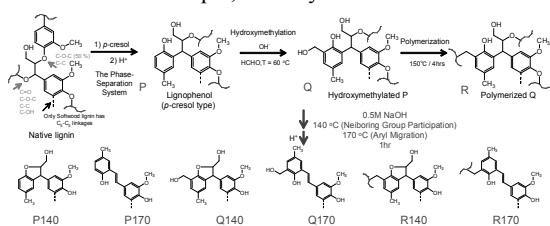


Fig.1 Reaction scheme and characteristic structures of Hinoki cypress-lignophenol (*p*-cresol type, HCLC) derivatives. P, Q and R are HCLC, hydroxymethylated HCLC (HCLC-HM) and polymerized HCLC-HM (HCLC-HM-P). P140, P170, Q140, Q170, R140 and R170 show second derivative-I(140) and II (170) of P, Q and R, respectively. Both 140 and 170 mean treatment temperatures under 0.5 N NaOH.

native lignin. After evaporation of acetone, 72 % H_2SO_4 aq. solution was poured into the material adsorbed by *p*-cresol at 30 °C in a reactor in system plant No.1 (established in Mie University, JST-CREST). Then the mixture was stirred vigorously for 60 min. The mixture was quickly poured into 20 L of de-ionized water with vigorously stirring by a homogenizer for 5 min. Then the purple precipitation was washed until pH = 5. After drying the solid, LP was extracted by acetone. The LP solutions were dropped into diethylether (EtOEt) under vigorously stirring in chilled condition. After evaporating and drying on P_2O_5 , both Hinoki cypress-lignophenol (*p*-cresol type, HCLC) and Birch-lignophenol (*p*-cresol type, BILC) were obtained.

2.2 Preparation of Derivatives

Hydroxymethylated HCLC (HCLC-HM) was synthesized from 15 g of LP in 0.5 M NaOH solution by mixing 20 mol of formaldehyde for an amount of aromatic rings in LP at 60 °C under N_2 atmosphere with a stirring system and a reflux condenser. After 3 hrs, 1.0 M HCl was dropped into the reaction mixture at 5 °C to pH = 2.0. The resulting precipitation was washed to pH = 5.0. The solid was dried on P_2O_5 vacuum drying. Polymerization of HM-LP (HCLC-HM-P) by heat-set was carried out at 150 °C for 7 hrs under an aerobic condition.

2.3 Functionality Controls

Both second derivatives I of HCLC (HCLC140), HCLC-HM (HCLC-HM140) and HCLC-HM-P (HCLC-HM-P140) were derived under alkaline condition at 140 °C in SUS autoclaves. Second derivative-II of HCLC (HCLC170), HCLC-HM (HCLC-HM170) and HCLC-HM-P (HCLC-HM-P170) were synthesized in the same ways under 170 °C. HCLC samples were dissolved in 0.5 M NaOH. The solutions were heated to 140 °C or 170 °C. After 60 min, the reaction mixtures were neutralized by 1.0 M HCl to pH = 2.0. The resulting precipitation was washed by chilled de-ionized water. The insoluble residue was dried over P_2O_5 .

2.4 Characterization of LPs

The structure of LP was characterized by Gel Permeation Chromatography (GPC), $^1\text{H-NMR}$, FT-IR and Ionization Different Spectra (UV-Vis). GPC was carried out by LC-10 with four columns (KF801, KF802, KF803 and KF804, Shodex Co.), using rectified tetrahydrofran (THF) as an effluent. Both M_w and M_n were determined based on standard polystyrene. $^1\text{H-NMR}$ spectrum was measured by NMR500 (JASCO Co.) in CDCl_3 or $\text{CDCl}_3 / \text{C}_5\text{D}_5\text{N} = 3 / 1$ (v / v). FT-IR spectroscopy was also carried out on a Spectrum GX (Perkin Elmer Co.), using the KBr pellet technique for sample preparation. Ionization Difference Spectrum was obtained on UV-560 (JASCO Co.) by differential spectrum between 2-methoxyethanol solution and 2-methoxyethanol / 2 N NaOH = 13 / 12 (v/v) solution.

2.5 Preparation of LP Solar Cells

Photochemical cells with TiO_2 thin film on FTO glasses employing LPs were prepared. TiO_2 pastes were obtained by well mixing of HPA-15-R TiO_2 dispersion

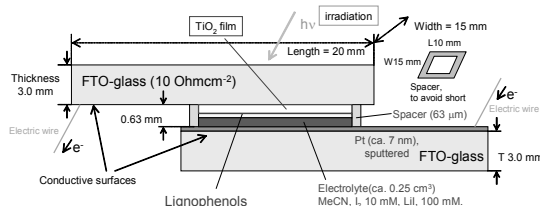


Fig.2 A schematic model of a dye-sensitized solar cell with lignophenols.

(Shokubai Kasei Co.), P25 (Nippon Aerogel Co.) and polyethylene glycol ($F_w = 20\,000$, Wako Co.) at a ratio of 100 : 10 : 4 (w/w/w). Well-ground pastes were coated on FTO-glasses ($30\ \text{Ohmcm}^{-2}$) using bar-coating technique with $63\ \mu\text{m}$ spacers. The dried films on FTO-glasses were sintered at 450 °C for 60 min under an aerobic condition. After cooling to 80 °C, the film on FTO was immersed into $5.0\ \text{g L}^{-1}$ of LP solution. The TiO_2 electrodes employing LP-electrolytes (0.5 M LiI, 0.05 M I_2 in acetonitrile)-Pt-FTO was composition of cells (Fig.2). Performances of the cells were estimated by potentiostat (HA-105, Hokuto Denko Co.) under 150-W Xe lamp (Hamamatsu Photonics Co.) irradiation through L41 UV-cut filter.

2.6 Polymerized Electrodes

The TiO_2 electrodes were immersed into each $5.0\ \text{g L}^{-1}$ of THF solution of HCLC-HM and BILC-HM. After 24 hrs, the electrodes were evaporated and heated for 4 hrs.

3 RESULTS AND DISCUSSION

3.1 LP Derivatives

Though the phase-separation system, HCLC was obtained with 24.7 % and 80.3 % yield based on wood and lignin contents, respectively. HCLC-HM was synthesized with 89.2 % of yield. After heat set of HCLC-HM, polymerized HCLC-HM (HCLC-HM-P) was obtained quantitatively.

The second derivatives, HCLC140, HCLC170, HCLC-HM140, HCLC-HM170, HMLC-HM-P140 and HCLC-HM-P170 were derived with yields of 88.4 %, 84.6 %, 92.5 %, 82.0 %, 75.4 % and 71.1 %, respectively. As shown above, most of LP derivatives were obtained with high yields. Almost all these derivatives were dissolved into acetone or THF except HCLC-HM-P.

3.2 Characteristics of LP Derivatives

The resulted HCLC derivatives showed dark beige or brown appearances due to generated conjugated structure, although HCLC showed light beige. Ionization difference spectra, which demonstrated differences in structural features from neutral and alkaline conditions, indicated generations of conjugations by peaks from 320

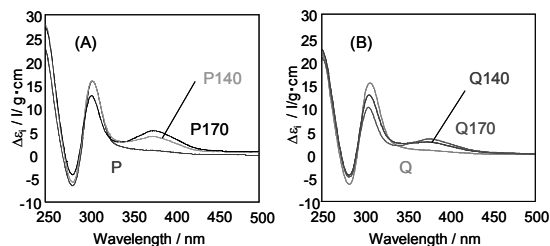


Fig.3 Ionization difference spectra of HCLC derivatives. (A) P, P140, P170 showed HCLC, HCLC140 and HCLC170, respectively. (B) Q, Q140, Q170 showed HCLC-HM, HCLC-HM140 and HCLC-HM170, respectively.

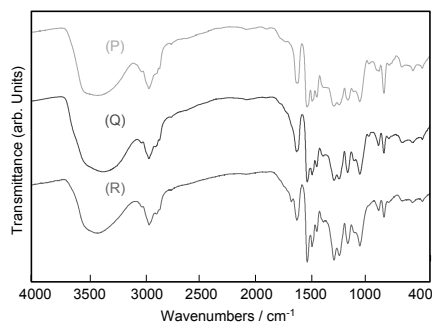


Fig.4 FT-IR spectra of (P) HCLC, (Q) HCLC-HM and (R) HCLC-HM-P.

nm to 470 nm (Fig.3). There were no data of HCLC-HM-P and its derivatives because of little solubility for 2-methoxyethanol. As both HCLC and HCLC-HM showed only peaks at 320 nm, there generated only phenoxide ions. On the other hand, second derivatives had broad peaks around 370 nm to visible region. The absorbance depended on arylcoumaran, stilbene and quinoid type structures [18].

FT-IR spectra supported these results. As shown in Fig.4, there were new shoulder peaks around 1740 cm^{-1} , quinoid carbonyls, in only HCLC-HM-P. In addition, decrease of 815 cm^{-1} , which showed vibrations of neighbouring aromatic H out of plain of *p*-cresol, were observed in both HCLC-HM and HCLC-HM-P due to generations of HM bridges. Moreover differences in hydroxyl groups peaks around 3400 cm^{-1} , but other characteristic peaks were almost the same.

Base on $^1\text{H-NMR}$ spectra, both structures of *p*-cresol

Table I Contents of hydroxyl groups in HCLC derivatives determined by $^1\text{H-NMR}$.

Derivatives ¹⁾	<i>p</i> -Cresol mol/ C_0	Phenolic-OH mol/ C_0	Aliphatic-OH mol/ C_0	HM-OH ²⁾ mol/ C_0
P	0.75	1.55	0.59	----
P140	0.89	1.33	1.15	----
P170	0.83	1.58	0.48	----
Q	0.80	0.99	1.37	0.60
Q140	0.75	1.18	0.64	0.12
Q170	0.93	1.27	0.32	0.05
R140	0.83	1.23	0.31	0.04
R170	0.71	1.29	0.83	trace

1) P, Q, R are HCLC, HCLC-HM and HCLC-HM-P, respectively. Both 140, 170 showed second derivatives-I and II of P, Q and R. 2) Hydroxymethyl -OH

grafted on native lignin and phenolic -OH were stored through the various chemical treatments as confirmed in FT-IR (Table I). Decrease on amounts of HM-OH indicated that detachments of H_2O under high temperatures. But other -OH were existed after such severe conditions. There data of HCLC-HM derivatives implied that resistances for NGP or AM reactions.

Interestingly, second derivatives of HCLC-HM-P showed relatively large amounts of hydroxyl -OH groups. In other words, phenolic resin based on HCLC was liberated its strong structures through simple alkaline treatments [22]. Although both arylcoumaran and stilbene type structures of the derivatives showed peaks around 4.5 and 6.4 ppm, respectively, but amounts of these structures could not be calculated because these peaks were overwrapped on aromatic-H or methoxyl groups. As shown in previous reports [18], hydroxyl groups probably acted as good linkers onto surfaces of

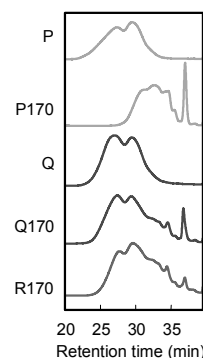


Fig.5 GPC profiles for HCLC derivatives based on standard PS in THF. P, Q, R were HCLC, HCLC-HM and HCLC-HM-P, respectively. Both 140 and 170 showed second derivative-I and II with reaction temperatures.

TiO_2 electrodes. Both FT-IR and $^1\text{H-NMR}$ data supported these results more strongly.

Fig.5 demonstrated molecular weight distributions of HCLC170 ($M_w = 1610$, $M_w/M_n = 2.14$)[18] decreased drastically from HCLC. On the other hand, both HCLC-HM170 ($M_w = 11150$, $M_w/M_n = 6.25$)[18] and HCLC-HM-P170 ($M_w = 7400$, $M_w/M_n = 4.25$)[18] showed both high molecular weights and low ones with broad type distributions. Though there remained larger fractions of HCLC-HM170 than HCLC-HM-P170, both polymerizations and de-polymerizations of HM-hydroxyl groups of the former occurred with generating quinoid type structures under such severe conditions. As $^1\text{H-NMR}$ data implied that polymeric structures of derivatives of HCLC-HM, these profiles supported such results.

3.3 Photo-Voltaic Performance

As shown in Table II, HCLC derivatives were used as photo-sensitizers for nano- TiO_2 electrodes under visible and infrared light with intensity of 100 mWcm^{-2} . HCLC140 demonstrated relatively better results than HCLC or HCLC170 as we reported [16]. On the other hands, second derivative-II of both HCLC-HM and HCLC-HM-P showed better performances. As shown in various spectra and GPC profiles, these samples involved large molecules with rich hydroxyl groups and conjugations. Moreover both HCLC-HM170 and HCLC-HM-P170 showed high photo current densities about 3 mAcm^{-2} . These currents meant two important facts: first, simply large amounts of electrons jumped over energy barriers of TiO_2 through excited states of these structures such as quinoid type structures which generated easily from HM-groups. Second, there were advantages on efficiencies of electron transfers between HCLC derivatives and TiO_2 surfaces. Therefore polymerization of HCLC-HM-P directly on TiO_2 surfaces was carried out because of utilization of these two important factors. In addition to these, in order to observe influences of structural features of native lignin, HM-P derivatives of Birch-ligninophenol (*p*-cresol type) were tried at the same time.

As demonstrated in Fig.6 and bottom of Table II, direct polymerization largely improved photo current densities due to both increase excited electrons from conjugated structures and to decline of energy barrier by approaching. Especially a result of birch was drastically improved because electron transfers increased close to

Table II Photovoltaic performances of Hinoki cypress-lignophenol-cells under 100 mWcm⁻² of visible light (150-W Xe lamp through L41-UV-cut filter)

Sensitizers ¹⁾	V _{oc} / V	I _{sc} / mAcm ⁻²	FF	η / %
P ²⁾	0.514	3.28	0.60	0.81
P140	0.484	3.71	0.58	0.87
P170 ²⁾	0.521	2.67	0.58	0.79
Q ²⁾	0.519	2.38	0.64	0.77
Q140	0.471	2.43	0.65	0.67
Q170	0.491	3.00	0.65	0.77
R ²⁾	0.395	1.38	0.62	0.33
R140	0.446	2.67	0.64	0.64
R170 ²⁾	0.475	3.17	0.60	0.89
QP ³⁾	0.483	4.00	0.61	1.06
Q(Birch) ⁴⁾	0.525	1.00	0.64	0.33
QP(Birch) ^{3,4)}	0.477	2.42	0.61	0.94

1) P, Q, R were HCLC, HCLC-HM and HCLC-HM-P, respectively. Both 140 and 170 showed second derivative-I and II, respectively. 2) already pressed in *Trans. Mater. Res. Soc. J.*, 32(4), 1107(2007). 3) Birch-lignophenol (*p*-cresol type)-HM, and its polymer by heat set on TiO₂ electrode. 4) lignophenol-phenolic resin polymerized direct on TiO₂ electrodes at 150 °C for 4 hrs.

energy band of TiO₂ charge band. These results implied that relative low photo-electricity conversion partly depended on difficulty for electron orbital of hardwood LP derivatives to approach onto the surface of TiO₂ due to rich 3,5-dimethoxy structures (syringyl structures), (Fig.7). Also based on these structures, there are less reactive sites for HM reactions than HCLC. Moreover there were more rich natural conjugated system such as C₅-C₅ diaryl structures for 10 % of all linkages in native lignin, but hardwood has only 5 %. In conclusion, effective conjugated structures for LP cells were quite different. For example, the characteristic conjugation of lignophenol such as arylcoumaran was good just for HCLC. On the other hand, it is effective to be prepared quinoid type structures for LP-HM. Moreover, shortening distance for electron transfer was effective to improve efficiencies.

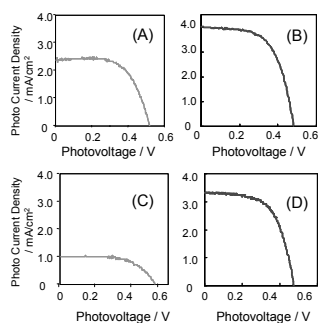


Fig.6 I-V curves for lignophenol cells under 100 mWcm⁻² visible and infrared light irradiations. (A) HCLC-HM, (B) direct polymerization HCLC-HM-P on TiO₂, (C) Birch (BI)-LC-HM and (D) direct polymerization of BILC-HM-P on TiO₂.

4. CONCLUSIONS

LP derivatives through the NGP or AM reactions based on HCLC, HCLC-HM and HCLC-HM-P were used as photo-sensitizers for TiO₂ electrodes. Arylcoumaran and stilbene type structures for HCLC derivatives contributed to high photo-electricity conversions. But for LP-HM, contribution of quinoid seemed to be more than HCLC because polymeric structures remained after both NGP and AM reactions. Direct polymerization of LP-HM on TiO₂ electrodes demonstrated large

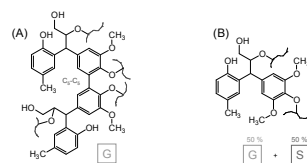


Fig.7 Differences of structural features on 1,1-bis(aryl)propane-2-O-arylether type structures between (A) HCLC and (B) BILC. G and S means guaiacyl and syringyl structures which are main units of native lignins. In general, softwood lignin consists of only G, but hardwood consists of G / S = 1 / 1.

improvements photo electron transfers. Based on these fundamental results, both optimization and improvement are expected for LP cells.

5. REFERENCES

- [1] B. O' Regan, M. Gratzel, *Nature*, **353**, 737-740(1991)
- [2] M. K. Nazeeruddin, F. D. Angelis, S. Fantacci, A. Selloni, G. Viscardi, P. Liska, S. Ito, B. Takeru, M. Grätzel, *J. Am. Chem. Soc.*, **127**, 16835-16847 (2005)
- [3] S. Hao, J. Wu, Y. Huang, J. Lin, *Solar Energy*, **80**, 209-214(2006)
- [4] S. Meng, J. Ren and E. Kaxiras, *Nano Lett.*, **8** (10), 3266-3272(2008)
- [5] Z. Dongshe, N. Yamamoto, T. Yoshida, H. Minoura, *Trans. Mater. Res. Soc. J.*, **27**(4), 811-814(2002)
- [6] Q. Dai, J. Rabani, *J. Photochem. Photobiol. A Chem.* **26**,421-429(2002)
- [7] W. M. Campbell, K. W. Jolly, P. Wagner, K. Wagner, P. W. Walsh, K. C. Gordon, L. Schmit-Mende, M. K. Nazeerudin, W. Wang, M. Gratzel, D. L. Officer, *J. Phys. Chem. C Lett.*, **111**, 11760-11762(2007)
- [8] R. Espinosa, I. Zumeta, J. L. Santana, F. M-Luzardo, B. Gonzalez, S. Docteur, E. Vigil, *Sol. Energy. Mater. Sol. Cells*, **85**, 359-369(2005)
- [9] A. Todaro, F. Cimino, P. Rapisarda, A. E. Catalano, R. N. Barbagallo, G. Spagna, *Food Chemistry*, **114**, 434-439(2009)
- [10] G. A. Garzon, R. E. Wrolstad, *Food Chemistry*, **114**, 44-49(2009)
- [11] Z. Huang, B. Wang, P. Williams, R. D. Pace, *LWT-Food. Sci. Tech.*, **42**, 819-824(2009)
- [12] Y-S. Shyu, J-T. Lin, Y-T. Chang, C-J. Chiang, D-J. Yang, *Food Chemistry*, **115**, 515-521(2009)
- [13] J. Lachman, K. Hamouz, M. Sulc, M. Orsak, V. Pivec, A. Hejtmanova, P. Dvorak, J. Cepel, *Food Chemistry*, **114**, 836-843(2009)
- [14] M. Aoyagi, M. Funaoka, *J. Photochem. Photobiol. A. Chem.*, **164**, 53-60(2004)
- [15] M. Aoyagi, M. Funaoka, *Jpn. J. Polym. Sci. Tech.*, **62**(6), 283-290(2005)
- [16] M. Aoyagi, M. Funaoka, *J. Photochem. Photobiol. A. Chem.*, **181**, 114-119(2006)
- [17] M. Aoyagi, M. Funaoka, *Journal of Network Polymer*, **27**(1), 20-29(2006)
- [18] M. Aoyagi, N. Umetani, M. Funaoka, *Trans. Mater. Res. Soc. J.*, **32**(4), 1107-1110(2007)
- [19] M. Funaoka and I. Abe, *Tappi*, **72**(8), 145-149 (1989).
- [20] M. Funaoka, *Polym. Int.*, **47**, 277-290(1998)
- [21] M. Aoyagi, M. Funaoka, *Trans. Mater. Res. Soc. J.*, **32**(4), 1103-1106(2007)
- [22] E. Ohmae, M. Funaoka, S. Fujita, *Mater. Sci. Res. Int.*, **10**, 78-84(2004)

(Received December 12, 2008; Accepted September 16, 2009)

Separation by Molecular Weight during Purification Process of Lignophenol

Mitsuru Aoyagi and Masamitsu Funaoka

Graduate School of Bioresources, Mie University, Japan Science and Technology Agency (JST)-Solution Oriented Research for Science and Technology (SORST), 1577 Kurimamachiya-Cho, Tsu, 514-8507, Japan
 Fax: +81-59-231-9591, E-mail: aoyagi@bio.mie-u.ac.jp

Separations of Hinoki cypress (*Chamaecyparis obtusa*)-lignophenol (*p*-cresol type, HCLC), which are phenolic lignin-based polymers derived directly from lignocellulosics through the phase-separation system, by molecular weight using diethylether (EtOEt), cyclopentylmethylether (CPME), *tert*-Buthylmethylether (TBME) and EtOEt / CPME (1 / 1, v / v) in ordinary purification processes were carried out. After purification, each lignophenol showed different purification yields: HCLC-E, HCLC-C, HCLC-T and HCLC-B showed 63.7 %, 50.3 %, 71.0% and 62.8 %, respectively. These HCLC samples showed different average molecular weights estimated by GPC. To begin with number average molecular weight (M_n) were 7 870, 9 960, 11 850 and 8 920, respectively. Next, weight average molecular weight (M_w) were 17 960, 22 510, 24 770 and 20 370, respectively. These HCLC samples showed almost same chemical properties such as appearance, solubility for solvents. Moreover same structural features were confirmed by FT-IR and $^1\text{H-NMR}$. Since these HCLC samples also showed almost same thermal properties, there are just a little difference for 5 °C on TMA. In conclusion, Molecular weight separation can contribute to not only new advanced chemical modifications for lignophenols, but to investigate new structural features of both lignophenols and whole native lignins in lignocellulosics.

Key words: lignin, lignophenol, molecular weight, solubility, separation

1. INTRODUCTION

Recently biomass has been expected as a substitution for fossil carbon resources in front of both serious environmental crisis and of apprehension for exhaustion of petroleum. Especially lignocellulosic materials have been tried to be applied for various industrial materials because they are sustainable and common raw materials on the earth. In general, lignocellulosics has been utilized as fuel, woody materials, and pulps as papers or fibers. As lignocellulosics consists of cellulose (50%), hemicellulose (15%) and lignin (30 %), utilization of carbohydrate especially pulp has been often used because of its rich contents. On the conventional separation process with high temperature, high pressure and chemicals, sensitive lignin was destroyed and polymerized at random. Because almost all reactive sites of native lignin were exhausted, the resulting lignins have little chemical reactivity. The low reactivity caused almost all these lignins to be used as thermal sources. But lignins are abundant and important aromatic resources with long circulation loop, it is wrong to be burned out to CO_2 . Therefore in order to utilize whole lignocellulosics perfectly, it is important to separate components of lignocellulosics to keep the reactive sites of lignin. The phase-separation system is one of the solutions to utilize whole lignocellulosics [1-2]. On the reaction on the surface between phenols and acids, both separation of components and conversion of lignin to functional materials are realized under 1 atm and room temperature within 60 min (Fig.1). Through this reaction both native lignin and carbohydrates were quantitatively converted into 1,1-*bis*(aryl)propane-2-*O*-arylether-3-ol

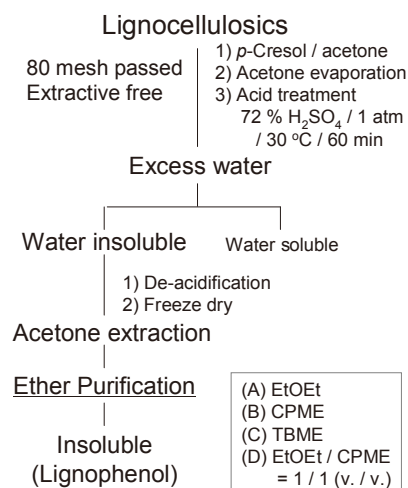


Fig.1 Synthesis flow of the phase-separation system. On the final step of purification, three different solvents were used.

type phenolic lignin based polymers (lignophenols) and hydrolyzed sugars. Lignophenols have appropriate properties for chemical applications such as high solubility for solvents, thermal plasticity, sustainable molecular designs, bio-degradability, bio-compatibility and so on [2]. Based on these appropriate chemical and physical analyses of lignophenols, various applications of lignophenols have been tried and realized [1-3].

In purification processes of lignophenols using ethers shown in bottom of Fig.1, both insoluble and soluble

moieties were separated. EtOEt-insoluble lignophenols have M_w around 8 000-20 000. While EtOEt soluble moieties have small M_w (1 590, $M_w/M_n = 1.81$) by using nano-TiO₂ collection method [3]. Interestingly these small molecules showed better performance on several applications [3]. These results implied that it is capable to separate fractions of lignophenols by molecular weight using various solvents. Moreover it is worthy to separate components by molecular size for various advanced applications. But in general, molecular weight separations are carried out by gel-permeation separation, membrane separation or ultra-filtration membrane mainly in bio-chemical, proteins DNA chemistry, medical [4-5] and waste water treatment [6]. Although these methods can cut-off molecular weights exactly, it is hard to treat large amount of materials.

Added this, EtOEt always has high risk of fire or productions of peroxides under aerobic conditions, but EtOEt is the best solvent. In order to overcome these problems, Cyclopentylmethylether (CPME, Zeon Co.)[7] and other ethers were tried to apply for purification. CPME is known for one of good substitutions for EtOEt or tetrahydrofran (THF) in organic synthesis [8-10]. Properties of CPME were 106 °C of boiling points, 0.809 cP of viscosity, 0.86 gcm⁻³ density and $\epsilon(25\text{ }^\circ\text{C}) = 8.4$. As CPME is hard to generate peroxides, it is safe and easy to be recycles and reused, compared to other alkyl ethers [7].

In this study, separations of lignophenol based on solubility through the ordinary purification processes using 4 different ether systems, (A) diethylether (EtOEt), (B) cyclopentylmethylether (CMPE), (C) *tert*-Butylmethylether (TBME) and (D) mixtures of EtOEt and CPME (1 / 1, v/v) in large scales were tried. After purification, comparisons of characteristics of HCLC samples by GPC, ¹H-NMR, FT-IR, TMA and TGA were carried out.

2. EXPERIMENTAL

2.1 The phase-separation system

Synthesis of lignophenol (*p*-cresol type) was followed by the phase-separation system (2-step method, process II) [2-3]. Hinoki cypress (*Chamaecyparis obtusa*) was used as softwood lignocellulosic material. Milled wood (80 mesh passed, 500 g) was defatted by acetone and dried before synthesis. The milled wood was mixed with *p*-cresol in acetone. Amount of *p*-cresol was 3 mol for phenylpropane units (C₉), which is basic unit of lignin structures. After 24 hrs acetone was evaporated. The obtained milled wood with *p*-cresol was reacted with 72 % H₂SO₄ at 30 °C for 1 hr in a reactor in system plant No.1 (established in Mie University since 2001, JST-CREST). The resulting mixture was quickly immersed into excess water under vivid stirring. The mixture was neutralized by changing water. After de-acidification, precipitates were collected and dried. After extraction by acetone, the concentrated acetone solution (54.2 gL⁻¹) was dropped into excess ethers such as EtOEt, CPME, TMBE and 1/1 (v/v.) mixture of EtOEt and CPME under vivid stirring in ice bath. The resulting precipitates were washed thoroughly to remove un-reacted *p*-cresol. After vacuum drying over P₂O₅, ether insoluble moieties of Hinoki cypress-lignophenol (*p*-cresol type, HCLC) were obtained. Each lignophenol

was noted as HCLC-E, HCLC-C, HCLC-T and HCLC-B, respectively.

2.4 Characterization of lignophenols

The structure of HCLC was characterized by Gel Permeation Chromatography (GPC), ¹H-NMR, FT-IR and Thermal Mechanical Analysis (TMA). GPC was carried out by LC-10 system with four columns (KF801, KF802, KF803 and KF804, Shodex Co.). Rectified tetrahydrofran (THF) was used as eluent with 1.0 mLmin⁻¹ of flow rate at 40 °C. UV-light at 280 nm was used for detection. Both M_w and M_n were determined based on standard polystyrene. ¹H-NMR spectrum was measured by FT-NMR500 (JASCO Co.) in CDCl₃ or CDCl₃ / C₅D₅N = 3 / 1 (v / v). *p*-Nitrobenzaldehyde and TMS were used as internal standards. TMA was also carried out by TMA-SS (Seiko Instruments Inc.) in the temperature range 50-280 °C at a rate of increase of 2 °Cmin⁻¹, using penetrating technique for a measurement. The samples were set on Al pan (5 mm). Geometry was quartz needle for penetration method. FT-IR spectroscopy was also carried out on a FT-IR8400 (Shimadzu Co.), using the KBr pellet technique for sample preparation.

3. RESULTS AND DISCUSSION

3.1 The phase-separation system

After the phase-separation system for Hinoki cypress, 97% yield of crude lignophenol based on lignin contents. Using four different solvent systems, purified HCLC showed just a little different characteristics. But almost all the properties were quite same. After purifications, yields of insoluble moieties of HCLC-E, HCLC-C, HCLC-T and HCLC-B were 63.7%, 50.3%, 71.0% and 62.8%, respectively. These all HCLC solids were sufficiently purified by removing un-reacted *p*-cresol and small fractions confirmed by GC and TLC. These HCLC solids had light beige appearances and were

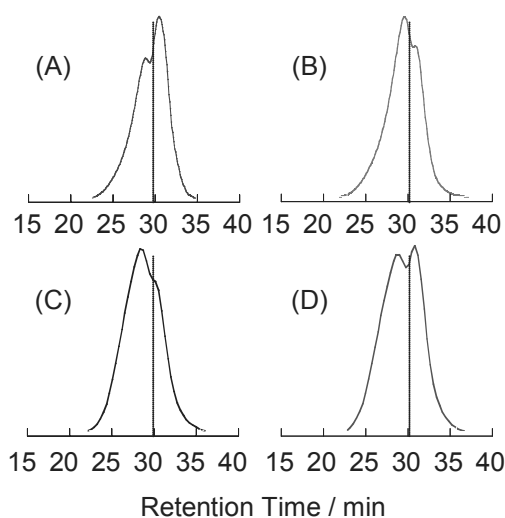


Fig.2 Normalized GPC profiles for (A) HCLC-E, (B) HCLC-C, (C) HCLC-T and (D) HCLC-E/C. Dotted lines were fixed on $t = 30$ min.

Table 1 Average molecular weights of HCLC.

Solvents	M_n	M_w	M_w / M_n
EtOEt	7 870	17 960	2.28
CPME	9 960	22 510	2.26
MTBE	11 850	24 770	2.09
Blend ¹⁾	8 920	20 370	2.28

1) EtOEt / CPME = 1 / 1 (v. / v.)

perfectly dissolved in acetone, ethanol, THF, pyridine and 1.0 M NaOH. Moreover the yield of HCLC-B was similar to HCLC-E. This result implied that properties of the solution were much dominated by EtOEt.

3.2 Average Molecular Weight

As shown in Fig.2, molecular weight distributions were different by using different ethers. All HCLC samples showed bimodal peaks with valley around $t = 30$ min. These bimodal peaks were due to main structures of native lignin. The higher molecular weight was mainly due to native lignin in intercellular layer, which contains rich network type lignin generated on the first growing step in bio-synthesis through bulk polymerization in plant cell. On the other hand, the lower one was characterized by second wall lignin, which contains rich linear type lignin synthesized on the final lignifying step through endwise polymerization on inner wall in a plant cell.

HCLC has rich $C\beta-O-C_4$ structures, which are most major linkages of lignins, after cleavages from $C\alpha$ (benzyl) aryl ether structures by both acid treatments and phenol grafting reactions [3]. In general, softwood native lignins have rich conjugated network type structures such as C_5-C_5 biphenyl type (10-11%), $C\beta-O-C_5$ phenylcoumaran type (9-12 %) and C_4-O-C_5 diarylether type structures (4%) [11]. These structures remained through the phase-separation system. Therefore due to these two different type molecular structures, GPC patterns were divided.

As compared Fig.2 (A) and (B), HCLC-E included

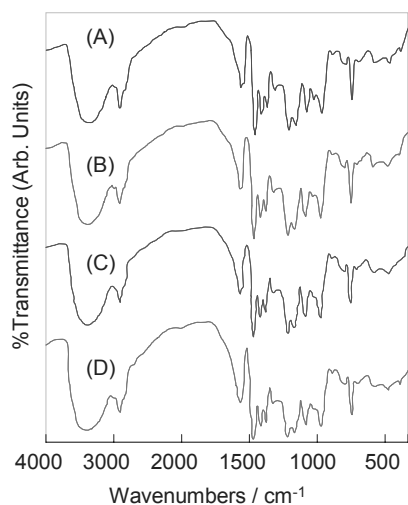


Fig.3 FT-IR spectra of (A) HCLC-E, (B) HCLC-C, (C) HCLC-T and (D) HCLC-E/C.

lower molecular weight moieties than HCLC-C. In fact average molecular weight (Table 1) M_w (M_n) of both HCLC-E and HCLC-C were 17 960 (7 870) and 22 510 (9 960), respectively. This result showed solubility of HCLC for CPME was larger than EtOEt. Moreover HCLC-T showed larger both M_w and M_n (Fig.2, Table 1) with high yield. This result implied that TBME dissolved more linear type molecules selectively.

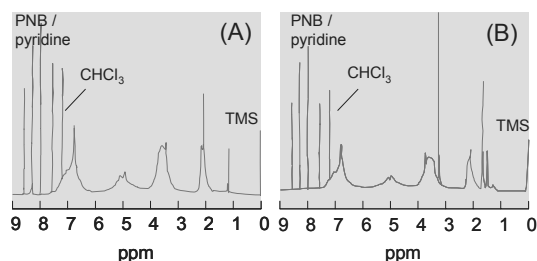


Fig.4 ¹H-NMR spectra of (A) HCLC-E and (B) HCLC-C.

3.3 Chemical features

As shown in Fig.3, spectra of FT-IR were quite same. This result clearly demonstrated that all HCLC samples had same functional groups such as grafted *p*-cresol (815 cm^{-1}), ether linkages of lignin units (1 300 - 1 000 cm^{-1}), aromatic skeltones (1 650 - 1 450 cm^{-1}), no carbonyls (1 700 cm^{-1}) no aldehydes (2 000 cm^{-1}), rich methylene linkages (2 900 cm^{-1}) and rich hydroxyl groups (3 400 cm^{-1}). The same chemical features can be contributed to various advanced modifications.

As ¹H-NMR spectra showed also same chemical features such as methylene groups of grafted *p*-cresol (2.5-2.0 ppm), methoxyl groups (4-3 ppm), aromatic rings (8-6 ppm) and no carbonyl and carboxyl groups (> 9 ppm) were obtained (Fig.4). For example, HCLC-E and HCLC-C had 1.59 mol/ C_9 and 1.69 mol/ C_9 of phenolic-OH, 0.93 mol/ C_9 and 0.75 mol/ C_9 of aliphatic-OH and 0.81 mol/ C_9 and 0.82 mol/ C_9 of grafted *p*-cresol, respectively. This comparison indicated that low molecular fractions included rich aliphatic-OH groups. Although there were same amounts of grafted *p*-cresol, total phenolic groups were decreased in HCLC-C. This showed natural phenolic moieties existed in lignopheols tends to be dissolved into CPME. But there were few differences on other parameters between HCLC-E and HCLC-C.

3.4 Thermal Properties

There are some relationships between thermal properties and molecular weights. Thermal behaviors of lignin materials are often measured by TMA using penetration method [12]. All HCLC samples were perfectly plasticized around 170 °C (Fig.5). The Solid-Liquid phase transition temperatures of HCLC-E, HCLC-C, HCLC-T and HCLC-B were 174.2 °C, 178.2 °C, 179.2 °C and 177.0 °C, respectively. The TMA patterns showed that HCLC molecules had almost same thermal properties because all HCLC samples plasticized smoothly within 30 °C with low viscosities.

Although there are large differences of both M_n for 5 000 and M_w for 6 000 among HCLC samples, TMA temperatures showed slight dependences on the molecular weights. This result implied there were strong

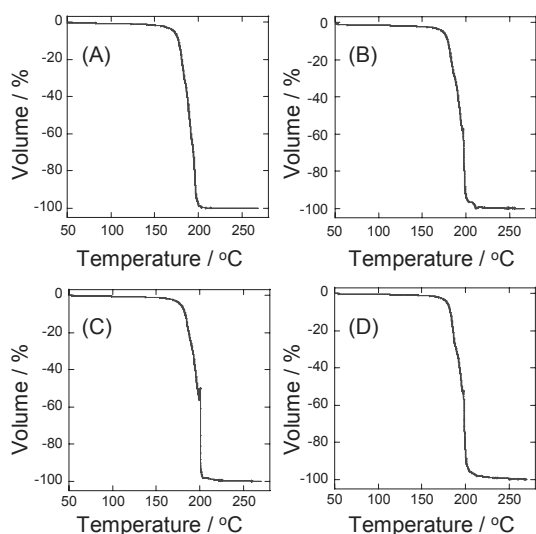


Fig.5 TMA charts for (A) HCLC-E, (B) HCLC-C, (C) HCLC-T and (D) HCLC-B. Volume (-100 %) means quartz needle reached the bottom of Al-Pan.

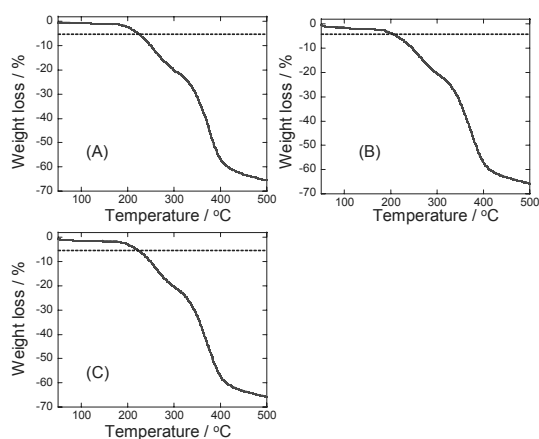


Fig.6 TG curves for (A) HCLC-E, (B) HCLC-C and (C) HCLC-T.

and dominant both inter- and intra-molecular interactions such as hydrogen bonds due to both rich phenolic and aliphatic -OH groups.

As shown in Fig.5, all HCLC samples showed good plasticity, but there were little decompositions in HCLC molecules. As Fig.6 demonstrated, HCLC-E, HCLC-C and HCLC-T had only little weight losses under 200 °C. There was also little difference among these three HCLC samples. As described in our previous report [13], weight loss observed under 250 °C was mainly due to release of small fractions such as HCHO or H₂O detected using TG-GC/MS. Therefore 5 % weight loss under 250 °C depended on releasing these small fractions or solvents. Over 250 °C same TG curves were obtained to 500 °C for all HCLC samples. Since amounts of remained moieties which were carbon rich materials obtained around 500 °C, all HCLC samples had same amounts (65%). This result indicated that there were same carbon skeletons in polymeric structures after

removed small fractions by solvents.

4. PERSPECTIVE FOR APPLICATIONS

Base on this separations, two important perspectives on applications of lignophenol were obtained.

First, these separations of contents in these bimodal peaks will contribute to discuss structures of native lignin, because analyses of whole lignin without heat or pressure have never been investigated. Although milled wood lignin is regarded as better sample of native lignin, yield of this lignin is very low. On the other hand, lignophenol is derived directly from native lignin under mild physical condition almost quantitatively. Therefore lignophenol can be applied for the first lignin derivatives to analyze whole lignin in lignocellulosics. Moreover by separation of contents using these solvents, new information about two different types lignin such as lignophenol of bulk polymerization and endwise polymerization can also contribute to investigate the structures of native lignin in cell walls.

Secondly, using EtOEt, CPME and TBME, average molecular weight of HCLC was divided by 2 000 for both M_n and M_w . These exact division can be contributed to various chemical applications.

5. CONCLUSION

Using EtOEt, CPME, TBME and EtOEt / CPME solution for purification of HCLC, components were separated by molecular weight in the ordinary purification process of lignophenols. Not only these ethers, but changing structures of ethers characteristics of lignophenols can be controlled. Though there were few differences in chemical properties, a little difference of thermal properties was observed. As each component of the bimodal peaks in the GPC profiles was separated, new advanced investigates on both lignophenols and native lignin are expected.

6. REFERENCES

- [1] M. Funaoka and I Abe, *Tappi*, 72, 145-155 (1989)
- [2] M. Funaoka, *Polym. Int.*, 47, 277-290 (1998)
- [3] M. Aoyagi and M. Funaoka, *Trans. Mater. Res. Soc. J.*, 32, 1103-1106 (2007)
- [4] Y. Mohadger, A. V. Tobolsky and T. K. Kwei *Macromolecules*, 7, 924-929 (1974)
- [5] S. Song, A. K. Singh, T. J. Sheppard, and B. J. Kirby *Anal. Chem.*, 7, 2367-2373 (2004)
- [6] H. Yanagishita, K. Nouzaki, M. Nagaea, J. Arai, D. Kitamoto, T. Ikegami, H. Negishi and K. Haraya, *Desalination*, 144, 53-59 (2002)
- [7] K. Watanabe, K. Goto, *J. Synth. Org. Chem. Jpn.*, 61, 806-808 (2003).
- [8] Y. Sawada, M. Sasaki and Kei Takeda, *Org. Lett.*, 6 (13), 2277-2279 (2004)
- [9] H. Tokimoto, Y. Fujimoto, K. Fukase, and S. Kusumoto, *Tetrahedron: Asymmetry*, 16(2), 441-447 (2005)
- [10] K. Matsui, S. Takizawa, and H. Sasai, *J. Am. Chem. Soc.*, 127, 3680-3681 (2005)
- [11] E. Adler, *Wood Sci. Technol.*, 11, 169-218 (1977)
- [12] D. Goring, *Pulp Pap. Mag. Can.*, 64, T517-T527 (1963)
- [13] M. Aoyagi, K. Iwasaki and M. Funaoka, *Trans. Mater. Res. Soc. J.*, 32, 1119-1122 (2007)

(Received December 12, 2008; Accepted September 16, 2009)

Preparation of Novel Lignophenol-based Polymers using Cellulose Fibers as Vanishing Reaction-Supports

Mitsuru Aoyagi, Satoko Yonekura, Chika Miyasaka and Masamitsu Funaoka

Graduate School of Bioresources, Mie University, Japan Science and Technology Agency (JST)-Solution Oriented Research for Science and Technology (SORST), 1577 Kurimamachiya-Cho, Tsu, 514-8507, Japan
Fax: +81-59-231-9591, e-mail: aoyagi@bio.mie-u.ac.jp

Two syntheses of novel lignophenol (LP) derivatives via hydroxymethylated (HM) lignophenol (*p*-cresol type) under conditions of the phase-separation system were carried out. First, brush-type derivatives were carried out using HM-Western Hemlock (*Tsuga Heterophilla*)-lignophenol (*p*-cresol type, HMLC1) as benzyl compounds. Resulting derivatives were obtained with high yields. Due to high reactivity and high affinity between *p*-cresol and HMCL1, there are no influences with or without reacting supports. Resulting LC2, LC3 and LC4 showed almost same characteristic properties as LP estimated by ¹H-NMR, TMA, GPC. Secondly, bulky alkyl phenols were also tried to apply for second grafting phenols to HM-Hinoki cypress (*Chamaecyparis obtusa*)-lignophenol (*p*-cresol type, HM-HCLC1). Without vanishing reaction-supports (pulp, freeness100), all derivatives were aggregated. On the other hand, using reaction-supports, 4-*sec*-buthylphenol (4SBP), 4-(1,1,3,3-tetramethyl)buthyl phenol (4TMBP) and 4-pentylphenol(4PP) generated derivatives with 47.6 %, 25.4 % and 59.4 % yields, respectively. A part of derivatives were dissolved into purification solvents such as EtOEt. Resulting derivatives were estimated by GPC, TMA and ¹H-NMR.

Key words: lignin, lignophenol, benzyl structure, cellulose, reaction support

1. INTRODUCTION

Recently serious environmental problems such as global warming concerning exhaustion of CO₂ have been paid a lot of attentions. Moreover apprehension for exhaustion of petroleum has also been attracted. To overcome a part of these problems, utilization of biomass has been tried for substitution of petroleum as both fuel and materials because of its sustainability. Especially lignocellulosics such as wood, glasses were regarded as one of best substitutions. However it has been almost impossible to be utilized whole lignocellulosics after separation of contents due to complicated and enforced inter-penetrating complexes (IPN structures) of both lignin and carbohydrates[1]. Therefore in an aspect of material utilization, only carbohydrates have been utilized as pulps, which amounts are corresponded to only 50 % of materials, in industry. As chemical reactivity of lignin was exhausted through the separation process under high temperature and pressure, lignin has been utilized as only fuel.

In order to utilize whole lignocellulosics, new reaction system, the phase-separation system, with both separations and structural conversions which consist of heterogeneous surface reactions has been developed [2-4]. Through the surface reactions between phenol / concentrated acids, both carbohydrates and lignin are separated and converted into aqueous carbohydrates and

lignin-based polymers, lignophenols (LPs), quantitatively under 1 atm and room temperature.

Through the reaction, at first step, 3-dimensional linkages of native lignin were quickly released on both benzyl aryl ether structures or benzyl units which included about 5-10 % [5] in softwood under acidic conditions [6-7]. However, main structures, Cβ-O-4 arylether linkages were not cleft. On the cleavages benzyl aryl ethers, rich phenols around native lignin selectively attacked to Cα carbocations. The resulting lignin-based polymers have 1,1-bis(aryl)propane-2-O-arylether-3-ol type structures with rich Cβ-O-4 linkages about 80 % [4,8].

On the other hand, benzyl structures are good reaction sites for nucleophilic attacks due to stable benzyl cations because of high reactivity especially under both acidic and heated conditions. For example, benzyl alcohol easily reacted to aliphatic-OH under only pH=6 buffer at 60 °C with self-condensations [9-11].

In fact, catechol was easily grafted to hydroxymethylated Hinoki cypress-lignophenol (*p*-cresol type, HCLC-HM) through the phase-separation system (72 % H₂SO₄) with almost 100 % of yields without condensations, although catechol without a reaction-support was easily dissolved and self-condensed under strong acid condition [12]. In general, lignin-based materials are likely to be aggregated and then self-condensed by itself. Therefore, to prevent from aggregating, cellulose reaction supports were used as vanishing reaction-supports through the phase-separation system. These reaction-supports acted to keep heterogeneous reaction surfaces with degrading by hydrolysis gradually [12].

Therefore using benzyl structures of HM structures,

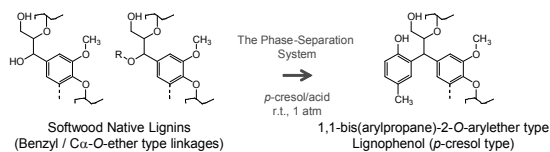


Fig.1 Initial reactions with *p*-cresol of benzyl and C_α-O-ether type structures in native lignin under acidic conditions through the phase-separation system.

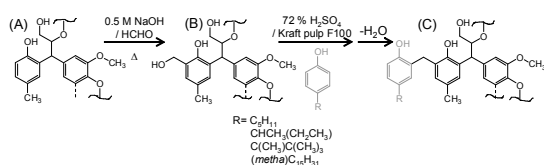


Fig.2 Reaction schemes of hydroxymethylation (HM) and second phenol grafting on hydroxymethylated lignophenol(*p*-cresol type, LCHM). The second phenolation was carried out through the phase-separation system. (A) LC, (B) HCLC-HM and (C) LCHM-Phenols.

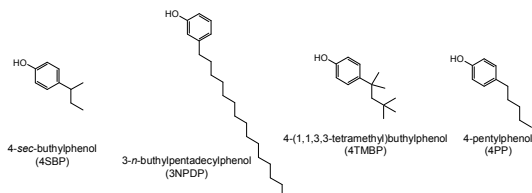


Fig. 3 Structures of (A) 4SBP, (B) 3NPDP, (C) 4TMBP and (D) 4PP.

more well-designed products can be synthesized. Moreover various phenols, which have been considered that it is impossible to be grafted because of poor affinity with lignocellulosics, can be grafted to LP.

In this study, two grafting reactions were carried out. First, synthesis of blush-type LP derivatives by successive grafting of *p*-cresol via methylene chains was tried (Fig.2). Secondly, several alkyl phenols were tried to be grafted. Although direct grafting to lignin of several alkyl phenols such as *o*-, *m*-cresol, xylenols, ethylphenol, 4-*n*-propylphenol, guaiacol has been tried and succeeded already [3], more bulky phenols have not tried yet. Therefore four bulky alkyl phenols such as 4-*sec*-buthylphenol (4SBP), 3-*n*-pentadecylphenol (3NPDP), 4-(1,1,3,3-tetramethyl)buthyl phenol (4TMBP) and 4-pentylphenol(4PP) were tried to grafting on LPHM with vanishing reaction-supports under the phase-separation system (Fig.2, 3).

2. EXPERIMENTAL

2.1 Synthesis of lignophenols

Western Hemlock (*Tsuga Heterophyll*) and Hinoki cypress (*Chamaecyparis obtusa*) were used as softwood materials for the phase-separation system. The woody materials were milled for 80 mesh passed. Extractives in the material were removed by acetone at room temperature for 72 hrs. The milled woods (500 g) were thrown into acetone solution of *p*-cresol with concentration of 3 mol / phenylpropane units (C₉ units), which were subunits of native lignin determined by Klason method. After evaporation of acetone, 72 % H₂SO₄ aq. solutions were poured into the material adsorbed with *p*-cresol at 30 °C. Then the mixtures were stirred vigorously for 60 min soon after mixing. After 60 min, the reaction mixtures were thrown into 20 L of de-ionized water with vigorously stirring by a homogenizer for 5 min. Then the purple precipitations were washed until pH = 5. After drying, the precipitations were extracted by acetone. The acetone solutions were purified by dropped into EtOEt under vigorously stirring at 0 °C. After evaporating and drying on P₂O₅, both Western Hemlock-lignophenol (*p*-cresol type, LC1), and Hinoki cypress-lignophenol (*p*-cresol

type, HCLC1) were obtained [2-4].

2.2 Preparation of vanishing reaction-supports

Kraft pulp was dispersed in de-ionized water. The suspension was beaten to freeness 100 estimated using Canadian freeness-tester [12-13].

2.3 Synthesis of derivatives

Hydroxymethylated LC1(HMLC1) and HCLC (HM-HCLC1) were synthesized in 0.5 M NaOH solution by mixing 20 mol of formaldehyde for a amount of aromatic rings in lignophenol at 60 °C under N₂ atmosphere with a stirring system and a reflux condenser. After 3 hrs reaction, 1.0 M HCl was dropped into the mixture at 5 °C to pH = 2.0. The resulting precipitation was washed to pH = 5.0. After the insoluble residues were dried over P₂O₅, both HM-LC1 and HM-HCLC1 were obtained.

2.4 Second phenol grafting

Second phenol grafting lignophenol was synthesized from HM-LC1 or HM-HCLC1, with or without reaction-supports through the phase-separation system (Two-step method, process-I). *p*-Cresol, 4SBP, 4-TMBP, 3NPDP and 4PP were used as the second grafting phenols. HM-LC1 (0.15 g) and phenols (20 mol/C₉) were adsorbed on 1.50 g of dry Kraft pulp (freeness 100) in 35.0 mL of THF. After evaporation of THF the resulting compound was reacted through the phase-separation system (2 step method, process-I) with 20.0 mL of 72 % H₂SO₄ under 30 °C. After 30 min, 20.0 mL of *p*-cresol was added to the reaction mixture as an extracting solvent under stirring. After 20 min, the organic layer and aqueous layer were separated by centrifugation (3 500 rpm). The organic layer was washed by EtOEt. Insoluble moiety was refined in the same way as LC1. After evaporation and dry on P₂O₅, lignophenol, the second phenol grafted (LC2) was obtained. Moreover only *p*-cresol type was repeated to be derived into LC3 and LC4.

2.5 Characterization of lignophenols

The structures of LP were characterized by Gel Permeation Chromatography (GPC), ¹H-NMR and Thermal Mechanical Analysis (TMA). GPC was carried out by LC-10 system (Shimadzu Co.) with four columns (KF801, KF802, KF803 and KF804, Shodex Co.), using tetrahydrofuran (THF) after rectification as eluent. Both *M_w* and *M_n* were determined based on standard polystyrene. ¹H-NMR spectrum was measured by FT-NMR500 (JASCO Co.) in CDCl₃ or CDCl₃ / C₅D₅N = 3 / 1 (v / v). TMA was also carried out by TMA-SS (SII Inc.) in the temperature range 50-280 °C at a rate of increase of 2 °Cmin⁻¹ with vertical 49 mN force, using penetrating technique for a measurement. UV-Vis spectroscopy was carried out on an UV-560 (JASCO Co.). FT-IR spectroscopy was also carried out on a FTIR8400 (Shimadzu Co.), using the KBr pellet technique for sample preparation.

Table I Yields, weight average molecular weights and amounts of hydroxyl groups in lignophenols derived based on LC1(Western Hemlock-LC).

Lignophenols	Yield / %	M_w ^{d)}	M_w/M_n ^{d)}	Grafting <i>p</i> -cresol ^{e)} mol/C ₉	Phenol mol/C ₉	-OH ^{e)} Aliphatic mol/C ₉
LC1 ^{a)}	18.9 ^{c)}	14 200	2.8	0.76	1.11	0.95
LCHM1 ^{b)}	98.7	15 100	2.8	0.84	1.69	1.63
LC2	75.1	10 600	1.8	1.10	1.86	1.16
LCHM2	98.2	10 300	2.5	1.02	2.09	2.60
LC3	75.7	10 800	1.9	1.65	2.13	1.61
LCHM3	92.3	11 400	2.3	1.49	2.24	2.61
LC4	81.9	14 400	1.9	1.92	2.20	0.92

a) Western Hemlock-lignophenol (*p*-cresol type), b) Hydroxymethylated LC1, c) based on native lignin in wood meals, d) M_w and M_n were determined by GPC, e) calculated based on ¹H-NMR.

3. RESULTS AND DISCUSSION

3.1 Brush type derivatives

LC1 was obtained with 60.9 % and 18.9 % yields based on wood meal and Klason lignin, respectively. As LC1 had 0.76 mol/C₉ of *p*-cresol, 0.24 mol/C₉ of un-reacted benzyl structures remained after reaction of the phase-separation system (Table I). After hydroxymethylation, LCHM1 was derived from LC1 with 98.7 % yield and with 0.69 mol/C₉ of hydroxymethyl-OH in 1.63 mol/C₉ aliphatic-OH. Next, grafting reaction between LCHM1 and *p*-cresol on the surfaces of *p*-cresol / 72 % H₂SO₄ heterogeneous conditions resulted in LC2 with rich phenolic-OH. As *p*-cresol had affinity with lignophenol derivatives, reactions were carried out perfectly without reaction supports [12]. In these ways, both LC3 and LC4 were also synthesized. Interestingly, average molecular weights of both LC2 and LC3 were smaller than LC1 with low M_w/M_n values. This implied that the un-reacted C α -ethers were cleft through the 2nd and the 3rd acid treatments. After cleavages of these linkages, generating small fractions were dissolved into EtOEt during purification processes. On the contrary, LC4 showed relatively high M_w because there were few un-reacted arylethers already, therefore almost all C α carbon were grafted by *p*-cresol. In fact, the yields of both LC2 and LC3 decreased, but only LC4 showed high yield. This indicated that after 4th *p*-cresol grafting via HM bridges there were few un-stable reaction sites in the molecules.

As shown in Table I, there were clear correlations between amounts of *p*-cresol and reaction frequencies. Moreover there were new signals of methylene proton at 4 ppm in ¹H-NMR (data not shown). These results indicated that successive linkages of *p*-cresol via methylene chains from C1-phenol nuclei. In addition to these results, TMA results showed LC2, LC3 and LC4

were plasticized near 150 °C. Therefore these derivatives have relatively linear type polymeric structures.

Fig.4 demonstrated a structure of LC4 and drastic molecular weight variations after alkaline treatments. In general, lignophenols with ortho-OH phenols cleaved C β -O-4 main chains by nucleophilic attacks by lone-pairs on oxygen on phenoxide ions under alkaline condition over 100 °C[8, 14-15]. After the reactions, phenol structures were switched to counter parts. These reactions were based on neighbouring group participation [16] and arylmigration [17] of lignin-based materials. Interestingly, all LC materials showed convergence to $M_w = 1 000$. These results implied phenol-switching reactions occurred on the 1st phenols grafted to C α positions. Consequently, using HMLC as combination sites for phenols, new precise and practical applications with controls of both network density and branches are expected.

3.2 Grafting of alkyl phenols using reaction-supports

In general, it has been difficult to use alkyl phenols with long or bulky chains as phenolic media for lignocellulosics through the phase-separation system, because of hydrophobicity. Due to this high hydrophobicity, alkyl phenols can not solvated native lignin. Without solvation of phenols, effective grafting reactions can not be occurred. Therefore only limited phenols with small alkyl substitutions (mainly under C3) were often used. If various phenols which have low affinity for lignocellulosics can be grafted into lignophenol molecules, possibility of lignophenols will be developed.

Both HCLC and HM-HCLC were obtained with high yields (Table II). In addition to these results, *p*-cresol contents were 0.74 and 0.79 mol / C₉, respectively. Although direct grafting reactions with HM-LC1 were tried, reactions have not occurred sufficiently with generating aggregations. On the other hand, using vanishing reaction-supports, solid of lignophenols with 4SBP, 4TMBP and 4PP were obtained but 3NPDP (Table II). Though some part of a derivative with 3NPDP was obtained as an acetone extraction, there was no solid of lignophenol derivatives after EtOEt or Benzene / *n*-Hexane purification systems. Both 4SBP and 4PP showed 47.6 % and 59.4 % yields, respectively.

Table II Results of synthesis of HCLC-HM-alkylphenols through the phase-separation system using Kraft pulp as vanishing reaction supports under r.t. and 1 atm. Acid was 72 % H₂SO₄. Hydrophobic moieties were taken up by 10.0 mL of *p*-cresol after 30 min reaction. Extractions and purifications were carried out by both acetone and EtOEt.

Phenols ^{a)}	Yield ^{c)} / %	M_n ⁱ⁾	M_w ⁱ⁾	M_w/M_n ⁱ⁾
HCLC	83.7	5 670	21 630	3.81
HCLC-HM	97.4	5 040	19 812	3.93
4SBP	47.6	5 290	19 270	3.64
3NPDP ^{d)}	N/A	-----	-----	-----
4TMBP	25.4	4 510	6 030	1.34
4PP	59.4	10 860	23 080	2.12

a) 4SBP: 4-*sec*-butylphenol, 3NPDP: 3-*n*-pentadecylphenol, 4TMBP: *p*-(1,1,3,3-tetramethylbutyl) phenol, 4PP: 4-pentylphenol. c) HCLC-HM-3NPDP was dissolved in EtOEt. c) Yields were based on HCLC-HM, d) products did not obtained as a solid.

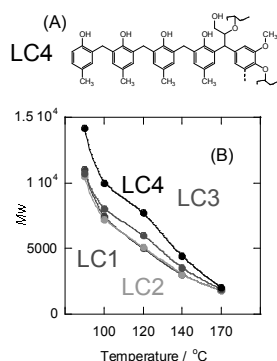


Fig.4 (A) Structures of brush-type derivatives (LC4) synthesized and (B) molecular weight variations after phenol switching treatments under 0.5 M NaOH aq.

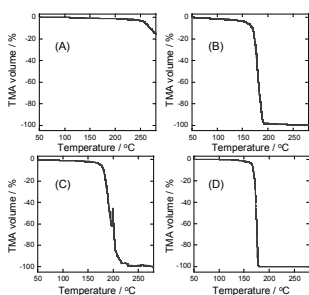


Fig.5 Thermal mechanical analyses (TMA) profiles for (A) HCLC-HM1, (B) HCLC-HM-4SBP, (C) HCLC-HM-4TMBP and (D) HCLC-HM-4PP.

As after EtOEt purification the aliquots showed light brown appearances, large parts of products would be dissolved like 3NPDP. As these phenols derived almost same M_w as HCLC or HCLC-HM1, reactions between HM-groups and phenols seemed to be occurred sufficiently. But 4PP showed large M_n probably due to polymerization at un-reacted α -positions because these products were dissolved easily in acetone. Low yield of 4TMBP was due to both rich aggregations during acid treatments and high solubility in EtOEt. Therefore only small fraction of EtOEt insoluble fractions was obtained.

In addition to low polydispersities of 4SBP, 4TMBP and 4PP derivatives, results of TMA supported linear structures of resulting products. As shown in Fig.5, 4SBP, 4TMBP and 4PP derivatives showed clear solid-liquid transition points around 170 °C, but HCLC-HM1 showed no plasticity. As there were few weight losses in HCLC-HM1 over 170 °C to 250 °C confirmed by thermal gravity analysis (TGA, data not shown), polymerization by heat-set was occurred. By intervals between start and end points of plasticity, information of viscosity was obtained. 4PP showed low viscosity but both 4SBP and 4TMBP showed relatively high viscosities. Moreover as Fig.5(C) showed there is a kick back type keen variation due to bubble up by gases such as H₂O from liquid 4TMBP derivatives. These differences on viscosity were due to alkyl chains combined to C1 phenol via methylene chains. As HCLC showed clear plasticity around 170-180 °C, main thermal properties were dominated by HCLC.

As shown in Fig.6, there were characteristic ¹H-NMR spectra of 4SBP, 4TMBP and 4PP derivatives. In all spectra there were 8-6 ppm (aromatic ring-H), 5 ppm (phenol-OH and un-reacted benzyl-H), 4 ppm

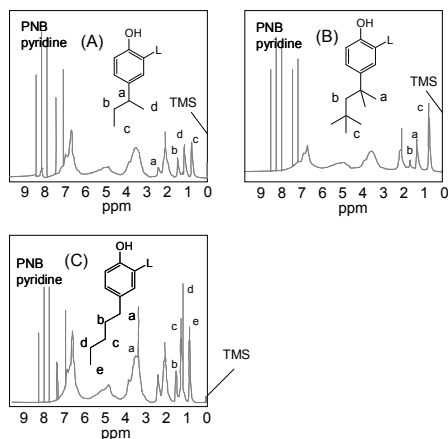


Fig.6 ¹H-NMR spectra for (A) HCLC-HM-4SBP, (B) HCLC-HM-4TMBP and (C) HCLC-HM-4PP. L means lignin structures.

(methylene bridges), 4-3 ppm (methoxyl groups), 2.5-2.0 ppm (methyl groups of *p*-cresol) and 2.5-0.5 ppm (characteristic alkyl groups) were observed. Unfortunately, it was impossible to calculate amount of phenols or hydroxyl groups because signals corresponded to alkyl chains were overlapped over methyl signals of *p*-cresol. But these spectra showed there remained un-reacted benzyl groups with small amounts. Therefore it is necessary to improve efficiency on reactions by increasing stirring efficiency such as ultra sonic irradiations without heating [18].

4. CONCLUSION

Using hydroxymethylated lignophenols as reaction sites for second or more phenol grafting reactions were carried out. First, successive *p*-cresol grafting reactions produced brush type-derivatives, LC2, LC3 and LC4, with typical characteristic properties of LP such as thermal plasticity, solubility for solvents, phenolic properties and switching functionality. Due to high reactivity, syntheses using *p*-cresol have not required reaction supports. Secondly, grafting of alkylphenols such as 4SBP, 4TMBP and 4PP to HCLC-HM1 using pulps with freeness100 as vanishing reaction supports were carried out. Resulting LPs showed properties of linear type polymers with M_w , thermal plasticities. Using these synthesis methods with benzyl structures mimic to the phase-separation system, developments on lignophenol molecules under precise control to generate novel functional materials are expected.

5. REFERENCES

- [1] K. V. Sarkanen, C. H. Ludwig, "Lignins: Occurrence, Formation, Structure and Reactions", Wiley-Interscience, New York, 95, 165(1971)
- [2] M. Funaoka, I. Abe, *Tappi*, **72**, 145-155 (1989)
- [3] M. Funaoka, M. Matsubara, N. Seki, S. Fukatsu, *Biotechnology and Bioengineering*, **46**, 545-552(1995)
- [4] M. Funaoka, *Polym. Int.*, **47**, 277-290 (1998)
- [5] E. Adler, *Wood Sci. Technol.*, **11**, 169-218 (1977)
- [6] M. Funaoka, M. Shibata, I. Abe, *Holzforshung*, **44**, 357-366(1990)
- [7] Y. Matsushita, S. Yasuda, *Mokuzai Gakkaishi*, **48**, 55-62(2002)
- [8] M. Funaoka, H. Ioka, T. Hoshio, Y. Nagamatsu, *Journal of Network Polymer Japan*, **17**, 121-129(1996)
- [9] J. A. Hemmingson, G. J. Leary, W. A. Thomas, A. D. Woolhouse, *J. Chem. Soc. Chem. Comm.*, 92-93(1978)
- [10] J. A. Hemmingson, *Aust. J. Chem.*, **32**, 225-229(1979)
- [11] G. J. Leary, D. A. Sawtell, H. Wong, *Holzforshung*, **37**, 11-16(1983)
- [12] M. Aoyagi, S. Yonekura, M. Funaoka, *Trans. Mater. Res. Soc. J.*, **32**, 1111-1114(2007)
- [13] TAPPI-T227
- [14] Y. Nagamatsu, M. Funaoka, *SEN'I GAKKAISHI*, **57**, 54-59(2001)
- [15] Y. Nagamatsu, M. Funaoka, *SEN'I GAKKAISHI*, **57**, 82-87(2001)
- [16] J. Gierer, C. R. Nelson, *J. Org. Chem.*, **43**, 4028(1978)
- [17] J. Gierer, *Wood Sci. Technol.*, **19**, 289(1985)
- [18] K. Nagamatsu, Y. Nagamatsu, M. Funaoka, *Journal of Network Polymer Japan*, **24**, 30-39 (2003)

(Received December 12, 2008; Accepted September 16, 2009)

Pre-processing By Shock Loading For Freeze-drying

Toshiaki WATANABE^{1*}, Ayumi TAKEMOTO², Daisuke SAWAMURA¹,
Yusuke YAMASHITA², Hironori MAEHARA², and Shigeru ITOH²

¹ Dept. of Ocean Mech. Eng., Nat. Fisheries Univ., Shimonoseki 759-6595, Japan

Fax: 81-83-286-7433, e-mail: watanabe@fish-u.ac.jp

² Shock Wave and Condensed Matter Research Center, Kumamoto Univ., Kumamoto, Japan

Fax: 81-96-342-3299, e-mail: itoh@mech.kumamoto-u.ac.jp

Abstract: In the food industry, it is hoping high value-aided product and the increase in efficiency of food processing. On the other hand, we get an experimental result that the load of the shock wave improves an extraction of food, and soften food. We tried to examine the effectivity of the shock wave as pre-processing for freeze-drying from the result in permeation character seen in the radish and so on. In the case of freeze-drying, the object tends to be limited to the small or thin one with size, from the sublimability in processing, the performance in case of the restoration and the viewpoint of the cost performance ratio. We report the result that shock wave loading was done to shrimp as pre-processing of freeze-drying.

Key words: Freeze-drying, Pre-processing, Shock loading

1. INTRODUCTION

In the food processing field, static pressure was mainly used for high pressure processing. For example, in the case of meat, experiments were carried out very much by Macfarlane in the 1970's [1]. They reported about the softening of the meat and the effect of the improvement of the water-holding by high pressure processing [2-4]. The following is reported about the meat fiber: High pressure processing makes the structure of the meat change and some of the proteins of that become solubilization. Effect of solubilization of the proteins proceeds as much as time is long as much as pressure is high [5-8].

On the other hand, These technique using shock waves from explosion of explosives or discharge of high current in water results in new industrial development as non-thermal food sterilization[9, 10]. Shock waves from explosion of explosives or discharge of high current in water can get high pressure comparatively easily though action time is short. When an underwater shock wave incidents into food and the structure, it is known to propagate as an incident wave and a reflected wave. An extraction and the softening of food are achieved by the incident wave, the reflected wave, and the difference of impedance in food. Shock wave processing has the possibility to bring the effect for which to be different from the pressure processing by the static pressure.

We tried to examine the effectivity of the shock wave as pre-processing for freeze-drying from the result in permeation character seen in the radish and so on. In the case of freeze-drying, the object tends to be limited to the small or thin one with size, from the sublimability ability in processing, the performance in case of the restoration and the viewpoint of the cost performance ratio. Therefore, we used comparatively large beheaded shrimps and attempted to review the effectivity of the shock wave processing about being freeze-drying.

2. EXPERIMENTAL APPARATUS AND METHOD

The outline of the shock loading experiment device is shown in Fig.1. The food samples bottled in polycarbonate vessel and a detonating fuse (Japan Carlit Co. Ltd., The 2nd kind detonating fuse, principal ingredient: PENET, loading density: 1200kg/m³, outer diameter: 5.4mm, detonation velocity: 6308m/s) were

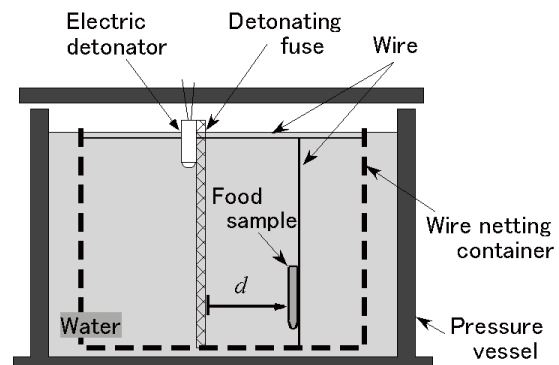


Fig.1 Outline of the shock loading experiment device

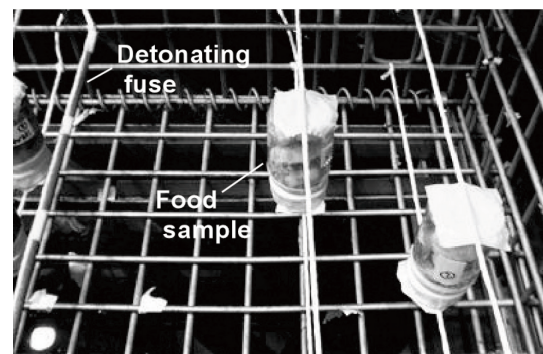


Fig.2 Photograph of experimental set up

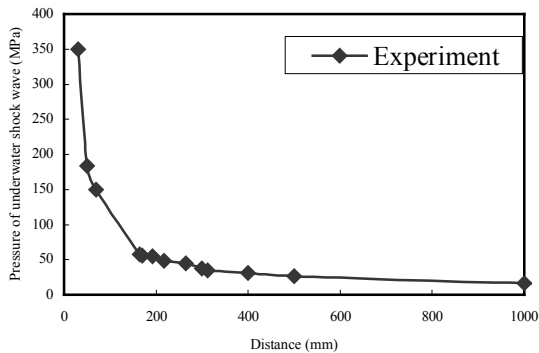


Fig.3 Relationship between pressure of underwater shock wave and distance

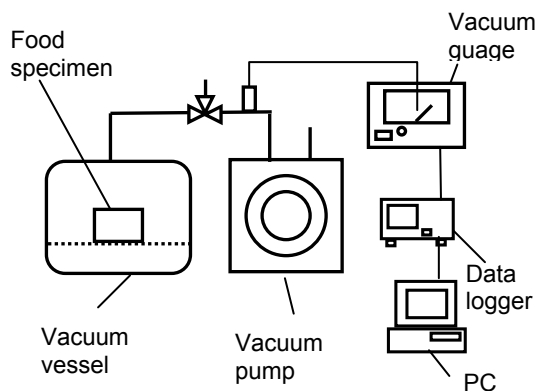


Fig.4 Schematic diagram of freeze-drying set up

fixed on the wire netting container (see in Fig.2). The wire netting container was put in the water-proof pressure vessel made by steel, and the water-proof pressure vessel was filled with the water. The initiation is made by the No.6 electric detonator (Asahi Chemical Industry Co. Ltd., Japan).

The relation between the pressure value of underwater shock wave and the distance from the detonating fuse obtained by the pressure measurement is shown in Fig.3. The pressure measurement of underwater shock wave generated by the detonating fuse was performed at the point's 30mm, 50mm, 70mm, 165mm, 300mm, 500mm 1000mm and others from the detonating fuse. The underwater shock wave generated from the detonating fuse attenuates gradually while propagating in water.

The shock-loaded specimens were frozen in a freezer and were set in the vacuum equipment to process freeze-drying. Freeze-drying process has been carried out without cold trap to monitor a sublimation condition by the vacuum pressure at this time. Also, it implemented freeze-drying processing by the only vacuum pump without overheating by the heater and so on to prevent from effect in heat-of-sublimation supply. The setup of the equipment to have used for freeze-drying processing is shown in Fig.4. The equipment for freeze-drying, it is simply composed of vacuum vessel, vacuum pump and vacuum gauge. The vacuum gauge

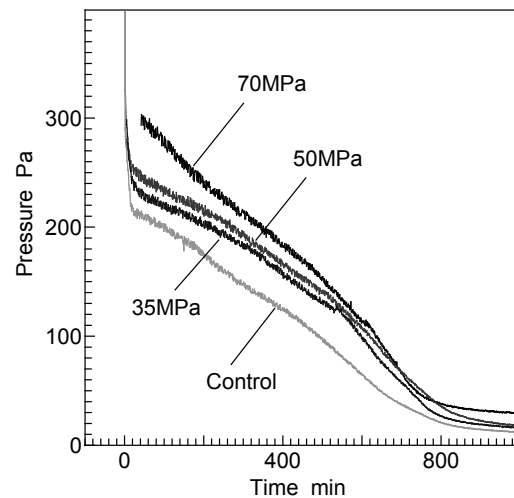


Fig.5 Pressure-time histories in the case of shrimp

connected with the PC through the data logger, and always monitored and recorded a vacuum pressure during freeze-drying.

RESULTS AND DISCUSSIONS

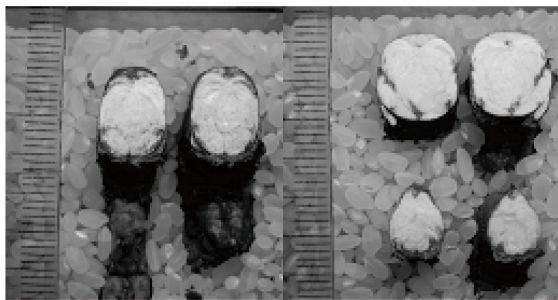
We divided the scalded beheaded shrimp of 12 tails into four groups; ① 70MPa shock loaded, ② 50MPa shock loaded, ③ 35MPa shock loaded and ④ control (un-shock loaded) for comparison respectively, as shown in Table I and experimented.

Pressure-time histories in the vacuum vessel are shown in Fig.5. The pressure value reaches to equal or less than about 600Pa of sublimation conditions within about 1minute without using a cold trap after the frozen specimen set in the vacuum vessel. From this result, the pressure of the specimen to have strong shocked processing is changing in the high condition and it shows that sublimation speed is fast. This is one of the problem which it should review, being detailed in the future with the possibility that the freeze-drying operation time can be abridged by the shock wave processing shown. This leads to the reduction of the freeze-drying cost.

These shrimps processed freeze-drying were attempt to reconstitute using boiling hot water with 1minute. To understand the state of the penetration of the case, hot water was colored with the food red. The representative example of each group is shown in Fig.6. The photograph shows a section of the division into the two equal parts in central and the section when quartering more. In case of control (un-shocked), the reconstitution by hot water is only the surface neighborhood and reconstitution of core part is nothing. In the case of 70MPa shocked, reconstitution is approximately sufficient by hot water, body collapse is seen, too. In case of shock wave processing of 50 MPa, reconstitution is sufficient in part from head to center, but reconstitution of the tail part is not enough. There are few body collapses. In case of shock wave processing of 35 MPa, reconstitution is not sufficient overall, body collapse cannot be seen absolutely. A restoration result in case of the shrimp is shown in

Table I Results of shrimp reconstituted by hot water

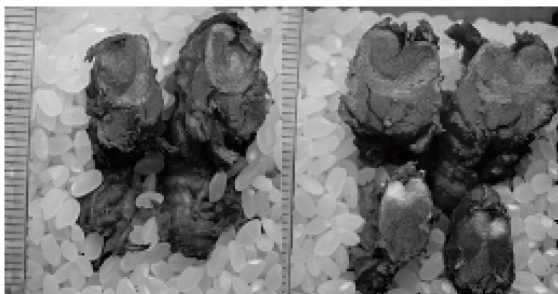
Shock condition	Freezed mass(g)	Dried mass(g)	Reconstituted mass(g)	Rehydration ratio(%)	Reconstitution ratio(%)	Average of rehydration ratio(%)	Average of Reconstitution ratio(%)
Control (Un-shocked)	7.43	2.50	5.11	52.9	68.8	35.3	56.8
	8.25	2.66	4.47	32.4	54.2		
	6.34	2.13	3.00	20.7	47.3		
70MPa	10.56	3.20	9.18	81.3	86.9	73.9	82.2
	8.14	2.66	6.64	72.6	81.6		
	10.01	3.17	7.81	67.8	78.0		
50MPa	10.38	3.37	7.33	56.5	70.6	47.4	64.5
	8.26	2.66	5.20	45.4	63.0		
	9.20	3.00	5.51	40.5	59.9		
35MPa	8.01	2.46	5.23	49.9	65.3	50.6	66.2
	8.40	2.78	5.86	54.8	69.8		
	8.25	2.56	5.24	47.1	63.5		



(a) Control (un-shocked)



(c) 50MPa shock loaded



(b) 70MPa shock loaded



(d) 35MPa shock loaded

Fig.6 Photographs of shrimp after reconstitution by hot water

Table I. The change of the re-hydration-ratio and re-constitution-ratio by the shock wave processing is shown in Fig.7. When attempting to see about the result including Table I, there is each sample individual difference, too, and its fluctuation is big, too. The result of re-hydration-ratio and re-constitution-ratio shows that the restore quality of specimen using hot water improves by shock wave pre-processing, when catching broadly. Means value of re-hydration-ratio and re-constitution-ratio in case of 35MPa shocked is higher than in case of 50MPa shocked. It is thought of as the irregular reflection of shock wave in the vessel wall, in addition to individual difference of shrimp being big. In the future, we add the evaluation of the food sense and so on, too, and proceed

with the reviewing such as the best value of shock pressure to each food, the best way to load.

The SEM photograph of shrimp in the case of un-shocked (control) is shown in Fig.8. The SEM photograph of shrimp in the case of 50MPa shocked is shown in Fig.9. In the case of shrimp, cells are collected, and it forms like a string. They gather more, and it feels to be a bundle. We think that the extent of the interval between that organization influences improvement in the re-hydration and re-constitution ratio. In the case of un-shocked (control), bundle forms a surface. But, in the case of 50MPa shocked, gap like a net is a little seen.

CONCLUSIONS

We tried to examine the effectivity of the shock wave as pre-processing for freeze-drying using beheaded shrimp as specimen. The improvement of the sublimation speed was gotten from the result that the pressure change during freeze-drying processing and the improvement of

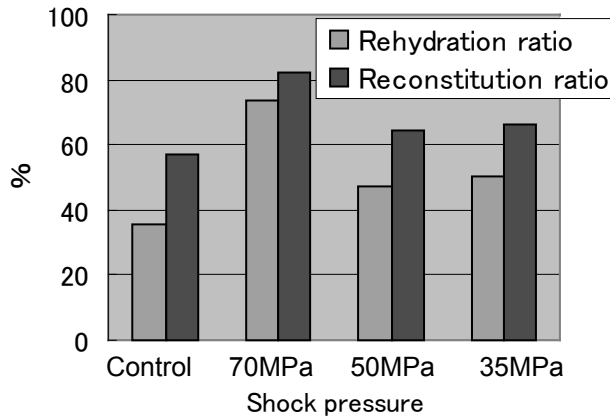


Fig.7 The improvement of the re-hydration ratio and re-constitution ratio by the shock wave loading

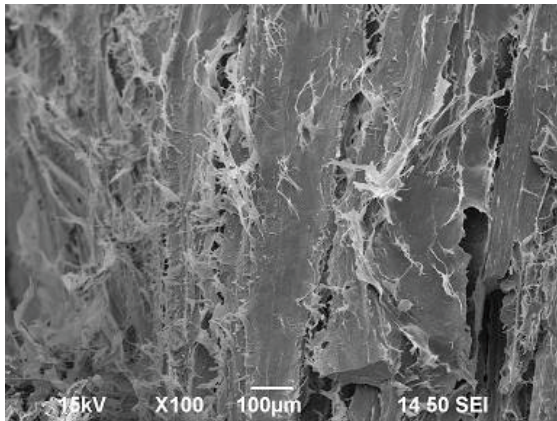


Fig.8 SEM photograph of shrimp after re-constitution by hot water in the case of control (un-shocked)

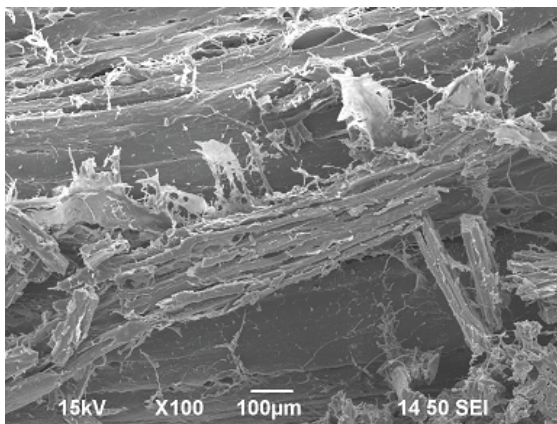


Fig.9 SEM photograph of shrimp after reconstitution by hot water in the case of 50MPa shocked

the reconstitution was gotten from the result using hot water. It was expected that the reconstitution of the freeze-dried food is improved and that a processing time is abridged, by shock wave loading as pre-processing for freeze-drying.

ACKNOWLEDGMENTS

The authors would like to express their appreciation to Mr. Akimaru, S., Shock Wave and Condensed Matter Research Center of Kumamoto University, for their great advice and assistance during the course of the experiments.

REFERENCES

- [1] J. J. Macfarlane, 1985, "Developments in Meat Science-3", Ed. R. Lawrie, Elsevier Applied Science Publishers, Barking.
- [2] J. J. Macfarlane, 1973, *J. Food Science*, 38, 294.
- [3] P. E. Bouton, P. V. Harris, J. J. Macfarlane and J. M. O'shea, 1977, *Meat Science*, 1, 307.
- [4] J. J. Macfarlane, I. J. Mckenzie, R. H. Tuerner and P. N. Jones, 1984, *Meat Science*, 10, 307.
- [5] J. J. Macfarlane, and D. J. Morton, 1978, *Meat Science*, 2, 281.
- [6] A. Suzuki, M. Watanabe, K. Iwamura, Y. Ikeuchi and M. Saito, 1990, *Agric. Biol. Chem.*, 54, 3085.
- [7] J. J. Macfarlane, 1974, *Food Science*, 39, 543.
- [8] A. Suzuki, N. Suzuki, Y. Ikeuchi and M. Saito, 1991, *Agric. Biol. Chem.*, 55, 2467.
- [9] Acim M. Loske, Ulises M. Alvarez, Claudia Hernandez-Galcia, Eduardo Catano-Tostado, and Fernando E. Prieto, *Innovative Food Science & Emerging Technologies* 3, 2002, pp.321-327.
- [10] Ulises M. Alvarez, Achim M. Loske, Eduardo Castano-Tostado, and Fernando E. Prieto, *Innovative Food Science and Emerging Technologies* 5, 2004, pp.459-463.

(Received December 12, 2008; Accepted September 16, 2009)

Properties of Humidity-Controlling Charcoal Produced from Wood Waste

Takahisa Nakai^{*}, Kentaro Abe^{**}, Tadashi Ohtani^{***}, and Yuuji Ishitobi^{****}

^{*}Department of Natural Resources Process Engineering, Shimane University,
1060 Nishikawatsu-cho, Matsue, Shimane 690-8504, Japan
Fax: +81-852-32-6071, E-mail: jaja@riko.shimane-u.ac.jp

^{**}Research Institute for Sustainable Humanosphere, Kyoto University,
Gokasho, Uji, Kyoto 611-0011, Japan
Fax: +81-774-38-3658, E-mail: abekentaro@rish.kyoto-u.ac.jp

^{***}Collage of Education, Ibaraki University,
2-1-1 Bunkyo, Mito, Ibaraki 310-8512, Japan
Fax: +81-29-228-8272, E-mail: t-ohtani@mx.ibaraki.ac.jp

^{****}Izumo Carbon Co., Ltd.,
1819-121 Shimokoshi-cho, Izumo, Shimane 693-0032, Japan
Fax: +81-853-24-8878, E-mail: sumiken@m1.izumo.ne.jp

Abstract: We carbonized the wood waste generated in Shimane Prefecture into humidity-controlling charcoal for use in housing and examined its properties. Though the moisture adsorption isotherm curve of the wood waste was a reverse S-shaped sigmoid curve, that of the charcoal produced was an S-shaped sigmoid curve. This suggests the possible presence of new mesopores (2-50 nm) resulting from carbonization. As the relative humidity increased, the percentage of moisture retained by the charcoal in the process of moisture adsorption and desorption increased, but the overall amount slightly decreased.

Key words: humidity-controlling charcoal, wood waste, adsorption, desorption, S-shaped sigmoid curve

1. INTRODUCTION

In recent years, the rise of a recycling-oriented society has been promoted in which the socioeconomic activity structures for mass production, consumption, and waste are being fundamentally reviewed. In May 2000, the Construction Materials Recycling Law was promulgated, and there were high expectations for the reuse and recycling of construction and demolition waste such as concrete, asphalt, and wood. A survey conducted in 2002 after the law came into force showed that about 4,640,000 tons of construction wood waste was generated, of which about 61% was reused and about 40% was incinerated or landfilled. A 2005 survey showed that about 5 million tons of construction wood waste was generated, of which about 68% was reused, a slight increase from 2002. When compared to concrete and asphalt waste, which are now nearly 100% recycled, further efforts are needed to increase the reuse rate of wood waste.^[1] In addition, large amounts of non-construction wood waste such as thinned wood and transporting wood pallets are generated. The beneficial use of wood waste is one of the social issues that need to be solved.

Conventionally, wood waste is chipped for use as feedstock for particle boards and paper or a substitute for litter; it is also carbonized into charcoal to be used as an agricultural soil

improvement agent. In recent years, there has been a shift from these types of material recycling to thermal recycling; large-scale wood biomass power plants have been built across the country. However, material recycling has been given a higher priority and is ranked higher than thermal cycling. In order to effectively use natural resources and prevent global warming by reducing CO₂ emissions, the importance of material recycling should be stressed again.

We purchased and chipped some of the wood waste generated in Shimane Prefecture; we carbonized all of it into humidity-controlling charcoal for use in housing and examined its properties.^[2]

2. EXPERIMENT

2.1 Test sample

Wood waste (coniferous wood: 40%; south-sea wood: 60%) generated in Shimane Prefecture was chipped to prepare the test samples. The wood waste for the test samples was carefully selected. Preserved wood waste and wood with nails, wire or other metals, and insulator cords were not accepted. Only wood waste that passed strict selection criteria was chipped.

The chipped wood waste was dried at 105°C for 24 h (this condition is defined as “absolutely dried”) and was then placed in a crucible with a

cover. The crucible was placed in an electric furnace, heated at a heating rate of 10 °C/min with a controlled air supply, and maintained at 800°C for 30 min to carbonize the wood chips. Then, it was gradually cooled by introducing nitrogen gas into the furnace; the crucible was left to stand to cool.

2.2 Measurement method

2.2.1 Measurement of specific area and pore distribution

The nitrogen adsorption-desorption isothermal curve of the charcoal produced at a relative pressure range of 0.01 to 0.15 was obtained using a nitrogen adsorption measuring apparatus. The specific area and pore distribution of the charcoal were measured by MP-method analysis using the obtained data.

2.2.2 Moisture adsorption-desorption test according to JIS A 1470-1

Since there is no established test method to evaluate the moisture adsorption-desorption performance of charcoal, the Test Method for Adsorption and Desorption Efficiency of Building Materials to Regulate Indoor Humidity (JIS A 1470-1) was modified for the test.

Absolutely dried charcoal or wood waste was placed in a glass Petri dish and then placed on a balance in a constant temperature/humidity chamber to measure the change in weight every 5 min. The temperature inside the chamber was kept constant at 23°C, and the humidity level was adjusted to 33%, 53%, 75%, 93%, 75%, 53%, and back to 33%. Each humidity level was maintained for 36 h. Each humidity change took place over 30 min.

2.2.3 Moisture adsorption-desorption test using a saturated salt solution

Weighing bottles containing absolutely dried charcoal or wood waste were placed in sealed containers containing ten different saturated salt solutions (LiCl (RH: 11%), CH₃COOK (RH: 22%), MgCl₂ (RH: 33%), K₂CO₃ (RH: 43%), Mg(NO₃)₂ (RH: 53%), NH₄NO₃ (RH: 62%), NaCl (RH: 75%), (NH₄)₂SO₄ (RH: 80%), KNO₃ (RH: 92%), K₂SO₄ (RH: 97%)); the weight change was measured continuously until the weight became constant with the humidity maintained at 23°C. After humidity adjustment, the weight of each charcoal and wood waste sample was measured to calculate the moisture content.

The weighing bottles containing absolutely dried charcoal and wood waste were placed in the sealed containers of the saturated K₂SO₄ solution until the weight became constant; the bottles were

then moved to the sealed containers of the saturated LiCl solution to conduct moisture-desorption test. The same measurement procedure as in the humidity adsorption test was used.

3. RESULTS AND DISCUSSION

3.1 Properties of the charcoal

A pyrogenicity test showed that the charcoal had a fixed carbon content of about 94%, a volatile content of about 3%, and an ash content of about 2%.

Nitrogen adsorption measurements showed that the charcoal had, on average, a specific surface area of 238.97 m²/g, pore area of 257.70 m²/g, and pore volume of 0.105 m³/g; these properties are nearly twice those of Bincho charcoal (Table I). The peak of the pore distribution of the charcoal was 0.63 nm, which is about 80% of that of Bincho charcoal (Table I).

FE(Field Emission)-SEM observation of the charcoal surface showed granular projections on the order of a few to a dozen nanometers (Fig. 1(a)); they appeared to be at the end of microfibrils and crack-like gaps (Fig. 1(b)).

3.2 Moisture adsorption-desorption properties of the charcoal

The experiment showed that the charcoal can control moisture by adsorbing or desorbing moisture according to an increase or decrease in humidity.

Investigation of the moisture adsorption and desorption capacity of the charcoal showed about 102.5% in a low relative humidity range (33% ⇔ 54%), about 73.6% in a medium relative humidity range (54% ⇔ 75%), and about 58.3% in a high relative humidity range (75% ⇔ 93%) (if the adsorbed moisture is not desorbed at all: 0%). As the relative humidity increased, the percentage of moisture retained by the charcoal in the process of moisture adsorption and desorption increased, but the overall amount slightly decreased (Table II).

3.3 Analysis of the adsorption-desorption process of the charcoal

It has been reported that generally, the adsorption-desorption isothermal curve of wood is a reverse S-shaped sigmoid curve. In this study, a similar reverse S-shaped sigmoid curve was obtained for the wood waste. The adsorption isotherm curve of the charcoal is an S-shaped sigmoid curve that, as shown in Fig. 2, is concave, convex, and steep in the low, high, and medium relative humidity ranges respectively. This suggests the possible presence of new mesopores

Table I. Characteristics of the charcoal produced with nitrogen adsorption measurements.

	Specific surface area (m ² /g)	Pore area (m ² /g)	Pore volume (m ³ /g)	Peak value of pore distribution (nm)
Charcoal produced	238.97	257.70	0.105	0.63
Bincho charcoal	118.49	124.02	0.050	0.78

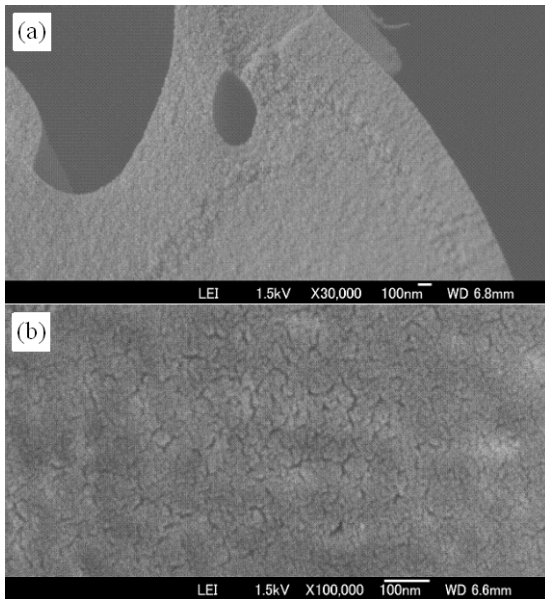


Fig. 1. Cross-sectional photograph of the charcoal produced with FE-SEM observation.
 Note: The following two types were observed on the charcoal surface: (a) granular projections on the order of a few to a dozen nanometers which appeared to be at the end of microfibrils (b) crack-like gaps.

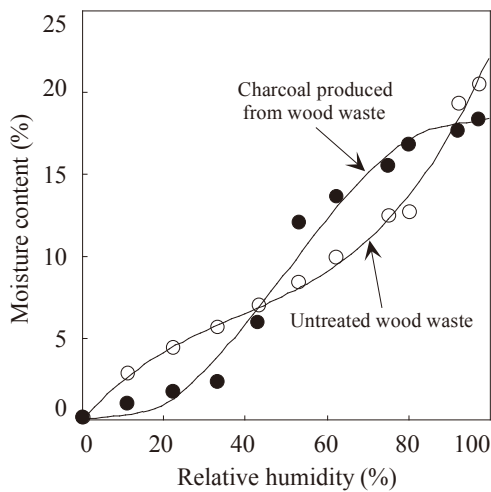


Fig. 2. Adsorption-desorption isothermal curves of charcoal produced and wood waste.
 Legend: ●: charcoal produced, ○: wood waste, moisture content: ((weight of sample under test)-(absolutely dried weight of sample))/(weight of sample under test) × 100 (unit: %).

(2–50 nm) resulting from carbonization.

Fig. 3 shows the change in moisture content in the adsorption-desorption process. The figure shows that the adsorption-desorption process is a typical logistic function curve. In order to quantitatively compare the adsorption-desorption process, the parameters characterizing the process were determined as follows.

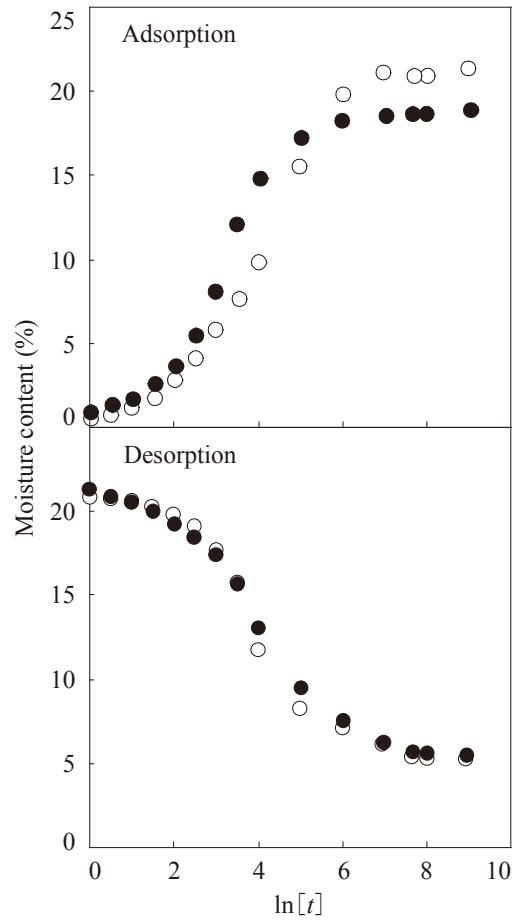


Fig. 3. Changes during the adsorption-desorption process of the charcoal produced.
 Legend: ● and ○: See the legend in Fig. 2, t : time which passed from the test start (unit: hour).

The adsorption process is the adsorption of the adsorbate on the surface of the adsorbent. The adsorption rate is high in the beginning, decreases gradually, and then levels off. If the adsorption process is represented by a moisture content-time ($\ln[t]$) curve, the curve is similar to the logistic function. Here t is time which passed from the test start. For the same reason, the desorption process is expected to be similar to the logistic function. In this study, an attempt was made to characterize the adsorption process via logistic function regression for comparison.^[3]

The logistic function is a function described as a solution to the following differential equation, which is a typical nonlinear differential equation:

$$\frac{dy}{dx} = \frac{a}{b} y(b - y) \tag{1}$$

The solution of equation (1) is given by the following equation:

$$y = \frac{b}{1 + c \exp[-ax]} \tag{2}$$

This equation is well known as describing self-catalytic processes such as growth and demand curves. Equation (2) can be expressed as $1/y = (1/b) + (c/b) \cdot \exp[-ax]$; therefore, the constants a , b and c can relatively easily be determined. From the above equation, the three constants are obtained as characteristic parameters. In equations (1) and (2), b is the level-off value (equilibrium moisture content) of the function, ab is the fraction of the adsorption site, $ab/4$ is the maximum adsorption rate, and $\ln[c]/a$ is the time of the maximum adsorption rate. The adsorption characteristics can be determined by these values.

It should be noted that these parameters do not correspond directly to physical characteristics but describe the characteristics of change. They

describe the trend of change and do not necessarily correspond directly to structural or physical factors. The correspondence between the parameters and structural or physical factors remains to be clarified.

The logistic function regression curve obtained from Fig. 3 was normalized by the level-off value to calculate the parameters (Table III). As a result, it was shown that in the adsorption process, the carbonization of wood waste increases the fraction of the adsorption site and maximum adsorption rate and decreases the time of the maximum adsorption rate; in the desorption process, the fraction of the desorption site and maximum desorption rate decrease and the time of the maximum desorption rate increases compared to the wood waste.

Table II. Moisture adsorption and desorption capacity of the charcoal under various relative humidity ranges.

RHR	Charcoal produced			Wood waste		
	AA (mg/g)	DA (mg/g)	MADC (%)	AA (mg/g)	DA (mg/g)	MADC (%)
33⇔54%	60.0	61.5	102.5	24.2	16.6	68.6
54⇔75%	29.2	21.5	73.6	37.7	43.4	115.1
75⇔93%	13.9	8.1	58.3	56.3	33.6	59.7

Legend: RHR: Relative humidity ranges, AA: Adsorption amount, DA: desorption amount, MADC: Moisture adsorption and desorption capacity.

Note: Moisture adsorption and desorption capacity; (Desorption amount) / (Adsorption amount) × 100.

Table III. Characteristics of the adsorption and desorption of the charcoal produced.

		Charcoal produced		Wood waste		Ratio	
		AP	DP	AP	DP	AP	DP
	ab	0.259	0.192	0.207	0.226	1.251	0.850
	$ab/4$	0.065	0.048	0.052	0.056	1.250	0.857
	$\ln[c]/a$	3.362	4.769	3.845	4.205	0.874	1.134

Legend: Ratio: (Charcoal produced) / (Wood waste), AP: Adsorption process, DP: Desorption process

Note: $|ab|$: fraction of the adsorption (or desorption) site, $|ab/4|$: maximum adsorption (or desorption) rate, $|\ln[c]/a|$: time of the maximum adsorption (or desorption) rate.

4. CONCLUSION

We carbonized the wood waste generated in Shimane Prefecture into humidity-controlling charcoal for use in housing and examined its properties.

The results obtained were summarized as follows.

1. Charcoal produced had, on average, a specific surface area of 238.97 m²/g, pore area of 257.70 m²/g, pore volume of 0.105 m³/g and the peak of the pore distribution of the charcoal was 0.63 nm with nitrogen adsorption measurements.

2. There were two types on the charcoal surface with the FE-SEM observation; one was granular projections on the order of a few to a dozen nanometers which appeared to be at the end of microfibrils and the other crack-like gaps.

3. Investigation of the moisture adsorption and desorption capacity of the charcoal showed about 102.5% in a low relative humidity range, about 73.6% in a medium relative humidity range, and about 58.3% in a high relative humidity range (if the adsorbed moisture is not desorbed at all: 0%).

4. The adsorption isotherm curve of the charcoal produced was an S-shaped sigmoid curve.

5. In the adsorption (or desorption) process, the carbonization of wood waste increased (or decreased) the fraction of the adsorption site and maximum adsorption rate and decreased (or increased) the time of the maximum adsorption rate compared to the wood waste.

Acknowledgments We thank Prof. Dr. Toshihiro Kitamura of Shimane University for their helpful suggestions and comments.

REFERENCES

- [1] Ministry of land, infrastructure, and transport, Report on investigation of actual conditions of construction by-product (in Japanese) (2005).
- [2] Kitamura, T., Tanaka, T., Katayama, H., and Ishitobi, Y., *J. Jpn. Soc. Waste Mgt. Experts*, Vol.16, No.6, pp.501-507 (in Japanese) (2005).
- [3] Bessho, K. and Nakano, T., *J. Soc. Mat. Sci., Jpn.*, Vol.58, No.1, pp.53-56 (in Japanese) (2009).

(Received December 12, 2008; Accepted September 16, 2009)

Development of Smokeless Carbonization and Combustion Technique Aiming at Versatile Use of Woody Biomass

Kiyotoshi Ogami¹, Ginji Sugiura², Takemichi Tsurumi¹ And Osamu Kobayashi¹

¹Faculty of Agriculture, Ehime University, Matsuyama, Japan

²Charcoal Burner Group, International Charcoal Cooperative Association, Tokyo, Japan

Fax:+81-89-941-1098,E-mail: chan@stu.ehime-u.ac.jp

As a replacement for oil burning boilers used for out-of-season culture in greenhouse, we have developed a new-type greenhouse heating apparatus using woody biomass, which is lumber from thinning, since 2002. The result of this research will be reported in this paper. We have obtained a basic patent on the heating apparatus in 2007 (patent no. 4048488: application in 2003).

Key words: Woody Biomass, Tree, Pyrolysis, Smokeless, Boiler

1. Introduction

Consuming vast amounts of fossil fuel results in emissions of carbon dioxide gas originating from underground resources into the atmosphere, which induces serious global warming. This situation requires people to end their excessive reliance on underground energy resources and to move toward using environmentally compatible energy resources. According to a report on climate change, issued by Intergovernmental Panel on Climate Change of United Nations, the average atmospheric temperature on the Earth will rise from 1.4°C to 5.8°C during the period from 1990 to 2100. This atmospheric temperature rise may induce water shortages, droughts, and forest fires in Southern Europe, as well as the receding of glaciers in the Alps. Furthermore, central Europe has a large possibility of suffering from floods and thermal waves. Emissions of CO₂ caused by the combustion of fossil fuels are pointed to as a cause of the above phenomena. The concentration of CO₂ in the atmosphere is predicted to continue increasing from 280 ppm in 1750, thus reaching a maximum level of as high as 250%.¹⁾ Corn and other crops, which are plant biomass (food), have become candidates as starting materials for producing ethanol, which is a substitute for underground resources. The use of corn and other crops, however, is expected to induce a new and worldwide food crisis.

The recent price increases of crude oil have had significant and widespread effects in Japan, which is an oil-dependent country. Agriculture is no exception and faces serious impacts. Specifically, some farms engaging in greenhouse cultivation are changing crops or are abandoning cultivation because it is not profitable due to price increases of boiler fuel used for providing heat in off-season cultivation. The situation of forestry is also severe as it faces a slump in lumber prices.

Against the background of above social situation, studies are underway to develop a mobile smokeless carbonization apparatus that applies the buried firewood method²⁾, which was once used on silkworm-breeding farms and other farms for heating. The apparatus is composed of a drum and uses woody biomass as fuel. This paper describes observation results for the equipment in terms of temperature change of generated heat, nature and quantity of gas generated, and also technological development aiming at practical applications.

2. Experimental method

2-1. Preliminary experimental apparatus using a pail can

A preliminary experiment using the smokeless combustion apparatus adopted a pail can. The inner wall surface of the apparatus was lined with ceramic wool (high-temperature fire-resistant insulation fiber ACE FIGHT CS, density 100 kg/m³, thickness 50 mm, and width 600 mm, manufactured by Shinnikka Thermal Ceramics Corporation). The bottom of the apparatus was covered with refractory to a depth of 6 cm. Above the refractory, a grate was formed using a wire mesh with a 5-mm mesh opening.⁴⁾

2-2. Smokeless carbonization apparatus using a drum

Similar to the pail can, the drum smokeless carbonization apparatus was prepared by forming a 6-cm thick refractory on the bottom of a drum to support a grate, laying a wire mesh with a mesh opening of 5 mm, and covering the bottom and the inner periphery with ceramic wool. The same wire mesh was laid inside the peripheral ceramic wool.⁵⁾

2-3. Fabrication of gas exchanger

A gas exchanger was fabricated above the drum to prevent gas from leaking outside. The outer frame of the gas exchanger was securely attached to the opening of the drum, while locating an inner frame inside the outer frame, and the inner frame was positioned above the ceramic wool inside the drum.⁶⁾ One liter of catalyst bed

(NM-103, manufactured by N.E.CHEMCAT CO., LTD.) was placed at the center of the flue. It was speculated that carbon monoxide gas generated by thermal decomposition in the drum would rise by convection through the catalyst bed where it would be converted into carbon dioxide. Eight pipes were attached to the air inlet (20 mm x 60 mm) of the gas sampler at a downward angle, and a flue (inner diameter of 100 mm and height of 150 mm) was mounted. In addition, two peepholes (50 mm x 20 mm square) for observing internal conditions were opened. The catalyst-supplying unit connected to the top lid had an inner diameter of 100 mm, which allowed catalyst pellets of 125 mm by 150 mm to be supplied, and a punched metal having 2-mm holes was welded to the lower section of the catalyst-supplying unit. The top lid, also made of the same punched metal, was placed at the top of the catalyst-supplying unit. A detachable roof shaped like a cylinder and cone was placed above the top lid to allow catalyst to be replaced. With a structure whereby the gas exchanger can be disassembled into three pieces, catalyst replacement and measurement could be readily executed. The photo-catalyst, spray-type photo-catalyst phosphorus coating (manufactured by Tokai Kiki Kogyo, Inc.), was applied on the glass wool, which was then attached to the tip of the air supply duct.⁷⁾

2-4. Method and apparatus for measuring C₂H₄ gas

The C₂H₄ gas concentration was determined by sucking in air in the greenhouse using a syringe, and sealing the syringe. The gas was analyzed later using a SHIMADZU gas chromatograph (GC-9A, manufactured by Shimadzu Corporation).

2-5. Fabrication of gas exchanger equipped with fan

Because thermal convection alone cannot increase the efficiency of oxidation of the catalyst, an air supply duct equipped with a fan was fabricated for the gas exchanger. A stainless steel cylinder (123.0 mm in diameter, 1.0 mm in thickness, and 200.0 mm in length) was welded to the side of the catalyst-supplying section, and a fan was mounted in the cylinder.⁸⁾

2-6. Attaching fan controller

A fan controller was attached⁹⁾ to investigate temperature changes generated when changing the fan's rotational speed to induce variations of the thermal decomposition rate. The fan cylinder of the gas exchanger was designed to allow the fan to be mounted to/dismounted from inside the cylinder using the flue. A VIZO window storm 8 cm fan (VZ-WS8038, manufactured by Vizo Technology, Corp.) was mounted on the fan base plate, which was slid into the chimney, and then was bolted in place. A round PVC-sheathed cable (VCIF) was used to connect the fan to the power source, and a fan controller (ZM-MFC1PLUS, manufactured by Selling Co., Ltd.) was mounted. The power source of the fan controller was the power source of the computer.

2-7. Measuring devices

2-7-1. CO and CO₂ gas measuring devices

Gas sampling was done with a Kitagawa gas sampler AP-20 (manufactured by Komyo Rikagaku Kogyo K.K.)

Qualitative gas detection was done with LOT No. 017052 (Kitagawa gas detection tube for qualitative organic gas detection). The gas detection tubes applied were made by Gastec Corporation, No.2L and No.2LC for CO₂, and No.1L and No.1La for CO. The CO tester applied was the testo330-2 manufactured by Testo Inc., and the CO₂ tester was the testo535 manufactured by Testo Inc.

2-7-2. Temperature measuring devices

Progressive temperatures inside the drum were determined using three high-temperature thermocouples, at the center of the drum, inside the gas exchanger, and outside the fan. Data were recorded at 10-min intervals using a data logging system NR1000 (manufactured by Keyence).

2-7-3. Wood moisture meter and combustion material

The water content of the combustion material was measured using a wood moisture meter (turku H, keet). The combustion material applied was 29.8 kg of Japanese cedar logs, with 8.1% average water content. The gaps between logs were filled with 9.5 kg of pulverized coal, and more pulverized coal was laid over the combustion material to a depth of 3 cm. On the pulverized coal layer was placed 2.1 kg of charcoal, which was then ignited.

3. Results and Consideration

3-1. Preliminary experiment using pail can

For the experiment using a pail can, the combustion material was successfully treated by high-temperature thermal decomposition in a smokeless state for about 10 continuous days.

3-2. Smokeless carbonization experiment using a drum

Maximum internal temperature of the mobile smokeless carbonization apparatus using a drum recorded was 624°C. Heat generation free from smoke was observed for a long period of 43 days from Feb. 15 to Mar. 29.

3-3. Gas determination using a gas exchanger

According to the measurement results for qualitative organic gas detection, CO, CO₂, and C₂H₄ gases were detected, (Fig. 1). Inside the flue, a CO concentration as high as 8,000 ppm was recorded immediately after ignition. After that, however, the CO concentration rapidly decreased to 1,612 ppm after two days. The CO concentration gradually decreased to a level of about 600 ppm. After 23 days from ignition, the CO concentration increased to 1,186 ppm, and stayed at around 600 ppm afterward.

On the other hand, the CO concentration after the gas passed through the catalyst bed increased after ignition, then decreased abruptly two days later. On the 6th day, the CO concentration increased to 130 ppm. However, the CO concentration on the next day decreased to 61 ppm, and then stayed at 35 ppm or less afterward.

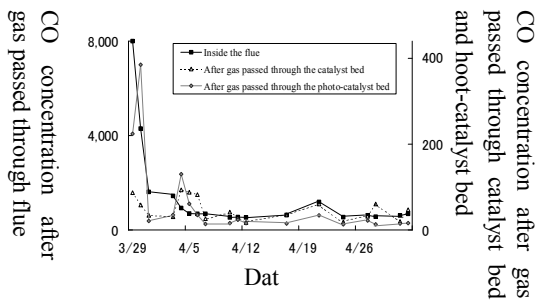


Fig. 1 Progressive concentration of CO in gas exchanger

Regarding CO concentration after gas passed through the catalyst bed, a gradual decrease occurred from 79 ppm, and the CO concentration showed an increase to 85 ppm on the 6th day, and then fell to 55 ppm or less. In the initial state of a high CO concentration, the level was less than half of that after passing through the catalyst bed. However, at the 6th day or later after ignition, the CO concentration gave a higher value than that after passing through the catalyst bed. Nevertheless, the maximum level was 85 ppm, and no higher level was observed.

In the verification experiment for the CO concentration using 1 liter of NM-103 catalyst in the gas exchanger, when the CO concentration after the gas passed through the catalyst bed, was compared to that before the gas passing through the catalyst bed, the values during the period of six days after ignition fluctuated in the range from 1.3% to 13.9%. After that, however, the CO concentration stayed at 10% or less. The experimental results suggest that the CO concentration can be further decreased by increasing the quantity of catalyst and by supplying oxygen or another gas to enhance oxidation.

3-4. C₂H₄ gas concentration

The C₂H₄ gas concentration was centered at 0.005 ppm, with a maximum of 0.0102 ppm. According to Abeles (1973)¹⁰, the 1/2 maximal concentration of C₂H₄ affecting plant growth is 0.1 ppm in many cases. However, as shown in Fig. 2, the measurements showed that the C₂H₄ gas concentration was centered at 0.005 ppm, with a maximum of 0.0102 ppm. Consequently, it is speculated that the quantity of C₂H₄ generated when the smokeless carbonization apparatus is placed does not affect plants in a greenhouse.

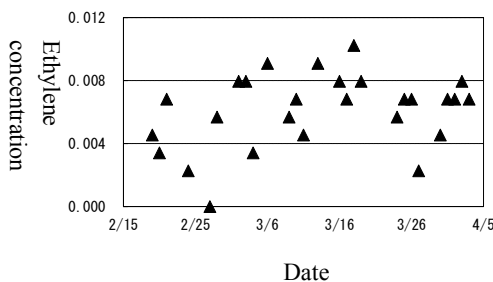


Fig. 2 Quantity of ethylene generated in buried firewood

3-5. Combustion experiment with gas exchanger equipped with fan

In the experiment with a drum using a gas exchanger equipped with a fan, the temperature also increased abruptly immediately after ignition and after starting the fan. However, when the fan was stopped, the temperature rapidly decreased, and then increased again. During the period of 15 hours from stopping the fan, the temperature increased similar to the case of the can. When the fan was started again, the temperature increased rapidly, and reached 1,192°C within about eight hours. The temperature of the can during that period was about 450°C. In the can, thermal decomposition continued for about 12 days. For the buried firewood can equipped with a fan, however, thermal decomposition was completed within about three days, although the fan was stopped once.

The experiment showed that, in the buried firewood can, smokeless thermal decomposition proceeds when air is sucked from beneath the grate. Thus, the temperature rises. It was also confirmed that 18 kg of logs can continue high-temperature thermal decomposition at 800°C or above for about 41 hours free from smoke. The apparatus was confirmed to be a heat-generating apparatus that is fully applicable as a wooden biomass boiler, substituting for existed fossil fuel boilers. It was confirmed that the smokeless heat generation apparatus has a large possibility of being applied as a greenhouse heating apparatus.

3-6. Combustion experiment using a fan controller

In the fan controller control experiment, (Fig. 3), the rotational speed of the fan was changed by the controller from 50% to 100% at 14:13, and was changed to 50% at 40 min. after that. The temperature outside the fan decreased from 90.1°C to 78.6°C, or more than 11°C, within 10 min. After that, the temperature gradually decreased, and the reduction range became 18°C or more after 70 min.

The rotational speed of the fan was then changed by the controller from half to full at 18:20. The temperature increased from 72.3°C to 83.3°C, or by more than 10°C, within 10 min. In both cases, when the rotational speed of the fan was increased by the controller, the temperature increased immediately, and when the rotational speed of the fan was decreased, the temperature decreased. This phenomenon suggests that temperature control by the controller is fully applicable.

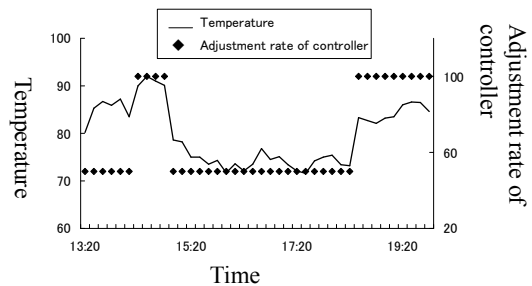


Fig. 3 Adjustment rate of controller and temperature change (2008)

[Literature cited]

- (1) Summary of the Third Evaluation Report of IPCC, translated by the Japan Meteorological Agency
- (2) Ginji Sugiura (2001), "Buried firewood" ("Current Miscellaneous Trees Dictionary" edited by Japan Miscellaneous Trees Congress), Hyakusui Sha Co., Ltd., pp244-245
- (3) Masakatsu Miura, "Recovery of Natural Resources from Biomass – New Macrowave Method –," AIST
- (4) Kiyotoshi Ogami, Takemichi Tsurumi, and Osamu Kobayashi, (2003), Summary Papers of The 53rd Research Presentation Meeting of Japan Wood Research Society, pt05
- (5) Kiyotoshi Ogami, Ginji Matsuura, Takemichi Tsurumi, and Osamu Kobayashi, (2004), Summary Papers of The 2nd Research Presentation Meeting of The Wood Carbonization Research Society, pp3-7
- (6) Kiyotoshi Ogami, Ginji Matsuura, Takemichi Tsurumi, and Osamu Kobayashi, (2005), Summary Papers of The 3rd Research Presentation Meeting of The Wood Carbonization Research Society, pp11-14
- (7) Kiyotoshi Ogami, Ginji Matsuura, Takemichi Tsurumi, and Osamu Kobayashi, (2006), Summary Papers of The 4th Research Presentation Meeting of The Wood Carbonization Research Society, pp11-12
- (8) Kiyotoshi Ogami, Ginji Matsuura, Takemichi Tsurumi, and Osamu Kobayashi, (2007), Summary Papers of The 5th Research Presentation Meeting of The Wood Carbonization Research Society, pp65-68
- (9) Kiyotoshi Ogami, Ginji Matsuura, Takemichi Tsurumi, and Osamu Kobayashi, (2008), Summary Papers of The 6th Research Presentation Meeting of The Wood Carbonization Research Society, pp1-4
- (10) ABELES, FREDERICK B, (1973), 『ETHYLENE IN PLANT BIOLOGY』, ACADEMIC PRESS New York and London, pp 228–230
- (11) Ichiro Watabe, (1987), "Experimental Methods on Agriculture Environment," Science House Co., Ltd.

(Received December 12, 2008; Accepted September 16, 2009)

Bending Creep of Sugi Glulam with Low Young's Modulus Laminae for the Inner Layer

Shiro Aratake, Akihiro Matsumoto, Hideki Morita and Takanori Arima *

Miyazaki Prefectural Wood Utilization Research Center, 21-2 Hanaguri Miyakonojo-shi, Miyazaki, 885-0037, Japan,
Fax: +81-986-46-6047, e-mail: aratake-shiro@pref.miyazaki.lg.jp

Bending creep tests for sugi (*Cryptomeria japonica* D.Don) glulam with extremely low Young's modulus laminae (3-4GPa) for the inner layer, along with the tests for hybrid glulam with the Douglas-fir (*Pseudotsuga menziesii* Franco) laminae (14-15GPa) for the outermost layer and the sugi laminae including 3-4GPa laminae for the inner layer, have been carried out since October, 2005. For the test, eight different composition glulam beams with the dimensions of 105mm in width, 210mm in depth and 3980mm in length were prepared. The results are summarized as follows. (1) There was no big difference between the Young's modulus or bending creep of glulam with L30 (Laminae with 3-4GPa Young's modulus) for the inner layers and that of glulam with L50 (Laminae with 5-6GPa Young's modulus) for the inner layers regardless of the glulam types. (2) Hybrid glulam with sugi laminae for the inner layers and the Douglas-fir laminae for the outermost layers showed higher Young's modulus and lower creep deflection than the glulam composed of only sugi laminae. However there was no big difference between their relative creep in 50 years, showing the values of approximately "2". (3) The relation between the change of humidity and that of creep deflection was not clear for the symmetry composite glulam, while it was very clear for the asymmetry one.

Key words: creep, sugi, glulam, mechano-sorptive deflection, Young's modulus

1. INTRODUCTION

Glulam used in Japan is mainly applied as columns and beams for Japanese conventional construction today, while it was used as a structural material for large-scale buildings. However, 90% or more of the glulam is composed of imported species of wood [1], and the ratio of domestic wood used in Glulam is very low under the present conditions. Unfortunately, this was caused by the Japanese Agricultural Standards (JAS) of glulam that set the guidelines for the glulam based on the strength ratios of steel used in large-scale construction. In order to compete and perform to the same standards of steel, it was imperative to develop standards for glulam. Therefore, creating higher strength glulam was the top priority when JAS was enacted [2].

To solve this dilemma, Japanese researchers carried out joint research to ascertain that domestic glulam, focusing on using Japanese cedar or known locally as "sugi", has ability to be used as glulam via the data gleaned from this research [3]. One part of this research was to create sugi glulam with extremely low Young's modulus laminae (3-5GPa) used in the inner layer. In fact, sugi with relatively low Young's modulus has been increasing especially in southern Japan because of its mild and humid climate, so we needed to find out the place where this kind of sugi can be effectively used. Data was taken and its mechanical properties were recorded [4-5]. Armed with this new data, the researchers petitioned the Forestry Agency to amend the JAS to include

extremely low Young's modulus laminae (3-5GPa) as inner members of glulam. The agency accepted the researcher's argument and amended the JAS for glulam to reflect the new findings recently. However, the next stage of research mandates long-term performance tests to determine where and how the glulam may be used.

Therefore, we have been conducting bending creep tests for sugi glulam with extremely low Young's modulus laminae for the inner layer, along with the tests for hybrid composite glulam with the Douglas-fir (*Pseudotsuga menziesii* Franco) laminae for the outermost layer and the sugi laminae for the inner layer since October, 2005. As this study is still ongoing, our report will focus on the tendencies of bending creep until October, 2008, along with the comparison of Young's modulus by the lamina's composition carried out in advance.

2. MATERIALS AND METHODS

2.1 Specimens

For the test, 8 different composition glulam beams with the dimensions of 105mm in width, 210mm in depth and 3980mm in length, were prepared (See Fig.1). Here, 6 of them are composed of only sugi laminae, whereas the other 2 beams are hybrid glulam composed of sugi laminae for the inner layers and the Douglas-fir laminae with the Young's modulus of 14-15GPa (L140) for the outermost layers. In this case, 2 out of 6 sugi glulam beams and 2 hybrid glulam beams are symmetric composition with L50 or

L30 as inner laminae. We call them “Sugi L50”, “Sugi L30”, “Hybrid L50” and “Hybrid L30” here. Remaining 4 out of 6 sugi glulam beams are asymmetry with also L50 or L30 as inner laminae. We call the ones with L50 “Sugi LH-L50”, “Sugi HL-L50” and the other ones with L30 “Sugi LH-L30”, “Sugi HL-L30” here. At the same time, these asymmetric beams are also classified into 2 groups by loading directions like “Sugi LH-L30”, “Sugi LH-L50” (loaded from the side of lower Young's modulus) and “Sugi HL-L30”, “Sugi HL-L50” (loaded from the side of higher Young's modulus) as shown in Fig.1. The properties of each glulam are shown in Table 1.

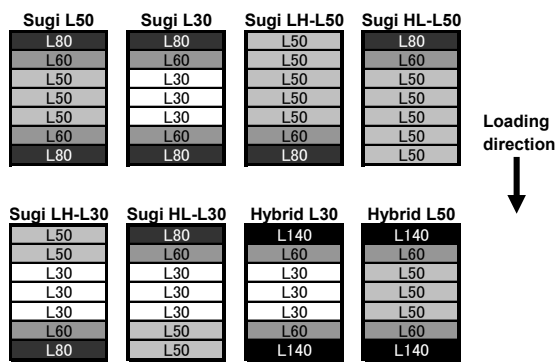


Fig.1. Cross section of glulam with different grade of laminae.

※ The thickness of laminae: 30mm, Species: L140: Douglas-fir, The others: sugi, Dimensions of glulam: 105W×210H×3980L (mm), Adhesive: Resorcinol resin.

Table 1. Properties of glulam.

Classification	Composition	Density (g/cm ³)	MOE (GPa)	MC (%)
Sugi L50	Symmetry	0.463	7.10	14.3
Sugi L30	Symmetry	0.409	6.83	16.3
Sugi LH-L50	Asymmetry	0.446	5.22	9.8
Sugi HL-L50	Asymmetry	0.415	5.34	17.0
Sugi LH-L30	Asymmetry	0.421	5.45	12.3
Sugi HL-L30	Asymmetry	0.431	5.36	10.5
Hybrid L30	Symmetry	0.448	10.8	14.8
Hybrid L50	Symmetry	0.447	10.6	16.0

※ MOE: Young's modulus in bending, MC: Moisture content measured by radio-frequency type moisture meter.

2.2 Bending creep test

Bending creep test has been conducted under 4 point loading conditions with the span lengths of 3655mm, the share span length of 1260mm, and the load span length of 1135mm for about 3 years. In this case, applied load was calculated supposing second floor of two-story general wooden house. Concretely, the load per area was considered as 190kgf/cm² (dead load 60kgf/cm² + live load 130kgf/cm²), then the total load 695kgf was calculated. This calculation method is based on the Building Standards Law in Japan.

The displacement has been measured via a data

logger and displacement transducers (stroke: 50mm) set up at a center, near load points, and fulcrums on the beams at 24-hour intervals. Along with this measurement, temperature and humidity has been measured at the same intervals.

Before the creep test above, effects of composition of laminae and loading direction on Young's modulus were examined in order to clarify the difference of short-term deformation by composition of laminae using the same span condition as the creep test.

3. RESULTS AND DISCUSSIONS

3.1 Effects of composition of laminae and loading direction on bending Young's modulus

Fig.2 shows relationships between the bending Young's modulus when the glulam was loaded from the side of lower Young's modulus (*MOE-LH*) and the side of higher Young's modulus (*MOE-HL*). Here, the data of symmetric composition (Sugi L30, L50 and Hybrid L30, L50) is also plotted to compare with those data.

According to Fig.2, there is almost no difference between the value of *MOE-LH* and *MOE-HL* regardless of the loading directions for the asymmetric glulam or the composition of laminae (symmetry or asymmetry). This result shows that there is no need to consider loading directions to the layer directions of laminae when glulam is installed as a member of constructions at least in terms of short-term conditions.

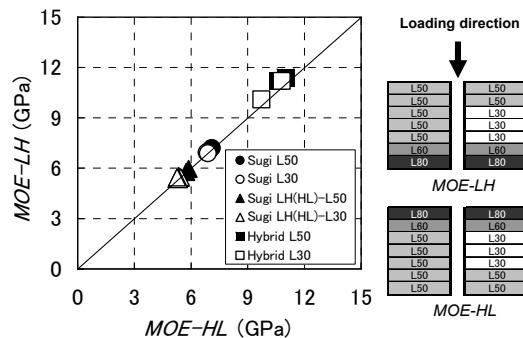


Fig.2. Relationships between the Young's modulus loaded from the side of lower Young's modulus laminae (*MOE-LH*) and the one loaded from the side of higher Young's modulus laminae (*MOE-HL*).

※ ○△□: Glulam used L30 for the Inner Layer, ●▲■: Glulam used L50 for the Inner Layer. ※ Data of symmetrical glulam (●○■□) is also shown for a comparison.

Fig.3 shows relationships between *MOE-LH* and Young's modulus obtained by longitudinal vibration (*Et*). According to this figure, there is almost no difference between the values of *MOE-LH* and *Et* for asymmetric glulam (Sugi LH-L50, L30). However, the

tendency which shows $MOE-LH > Et$ can slightly be recognized for Sugi L50, L30. Furthermore, this tendency becomes conspicuous for Hybrid L50, L30. In this case, $MOEs$ between the glulam with L30 and L50 for the inner layers are very close to each other as shown in this figure (Fig.3), along with Table 1 and Fig. 2.

These results show that the bending Young's modulus of glulam hardly depends on that of inner layer laminae, whereas greatly depends on that of outermost layer laminae.

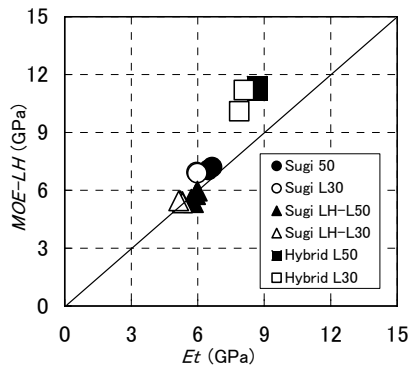


Fig.3. Relationships between $MOE-LH$ and the Young's modulus obtained by longitudinal vibration (Et).

3.2 Effects of composition of laminae and loading direction on bending creep

Fig.4 shows the changes of deflections with loading time. According to this figure, deflections are in order of sugi asymmetric composition, the highest value at the moment, followed by sugi symmetric composition and hybrid one, showing the clear difference from each other. These tendencies seem to make sense, considering the composition of lamina's Young's modulus of each glulam.

Fig.5 shows the changes of relative creep with loading time. Unlike the case of deflections in Fig.4, there is no big difference among the 8 conditions, while the tendency of Sugi L30 is little more stable than others. In both Fig.4 and Fig.5, deflections and relative creep between the glulam with L30 and L50 for the inner layer are not different from each other like the case of $MOEs$ shown in Fig.2.

Incidentally, the right figure in Fig.5 shows that the tendency of increase and decrease between Sugi LH-L50, L30 and Sugi HL-L50, L30 is totally opposite from each other. Namely, the creep recovery and increase in the case of sugi LH-L50, L30 almost correspond to the humidity increase and decrease, while totally opposite behavior is shown in the case of Sugi HL-L50, L30 as shown in Fig 6. Although the cause for these tendencies is not clear at the moment,

it seems that the response of deflection to humidity changes was influenced by lamina's composition, especially the properties of outermost laminae.

These results show that there is no problem to use laminae with extremely low Young's modulus, like L30, as inner layer laminae for not only short-term conditions but also long-term ones, and also shows that the relation between lamina's composition and loading direction should be considered when asymmetric glulam is practically used as a beam.

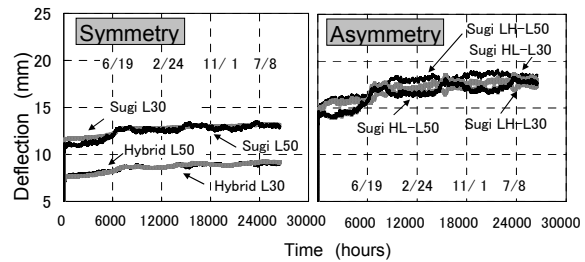


Fig.4. Changes of deflection with loading time.

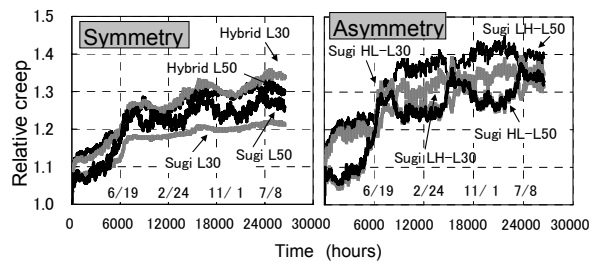


Fig.5. Changes of relative creep with loading time.

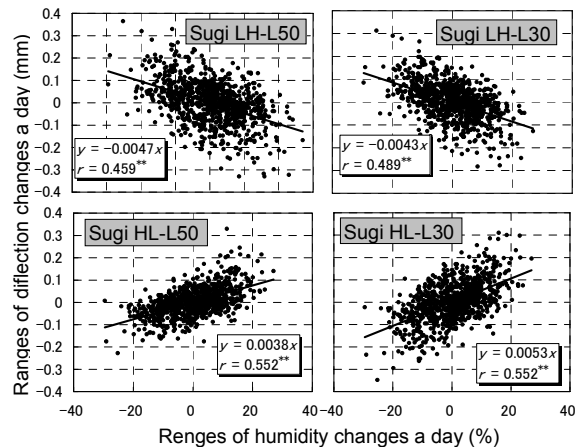


Fig.6. Relationships between ranges of deflection changes and that of humidity changes a day.

3.3 Estimation of bending creep

Fig.7. shows the comparisons between measured creep deflections (black thick lines) and creep deflections calculated by following power law $[\delta_c(t)]$ at the measuring term of 3 months (gray thick lines) and that of 3 years (black thin lines).

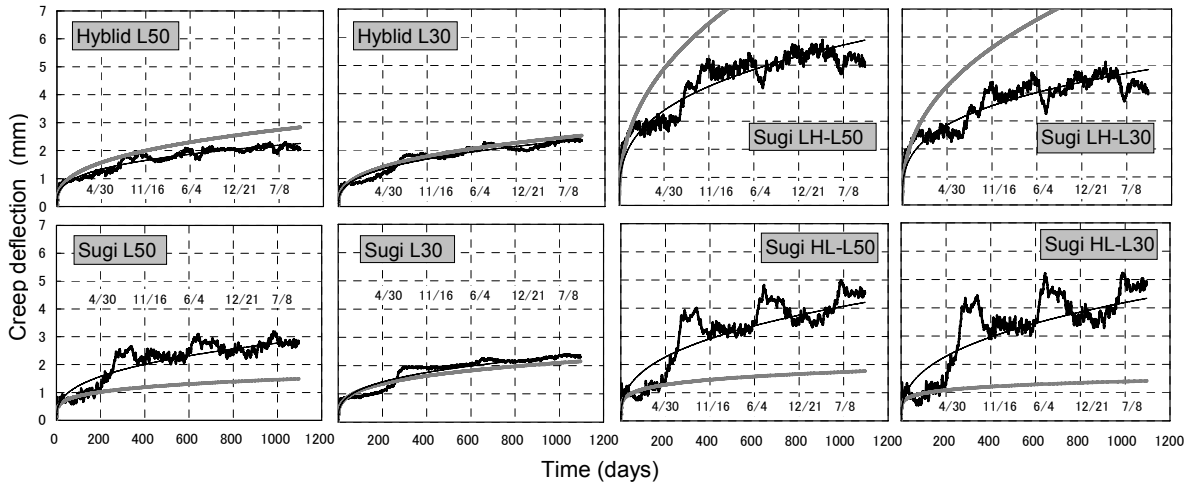


Fig.7. Comparisons between measured creep deflections and creep deflections calculated by power law at the measuring terms of 3 months and 3 years.

※ — : Measured value
 — : Calculated value by power law at the measuring term of 3 months
 - - - : Calculated value by power law at the measuring term of 3 years

$$\delta_c(t) = At^N \quad [1]$$

Here, the constants (A and N) were obtained from the curves from the beginning to each measuring term (3 months or 3 years).

As shown in this figure, it is hard to estimate creep curves by the short-term measurement (3 months), especially in the case of asymmetric glulam shown in the right 4 figures. On the other hand, relatively accurate estimated curves are obtained in the case of the long-term measurement (3 years) regardless of the condition. This result shows that a required experimental term should be cleared to estimate creep curve as efficiently and accurately as possible.

Fig.8 shows the relative creep in 50 years (δ_{50}/δ_0) calculated by equation [2] based on the power law at several measuring terms (1, 3, 6, 9 months, 1, 2, 3 years).

$$\delta_{50}/\delta_0 = 1 + at^N \quad [2]$$

Here, δ_0 is initial deflection, δ_{50} is deflection in 50 years, and a is A/δ_0 , the ratio of creep deflection in 1 day to initial deflection.

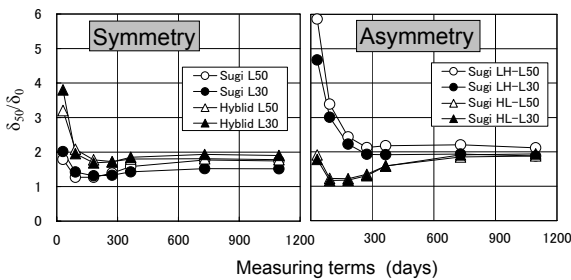


Fig.8. Relative creep in 50 years (δ_{50}/δ_0) calculated by power law at several measuring terms.

As shown in Fig.8., δ_{50}/δ_0 becomes rather stable when the measuring terms are longer than 1 year for the symmetric composition and 2 years for the asymmetric one, showing the values of approximately “2”, which is the standard value set by the Notification No.1459 of the Ministry of Construction in Japan. This result shows that the required experimental term is longer than 1 or 2 years to obtain a reliable estimated value of δ_{50}/δ_0 when this method is taken.

Incidentally, δ_{50}/δ_0 s between the glulam with L30 and L50 for the inner layers are not different from each other like in the case of MOE (See Fig.3).

4. CONCLUSION

The following results were obtained in this test. (1)Considering the bending performance, there is practically no problem to use laminae with extremely low Young's modulus (3-4GPa) for the inner layers regardless of the glulam types. (2)The experimental term should be at least 1 or 2 years to estimate an accurate creep curve when power law is applied.

REFERENCES

[1] F. Kamiya, *Reports of the Forestry and Forest Products Research Institute.*, **68**, (2004).
 [2] F. Kamiya, *JOURNAL OF TIMBER ENGINEERING.*, **63**, 17-20(2005).
 [3] F. Kamiya, *Jyutaku to Mokuzai*, **28**, 14-17 (2005).
 [4] H. Tanaka, H. Morita, Y. Murase, “*Proceeding of 10th World Conference on Timber Engineering, WCTE 2008*, Miyazaki Japan ., 402 (2008).
 [5] A. Matsumoto, H. Morita, Y. Fujimoto, A. Shiiba, Y. Iimura, “*Proceeding of 10th World Conference on Timber Engineering, WCTE 2008*, Miyazaki Japan ., 363 (2008).

(Received December 12, 2008; Accepted September 16, 2009)

Analysis of Allergy from the Standpoint of Ecology -Safety and Clinical Use of Hinokithiol Derived from Aomori Hiba

Fumiko Juji¹, Shigetoshi Kobayashi², Tsutomu Iwata³, Yutaka Morita⁴, Hidemi Nakagawa⁵,

Tooru Fukui⁶, Yoshihiko Inamori⁷ and Toshihiro Okabe⁸

¹Japan Allergy Research Institute, Shinbashi Allergy and Rheumatic Clinic, 2-16-1-318, Tokyo 105-0004, Japan

FAX: 81-3-3591-8404, E-mail: jujif-ky@umin.ac.jp

²Teikyo Medical School, Tokyo 173-8605, Japan

³Tokyo Kasei University, Tokyo 173-8602, Japan

⁴Ochanomizu University, Tokyo 112-8610, Japan

⁵The Jikei University School of Medicine, Tokyo 105-8471, Japan

⁶Byotaiseri Laboratory, Tokyo, 173-0025, Japan

⁷Osaka University of Pharmaceutical Science, Osaka 569-1094, Japan

⁸Aomori Industrial Research Center, Aomori 030-0113, Japan

Recent increases of allergenic diseases are tremendous. Multiple chemical ingredients may possibly be the allergens or deteriorants. We chose the daily used products mainly applied on the skin. This paper shows the safe and proper application of Hinokithiol as for the antiseptics and preservatives.

Hinokithiol (synthetic one, and natural one derived from Aomori-Hiba dissolved in alcohol and Tween, whose concentrations were 0.1%, 0.05%, 0.005%) were patch-tested on 15 healthy adults. Stimulation Indices (SI) were analyzed both after 48 hours and 72 hours. Synthetic Hinokithiol showed the mean SI 11.6 after 48 hours and 4.5 after 72 hours. Natural Hinokithiol dissolved in alcohol showed SI 6.6 after 48 hours and 2.2 after 72 hours. SI by Hinokithiol dissolved in Tween showed 0. For the daily use of products applied on the skin, natural ingredients rather than artificial (synthetic) ones are safer for the skin, especially for allergic patients.

Key word: Allergy, Ecology, Daily use products, Hinokithiol

1. INTRODUCTION

Allergy-strange disease has been increasing tremendously recently [1]. Conventional evaluation and management could show the limit of management. Therefore we introduced new ideas of understanding the allergy, from the standpoint of ecology [2].

Major allergy were 1. Bronchial asthma 2. Allergic rhinitis and 3. Atopic dermatitis.

Major allergens were determined, and elimination is the first procedure as well as immunotherapy and medications. But recently, allergic skin or atopic dermatitis were increasing and some cases were difficult to treat.

Allergens such as inhalants (house dust mite, pollens, or molds) and foods were managed well [3, 4, 5] but we thought there might be some other factors which cause the worsening and deterioration for body surface (=skin).

Therefore we compared the products for daily use on the skin; shampoo, rinse, detergents, soap, cosmetics and house dust mite (*Dermatophagoides pteronissinus*: D. P.) by patch tests. Many chemical ingredients were used which were derived from chemical oil. We happened to know the products from Aomori-Hiba derived Hinokithiol. Which has been coming to be used widely. Therefore we compared the products to show whether it's safer and applicable for the allergic patients.

2. EXPERIMENTAL METHOD

2.1 Method for Patch Test

Patch tests were done using Finn-chamber. 0.03ml of materials were applied on the skin, sealed and after 48 hours and 72 hours reactions were scored by International Contact Dermatitis Research Group (ICDRG) criteria, and SI are calculated.

2.2 Cellular antigen stimulation Test (CAST)

CAST analyses were done using food additives. Peripheral blood was drawn and mononuclear cells were separated. Monosodium glutamate 10^2 , 10^3 , 10^4 , 10^5 ($\mu\text{g/ml}$), Na-anhydride 10 , 10^2 , $10^3\mu\text{g/ml}$, Tartrazine 10 , 10^2 , $10^3\mu\text{g/ml}$ were added for cell suspension. After 48 hours incubation, Leukotrienes C_4 , D_4 , E_4 were measured and SI were calculated, compared to control stimulation.

3. RESULTS

3.1 Comparison of Daily use products

Table 1 shows the results. They showed that shampoo 60%, detergent 56.2% and soap 44.0% positive. Major inhalant allergen, HD mite (D. P.) was 9.5%, which means shampoo, rinse and soap are more affecting rather than major inhalant allergen.

Table 1 Patch Test of Daily use products

	3+	2+	1+	±	0	No. of cases positive	%
Shampoo	5	10	3	4	8	18/30	60.0
Rinse	2	1	1	0	11	5/15	33.3
Detergent							
for dishes	0	7	2	2	11	9/22	40.8
for clothing	2	6	1	5	2	9/16	56.2
Soap	1	10	0	7	7	11/25	44.0
Cosmetics	1	5	1	5	3	27/44	15.9
Others							
house dust	0	1	0	2	12	1/12	0.8
Mite (D.P)	0	2	0	2	17	2/21	9.5

3.2 Comparison of Baby shampoos

The baby shampoos for which pediatricians or dermatologists recommend, and two kinds of herbal shampoos were patch tested. Table 2 shows shampoo E shows less SI after 72 hours. Where is the difference? If one looks at the ingredients, there is the answer. Baby shampoos contain much surfactants, preservatives, coloring and perfume. Herbal shampoo F contains mostly the same. But Herbal shampoo E contains surfactant 1.35% - about 1/10 of usual one. And ingredients come from herbs, coconut oils—all from vegetative origin and Hinokithiol. Therefore we recommend this for the patients. After 4 weeks the skin condition improved 83% or more.

Those results showed daily use of detergents, especially shampoos, could bring irritation of the skin and make symptoms harder and difficult to treat [6].

Table 2 Comparison of Baby Shampoos and Herbal Shampoos by Patch Test

sampoo	Stimulation Index(mean)		Ingredients
	48h	72h	
A	20.5	7.6	Sodium anhydrate, Progprene glycol, Perfume
B	26.5	10.1	Paraben, Perfume, Yellow No.5, Yellow No.203
C	46.1	25.8	Edetic acid, Paraben, Sodium Anhydrate
D	36.1	38.0	Perfume, Edetic acid, Polyoxy-ethylene laureate Dibutyl-hydroxy Toluene Triethanol amine
E	15.4	2.6	Polyoxy-ethylene laureate, Perfume
F	14.1	15.5	Polyoxy-ethylene laureate, Parabene, Salicylate, Dehydro acetic acid, Edetic acid, Dibutyl-hydroxy toluene, Yellow No.4, Green No.3, Perfume

baby shampoo: A, B, C, D herbal shampoo: E, F

3.3 Comparison of Soaps

Next we compared soaps which are recommended to be safer for the allergic skin. Table 3 shows soap E which is made from Hiba-oil shows less SI. That means it is the safest for the skin.

Table 3 Comparison of Soaps by skin irritation

soap	Main Ingredients	SI (48h)	Safety
A	Na laureate	89.8	x
B	Na-glutamate	36.7	x
C	Triethanol amine	22.7	x
D	Arginine	14.6	○
E	Hiba oil	5.7 0 (72h)	○ ◎

SI: Stimulation Index

◎ : safe < 5.0
○ : permitting 5.0 ~ 15.0
△ : doubtful 15.0 ~ 30.0
x : dangerous 30.0 <

3.4 Comparison of bath flavors

Next we compared bath flavors. Table 4 show A and B contain extracts from white cedar (Hiba boiled at 40°C and 50°C extract), C and D are commercial products. One derived from Hiba extracts (A) showed less irritation after 72 hours at 0.01%.

Table 4 Comparison of Bath flavors

Flavor	SI	
	48h	72h
A Hiba-water (40°C, 1h extract)	11.8	5.9
B Hiba-water (50°C, 1h extract)	17.0	29.4
C Hiba-oil	33.3	25.0
D Hiba-water	33.3	8.6
E Garlic extract	33.3	6.6
F Ricebran extract	20.0	10.0
G Herbal extract	30.3	10.0

SI: Stimulation Index (± or more)
safe < 5.0
permitting 5.0 ~ 15.0
doubtful 15.0 ~ 30.0
dangerous 30.0 <

3.5 Comparison of Hinokithiol

Next we compared Hinokithiol. Table 5, A is Hinokithiol synthetic, B derived from Aomori Hiba dissolved in alcohol and C Hinokithiol derived from Aomori Hiba dissolved in Tween. Synthetic Hinokithiol showed higher SI than one derived from Aomori Hiba. Moreover SI by Hinokithiol derived from Aomori Hiba dissolved in Tween are 0 at all the concentration after 48 hours and 72 hours.

Table 5 Comparison of Hinokithiol by Patch Test

	%	48h				72h			
		0.1	0.05	0.005	mean	0.1	0.05	0.005	mean
A	Hinokithiol (synthetic)	—	16.6	6.6	11.6	11.6	6.6	3.3	4.5
B	Hinokithiol (derived from Aomori Hiba Dissolved in Tween)	0	0	0	0	0	0	0	0
C	Hinokithiol (derived from Aomori Hiba Dissolved in alcohol)	6.6	3.3	10	6.6	3.3	3.3	0	2.2

safe < 5.0
 permitting 5.0~15.0
 doubtful 15.0~30.0
 dangerous 30.0 <

3.6 CAST by food additives

Cellular antigen stimulation test (CAST) were developed to analyze unknown causes of allergen such as pseudo-allergen or drugs. We thought it might be helpful to analyze chemicals, especially food additives which cause allergic symptoms.

Patients who showed anaphylactic reactions by food show higher SI and atopic patients show second higher indices compared to control.

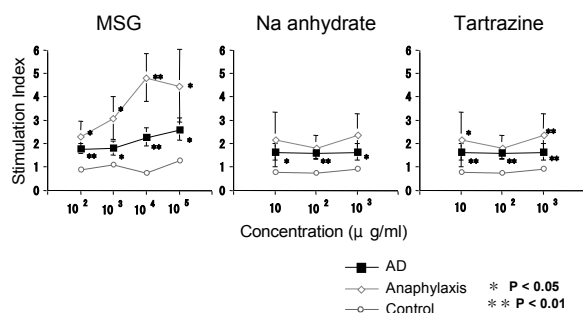


Fig. 1 Cellular antigen Simulation Test (CAST) by Food Additives

Allergic diseases, especially more difficult cases, are increasing although many efforts are proposed. We showed that products used daily could be the irritants for allergic skin, atopic dermatitis. So if one eliminates those irritants, it could bring the symptoms better. So far, allergic disease has been evaluated by inhalants (House dust, mites, pollens...), or foods (egg, milk...), but the involvements of chemical ingredients were very difficult to show. Our papers first showed the involvement of chemical products for the deterioration of allergic skin. Also the food additives contribute to the allergic symptoms. Again if one eliminates food additives, another pollutants, they serve the allergic conditions in better way.

4. CONCLUSIONS

Increases of Allergy were mainly from the environmental pollution such as air pollutant (Diesel Exhaust Particles: DEP, NO_x, SO_x...), food additives and chemical pollutants for daily-use skin products.

Elimination of such pollutants—choosing the safer ingredients could be the important thesis for allergic diseases and decrease of vicious environmental cycle might serve the decrease of allergic diseases.

Hinokithiol first showed us [7, 8, 9] the clues to decrease the environmental pollutant all over. And if one chooses safer materials and safer products, it will contribute to the allergic conditions in better way.

6. Acknowledgement

We are deeply grateful to Mr. Y. Inokuchi (IKEHIKO Corporation, Co.Ltd.), Mr. T. Kabashima for useful suggestions and Ms Yasuko Asada for secretarial help.

7. REFERENCES

- [1] RK. Chandra, B. Gill, S. Kumari.: Food allergy and atopic disease. Clin Rev Allergy Immunol. Vol.13, No.4, 293-314(1995).
- [2] F. Juji et al.: Childhood atopic dermatitis, from the standpoint of Ecology, Allergia No25, 54-57(1996).
- [3] G. Fuglsang, et al.: Adverse reactions to food additives in children with atopic symptoms. Allergy. Vol.49, 31-37(1994).
- [4] B. Wuthrich.: Adverse reactions to food additives. Ann Allergy. Vol.71, No.4, 379-384(1993).
- [5] RW. Weber.: Food additives and allergy. Ann Allergy. Vol.70, No.3, 183-190(1993).
- [6] F. Juji et al.: Pediatrics, No54(12), 2857-2861(1991).
- [7] T. Okabe, et al.: MROMA RESEARCH. Vol.5, No.4, 18-326(2004).
- [8] Y. Inamori, et al.: Biol Pharm Bull. Vol.22, No.9, 990-993(1999).
- [9] JG. Selner.: Unproven Diagnostic and Therapeutic Technique for Allergy in Allergy Principle and Practice (edited by Middleton E, Reed CE, Ellis EF, et al), Mosby, St.Louis. Vol. 1, 1571(1988).

(Received December 12, 2008; Accepted September 16, 2009)

New Utilization Methods of Essential Oils from Woody Biomass

Yoshito Ohtani¹, Pornpun Siramon¹, Rini Pujiarti², and Hideaki Ichiura¹

¹ Kochi University, Nankoku, Kochi 783-8502 Japan

² Gadjah Mada University, Yogyakarta, Indonesia

E-mail: ohtani@kochi-u.ac.jp

The new methods to utilize the essential oil, especially taken from hinoki (*Chamaecyparis obtuse* Endl.) and eucalypt (*Eucalyptus camaldulensis* Dehnh.) were developed in order to raise the total value of hinoki and eucalypt woods. Evaluation and value-added utilization of the essential oils was carried out concerning the chemical recycling of expanded polystyrene (EPS) with essential oil and creating the antifungal and antitermitic agents, cleaning and detoxifying the diesel exhausting gas with hinoki oil fumigant, functional fragrance for human physiological behavior controlling and so on.

Key words: essential oil, *Chamaecyparis obtusa*, *Eucalyptus camaldulensis*, biomass utilization

1. INTRODUCTION

Biomass has drawn a large attention as an eco-friendly resource for energy and chemicals etc. Although woody biomass amounts to more than 90% of global biomass on the land, it is rather difficult to be utilized for many purposes compared to the agro-biomasses.

Hinoki (*Chamaecyparis obtusa* Endl.) and eucalypt (*Eucalyptus camaldulensis* Dehnh.) are typical reforesting tree species in Japan and Thailand¹⁾, respectively. Both trees are planted widely and therefore evaluated as huge promising biomasses. Usually they are used as construction wood and pulpwood, but large amount of wastes including twig, leaves, cutting edges, stumps etc. are generated during harvesting and processing them. The essential oil is a quantitatively minor component (only a few percentages based on the dry woody materials), but it is quite important for not only tree itself but also the other livings²⁾ and is of high price as a commercial product. Woody biomass is expected for energy production, but it may not be still competitive to the fossil oil or coal. That is, the energy such as electricity from it is more costly than that from fossil oil or charcoal. So, to obtain and utilize the essential oils from the wastes enhance the value of whole trees.

Generally essential oils from the woody biomass reveal the notable features of wood, such as aromatics, antiviral, antifungal, antitermitic and insecticidal properties etc.³⁾, and therefore, the attempts to extract the essential oils from woody biomass have recently been carried out in many places. In this report some new utilization methods for the essential oils are introduced and discussed.

2. MATERIALS AND METHODS

2.1 Wood essential oil

Hinoki leaf and wood oils were supplied by Kochi Seiko Co. and Green Co., Kochi, Japan, respectively.

Both oils were obtained by steam distillation of the leaves and the whole woods taken from the thinning trees, respectively. Sugi (*Cryptomeria japonica* D. Don) essential oil was obtained by the steam distillation of the whole wood chips. Eucalypt (*Eucalyptus camaldulensis*) leaves were supplied by Siam Forestry Co. Ltd., Kanchanaburi province, Thailand. Their oils were prepared by water distillation. Both essential oils were analyzed by GC-MS spectroscopy, Shimadzu QP5050A using capillary column, TC-1 0.25mm ϕ x 15m, GL Science Co. The detailed conditions are the same in the previous paper.⁴⁾

2.2 Preparation of the solution of expanded polystyrene (EPS) and essential oil

Bulky EPS was dissolved in the hinoki essential oil. Solution of 25 and 50 w/w% were prepared. Apparent specific gravities of EPS and essential oil are 0.01 and 0.9, respectively.

The solution was applied on the surface of wood samples (sugi wood cubic sample (25 x 25 x 5 mm) and cylindrical sample (8cm ϕ x 30cm)), then the resulting samples were subjected to biological degradation tests in order to evaluate antifungal and antitermitic abilities. They were placed in the bait station set around the termite colony, then their deteriorations were checked periodically.

The fungal growth and termiticidal tests were also conducted on the PDA culture medium and the filter paper in the Petri dishes, respectively.

The PDA culture media were sterilized at 120°C for 30 min, then cooled down. The methanol solution of essential oil was added onto the PDA culture medium and only methanol was volatilized off in the clean bench. The PDA culture media prepared with only methanol were used as the control. The fungi, *Trametes versicolor* NBRC 4937 and *Fomitopsis palustris* NBRC 30339 were inoculated at the center of PDA culture media in

the Petri dishes containing 10 mg/ml of the essential oils, then the colony area were measured at each day for a week as described in the .⁵⁾

Antifungal index was calculated as follow;

$$\text{Antifungal index (\%)} = (1 - Sa/Sb) \times 100$$

Sa: Area of mycelial colony grown with oil sample (cm²)

Sb: Area of mycelial colony grown in control (cm²)

Twenty eight workers and 2 soldiers of *Coptotermes formosanus* Shiraki were introduced onto the filter paper with the essential oil and distilled water in the Petri dish, then the dead termites were counted everyday and the antitermitic activity was determined by the termite mortality.⁴⁾

2.3 Treatment of diesel exhausting gas with hinoki oil fumigant

The diesel exhausting gas was generated by the diesel engine and passed through the apparatus (diameter:32mm, length:10cm) filled with ceramic ball (diameter:3mm, Toyo Denka Co.) and hinoki oil solution (1% in water) at the flow rate of ca. 60 ml/min. The concentrations of diesel gas particulate (DEP), NO_x, CO_x, and SO_x in the diesel gas were measured at the inlet and outlet of the apparatus. Concentration of DEP was measured by digital fine particle counter (Dustmate LD-3K2, Fujirika Co.), NO_x, CO_x and SO_x were evaluated by inspection tubes (Gastech Co.).

2.4 Influence of essential oils on human physiological behaviors

Four kinds of essential oils, hinoki wood, hinoki leaf, sugi wood (Marusichi sangyo Co. Shizuoka), eucalypt leaf oils were utilized. Totally 41 persons (27 males and 14 females) were tested. Before and after sniffing these oils, maximum and minimum blood pressures, pulse rate, stress index, intensities of brain waves were measured. The former three were measured by conventional sphygmometer. The stress index was measured by cocorometer (CM-1.1, NIPRO Co.) based on the amylase activity of saliva.⁶⁾ The intensities of brain waves (α (slow:7-8Hz (α_s), mid:9-11Hz (α_m), fast:12-14Hz (α_f), β (15-23Hz), θ (4-6Hz) - waves) were measured by Mind Sensor II (Noryoku Kaihatsu Kenkyusho Co.). The mental condition was evaluated as the relaxation value = $(3\alpha_m + \alpha_s + \theta) \times 100\%$.

Change in sympathetic nervous action was evaluated by the above parameters. The control tests were also conducted by sniffing the distilled water in place of the essential oils.

All results were statistically evaluated by Excel Statistics for Windows, The Social Information Service Inc., Japan. Significance of difference was calculated by t-test.

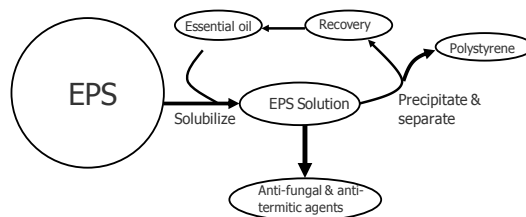
3. RESULTS AND DISCUSSIONS

3.1 Effects of EPS-essential oil solution on antifungal and antitermitic activities

The wood samples were set around the termite colony of *C. formosanus* in the field. Treated and untreated wood blocks were placed together in a bait station. After 1 and 3 months, the untreated wood blocks reduced their weights about 50% by termitic attacks, but the wood blocks coated with EPS-essential oil solution hardly changed even after 3 months. Only the treated wood blocks were wholly covered with frass produced by termites, it means the termites tend to strongly avoid the treated samples.

The cylindric wood samples from thinning forest were subjected to the weather test in the field for three years. After 3 years wood samples had many small cracks, but they were not damaged by biological attacks, like fungal and termitic ones. Hinoki essential oil has a strong antitermitic activity⁷⁾, but even if only hinoki essential oil is applied on surface of the wood sample, it mostly disappears within a few weeks because of its volatility. The polystyrene coating layer formed by EPS-essential oil solution acts as barrier for emission of essential oil, so the essential oil can be maintained on the wood sample and its function is kept for longer time.

The latter scheme shows the chemical recycling system of EPS with hinoki essential oils. In this system the essential oil is able to be utilized repeatedly.⁸⁾



Scheme Recovery of polystyrene from expanded polystyrene (EPS) waste with wood essential oils

Two essential oils were used for antifungal tests against *T. versicolor* and *F. palustris*. The results are shown in Table 1. Growings of two fungi were reduced by each essential oil at 10mg/ml. Especially *F. palustris* was highly inhibited by eucalypt leaf oil. Several other fungi are also tested.⁵⁾

Table 1 Antifungal activities of hinoki leaf oil and eucalypt leaf oil at 10 mg/ml for a week

	Antifungal indices (%)	
	<i>Trametes versicolor</i>	<i>Fomitopsis palustris</i>
Hinoki leaf oil	57.5 ± 2.3	48.5 ± 12.1
Eucalypt leaf oil	39.5 ± 3.9	84.9 ± 2.3

± values mean the standard deviation

3.2 Treatment of diesel exhausting gas with hinoki essential oil

The diesel exhausting gas particulates (DEP) were completely removed by the apparatus tube filled with ceramic balls and hinoki essential oil solution. The microscopic observation indicated that the fine DEP was agglomerated during passing through the vaporized essential oil and easily filtered off. However the

agglomeration mechanism is not known yet, so further investigation is necessary.

The oxygenated nitrogen (NOx) and the carbon monoxide were also effectively removed as described in Fig. 1 and Fig. 2, respectively. The symbols A, B, C mean the concentration of NOx or CO in the gasses passed through (A) ceramic ball only, (B) ceramic ball with water, and (C) ceramic ball with hinoki essential oil solution. It is considered that some components of the essential oil react with the oxygenated nitrogen and the carbon monoxide. Especially the oxygenated nitrogen is effectively removed by this apparatus. Most of NOx in diesel exhausting gas is removed by ceramic balls, furthermore, hinoki essential oil enhances its effect and can completely reduce the NOx. Carbon monoxide (CO) is also effectively removed by ceramic ball and hinoki essential oil.

This technology may be available for cleaning the diesel exhaust gas not only at the exit of muffler but also in the mostly closed spaces such as tunnel, construction site etc. These wide adaptabilities are one of the most advantages of this technology.

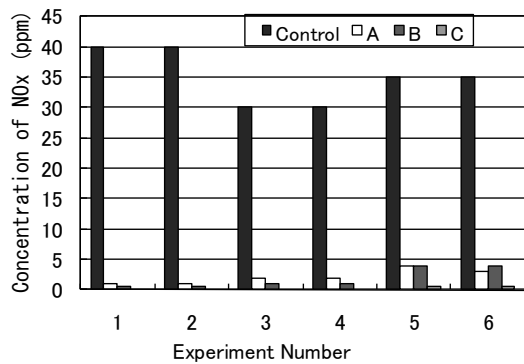


Fig. 1 Concentration of NOx before and after the treatment
 A: Ceramic ball only
 B: Ceramic ball with water
 C: Ceramic ball with hinoki essential oil solution

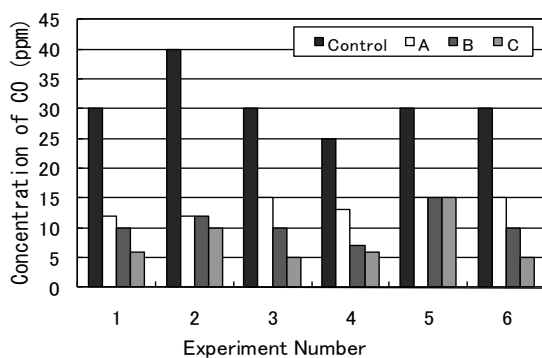


Fig. 2 Concentration of CO before and after treatment
 A: Ceramic ball only
 B: Ceramic ball with water
 C: Ceramic ball with hinoki essential oil solution

3.3 Effect of essential oil on human physiological conditions

Maximum blood pressures before and after sniffing essential oils are shown in Fig. 3. Testing groups were different for each essential oil, so the initial maximum blood pressures were not identical each other. The maximum blood pressure was decreased after sniffing each essential oil. Each essential oil can lower the maximum blood pressure. This effect is statistically significant with 1% level of significance. The minimum blood pressure was also mostly decreased, but its effect was not statistically significant. The pulse rate did not change before and after sniffing the essential oils.

The control test with sniffing the distilled water may indicate an influence of placebo effect. With only sniffing the distilled water, blood pressure and pulse rate were slightly changed, but the effects were negligible small.

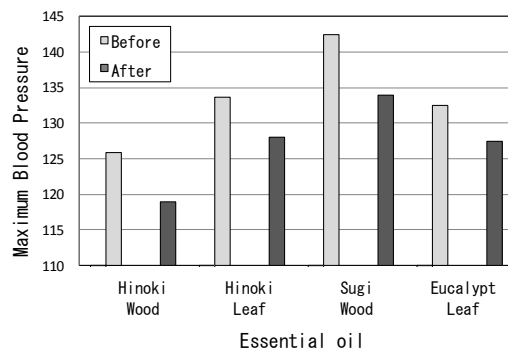


Fig. 3 Maximum blood pressures before and after sniffing several essential oils from hinoki wood, hinoki leaf, sugi wood, eucalypt leaf.

The stress index is evaluated by amylase activity of saliva. Higher values mean to be highly stressed. After sniffing the essential oils of hinoki wood, hinoki leaf and sugi wood, each stress index is decreased as shown in Fig. 4. On the other hand, eucalypt essential oil only increases the stress index. It means some essential oils make human relaxed, but some others give the opposite effects. However, the values of stress index are quite different from person to person, furthermore their changes after sniffing the essential oils largely depend on the individuals. These effects have not been confirmed with statistical significance due to large difference in the individual values so far.

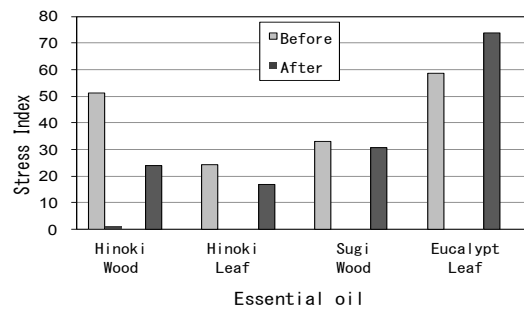


Fig. 4 Stress indices before and after sniffing several essential oils from hinoki wood, hinoki leaf, sugi wood, eucalypt leaf.

Average relaxation values of 27 males before and after sniffing the essential oils are shown in Fig.5. After sniffing the essential oils from hinoki leaf, sugi wood and eucalypt leaf the relaxation values were increased, but only the hinoki wood essential oil didn't show positive effects although it showed very good effects for maximum blood pressure and stress index. Some essential oils are found to exert on strengthening α brain wave.⁹⁾ Hinoki leaf, sugi wood and eucalypt leaf oils can increase α brain wave.

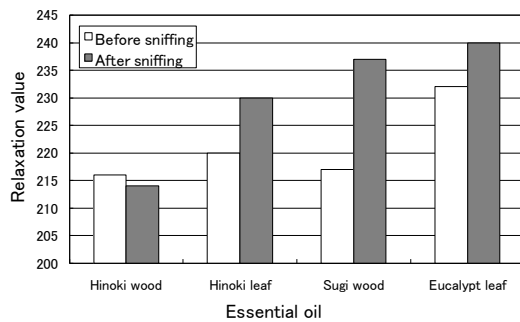


Fig. 5 Average relaxation values of 27 males before and after sniffing the essential oils.

It is found that the maximum blood pressures, stress indices and relaxation values before sniffing the essential oils are quite different. A set of the sniffing tests (before and after) is conducted once per day, therefore it means that these parameters vary daily to large extent. These tendencies may make it difficult to evaluate the physiological effects of the essential oils by statistical calculation.

4. CONCLUSION

New methods for wood essential oil utilization have been developed. They have been revealed effective and useful. Utilization of the essential oils from woody materials is promising for antifungal and antitermitic agents, detoxifying agent of diesel exhausting gasses, functional fragrance etc. The essential oils can be produced from wood processing wastes and before main utilization, such as energy generation, pulping etc. Higher potential of the essential oils enhance the total values of woods, which may be of benefit to the artificial forest management.

ACKNOWLEDGMENT

This work was partially supported by a Grant-in-Aid for Scientific Research from the Ministry of Education, Culture, Sports, Science and Technology, Japan (No. 20580364).

REFERENCES

- 1) P. Siramon and Y. Ohtani: J. Wood Sci. (2007) **53**:498-504
- 2) E. L. Rice: Allelopathy, Academic Press Second edition (1984)
- 3) M. Yatagai: Mori no fushigi, Gendai Shorin, p. 103~108 (1995)

- 4) P. Siramon, Y. Ohtani and H. Ichiura: J. Wood Sci. (2008) **55**:41-46
 - 5) P. Siramon, Y. Ohtani and H. Ichiura: Proc. of Intl. Symp. Wood Sci. Tech., p.311-312, Sept. 27-29, 2008, Harbin, China
 - 6) M. Yamaguchi and H. Yoshida: Chemical Sensors, **21**, 3, 92-98 (2005)
 - 7) Y. Ohtani, M. Hazama and K. Sameshima: Mokuzai Gakkaishi, **43**, 12, 1022-1029 (1997)
 - 8) Japan Patent Kokai: 2006-160648
 - 9) F. Yamashita et. al.: Japanese J. Aromatherapy, **7**, 1, 15-28 (2007)
- (Received December 12, 2008; Accepted September 16, 2009)

Cellulose / Copper Blend and Porous Copper Prepared by Mechano-Chemical Treatments

Hitomi Miyamoto, Chisato Ueda, Chihiro Yamane, Mariko Ago*, Kunihiro Okajima*, Takashi Endo**, Makiko Hattori***

Faculty of Home Economics, Kobe Women's University, Aoyama 2-1, Higashisuma Suma-ku, Kobe 654-8585, Japan

FAX:81-78-732-5161, e-mail: yamane@suma.kobe-wu.ac.jp

*Faculty of Engineering, Tokushima Bunri University, Shido 1314-1, Sanuki-shi, Kagawa 100-0004, Japan

FAX:81-87-894-4201, e-mail: okajima@fe.bunri-u.ac.jp

** Advanced Industrial Science and Technology, 2-2-2, Hiro-suehiro Kure, Hiroshima 737-0197 Japan

FAX:81-823-72-1990, e-mail: t-endo@aist.go.jp

*** Central R&D Laboratories, Asahi Kasei Corporation, 2-1, Samejima, Fuji, Shizuoka, 416-8501, Japan

FAX:81-545-62-3179, e-mail: hattori.mb@om.asahi-kasei.co.jp

A cellulose/copper blend was prepared by a mechano-chemical treatment using a high-speed ball mill called a planetary mill. Cellulose and copper in the blend were mixed in the submicron scale, as observed by scanning probe microscopy using the surface potential microscopic mode. The treatment made the cellulose crystal almost amorphous while the molecular weight of the cellulose retained 70% of its original value. X-ray diffraction patterns of the copper remained unchanged. Removal of cellulose from the blend by firing or enzymatic decomposition yielded porous copper, the surface area of which was 18 m²/g. The copper fragments appeared not to be isolated but rather were connected to each other at junction points. Such a porous structure must prevent cohesion of each metal fragment to retain its effective surface area. Many nano-metals have a problem, in that the cohesion of the particles decreases their apparent surface area resulting in a decrease in the efficiency for their practical use. Therefore, if porous metals prepared by this method are applied as catalysts or electrodes, a high efficiency can be expected.

Key words: cellulose, mechano-chemical, blend, metals, composite

1. INTRODUCTION

Mechanical alloying has been widely studied for many materials, such as metal alloys and polymer blends, because of the wide range of its applicability. Conventional polymer blends are mainly prepared from the melt mixtures of the polymers or solutions, which require the polymers to be melts or co-solvents of them. Cellulose is thus not suitable as a material for such blendings because it can not melt under the temperature of thermal decomposition and has few co-solvents with commonly used polymers. Mechanical alloying however has been used for forming blends whose components are not chemically miscible with each other. Blends of cellulose and thermoplastic polymers were recently prepared for the first time by mechano-chemical treatment using a high-speed ball mill called a planetary mill^{1, 2}. By the treatment, the blends with cellulose content over 80% were thermally flow-able as to be applied to injection molding. It is to be noted that blends mixed by a conventional extruder cannot be shaped by

injection molding. In this context, mechanical alloying offers a new avenue for preparing polymer/metal blends with fine dispersion.

Recently, polymer/metal nano-composites have been prepared using various methods, including (1) evaporation of metals on a polymer surface followed by dispersion into the polymer by molecular movement of the polymer segments above the glass transition temperature^{3,4}; (2) independently evaporating organic and metallic raw materials and thereby covering the metal with the organic material⁵; (3) selective localization of metal particles in a polymer domain using a micro-phase separation method⁶; (4) absorption of hydrophobic parts of polymers on a metal surface forming a polymer/metal composite in order to prevent aggregation of these metals⁷. Various additional studies relating to polymer/metal nano-composites have been conducted, and a complete review is beyond the scope of this paper. However, it is to be noted that mechanical alloying has not been attempted thus far to prepare polymer/metal composites.

In this study, we prepared cellulose/copper blends using a planetary mill and examined the structure of the blends. In addition, porous copper prepared by removing cellulose from the blend by firing or enzymatic decomposition was also investigated.

2. EXPERIMENTAL

2.1 Blend of Copper and Cellulose

Copper powder, under 80 μm in diameter, prepared using an atomizing method was purchased from Kojundo Chemical Laboratory Co Ltd., Japan. Cellulose powder supplied by Whatman International Ltd., England, was used as the cellulose sample; the sample name was CF-11. Fourteen grams of copper, 6 g of cellulose and 25 zirconia balls (20-mm diameter) were placed in a zirconia vessel with a 500 ml volume. The vessel was set in the high-speed ball mill (Model P-5, Fritsch GmbH, Germany) and subjected to planetary motion capable of moving the balls with a high acceleration over 10 times the gravitational acceleration. The copper and cellulose mixture was ball milled using this apparatus at 250 rpm, which is equivalent to 10 times the acceleration of gravity, at under 80°C for given times. This treatment was conducted intermittently, 30 minutes running followed by a 15 minute pause, such that the sample temperature did not exceed 80°C.

2.2 Preparations of Porous Copper

Porous copper was prepared by removing cellulose from the blend. Two methods were employed to remove cellulose. In the first method, the copper and cellulose blend was fired at 600°C for 3 hours to remove the cellulose. In the second method, the copper and cellulose blend was treated with 1 wt% aq. cellulase (Onozuka R-10 derived from *Trichoderma viride*, Yakult Co. Ltd., Japan) at 50°C and at a pH of 4.5 in an acetic acid buffer (0.1 N acetic acid / 0.1 N sodium acetate = 10/7 v/v) for one week. Complete removal of cellulose from the blend was confirmed by the weight loss of the sample, equal to the cellulose content in the blend.

2.3 Measurements

Scanning Electron Microscopy (SEM): The blend of copper and cellulose was observed using a S-4700 (Hitachi, Ltd.) SEM operated at an accelerating voltage of 15 kV. This microscope is also equipped with an energy dispersive X-ray micro analyzer (EMAX-7000, HORIBA, Ltd.).

Scanning Probe Microscopy (SPM): The blend sample was placed on a stainless steel sample holder covered with carbon paste, and observed with a scanning probe microscope (Nano Scope IV D3100 with Cr/Au coated probes named MESP, Veeco Instruments Inc.) using a surface potential microscopic mode (SPoM).

Wide-Angle X-ray Diffraction: X-ray diffraction patterns were measured using a reflection

method and recorded on an X-ray diffraction apparatus with a scintillation counter (Rotaflex Ru-200PL, Rigaku Denki Co. Ltd., Japan) with an inner reference (SiO_2 ; $2\theta = 28.45^\circ$).

Surface Area: The surface area of the porous copper was measured by the amount of nitrogen adsorbed on the surface of the copper, which is known as the Brunauer-Emmett-Teller (BET) method⁸, using a NOVA2200e apparatus (Quantachrome Instruments, USA).

3. RESULTS AND DISCUSSION

3.1 Scanning Electron Microscopy (SEM)

Figure 1 shows an SEM image of the blended particles of copper and cellulose prepared by the high-speed ball milling for 3 hours. The sizes of these particles ranged from 4.7 μm to 58.6 μm , which average out to 18.8(11.2) μm calculated from randomly selected 100 particles; the size of a particle is the average of the longest and shortest length of the particle and the value in parenthesis represents the standard deviation.



Fig.1 SEM image of cellulose/copper blend prepared by the high speed ball milling for 3 hour

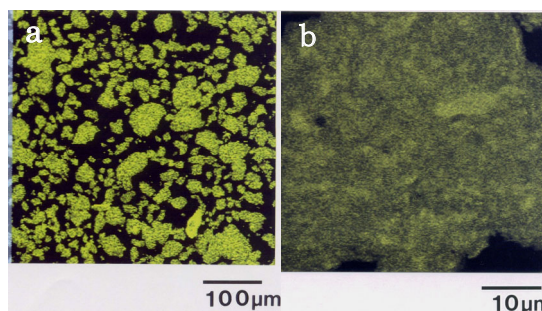


Fig.2 Distribution maps of cellulose / copper blend observed with energy dispersive X-ray micro analyzer.

Figure 2a shows the distribution map of copper for the same image shown in Figure 1. Yellow indicates domains where copper exists. The yellow regions had the same shapes as the particles shown in Figure 1, meaning that

copper fragments were distributed homogeneously in the particles. A magnified view of the copper distribution shown in Figure 2b also indicates the homogeneous existence of copper. However, the resolution of the apparatus used for this copper mapping was not so high (about 1 μm) as to examine the blended state of copper and cellulose.

3.2 Scanning Probe Microscopy (SPM)

The copper/cellulose blend materials were imaged by SPM using the surface potential microscopic mode. This mode can distinguish between copper and cellulose because the electrostatic potentials of the two materials are very different. In the SPM image (Figure 3), the black and white parts indicate copper and cellulose, respectively. The copper fragments were dispersed in the cellulose matrix in the sub-micron and nanometer scale. During the high-speed milling, the impact of heavy ceramic balls possibly caused amalgamations of copper and cellulose followed by breakdown of the fused pieces. It seemed reasonable to assume that the countless repeats of amalgamations and breakdowns mixed the copper/cellulose blend materials together on a sub-micron scale. The highest surface energy of cellulose (45 mN/m)⁹ among polymers probably provides strong contact between cellulose and copper. If it were not for the strong interaction between cellulose and copper, the two materials would be divided along the interface and would not be blended in this small scale. This is the main reason to use cellulose as the first polymer material for this study. When the copper alone was treated by the high speed ball milling for 3 hours, the size of the copper particles did not reduce, but became much larger, up to 0.2 – 0.5 mm, with a scale-like shape. This is probably due to the ductility of copper, which makes the copper powders stick together to form larger granules rather than being crushed to small pieces.

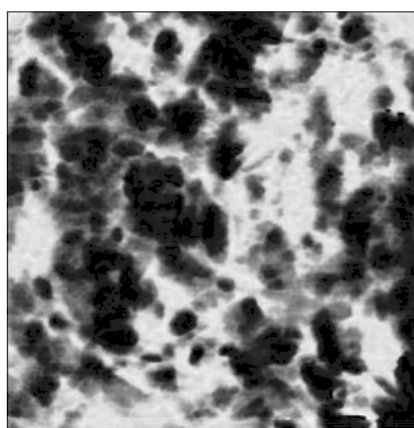


Fig.3 SPM image of cellulose/copper blend using surface potential microscopic mode.

3.2 Structural change during high-speed ball milling

Figure 4 shows changes in the X-ray diffraction patterns of cellulose during high-speed ball milling. Clear diffraction peaks from the (1-10), (110) and (200) crystal planes of the cellulose I crystal from the lower diffraction angle were observed for the original cellulose (Figure 4(a)). The diffraction peaks abruptly decreased after a 10 minute treatment (Figure 4(b)) leading to one broad peak after 2-3 hours treatment (Figure 4(d,e)). In spite of the drastic change in crystallinity, decreases in molecular weight (M_w) were not very high, i.e., 36,700 for original cellulose, 26,100 for 2 hour ball milling and 26,200 for 3 hour ball milling. On the other hand, the X-ray diffraction pattern of copper remained unchanged even for the 3 hour treatment. The diffraction peak at $2\theta = 28.45^\circ$ is from SiO_2 used as an internal reference.

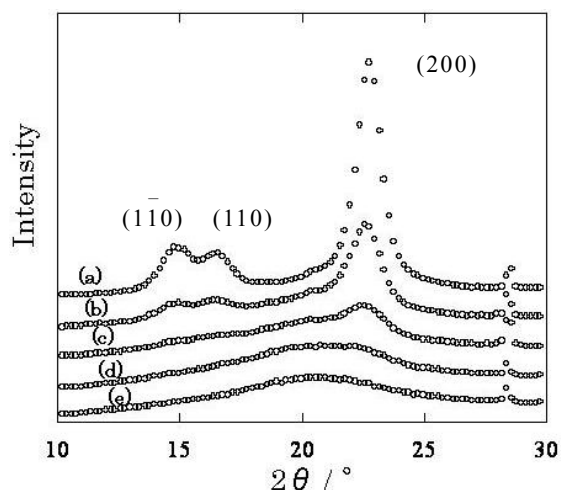


Fig.4 Changes in X-ray diffraction patterns of cellulose during high speed ball milling: (a), original cellulose; (b), ball milled for 10min.; (c), 30min.; (d), 2 hr.; (e), 3 hr.

3.3 Porous Copper

When cellulose in the blend materials was removed by firing or enzyme decomposition, porous copper could be obtained. Figure 5 shows an SEM image of porous copper prepared by firing at 600°C for 3 hours. The starting blend material subjected to firing was the same one shown in Figures 1 – 3. The surface area of the fired particles was 9.60 m^2/g , which was much higher than that of the starting copper powder (0.3 m^2/g) prepared by an atomizing method. Every copper fragment seemed to be connected by sintering. It is not surprising that sintering took place at a far lower temperature (600°C) than the melting point of copper (1085°C), because the melting temperature decreases with decreasing size; for instance, the melting point of bulk gold (1064°C) decreases to 330°C for gold particles with a diameter of 2 nm ¹⁰. This suggests that the copper fragments in the blend materials include very small ones.

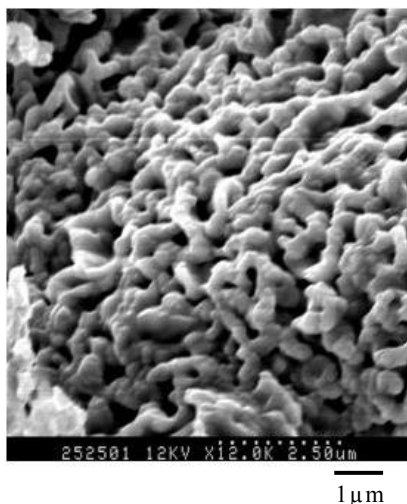


Fig.5 The SEM image of porous copper prepared by firing at 600°C for 3 hour in order to remove cellulose from the blend.

Porous copper can also be prepared by another method. Figure 6 shows the porous copper obtained from the same blend particles as the ones mentioned above using enzymatic decomposition of cellulose. The surface area of these particles was 18.32 m²/g, which was higher than that of the fired particles (9.60 m²/g), probably because no sintering occurred during the enzyme treatment. The shape and the size of the copper fragments were almost the same as those shown in Figure 3, indicating that Figure 6 shows the skeleton of the copper buried in the cellulose matrix.

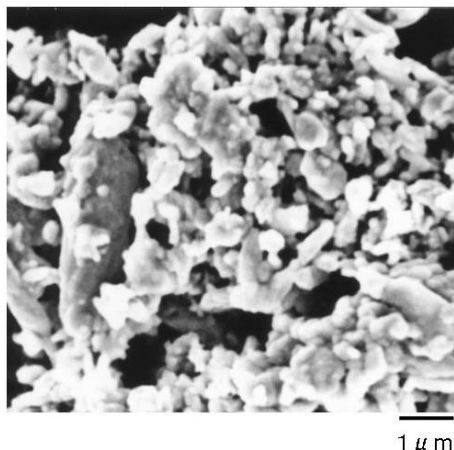


Fig.6 The SEM image of porous copper prepared by enzymatic decomposition of cellulose.

A closer look at Figure 6 shows some junction points present among the copper fragments. In addition to this, the blending mechanism, amalgamations and breakdowns, support the possibility that the copper fragments were not isolated from each other but rather were connected to each other at the junction points. Therefore, such a porous structure must prevent

cohesion of the metal fragments to retain its effective surface area. Various nano-metals have a problem that needs to be solved, that is, cohesion of the particles decreases the apparent surface area resulting in a decrease in the efficiency for their fine use. Therefore, if the porous metals prepared by this method are applied as catalysts or electrodes, a high efficiency can be expected and anticipated.

4. REFERENCES

1. T. Endo, R. Kitagawa, F. Zhang, T. Hirotsu and J. Hosokawa, *Chem. Lett.*, 1155(1999).
2. H. Kitagawa, M. Iseya, N. Kubo, T. Endo, K. Moriya and K. Okita, Woody Composition for Molding and Its Manufacturing Method, publication number (2002-225011), Japan, date of publication of application, 14/08/2002.
3. Y. Yamaguchi, T. Noguchi and K. Goto, *Sen-i Gakkaishi* (Journal of the Society of Fiber Science and Technology, Japan), **49**, 124(1993).
4. Y. Nakamichi, Preparation of Polymer/Metal Cluster Composite; patent number (3062748), Japan, issue date 10/03/1999.
5. J. Hasegawa, M. Ito, K. Niihara, T. Nakayama, Method for Manufacturing Composite Material, publication number (2006-089523), Japan, date of publication of application, 06/04/2006.
6. R. Saito and K. Ishizu, *Polymer*, **33**, 1099(1992).
7. M. Harada, K. Asakura, Y. Ueki and N. Toshima, *J. Phys. Chem.*, **98**, 2653(1994).
8. S. Brunaur, P.H. Emmett and E. Teller, *J. Amer. Chem. Soc.*, **60**, 309(1938).
9. "Polymer Handbook - Fourth Edition -", Ed. by J. Brandrup, E.H. Immergut, and E.A. Grulke, Wiley Interscience, (1999) p.VI 533.
10. P. Buffat and J. Borel, *Physical Review A*, **13**, 2287-2298(1976).

(Received December 12, 2008; Accepted September 16, 2009)

Potential of bamboo forest as molecule forming fields

Hao REN and Masamitsu FUNAOKA

Graduate School of Bioresources, Mie University, 1577 Kurima-machiya, Tsu, Mie, 514-8507, Japan

Fax: 81-59-231-9517, e-mail: funaoka@bio.mie-u.ac.jp

In this study, the structural characteristics of bamboo lignophenol were discussed in detail. As a part of *p*-hydroxyphenolic units (H units) esterified to native core lignin still remained in ligno-*p*-cresols, the separation of H units from core lignin has been done in alkali conditions. The structure analysis of hydrolyzed H units is done with UV spectroscopy measurement (UV), Fourier Transform Infrared (FT-IR) etc.. They are composed of *p*-coumaric acid, ferulic acid and 4-hydroxybenzoic acid. *p*-Coumaric acid has antioxidant properties; ferulic acid, being highly abundant, may be useful as a precursor in the synthetic chemistry industry; *p*-hydroxybenzoic acid is primarily known as the basis for the preparation of cosmetics. That is, *p*-coumaric acid and ferulic acid and *p*-hydroxybenzoic acid are important as the industrial raw materials such as the medicine, the spices, and cosmetics. Therefore, the potential of bamboo forest as a sustainable molecule forming fields can be evaluated through the phase-separation system by the performance analysis on a molecular refining characteristics.

Key words: bamboo forest, ligno-*p*-cresol, H-units, molecular forming fields

1. INTRODUCTION

Recently environmental protection and sustainable development have been considered significant. It is very important to exploit biomaterials instead of petrochemical resources. Bamboo species are distributed throughout the tropics, subtropics and temperate zones in the world. Due to its low cost, utilization of bamboo has attracted increasing attention in the world. However, the research is limited to carbohydrates, and completely effective use of the bamboo resources has not been achieved yet.

In the concrete, the accumulation of bamboo in Japan is in the range of 3~3.6 million tons in the dry weight. It is estimated to be 360 million tons as an amount of the resource in the world. The annual production of bamboo is 20-30 tons/ 100-120 tons of present stock. It is higher than either of the rainforest, temperate-zone hardwood forest and field of grass [1]

In our previous study, the conversion and separation patterns of bamboo lignocellulosics through the phase-separation system have been investigated. Through short time phase-separation treatment without ultrasonic irradiation, bamboo lignocellulosics were separated into carbohydrates and ligno-*p*-cresols more rapidly than woody materials. The yield of ligno-*p*-cresols (ether insoluble) derived from bamboo is ca. 80% to its Klason lignin, and the other ca. 20% is ether soluble. The yield of carbohydrates derived from bamboo is nearly 100% to holocellulose [2]. The ¹H-NMR (Nuclear Magnetic Resonance), FT-IR (Fourier Transform Infrared absorption spectrum), pyrolysis GC/MS (Gas Chromatography/Mass) and TMA (Thermo mechanical analysis) analytical data indicated that the

characteristics of bamboo ligno-*p*-cresols were basically similar to hardwood ligno-*p*-cresols. However, a part of *p*-hydroxyphenolic acid in bamboo lignins remained in the molecule even after phase-separation treatment, due to the solvation effect of cresol [3,4]. Bamboo ligno-*p*-cresols had high protein-adsorption capacities, comparable to wood ligno-*p*-cresols, which were 5~10 times higher than conventional lignin preparations.

In conventional researches, it has been known as a unique feature of bamboo and grass lignins that they contain 5-10% of esters of *p*-coumaric acid accompanied by ferulic acid in small amounts [5]. The occurrence of the esters of *p*-coumaric acid in bamboo was demonstrated by Shimada et al., in indicating that the majority of *p*-coumaric molecules in bamboo and grass lignins are linked to the α -position of the side chain of lignin molecules [3].

Furthermore, in this study, the structural characteristics of bamboo ligno-*p*-cresols were discussed in detail. As a part of *p*-hydroxyphenolic units (H units) esterified to native core lignin still remained in ligno-*p*-cresols, the separation of H units from core lignin has been done in alkali conditions. The structure analysis of hydrolyzed H units is done with UV spectroscopy measurement. Bamboo species are distributed throughout the tropics, subtropics and temperate zones of the world. Many bamboo species, ca 1000 species and 100 genera are known [6,7]. They generally possess some unique features in common, such as the culms are connected by dense rhizomes, new culms are reproduced asexually every year with a rapid growth rate, culms do not carry out secondary growth and sexual reproduction is conducted at long intervals ranging from 3 to 120 years

[8]. The genus *Phyllostachys* is one of the largest genera of bamboo and about 30 species are known in the East Asia [9]. The accumulation of bamboo in Japan is in the range of 3 ~ 3.6 million tons in the dry weight. It is estimated to be 360 million tons as an amount of the resource in the world. The year production of bamboo is 20-30 ton/ 100-120 ton. It is higher than either of the rainforest, temperate-zone hardwood forest and field of grass [10,11].

The potential of bamboo forest as a sustainable molecule forming fields is evaluated through the phase-separation system by the performance analysis on molecular refining characteristics.

2. EXPERIMENTS

2.1 Alkaline hydrolysis

Bamboo ligno-*p*-cresols (500 mg) was dissolved in 200 mL of 1N NaOH solution was kept for 72 hrs at 40°C. The solution was acidified (PH=4) with 1N HCl and the precipitate was filtered off. Lignin residue was washed with a small amount of hot water. Filtrate and washings were combined and extracted with ether (100 mL×4). The ether layer was extracted with saturated NaHCO₃ solution (100 mL×5), and the aqueous layer was acidified with conc. HCl and re-extracted with ether (100 mL×4). The ether fraction was then washed with saturated NaCl solution and dried over anhydrous Na₂SO₄. Removed of the solvent in vacuo gave crude crystals of *p*-coumaric acid (*p*-CA), which were determined by measurement of the absorbance at 336 nm in the alkaline 2-methoxyethanol solution [4]. The ligno-*p*-cresols received after alkaline hydrolysis is called for sap-ligno-*p*-cresols in this study.

2.2 NaBH₄-reduction difference curves

To 10 mg ligno samples (bamboo ligno-*p*-cresols and bamboo sap-ligno-*p*-cresols), 0.1 N NaOH solution was used to measure it up to 25 mL, which was defined as original solution. Furthermore, 3 mL original solutions was diluted to 25 mL with 0.1 N NaOH as reference solution. On the other, 3 mL original solutions was added in 0.6 mg NaBH₄ and then diluted into 25 mL with 0.1 N NaOH solution as reduced solution. The NaBH₄-reduction difference curves were measured on a JASCO V-560 spectrophotometer. They are measured continuously in wavelength region of 200-600 nm [12,13].

2.3 FT-IR spectra

FT-IR spectra were obtained on Perkin Elmer Spectrum GX FT-IR Spectroscopy using KBr discs (sample: KBr=3 mg; 200 mg). The spectra were recorded in the range from 400 to 4000 cm⁻¹ with a resolution of 4 cm⁻¹ over 32 scans. The regions from 1600 to 1700 cm⁻¹ of FT-IR spectra were compared between bamboo ligno-*p*-cresols and bamboo sap-ligno-*p*-cresols.

2.4 UV-Vis spectra

Ultraviolet and Visible spectra of bamboo sap-ligno-*p*-cresols were determined on a JASCO V-560 spectrophotometer. They are measured continuously in the wavelength region of 200-600 nm. The absorbance at 300-400 nm was compared to original spectrum.

2.5 Thermo mechanical analysis (TMA)

Thermo mechanical analyses of ligno-*p*-cresols were performed on a SEIKO EXSTAR 6000 TMA/SS. The method for measurement was the same with that in [2]. The solid-liquid transitions of sap-ligno-*p*-cresols were measured by programmed heating from 50 to 250°C (2°C/min) under 200 mL/min of N₂.

2.6 Molecular weight distribution of bamboo sap-ligno-*p*-cresols

Gel permeation chromatography (GPC) of ligno-*p*-cresols was determined on SHIMADZU CLASS LC-10 system in the same conditions with ligno-*p*-cresols [2].

3. RESULTS AND DISCUSSION

It has been known that *p*-coumaric acids (*p*-CA) is connected to bamboo and grass lignins through an ester linkage [5,14,15]. Nakatsubo et al. [16] recently reported that several aliphatic carboxylic acids were introduced to α -position of quinonemethide of guaiacylcerol- β -aiacyl ether which is a model compound of an important intermediate in dehydropolymerization of lignin monomers. According to the reaction mechanism between quinonemethide and carboxylic acid, *p*-CA is possibly incorporated to α -position of the lignin side chain. On the other hand, Shimada et al. [3] indicated from the modification reactions of lignin that the major portion of *p*-CA in bamboo lignin is linked to the terminal γ -carbon of side chain, although the minor portion of *p*-CA is present at α -position. Furthermore, the amounts of α - and γ -esters of *p*-CA in bamboo MWL (Milled Wood Lignin) had been estimated on the basis of the results obtained using model compounds. The results suggested that the portion (about 80%) was esterified with γ -hydroxyl groups of side chains, especially of α , β -saturated ones, in lignin molecules [17]. Our researches indicated that the characteristics of bamboo ligno-*p*-cresols are similar to hardwood ligno-*p*-cresols, however a part of esterified *p*-hydroxyphenolic acids remained. In this study, the structure characteristics of bamboo ligno-*p*-cresols was analyzed with alkaline hydrolysis in more detailedly.

3.1 Yield of bamboo sap-ligno-*p*-cresols and H units

After the bamboo ligno-*p*-cresols (500 mg) treated with alkaline hydrolysis as shown in 2.1, the weight of insoluble lignin residue was 288 mg, the yield of bamboo sap-ligno-*p*-cresols was 57.6%. The structure characteristics of separated H units was analyzed with UV-vis spectra, but the quantification was difficult to do in fluffy for the two many steps of extracting it.

3.2 NaBH₄-reduction difference curves

The original bamboo ligno-*p*-cresols and bamboo sap-ligno-*p*-cresols were treated with NaBH₄ in alkaline conditions. The NaBH₄-reduction difference spectra were compared with each other (Fig.1). Both the original sample and sap-ligno-*p*-cresols can not be detected absorption after one hour reduction treatment. However, after 24 hours and 48 hours respectively, shoulder peaks were observed obviously at 310-360 nm of the original sample, smaller absorptions

were observed at the same region of the saponification

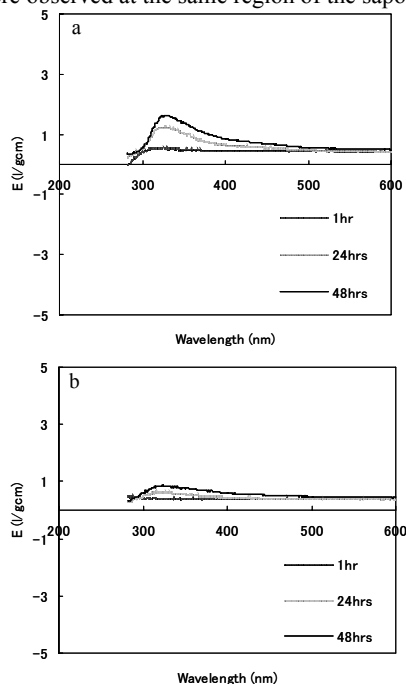


Fig.1 NaBH_4 -reduction difference of bamboo original (a) and sap-ligno-*p*-cresols (b). Reduction treatment time is 1hr, 24hrs and 48 hrs respectively.

samples. The esterified *p*-hydroxyphenolic acids in the γ -position were separated from core lignin through the alkaline hydrolysis. But a few of phenolic aryl- α -CO groups might not be hydrolyzed in the alkaline condition, so that the smaller absorptions were seen. This is based on the conclusion that NaBH_4 reduction method differentiated between different types of conjugated CO groups present in MWL [18]. Etherified aryl- α -CO groups and coniferylaldehyde group are reduced very quickly, while the reduction of phenolic aryl- α -CO groups might take several days.

3.3 FT-IR spectra

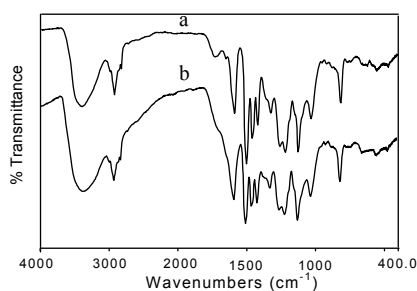


Fig.2 FT-IR spectra of bamboo original (a) and sap-ligno-*p*-cresols (b).

In our conventional studies, it was reported that a distinct C=O vibration belonging to carboxyl or ester group at 1730 cm^{-1} is found in bamboo ligno-*p*-cresols, the peak was disappeared completely after alkaline hydrolysis (Fig.2b). It can be concluded that the separation of *p*-hydroxyphenolic acid from bamboo core lignin had been succeeded.

3.4 UV-Vis spectra

As same as original bamboo ligno-*p*-cresols, UV-vis spectrum of bamboo sap-ligno-*p*-cresols was characterized by a sharp band at 280 nm, a shoulder at 300-370 nm was not observed (Fig.3). The UV-vis spectrum pattern of bamboo sap-ligno-*p*-cresols is agreeable to its of softwood ligno-*p*-cresols. That is to say, bamboo ligno-*p*-cresols have the addition structure of a useful mono-phenol to the core lignin by the ester bond. It is possible to separate it according to the purpose.

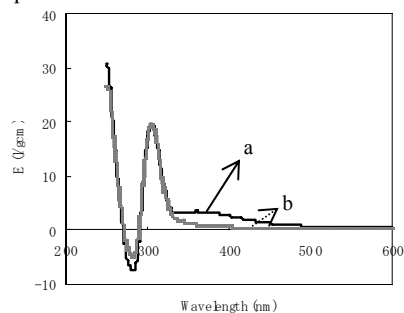


Fig.3 UV spectra of bamboo original (a) and sap-ligno-*p*-cresols (b).

3.5 Thermo mechanical analysis (TMA)

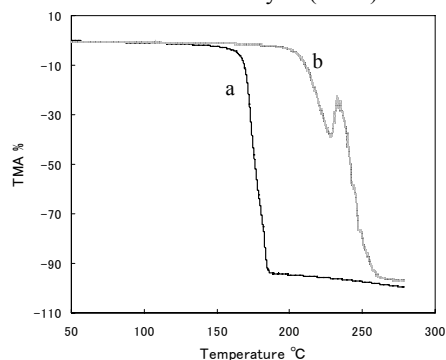


Fig.4 TMA profiles of original bamboo ligno-*p*-cresols (a) and sap-ligno-*p*-cresols (b).

The TMA curves of bamboo sap-ligno-*p*-cresols revealed volume decreasing at $205\text{ }^\circ\text{C}$ due to the solid/liquid phase transition. The transition points of bamboo sap-ligno-*p*-cresols showed $30\text{ }^\circ\text{C}$ higher values than bamboo original ligno-*p*-cresols. After saponification treatment, the ester bonds posited in -carbon were cleaved, and many aliphatic hydroxyl groups were exposed. The H bonds between the hydroxyl groups made to have so higher solid/liquid phase transition point.

3.6 Molecular weight distribution of bamboo sap-ligno-*p*-cresols

Weight average molecular weight (Mw) of original bamboo ligno-*p*-cresols are 3877, number-average molecular weight (Mn) is 2243, polydispersity $\text{Mw}/\text{Mn}=1.73$. Mw of bamboo sap-ligno-*p*-cresols is 2839, Mn is 1621, polydispersity $\text{Mw}/\text{Mn}=1.75$. Weight average molecular weight of bamboo sap-ligno-*p*-cresols is a little lower than bamboo ligno-*p*-cresols for the reason of cleaved of ester bonds of *p*-hydroxyphenolic acids, but the polydispersity showed almost the same data with bamboo ligno-*p*-cresols.

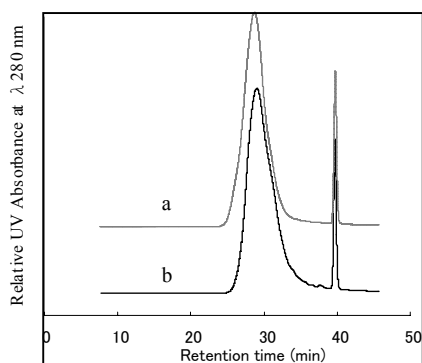


Fig.5 GPC profiles of original bamboo ligno-*p*-cresols (a) and sap-ligno-*p*-cresols (b).

3.7 UV absorption spectra of *p*-coumaric acid and ester *p*-hydroxyphenolic acid in bamboo ligno-*p*-cresols

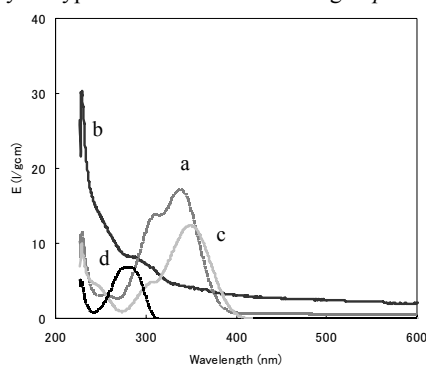


Fig.6 UV/vis spectra of *p*-coumaric acid in alkali conditions.(a) ether extractives (b) ferulic acid (c) *p*-coumaric acid (d) *p*-hydroxybenzoic acid.

The ether extractives of the resulted soluble fractions after acidification through alkali hydrolysis were achieved as yellow mucilage. The UV/vis spectrum of its dry sample was compared to *p*-coumaric acid in alkali conditions in the method same to it was accounted in 2.4. For the region of absorption is not completely accord to a, b, c and d, it can not be concluded that the H-units are mainly composed with *p*-coumaric acid here. The ester stabilizer has to be paid attention, it need to be confirmed with GC in detail.

3.8 Potential of bamboo forest as molecule forming fields

Based the data showed in literatures [2,19,20] through the phase-separation system, the yield of aliphatic compounds (carbohydrates) is about 80% to bamboo meal, and the yield of aromatic compounds (lignophenols) is about 16% to bamboo meal. Therefore, bamboo resources have the potential of providing 5.76×10^5 ton of aromatic compounds and 28.8×10^5 ton of aliphatic compounds with the increase of 4.8 ton/year of aromatic compounds and 24 ton/year of aliphatic compounds every 100-120 ton of present stock. Furthermore, the H units included in bamboo lignin can be separated for the different purposes. *p*-Coumaric acid is believed to reduce the risk of stomach cancer[21], by reducing the formation of carcinogenic nitrosamines[22]; ferulic acid may be useful as a precursor in the manufacturing of vanillin[23]; *p*-hydroxybenzoic acid is known as preparation of its esters, which are used as preservatives in cosmetics[24].

4. CONCLUSIONS

As distributed before, after the phase separation treatment, H-units were still remained for the *p*-cresols solvation effect in bamboo ligno-*p*-cresols. In this study we separated H-units from bamboo ligno-*p*-cresols, the analytical data had shown the core bamboo ligno-*p*-cresols have same features with wood ligno-*p*-cresols. And the H-units are not only composed of *p*-CA, but also ferulic acid and *p*-hydroxybenzoic acid. All of them are useful resource in organic chemical industry. In summary, through phase separation system, we can get both additional structure of useful mono-phenols and lignin-based polymer from bamboo. Bamboo can be thought as a kind of developed biomass resources compared to wood in the phase-separation system.

5. REFERENCES

- [1] Y. Isagi et al., *Ecological Research*, **8**, 123-133(1993)
- [2] H.Ren and M. Funaoka, *Trans. Mater. Res. Jpn.*, **32(4)**, 1095-1098 (2007).
- [3] M. Shimada, T. Fukuzuka and T. Higuchi, *Tappi*, **54(1)**, 72-78(1971).
- [4] Y. Nakamura and T. Higuchi, *Holzforchung*, **30**, 187-191(1976).
- [5] T. Higuchi, Y. Ito et al., *Phytochem.*, **6**, 1551(1967).
- [6] D. Ohrnberger, *J.Am.Bamboo Soc.*, **4**, 43-52 (1983).
- [7] M. Watanabe, *Japan Society of Bamboo Development and Protection*, Kyoto (1987).
- [8] D.H. Janzen, *Ann. Rev. Ecol. Syst.*, **7**, 347-391(1976).
- [9] J.M.O. Scurlock, D.C. Dayton and B. Hames, *Biomass and Bioenergy*, **19**, 229-244 (2000).
- [10] Y. Isagi, T. Kawahara, K.Kamo et al., *Plant Ecology*, **130**, 41-52 (1997).
- [11] M. Sai Ram and G. Seenayya, *World Journal of Microbiology and Biotechnology*, **7**, 372-378 (1991).
- [12] J. Marton, *Tappi*, **47(11)**, 713-719 (1964).
- [13] C.W. Dence, in "Methods in Lignin Chemistry," S.Y.Lin and C.W. Dence, Ed., Berlin Heidelberg: Springer-Verlag, 1992, p326-327.
- [14] D.C.C.Smith, *Nature*, **176**, 267-268 (1955a).
- [15] J.Kuc and N.E. Nelson, *Arch. Biochem. Biophys.*, **105**, 103-113 (1964).
- [16] F. Nakatsubo, K.Sato and T. Higuchi, *Makuzai Gakkaishi*, **22**, 29-33 (1976).
- [17] J. Nakano, A. Ishizu and N. Migita, *Tappi*, **44**, 30-32 (1961).
- [18] G.X. Pan, J.L.Bolton and G.J. Leary, *J. Agric. Food Chem.*, **46**, 5283-5288(1998).
- [19] H.Ren and M. Funaoka, *Trans. Mater. Res. Jpn.* **33(4)**, 1141-1144 (2008).
- [20] H.Ren and M. Funaoka, *Trans. Mater. Res. Jpn.*, **33(4)**, 1145-1148 (2008).
- [21] K. Kikugawa et al, *Journal of Agricultural and Food Chemistry*, **31(4)**, 780-785(1983).
- [22] L. Ferguson et al., *Harris Philip J. Molecular Nutrition & Food Research*, **49(6)**, 585-593(2005).
- [23] S. Mathew et al., *Crit.Rev. Biotechnol.*, **24(2-3)**, 59-83(2004).
- [24] C. Moumita et al., *Biochemical Systematics and Ecology*, **34**, 509-513(2006).

(Received December 12, 2008; Accepted September 16, 2009)

Potential of herbaceous lignocellulosics as industrial raw materials

Hao REN and Masamitsu FUNAOKA

Graduate School of Bioresources, Mie University, 1577 Kurima-machiya, Tsu, Mie, 514-8507, Japan
Fax: 81-59-231-9517, e-mail: funaoka@bio.mie-u.ac.jp

Alpinia zerumbet is a perennial plant growing widely in the subtropical and tropical regions. *Alpinia zerumbet* leaves and rhizomes have been extensively studied for their chemical compositions and biological activities. It is traditionally used for the treatment of cardiovascular hypertension and as an antispasmodic agent [1-4]. Kaoliang is another kind of lignocellulose, it has been widely used as natural dyes in the coloring of foods, clothes, and cosmetics. The main components of Kaoliang color have been reported to be apigeninidin and luteolinidin [5], however, the structures of other compounds present in the color have not been elucidated clearly until now [6]. Bagasse is the fibrous residue remaining after sugarcane or sorghum stalks are crushed to extract their juice and is currently used as a renewable resource in the manufacture of pulp and paper products and building materials [7-8]. In this study, lignocellulosics characteristics of *alpinia zerumbet*, kaoliang and bagasse were investigated to compare with other gramineae plants through the phase-separation system.

Key words: *alpinia zerumbet*, kaoliang, bagasse, lignocellulosics characteristics, gramineae plant

1. INTRODUCTION

Lignocellulosic biomass is the world's most abundant renewable material and has long been recognized as a potential feedstock for producing chemicals, fuels, and materials [9-11]. It is primarily composed of the two carbohydrate polymers cellulose and hemicellulose, and lignin. Lignin is a phenolic high molecular mass biopolymer, composed of a highly branched phenylpropanoid framework that is unique to vascular land plants. *Alpinia zerumbet*, kaoliang and bagasse are three kinds of special lignocellulosic biomass.

Alpinia zerumbet is a perennial plant growing widely in subtropical and tropical regions. With fast growth and strong resistance to pests and diseases, this species grows abundantly in the Ryukyu Islands, and has been a traditionally important and economic plant in Okinawa [12]. *Alpinia* essential oils were obtained by steam distillation of *alpinia* leaves. From about 100 kg *alpinia* leaves, 100 L of distillate was obtained, which yielded 100 mL of essential oils [13-15]. In Okinawa, *alpinia* oils are used as cosmetics, perfumes, and soaps. Using *alpinia* stems, the fiber is squeezed and more than 20 products are commercialized, which include Japanese paper, kariyushi-wear, and cloth. The rhizomes can be used as spices and in beverages. The contents of essential oils, total phenolics, dihydro-5,6-dehydrokawain (DDK) and their antioxidant and antibacterial actives were investigated in *alpinia*, which had been sprayed with copper sulphate 24 hrs earlier [16]. The main components determined in leaf oils were 1,8-cineol, camphor and methyl cinnamate, whereas the major oils in the rhizome were DDK and methyl cinnamate [17].

Kaoliang color is a brown coloring agent used in East Asia, mainly China, Korea, and Japan.

According to the "Japan Food Additives Association Standard", this color is prepared by extraction of kaoliang, seed coat, either in neutral or alkaline conditions and slightly warmed water or with acidic aqueous ethanol. The main components are two flavonoids; apigeninidin and luteolinidin [5,18,19]. Other flavonoids and their derivatives have been isolated from this color in previous studies [20,21], but the structures of many components have not yet been determined.

On the other hand, many research efforts have attempted to use bagasse as a renewable feedstock for power generation and for the production of bio-based materials [22-26].

As distributed above, both *alpinia zerumbet*, kaoliang and bagasse play important roles in strengthening the economy of the region from its products such as essential oil and coloring agent. However, the whole lignocellulosics characteristics of them have never been investigated until now.

In this study, five herbaceous [*Alpinia zerumbet* (leaves and rhizomes), Kaoliang (Hull and Culm), Bagasse] were estimated for the utilization as industrial raw materials. All the lignocellulosics were converted into sugars and lignin-based polymers (lignopluls) through the phase-separation system.

2. EXPERIMENTAL

2.1 Materials

Air dried *Alpinia zerumbet*, Kaoliang, Bagasse were ground respectively in a Wiley mill and a vibrational mill to pass an 80 mesh screen, and extracted with ethanol-benzene (1:2, v/v) for 48hr.

2.2 Composition analyses of five lignocellulosics

Dry matter content

The dry matter content of bamboo meals were gravimetrically determined by drying samples at 105 °C

to constant weight.

Extractives

Bamboo meals (40~60 mesh, 1 g) were extracted with cold water for 48h, hot water for 3h with refluxing, and 1% NaOH solutions for 1h with refluxing respectively. The extractives contents were gravimetrically determined by drying treated samples at 105 °C to constant weight.

Lignin

Lignin contents were determined on Klason method (TAPPI T 13 m-54) with acid-pepsin pretreated bamboo meals [27].

2.3 Synthesis and isolation of ligno-*p*-cresols

Synthesis and isolation of ligno-*p*-cresols were carried out with the method in literature [28]. Physicochemical characterization analysis of ligno-*p*-cresols

Amounts of combined *p*-cresols

¹H-NMR analyses of ligno-*p*-cresols were acquired with a JOEL JNM-A500 FT-NMR System. The amounts of combined cresols were calculated on the signal intensity of cresolic methyl protons (1.6-2.4 ppm) against aromatic protons (7.8-8.4 ppm) of internal standard (*p*-nitrobenzaldehyde) on ¹H-NMR spectra.

FT-IR spectra of ligno-*p*-cresols

FT-IR spectra were obtained on Perkin Elmer Spectrum GX FT-IR Spectroscopy using KBr discs. The spectra were recorded in the range from 400 to 4000 cm⁻¹ with a resolution of 4 cm⁻¹ over 32 scans.

UV-Vis spectra of ligno-*p*-cresols

Ultraviolet and Visible spectra of ligno-*p*-cresols were determined on a JASCO V-560 spectrophotometer. They are measured continuously in the wavelength region of 200-600 nm.

Thermo mechanical analysis (TMA) of ligno-*p*-cresols

Thermo mechanical analyses of ligno-*p*-cresols were performed on a SEIKO EXSTAR 6000 TMA/SS. About 3 mg sample powder was set in an aluminum pan (5mm × 2 mm) and a smaller aluminum operculum (2 mm) was put on the center over the sample. Under 49 mN loading by quartz needle, the solid-liquid transitions of ligno-*p*-cresols were measured by programmed heating from 50 °C to 250 °C (2 °C/min) under 200 mL/min of N₂.

3. RESULTS AND DISCUSSION

3.1 Chemical compositions of five herbaceous and yields of ligno-*p*-cresols

The five kinds of lignocellulose samples were compared with the bamboo through phase separation treatment. Alpinia culm, kao liang culm, and bagasse were converted into the ligno-*p*-cresols and carbohydrates promptly just like the bamboo sample. Yields of ligno-*p*-cresols are 55-69% to each Klason lignin contents, and this comparatively low yields originated in the molecular weight of lignin sample derived from the herbs plant is low and a part of them had been lost as ether soluble fractions during the refinement process. Moreover, when the Alpinia blade and Kaoliang hull are used as raw material, the amounts of the aromatic compounds collected from the phenol layer are a little fewer, it was 20-30% to their acid insoluble fractions amounts received by Klason method. It originated the alcohol/benzene extraction can not completely take all of the oil elements out, a large quantities of the extraction elements such as the

monoterpene are remained in the sample meals, and during the phase-separation process, oil elements can be connected with lignin or themselves then a thick interlayer was formed. The amounts of phenol soluble decreased and the yields became low. In the case of Kaoliang hull, a large amount of two flavonoids (apigeninidin and luteolinidin) are the two main components in it. In the acid conditions, it is possible to have condensed structures to form a phenol insoluble composition. As a result, it is the same to Alpinia blade which can not receive high yields of ligno-*p*-cresols.

Table1 Yields of acid insoluble fractions with klason method

Sample name	Extractives to dry Wt.(%)	Moisture content (%)	Yields of Klason (%)
Alpinia blade	13.46	10.02	20.41
Alpinia culm	4.67	9.97	16.24
Kao liang hull	9.95	10.07	15.49
Kao liang culm	19.50	10.36	9.16
Bagasse	4.45	10.1	15.88

Table2 Yields of acid soluble fractions with klason method

Sample name	Weight of wood meal	Moisture content (%)	Yields of acid soluble lignin(%)
Alpinia blade	0.2633	10.02	3.75
Alpinia culm	0.2549	9.97	1.74
Kao liang hull	0.2621	10.07	2.90
Kao liang culm	0.1158	10.36	1.80
Bagasse	0.9514	10.10	1.53

Table3 Yields of lingo-*p*-cresols

Sample name	Wt. of wood meal after extraction (g)	Wt. of ligno- <i>p</i> -cresols after dry(g)	Yields of ligno- <i>p</i> -cresols (to dry wood meal) (%)
Alpinia blade	1.0972	0.0411	4.16
Alpinia culm	1.0351	0.0782	8.39
Kao liang hull	1.0932	0.0521	5.30
Kao liang culm	1.0742	0.0605	6.28
Bagasse	1.0464	0.0834	8.86

3.2 Amounts of combined cresols

With the same method of ref.[28], the amounts of combined cresols were also accounted here. For the reason that Kaoliang hull ligno-*p*-cresols can not be dissolved into pyridine completely, we can not measure it by ¹H-NMR. For the other four kinds of samples, we compare their ¹H-NMR charts with bamboo, the same pattern with the bamboo was shown, and the amount of the calculated combined cresols in the kaoliang culm and bagasse also shown almost the same data with bamboo (0.8mol/C₉), but the amount of the combined cresols of alpinia culm is 1.15 mol/C₉. This is because there are a lot of low moleculars which were formed by combining cresol. They were refined as alpinia culm ligno-*p*-cresols from organic layer. Moreover, only the spectrum of alpinia blade, a sharp peak was observed in about 1.0 ppm. This originates in hydrogen in the ring of the >CH-C-R structure and the cyclic compound that exists on the straight chains of the mono-terpene,

sesquiterpenes, and the mono-terpene alcohol contained in the refinement of oil element of the alpinia blade as well.

3.3 FT-IR of ligno-*p*-cresols

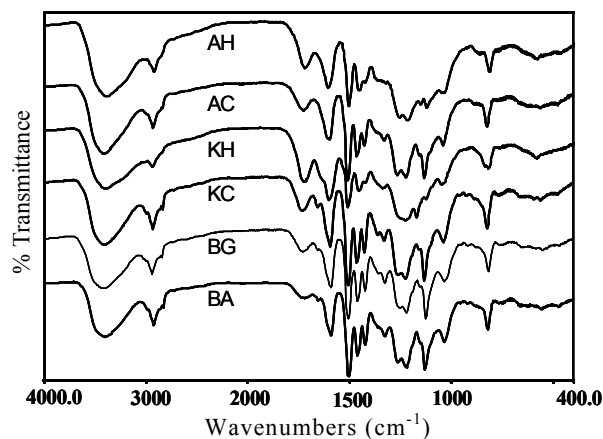


Fig.1 FT-IR spectra of ligno-*p*-cresols. (AH: Alpinia blade; AC: Alpinia culm; KH: Kaoliang Hull; KC: Kaoliang Culm; BG: Bagasse; BA: Bamboo)

As we reported before, the FT-IR spectra of three species bamboo ligno-*p*-cresols show bands at 1325, 1220, 1130 cm^{-1} which belong to vibrations of syringyl group and 1270, 1040 cm^{-1} which belong to vibrations of guaiacyl group, 815 cm^{-1} resulted from combined cresols, which are similar to hardwood ligno-*p*-cresols. A distinct C=O vibration belonging to carboxyl or ester group at 1730 cm^{-1} is found. We concluded that, a part of esterified *p*-coumaric acid in bamboo native lignin is remained through the phase-separation system. They also may be resulted from the non-conjugation carbonyl groups coming from polysaccharides[29].

In this study, all of the five kinds of herbs ligno-*p*-cresols were observed to have absorption at 1730 cm^{-1} , which were the same with bamboo. The absorption based on the expansion and contraction vibration of the ester linkage was confirmed to the vicinity. Moreover, Alpinia culm, kaoliang culm, and bagasse showed the completely same FT-IR absorption pattern with bamboo, and alpinia blade and kaoliang hull were observed absorptions at 1000-1100 cm^{-1} and 1100-1300 cm^{-1} respectively(Fig.1). This was a result of connecting refinement of oil and the pigment composition included in of each with the lignin main structures [32].

3.4 UV/vis spectra of ligno-*p*-cresols

In the case of bamboo, UV-Vis spectra were characterized by a sharp band at 280 nm, a shoulder at 305 to 370 nm [29]. During the phase-separation treatment, selective and effective grafting of cresol at reactive sites in the side chains, leading to the disappearance of conjugated systems had been known by the previous researches. The shoulder peaks of bamboo ligno-*p*-cresols come from the conjugation structures of the esterified *p*-coumaric acid.

The UV/vis spectra of five kinds of herbs sample

were compared to bamboo ligno-*p*-cresols. As same as bamboo, in the neutral solution the absorption at 280 nm and in alkaline solution the absorptions at 300 nm were observed. Furthermore, in the ionization difference spectra of herbaceous ligno-*p*-cresols, either of them was observed big shoulder peak at 350-450nm (Fig.2). Among them, the kaoliang hull and alpinia blade sample showed the largest ones. This is because essential oil and pigment composition were included except that a peculiar *p*-hydroxyphenolic unit to herbs was contained for alpinia blades and kaoliang hulls[33].

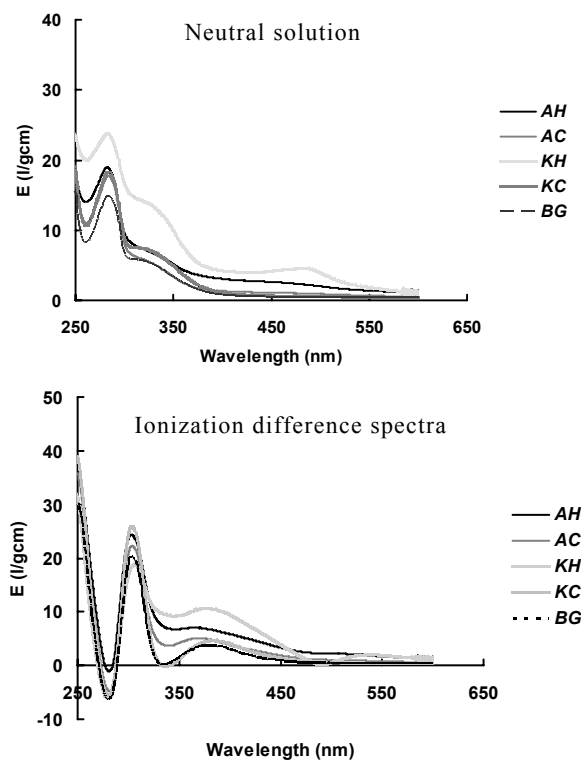


Fig.2 UV/vis spectra in neutral solution and ionization difference spectra of herbaceous ligno-*p*-cresols.

3.5 TMA analysis of ligno-*p*-cresols

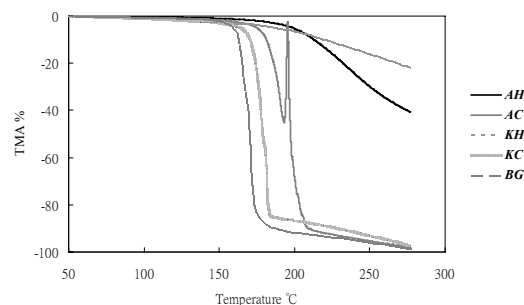


Fig.3 TMA profiles of ligno-*p*-cresols.

As we reported before, the TMA curves of ligno-*p*-cresols from bamboo and woody materials revealed volume decreasing at 150-160 $^{\circ}\text{C}$ due to the solid/liquid phase transition. The transition points of bamboo ligno-*p*-cresols indicate higher values than

wood ligno-*p*-cresols[29]. The polydispersity of bamboo ligno-*p*-cresols (by GPC) is lower than wood materials. Therefore this is based on the scarcity in low molecular compositions that function as internal plasticizer.

The weight average molecular weight, the amount of the combined cresols of three kinds of bamboo were almost the same, and the phase transition point were not admitted the great disparity, and were about 6,000, and were 0.8 mol/C₉ and 155 °C respectively. While, lignophenols derived from alpinia culm, kaoliang culm, and bagasse showed thermal liquidity as excellent as bamboo, and the phase transition point was 150-170 °C. On the other hand, the thermal liquidity of the aromatic compounds derived from alpinia blade and kaoliang hull were low. It originated that a toroidal or a straight-chain structure of the essential oil elements or the pigment compositions exist, the steric hindrance was caused when heating, so that the thermal liquidity was decreased. These were all for the reason of essential oil and pigment composition which were included in alpinia blade and kaoliang hull connected with lignin body in some shape. Moreover, all the ligno-*p*-cresols that had been derived from bamboo and these five kinds of herbs plant showed higher solid-liquid transition points (20-40 °C higher) than wood samples through the thermomechanical analysis (TMA). This result based on the polydispersity of herbs ligno-*p*-cresols (by GPC) is lower than wood materials, on the other hand the amounts of hydroxyl groups are higher in herbs ligno-*p*-cresols, it was also thought as the intermolecularly linked hydroxyl groups made the solid-liquid transition points high.

In summary, though the herbs plant resource such as the alpinia, kaoliang, bagasses, and bamboos have been hardly used at the molecular material level as a result of examining the total characteristic of other five-kind lignocellulosic resource so far. It was shown that through the phase-separation system they can be conversed into ligno-*p*-cresols and carbohydrates, the molecular potential was equal to bamboo and woody resources [30,31]. And the prompt growth, it updated in addition, and was extremely useful as continued lignocellulose formation body. The features of H-units structure or essential oil and pigment compositions structures connected with lignin body can be thought as the addition of a useful monophenol etc. to the core lignin by the ester linkage. The potential of herb lignocellulosics as a sustainable molecule forming fields is very huge. We can control the reaction process according to purpose.

4. REFERENCES

- [1] R., Soares de Moura; A.F., Emiliano et al., *Journal of Cardiovascular Pharmacology*, **46(3)**, 288-294 (2005).
- [2] S., Marakami; W., Li et al., *Journal of Natural Medicines*, **63(2)**, 204-208 (2009).
- [3] A.A. Elzaawely, T.D. Xuan, H. Koyama, S. Tawata, *Food Chemistry*, **104**, 1648-1653 (2007).
- [4] S. Tawata, M. Fukuta, T.D. Xuan et al., *J.Pestic. Sci.*, **33(1)**, 40-43(2008).
- [5] K. Wada, T. Koda, H. Aoki, *Journal of Liquid Chromatography & Related Technologies*, **28**, 2097-2106(2005).
- [6] G. Mitchell, *Brain Research Bulletin*, **50**, 427(1999).
- [7] H. Y. Zhang and Y. Zhao, *Progress in Paper Recycling*, **17(4)**, 11-14 (2008).
- [8] S.B. Wu; L.L. Guo; S.G. Wang et al., *Forestry Studies in China*, **8(3)**, 34-37 (2006).
- [9] S.K., Uppal; R., Gupta; R.S.,Dhillon et al., *Sugar Tech*, **10(4)**, 298-301 (2008).
- [10] S.Y., Ou; Y.L., Y.L., Luo; C.H., Huang et al., *Innovative Food Science & Emerging Technologies*, **10(2)**, 253-259 (2009).
- [11] S.B., Wu; Y.L., Guo et al., *Forestry Studies in China*, **8(3)**, 34-37(2006).
- [12] S., Murakami, W., Li et al., *Journal of Natural Medicines*, **63(2)**, 204-208 (2009).
- [13] M.A.C., Bezerra, J.H.Leal-Cardoso, A.N. Coelho-de-Souza et al., *Phytotherapy Research*, **14**, 549-551 (2000).
- [14] S.T., Chang, P.F., Chen, S. Y., Wang et al., *Journal of Medical Entomology*, **38**, 455-457(2001).
- [15] A. Djeridane, M. Yousfi, B. Nadjemi et al., *Food Chemistry*, **97**, 654-660 (2006).
- [16] H. Itokawa, M. Morita et al., *Phytochemistry*, **20**, 2503-2506 (1981).
- [17] L. Jirovetz, G. buchbauer et al., *Acta Pharmaceutica*, **53**, 73-81 (2003).
- [18] J.P., Song, H.Z., Chen, R.Y., Ma, *NiangJiu*, **34(4)**, 52-53 (2007).
- [19] C.L., McIntyre, J., Drenth, N., Gonzalez et al., *Gensome*, **51(7)**, 524-533(2008).
- [20] D. Cook, F.E., Dayan, A.M., Rimando et al., *Recent Advances in Phytochemistry*, **40**, 157-177 (2006).
- [21] E.I., Adeyeye, *Bulletin of the Chemical Society of Ethiopia*, **22(1)**, 11-17 (2008).
- [22] S.K., Uppal; R.,Gupta; R.S., Dhillon; S., Bhatia, *Sugar Tech*, **10(4)**, 298-301 (2008).
- [23] B.A., Prior; D.F., Day, *Applied Biochemistry and Biotechnology*, **146(1-3)**, 151-164 (2008).
- [24] S.C., Rabelo; M.F., Rubens; A.C., Costa, *Applied Biochemistry and biotechnology*, **148(1-3)**, 45-58(2008).
- [25] A. Ilindra; J.D.M.,Dhake, *Indian Journal of Chemical Technology*, **15(5)**,497-499 (2008)
- [26] A.K., Saroha; K. Parmod; P. Komsal; S. Shishir, *IPPTa Journal*, **20(3)**, 179-184 (2008).
- [27] C.W. Dence, in "Methods in Lignin Chemistry," S.Y. Lin and C.W. Dence, Ed., Berlin Heidelberg: Springer-Verlag, 1992, p24-25.
- [28] M. Funaoka and I. Abe, *Tappi Journal*, **August**, 145-149 (1989).
- [29] H.Ren and M. Funaoka, *Transactions of the Materials Research Society of Japan*, **32(4)**, 1095-1098 (2007).
- [30] H.Ren and M. Funaoka, *Transactions of the Materials Research Society of Japan*, **33(4)**, 1141-1144 (2008).
- [31] H.Ren and M. Funaoka, *Transactions of the Materials Research Society of Japan*, **33(4)**, 1145-1148 (2008).
- [32] T. Masuda, S. Mizuguchi, T. Tanaka et al., *Journal of Agricultural and Food Chemistry*, **48**, 1479-1484 (2000).
- [33] S. Tawata, S. Taira, N. Kobamoto et al., *Bioscience, Biotechnology and Biochemistry*, **60**, 1643-1645 (1996).

(Received December 12, 2008; Accepted September 16, 2009)

New EFB Refining System Using Structural Units of EFB Lignin

Takanori Shinano¹, Masamitsu Funaoka^{1*}, Yoshihito Shirai² and Mohd Ali Hassan³

¹Graduate School of Bioresources, Mie University, SORST JST

²Kyushuu Institute of Technology

³Universiti Putra Malaysia

*Fax: 059-231-9591, e-mail: funaoka@bio.mie-u.ac.jp

In order to achieve sustainable conversion of lignocellulosics through the phase-separation process, *p*-hydroxybenzoic acid (*p*-HBA) attached to core lignin through ester linkage was used as a reagent for lignin conversion. During the phase-separation treatment with *p*-HBA, the viscosity of reaction mixture was higher, compared with the phase-separation treatment with *p*-cresol. By centrifugation of the reaction mixture, the thick interfacial solid materials were formed. The yields of lignophenol, its low molecular weight fraction (separated to the organic layer) and the interfacial solid fraction were about 30%, 30% and 40%, respectively. In case of phase-separation treatment with *p*-cresol, the yields of lignophenol and its low molecular weight fraction (separated to the organic layer) were about 73% and 27%, respectively. The peak ratio of phenol to guaiacol plus syringol in the pyrogram of lignophenol (*p*-HBA type) was higher than those of lignophenol (*p*-cresol type) and Klason lignin. The peak of non-conjugated carbonyl group in the FT-IR spectrum of lignophenol (*p*-HBA type) was higher than that of the material synthesized without *p*-HBA. These results indicated that *p*-HBA was grafted to EFB lignin. The lignophenol (*p*-HBA type) had higher thermal stability, compared with lignophenols (*p*-Cresol type). The interfacial solid material between the organic and aqueous layers had higher thermal stability than sulfuric acid lignin. These results suggest the formation of lignin network through *p*-HBA.

Key words: Oil Palm, EFB (Empty Fruit Bunch), Phase-Separation System, Lignophenol, Resource Circulation

1. INTRODUCTION

EFB (Empty Fruit Bunch, *Elaeis guineensis*) has been discharged from palm oil industry. The amount is 14 million tons / year [1]. The potential of EFB as industrial raw materials and the characteristics of EFB lignin have been formulated through the phase-separation system [2-3]. EFB core-lignin consists of guaiacyl and syringyl units. *p*-Hydroxybenzoic acid (*p*-HBA) is linked to the side chain of EFB lignin through ester linkage. The ester linkages were hydrolyzed easily. This result shows that *p*-HBA can be collected from original EFB meals and EFB lignophenol (lignin derivative synthesized by the phase-separation system). In place of phenols obtained from petroleum, if *p*-HBA obtained from EFB itself can be used for the conversion and separation of lignin and carbohydrate, the amount of the used petroleum can be reduced.

In this study, the possibility of sustainable phase-separation system composed of *p*-HBA and acid was investigated.

2. EXPERIMENTAL

2.1 Preparation of alkaline treated EFB.

EFB meals (extractives-free, 80 mesh pass) were treated with 1.0 N NaOH [10 mg of lignin content / 4 mL of 1.0 N NaOH solution] under N₂ condition at 40°C for 96 hrs. After that, EFB meals were washed with hot water to pH 7 and dried at 40 °C. The alkaline treated EFB were milled by mill [Retsch, ZM 100, 60 mesh screen]. The lignin contents of alkaline treated EFB were estimated [4].

2.2 Preparations of lignin derivatives.

2.2.1 Conversion of alkaline treated EFB with *p*-HBA (2 step process I).

Three mol / C₉ of *p*-HBA were solvated to alkaline treated EFB meals with acetone. Seventy-two wt % sulfuric acid [1g of meals / 10 mL of the acid] was added to the solvated meals and the reaction mixture was stirred vigorously. After 40 min, 10 mL of *p*-cresol was added. The total reaction time was 60 min. The reaction mixture was centrifuged. The organic phase was added drop wise to 250 mL of diethyl ether. The precipitate was dissolved with 80 mL of acetone. The insoluble fraction was removed by centrifugation and filtration. The soluble fraction was concentrated under reduced pressure until 10 mL. The concentrated acetone solution was added drop wise to 200 mL of diethyl ether. The insoluble fraction (1st ligno-*p*-HBA) was collected by centrifugation and dried with P₂O₅.

The interfacial phase (1st interfacial solid material) was added to excess deionized water and collected by centrifugation. The material was washed with deionized water until no smelling *p*-cresol and dried with P₂O₅. In order to remove sugars and non-polymerized lignin part of the washed material, the material was treated by 1step process of the phase-separation system composed of *p*-cresol and 72 wt % sulfuric acid [2]. 2nd ligno-*p*-HBA was separated and purified from the organic phase as described above. The 2nd interfacial solid material was separated from the interface phase as described above.

2.2.2 Conversion of alkaline treated EFB with *p*-cresol (1 step process).

In order to compare the roles of phenol derivatives for conversion of lignin, the alkaline treated EFB was converted by 1 step process composed of *p*-cresol and 72 wt % sulfuric acid. The lignophenol was separated and purified from the organic phase.

2.2.3 Conversion of alkaline treated EFB without

p-HBA.

In order to compare the roles of *p*-HBA for lignin conversions, the alkaline treated EFB was treated with 72 wt % sulfuric acid, followed by *p*-cresol treatment. The lignin derivative was separated and purified from the organic phase.

2.2.4 Conversion of alkaline treated EFB with only 72 wt % sulfuric acid (Klason method).

In order to compare the characteristics of the polymerized materials, the EFB Klason lignin was prepared by Klason method. The remained precipitate was collected by filtration.

2.3 Analysis of lignin derivatives.

FT-IR spectra (KBr disks) of lignin derivatives were determined by Spectrum TM GX FT-IR Spectrometer (PERKIN ELMER). In order to measure molecular weight, gel permeation chromatograms of lignophenols were determined by LC-10 system with four columns (KF801, KF802, KF803 and KF804) and UV detector (280 nm). Tetrahydrofuran was used as the eluent. In order to estimate grafted *p*-cresol contents, ¹H-NMR spectra of original lignophenols were determined in C₅D₅N-CDCl₃ (1/3, v/v) on a JNM-A500 FT-NMR SYSTEM and ALPHA FT-NMR Spectrometer (JEOL, 500 MHz). UV-Vis (in methyl cellosolve) spectra of lignophenols were determined by a JASCO V-560 spectrophotometer. TMA profiles of lignophenols were determined by a Seiko Instruments Inc TMA / SS6100 [Rate: 2°C/min, 50 °C-250°C (370°C), Flow: N₂]. TG profiles of lignophenols were determined by a Seiko Instruments Inc TG / DTA 6200 (Rate: 2°C/min, 50 °C-450°C, Flow: N₂). In order to estimate the compositions of lignophenols, lignophenols were pyrolyzed at 550°C for 12 s, using a pyrolyzer (Frontier Lab., PY-2020D) coupled to a gas chromatograph with EI-MS detector (Shimadzu GC/MS-QP5050A, Carrier gas: He). The gas chromatographs were fitted with an 007-1 column programmed from 90 to 280°C at 4°C/min.

2.4 Conversions of lignin derivatives by neighboring group participation reaction of grafted phenol derivatives.

Lignin derivatives (5 mg) were dissolved in 0.5 N NaOH (2 mL) and treated at 140 °C and 170 °C. After reactions, the reaction mixture was acidified with 1 N HCl to pH 2. The precipitations were collected by centrifugation, washed with a small amount of water and dried under P₂O₅. The average molecular weights of lignophenols (2nd derivatives) were estimated by GPC.

3. RESULT AND DISCUSSION

The viscosity of reaction mixture in the conversion with *p*-HBA was higher than that in the conversion with *p*-cresol. After centrifugation of the reaction mixture in the conversion with *p*-HBA, about 5 mm of the interface layer between the organic layer and aqueous layer appeared. The interfacial solid material did not disappear even after treated by 2nd phase-separation treatment. In case of the conversion with *p*-cresol, the centrifuge tube had a thin layer. But the layer disappeared after 80 min treatment. The yields of 1st ligno-*p*-HBA, 2nd ligno-*p*-HBA and 2nd interfacial solid material were 18.6%, 8.91% and 37.7% of alkaline treated EFB lignin (Acid insoluble lignin: 17.7%, Acid soluble lignin:

2.44%). In case of the conversion with *p*-cresol, the yield of lignophenol (*p*-cresol type) was 73.3% of the lignin. These results suggest that polymerized materials of lignin and *p*-HBA are formed in the conversion reaction. The amount of grafted cresol contents of 1st ligno-*p*-HBA and lignophenol (*p*-cresol type) were 14.0 % and 27.4 %, respectively.

The FT-IR spectrum of lignophenol (*p*-cresol type) from alkaline treated EFB did not have a peak of 1714 cm⁻¹ assigned to ester linkages and was similar to that of hardwood lignophenol (Fig. 1). These results show that ester linkages of *p*-HBA and *p*-coumaric acid in EFB native lignin are hydrolyzed to give guaiacyl (G)-syringyl (S) type lignin. The peaks of about 1700 cm⁻¹ assigned to non-conjugated carbonyl groups of lignin derivatives synthesized with *p*-HBA (Fig. 1, c, d, e and f) were higher than that of lignin derivative synthesized without *p*-HBA (Fig. 1, f). The pyrogram of 1st ligno-*p*-HBA mainly had the peaks of phenol, *o*-cresol, *p*-cresol guaiacol and syringol. The peak ratio of phenol for guaiacol plus syringol in the pyrogram of 1st ligno-*p*-HBA was higher than those of lignophenol (*p*-cresol type), Klason lignin and the lignin derivative synthesized without *p*-HBA (Fig. 2). These results indicate that *p*-HBA is grafted to EFB lignin at *o*-position of *p*-HBA.

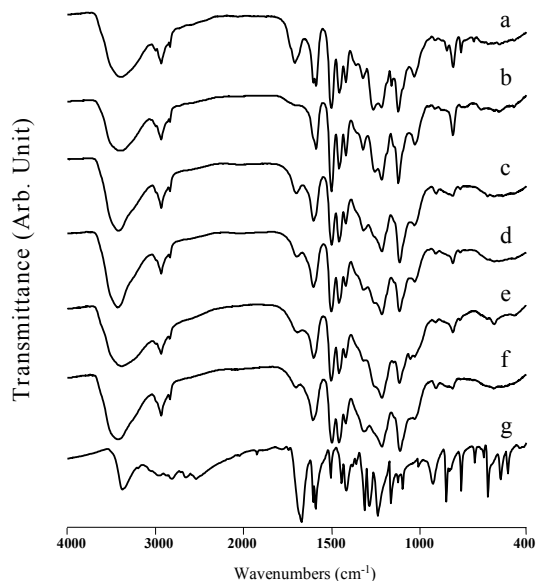


Fig. 1 FT-IR spectra of lignin derivatives. [a: Lignophenol synthesized by 1 step process from original EFB, b: Lignophenol synthesized by 1 step process from alkaline treated EFB, c: 1st Ligno-*p*-HBA synthesized by 2 step process I with *p*-HBA from alkaline treated EFB, d: 2nd Ligno-*p*-HBA, e: 2nd Interfacial solid material, f: Lignin derivative synthesized by the process without *p*-HBA from alkaline treated EFB, g: *p*-HBA.]

The ionization difference spectrum of 1st ligno-*p*-HBA had a peak of about 365 nm, indicating that 1st ligno-*p*-HBA has the conjugated system in the molecule (Fig. 3).

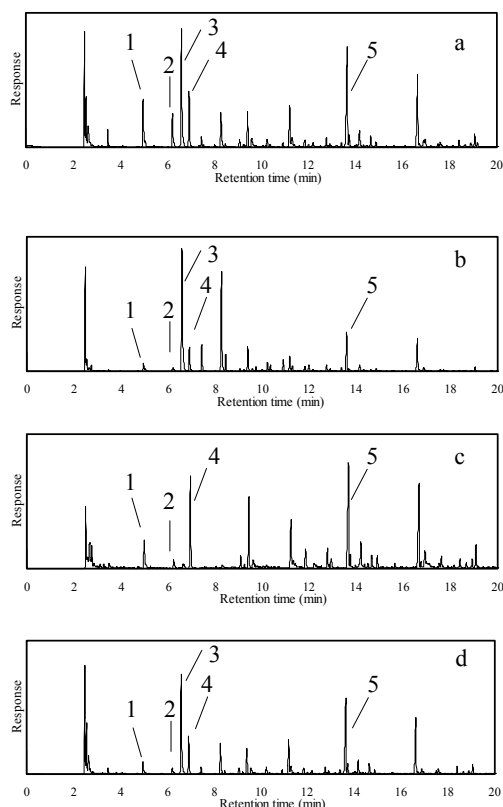


Fig. 2 Pyrograms of lignin derivatives. [a: 1st Ligno-*p*-HBA synthesized by 2 step process I with *p*-HBA from alkaline treated EFB, b: Lignophenol synthesized by 1 step process from alkaline treated EFB, c: Sulfuric acid lignin from alkaline treated EFB, d: Lignin derivative synthesized by the process without *p*-HBA from alkaline treated EFB, 1: Phenol, 2: *o*-Cresol, 3: *p*-Cresol, 4: Guaiacol, 5: Syringol, Conditions: 550 °C, 12s.]

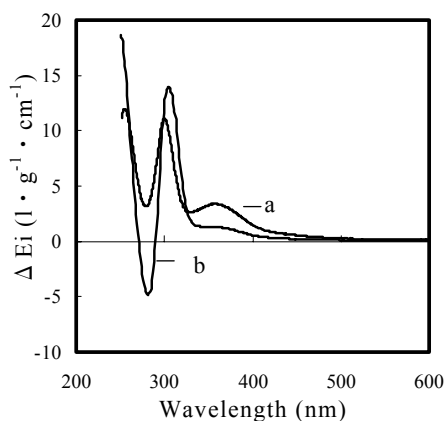


Fig. 3 Ionization difference spectra of lignin derivatives. [a: 1st Ligno-*p*-HBA synthesized by 2 step process I with *p*-HBA from alkaline treated EFB, b: Lignophenol synthesized by 1 step process from alkaline treated EFB.]

The TMA and TG profiles of 1st ligno-*p*-HBA and lignophenol (*p*-cresol type) were shown in Fig. 4. The phase transition points of 1st ligno-*p*-HBA and lignophenol (*p*-cresol type) were about 205°C and 142°C respectively. The 10% weight loss point of 1st ligno-*p*-HBA and lignophenol (*p*-cresol type) were about 253°C and 224°C, respectively. These results suggest that the amount of C-C linkage and the intermolecular interaction of 1st ligno-*p*-HBA are higher than those of lignophenol (*p*-cresol type). Judging from TG profile of 1st ligno-*p*-HBA, the kickback around 300°C in the TMA profile of 1st ligno-*p*-HBA shows the decomposition of the molecule.

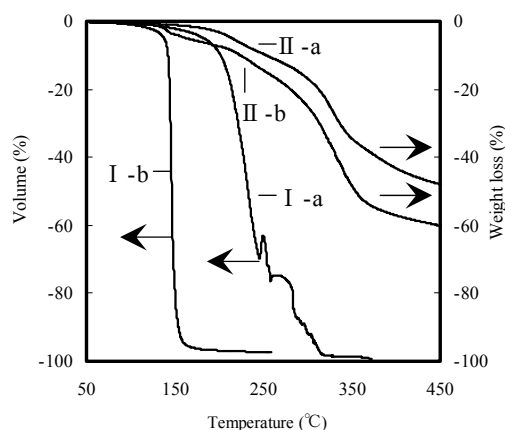


Fig. 4 TMA (I) and TG (II) profiles of lignin derivatives. [a: 1st Ligno-*p*-HBA synthesized by 2 step process I with *p*-HBA from alkaline treated EFB, b: Lignophenol synthesized by 1 step process from alkaline treated EFB.]

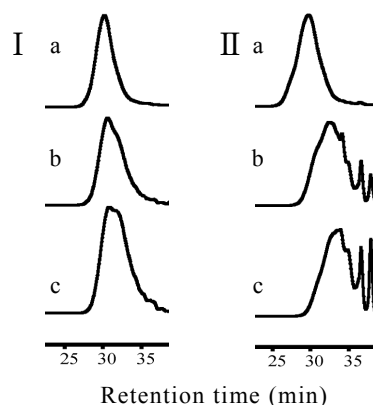


Fig. 5 GPC profiles of lignin derivatives. [I: 1st Ligno-*p*-HBA synthesized by 2 step process I with *p*-HBA from alkaline treated EFB, II: Lignophenol synthesized by 1 step process from alkaline treated EFB, a: Original (non-treated), b: 2nd derivative (140 °C treatment in alkaline solution), c: 2nd derivative (170 °C treatment in alkaline solution).]

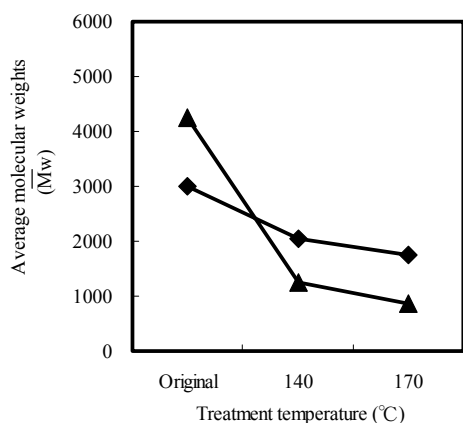


Fig. 6 Variations of average molecular weights of lignin derivatives for neighboring participation reaction of grafted phenol derivatives. [◆: 1st Ligno-*p*-HBA synthesized by 2 step process I with *p*-HBA from alkaline treated EFB, ▲: Lignophenol synthesized by 1 step process from alkaline treated EFB.]

The GPC profiles and the variations of average molecular weights of 1st ligno-*p*-HBA and lignophenol (*p*-cresol type) were shown in Fig. 5 and Fig. 6, respectively. After 140 °C and 170 °C treatment of lignophenol (*p*-cresol) with 0.5 N NaOH, the molecular weight distribution was moved to right hand side with increasing treatment temperature, indicating the conversion into low molecular weight parts. In case of 1st ligno-*p*-HBA, the molecular weight distribution slightly changed. These results suggest that the lignin molecules are tied up by *p*-HBA and the network structures are formed through the phase-separation treatment.

In order to compare the characteristics of high polymerized materials, the TMA and TG profiles of 2nd interfacial material and sulfuric acid lignin were analyzed (Fig. 7 and Fig. 8). The volume of 2nd interfacial material slightly decreased with the decrease of weight. In case of sulfuric acid lignin, the volume dramatically decreased with the decrease of weight. These results suggest that as

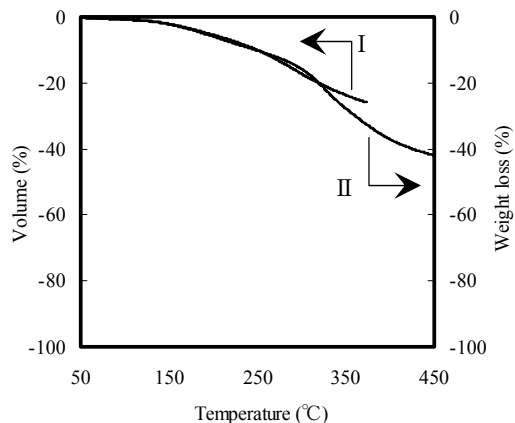


Fig. 7 TMA (I) and TG (II) profiles of 2nd interfacial solid material.

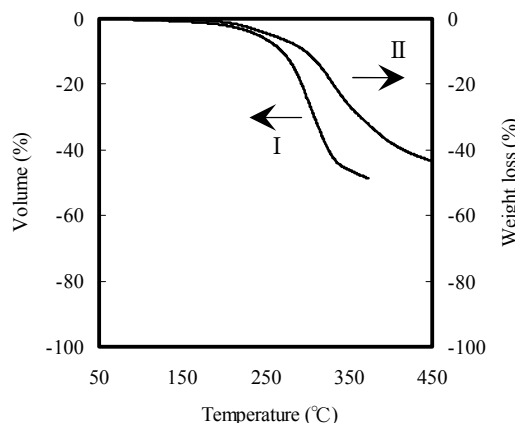


Fig. 8 TMA (I) and TG (II) profiles of Klason lignin obtained from alkaline treated EFB.

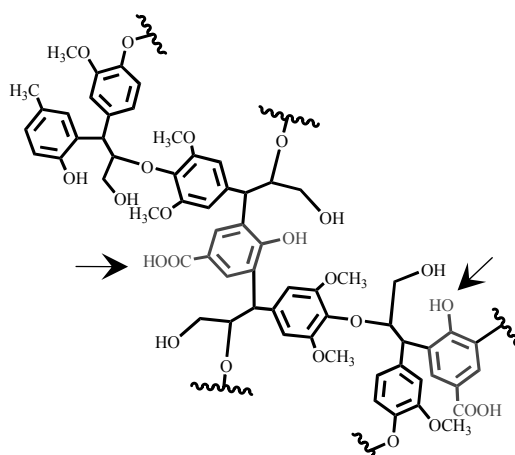


Fig. 9 Model structure of lignin/*p*-HBA hybrid.

the lignin molecules are tied up by *p*-HBA, the degree of freedom of the lignin molecule decreases, and the amount of C-C linkage in the molecule and the intermolecular interaction increases (Fig. 9).

4. CONCLUSION

Through the phase-separation process with *p*-HBA, lignin / *p*-HBA hybrid (ligno-*p*-HBA) was synthesized. Lignin / *p*-HBA hybrids had higher thermal stabilities, compared with lignin / *p*-cresol hybrids, suggesting the formation of network structures through *p*-HBA.

5. ACKNOWLEDGEMENT

We thank Dr. Nonaka for helpful discussion.

6. REFERENCE

- [1] Wakisaka, M. et al. *Baiomasu Kagaku Kaigi Happyo Ronbunshu*, **2**, 42-43 (2007)
- [2] Shinano, T. et al. *Trans. Mater. Res. Soc. J.*, **33**, 1181-1184 (2008)
- [3] Shinano, T. et al. *Trans. Mater. Res. Soc. J.*, **33**, 1185-1188 (2008)
- [4] Chemical Institutes of Forest Products, University of Tokyo, *Experiments in Chemistry of Forest Products*, Sangyo Tosho Publishing Co., Ltd.

(Received December 12, 2008; Accepted September 16, 2009)

Response of lignophenols for oxidation and reduction systems

Shimpei HORII and Masamitsu FUNAOKA

Graduate School of Bioresources, Mie University, SORST JST, Tsu, Japan

Fax: 059-231-9521, e-mail: funaoka@bio.mie-u.ac.jp

Lignin is one of the most abundant renewable materials. It has perfect biodegradability in soil. This biodegradation proceeds oxidatively and reductively. In order to utilize along the material flow in the ecosystem, it is important to obtain information for oxidative and reductive responses of lignophenols, which were synthesized through the phase-separation system. Lignocresol was synthesized from Hinoki cypress (*Chamaecyparis obtusa*) through the phase-separation system with 72% H₂SO₄ and *p*-cresol. Responses under both oxidation and reduction environments were estimated by FT-IR, TGA and TMA. Both lignocresol and wood meals were oxidized with sodium periodate. FT-IR spectra of oxidized lignocresol indicated the formation of muconic acid type structures. FT-IR spectra of lignocresol derived from oxidized wood meals indicated the phenolation of conjugated carbonyl structures. Thermal stability of lignophenols was improved by the reduction treatments with sodium borohydride.

Key words: Lignin, Phase-separation system, Lignophenol, Oxidation, Reduction

1. INTRODUCTION

Lignin is one of the most abundant renewable materials on the earth, accounting for approximately 25-35% of the organic matrix of lignocellulosic biomass. It has high potential as a feedstock for producing chemicals, fuels and materials. Lignin has been mainly used as an energy source in pulp and paper industries. During pulping process at high temperature and pressure, structures of lignin become complex. These random structures make the utilization difficult as a functional polymer.

However, selective structural control of lignin can be achieved through the phase-separation system, which has been developed by Funaoka since 1988 [1-3]. Lignocellulosics are rapidly separated to water-soluble saccharides and lignin derivatives with concentrated acid and phenol derivatives under ordinary pressure at room temperature through the system. The separated lignin derivatives (lignophenol) have 1,1-bis(aryl)propane type structures. Lignophenols also have several structural characteristics. They are highly phenolic and very lightly colored *etc.* Additionally, lignophenols were designed to be able to control the functionalities such as molecular weight. Lignophenols have been expected to be effectively utilized as alternative resources to fossil materials.

In order to utilize lignin along a material flow in the ecosystem, it is important to obtain information for oxidative and reductive responses. Lignin is biodegraded in soil with creating various functions such as adsorption of metallic ions or proteins. That degradation proceeds oxidatively and reductively.

In this work, periodate oxidation and borohydride reduction were applied to wood meals and lignophenols, and the structural features of the resulting lignins were discussed in the point of view of functionality control for successive utilization. Generally periodate oxidation has been used for estimation of phenolic hydroxyl groups in lignin [4, 5]. One mole of methanol per mole of phenolic hydroxyl group is released during the oxidation. At this time, aromatic ring of lignin with phenolic hydroxyl group was converted to muconic acid

type structures via *o*-quinone structure. Borohydride reduction has been investigated for bleaching of pulp [6, 9]. The combination of oxidation and reduction might enable selective functionality control of lignophenol.

2. EXPERIMENTAL

2.1 Synthesis of lignophenol

The chips of Hinoki cypress (*Chamaecyparis obtusa*) were milled to 60 mesh. Extractives in the wood meals were removed with benzene / ethanol = 2 / 1 (v/v) using Soxhlet system for 72 hrs. Lignocresol (LC) was synthesized through the phase-separation system, using two-step method (process II) (Fig. 1). The wood meals (50 g) were immersed in acetone solution of *p*-cresol with concentration of 3 mol / phenylpropane units (C₉

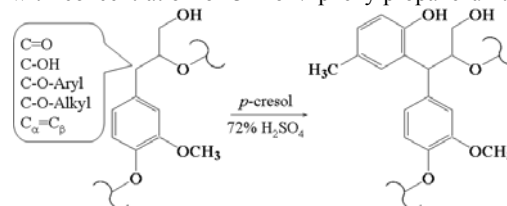


Fig. 1 Synthesis of lignophenols through the phase-separation system with *p*-cresol and 72% H₂SO₄.

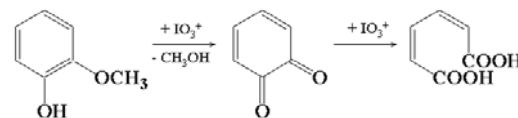


Fig. 2 Periodate oxidation of lignin model.

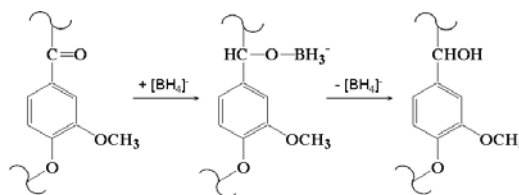


Fig. 3 Borohydride reduction of lignin.

units). After evaporating acetone, 72% H₂SO₄ was poured into the wood meals at 30°C. Then, the mixture was stirred vigorously for 60 min. Then, the mixture was poured into 2 L of de-ionized water with vigorously stirring. Then the precipitation was washed until neutral. After drying, the precipitates were dissolved in acetone, and insoluble materials were removed by centrifugation and filtration. The acetone solution was concentrated under reduced pressure and added dropwise to excess amount of diethyl ether with stirring. The precipitated lignocresol was collected by centrifugation. After evaporating and drying on P₂O₅, lignocresol was obtained.

2.2 Periodate oxidation

Periodate oxidation was carried out, according to the procedure by Funaoka (Fig. 2) [2]. Oxidation of wood meals: A saturated sodium periodate (NaIO₄) solution kept at 4°C (15 mL/g) was added to wood meals. The suspension was homogenized and placed in a refrigerator at 4°C with occasional stirring for 48 hrs. After the treatment, the materials were filtered and washed with cold de-ionized water. After freeze-drying and drying on P₂O₅, oxidized wood meals were obtained.

Oxidation of lignocresol: Lignocresol was dissolved in glacial acetic acid (1 mL/100 mg), to which the sodium periodate (NaIO₄) solution (15 mL/100 mg) was added. The reaction mixture was kept with occasional stirring at 4°C for 72 hrs. Then, it was added dropwise to an excess amount of cold water with vigorous stirring and the precipitated oxidized lignocresols were collected by centrifugation and washed with cold water. After freeze-drying followed by drying on P₂O₅, oxidized lignocresol (OLC) was obtained.

2.3 Synthesis of lignophenols from oxidized wood meals

Lignocresol was synthesized from oxidized wood meals through the phase-separation system, using one-step method. *p*-Cresol (10 mL/g wood) was added to wood meals with stirring. After 10 min, 72% H₂SO₄ (20 mL/g wood) was added to the mixture and the vigorous stirring was continued at room temperature for 60 min. The separated cresol phase was added dropwise to an excess of diethyl ether with vigorous stirring. The precipitates were dissolved in acetone, and insoluble materials were removed by centrifugation and filtration. The acetone solution was concentrated under reduced pressure and added dropwise to an excess of diethyl

ether with stirring. The precipitated lignocresol was collected by centrifugation. After evaporating and drying on P₂O₅, lignocresol derived from oxidized wood meals (LCO) was obtained.

2.4 Sodium borohydride reduction

Lignocresol, oxidized lignocresol and lignocresol derived from oxidized wood meals were dissolved in 0.1 N NaOH under a nitrogen atmosphere, to which sodium borohydride (NaBH₄) was added (Fig. 3). The reaction mixture was kept with occasional stirring at room temperature for 72 hrs. Then, it was acidified to pH 2 with 1 N HCl. The precipitates were collected by centrifugation, washed until neutral. After freeze-drying following by drying on P₂O₅, reduced lignocresol (RLC), reduced oxidized lignocresol (ROLC) and reduced lignocresol derived from oxidized wood meals (RLCO) was obtained.

2.5 Alkaline treatment of lignophenol

Lignocresol was dissolved in 0.1 N NaOH under a nitrogen atmosphere. The reaction mixture was kept with occasional stirring at room temperature for 72 hrs. Then, it was acidified to pH 2 with 1 N HCl. The precipitates (ALC) were collected by centrifugation and washed until neutral.

2.6 Analytical methods

The structures of lignophenols were characterized by Fourier Transformation Infra-Red spectroscopy (FT-IR), Thermogravimetry analysis (TGA) and Thermo Mechanical Analysis (TMA). FT-IR spectroscopy was carried out on a Spectrum GX (Perkin Elmer Co.), using the KBr pellet technique for sample preparation. TGA was carried out by TG/DTA-6200 (SII Inc.) at a rate 2°C min⁻¹ under 300 mL min⁻¹ of N₂ flow. TMA was also carried out by TMA-SS (SII Inc.) in the temperature range 50-280°C at a rate of 2°C min⁻¹, using penetrating technique for a measurement.

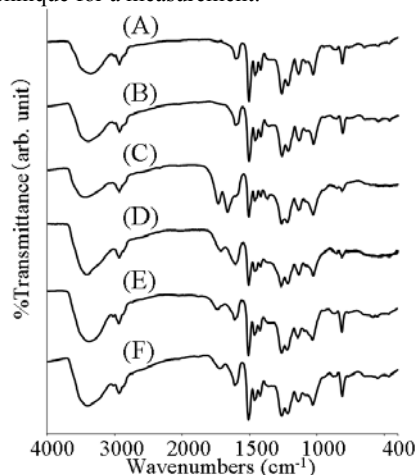


Fig. 4 FT-IR spectra of lignophenols. (A) Lignocresol; LC, (B) Reduced lignocresol; RLC, (C) Oxidized lignocresol; OLC, (D) Reduced oxidized lignocresol; ROLC, (E) Lignocresol derived from oxidized wood meals; LCO, (F) Reduced lignocresol derived from oxidized wood meals; RLCO

Table I Yields of lignophenols.

	Yields	
	(%) of wood meal	(%) of Klason lignin*
LC	27.3	93.3
OLC	25.4	86.6
LCO	37.7	128.7
RLC	24.1	82.1
ROLC	22.7	77.3
RLCO	26.9	91.9

* Klason lignin means the amount of lignin in the plant.

3. RESULTS AND DISCUSSION

3.1 Yields of lignophenols

Yields of lignophenols were shown in Table 1. LC was effectively synthesized from Hinoki cypress wood meals. OLC was obtained in 93.3% yield from LC. In contrast, LCO was obtained in 128.7% yield based on Klason lignin. This would be attributed to large amount of introduced *p*-cresol. Through the phase-separation treatment after the oxidation, the phenolation for conjugated structures in muconic acid type structures occurred. However, LCO includes adsorbed *p*-cresol. RLC, ROLC, RLCO were obtained in about 88%, 89% and 71% yields, respectively. *p*-Cresol adsorbed on LCO would be washed away during the reduction treatment in the alkaline solution.

3.2 Structural characterization of lignophenols

FT-IR spectrum of LC had a sharp peak at 815 cm^{-1} , assigned to C-H deformations (two adjacent) of cresol (Fig. 4A) [2]. The spectrum of RLC reveals the presence of less carbonyl structures in LC (Fig. 4B). OLC had smaller peaks at 815 cm^{-1} and 1600 cm^{-1} (Fig. 4C). Moreover, it had a peak assigned to conjugated carbonyl group at 1660 cm^{-1} . These suggested that muconic acid type structures were formed by the cleavage of aromatic rings. The peak at 1740 cm^{-1} indicated that OLC had unconjugated carbonyl groups in C γ position. On the other hand, LCO had weak absorption around 1660 cm^{-1} and sharp absorption at 815 cm^{-1} , indicating the introducing of *p*-cresol to conjugated carbonyl structures. By the reduction of OLC and LCO with NaBH_4 , only a weak band remains around 1720 cm^{-1} due to the slow reactivity of the unconjugated carbonyl groups (Fig. 4D, F) [7, 8, 9].

3.3 Thermal properties of lignophenols

The results of TGA were shown in Fig. 5. T_{d5} and T_{d10} of LC were observed at 175 and 242°C , respectively (Fig. 5A). On the other hand, OLC showed 191°C and 233°C respectively. Due to molecular associate of carboxyl groups in muconic acid type structures, thermal stability was improved (Fig. 5B). However, the improvement could be due to the loss of the certain parts during oxidation treatment, which is the lower resistant fraction under the heat condition. The weight loss of LCO was observed at lower temperatures than LC (Fig. 5C). This is attributed to adsorption of *p*-cresol at the surface of LCO structures. Therefore LCO seems to have higher adsorption ability. After the reduction with NaBH_4 in alkaline solution, thermal stabilities of LC, OLC and LCO were improved drastically (Fig. 5D, E, F).

The results of TMA were shown in Fig. 6. TMA profiles showed that solid-liquid transition temperature of LC was 157.7°C (Fig. 6A). This flux indicated that LC is a liner-type polymer. OLC showed no fluidity, indicating that thermal stability was improved as well as the result of TGA (Fig. 6B). LCO has the transition point at 161°C and remarkable swelling during the flux (Fig. 6C). This swelling was due to the increase of viscosity. The increase of viscosity is due to the improvement of the interaction among molecules. Higher adsorption ability of LCO can be accounted by this improvement. In agreement with the results of TGA, reduced lignophenols have higher thermal stability than before.

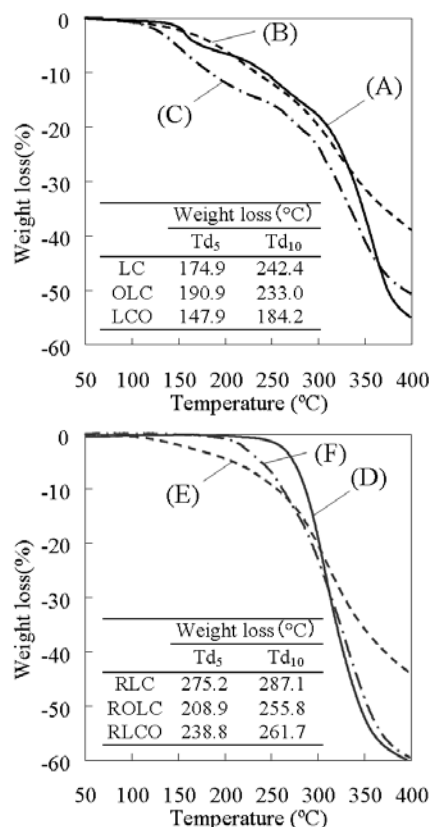


Fig. 5 TGA profiles of lignophenols. (A) LC, (B) OLC, (C) LCO, (D) RLC, (E) ROLC, (F) RLCO

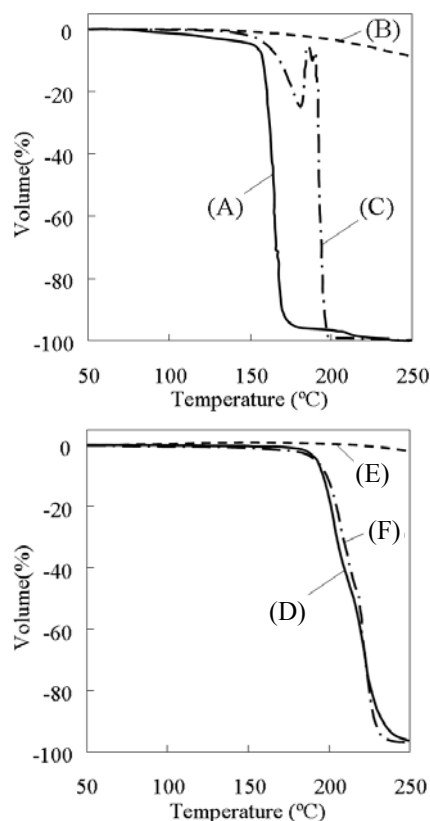


Fig. 6 TMA profiles of lignophenols. (A) LC, (B) OLC, (C) LCO, (D) RLC, (E) ROLC, (F) RLCO

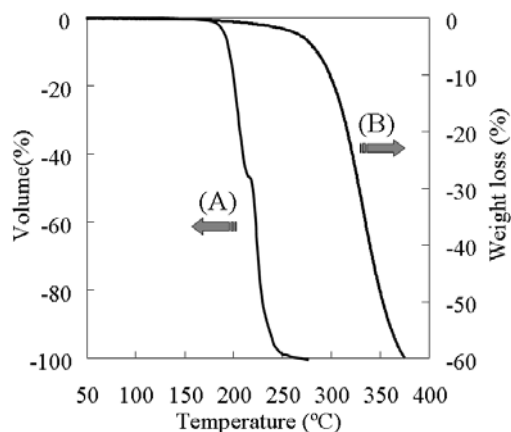


Fig. 7 TGA and TMA profiles of ALC. (A) TMA (B) TGA

This improvement of thermal stability would be affected by the amount of hydroxyl groups. Probably, reduced lignophenols have high hydroxyl contents. Its hydroxyl groups have some hydrogen bonds, which improve the interactions among molecules. However, alkaline treatments also effect on thermal stability. TGA and TMA profiles of ALC were shown in Fig. 7. Td_5 and Td_{10} were observed at 281.1 and 298.5°C respectively. The solid-liquid transition temperature was 194.2°C. The improvements of thermal stability were in the same range with reduced lignophenols. By alkaline treatment, the linkage at C α position such as benzyl aryl ether bond can be cleaved. The low-molecular lignin fractions eliminated during alkaline treatment would behave as an internal plasticizer in lignophenol without alkaline treatment. Therefore, the cleavages of the linkage at C α position would improve thermal stability.

3.4 Proposed structures of lignophenols

Periodate oxidation of LC cleaves the aromatic ring, and then muconic acid type structures are formed (Fig. 8A). Through the phase-separation treatment after the oxidation, conjugated structures are disappeared by the introducing *p*-cresol (Fig. 8B). The main structures of RLC are similar to LC because of a small amount of carbonyl structures. After the borohydride reduction, carbonyl groups in OLC and LCO are converted to alcohol (Figs. 8C and D, respectively). Especially, conjugated carbonyl groups are reduced rapidly than unconjugated ones.

3.4 Potential of these materials as the feedstock

Lignophenols have been investigated as the feedstock for bio-based products such as lignophenol-fiber complex [3], dye-sensitized solar cell [10], bioreactor with enzyme-immobilized ability [3] etc. A unique characteristic of OLC is to have the strong hydrogen bonds due to many carboxyl groups, which can be applied as the reinforcement such as adhesive reagent. LCO has a high adsorption ability. This is expected the application as controlled-release formulation. RLC, ROLC and RLCO have high thermal stability. These would be utilized as molded materials with thermal process.

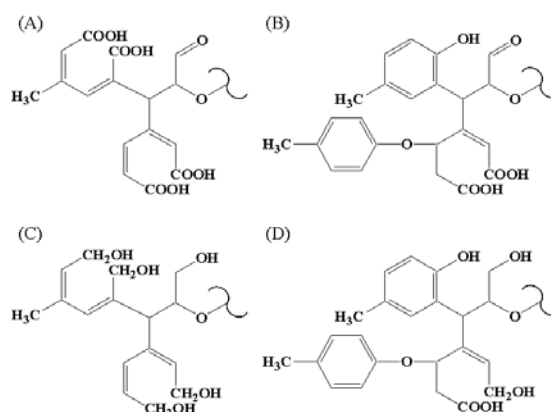


Fig. 8 Proposed structures of lignophenols after oxidation and reduction treatments. (A) OLC, (B) LCO, (C) ROLC, (D) RLCO

4. CONCLUSION

The structural characteristics of lignophenols treated under the oxidative and reductive environments were mainly discussed with FT-IR. After oxidation, OLC had muconic acid type structures. In the results by TGA and TMA, these high thermal stabilities were observed. This is due to hydrogen bonds between carboxylic groups. LCO was obtained in higher yield from oxidized wood meals. This is attributed to a high content of *p*-cresol. The interactions between the molecules of LCO were improved. Reduction treatments in alkaline solution provided higher thermal stability. This would be due to the increase of hydroxyl group. Alkaline treatments also improved the thermal stability.

Oxidation and reduction treatments of lignophenols create new functions. These results indicated that these methods are effective for selective functionality control along the material flow in the ecosystem. These methods have the potential as new application of lignophenols.

5. ACKNOWLEDGEMENT

We thank Dr. Nonaka for helpful discussion.

6. REFERENCES

- [1] M. Funaoka and I. Abe, *Tappi journal*, 72, 145-149 (1989)
- [2] M. Funaoka and S. Fukatsu, *Holzforchung*, 50, 245-252 (1996)
- [3] M. Funaoka, *Polymer International*, 47, 277-290 (1998)
- [4] E. Adler and S. Hernestam, *Acta Chem. Scand.*, 9, 319-334 (1955)
- [5] E. Adler, S. Hernestam and I. Wallden, *Svensk Papperstidn.*, 61, 641-647 (1958)
- [6] W. C. Mayer and C. P. Donofrio, *Pulp and Paper Magazine of Canada*, 59, 157-163, 166 (1958)
- [7] E. Adler and J. Marton, *Acta Chem. Scand.*, 13, 75-96 (1959)
- [8] J. Marton, E. Adler and K. I. Persson, *Acta Chem. Scand.*, 15, 384-392 (1961)
- [9] S. Y. Lin and K. P. Kringstad, *Tappi*, 53, 1675-1677 (1970)
- [10] M. Aoyagi and M. Funaoka, *J. Photochem. Photobiol. A Chem.*, 164, 53-60 (2004)

(Received December 12, 2008; Accepted September 16, 2009)

Rearrangement of Lignin Polymer Network with Lignin Precursors

Maiko OKURA and Masamitsu FUNAOKA

Graduate School of Bioresources, Mie University, SORST JST, Tsu, Japan

Fax: +81-59-231-9521, E-mail: funaoka@bio.mie-u.ac.jp

The exhaustion of petroleum oil has been concerned as the consumption of them increases. In response to the trend, biomass resources, in particular lignocellulosics, recently attracts a lot of attention as a substitute for petroleum oil. The phase-separation system accomplishes conversion and separation of lignocellulosics into both carbohydrates and lignin based polymers by the hydrolysis of carbohydrates and the phenolysis of lignin. Through the system under typical conditions, native lignin is converted into linear type polymer (lignophenol) with *p*-cresol. In this study, the phase-separation treatments with both *p*-coumaric acid (CA) and ferulic acid (FA) were carried out. The lignin derivatives with CA and FA were distributed into the organic and interface layers, termed L-CA/FA and I-CA/FA, respectively. Through the treatments with CA and FA, most part of native lignins were derived as I-CA or I-FA, having black color and poor solubility. The FT-IR spectra of these derivatives showed bands at 1715 and 1610 cm^{-1} assigned to unconjugated and conjugated carbonyl groups, respectively. These results suggested that lignin derivatives were derived by rearrangement of lignin polymer network with CA or FA.

Key words: phase-separation system, lignophenol, lignin precursor, lignin polymer network, natural phenol

1. INTRODUCTION

Oil & Gas Journal (2007) showed that the reserve to production ratio of crude petroleum is around 50 years [1]. Furthermore, mass consumption of fossil fuels has been considered to result in global warming, due to the emission of greenhouse gases.

Lignocellulosics consist of both aliphatic (carbohydrates) and aromatic (lignin) polymers, having potential as chemicals comparable to petroleum. However, since both polymers form a complex interpenetrating polymer network, it is difficult to separate them without disturbing original functions for conversions and applications to chemical materials.

Although some methods to separate lignocellulosics into carbohydrates and lignin have been developed, only carbohydrates have been utilized for various applications, such as wood pulps, chemical feedstocks, and food products. On the other hand, since lignin is out of control due to random rearrangement by conventional methods, it has been scarcely utilized as materials except thermal use until now.

The development of the phase-separation system by Funaoka et al. [2-4] has overcome such problems. The system accomplishes conversion and separation of lignocellulosics into both carbohydrates and lignin based polymers by the hydrolysis of carbohydrates and the phenolysis of lignin under a mild condition. Through the system, native lignin is converted into linear type polymers (lignophenols) with phenol derivatives, such as *p*-cresol, while carbohydrates are converted into polysaccharides with low molecular weight [2]. Lignophenols has 1,1-bis(aryl)propane-2-O-arylether type structures. Selectively grafted phenolic nuclei and aromatic nuclei in lignin are equivalently connected at benzyl positions, leading to hybrids with characteristics of grafted phenols and lignin [5]. In other words,

characteristics or functions of derived materials can be controlled by the phenols use in the system. Applications of *p*-cresol, phenol, *m*- and *p*-ethylphenol, *p*-*n*-propylphenol and guaiacol as grafted phenols in the system have ever been studied [6].

In this study, 3-(4-hydroxyphenyl)-2-propenoic acid (*p*-coumaric acid, CA) and 3-(3-methoxy-4-hydroxyphenyl)-2-propenoic acid (ferulic acid, FA) were applied as grafted phenol in the system. They are included in plant extractives from grass and covalently linked to polysaccharides by ester bonds and to lignin units by ester or ether bonds [7]. These natural phenols, referred as lignin precursors, are bio-synthesized from glucoses through shikimic acid pathway and converted into cinnamic alcohol derivatives, constructing lignin polymer via random coupling. Therefore, all-lignin-derived materials can be produced by the phase-separation treatment with CA or FA.

In this work, hinoki cypress (*Chamaecyparis obtusa*) lignin was treated with CA, FA, and *p*-cresol by the phase-separation processes using sulfuric or phosphoric acid as aqueous solvent. By the treatment using sulfuric acid, native lignins were converted into lignophenols (ligno-cresol, ligno-coumaric acid and ligno-ferulic acid) and interface fractions (interface-coumaric acid and interface-ferulic acid). These lignophenols are described respectively as L-cresol, L-CA and L-FA. These interface fractions are described respectively as I-CA and I-FA. In the case with phosphoric acid, lignin derivatives are described as L-CAP/L-FAP for lignophenols and I-CAP/I-FAP for interface fractions, respectively. The characteristics of lignin derivatives were analyzed by FT-IR, GPC, TMA and TGA.

2. EXPERIMENTAL

2.1 Materials and Preparations

Wood chips of hinoki cypress (*Chamaecyparis obtusa*) were ground to pass a 60-mesh screen using an ultracentrifugal mill (ZM100, Retch, Germany). Then extractives in the wood meal were removed with ethanol/benzene (1:2, v/v) using Soxhlet system for 48 h, and air-dried.

CA and FA were obtained from Tokyo Chemical Industry Co., and *p*-cresol were obtained from Wako Pure Chemical Industries, Ltd. Sulfuric acid (Wako Pure Chemical Industries, Ltd., 97%) was diluted into 72% with deionized water. 95% phosphoric acid were prepared from *o*-phosphoric acid (Merck KGaA, 99% solid).

2.2 Synthesis of L-cresol

Synthesis of L-cresol was carried out by the phase-separation treatment (2 step process I) [6]. Three mol/C₉ units of *p*-cresol is dissolved in acetone and allowed to penetrate within the extractive-free wood meal (1 g) for 24 h. After evaporating acetone, 72% sulfuric acid (10 mL) was added into wood meal sorbed with *p*-cresol. Then the mixture was stirred vigorously for 30 min at 30°C, followed by the addition of *p*-cresol (10 mL) and further stirring for 20 min. After centrifugation of the reaction mixture (3500 r.p.m., 25°C, 10 min), the mixture was separated into two layers in centrifuge tube. The upper layer is organic phase and another layer is aqueous phase. The organic phase was dropped into diethyl ether in chilled conditions. Precipitation in diethyl ether was picked up by centrifugation and extracted with acetone. The acetone-soluble material was purified by the above procedure with diethyl ether, evaporated and dried on P₂O₅, leading L-cresol (Fig. 1).

2.3 Syntheses of L-CA and L-FA

The extractive-free wood meals (1 g) were treated with CA or FA by the process using 72% sulfuric acid, like above (2.2). After centrifugation of the reaction mixture (3500 r.p.m., 25°C, 10 min), the mixtures were separated into three layers in centrifuge tube. The upper layers are organic phase, the middle layers are insoluble interface and other layers are aqueous phase, respectively. The organic phases were treated by above process with diethyl ether and acetone, leading 1st L-CA or L-FA (Fig. 1). While the insoluble interfaces were thrown into an excess amount of deionized water and washed to around pH 7. After deacidified, the interfaces were freeze-dried and dried on P₂O₅.

2.4 Second phase-separation treatment with interfaces

The dried insoluble interfaces with CA or FA obtained through the above process (2.3) were consecutively treated by the phase-separation process (1 step process) [6], to hydrolyze undegraded carbohydrates and to release lignin derivatives. *p*-Ethylphenol/benzene (7:3, v/v, 5 mL) was added to the dried interfaces, followed by the addition of 72% sulfuric acid (10 mL). The reaction mixtures were stirred vigorously for 60 min at 30°C and centrifuged (3500 r.p.m., 25°C, 10 min), then three layers were obtained like above. The insoluble interfaces and the organic phases were treated as described above, leading I-CA/I-FA and 2nd L-CA/L-FA, respectively (Fig. 1). In

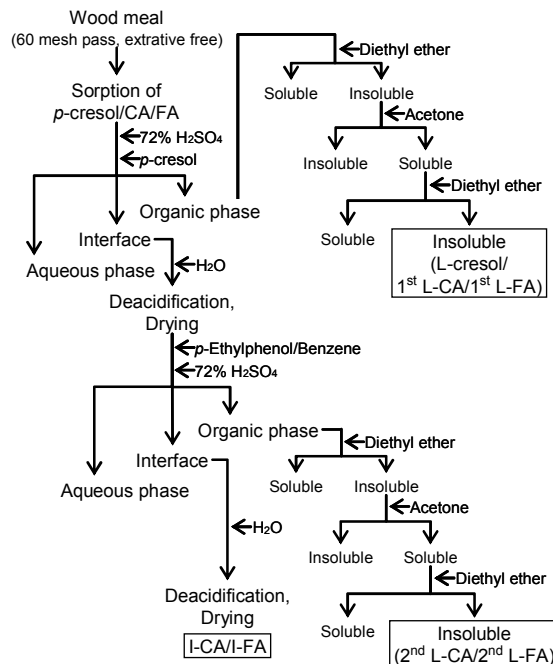


Fig. 1 Syntheses of lignin derivatives through the phase-separation treatment with 72% sulfuric acid.

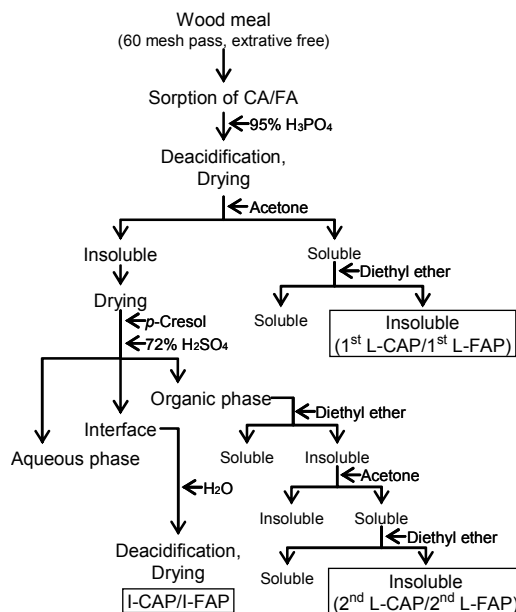


Fig. 2 Syntheses of lignin derivatives through the phase-separation treatment with 95% phosphoric acid.

this study, 2nd L-CA and L-FA were not analyzed.

2.5 Syntheses of L-CAP and L-FAP

Syntheses of L-CAP and L-FAP with phosphoric acid were carried out by the phase-separation treatment (2 step process II) [6]. 95% phosphoric acid (10 mL) was added into wood meal sorbed with CA or FA like above (2.3), and then the mixtures were stirred vigorously for 60 min at 50°C. The reaction mixtures were thrown into an excess amount of deionized water and washed to around pH 7. After deacidified, the water-insoluble materials were freeze-dried, dried on P₂O₅ completely,

Table I Yields of lignin derivatives with CA, FA and *p*-cresol through the phase-separation system.

Used acid	Lignin der.	Yields of lignin derivatives	
		(% of wood)	(% of Klason lignin)
H ₂ SO ₄	1 st L-CA	2.7	8.5
	2 nd L-CA	1.0	3.2
	I-CA	44.5	141.1
	1 st L-FA	10.4	33.0
	2 nd L-FA	2.4	7.6
	I-FA	34.3	108.8
	L-cresol	26.2	83.0
H ₃ PO ₄	1 st L-CAP	6.4	20.4
	2 nd L-CAP	3.6	11.3
	I-CAP	36.4	115.4
	1 st L-FAP	11.8	37.5
	2 nd L-FAP	8.9	28.3
	I-FAP	21.5	68.0

and then extracted with acetone. The acetone-soluble materials were purified by the above procedure with diethyl ether, leading 1st L-CAP or L-FAP (Fig. 2).

The acetone-insoluble materials were evaporated and consecutively treated by phase-separation process (1 step process) with *p*-cresol and 72% sulfuric acid, like above (2.4). The treatment led I-CAP/I-FAP and 2nd L-CAP/L-FAP, respectively (Fig. 2). In this study, 2nd L-CAP and L-FAP were not analyzed.

2.6 Characterization of lignin derivatives

Characteristics of lignin derivatives were estimated by Fourier Transform Infrared Spectroscopy (FT-IR), Gel Permeation Chromatography (GPC), Thermo Mechanical Analysis (TMA) and Thermo Gravimetric Analysis (TGA). FT-IR was carried out on Spectrum GX (Perkin Elmer Co.) in the wavelength range from 4000 to 400 cm⁻¹, using the KBr pellet technique for sample preparation. GPC was carried out by LC-10 system (Shimadzu Co.) with four columns (KF801, KF802, KF803, and KF804, Shodex Co.), using distilled tetrahydrofuran after distillation with a flow rate of 1 mL/min. M_w and M_n were determined based on standard polystyrenes. TMA was carried out by TMA/SS6100 (SII Inc.) in a temperature range from 50 to 260°C at a rate of 2 °C/min under N₂ flow, using penetrating technique. TGA was carried out TG/DTA-6200 (SII Inc.) at a rate of 2 °C/min under 300 mL/min of N₂ flow.

3. RESULT AND DISCUSSION

3.1 Presumable structures of lignin derivatives

Table I shows the yields of lignin derivatives with CA, FA and *p*-cresol synthesized through the phase-separation system with 72% sulfuric acid. Through the treatments, the yields of L-CA and L-FA fell much below that of L-cresol. In other words, most of native lignins were obtained as I-CA or I-FA, insoluble in both organic and aqueous phases. This result demonstrates that I-CA and I-FA have consisted of undegraded (or released) lignin and carbohydrate polymers. Interfaces have black color and poor solubility for solvents such as acetone, tetrahydrofuran, methyl cellosolve and pyridine.

FT-IR spectra of lignin derivatives with CA and FA (Fig. 3) show particular peaks for unconjugated carbonyl groups around 1717 cm⁻¹ and for conjugated carbonyl

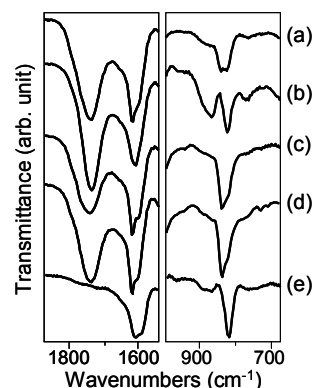


Fig. 3 FT-IR spectra of lignin derivatives through the phase-separation system with 72% sulfuric acid. (a) 1st L-CA, (b) 1st L-FA, (c) I-CA, (d) I-FA, and (e) L-cresol.

groups around 1610 cm⁻¹. These peaks suggest the presence of CA or FA in the molecules. Although, it is not clear what combines to lignin-based polymer, since lignin derivatives with CA and FA can trap other solvents or molecules intermolecularly, not intramolecularly. Furthermore, these derivatives have several types of bands around 800-900 cm⁻¹, assigned to C-H deformations in aromatic nuclei, indicating that lignin derivatives with CA or FA can have random linking pattern.

GPC profiles of both L-CA and L-FA (Fig. 4) showed low elution peaks corresponding to CA or FA monomers, demonstrating that CA and FA have combined with lignin polymers with regard to L-CA or L-FA. Namely, L-CA and L-FA would be derived by rearrangement of lignin polymer network with CA or FA.

Fig. 5 and Fig. 6 are TMA profiles and TG curves of lignin derivatives, respectively. TMA profiles show that lignin derivatives with CA and FA have much lower volume decrease than that of L-cresol. Additionally TG curves show that L-CA and L-FA are more thermally resistant than L-cresol. These results demonstrate that both L-CA and L-FA are more thermostable than L-cresol, because the rigid linkages in network structure inhibit thermally degradation or release of polymer structures. This confirms structural rigidity of these derivatives. On the other hand, thermal behaviors of I-CA or I-FA are characteristic; thermally degradation (or release) of molecular structures is initiated at low temperature and proceeds mildly. These results imply that both I-CA and I-FA have constructed rigid network polymer in which other solvents or molecules, could be trapped like capsules.

3.2 Synthesis of lignin derivatives with phosphoric acid

As indicated above, most of native lignins were derived as I-CA or I-FA through the phase-separation treatment using 72% sulfuric acid. It is proposed that strong acid accelerated excess cross-linking with CA and FA in lignin network, because these phenols poorly prevent electrophilic attack by proton to benzyl position in lignin due to hydrophilic carboxyl groups. This hypothesis suggested that strength of a used acid can control the extent of cross-linking with CA and FA in lignin network. Thus, the phase-separation treatments using phosphoric acid, milder than sulfuric acid, were

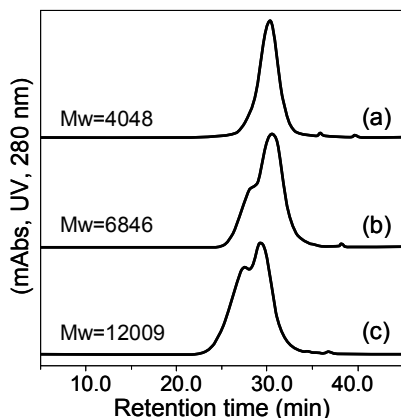


Fig. 4 GPC profiles of lignophenols through the phase-separation system with 72% sulfuric acid. (a) 1st L-CA, (b) 1st L-FA, and (c) L-cresol.

carried out (Fig. 2).

Yields of both L-CAPs and L-FAPs synthesized with 95% phosphoric acid were higher than that of L-CAs and L-FAs synthesized with 72% sulfuric acid (Table I). These results indicate that the extent of cross-linking with CA and FA in lignin network depends on the strength of a used acid. Additionally, FT-IR spectra of these lignophenols (Fig. 7) show that both L-CAP and L-FAP have similar structure to L-CA and L-FA, respectively. In other words, L-CAP and L-FAP are also expected to have network structures, such as L-CAs and L-FAs synthesized with 72% sulfuric acid.

4. CONCLUSION

The phase-separation treatments of native lignins with lignin precursors, CA and FA were carried out to rearrange lignin polymer networks leading to new functions. FT-IR spectra and GPC profiles indicated that lignin derivatives through these treatments have linkages with CA and FA intramolecularly. Furthermore, TMA profiles and TG curves indicate that these derivatives have higher rigidity and thermostability than L-cresol. Through the phase-separation treatment using phosphoric acid, the yields of lignophenols increased due to limited cross-linking. These derivatives are also

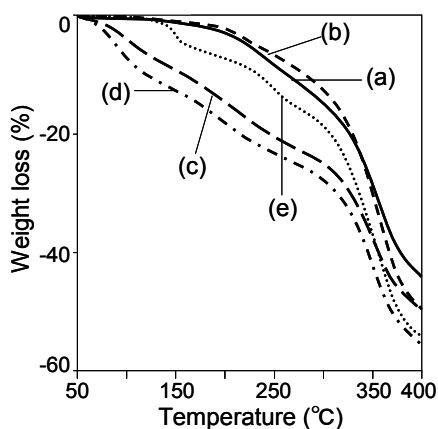


Fig. 6 TG curves of lignin derivatives through the phase-separation system with 72% sulfuric acid. (a) 1st L-CA, (b) 1st L-FA, (c) I-CA, (d) I-FA, and (e) L-cresol.

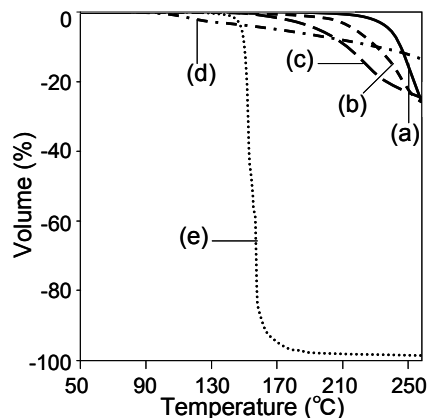


Fig. 5 TMA profiles of lignin derivatives through the phase-separation system with 72% sulfuric acid. (a) 1st L-CA, (b) 1st L-FA, (c) I-CA, (d) I-FA, and (e) L-cresol.

expected to have network structures, such as that with 72% sulfuric acid.

These all-lignin-derived polymers with novel characteristics can be utilized for various applications, such as controlled-release membrane for manure and medicines.

5. ACKNOWLEDGMENT

We thank Dr. Nonaka for helpful discussion.

6. REFERENCES

- [1] PennWell Corporation, *Oil & Gas Journal* (December, 2007).
- [2] M. Funaoka and I. Abe, *Tappi*, 72, 145-149 (1989).
- [3] M. Funaoka, M. Matsubara, N. Seki and S. Fukatsu, *Biotechnol. Bioeng.*, 46, 545-552 (1995).
- [4] M. Funaoka and S. Fukatsu, *Holzforchung*, 50, 245-252 (1996).
- [5] M. Funaoka, *Polymer application*, 48, 66-73 (1999).
- [6] M. Funaoka, *Polym. Int.*, 47, 277-290 (1998).
- [7] A. Scalbert, B. Monties, J. Y. Lallemand, E. Guittet and C. Rolando, *Phytochemistry*, 24, 1359-1362 (1985).

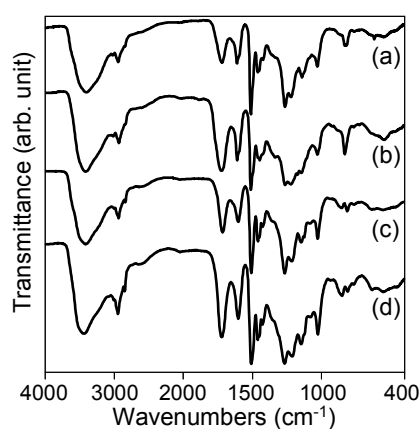


Fig. 7 FT-IR spectra of 1st lignin derivatives through the phase-separation system. (a) 1st L-CA, (b) 1st L-CAP, (c) 1st L-FA, and (d) 1st L-FAP.

(Received December 12, 2008; Accepted September 16, 2009)

CO₂ adsorption/desorption on mesoporous silica at various pressuresRyosuke Nakanishi, Masaya Suzuki¹, Keiichi Inukai, Masaki Maeda

AIST, Materials Research Institute for Sustainable Development, 2266-98 Anagahora, Shimoshidami, Moriyama-ku, Nagoya, 463-8560

¹ AIST, Institute for Geo-Resources and Environment, AIST Central 7, 1-1-1 Higashi, Tsukuba, 305-8567

CO₂ adsorption/desorption on zeolite X and mesoporous silica (MCM-41) was examined under high pressure up to 950 kPa for carbon capture and storage (CCS). The pressure swing adsorption (PSA) method for CO₂ separation and capture was used, because of its energy efficiency. In the range of 100-950 kPa, the amounts of CO₂ adsorbed on MCM-41 and zeolite X were 14.6 wt% and 5.4 wt%, respectively. The amount of CO₂ adsorbed on MCM-41 was 2.5 times greater than that of zeolite X with respect to atmospheric pressure.

Key words: CO₂ adsorption, PSA, atmospheric pressure, mesoporous silica, global warming

Introduction

In recent years, the CO₂ concentration in the atmosphere has been increasing. It is commonly considered that the increase in CO₂ concentration contributes to global warming; therefore, it is very important to reduce CO₂ emission. One effective method to decrease CO₂ emission in the short term is CO₂ capture from concentrated generation sources, such as thermal power plants, steel plants and cement manufacturing plants. Currently, conventional CO₂ capture methods are chemical absorption, physical absorption, pressure swing adsorption (PSA), membrane separation and hybrid processes of these. The chemical absorption process comprises a rotation of CO₂ absorption in amine solutions, such as monoethanolamine (MEA) and methyldiethanolamine (MDEA), with subsequent dissociation by heating at 110-140 °C [1-4]. The PSA method consists of a cycle of CO₂ adsorption on adsorbents such as zeolite by increasing pressure, and desorption by decreasing the pressure [5-7]. Recovery of CO₂ by membrane processes is affected by the transmission rates of other gases (e.g. CH₄, N₂ etc.) and the selectivity of CO₂ [8-9]. Hybrid methods using membranes and amine solutions have been proposed as improved technologies [10-12]. Underground CO₂ storage is one method for the disposal of captured CO₂, and has been researched and assessed with respect to safety and cost [13-14]. Some large-scale experiments regarding underground CO₂ storage are soon to be conducted in Japan. It is, however, necessary to reduce the expense of carbon capture and storage (CCS).

In this study, the PSA method was selected for the improved capture CO₂ with respect to small-scale and energy efficiency. Zeolite has been conventionally used as an adsorbent for the PSA method, and the process requires a vacuum to release CO₂ from the adsorbent [15]. However, the energy required to produce the vacuum is excessive; therefore, the process is not cost-efficient for practical applications. A more energy-efficient method

would be to adsorb CO₂ at high pressure and extract it by returning to atmospheric pressure, rather than by evacuation of the air. Using this method, it was found that the amounts of CO₂ adsorbed/desorbed on mesoporous silica were twice as much as those on zeolite X at 100-950 kPa. In this paper, we report CO₂ adsorption/desorption on mesoporous silica and zeolite X under high pressures.

Experimental

Synthesis of Mesoporous Silica (MCM-41)

Mesoporous silica (MCM-41) was prepared by the following procedure. Cetyltrimethylammonium bromide (2.4 g), as a surfactant, was dissolved in 100 mL of distilled water to prepare a 0.066 mol L⁻¹ solution, followed by the addition of 12.4 mL of ethylamine. After a homogeneous mixture was formed, 10 mL of tetraethoxysilane (TEOS) was added dropwise to the surfactant solution. The mixture was stirred for 5 h and poured into a 100 mL Teflon bottle followed by heating at 100 °C for 48 h. The white product was washed using 1 L of distilled water with centrifugation and then dried in air. The sample was then calcined at 550 °C in a muffle furnace under static air for 5 h [16-17].

Characterization of samples

The MCM-41 sample was evaluated using X-ray diffraction (XRD; RINT 2100V, Rigaku Co.). The surface areas and pore volumes of the samples were measured using N₂ adsorption apparatus (NOVA, Quantachrome Co.), prior to which the samples were degassed at room temperature (25 °C) for 3 h, followed by heating at 110 °C (MCM-41) and at 330 °C (zeolite X) for 6 h.

CO₂ adsorption/desorption measurements

The amounts of adsorbed/desorbed CO₂ on the MCM-41 and zeolite X (Mizusawa Co.) samples were measured at 298 K using an automatic gas adsorption

apparatus (Belsorp HP, Bel Japan). Before the CO₂ adsorption test, the samples were deaerated under vacuum at 110 °C for 2 h and the dry weight value was used for the test.

Results and discussion

The XRD pattern of MCM-41 is shown in Figure 1. Peaks were evident at 2.7, 4.7, 5.4 and 7.3°, which confirmed the successful synthesis of MCM-41 [18]. Table 1 shows the characteristics of zeolite X and MCM-41 obtained from the N₂ adsorption experiments. The diameter of zeolite X and MCM-41 were determined by SF method and BJH method, respectively. The BET surface area of MCM-41 was 870 m² g⁻¹, while that of zeolite X was 490 m² g⁻¹.

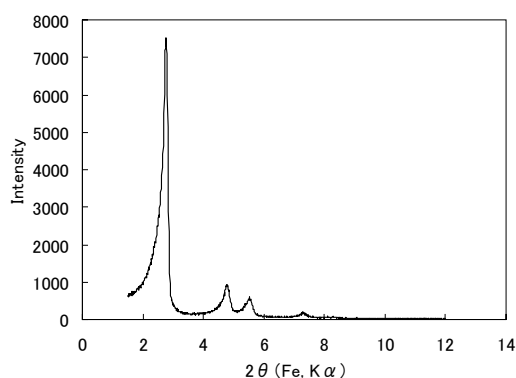


Figure 1. XRD pattern of mesoporous silica (MCM-41).

CO₂ adsorption/desorption isotherms for MCM-41 and zeolite X with respect to (a) the absolute pressure and (b) atmospheric pressure (103 kPa) are shown in Figure 2. The filled and opened symbols represent the amounts of adsorbed CO₂ during the adsorption and desorption processes. The CO₂ contents adsorbed on zeolite X and MCM-41 at 900 kPa with respect to the absolute pressure were 23 wt% and 18 wt%, respectively. However, with respect to the atmospheric pressure, the amounts of CO₂ adsorbed on zeolite X and MCM-41 were 5.4 wt% and 14.6 wt% at the same pressure, respectively. The amount of CO₂ adsorbed on MCM-41 was approximately two and a half times that on zeolite X at 900 kPa with respect to atmospheric pressure. No hysteresis was observed in the adsorption/desorption isotherms of zeolite X. In contrast, the isotherms of MCM-41 exhibited a slight hysteresis. The recovery rate of CO₂ was calculated by dividing the amount of CO₂ desorption at different equilibrium pressures by the adsorbed amount in the range of same pressures. Considering the application of MCM-41 as a CO₂ adsorbent for PSA, hysteresis effects are problematic, as they would cause a decrease in the recovery rate of CO₂.

The experimental results lead us to two possible speculations. (i) The average pore size of zeolite X was 1.5 nm, so that CO₂ was easily adsorbed into the large amount of micropores by capillary tube condensation under vacuum state. However, MCM-41 had an average pore size of 3.1 nm; therefore, it was difficult for CO₂ molecules to enter the pores at around 100 kPa compared

Table 1. Characteristics of zeolite X and MCM-41 from N₂ adsorption. (Pore diameters of zeolite X and MCM-41 were calculated using the Saito-Foley (SF) method and Barrett-Joyner-Halenda (BJH) methods, respectively. Surface areas were calculated using the Brunauer-Emmett-Teller (BET) method.)

	Zeolite X	MCM-41
Pore Diameter (nm)	1.5	3.1
Total Pore Volume (cm ³ g ⁻¹)	0.252	0.908
BET Surface Area (m ² g ⁻¹)	490	870

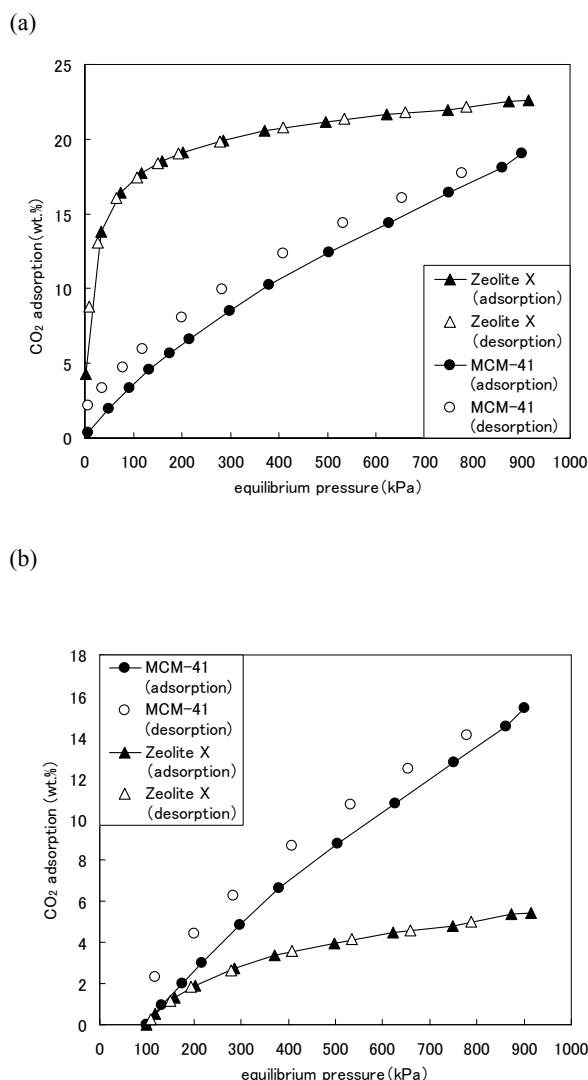


Figure 2. CO₂ adsorption/desorption isotherms of MCM-41 and zeolite X at 298 K with respect to (a) absolute pressure, and (b) atmospheric pressure.

to zeolite X. However, more CO₂ molecules could be forced into the pores of MCM-41 with increasing pressure. It was speculated that the amount of CO₂ adsorbed on zeolite X would remain at approximately the same level at more than 900 kPa. On the other hand, the amount of CO₂ adsorption on MCM-41 would increase until the total pore volume became saturated as the equilibrium pressure increased. The total pore volume of MCM-41 was larger than that of zeolite X (Table 1), so that there would be space for CO₂ molecules to adsorb. (ii) CO₂ molecules can move more easily into zeolite X pores, because it has a three-dimensional pore shape. However, MCM-41 has a one-dimensional pore form [17, 19]. These different pore shapes have an effect on the distinct type of adsorption. From these speculations, adsorbents with large pore size, large total pore volume and the type of pore shape could be utilized for the adsorption/desorption of large amounts of CO₂ above atmospheric pressure.

In CO₂ adsorption/desorption, there is also the possibility of electronic interaction between the surface atoms of solids and CO₂ molecules [20]. The surface of MCM-41 consists of silicon (Si), oxygen (O) and hydroxyl radical (OH). Zeolite X consists of Si, aluminum (Al), O and cation such as sodium (Na⁺) and calcium (Ca²⁺). Hydroxyl radical would presumably be available on the surface of zeolite X. Considering the electron configuration of each element or hydroxyl group, the surface electric states of MCM-41 and zeolite X are different. The presence of hysteresis effects in isotherms may be due to pore shape or to the different surface electronic states of adsorbents. Therefore, it would be necessary to examine the effect of the surface electronic states of adsorbents on CO₂ adsorption/desorption in future research.

References

- 1 J.T. Yeh, K.P. Resnik, K. Rygle, H.W. Pennline, *Fuel Proc. Technol.*, 86, 1533-1546 (2005)
- 2 L.M. Romeo, I. Bolea, J.M. Escosa, *Appl. Therm. Eng.*, 28, 1039-1046 (2008)
- 3 T. Yagi, H. Shibuya, T. Sasaki, *Energy Convers. Manag.*, 33, 349-355 (1992)
- 4 D.A. Glasscock, J.E. Critchfield, G.T. Rochelle, *Chem. Eng. Sci.*, 46, 2829-2845 (1991)
- 5 A. Macario, A. Katovic, G. Giordano, F. Iucolano, D. Caputo, *Micropor. Mesopor. Mater.*, 81, 139-147 (2005)
- 6 P.J.E. Harlick, F.H. Tezel, *Micropor. Mesopor. Mater.*, 76, 71-79 (2004)
- 7 K. Bonnot, D. Tondeur, L.A. Luo, *Chem. Eng. Resear. Desig.*, 84 (A3), 192-208 (2006)
- 8 K.Okabe,, N. Matsumiya, H. Mano, *Sep. Purif. Technol.*, 57, 242-249 (2007)
- 9 Y. Fujioka, "Carbon Dioxide Capture and Storage Technology", Ed. by CHIKYU KANKYO SANGYO GIJYUTU KENKYUKIKO, KOUGYO CHOSAKAI press, Tokyo (2006) pp. 77-126.
- 10 M. Teramoto, N. Takeuchi, T. Maki, H. Matsuyama, *Sep. Purif. Technol.*, 27, 25-31 (2002)
- 11 M. Teramoto, N. Ohnishi, N. Takeuchi, S. Kitada, H. Matsuyama, N. Matsumiya, H. Mano, *Sep. Purif. Technol.*, 30, 215-227 (2003)
- 12 M. Teramoto, S. Kitada, N. Ohnishi, H. Matsuyama, N. Matsumiya, *J. Membr. Sci.*, 234, 83-94 (2004)
- 13 C.A. Hendriks, K. Blok, *Energy Convers. Manag.*, 36, 539-542 (1995)
- 14 S. Holloway, *Energy*, 30, 2318-2333 (2005)
- 15 A. Saji, Y. Takamura, H. Noda, F. Watanabe, H. Matsuda, M. Hasatani, *KAGAKU KOUGAKU RONBUNSHU*, 23, 149-156 (1997)
- 16 W. Lin, Q. Cai, W. Pang, Y. Yue, B. Zou, *Micropor. Mesopor. Mater.*, 33, 187-196 (1999)
- 17 J.S. Beck, J.C. Vartuli, W.J. Roth, M.E. Leonowicz, C.T. Kresge, K.D. Schmitt, C.T-W. Chu, D.H. Olson, E.W. Sheppard, S.B. McCullen, J.B. Higgins, J.L. Schlenker, *J. Am. Chem. Soc.*, 114, 10834-10843 (1992)
- 18 S.K. Jana, A. Mochizuki, S. Namba, *Catal. Surv. Japan*, 8, 1-13 (2004)
- 19 C. T.Kresge, M. E. Leonowicz, W.J. Roth, J.C. Vartuli, J.S. Beck, *Nature*, 359, 710-712 (1992)
- 20 K. Kaneko, "HANDBOOK OF INTERFACES: CHEMISTRY AND ENGINEERING", N.T.S., Tokyo (2001) pp. 132-138.

(Received January 8, 2009; Accepted May 26, 2009)

Hydrogen Generating Gel Systems Induced by Visible Light and Application to Artificial Photosynthesis

Kosuke Okeyoshi and Ryo Yoshida*

Department of Materials Engineering, Graduate School of Engineering, The University of Tokyo
7-3-1, Hongo Bunkyo-ku, Tokyo 113-8656, Japan
Fax: 81-3-5841-8844, e-mail: okeyoshi@cross.t.u-tokyo.ac.jp
Fax: 81-3-5841-7112, e-mail: ryo@cross.t.u-tokyo.ac.jp

We tried to achieve artificial photosynthesis systems by using gel to generate hydrogen when visible light and water are supplied. Three types of gels involving electronic transmission circuit with sensitizer, electron acceptor and catalyst were designed and the amount of generated H₂ gas was measured. In the gel systems, hydrogen was generated more efficiently than in the solution systems, and all the functional groups constructed in the gel network worked effectively and cooperated each other to generate hydrogen.

Key words: gels, colloids, photosynthesis, hydrogen

Introduction

Toward the hydrogen-energy society, researches on artificial photosynthesis have been done enthusiastically by using organic and inorganic materials. Grätzel et al. have devised the reaction circuit for solar energy conversion,^[1] which consists of multi-electronic redox reactions to generate hydrogen and oxygen when visible light and water are supplied. But it was difficult to operate this circuit in an aqueous solution because each chemical component is randomly distributed in the medium. Therefore, many researchers have tried to realize this circuit by systematic design using vesicle, micelle, antibody, solid phase, etc. In addition, molecular arrangements for each component have been attempted by using supramolecules such as dendrimers and fullerenes to improve the intramolecular electron-transfer. In these studies, linking of the multiple functional molecules enabled long-lived charge separation between the sensitizer and the electron-acceptor. However, these systems are still incomplete and the conversion efficiency is low to generate hydrogen mainly because the components do not coordinate in the mediums due to self-quenching which significantly occurs at high concentration.

In order to overcome the self-quenching of the photoexcited state, in this study, we used polymer gel as a medium. Gel is a soft and wet material and defined as a crosslinked-polymer network involving solvent. It is possible to arrange functional groups in the network and control molecular behavior by the network. Besides, by using stimuli-responsive polymer, it is possible to control network structure dynamically by external stimuli. Here, we designed functional gels involving the reaction circuit to generate hydrogen when visible light and water were supplied (Fig. 1). By irradiating visible light to the gel, the functional groups constructed in the polymer network decompose water and generate hydrogen. In the gel systems, the necessary components are not dispersed like solution systems. The Pt catalyst is trapped as a nanoparticle in

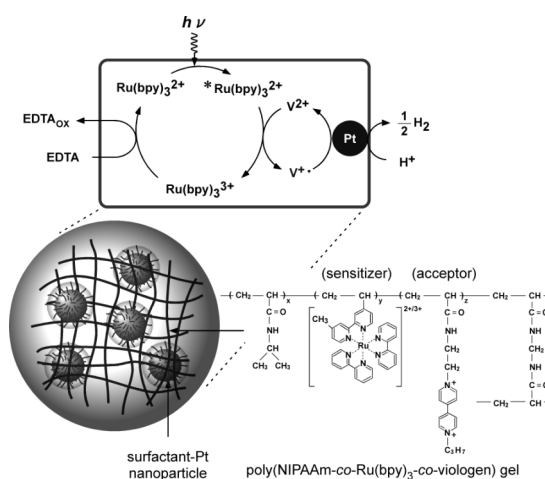


Figure 1. Mechanism of hydrogen generating gel systems using poly(NIPAAm-co-Ru(bpy)₃-co-viologen) gel.

Table I. Components of L and G systems.

System	Gel	Outer solution
L	-	EDTA/Ru(bpy) ₃ ²⁺ /MV ²⁺ /Pt NPs
G1	PNIPAAm gel containing Pt NPs	EDTA/Ru(bpy) ₃ ²⁺ /MV ²⁺
G2	Poly(NIPAAm-co-Ru(bpy) ₃) gel containing Pt NPs	EDTAMV ²⁺
G3	Poly(NIPAAm-co-Ru(bpy) ₃ -co-viologen) gel containing Pt NPs	EDTA

the network, and the sensitizer and the acceptor units are arranged in the gel network organically. The Pt nanoparticles are prepared by using anionic surfactant as a protector. Thus, we designed the electronic transmission circuit to operate smoothly by close arrangement of molecules and by utilizing electrostatic

interaction between the cationic molecules and the anionic surface of Pt nanoparticle. As a result of immobilization of cationic molecules and catalyst with negative surface in gel systems, the multivalent interaction between them enhances the electronic transmission to generate hydrogen.

In order to construct such a gel system, the necessary components were introduced one by one. Three types of gel systems (G1 ~ G3), that is, microgel suspension composed of microgels and reactants in the aqueous phase are prepared (Table I). Each function was verified by visible light irradiation.

Experimental

Materials. *N*-isopropylacrylamide (NIPAAm; Wako Pure Chemical Industries, Co., Ltd., Osaka, Japan) was purified by recrystallization from its toluene solution with hexane. Ruthenium(4-vinyl-4-methyl-2,2'-bipyridine)bis(2,2'-bipyridine)bis(hexafluorophosphate) ($\text{Ru}(\text{bpy})_3$ monomer) was synthesized according to previous work.^[2] *N*- β -acrylamidoethyl-*N*'-*n*-propyl-4,4'-bipyridinium bromide chloride (viologen monomer) was synthesized according to the procedure reported before. Other reagents were used without further purification.

Preparation of Gels. Firstly, surfactant-modified Pt nanoparticle was prepared by alcohol reduction method with chloroplatinic acid ($\text{H}_2\text{PtCl}_6 \cdot 6\text{H}_2\text{O}$) (Wako Pure Chemical Industries, Co., Ltd., JAPAN), reactive surfactant^[3-4] (S180A) (Kao Co., JAPAN) as a protector and ethanol-water mixed solvent. The diameter of surfactant-modified Pt nanoparticle was about 1.7 nm from the observation of transmission electron microscopy (TEM). Secondly, NIPAAm, Pt-colloidal suspension, $\text{Ru}(\text{bpy})_3$ monomer, viologen monomer, and *N,N'*-methylenebisacrylamide as a cross-linker were dissolved in ethanol. Under nitrogen atmosphere for 20 min, 2,2'-azobis-2,2,4-dimethylvaleronitrile as an initiator were added to this pre-gel solution. The microgels were prepared by suspension polymerization using liquid paraffin as oil phase. After gelation, they were thoroughly washed to remove unreacted compounds. The diameter of the poly(NIPAAm-co- $\text{Ru}(\text{bpy})_3$ -co-viologen) microgel containing Pt nanoparticle at swollen state (20 °C) in water was about 300 μm from optical microscopy observation.

Measurements of H_2 generation for Gel Systems. Three types of gel systems (G1~G3), that is, microgel suspension composed of microgels and reactants in the aqueous phase are prepared as follows (Table I). The PNIPAAm microgel containing Pt nanoparticle (50 mg) was dispersed in the mixture (3.0 ml) of $\text{Ru}(\text{bpy})_3^{2+}$ / methylviologen (MV^{2+}) / ethylenediaminetetra acetic acid (EDTA) (the G1 system). Similarly, the poly(NIPAAm-co- $\text{Ru}(\text{bpy})_3$) microgel containing Pt nanoparticle was dispersed in the mixture of MV^{2+} / EDTA (the G2 system), and the poly(NIPAAm-co- $\text{Ru}(\text{bpy})_3$ -co-viologen) microgel containing Pt nanoparticle was dispersed in EDTA solution (the G3 system). These microgel suspensions were stirred sufficiently at 20 °C for 1 day, and then visible light was irradiated by using a 100 W halogen lamp (TECHNO LIGHT KTS-100RSV, Kenko). At

given times, the absorption spectra was measured by UV-vis spectrophotometer (UV-2500PC, SHIMADZU), and the generated gas was collected and analyzed by gas chromatography (GC-8APT, SHIMADZU).

Result and Discussion

When the G1 system was irradiated by visible light, absorption strength caused by $\text{MV}^{+ \cdot}$ increased. Abilities to sensitize and accept electron in the G1 system was confirmed. Simultaneously, the bubbles were generated continuously (Fig. 2a). Hydrogen was generated by way of Pt nanoparticle in gel. It was indicated that water decomposition by visible light in gel was possible. The amount of generated H_2 gas in the G1 system was compared with that of homogeneous solution system (L) at 20 °C (Fig. 2b). Under the same concentration for all components, G1 generated H_2 gas more efficiently by 1.5 times than L. It was considered that this result was caused by concentration of Pt nanoparticle in the network of the gel and improvement of electron transmission efficiency by (i) enrichment of Pt nanoparticles in gel phase, (ii) stable dispersion of Pt nanoparticles in the gel, and (iii) physical effect of polymer chain to the electronic transmission.

In the gel systems, PNIPAAm was used as main chain, a thermo-responsive polymer. The relation between the temperature and hydrogen generation was

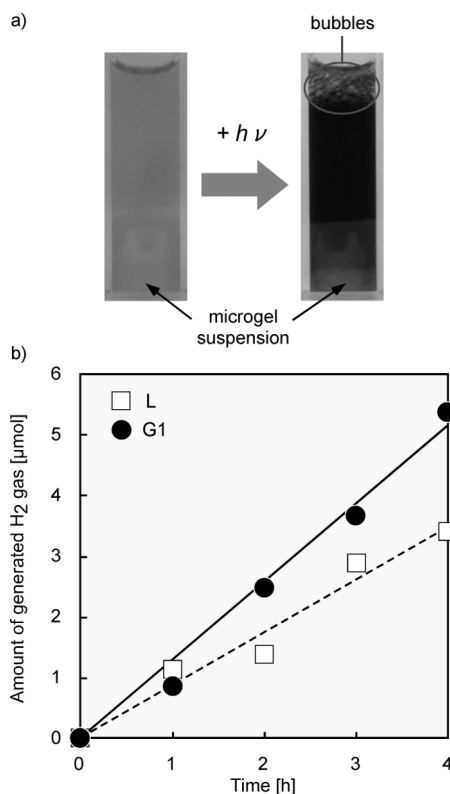


Figure 2. a) Color change of microgel suspension and the bubbles generation. b) H_2 generation for solution and microgel systems. L1: Pt colloidal suspension ($[\text{Pt}] = 0.017 \text{ mM}$) and the mixture [A] ($[\text{Ru}(\text{bpy})_3^{2+}] = 0.050 \text{ mM}$, $[\text{MV}^{2+}] = 5.0 \text{ mM}$, $[\text{EDTA}] = 50 \text{ mM}$). G1: Pt nanoparticles in PNIPAAm gel (50 mg) and the mixture [A].

investigated. By irradiating visible light to the G2 system under stepwise temperature changes between 20 °C and 40 °C, the amount of generated H₂ gas changed remarkably (Fig. 3). When the gel was in swelling state (20 °C) with hydrophilic environment, electron transmission occurred smoothly and H₂ gas was generated. On the other hand, when the gel was in shrinking state (40 °C) with hydrophobic environment, decreased diffusivity in gel and skin layer of gel stopped electron transmission and H₂ generation. Thus, by changing temperature, on-off control of H₂ gas generation was possible. This function is useful for the stopper of the over generation.

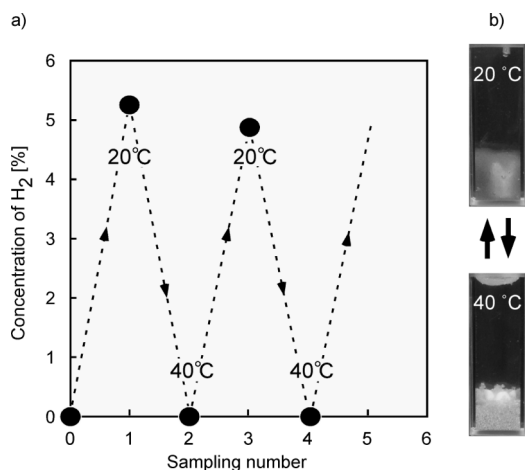


Figure 3. H₂ generation by photocatalytic reaction under stepwise temperature change between 20 °C and 40 °C. Sampling number: (0) before irradiation (20 °C), (1) cumulative amount of H₂ gas during 0 ~ 2 h (20 °C), (2) 2 ~ 4 h (40 °C), (3) 4 ~ 6 h (20 °C), (4) 6 ~ 8 h (40 °C) after irradiation.

In the G3 systems, the viologen unit was also introduced in the gel network. By irradiating visible light to the system, absorbance at 603 nm originating from viologen radical at reduced state increased and the color of microgels changed from orange to blue green. This suggested that electrons actually transmitted from Ru(bpy)₃ unit to viologen unit constructed in the network (Fig. 4a). Moreover, H₂ gas generated continuously. This result means that electrons transmitted effectively to generate H₂ gas among three components constructed in the gel (Fig. 4b).

In future, by coexistence of catalyst for O₂ generation such as RuO₂, it would be possible to construct gel systems performing complete artificial photosynthesis to generate both of hydrogen and oxygen when visible light and water are supplied. They are necessary for fuel cells and the gel systems are useful as a solar energy-conversion system.

Conclusions

Firstly, Pt nanoparticle as a catalyst was immobilized in PNIPAAm gel. Hydrogen was generated more efficiently in the gel system than in solution system. Secondly, Pt nanoparticle and Ru(bpy)₃ complex as sensitizer was immobilized and copolymerized in the gel. By changing temperature,

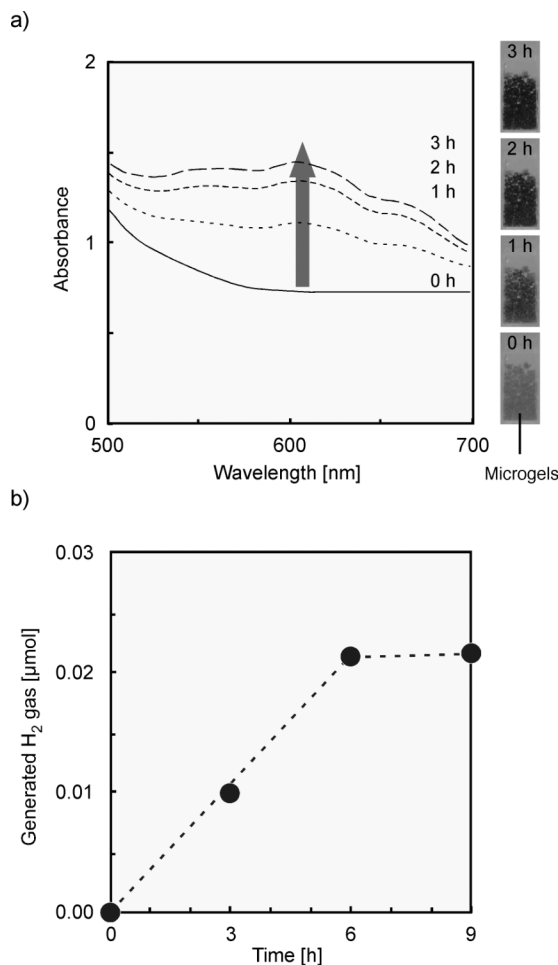


Figure 4. a) Change in absorption spectra for the mixture of poly(NIPAAm-co-Ru(bpy)₃-co-viologen) gel containing Pt nanoparticles and EDTA. b) The amount of generated H₂ gas for the G3 system.

the amount of generated H₂ gas could be controlled because diffusivity of components in the gel was changed remarkably. As well as Pt nanoparticle and Ru(bpy)₃ complex, viologen as acceptor was copolymerized in the gel. By irradiating visible light to poly(NIPAAm-co-Ru(bpy)₃-co-viologen) gel containing Pt nanoparticle, electron was transmitted effectively and hydrogen was generated.

Acknowledgements

K. O is grateful for the research fellowships of the Japan Society for the Promotion of Science for Young Scientists.

References

- [1] K. Kalyanasundaram and M. Grätzel, *Angew. Chem. Int. Ed.*, **18**, 701 (1979).
- [2] R. Yoshida, T. Takahashi, T. Yamaguchi, H. Ichijo, *J. Am. Chem. Soc.* **118**, 5134 (1996).
- [3] Y. Noguchi, K. Okeyoshi, R. Yoshida, *Macromol. Rapid Commun.*, **26**, 1913 (2005).
- [4] K. Okeyoshi, T. Abe, Y. Noguchi, H. Furukawa, R. Yoshida, *Macromol. Rapid Commun.*, **29**, 897 (2008).

(Received December 8, 2008; Accepted October 8, 2009)

Low Driven Voltage Electrochromic Devices Using Aqueous Polyaniline/poly(4-styrenesulfonic acid)

Atsushi Aoki* and Maiko Yoshida

Materials Science & Engineering, Graduate school of Engineering, Nagoya Institute of Technology, Gokiso, Showa-ku, Nagoya 466-8555, Japan

Fax: 81-52-735-5251, e-mail: aaoki@nitech.ac.jp

Aqueous polyaniline (PANI)/poly(4-styrenesulfonic acid) (PSS) was prepared by chemical oxidative polymerization in PSS solution. The electrochemical, spectroscopic and electrochromic (EC) properties of PANI/PSS spin-coated films have been investigated. The EC devices consist of emeraldine salt (ES) form of PANI/PSS films on the both of display and counter electrodes. Since ES can be oxidized or reduced to produce pernigraniline (PS) or leucoemeraldine salt (LES), respectively, each reaction takes place at the both electrodes and such a low driven voltage of 0.8 V has been achieved. The color of the display electrode shows green at no bias and is turned to dark blue at the bias. The EC properties, such as contrast and response time, were characterized.

Key words: conductive polymer, polyaniline, poly(4-styrenesulfonic acid), electrochromic device

1. INTRODUCTION

Conducting polymers have some attractive features, such as conductivity, electric charge, semiconducting behavior and electrochromic phenomenon to expect application to organic electronic and photonic devices. The electrochromic behavior takes place for the color change corresponding to the redox state of conducting polymers [1]. The conducting polymers are generally modified on the display electrodes and the electrochemical oxidation and reduction of the conducting polymers cause the color change. However, the opposite reaction is needed on the counter electrode to lead to electrochromic behavior reversibly. We assume that polyaniline (PANI) is suitable for this requirement because PANI has three redox states, which are fully reduced leucoemeraldine salt (LES), partially oxidized emeraldine salt (ES) and fully oxidized pernigraniline (PS) [2]. Moreover, the three redox states of PANI are known to show different color, which are yellow green, green and dark blue at LES, ES and PS, respectively. Therefore, when ES state of polyaniline is employed as the both display and counter electrodes, the operational voltage becomes low to compare with a bare counter electrode. PANI is one of the most frequently investigated conducting polymers because of ease of chemical and electrochemical polymerization, chemical stability and inexpensiveness. However, PANI has less processability for infusible and insoluble into common organic solvents except a few solvents, such as *N*-methyl-2-pyrrolidone (NMP) [3] and formic acid [4]. Attempts to make PANI soluble into organic or aqueous solvents have been carried out by many researchers [5-7]. Recently, we have reported that PANI/dodecylbenzenesulfonic acid (DBSA) polyion complex is soluble into chloroform and forms LB film [8] and EC property [9]. In this study, aqueous polyaniline was prepared by chemical oxidative

polymerization of aniline monomer in PSS solution. We think that the aqueous PANI/PSS is more environment-friendly than the organic solvent-soluble polyaniline derivatives. The electrochemical and spectroscopic characterization was performed by cyclic voltammetry and UV-vis absorption spectroscopy. Moreover, we fabricated EC devices composed of the same PANI/PSS films at the both of display and counter electrodes. The PANI/PSS film EC device was characterized by spectroelectrochemistry.

2. EXPERIMENTALS

Aqueous PANI/PSS solution was typically prepared by chemical oxidative polymerization of 2.52 mmol aniline in 33 mM HCl solution including 2.50 mmol poly(4-styrenesulfonic acid) using 2.72 mmol ammonium peroxodisulfate as an oxidant at 0 °C for overnight. The PANI/PSS films on ITO electrodes were prepared by spin-coating of the aqueous PANI/PSS solution at 500 rpm. The resulting film thickness was determined to be 210 nm from the cross-section observed by profilometer. UV-vis absorption spectra and electrochemical spectroscopy were measured with Hitachi U-2800 spectrometer. Cyclic voltammetry was carried out by three electrode cell which was composed

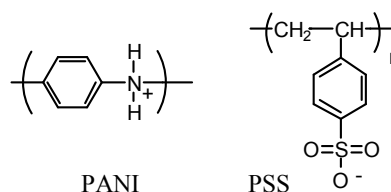


Fig. 1 Chemical structures of polyaniline (PANI) and poly(4-styrenesulfonate) (PSS).

of the PANI/PSS film on an ITO electrode as a working electrode, Ag/Ag⁺ electrode as a reference electrode and Pt wire as a counter electrode in the potentiostat (Princeton Applied Research VersaSTAT3) in 0.1 M tetrabutylammonium hexafluorophosphate (TBN⁺PF₆⁻) as an electrolyte acetonitrile (AcCN) solution with 50 mM H₂SO₄. Current-voltage curve was carried out by two electrode cell which was composed of two PANI/PSS films on ITO electrodes as a display electrode and as a counter electrode in the potentiostat. Electrochemical spectroscopy was carried out by insertion of EC devices into quartz cell and the source meter (Keithley 2400) in 0.1 M TBN⁺PF₆⁻ AcCN solution with 50 mM H₂SO₄.

3. RESULTS AND DISCUSSION

Color of the reaction solution after addition of the oxidant gradually started to turn to light green within 10 min and become dark green after 40 min. Since the resulting solution is viscous but does not include any precipitate, aqueous PANI/PSS polyion complex were formed. We think that formation of polyion complex between insoluble PANI polycation and soluble PSS polyanion makes PANI/PSS soluble in water. UV-vis absorption spectrum of the aqueous PANI/PSS solution is shown in Fig.2. The spectrum of PANI/PSS in aqueous solution exhibits three typical bands at 750, 430 and 350 nm, which are assigned to polaron transition and π - π^* transition, respectively, indicating that the state of PANI is emeraldine salt. The PANI/PSS films were prepared by spin-coating of the aqueous PANI/PSS solution on ITO electrodes. The prepared film is uniform with green color. The film dissolves in water but does not in AcCN. So, the electrochemical properties of PANI/PSS films were investigated by cyclic voltammetry in 0.1 M TBN⁺PF₆⁻ AcCN solution with 50 mM H₂SO₄ as shown in Fig. 3. The voltammogram shows that the open-circuit potential of PANI/PSS film is 0.55 V vs. Ag/Ag⁺, indicating ES state. It's also a surface wave voltammogram, indicating that PANI/PSS film is stable on ITO electrode in AcCN solution. In fact, the peak currents do not depend on the root square of the scan rate but are proportional to the scan rate. The voltammogram shows that three anodic peak currents appear at 0.52, 0.74 and 0.88 V vs. Ag/Ag⁺, assigned to LES/ES, degradation products such as *p*-benzoquinone and ES/PS couples, respectively [10, 11]. The shape of the voltammogram is not changed

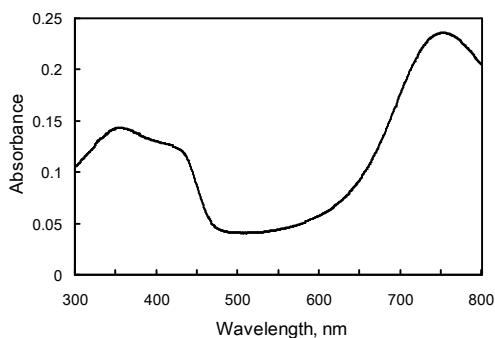


Fig. 2 UV-vis absorption spectrum for aqueous PANI/PSS solution.

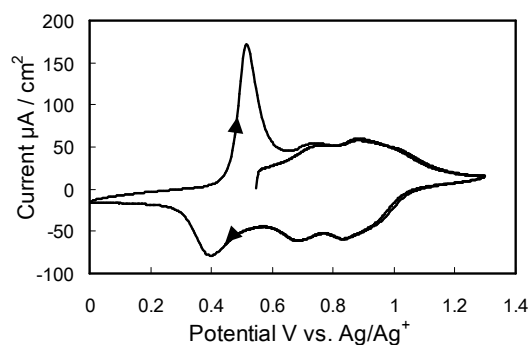


Fig. 3 Cyclic voltammogram for PANI/PSS film on ITO electrode in 0.1 M TBN⁺PF₆⁻ AcCN solution with 50 mM H₂SO₄ at the scan rate of 20 mV/s.

by repeating cycles of the potential scan, indicating the electrochemical reversibility of PANI/PSS film and stability of the film.

The EC device composed of PANI/PSS films on the both of display and counter electrodes is found to be operated at such a low voltage of 0.8 V. The Current-voltage curves (Fig. 4) show charging and discharging behavior like a capacitor with stable repeating cycles. The charging current results from the oxidative reaction from ES to PS at the display electrode and the reductive reaction from ES to LES at the counter electrode of the EC device. Thus, color of the display electrode turned from green to dark blue. The discharge current results from the reduction from PS to ES at the display electrode and the oxidation from LES to ES at the counter electrode of the EC device. Thus, color of the display electrode returned from dark blue to green. Meanwhile, there is almost no charging current at both of bare ITO electrodes because no redox species exist on the electrodes. Even, at the EC device using bare ITO as the counter electrode, the operating voltage is needed to be 1.8 V. This large difference in the operational voltage between PANI/PSS film on ITO electrode and bare one as a counter electrode is due to whether the opposite reaction is compensated at the

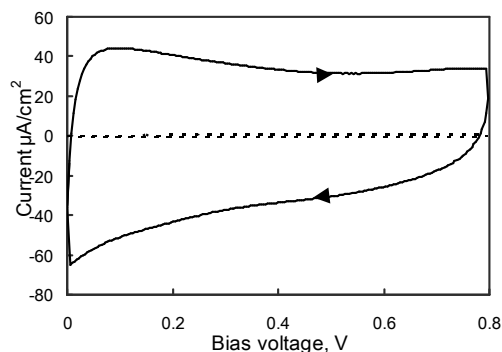


Fig. 4 Current-voltage curves of EC device using PANI/PSS film (solid line) and bare (dotted line) ITO electrodes at the scan rate of 50 mV/s.

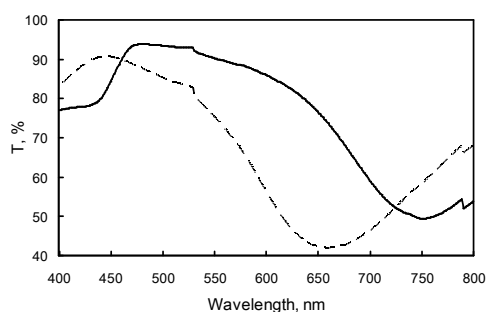


Fig. 5 Transmittance spectra of EC device composed of PANI/PSS films applied at 0.0 V (solid line) and 0.8 V (dotted line).

counter electrode. The opposite reaction that is reducing reaction from ES to LES occurs at small overpotential at the PANI/PSS film, whereas a large overpotential is needed to take place the reducing reaction which might be reduction of AcCN solvent, electrolyte or cathodic deposition of indium oxide at the bare ITO electrode.

The transmittance spectra of the PANI/PSS film on ITO electrode as a display electrode of the EC device applied at the voltage bias of 0 V and 0.8 V is shown in Fig. 5. The spectrum of the EC device at the zero bias indicates two typical absorption bands at 430 and 750 nm, which are assigned to π - π^* transition and polaron transition, respectively, indicating that the state of PANI is emeraldine salt [2]. The absorption peak at 750 nm is blue-shifted to 660 nm and the absorbance at 430 nm decreases when the EC device is applied at the voltage bias of 0.8 V. The spectrum obtained at the voltage bias of 0.8 V is not fully oxidized polyaniline but more oxidized state than emeraldine salt. The visible color change takes place from green at 0 V to dark blue at 0.8 V. In order to investigate the electrochromic switching characteristic, the wavelength of 637 nm where the difference in the transmittance is the largest value of 36 % is selected. The electrochromic switching is measured by monitoring the transmittance at 637 nm at the EC device applied at the step voltage between 0 V and 0.8 V during the interval of 10 sec (Fig. 6). The shape of transmittance response is almost corresponding to that of the step voltage. This switching is especially stable with little change in the transmittance during every step voltage cycles. The response time for 90 %

full transmittance changes is about 2 sec, which is quite fast.

4. CONCLUSIONS

We have prepared aqueous polyaniline by chemical oxidative polymerization in PSS solution. We demonstrate that the EC devices using PANI/PSS films on the both of display and the counter electrodes show lower driven voltage of 0.8 V and reversibility. The electrochromic properties are obtained to be the transmittance change of 36 %, the switching time of 2 sec. We expect that the aqueous PANI/PSS is one of candidate for EC materials.

References

- [1] L. B. Groenendaal, G. Zotti, P.-H. Aubert, A. M. Waybright and J. R. Reynolds, *Adv.Mater.*, **15** 855 (2003).
- [2] W. S. Huang and A. G. MacDiarmid, *Polymer*, **34** 1833 (1993).
- [3] M. K. Ram, M. Adami, M. Sartore, M. Salerno, S. Paddeu and C. Nicolini, *Synth.Metals*, **100** 249 (1999).
- [4] G. Li, C. Martinez and S. Semancik, *J.Am.Chem.Soc.*, **127** 4903 (2005).
- [5] R. Madathil, R. Parkesh, S. Ponrathnam and M. C. J. Large, *Macromolecules*, **37** 2002 (2004).
- [6] S. Shreepathi and R. Holze, *Langmuir*, **22** 5196 (2006).
- [7] S. Shreepathi and R. Holze, *Chem.Mater.*, **17** 4078 (2005).
- [8] A. Aoki, R. Umehara and K. Banba, *Langmuir*, **25** 1169 (2009).
- [9] A. Aoki, R. Umehara, Y. Kawai and M. Yoshida, *Mol.Cryst.Liq.Cryst.*, **504** 97 (2009).
- [10] D.-H. Han and S.-M. Park, *J.Phys.Chem.B*, **108** 13921 (2004).
- [11] S.-Y. Hong and S.-M. Park, *J.Phys.Chem.B*, **109** 9305 (2005).

(Received December 24, 2008; Accepted May 11, 2009)

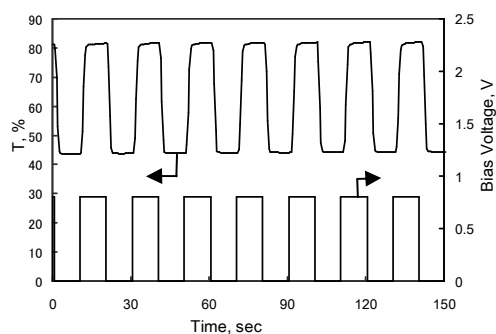


Fig. 6 Electrochromic switching between 0.0V and 0.8 V at 637 nm.

The Hall effect measurement in the high resistance In₂O₃-ZnO polycrystalline films

K. Yamada¹, T. Yamaguchi¹, N. Kokubo¹, B. Shinokazi¹, K. Yano², H. Nakamura²

¹Department of Physics, Kyushu University, Fukuoka, Japan

Fax: 81-92-726-4823, e-mail: yamada@phys.kyushu-u.ac.jp

²Advanced Technology Research Laboratory, Idemitsu Kosan Co.Ltd., Sodegaura, Japan

Sputtering In₂O₃-ZnO on the glass substrate by the DC magnetron method and annealing, granular films were obtained. Controlling the carrier density by the frequency and the power of the light, the carrier density and the mobility were measured by the Hall effect for the high resistance films (180kΩ - 32GΩ). For the samples with the ZnO concentrations 0, 0.5% and 1% (wt), the mobility increases with the carrier density. For the samples ZnO 2% and 3%, the variation of the mobility is relatively small.

Key words: hall effect, transparent conducting film, polycrystalline, photoconductivity

1. INTRODUCTION

The wide band gap semiconductor In₂O₃-ZnO films are used as the transparent conducting films for liquid crystal displays and solar cells[1,2]. The measurements of the mobility μ and the carrier density n are important for these applications. The temperature dependence of μ in amorphous In₂O₃-ZnO is explained by the electron-phonon scattering, the electron-electron interaction and weak localization[3,4,5]. On the other hand, the conductance enhancements due to lights have been reported in various metal oxide semiconductors such as titanium oxides[6,7,8], zinc oxides[9,10,11] and indium oxides[12]. P. Görm *et al.* have reported the influence of visible lights on transparent indium tin oxide thin films[13]. Controlling n by the ZnO concentrations and the frequency and the power of the light, we investigate the mobility and the carrier density by the special high resistance hall measurement technique. There are few studies about the hall measurements of the high resistance materials over 100MΩ[14]. We describe the hall measurement technique and their results in this paper.

2. EXPERIMENTAL METHOD

Sputtering In₂O₃-ZnO on glass substrates by the DC magnetron method, amorphous films with 25 nm thickness were obtained. By annealing, these films were crystallized and oxygen defects decreased and the conductance decreased. On the other hand, applying light to films, we can increase the carrier density. Controlling n by ZnO concentration and the frequency and the power of the light, the n dependence of μ is measured by the Hall effect. The schematic of the equipment is shown in Fig.1. The each terminals are insulated by Polytetrafluoroethylene (PTFE). The magnetic fields are induced by the normal conducting electromagnet ESR-360MR by JEOL Ltd. The normal conducting electromagnet was cooled by water. For the inversion of the magnetic field, we rotated the sample holder. The lights are emitted by LEDs listed in the

Table I. The sapphire plate insulates the sample film from the aluminum die casting shield box. The PTFE or the sapphires with high resistivity is needed for the enough insulation. We confirmed the insulation resistance $R > 100T\Omega$ between the ground and the sample inducing the high voltage 100V.

Color	wave length	FWHM	Bender
UV	400nm	60nm	BivarOpto
Blue	430nm	60nm	Kingbright
Green	565nm	30nm	Kingbright
RED	627nm	50nm	Kingbright
IR	870nm	60nm	Toshiba

Table I The list of used LEDs.

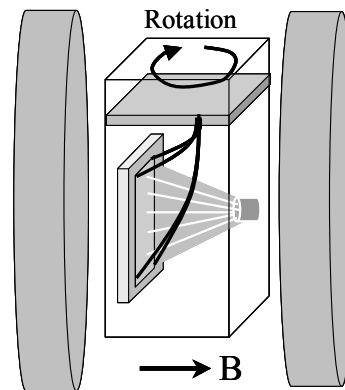


Fig.1 The schematic drawing of the hall measurement system. The magnetic fields are induced by the normal conducting electromagnet ESR-360MR by JEOL Ltd. The lights are emitted by LEDs listed in the Table I. The measurement circuit is shown in Fig.2.

By applying the magnetic field $B = 1T$, the Hall measurement was performed in the atmosphere at the room temperature by the van der Pauw technique[15]. The measurement circuit of the Hall measurement is

shown in Fig. 2. The current is induced by the Keithley 220 current power supply. The voltages of the high resistance films over 1GΩ are measured with the differential measurement using two electrometers (Keithley 6517 and 6514) as preamps[16]. The input resistances between high and low of electrometers are 200TΩ but the resistances between low and grand are only 10GΩ. Then two electrometers are needed for the measurement of the high resistance films. The coaxial cables are used for noise shields. We bonded the copper wire to the sample films by indium solders.

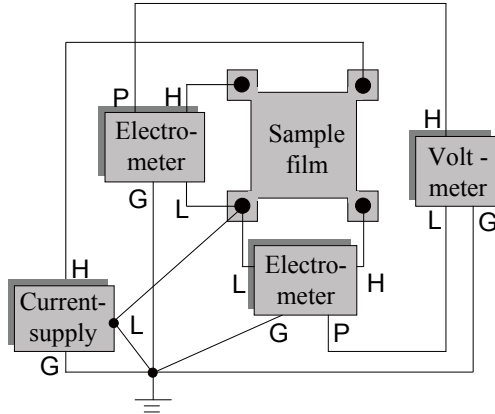


Fig.2 The measurement circuit for the high resistance films. The sample films are patterned by the metal mask. The Hall effect and the resistivity are measured by the van der Pauw method. The marks H, L, G and P indicate terminals of the instruments for high, low, grand and preout, respectively.

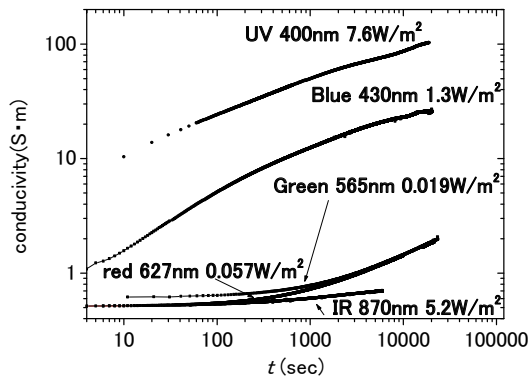


Fig.3 The time development of conductivity applying the light to the sample with ZnO 1%. The vertical axis indicates the elapsed time since starting of applying the light.

3. EXPERIMENTAL RESULTS AND DISCUSSION

After the long wait enough for the resistance to be constant in the dark, we applied the various LED lights listed in Table I to sample films. The time development of the conductivity applying the lights of various colors and the various power to the sample ZnO 1% is shown as Fig.3. The vertical axis indicates passed time since starting of applying the light. The conductance enhances even if applying of the lights with the low energy below the energy gap. Applying the light with the shorter wave

length, the conductivity increases more rapidly than longer wave length. The power-law like behavior is observed in the time dependence of the conductivity[7]. Controlling the carrier density n by the frequency and the power of the lights as the above, the Hall measurement was performed.

The transverse magnetoresistance ΔR_{XY} vs B plots are shown in Fig.3 for (a) the samples with the ZnO concentration 1% $R_{sq}=30M\Omega$ and (b) 3% $R_{sq}=32G\Omega$ in the dark. Here, $\Delta R_{XY}(B)$ is defined as $\Delta R_{XY}(B)=(V_Y(B)-V_Y(0))/I_x$. If the hole conduction is neglected in n -type semiconductors[17],

$$E_y = R_H J_x B_z$$

$$R_H = \frac{1}{ne} = \frac{dR_{xy}}{B}$$

$$R_{sq} = \frac{\pi V}{\ln 2 I}$$

$$\rho = \frac{R_{sq}}{d} = \mu en \quad (1).$$

Here, R_{sq} , V , I and d are the sheet resistance, the voltage, the current, the thickness, respectively.

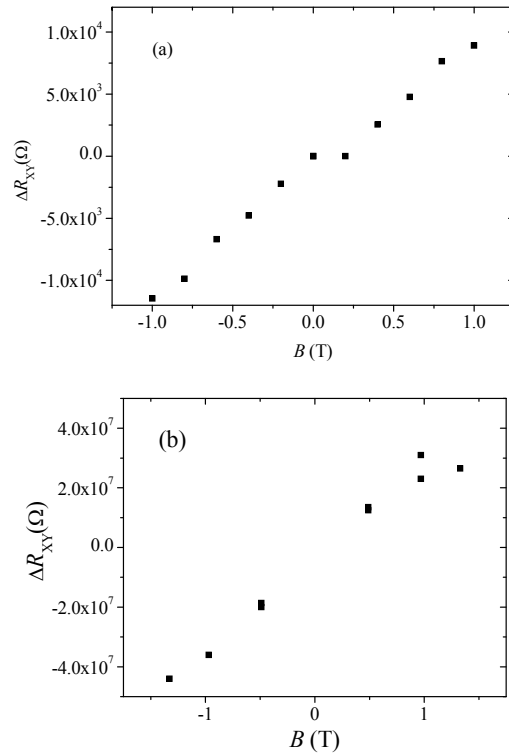


Fig.4 The transverse magnetoresistance ΔR_{XY} vs B plots for the samples with (a) the sample with the ZnO concentration 1% $R_{sq}=30M\Omega$ and (b) 3% $R_{sq}=32G\Omega$ in the dark. Here, $\Delta R_{XY}(B)$ is defined as $\Delta R_{XY}(B)=(V_Y(B)-V_Y(0))/I_x$.

Using the above equations, we obtained n and μ from the analysis of the $\Delta R_{XY}(B)$. The signs of measured R_H show that these samples are n -type. The R_{sq} dependence of n is shown in Fig.5 for films with various concentrations of ZnO. The R_{sq} dependence of μ is

shown in Fig.6. Decreasing ZnO, the oxygen defect increases and the carrier density increases. For the samples 0%, 0.5% and 1%, the mobility decreases with the increasing of the resistance. This behavior is similar to the amorphous films. As a reason for this dependence, we consider that carriers screen the disorder potential for the defects and the electron scattering decreases. For the samples 2% and 3%, the carrier density is too little to screen the disorder potential and the mobility does not seem to be dependent on the carrier density.

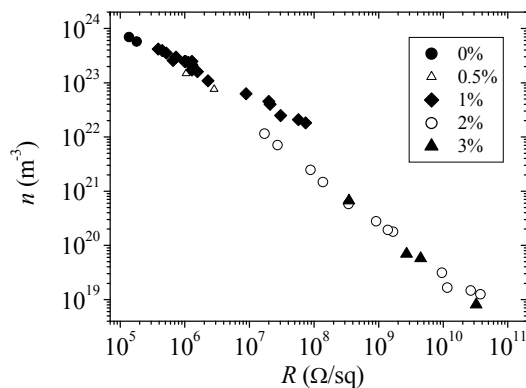


Fig.5 The carrier density n vs R_{sq} plots. Controlling n by the frequency and the power of the light, n is measured by the hall effect. The each marker indicates the sample with the various ZnO concentrations (wt%).

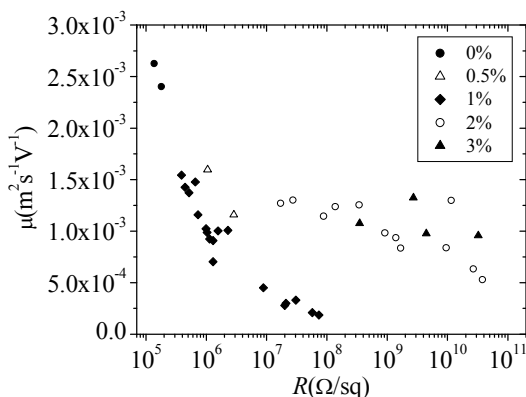


Fig.6 The mobility μ vs R_{sq} plots. Controlling n the frequency and the power of the light, μ is measured by the hall effect. The each marker indicates the sample with the various ZnO concentrations (wt%).

4. SUMMARY

Controlling n by the ZnO concentration and the frequency and the power of the light, the carrier density n and the mobility μ is measured by the Hall effect of the granular films. We measured the films whose resistance is very high 180k Ω - 32G Ω by the special high resistance hall measurement technique. For the samples ZnO concentration 0, 0.5% and 1%, μ increases with n . For the samples 2% and 3%, the variation of μ is relatively small.

5. ACKNOWLEDGEMENT

Authors thank Mr. S. Tomai for useful discussions.

6. REFERENCES

- [1] A. Kaijo, Proc. 3rd Int. Display Workshop, Vol. 2, p. 365 (1996).
- [2] Y. S. Jung, J. Y. Seo, D. W. Lee and D. Y. Jeon, Thin Solid Films, 445, 63 – 71 (2003).
- [3] K. Makise, M. Funaki, B. Shinozaki, K. Yano, K. Yano, Y. Shimane, K. Inoue and H. Nakamura, Thin Solid Films, **516**, 5805-5808 (2008).
- [4] M. Funaki, K. Makise, B. Shinozaki, K. Yano, F. Utuno, K. Inoue and H. Nakamura, J. Appl. Phys., **103**, 113701 1-6 (2008).
- [5] B. Shinozaki, K. Makise, Y. Shimane and H. Nakamura, J. Phys. Soc. Jpn., **76**, 074718 1-6 (2007).
- [6] Z. Xie, V. M. Burlakov, B. M. Henry, K. R. Kirov, H. E. Smith, C. R. M. Grovenor, H. E. Assender, G. A. D. Briggs, M. Kano and Y. Tsukahara, Phys. Rev. B **73**, 113317 (2006).
- [7] D. Comedi, S. P. Helunani, M. Villafuerte, R. D. Arce and R. R. Koropecki, J. Phys.: Condens. Matter **19** 486205 (2007).
- [8] J. Hao, S. A. Studenikin and M. Cocivera, J. Appl. Phys. **90**, 5056 - 5069 (2001).
- [9] S. A. Studenikin, N. Golego, and M. Cocivera, J. Appl. Phys. **87**, 2417 - 2421 (2000).
- [10] B. Clafin, D.C. Look, S. J. Park and G. Cantwell, J. Crystal Growth **287**, 16 - 22 (2006).
- [11] A. Tsukazaki, A. Ohtomo, M. Nakano and M. Kawasaki, Appl. Phys. Lett. **92**, 052105 (2008)
- [12] M. Bender, N. Katsarakis, E. Gagaoudakis, E. Hourdakis, E. Douloufakis, V. Cimalla, and G. Kiriakidis, J. Appl. Phys. , **90**, 5382 - 5387 (2001).
- [13] P. Görm, M. Lehnhardt, T. Riel, and W. Kowalsky, Appl. Phys. Lett., **91**, 193504 (2007).
- [14] A. Oprea, N. Barsan and U. Weimar, J. Phys. D: Appl. Phys. **40** 7217–7237 (2007).
- [15] L. J. van der Pauw, Phillips Research Reports, **13**, 1-9 (1958).
- [16] “Low Level Measurements Handbook 6th edition”, Keithley Instruments Inc. (2004) pp.4-32.
- [17] “Physics of Semiconductor Deices” S. M. Sze, A Wiley-Interscience publication, New York (1981) pp.30-35

(Received December 12, 2008; Accepted September 23, 2009)

Dependence of Size of Liquid Phase Pulsed Laser Ablated ZnO Nanoparticles on pH of the Medium

P.M. Aneesh, Arun Aravind, R. Reshmi, R.S. Ajimsha and M.K. Jayaraj

Optoelectronic Devices Laboratory, Department of Physics, Cochin University of Science and Technology, Kochi-682 022, India

Tel.: +91 484 2577404, Fax: +91 484 2577595, e-mail: mkj@cusat.ac.in

Highly transparent, luminescent, chemically pure and biocompatible zinc oxide (ZnO) nanoparticles (NPs) without any surfactants were synthesized by liquid phase- pulsed laser ablation (LP- PLA) of sintered ZnO pellets. Transmission electron microscopic study confirms the formation of crystalline ZnO nanoparticles. The size of the nanoparticles increases when oxygen is bubbled in the liquid during ablation and it remains same on bubbling with nitrogen. The yellow luminescence from ZnO NPs is due to the oxygen vacancies. The emission color can be tuned from yellow to bluish violet by suppressing the oxygen vacancies on bubbling oxygen during the ZnO ablation. The NPs were also grown by LP-PLA under surfactants free acidic and basic medium and the surface charge of the NPs provided the repulsive force between NPs which suppressed the growth through coagulation. These luminescent and nontoxic ZnO nanoparticles will find applications in biomedical imaging and cancer detections.

Key words: Zinc oxide, Nanoparticles, Liquid phase- pulsed laser ablation, Transmission electron microscopy, Luminescence

1. INTRODUCTION

In recent years liquid phase pulsed laser ablation (LP-PLA) has become an attractive method to prepare colloidal solutions containing nanoparticles of noble metals [1-3], alloys [4, 5], oxides [6, 7]. It involves the firing of laser pulses through liquids transparent to that wavelength on to the target surface. The ablation plume interacts with the surrounding liquid particles, creating cavitation bubbles which, upon their collapse, give rise to extremely high pressures and temperatures. These conditions are, however, localized and exist across the nanometer scale. It facilitates the production of crystallized nanoparticles without any further treatment because of high energetic state of ablated species [8, 9]. Another advantage is that the production system is simple and does not require costly vacuum equipment. The final product can be collected in solutions and the obtained colloidal solution is very easy to handle.

Zinc oxide (ZnO) is a wide band gap (3.37eV) promising semiconductor having large exciton binding energy (60 meV) at room temperature and has important applications in electroluminescent displays [10], optoelectronics [11, 12], sensors [13], lasers [14] etc. Because zinc is an important trace element of humans [15], ZnO is environmentally friendly and suitable for in vivo bioimaging and cancer detection.

There have been reports on synthesis of ZnO NPs by LP- PLA techniques from metal target [16, 17]. In this work, we report the synthesis of highly luminescent, transparent, chemically pure

and crystalline ZnO nanoparticles by LP- PLA technique without using any surfactant from sintered ZnO mosaic target. The dependence of oxygen and nitrogen bubbling during ablation and pH of the medium on the properties of the ZnO NPs was also investigated.

2. EXPERIMENTAL

A ZnO (99.99%) mosaic target sintered at 1000°C for 5hrs was used for the synthesis of ZnO nanoparticles. The ZnO target immersed in 15 mL of the liquid media having different pH was ablated at room temperature by third harmonic of Nd: YAG laser (355 nm, repetition frequency of 10 Hz, pulse duration of 9 ns). The experimental arrangement is shown in figure 1. The laser beam was focused using a lens and the ablation was done at a laser fluence of 15 mJ/pulse. The spot size of the laser beam is about 1mm. The duration of ablation was 1 hr in all the media. This simple room temperature method produced a highly transparent ZnO NPs well dispersed in the liquid.

The formation of ZnO NPs was confirmed by transmission electron microscopy (JEOL, TEM) operating at an accelerating voltage of 200 kV. The sample for TEM was prepared by placing a drop of the ZnO nanoparticle colloidal solution onto a standard carbon coated copper grid. The grids were dried before recording the micrographs. Photoluminescence (PL) spectra were recorded using Jobin Yvon Fluoromax-3 spectrometer equipped with 150 W xenon lamp.

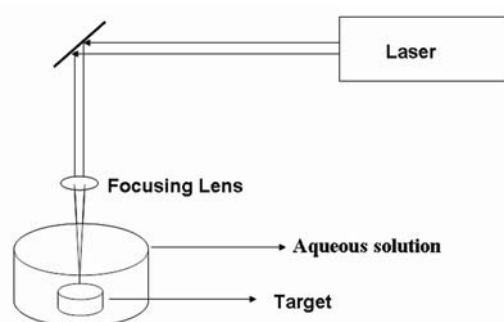


Figure 1. Experimental setup for the LP-PLA technique

3. RESULTS AND DISCUSSION

Transmission electron microscopic (TEM) studies confirm the resulting product after laser ablation in different media consisted of particles in the nanoregime. The selective area electron diffraction (SAED) pattern shows concentric rings corresponding to the hexagonal ZnO. This clearly shows the growth of crystalline ZnO NPs. From these studies, the formation of other molecules like $\text{Zn}(\text{OH})_2$ or ZnO/Zn core shell formation is not found. Because the ejected molten material from the target normally reacts with medium only at the outer surface, [18] the ejected plasma readily cools, thereby reforming ZnO itself. Because there are many surface oxygen deficiency, these nanoparticles are charged. The ZnO nano particles grown by LP-PLA in pure water is usually charged because the isoelectronic points of ZnO (~ 9.3) is well above the pH 7.0 of pure water.[19] This surface charge provides a shield, preventing further agglomeration and forming self stabilized particles even in the absence of surfactant. In the present study the ZnO NPs grown by LP-PLA is oxygen deficient which may also lead to positive charge. The fluence dependence on the mean size of the particle shows almost a linear increase (figure 2).

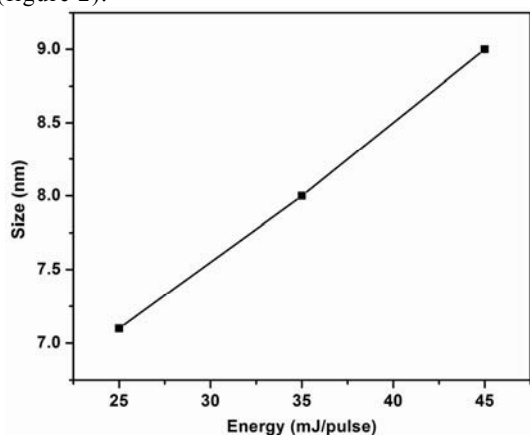


Figure 2. Variation of size of the ZnO NPs synthesized by LP-PLA method with laser fluence

However at higher laser fluence result in bigger

size and wide size distribution. The larger duration of LP-PLA at lower fluence does not increase the size of the NPs but increase the particle density. The transparency of the ZnO nanoparticle colloid remains as such even for ablation duration of more than 3 hrs at 45 mJ/pulse laser energy. The maximum concentration of ZnO NPs that was achieved while maintaining transparency was $17.5 \mu\text{g/mL}$ [20].

TEM analysis revealed that ZnO samples after laser ablation with energy 25 mJ/pulse in the neutral media (pH \sim 7) consists of particles in the nano regime as shown in figure 3a. The particle size distribution shows size distribution is in small range (figure 3(b)) and majority of the particles has size 7 nm. The $d = 0.26 \text{ nm}$ shown in the HRTEM image (figure 3(d)) corresponds to 002 plane of wurtzite ZnO. Almost all particles shows uniform size distribution. The selective area electron diffraction (SAED) (figure 3(c)) exhibit well distinguishable concentric ring pattern representing 100, 002, 102, 110 and 103 plane of hexagonal ZnO. This clearly shows the growth of crystalline ZnO NPs with random orientation. ZnO NPs were arranged in hexagonal shape as observed from high resolution TEM image (inset figure 3(d)). The stacking of the 85 hexagonal unit cells make 7 nm. The PL emission studies have reported by us earlier [20].

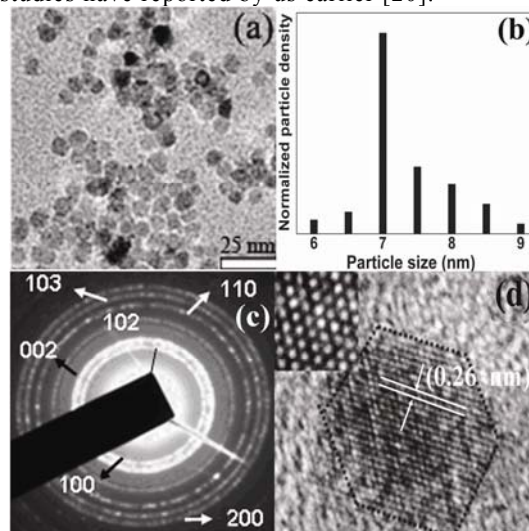


Figure 3. TEM image (a), particle size distribution (b) SAED pattern(c) of ZnO NPs synthesized by LP PLA method with a fluence of 25 mJ/pulse in water. HRTEM image (d) of a single ZnO nanoparticle and inset shows the arrangement in hexagonal close packed mode

The TEM image shows that the particles are in spherical shape and it has an average size about 7 nm and the colloid is transparent. The Zn/ZnO composite nanoparticles grown by Zeng et.al [21] have an average particle size 18 nm and colored due to turbidity. The size of the particle is found to increase when the experiment is done with oxygen bubbling into the water during laser

ablation of ZnO targets while size remains the same as that grown in pure water when ZnO NPs were grown in nitrogen atmosphere. Figure 4 (a) shows the TEM image of the ZnO NPs prepared in oxygen atmosphere and nitrogen atmosphere. The TEM image of NPs grown in nitrogen atmosphere keeping the other parameters of the experiment the same has same size as those grown in neutral deionized water (figure 4 (b) and (c)). The oxygen bubbling during the ablation increases the amount of dissolved oxygen and promotes the growth of ZnO. This leads to bigger ZnO NPs, where as nitrogen bubbling through the solution does not provide any extra oxygen other than the oxygen in the plasma produced by the laser interaction with the ZnO target. Thus the size of the particle is same as those obtained by LP-PLA in pure water.

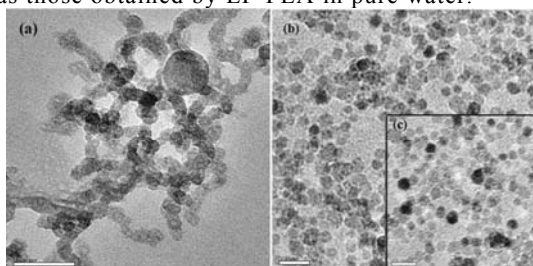


Figure 4. TEM image of the ZnO NPs prepared in oxygen atmosphere (a), nitrogen atmosphere (b), and TEM image of ZnO NPs synthesized in water (c)

PL measurement was performed in the NPs dispersed in neutral media at an excitation wavelength of 345 nm. Deep yellow luminescence (figure 5) was observed from the ZnO NPs dispersed in water. Inset bottom of figure 5 shows the photograph of highly transparent ZnO NPs dispersed in water and its yellow emission under UV excitation. This yellow luminescence originates from the native oxygen defects [20] of the prepared ZnO NPs.

The origin of yellow luminescence due to oxygen vacancy was further supported by the experiment done with oxygen bubbled into the water during laser ablation of ZnO targets. Figure 5 (curve II) shows PL emissions peaking at 408 nm and 427 nm in the violet blue region, suppressing the yellow emission when oxygen was bubbled through liquid during the ablation. Inset top of figure 5 shows the photograph of deep bluish-violet emission. Due to the bubbling of oxygen during ablation, defect density was considerably reduced tending to more stoichiometric ZnO NPs. Where as the ZnO NPs grown under nitrogen atmosphere has similar size and PL emission characteristic as of those grown in neutral water. This further supports that yellow luminescence originates from oxygen vacancies. Emission at 408 nm is due to the transition of electrons from shallow donor levels to valance band [7]. According to Lin *et al* [22] the energy gap between the valance band and energy level of interstitial zinc is 2.9 eV. This is very well

consistent with PL emission at 427 nm for the ZnO NPs. The weak Raman peak of the solvent corresponding to OH vibration was not detected in the PL spectra mainly because the PL emission intensity was very intense.

The ZnO NPs grown in the present study does not exhibit any green emission. The origin of green emission is still remains controversial. However there is convincing evidence that it is located at the surface [23]. The absence of green emission in the LP-PLA grown ZnO NPs suggest the possible presence of $Zn(OH)_2$ on the surface [24].

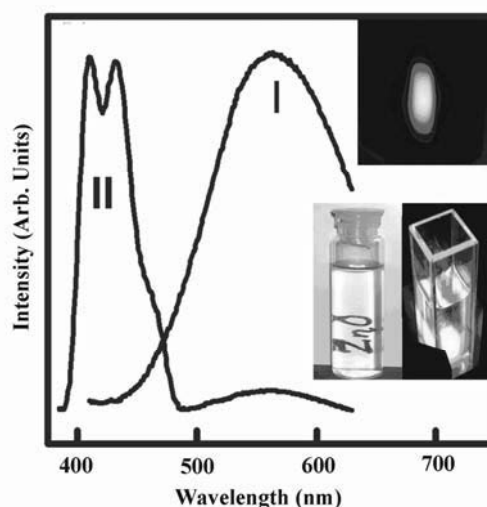


Figure 5. PL emission spectra of ZnO NPs prepared without (curve I) and with (curve II) oxygen atmosphere at an excitation wavelength of 345 nm. Inset bottom shows the photograph of transparent ZnO NPs synthesized by LP-PLA method and its yellow luminescence in water and inset top is the bluish-violet luminescence from the NPs grown in oxygen atmosphere

The growth of ZnO NPs by LP-PLA can be modeled as follows. The plasma consisting of ionic and neutral species of Zn and oxygen [25] along with water vapor is produced at the solid-liquid interface on interaction between the laser beam and the ZnO target. Due to the high intensity of the laser beam in the nano second scales, high temperature (10^4 - 10^5 K) and pressure of few GPa [26] in the volume is produced. The adiabatic expansion of the plasma leads to formation of ZnO. The ZnO thus formed interact with the solvent water forming a thin layer of $Zn(OH)_2$ since ZnO is extremely sensitive to H_2O environment [27]. Thus the ZnO NPs prepared by LP-PLA may have a thin passivation layer of $Zn(OH)_2$. The oxygen bubbling during the ablation increases the amount of dissolved oxygen and promotes the growth of ZnO. This leads to bigger ZnO NPs, where as nitrogen bubbling through the solution does not provide any extra oxygen other than the oxygen in the plasma produced by the laser interaction with the

ZnO target. Thus the size of the particle is same as those obtained by LP-PLA in pure water. The ZnO NPs grown by LP-PLA in the acidic medium pH=5 shows relatively bigger size in comparison with those grown in pure water under identical experimental conditions. The very thin passivation layer of $\text{Zn}(\text{OH})_2$ during the cooling of laser plasma interacting with the liquid medium may be slower owing to higher dissolution of hydroxide in acidic medium. Hence this favours the growth of bigger ZnO NPs. Whereas the ablation in alkali medium favours growth of $\text{Zn}(\text{OH})_2$ by providing hydroxyl group and hence result in smaller NPs.

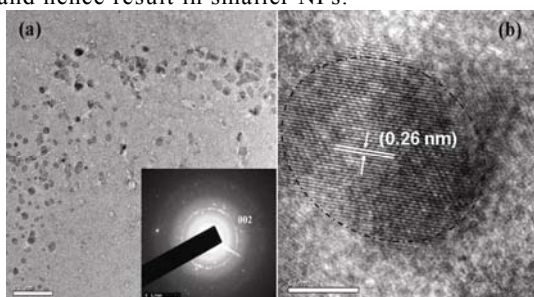


Figure 6. TEM image (a) and HRTEM image (b) ZnO NPs synthesized in acid media by LP-PLA method. Inset of (a) shows the corresponding SAED pattern

Figure 6 (a) shows TEM and figure 6 (b) is the high resolution transmission electron microscopic (HRTEM) image. The SAED pattern of the ZnO NPs prepared in acid media (pH~ 5) keeping all other experimental parameters the same shows the ring pattern corresponding to the 002 plane. The particles have an elliptical shape with 15 nm size in the elongated region and 11 nm in the compressed region is observed from the HRTEM image. From the diffraction rings in the SAED pattern, 002 plane of the wurtzite ZnO was identified.

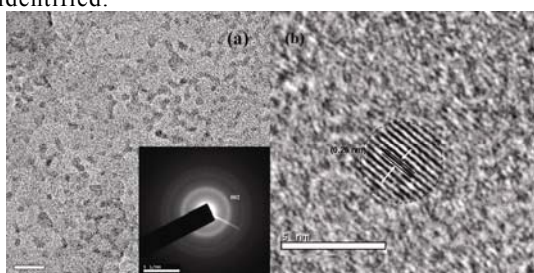


Figure 7. TEM image (a) and HRTEM image (b) ZnO NPs synthesized in basic media by LP-PLA method. Inset of (a) shows the corresponding SAED pattern

Figure 7 (a) shows the TEM and the SAED pattern (inset) of ZnO NPs prepared by pulsed laser ablation in basic media (pH~ 9). Spherical particles were observed in the HRTEM image (fig.7b) having a size about 4 nm. The 002 plane of wurtzite ZnO is observed in the SAED pattern. This confirms the formation of crystalline ZnO NPs by pulsed laser ablation in liquid.

The thermodynamic conditions created by the laser ablation plume in the liquid are localized to a nano meter scale which is not much influenced by the pH of the solution. The increase of laser energy for the ablation results in increase of size of the NPs due to ablation of more material. The hydroxide passivation layer formation is much influenced by the pH of the aqueous solution which may affect the growth and size of the particles. All the particles grown in acidic, alkali and neutral medium are well dispersed and no agglomeration of the particles are observed as in the case of ablation of zinc metal targets in aqueous solution [28]. In the present study the particles grown during oxygen bubbling of LP-PLA leads to the formation of bigger particles and agglomeration. This suggests that surface charge of ZnO NPs arise mainly from oxygen deficiency and pH of the medium has less pronounced effect.

4. CONCLUSIONS

Highly transparent, deep yellow and bluish-violet emitting, bio-compatible ZnO NPs were prepared in various liquid media using LP-PLA technique without using any surfactant. Transmission electron microscopic study confirms the formation of crystalline ZnO nanoparticles. The size of the nanoparticles increases when oxygen is bubbled during ablation and it remains same as in nitrogen atmosphere. The origin of yellow luminescence is due to oxygen vacancies. The surface charge of the NPs provided the repulsive force between the NPs and suppressed the growth through coagulation.

5. ACKNOWLEDGMENTS

The work is supported by department of science and technology, government of India under nanoscience and technology initiative. One of the authors (PMA) thanks Kerala state council for science, technology and environment for the award of research fellowship.

6. REFERENCES

1. G Compagnini, A A Scalisi, O Puglisi, *J. Appl. Phys.*, **94**, 7874 (2003).
2. T Tsuji, K Iryo, N Watanabe, M Tsuji, *Appl. Surf. Sci.*, **202**, 80 (2002).
3. F. Mafune, J. Kohno, Y. Takeda, T. Kondow, H. Sawabe, *J. Phys. Chem. B*, **104**, 9111 (1999)
4. S.H. Tsai, Y.H. Liu, P.L. Wu, C.S. Yeh, *J. Mater. Chem.* **13**, 978 (2003)
5. J. Zhang, J. Worley, S. Denommee, C. Kingston, Z.J. Jakubek, Y. Deslandes, M. Post, B. Simard, N. Braid, G.A. Botton, *J. Phys. Chem. B* **107**, 6920 (2003)
6. C H Liang, Y Shimizu, T Sasaki, N Koshizaki, *J. Phys. Chem. B*, **107**, 9220 (2003).

7. H B Zeng, W P Cai, J L Hu, G T Duan, P S Liu, Y Li, *Appl. Phys. Lett.*, **88**, 171910 (2006)
8. T. Sakka, S. Iwanaga, Y.H. Ogata, A. Matsunawa, T. Takemoto, *J. Chem. Phys.* **112**, 8645 (2000).
9. K. Saito, T. Sakka, Y.H. Ogata, *J. Appl. Phys.* **94**, 5530 (2003).
10. R Konenkamp, R C Word and C Schlegel, *Appl. Phys. Lett.* **85** 6004 (2004)
11. T Gruber, C Kirchner, R Kling and F Reuss, *Appl. Phys. Lett.* **84** 5359 (2004)
12. C W Sun, P Xin, Z W Liu and Q Y Zhang, *Appl. Phys. Lett.* **88** 221914 (2006)
13. K. S. Weissenrieder and J. Muller, *Thin Solid Films* **300**, 30 (1997)
14. M H Huang, S Mao, H Feick, H Q Yan, Y Y Wu, H Kind, E Weber, R Russo and P D Yang, *Science* **292**, 1897 (2001)
15. G. Thomas, *Chemistry for Pharmacy and Life Sciences: Including Pharmacology and Biomedical Science*, Ellis Horwood Ltd., London (1996).
16. H. Usui, Y. Shimizu, T. Sasaki, N. Koshizaki, *J. Phys. Chem. B* **109** (2005) 120.
17. S. C. Singh and R. Gopal, *Bull. Mater. Sci.* **30**, 291 (2007)
18. W. T. Nichols, T. Sasaki, and N. Koshizaki, *J. Appl. Phys.*, **100**, 114913 (2006)
19. F Kooli., I C Chsem, W Vucelic, *Chem Mater* **8**, 1969(1996)
20. R. S Ajimsha, G. Anoop, Arun Aravind, M.K Jayaraj, *Electrochemical and Solid-State Letters*, **11**, K14 (2008)
21. H.B. Zeng, W.P. Cai, Y.Li, J.L. Hu and P.S. Liu *J. Phys.Chem. B* **109**, 18260 (2005)
22. B. X. Lin, Z. X. Fu and Y. B. Jia, *Appl. Phys. Lett.* **79**, 943 (2001)
23. A. B. Djuricic and Y H Leung, *Small* **2**, 944 (2006)
24. H. Zhou, H.Alves, D.M.Hofmann, W.Kriegseis, B.K.Meyer, G.Kaczmarczyk, A.Hofmann *Appl. Phys. Lett.* **80**, 210 (2002)
25. N. V. Joshy, K. J. Saji and M. K. Jayaraj, *J. Appl. Phys.*, **104**, 053307 (2008)
26. L.Berthe, R.Fabbro, P.Peyre, L.Tollier and E.Bartnicki *J.Appl Phys.* **82**, 2826 (1997)
27. M.Nakagawa and H.Mitsudo *Surf Sci* **175**, 157 (1986)
28. C.He, T.Saski, H.Usui, Y.Shimizu, N.Koshizaki, *J. Photochem and Photobiology A: Chemistry* **191**, 66 (2007)

(Received December 12, 2008; Accepted October 28, 2009)

Hydrophilicity Switching of Silica Surface Incorporated with Thermoresponsive Polymer

Takeshi Higuchi*, Wataru Tanji, Tadahiro Aita and Shimio Sato

Department of Chemistry and Chemical Engineering, Yamagata University,
4-3-16 Jonan, Yonezawa, Yamagata 992-8510, Japan
* higuchi@yz.yamagata-u.ac.jp, Fax: +81-238-26-3414

It was attempted to switch the wettability of a glass surface by modification with the thermoresponsive polymer poly(*N*-isopropylacrylamide) (PNIPAAm). To strengthen the PNIPAAm layer, the polymer was fixed in a silica gel matrix by a sol-gel method and coated on a glass plate. The wettability of the silica-PNIPAAm composite layer was evaluated by contact angle measurements. The effect of silica on the wettability was investigated by altering the PNIPAAm/silica molar ratio. The effect of surface roughness on the contact angle was also evaluated using atomic force microscopy (AFM). The wettability of the surface drastically dropped by elevating the temperature from 305 K to 313 K through the lower critical solution temperature (LCST) of PNIPAAm.

Key words: thermoresponsive polymer, wettability, sol-gel method, surface modification

1. INTRODUCTION

Poly(*N*-isopropylacrylamide) (PNIPAAm), a thermoresponsive polymer, undergoes a reversible hydration-dehydration transition at its lower critical solution temperature (LCST) of 305 K. The swelling-shrinking behavior of PNIPAAm in aqueous media has attracted significant interest from the viewpoint of developing new drug delivery systems (DDS) [1-4], high-performance liquid chromatography (HPLC) [5,6] and molecular cutoff systems, which separate polydisperse macromolecules into different molecular weight ranges [7,8]. This is because PNIPAAm functions as a switch in aqueous media that can be used to control the permeability of target molecules. PNIPAAm has also been applied to temperature swing adsorption [9-11] that utilizes hydrophilicity switching of the polymer gel. In most of these studies, PNIPAAm was used as a polymer gel or grafted on a solid substrate. One disadvantage of this is that a PNIPAAm layer on a substrate lacks sufficient mechanical toughness and it can be easily damaged. For

applications that do not require the swelling-shrinking behavior, such as modification of surface hydrophilicity, the mobility of the PNIPAAm macromolecule is not considered to be essential because the PNIPAAm transition across LCST is attributed to the stability of the hydration state of the amide and alkyl groups in the PNIPAAm macromolecule. Therefore, immobilization of PNIPAAm by sol-gel could be an effective method for enhancing the toughness of the PNIPAAm layer.

In this study, we have attempted to switch the wettability of a glass surface by modification with PNIPAAm. To strengthen the PNIPAAm layer, the polymer was fixed in silica gel matrix by a sol-gel method and coated on a glass plate. The wettability of the silica-PNIPAAm composite layer was evaluated by contact angle measurements. The effect of silica on the wettability was examined by altering the PNIPAAm/silica molar ratio. The effect of the surface roughness on the contact angle was also evaluated using atomic force microscopy (AFM).

2. EXPERIMENTAL

2.1 Chemicals

PNIPAAm was synthesized from the corresponding monomer (*N*-isopropylacrylamide, from Wako Pure Chemical Industries, Ltd., Japan) using both ammonium peroxydisulfate and sodium sulfite as the polymerization initiators. The degree of polymerization was controlled using 3-mercaptopropionic acid. Redox polymerization was carried out for 2 h at 293 K. PNIPAAm was precipitated at 333 K, followed by washing in deionized water at 373 K several times and subsequent vacuum desiccation for 4 days. The number average molecular weight M_w of the obtained PNIPAAm was determined to be 4.5×10^4 using gel permeation chromatography (HLC-8120GPC, Tosoh Corp., Japan).

2.2 Preparation of Thermoresponsive Surface

PNIPAAm was dissolved in a mixture of 4 ml of ethanol and 0.8 ml of 0.1 M HCl. 2 g of tetraethoxysilane (TEOS, from Kanto Kagaku, Japan) was added to the solution and hydrolyzed under vigorous stirring for 6 h at 298 K. Dip-coating of the solution on a glass plate was carried out with a drawing-up rate of 20 mm/min. The coated plate was placed in a tightly sealed vessel for 2 days at room temperature for gradual desiccation, which provided sufficient time for polycondensation of silica and aging of the wet silica gel. Finally, the plate was desiccated at 298 K under ambient pressure for over 2 days. The PNIPAAm macromolecules were incorporated in the silica gel matrix through polycondensation of silica during the aging and desiccation.

2.3 Measurement of Wettability

The hydrophilicity and thermoresponsive transition of the silica-PNIPAAm composite layer coated on the glass plate were evaluated by contact angle measurements of a water droplet. The coated glass plate was placed in a sealed vessel saturated with water vapor, as shown in Figure 1. The temperature inside the vessel was controlled by a Peltier device. 15 μ l of water was dropped on the plate with a syringe and left for more than 1 h prior to each measurement for vapor saturation. The surface roughness of the coated layer was analyzed by AFM (Nanopics 1000, Seiko Instruments). The nominal diameter and apex angle of the tip of the probe,

which has a conical tip, were approximately 20 nm and 30°, respectively.

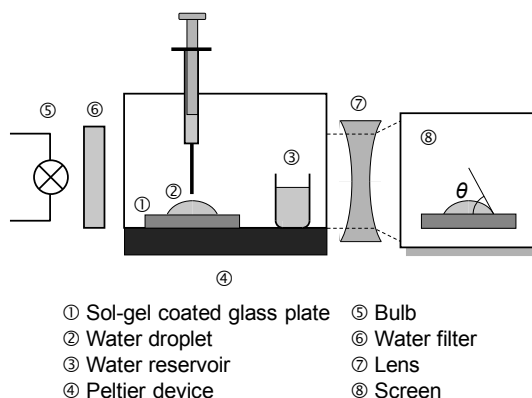


Fig. 1: Schematic drawing of the apparatus used for contact angle measurements at a controlled temperature

3. RESULTS AND DISCUSSION

3.1 Effect of Surface Roughness on Wettability

It should be noted that the apparent contact angle of water drops on the coated layers, θ_{app} , does not necessarily represent surface wettability of the coated layer because of the surface roughness as shown in Figure 2. The real contact angle, θ_{real} , which coincides with the contact angle on a smooth surface and represents the inherent surface wettability, can be estimated by the Wenzel theory [12,13]:

$$\frac{\cos \theta_{app}}{\cos \theta_{real}} = \frac{A_{real}}{A_{app}} \quad (1)$$

The real surface area of the layer is larger than the apparent surface area calculated from the dimensions of the layer because of the surface roughness. The right hand side of the above equation is the ratio of the real surface area (A_{real}) and the apparent one (A_{app}) of the corresponding surface of the layer, which was calculated by AFM image analysis in this study. A_{real}/A_{app} for various PNIPAAm content in the coated layer $r_{P/T}$, which is the molar ratio of PNIPAAm (in terms of the number of moles of the monomer) to TEOS in the starting solution, are shown in Figure 3. The silica-PNIPAAm composite has no mesopores, which increase A_{real} , and might not be detected by the AFM probe, because hydrolysis and polycondensation of TEOS was implemented in an acidic solution.

Micropores in the composite do not affect θ_{app} because the width of a micropore is less than approximately 10 times the diameter of a water molecule. In such a small space, water can no longer be considered to be a continuous liquid, rather it acts as if it is an ensemble of particles. Therefore, roughness analysis by AFM in this study is sufficiently accurate for evaluation of roughness effects on θ_{app} . As shown in Figure 3, a higher PNIPAAm content resulted in larger roughness of the surface.

Changes in θ_{app} and θ_{real} around the LCST of PNIPAAm are shown in Figures 4 and 5 respectively. While these features are similar to each other, θ_{real} was greater than θ_{app} by up to 5°. This is caused by the surface roughness and hydrophilicity of PNIPAAm on the surface of the coated layer because if the surface is hydrophilic (inherent contact angle θ_{real} is smaller than 90°), θ_{app} should decrease as roughness increases, as estimated by eq. 1.

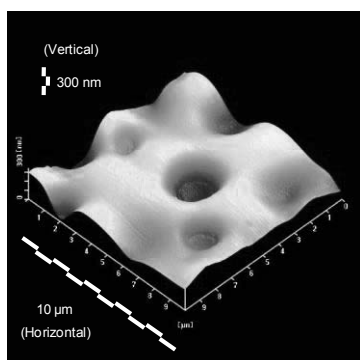


Fig. 2: Example of an AFM image of the coated layer. Molar ratio of NIPAAm to TEOS ($r_{P/T}$) is 2.0.

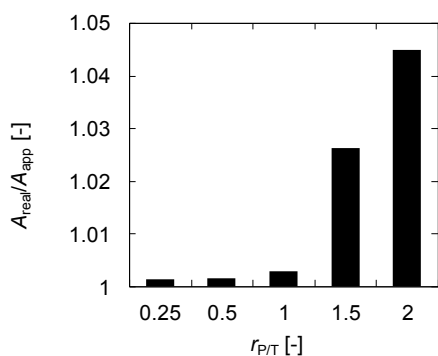


Fig. 3: Roughness factor of the surface of the coated layer as a function of the $r_{P/T}$ ratio calculated from AFM images.

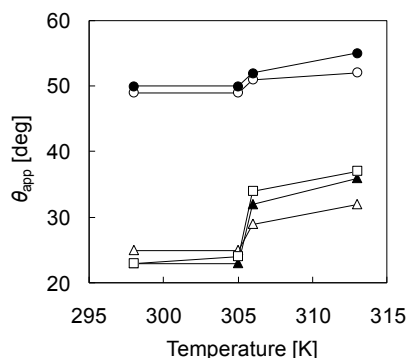


Fig. 4: Apparent contact angle of a water droplet on the thermoresponsive coated layer. The $r_{P/T}$ ratios are ○: 0.25, ●: 0.5, △: 1, ▲: 1.5 and □: 2.

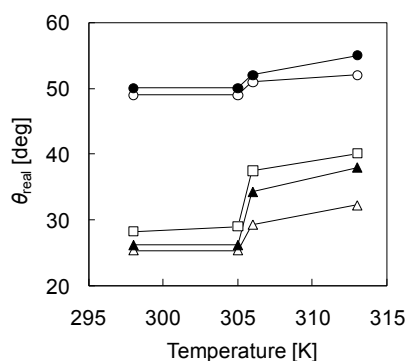


Fig. 5: Real contact angle estimated from Fig. 4 by Eq. 1. The symbols denote the same $r_{P/T}$ ratios as those in Fig. 4.

3.2 Thermoresponsive Change in Wettability

The first important feature in Figure 5 is that θ_{real} abruptly increases between 305 K and 306 K, and then gradually increases between 306 K and 313 K. The second feature is that the increase in θ_{real} from 305 K to 306 K and 313 K becomes larger with increasing $r_{P/T}$ as calculated in Figure 6. The third feature observed is that θ_{real} of $r_{P/T} = 0.25$ and 0.5 were much larger than the others, which might reflect a significant change in the microstructure of the silica-PNIPAAm composite gel.

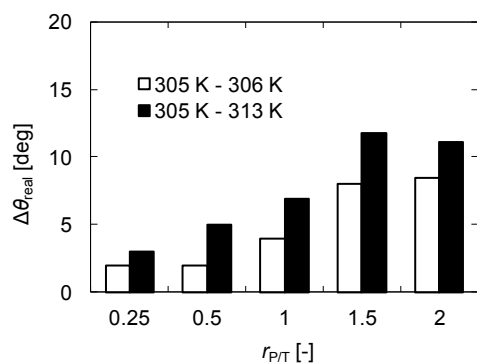


Fig. 6: Increase in real contact angle by hydrophobic transition of PNIPAAm calculated from Fig. 5

Obviously, the surface hydrophilicity of the coated layer dropped sharply around 306 K for each $r_{p/T}$. The results also suggest that the surface with higher $r_{p/T}$ has a lower hydrophilicity above 306 K. For PNIPAAm macromolecules in an aqueous media, dehydration of the alkyl and amide groups in PNIPAAm and the formation of intramolecular hydrogen bonds between amide groups take place above 305 K and proceed up to 313 K [14]. In this process, the PNIPAAm chain became hydrophobic because dehydration of PNIPAAm is endothermic. The intramolecular hydrogen bond between amide groups and hydrophobic interaction between alkyl groups, which might have smaller formation enthalpy than their hydration, should be predominant at higher temperatures. Thus, the conformation of the PNIPAAm chain changes from a coil to a globule as this transformation proceeds. However, in the coated layer in this study, a large portion of the PNIPAAm chains in the layer penetrates the silica gel matrix and forms hydrogen bonds between silica. The coil-globule transition of PNIPAAm is strongly suppressed because the mobility of the chain is restricted by the gel matrix. This situation compels the dehydrated amide group and alkyl group in the PNIPAAm chain to be exposed to aqueous media. The existence of such a hydrophobic group should decrease wettability and result in an increase in the contact angle. These results imply that PNIPAAm can exhibit a drastic change in hydrophilicity even though its mobility is lost by immobilization in the silica gel matrix.

4. CONCLUSIONS

This study showed that immobilization of the

thermoresponsive polymer on the substrate using the sol-gel method is a promising way to modify surface properties so that the wettability changes reversibly with temperature.

ACKNOWLEDGEMENTS

The authors are deeply grateful for technical support for the AFM measurements to Mr. Kiyohito Uryu in Yamagata University.

REFERENCES

- [1] Y. Shin, J. H. Chang, J. Liu, R. Williford, Y.-K. Shin and G. J. Exarhos, *J. Control. Release* **73**, 1-6 (2001).
- [2] S. K. Li and A. D'Emanuele, *J. Control. Release* **75**, 55-67 (2001).
- [3] K. Suzuki, T. Yumura, Y. Tanaka and M. Akashi, *J. Control. Release* **75**, 183-89 (2001).
- [4] L.-Y. Chu, S.-H. Park, T. Yamaguchi and S. Nakao, *Langmuir* **18**, 1856-64 (2002).
- [5] H. Kanazawa and Y. Matsushima, *Yakugaku Zasshi* **117**, 817-24 (1997).
- [6] H. Lakhari, T. Okano, N. Nurdin, C. Luthi, P. Descouts, D. Muller and J. Jozefonvicz, *Biochimica et Biophysica Acta* **1379**, 303-13 (1998).
- [7] G. V. R. Rao and G. P. López, *Adv. Mater.* **12**, 1692-95 (2000).
- [8] G. V. R. Rao, S. Balamurugan, D. E. Meyer, A. Chilkoti and G. P. López, *Langmuir* **18**, 1819-24 (2002).
- [9] Y. Seida and Y. Nakano, *J. chem. Eng. Jpn.* **29**, 767-72 (1996).
- [10] Y. Seida and Y. Nakano, *Kagaku Kogaku Ronbunshu* **25**, 1024-26 (1999).
- [11] K. Yamashita, T. Nishimura, K. Ohashi, H. Ohkouchi and M. Nango, *Polym. J.* **35**, 545-50 (2003).
- [12] R. N. Wenzel, *Ind. Eng. Chem.* **28**, 988-94 (1936).
- [13] C. W. Extrand, *Langmuir* **18**, 7991-99 (2002).
- [14] Y. Maeda, T. Higuchi and I. Ikeda, *Langmuir*, **16**, 7503-09 (2000)

(Received December 12, 2008; Accepted September 10, 2009)

Electrochemical Properties and Microstructure of C/LiFePO₄ Powders Prepared by Spray Pyrolysis

Motofumi Yamada, Koji Egawa, Takashi Ogihara and Takayuki Kodera

Graduate School of Fiber Amenities Engineering, University of Fukui

Fax: 81-76-27-8624, e-mail: ogihara@matse.u-fukui.ac.jp

9-1 Bunkyo 3, Fukui-shi, Fukui, 910-8507 Japan

Spherical C/LiFePO₄ cathode powders were successfully prepared by spray pyrolysis. The saccharides such as monosaccharide and disaccharide or organic acid were used as carbon sources. SEM observation showed that they had spherical morphology with particle size of about 1 μm. XRD analysis revealed that the olivine phase was obtained by heating at 700°C under the atmosphere of argon/hydrogen (5%). Electrochemical measurement revealed that the rechargeable capacity of C/LiFePO₄ cathode was significantly improved by the addition of carbon. The use of sucrose was most effective for the high rechargeable capacity and cycle stability.

Key words: Spray pyrolysis, Aerosol, Olivine, Lithium ion battery, Powders

1. INTRODUCTION

Lithium transition metal oxides such as LiMn₂O₄, LiCo_{1/3}Ni_{1/3}Mn_{1/3}O₂ and LiFePO₄ have been noted as cathode materials of lithium ion battery for EV (Electric vehicle) and HEV (Hybrid electric vehicle) or power supply for load leveling in wind power generation and solar power generation. [1,2]. Olivine-type LiFePO₄ was expected as cathode material for lithium ion batteries because of low cost, relatively high theoretical capacity of 170mAh/g and stable cycle performance at high temperature. However, the electrical conductivity of LiFePO₄ expires too low in order to use as cathode materials for lithium ion battery. Therefore, the conductive materials such as carbon, metal and metal oxide were doped to enhance the electrical conductivity of LiFePO₄ [4-7]. The advantages of spray pyrolysis were as follows: (1) As-prepared particles had spherical morphology with a high surface area, (2) The carbon or metal ion is directly doped during particle formation, (3) Oxide powders can be directly prepared and the synthesis time is much shorter than that required for solid state reaction and sol-gel method [9,10]. It is considered that above advantages are effective for the

use as the cathode of lithium ion battery. Yang et al reported the electrochemical properties of C/LiFePO₄ cathode materials prepared by spray pyrolysis [8]. By selecting the organic compounds and doping the foreign metal ion, we found that the rechargeable capacity and cycle performance of C/LiFePO₄ cathode derived from spray pyrolysis were improved at high rate charging and elevated temperature.

In this paper, spherical C/LiFePO₄ composite powders were prepared by spray pyrolysis using several type of organic compound as a source of carbon. The effect of organic compound for rechargeable capacity and cycle performance of C/LiFePO₄ cathode were also investigated. Furthermore, the foreign metal was doped to C/LiFePO₄ to improve the rechargeable properties.

2. EXPERIMENTAL PROCEDURE

LiNO₃, Fe(NO₃)₃•9H₂O, H₃PO₄ and Mg(NO₃)₂•6H₂O were used as starting materials. LiNO₃, Fe(NO₃)₃•9H₂O, and H₃PO₄ were weighted out to attain the molar ratio of metal components (Li:Fe:P = 1:1:1) and were dissolved in double distilled water to prepare aqueous solutions of 0.1mol/dm³. Various types of organic compounds such

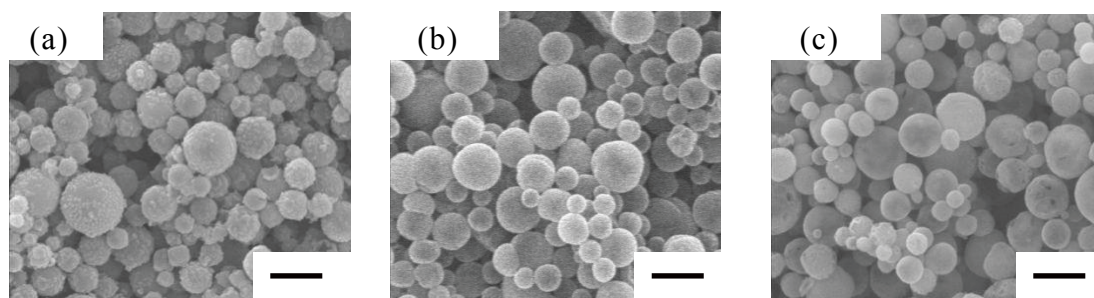


Fig.1 SEM photographs of carbon doped LiFePO₄ powders derived from (a)sucrose, (b)fructose, (c)citric acid (bar=2μm)

as sucrose, fructose, sugar or citric acid were added to aqueous solutions up to 60wt% as carbon source. Mg(NO₃)₂•6H₂O was used as dopant and then the concentration of it was 0.01mol%. The mist of aqueous solution was generated with ultrasonic atomizer (1.6MHz) with 0.08dm³/s of air carrier gas. The pyrolysis temperature was 500°C. As-prepared C/LiFePO₄ powders were corrected by the cyclone. Furthermore, as-prepared C/LiFePO₄ powders were heat-treated at 700°C for 10hr in the electric furnace under argon/hydrogen (5%) atmosphere. The average particle size, morphology and microstructure of C/LiFePO₄ powders were determined with a scanning electron microscope (SEM, Hitachi, S-2400). The crystal phase of C/LiFePO₄ powders was identified by powder X-ray diffraction (XRD, Shimadzu, XRD-6100). Specific surface area of them was measured by BET method using N₂ adsorption (Shimadzu, Tristar-3000). The chemical composition of them was determined by inductively coupled plasma analysis (ICP, SH, SPS3000). Powder density was determined by pycnometer (Shimadzu, AccupycII 1340). The carbon content in the C/LiFePO₄ particles was determined by differential thermal analysis - thermogravimetry (Shimadzu, DTG-60).

Cathode was prepared using 80wt% C/LiFePO₄ powders, 10wt% acetylene black and 10wt% fluorine resin. Metal lithium sheer (Honjo chemical) was used as an anode. The polypropylene sheet (Heist, celgard 2400) was used as a separator. 1mol/dm³ LiPF₆ in ethylene carbonate / 1,2-dimethoxyethane (EC : DEC = 1 : 1, Tomiyama pure chemical) was used as the electrolyte. Coin cell (2032 type, 20.0mmφ × 3.2mm) was built up in globe box under an argon atmosphere. The rechargeable capacity and cycle stability of C/LiFePO₄ cathode were measured with a battery tester (Hosen, BTS2004) at between 2.5V and 4.3V.

3. RESULTS AND DISCUSSION

Figure 1 shows typical SEM photographs of C/LiFePO₄ powders obtained by heat treatment at 700°C under the atmosphere of argon/hydrogen (5%). SEM

photographs revealed that C/LiFePO₄ particles had spherical morphology with non-aggregation regardless of the types of carbon sources. The average particle size of them determined by SEM photograph was about 1 - 2 μm. The geometrical standard deviation of average particle size ranged from 1.2 to 1.5 μm and these powders had relatively narrow size distribution. Specific surface area of LiFePO₄ powders was 1m²/g, but that of C/LiFePO₄ powders was about 40m²/g. It was found that specific surface area significantly increased by the addition of carbon. Specific surface area of them suggested that the particle microstructure of C/LiFePO₄ powders was porous by the addition of carbon. On the other hand, the powder density of LiFePO₄ powders and C/LiFePO₄ powders was 3.5kg/m³ and 3.2kg/m³, respectively. It was considered that the particle density of C/LiFePO₄ powders was reduced because of porous microstructure.

Figure 2 showed typical XRD patterns of LiFePO₄ and C/LiFePO₄ powders, respectively. The crystal phase of as-prepared C/LiFePO₄ powders was amorphous, but they were well crystallized by the heat-treatment under the atmosphere of argon/hydrogen (5%). XRD revealed that the diffraction patterns of all sample were good agreement with olivine structure (space group: Pnma) and other phases were not observed. The chemical composition of them was good agreement with starting solution composition from inductively coupled plasma analysis. The crystallinity of LiFePO₄ was higher than that of C/LiFePO₄. Therefore, no evidence of diffraction peaks for carbon appeared in the diffraction pattern, which indicates that the carbon generated from organic materials is amorphous and the presence of carbon does not influence the formation of LiFePO₄.

Figure 3 shows the rechargeable curves of LiFePO₄ and C/LiFePO₄ cathodes at the rate of 1C. The long plateau was observed at about 3.5V in the rechargeable curves. The charge and discharge capacity of carbon-free LiFePO₄ cathode was about 43mAh/g and 40mAh/g because of poor electrical conductivity. It was found that the rechargeable capacity of LiFePO₄ was considerably improved by the addition of carbon. The

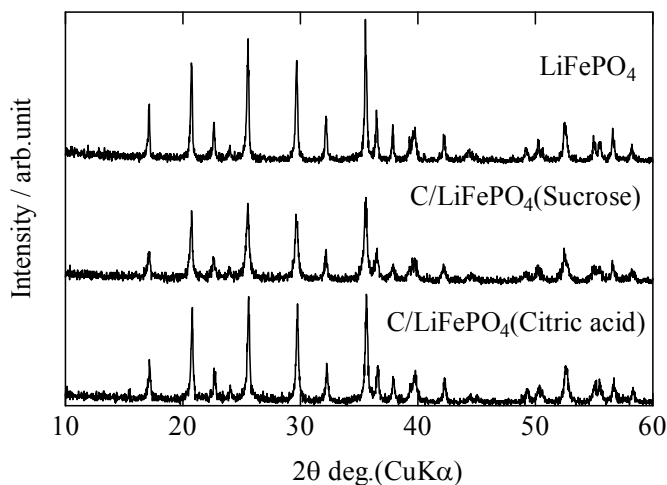


Fig.2 XRD patterns of LiFePO₄ and C/LiFePO₄ powders derived from sucrose and citric acid

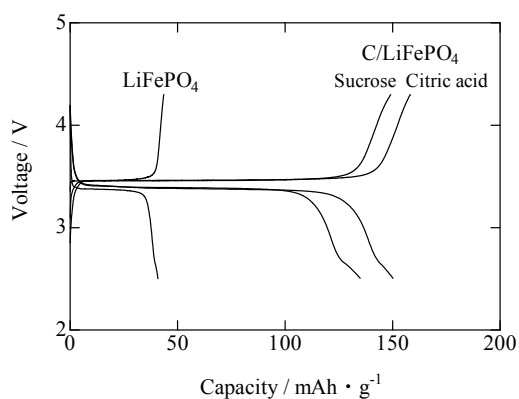


Fig. 3 Rechargeable curves of LiFePO_4 and C/LiFePO_4 cathode at rate of 1C

charge and discharge capacity of C/LiFePO_4 cathode derived from citric acid exhibited 158mAh/g and 150mAh/g, respectively. That of C/LiFePO_4 cathode derived from sucrose exhibited 150mAh/g and 130mAh/g, respectively. The discharge capacity of C/LiFePO_4 derived from other organic compound such as fructose, white sugar also exhibited 140mAh/g. The rechargeable capacity of C/LiFePO_4 cathode derived from citric acid was higher than that derived from sucrose. The carbon content was 2.6wt% in C/LiFePO_4 particles derived from citric acid. The carbon content was 7.1wt% in C/LiFePO_4 particles derived from sucrose. Because the particle size of C/LiFePO_4 particles derived from citric acid is close to that of C/LiFePO_4 particles derived from sucrose, the excess carbon content (4.5wt%) may lead to the loss for energy density of C/LiFePO_4 cathode derived from sucrose.

Figure 4 shows the change of initial discharge capacity of C/LiFePO_4 cathode derived from citric acid. The initial discharge capacity of C/LiFePO_4 cathode exhibited 157mAh/g at rate of 0.1C. The initial discharge capacity of it decreased to about 100mAh/g at rate of 5C. At rate of 10C, it exhibited 70mAh/g.

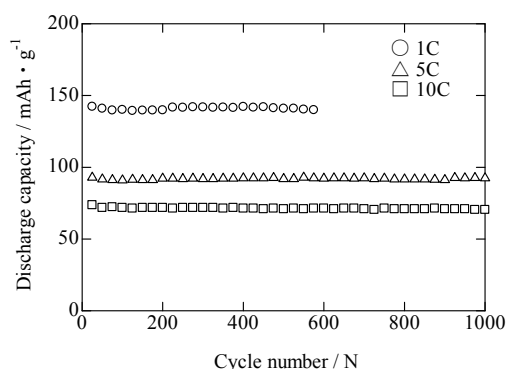


Fig. 5 Relation between discharge capacity and cycle number of C/LiFePO_4 cathode at rate indicated

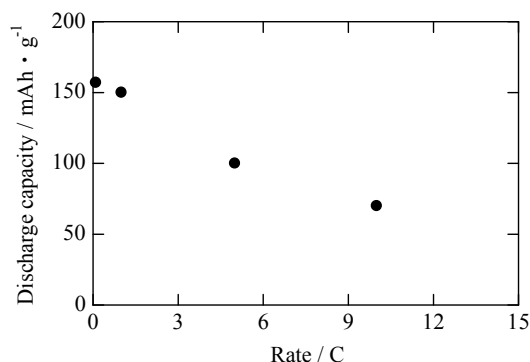


Fig. 4 Relation rate and discharge capacity of C/LiFePO_4 cathode derived from citric acid

Figure 5 shows the relation between cycle number and discharge capacity of C/LiFePO_4 cathode derived from citric acid at rate indicated. The rechargeable test was carried out up to 1000 cycles. It was clear that C/LiFePO_4 cathode had the excellent cycle stability. The discharge capacity of C/LiFePO_4 cathode maintained 90% of initial discharge capacity after 600 cycles at rate of 1C. The same tendency of cycle stability was also observed in the cycle data at rate of 5C and 10C. The discharge capacity of C/LiFePO_4 cathode maintained 92% of initial discharge capacity after 1000 cycles at rate of 10C.

Figure 6 shows the relation between cycle number and discharge capacity of C/LiFePO_4 cathode at 50°C. The rechargeable test of coin cell was examined up to 100 cycles, while it was heated on the hot plate which was kept to 50°C. The charge rate of it was 1C. The discharge capacity of C/LiFePO_4 cathode derived from citric acid exhibited 147mAh/g and the cycle life of it was also stable. The discharge capacity of C/LiFePO_4 cathode maintained 96% of initial discharge capacity after 100 cycles. It was found that C/LiFePO_4 cathode had high cycle stability at the elevated temperature.

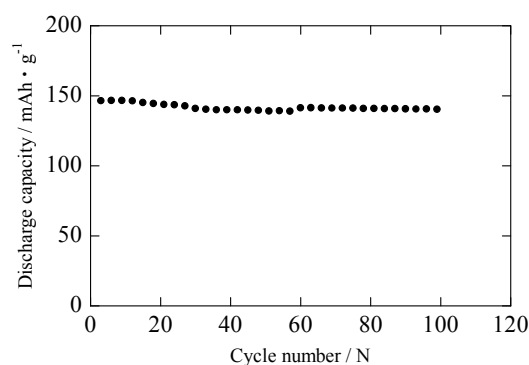


Fig. 6 Relation between discharge capacity and cycle number of C/LiFePO_4 cathode at 50°C

In order to improve the cycle stability of C/LiFePO₄ cathode at higher rate of charge/discharge, the addition of foreign metal to C/LiFePO₄ was examined. Magnesium ion was used as foreign metal in this work. Figure 7 shows the relation between cycle number and discharge capacity of C/LiFe_{0.99}Mg_{0.01}PO₄ cathode at rate of 5C and 10C, respectively. The initial discharge capacity of it increased to 110mAh/g and 96mAh/g at rate of 5C and 10C, respectively. However, the initial discharge capacity was not improved even if magnesium ion was added from 2 to 5mol%.

The cycle stability of it was as same as that of C/LiFePO₄ cathode. The discharge capacity of C/LiFe_{0.99}Mg_{0.01}PO₄ cathode maintained 95% of initial discharge capacity at rate of 10C after 200 cycles. It was found that C/LiFe_{0.99}Mg_{0.01}PO₄ cathode had high cycle stability for as well as C/LiFePO₄ cathode.

4. CONCLUSION

C/LiFePO₄ precursor powders were prepared by spray pyrolysis using aqueous solution with organic compounds. Spherical C/LiFePO₄ particles with size of 1µm and high specific surface area were obtained. XRD revealed that the crystal phase of C/LiFePO₄ powders was agreement with olivine phase. The rechargeable properties of LiFePO₄ cathode were significantly improved by addition of carbon. The electrochemical measurement revealed that the rechargeable capacity of C/LiFePO₄ cathode was 157mAh/g at rate of 0.1C and exhibited good cycle stability at 25°C. The addition of citric acid led to highest rechargeable capacity and most stable cycle life of C/LiFePO₄ cathode. 90% of initial discharge capacity was maintained after 600 cycles. The cycle stability was also kept at the elevated temperature. The addition of magnesium ion led to the cycle stability at higher rate.

ACKNOWLEDGEMENT

This work was supported by Development of an Electric Energy Storage System for Grid-connection with New Energy Resources in New Energy and Industrial Technology Development Organization (NEDO).

References

- [1] K. Matsuda, I. Taniguchi, *J. Power Sources*, 132, 156-160 (2004).
- [2] M.S. Whittingham, *Chem. Rev.*, 104, 4271-4301 (2004).
- [3] A. S. Andersson, J. O. Thomas, B. Kalska, L. Haggstrom, *Electrochem. Solid State Lett.*, 3, 66-68 (2000).
- [4] A.K. Padhi, K.S. Nanjundaswamy, J.B. Goodenough, *J. Electrochem. Soc.*, 144, 1188-94 (1997).
- [5] S.L. Bewlay, K. Konstantinov, G.X. Wang, S.X. Dou, H.K. Liu, *Mater. Lett.*, 58, 1788-91 (2004).
- [6] D. Wang, H. Li, S. Shi, X. Huang, L. Chen, *Electrochim. Acta*, 50, 2955-58 (2005).
- [7] J. Barker, M.Y. Saidi, J.L. Swoyer, *Electrochem. Solid State Lett.*, 6, A53-55 (2003).
- [8] M.R. Yang, T.H. Te, S.H. Wu, *J. Power Source*, 159, 307-311 (2006).
- [9] B. Dubois, D. Ruffier, P. Odier, *J. Am. Ceram. Soc.*, 72, 713-15 (1989).

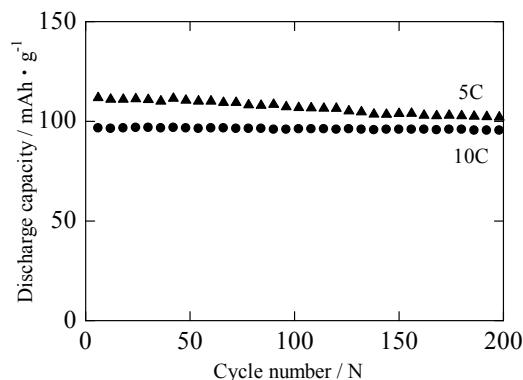


Fig.7 Relation between discharge capacity and cycle number of C/LiFe_{0.99} Mg_{0.01}PO₄ cathode at rate indicated

[10] G. L. Messing, S.C. Zhang, G. V. Javanthi, *J. Am. Ceram. Soc.*, 76, 2707-26 (1993).

(Received December 11, 2008; Accepted November 11, 2009)

Synthesis and Properties of Nitrogen Atom Encapsulated Fullerene

Jamal Uddin Ahamed, Sunao Miyanaga, Toshiro Kaneko, and Rikizo Hatakeyama

Department of Electronic Engineering, Tohoku University, Sendai 980-8579, Japan

Fax: +81-22-263-9225, e-mail: ahamed@plasma.ecei.tohoku.ac.jp

An electron spin resonance analysis confirms that an atomic nitrogen is encapsulated inside a sublimated fullerene (C_{60}) molecule in a radio frequency (RF) discharge plasma. It is observed that the electron beam superimposed RF plasma whose parameters are easily controlled has remarkable effects on the synthesis of the nitrogen atom encapsulated fullerene ($N@C_{60}$). Optical emission spectroscopy (OES) is used to characterize the nitrogen species in the plasma, and it is clarified that the moderately low gas pressure and high RF power effectively dissociate the nitrogen molecules, resulting in the enhancement of the purity of $N@C_{60}$.

Key words: fullerene, encapsulation, RF plasma, electron beam, nitrogen species.

1. INTRODUCTION

The fullerene such as C_{60} discovered in 1985, which has a soccer ball like structure with a hollow interior [1], can accommodate various atoms or molecules [2]. Up to now several kinds of endohedral fullerenes have been synthesized, such as metallofullerenes [3, 4], in which metallic atoms are incorporated inside the cage, noble gas endohedral fullerenes [5, 6], in which one or two noble gas atoms are inserted in the cage, and endohedral fullerenes with reactive atoms like as nitrogen or phosphorus stabilized inside the cage [7–9]. The insertion of different kinds of atoms or molecules into the cage of the fullerenes has been actively studied because of their unique structure and electric/magnetic/optical properties. The nitrogen atom encapsulated fullerene ($N@C_{60}$) is the first member of the endohedral fullerenes in which the highly reactive nitrogen atom is stabilized in its atomic ground state due to the protection provided by the C_{60} cage. The nitrogen atom in C_{60} is chemically inert and stable under ambient conditions. Among various endohedral fullerenes, $N@C_{60}$ attracts particular interest due to the atomic nature of the entrapped nitrogen atom and its half-filled P orbitals. Potential applications, such as in the field of spin quantum computation, have been proposed [10, 11]. $N@C_{60}$ has been yielded by ion implantation [7], glow [9, 12], radio frequency [13, 14], and electron cyclotron resonance [15, 16] discharge methods so far, where C_{60} films deposited on substrates are exposed continuously to the nitrogen ions accelerated by electric fields actively or passively. However, the synthesis yield of $N@C_{60}$ is extremely low (purity just after synthesis: $N@C_{60}/C_{60} = 10^{-3} \%$ to $10^{-2} \%$) at present. Although the purity can be improved by high performance liquid chromatography (HPLC) [17], HPLC takes an awfully long time to purify the extremely low yield of $N@C_{60}$. Therefore, to get the high purity of $N@C_{60}$, it is necessary to clarify the encapsulation mechanism and to improve the encapsulation yield.

The synthesis of $N@C_{60}$ requires a plasma containing a considerable amount of nitrogen-atom radicals N^* (N^* stands for excited atomic nitrogen) and/or ions N^+ as an encapsulated source of nitrogen atom. To produce N^*

and N^+ from nitrogen molecules N_2 ($N_2 + e \rightarrow N^* + N^+ + 2e$), a desorption/ionization energy of 25.4 eV should be supplied to N_2 by energy transfer from electrons [18]. In this respect an electron beam superimposed radio frequency (RF) plasma is useful, which leads to the energization of the electrons and the resultant dissociation and ionization of N_2 .

In this paper, the efficient synthesis of $N@C_{60}$ is demonstrated by actively controlling the plasma parameters such as nitrogen gas pressure, nitrogen species, RF power, substrate, and grid bias voltages using the electron beam superimposed RF plasma source.

2. EXPERIMENTAL APPARATUS

The schematic of an experimental apparatus is shown in Fig. 1. Nitrogen gas is input from the top of the apparatus, and the nitrogen plasma is generated by applying an RF power with a frequency of 13.56 MHz to a spiral-shaped RF antenna (no. of turns is 5) located at $z = 58 - 72$ cm, and controlled by the applied RF power P_{RF} , a nitrogen gas pressure P_{N_2} , a substrate potential V_{sub} , and a grid potential V_g . A stainless mesh grid (20 meshes/cm) with a supporting rod is set up at an upper part of the apparatus to control plasma parameters by applying V_g . The upper side and lower side of the grid are defined as “plasma production area” and “process area”, respectively. The plasma potentials in the two areas are controlled by V_g and V_{sub} , and a potential difference is formed between the two areas. The potential difference produces the electron beam flowing from the plasma production area to the process area and the electron beam dissociates nitrogen molecules. C_{60} is sublimated from an oven located at $z = 27$ cm and deposited on a cylindrical substrate at $z = 25 - 39$ cm. The nitrogen plasma is continuously irradiated to C_{60} on the substrate. The experiment lasts for around 1 hour and about 65 mg of C_{60} is sublimated. Since the produced $N@C_{60}$ is very sensitive to the ambient temperature [19], the substrate is maintained at low temperatures (below 20 °C) by water cooling during the plasma irradiation.

The plasma parameters are measured by Langmuir probes at $z = 30$ cm in the process area and at $z = 53$ cm in

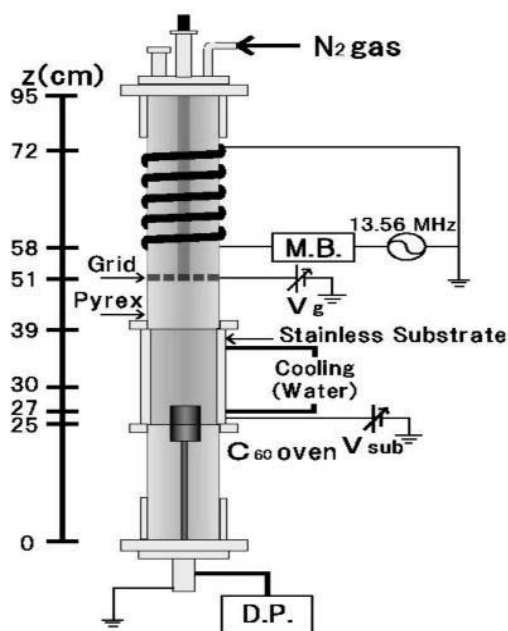


Fig. 1: Schematic of experimental apparatus.

the plasma production area. An irradiated ion energy E_i to the substrate is defined as the difference between plasma potential ϕ_p and V_{sub} . The nitrogen species are analyzed by optical emission spectroscopy (OES) at $z = 41$ cm in the process area and at $z = 53$ cm in the plasma production area. Experiments on the synthesis of $N@C_{60}$ are performed under the condition as follows: applied RF power $P_{RF} = 100 \sim 800$ W, nitrogen gas pressure $P_{N_2} = 0.5 \sim 3$ Pa, $V_g = -100 \sim 100$ V, and $V_{sub} = -100 \sim 100$ V.

A C_{60} compound including $N@C_{60}$ deposited on the substrate is scratched off and dissolved in toluene. The solution is then analyzed by electron spin resonance (ESR) and UV-vis absorption spectrometry to calculate the purity, and is refined by high performance liquid chromatography (HPLC).

3. RESULTS AND DISCUSSIONS

Figure 2 shows an ESR spectrum of the product of $N@C_{60}$. The hyperfine constants (5.67 G) and g values for this splitting are essentially the same as those reported [7, 20], which are attributed to the isotropic hyperfine interaction of the ^{14}N unpaired electron spins with the nuclear spins. The concentration of $N@C_{60}$ is very low. One of the possible reasons is that the polymerization probably takes place between $N@C_{60}$ and C_{60} , which is supported by the substantial line broadening of the dimmer $N@C_{60}-C_{60}$ compared to that of $N@C_{60}$ [21]. Further study is needed to isolate and characterize the polymerized $N@C_{60}$. The typical purity of $N@C_{60}$ is in the order of 10^{-3} to 10^{-2} %, which is calculated by comparing with a standard spin material.

In the nitrogen RF-plasma, there are various kinds of ionic and neutral species, such as nitrogen molecule radicals N_2^* , nitrogen molecule ions N_2^+ , nitrogen atom radicals N^* , and nitrogen atom ions N^+ . During evaporation, some C_{60} molecules are immediately ionized and excited by the high energy electrons in the plasma. Since C_{60} is the electron-affinitive molecule, C_{60}

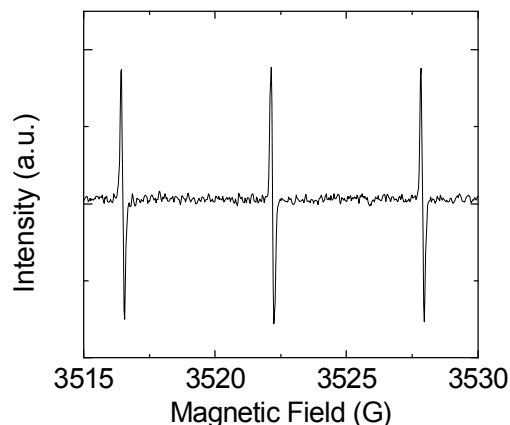


Fig. 2: X-band ESR spectrum of $N@C_{60}$.

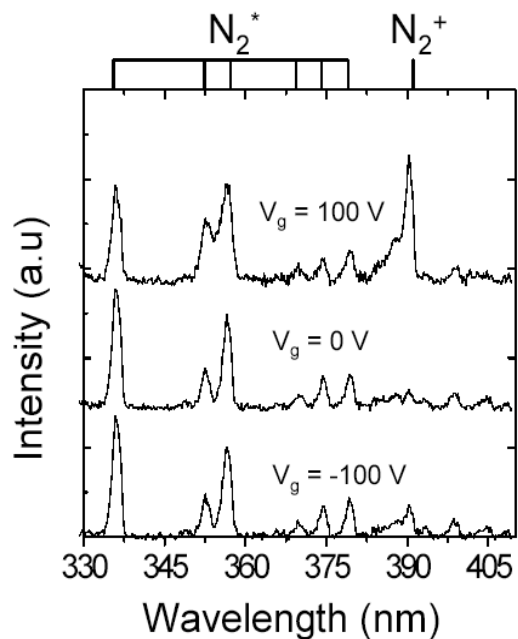
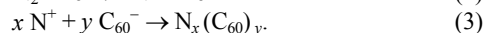


Fig. 3: Optical emission spectra of nitrogen species in the plasma process area for $P_{RF} = 450$ W, $P_{N_2} = 0.6$ Pa, $V_{sub} = 100$ V.

will be negatively charged in the plasma, and is expected to have mutual dissociative recombination reactions with N^+ ions. The main species and reactions in the plasma can briefly be expressed as follows [13, 18, and 23].



Reaction (3) represents the formation of both $\text{N}-C_{60}$ hybrid compounds and C_{60} polymers. Here x and y are integer larger than 0. By adjusting the input RF power, nitrogen gas pressure, and potential difference between plasma production area and the process area, the electron energy and flux which affect the generation of the atomic nitrogen species can be controlled, and furthermore, the substrate potential can vary the energy of the atomic nitrogen species irradiated to the substrate in the range of $10 \sim 100$ eV, which covers the energy suitable for ion

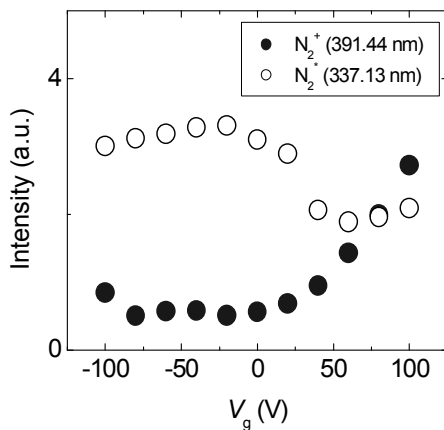


Fig. 4: Optical emission intensity of N_2^* and N_2^+ in the plasma process area as a function of V_g for $P_{RF} = 450$ W, $P_{N_2} = 0.6$ Pa, $V_{sub} = 100$ V.

implantation (~40 eV) [16, 22]. This reaction toward ion implantation can take place:



Figure 3 gives OES results observed in the plasma process area for $V_g = 100, 0,$ and -100 V, $P_{RF} = 450$ W, $P_{N_2} = 0.6$ Pa, and $V_{sub} = 100$ V. The nitrogen plasma is considered to be composed of nitrogen molecule radicals (N_2^*), nitrogen molecule ions (N_2^+), nitrogen atom radicals (N^*), and nitrogen atom ions (N^+) with their strong peak wavelengths at 337.13 nm, 391.44 nm, 746.83 nm and 500.52 nm respectively. Since the emission intensity of the N_2 and N_2^+ lines is proportional to the concentration of these species and the number of electrons having energy larger than their excitation threshold energy. The threshold excitation energy of N_2 (337.13 nm) is 11.1 eV and the threshold ionization energy of N_2 is 15.57 eV, while the threshold excitation energy of N_2^+ (391.44 nm) is 18.7 eV [18]. It is concluded that the excitation of the nitrogen molecule N_2 dominates lower energy, while dissociation process as well as molecular ionization N_2^+ dominates at higher electron energy. It is clear from the Fig. 3 that the peak intensity is changed by V_g . The high intensity peaks result from the emission of N_2^* and N_2^+ , but the peaks of N are not observed in our OES spectrometry because it is unable to detect the peak of ground state atomic nitrogen species. However, the increase in N_2^+ and the decrease in N_2^* in the plasma for high energy electrons imply that the density of the atomic nitrogen species is increased.

Figure 4 shows the dependence of the optical emission intensities of N_2^* and N_2^+ in the plasma process area on V_g for $P_{RF} = 450$ W, $P_{N_2} = 0.6$ Pa, and $V_{sub} = 100$ V. It is found that the peak intensities in the plasma process area are changed by V_g . For $V_g < -20$ V, the peak intensities are nearly constant, and the intensity of N_2^+ is lower than that of N_2^* . For $V_g > -20$ V, on the other hand, the intensity of N_2^+ starts to increase, and the intensity of N_2^* starts to decrease with increasing V_g . This change of the peak intensities in the process area can be explained by the high energy electrons going through the grid to the process area, and hence an increase in the density of atomic nitrogen species is expected. In our apparatus the plasma potential in the process area is higher than that in the plasma production area. In this case, the electrons that travel through the grid can be accelerated by the potential

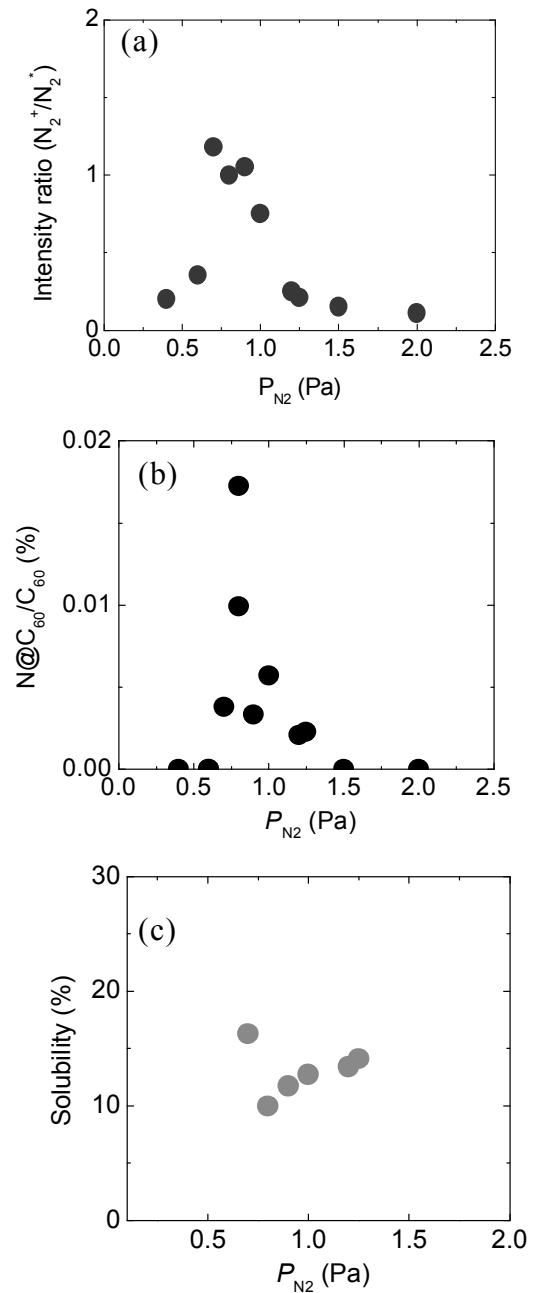


Fig. 5: Dependence of (a) intensity ratio (N_2^+/N_2^*), (b) purity of $N@C_{60}$, and (c) solubility on nitrogen gas pressure P_{N_2} for $P_{RF} = 450$ W, $V_g = V_{sub} = 100$ V.

difference between the plasma production areas and the process area.

Figure 5 presents the dependence of intensity ratio (N_2^+/N_2^*), purity of $N@C_{60}$, and solubility on P_{N_2} . It is found from the Fig. 5 (a) that the high intensity ratio (N_2^+/N_2^*) is achieved under the condition that the applied nitrogen gas pressure is around 0.8 Pa. At extremely low and high gas pressures the intensity ratio becomes low. Therefore, it can be considered that the moderately low nitrogen gas pressure improves the rate of dissociation/ionization and hence increases the density of the atomic nitrogen species in the plasma process area. These increased high density atomic nitrogen species enhances the purity of $N@C_{60}$ which can be noted from

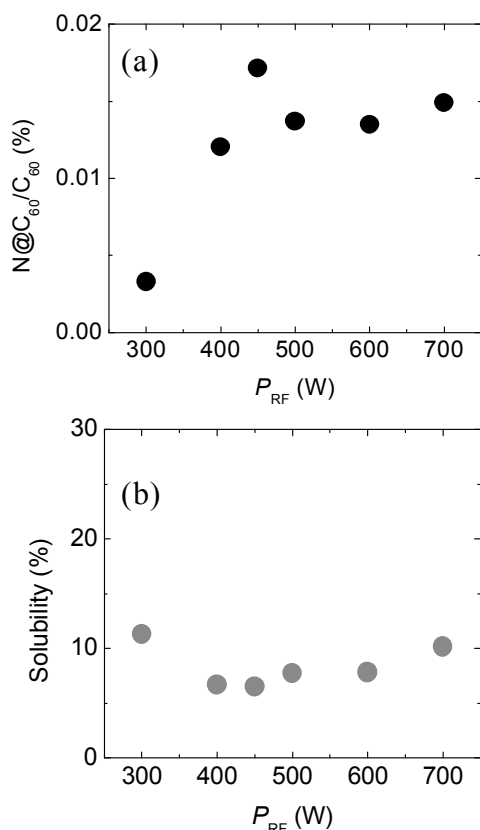


Fig. 6: Dependence of (a) purity and (b) solubility of N@C₆₀ in toluene on P_{RF} for $V_g = V_{sub} = 100$ V, $P_{N_2} = 0.8$ Pa.

the Fig. 5 (b). Since the solubility is observed to be independent of nitrogen gas pressure, maximum synthesis of N@C₆₀ is achieved at moderately low gas pressure which realizes the high purity of N@C₆₀.

Figure 6 shows the dependence of the purity of N@C₆₀ and solubility on P_{RF} . It is found that the purity increases with increasing the RF power and the maximum purity of about 0.02 % is achieved under the condition that the applied RF power is more than 400 W. It is considered that the electron density in the plasma production area and the electron beam density in the process area increase with increasing P_{RF} . This increased electron beam enhances the rate of dissociation/ionization of the nitrogen molecules in the process area, resulting in the improvement of the purity.

4. CONCLUSION

The nitrogen molecules are effectively dissociated/ionized by using an electron beam superimposed RF discharge plasma. A high intensity ratio (N_2^+/N_2^*) is obtained at moderately low nitrogen gas pressure, which implies that the rate of dissociation/ionization and hence the density of atomic nitrogen increase in the plasma process area. This high density atomic nitrogen enhances the purity of N@C₆₀. Also, the purity of N@C₆₀ increases with increasing the RF power and the maximum purity is obtained when the RF power is more than 400 W.

ACKNOWLEDGEMENTS

This work is supported by the Tohoku University

Electro-Related Departments Global COE Program. We are very much indebted to Professor M. Takahashi for his support in ESR measurements.

References

- [1] H. W. Kroto, J. R. Heath, S. C. O'Brien, R. F. Curl and R. E. Smalley, *Nature*, **318**, 162-163 (1985).
- [2] J. R. Heath, S. C. O'Brien, Q. Zhang, Y. Liu, R. F. Curl, H. W. Kroto, F. K. Tittel and R. E. Smalley, *J. Am. Chem. Soc.*, **107**, 7779-7780 (1985).
- [3] D. S. Bethune, R. D. Johnson, J. R. Salem, M. S. de Vries and C. S. Yannoni, *Nature*, **366**, 123-128 (1993).
- [4] H. Shinohara, H. Sato, M. Ohkohchi, Y. Ando, T. Kodama, T. Shida, T. Kato and Y. Sato, *Nature*, **357**, 52-54 (1992).
- [5] M. Saunders, H. A. Jiménez-Vázquez, R. J. Cross and R. J. Poreda, *Science*, **259**, 1428-1430 (1993).
- [6] M. Saunders, R. J. Cross, H. A. Jiménez-Vázquez, R. Shimshi and A. Khong, *Science*, **271**, 1693-1697 (1996).
- [7] T. A. Murphy, T. Pawlik, A. Weidinger, M. Höhne, R. Alcalá and J.-M. Spaeth, *Phys. Rev. Lett.*, **77**, 1075-1078 (1996).
- [8] H. Mauser, N. J. R. van E. Hommers, T. Clark, A. Hirsch, B. Pietzak, A. Weidinger and L. Dunsch, *Angew. Chem. Int. Ed. Engl.*, **36**, 2835-2838 (1997).
- [9] A. Weidinger, M. Waiblinger, B. Pietzak and T. A. Murphy, *Appl. Phys. A* **66**, 287-292 (1998).
- [10] W. Harneit, *Phys. Rev. A* **65**, 032322-1-6, (2002).
- [11] S. C. Benjamin, A. Ardavan, G. A. D. Briggs, D. A. Britz, D. Gunlycke, J. Jefferson, M. A. G. Jones, D. F. Leigh, B. W. Lovett, A. N. Khlobystov, S. A. Lyon, J. J. L. Morton, K. Porfyrakis, M. R. Sambrook and A. M. Tyryshkin, *J. Phys.: Condens. Matter*, **18**, S867-S883 (2006).
- [12] B. Pietzak, M. Waiblinger, T. A. Murphy, A. Weidinger, M. Höhne, E. Dietel and A. Hirsch, *Chem. Phys. Lett.*, **279**, 259-263 (1997).
- [13] H. Huang, M. Ata and M. Ramm, *Chem. Commun. (Cambridge)*, **2002**, 2076-2077 (2002).
- [14] M. Ata, H. Huang and T. Akasaka, *J. Phys. Chem., B* **108**, 4640-4646 (2004).
- [15] T. Kaneko, S. Abe, H. Ishida and R. Hatakeyama, *Phys. Plasmas*, **14**, 110705 1-3 (2007).
- [16] S. Abe, G. Sato, T. Kaneko, T. Hirata, R. Hatakeyama, K. Yokoo, S. Ono, K. Omote and Y. Kasama, *Jpn. J. Appl. Phys.*, **45**, 8340-8343 (2006).
- [17] M. Kanai, K. Profyrakis, G. A. D. Briggs and T. J. S. Dennis, *Chem. Commun. (Cambridge)*, **2004**, 210-211 (2004).
- [18] A. Qayyum, S. Zeb, S. Ali, A. Waheed and M. Zakauallah, *Plasma Chem. Plasma Process*, **25**, 551-564 (2005).
- [19] M. Waiblinger, K. Lips, W. Harneit and A. Weidinger, *Phys. Rev. B* **64**, 159901-5 (2001).
- [20] K. Lips, M. Waiblinger, B. Pietzak and A. Weidinger, *Phys. Status Solidi*, **177**, 81-91 (2000).
- [21] B. Goedde, M. Waiblinger, P. Jakes, N. Weiden, K. P. Dinse and A. Weidinger, *Chem. Phys. Lett.*, **334**, 12-17 (2001).
- [22] J. A. Larssona, J. C. Greer, W. Harneit and A. Weidinger, *J. Chem. Phys.*, **116**, 7849-7854 (2002).
- [23] R. F. Boivin and E. E. Scime, *Plasma Sources Sci. Technol.*, **14**, 283-292 (2005).

(Received December 11, 2008; Accepted October 5, 2009)

- Polar Coincident Site Lattice Figure - Multiple Domain Growth of Bismuth Cuprate Superconducting Film

S. Kaneko, K. Akiyama, Y. Hirabayashi, T. Ito, Y. Motoizumi, K. Yoshida, T. Horiuchi,
M. Soga, M. Yasui, M. Kano, M. Kumagai, H. Funakubo* and M. Yoshimoto*

Kanagawa Industrial Technology Center, Kanagawa Prefectural Government,
705-1 Shimo-Imaizumi, Ebina, Kanagawa 243-0435 JAPAN
Fax: 81-426-236-1500, e-mail: satoru@kanagawa-iri.go.jp

*Department of Innovative & engineered Materials, Tokyo Institute of Technology,
4259 Nagatsuda, Midori-ku, Yokohama, Kanagawa 226-8503 JAPAN
Fax: 81-45-924-5388

Bismuth cuprate superconducting film has a large-scale periodicity, supercell, other than an ordinal lattice cell. Although the supercell lies along b axis in bulk material, the structure lies along both a and b axes on thin film and shows asymmetric structure in reciprocal space along c axis. The asymmetric structure was described with triangle function, which modulates the structure to form the supercell. In the terms of the double domain along a and b axes were observed on three dimension X-ray reciprocal space mapping. Bismuth oxide film ($\text{Bi}_2\text{Sr}_2\text{Ca}_1\text{Cu}_2\text{O}_x$) grew with the relation of $\text{Bi-2212}[001]$ parallel to $\text{MgO}[110]$ (45° rotation growth), but the bismuth cuprate superconducting film often grows with lateral rotation from 45° growth. To describe such a relation, coincidence site lattice was visually expressed on polar coordinate system.

Key words: high Tc superconductor, thin film, supercell, reciprocal space mapping

1. INTRODUCTION

High Tc superconductor, bismuth cuprate oxides, is well known for structural modulation, supercell. The supercell is incommensurate modulation consisting of several unit cells along b axis with periods of 4.7 unit cells [1-4]. The supercell (SC) of $\text{Bi}_2\text{Sr}_2\text{Ca}_1\text{Cu}_2\text{O}_x$ (Bi-2212) is expressed as $\text{SC} = 4.7\mathbf{b} + 1.0\mathbf{c}$, where \mathbf{b} and \mathbf{c} are unit cell vectors along b and c axes. The modulation is incommensurate along b axis but is commensurate along c axis in bulk samples previously reported.

While bulk samples show symmetric structure of SC by high-resolution electron microscopy, electron diffraction, x-ray diffraction, and neutron diffraction [5-9], thin films show asymmetric peaks on X-ray Reciprocal Space Mapping (XRSM) [10]. The symmetric peaks observed on bulk samples can be generated by modulation vector as a sinus function modulating unit cells through its crystal, and the asymmetric peaks are described by triangle function [11]. Another XRSM shows the SC modulations exist along both a and b axes. An epitaxial Bi-2212 film deposited on $\text{MgO}(001)$ substrate grows with relation of $\text{Bi-2212}[100]$ parallel to $\text{MgO}[110]$ (45° rotation), indicating Bi-2212 grows epitaxially on MgO substrate in term of unit cells. However, from the view of long periodicity the SC structure has two domains along a and b axes.

Aliovalent substitution and extra oxygen had been

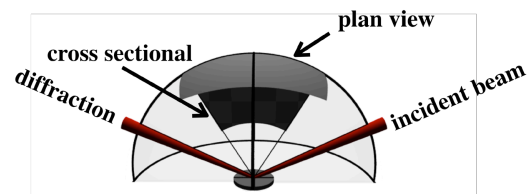


Fig.1 Schematic of X-ray Reciprocal Space Mapping (XRSM). X-ray irradiates a sample with an incident beam and is diffracted to the left. An ordinal cross sectional XRSM (black plane) and a plan view XRSM (top gray plane).

carried out to investigate the origin of SC structure [12-14]. The aliovalent substitution replaces cations with different radius, and the oxygen doping changes oxygen content by annealing or by high-pressure oxidization. The aliovalent substitution of cations changes also oxygen content by replacing divalent strontium with trivalent lanthanum, for instance, so that the aliovalent substitution might affect oxygen content as well as inducing strain into crystal. To emphasize the effect of strain, multilayered and thick films were prepared and investigated in detail [15,16]. In multilayered structure the strain must be prominent, to the contrary, the strain must be released in thick film. Interestingly in the thick

film other domains grow on MgO(001) substrates with $\sim 30^\circ$ lateral rotation relative to initial 45° rotation [16].

In this study, 45° rotation growth was addressed by the coincidence site lattice [17-19] expanded on polar coordinate system for visualization, and to verify double domain growth in terms of SC structure plan view XRSM was taken on the plane vertically crossing ordinal cross sectional XRSM around Bi-2212(0020) peak. By continuously taking slices of plan view XRSM, three dimensional XRSM was also presented.

2. EXPERIMENTAL

Bi-2212 thin films were prepared by pulsed laser deposition using “slower Q-switched Nd:YAG laser” [20] at the repetition rate of 2 Hz generated by 10 Hz modulated flash lamp with secondary function generation. Targets were prepared by stoichiometric ratio of Bi_2O_3 , SrCO_3 , CaCO_3 and CuO powders, which were ground and calcined for total four hours in oxygen atmosphere at 800°C . The mixture was pressed as pellets at the pressure of 400 kgf/cm^2 , and sintered again in oxygen atmosphere at 800°C .

Bi-2212 films were deposited on MgO(100) substrates at a temperature of 750°C with a substrate-target distance of 40 mm. A thick film $\sim 5,000 \text{ \AA}$ was also prepared in the same conditions. Epitaxial growth was verified by mainly x-ray diffraction (XRD) such as θ - 2θ and φ scan, and deposition rate was estimated using film thicknesses obtained by x-ray reflection (XRR). X-ray reciprocal space mapping (XRSM) was taken on a cross section ($\mathbf{b}^* \times \mathbf{c}^*$ plane) and a plan view ($\mathbf{a}^* \times \mathbf{b}^*$ plane) to observe SC peaks generated by SC structure, as shown in Fig.1. The series of plan view XRSMs were taken to visualize SC structure in three dimensions. Resistivity was measured by the Van der Pauw method with silver electrodes, and showed the transition temperature ($R=0$) of 70 K.

3. RESULTS AND DISCUSSION

XRD θ - 2θ and φ scan verified an epitaxial growth of Bi-2212 film with the relation of Bi-2212[001] parallel to MgO[001] and Bi-2212[100] parallel to MgO[110] (45° rotation), and XRR showed the film thickness of $\sim 1,000 \text{ \AA}$. The lattice mismatch of Bi-2212[100] is about 25 % to MgO[100] (cubic on cubic) and 5 % to MgO[110] (45° rotation), respectively. The thick film with thickness of $\sim 5,000 \text{ \AA}$ showed lateral rotation other than 45° rotation growth commonly obtained on MgO(001) substrate.

A cross sectional XRSM was taken around Bi-2212(2022) including a substrate peak of MgO(113) so that the lattice constants of Bi-2212 can be verified by those of MgO substrate. The two peaks lied on MgO[110] \times MgO[001] plane, which is equivalent to $\mathbf{b}^* \times \mathbf{c}^*$ plane of Bi-2212 film. The cross sectional XRSM observes a plane of reciprocal lattice by using $\omega \times (\omega - 2\theta)$ axes, so that reciprocal lattice units (rlu), Qx and Qy can be expressed as,

$$Q_x = \frac{2 \sin \theta}{\lambda} \sin(\omega - \theta) ; Q_y = \frac{2 \sin \theta}{\lambda} \cos(\omega - \theta),$$

where λ is the wave length of incident X-ray ($\text{CuK}\alpha_1 = 1.5406 \text{ \AA}$). Since these are rectangular coordinates, the lattice constants can easily be estimated on Qx-Qy

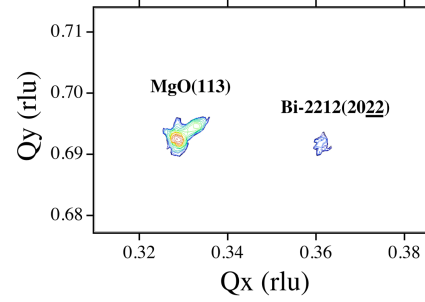


Fig.2 XRSM on MgO[110] \times MgO[001] plane, which is equivalent to the $\mathbf{b}^* \times \mathbf{c}^*$ plane of the Bi-2212 film. Bi-2212(2022) peak was observed with the substrate of MgO(113) peak.

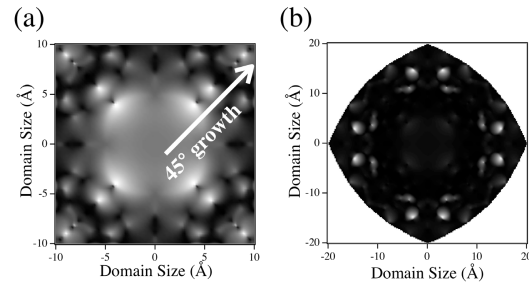


Fig.3 Polar CSL figure of Bi-2212 film grown on MgO(001) substrate (a) within domain size of 10 \AA , and (b) within 20 \AA . 45° rotation growth is dominant.

coordinate. The Bi-2212 thin film on a MgO(100) substrate showed the lattice constants, $b \sim 5.43 \text{ \AA}$, and $c \sim 30.88 \text{ \AA}$, which were estimated by XRSM observed around Bi-2212(2022) peak as shown in Fig.2.

Lattice mismatch is often mentioned for epitaxial growth, where the lattice coherent strain [21] e_ℓ is expressed as

$$e_\ell = 2 \frac{a_{\text{Bi}} - a_{\text{MgO}}}{a_{\text{Bi}} + a_{\text{MgO}}},$$

where a_{Bi} and a_{MgO} are lattice constants of Bi-2212 and MgO substrate, respectively. For an epitaxial growth the lattice coherent must be reasonably small. However, an epitaxial growth exists even with a large mismatch [22]. The lattice coherent strain is considered to be combinations of one each unit cells between a film and substrate. Epitaxial growth with a large lattice coherent strain is often described by domain epitaxial growth consisting of $(m \times n)$ unit cells of film growing on $(k \times \ell)$ ones of a substrate, and two lattices have a coincident site lattice (CSL) between $(k \times \ell)$ and $(m \times n)$ unit cells [17]. Domain coherent strain is often shown with only some combinations of k , ℓ , m and n in table.

In order to visualize domain coherent strain, a polar CSL has been proposed with all the combinations of $(k \times \ell)$ and $(m \times n)$ [22]. Domain coherent strain e_d is defined as

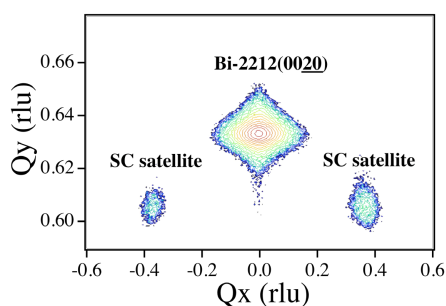


Fig.4 Cross sectional XRSM on ($\mathbf{b}^* \times \mathbf{c}^*$) plane of Bi-2212(0020) peak. Asymmetric intensity distribution of SC satellite peaks are observed around the main peak of Bi-2212(0020).

$$e_d = 2 \frac{\sqrt{m^2 + n^2} a_{\text{film}} - \sqrt{k^2 + \ell^2} a_{\text{sub}}}{\sqrt{m^2 + n^2} a_{\text{film}} + \sqrt{k^2 + \ell^2} a_{\text{sub}}},$$

where a_{film} and a_{sub} are lattice constants of film and substrate, respectively. Using polar coordinate, r and θ are defined as

$$r = \frac{\sqrt{k^2 + \ell^2} a_{\text{sub}} + \sqrt{m^2 + n^2} a_{\text{film}}}{2},$$

$$\phi = \tan^{-1}(n/m) - \tan^{-1}(\ell/k),$$

where r is the domain size and ϕ is the angle of lateral rotation between two lattice cells. The polar CSL is expressed on cylindrical polar coordinates r and θ with height z as domain matching, so that the figure shows domain size as the distance from the center point and in-plane epitaxial relation as angle of ϕ .

In spite of small lattice mismatch of 5% with 45° rotation growth, Bi-2212 film often grows with other domains than 45° rotation growth. Using a polar CSL, one can bird's-view domain coherent strain as well as lattice coherent strain. Figure 3(a) is the polar CSL figures of Bi-2212 film grown on MgO(001) substrate within domain size of 10 Å, which clearly shows the dominant is 45° rotation growth. As shown in Fig.3(b) with increasing domain size, CSL peaks are scattered around the angle ϕ , which is lateral rotation angle between film and substrate. For Bi-2212 film grown on MgO(001) 45° rotation growth is dominant, though it is possible to grow other domain in term of domain growth.

The SC structure was observed on XRSM taken around Bi-2212(0020) peak on ($\mathbf{b}^* \times \mathbf{c}^*$) plane as shown in Fig.4, and the SC size can be estimate in the same way to estimate lattice constants using the distance between main and SC peak on the Qx-Qy coordinate. The SC size in Bi-2212 film with thickness of ~1,000 Å was estimated to be SCb ~ 4.2b and SCc ~ 0.9c along \mathbf{b} and \mathbf{c} axes, respectively. Since the same mapping was obtained even on the plane laterally rotated 90° ($\mathbf{a}^* \times \mathbf{c}^*$ plane), unlike bulk sample the SC structure lies along both \mathbf{a} and \mathbf{b} axes; double domain in terms of SC structure. To verify the double domain of SC structure, continuous slice of plan view XRSM were taken on (\mathbf{a}^*

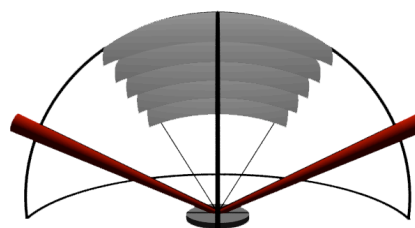


Fig.5 Slices of plan view XRSMs. Continuous plan view XRSM are taken along \mathbf{c}^* axis of Bi-2212 film.

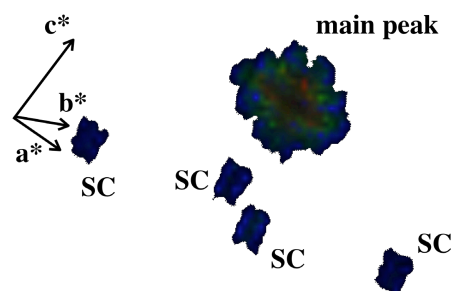


Fig.6 Three dimensional XRSM. 3D XRSM image is visualized from slices of plan view XRSMs by using an image processing software Osirix. Four SC satellite peaks are clearly observed on Bi-2212 film.

$\times \mathbf{b}^*$) plane of Bi-2212 film as shown in Fig.5. An image processing software “Osirix” dedicated to DICOM (Digital Imaging and Communications in Medicine) was employed to visualize three dimensional image from slices of plan view XRSM. Three dimensional (3D) XRSM was obtained as shown in Fig.6. Four SC satellite peaks were clearly observed under the main peak of Bi-2212(0020) peak at $\sim (\pm 0.2, \pm 0.2, 19)$.

In summary, Bi-2212 films were prepared by PLD method with slower Q-switched YAG laser. XRD θ -2 θ and ϕ scan verified the epitaxial growth of Bi-2212 film, though lateral rotation growth is often reported on Bi-2212 film. To describe the lateral rotation growth including 45° rotation growth, a polar CSL figure was proposed. To verify the SC structure lay along both \mathbf{a} and \mathbf{b} axes, slices of plan view XRSMs were taken around Bi-2212(0020) peak, and 3D-XRSM clearly showed the SC structure lay along both \mathbf{a} and \mathbf{b} axes.

REFERENCES

- [1] Y. Matsui, H. Maeda, Y. Tanaka and S. Horiuchi, *Jpn. J. Appl. Phys.*, **27**, L372-L375 (1988).
- [2] Y. Bando, T. Kijima, Y. Kitami, J. Tanaka, F. Izumi and M. Yokoyama, *Jpn. J. Appl. Phys.*, **27**, L358-L360 (1988).
- [3] Y. Hirotsu, O. Tomioka, T. Ohkubo, N. Yamamoto, Y. Nakamura, S. Nagakura, T. Komatsu and K.

Matsushita, *Jpn. J. Appl. Phys.*, **27**, L1869-L1872 (1988).

[4] V. Petricek, Y. Gao, P. Lee and P. Coppens, *Phys. Rev. B*, **42**, 387-392 (1990).

[5] M. B. Walker and W. Que, *Phys. Rev. B*, **45**, 8085-8090 (1992).

[6] J. Etrillard, P. Bourges and C. T. Lin, *Phys. Rev. B*, **62**, 8085-8090 (2000).

[7] Y. Matsui, S. Takekawa and S. Horiuchi, *Jpn. J. Appl. Phys.*, **27**, L1873-L1876 (1988).

[8] H. Nui, N. Fukushima, S. Takeno, S. Nakamura and K. Ando, *Jpn. J. Appl. Phys.*, **28**, L784-L786 (1988).

[9] J. G. Wen, C. Y. Yang and K. Fung, *Phys. Rev. B*, **42**, 4117-4121 (1992).

[10] S. Kaneko, K. Akiyama, Y. Shimizu, H. Yuasa, Y. Hirabayashi, S. Ohya, K. Saito, H. Funakubo and M. Yoshimoto, *J. Appl. Phys.*, **97**, 103904-1-7 (2005).

[11] S. Kaneko, Y. Shimizu, K. Akiyama, T. Ito, M. Mitsuhashi, S. Ohya, K. Saito, H. Funakubo and M. Yoshimoto, *Appl. Phys. Lett.*, **85**, 2301-2303 (2004).

[12] Z. Mao, C. Fan, L. Shi, Z. Yang and Y. Zhang, *Phys. Rev. B*, **47**, 14467-14475 (1993).

[13] Z. Mao, H. Zhang, M. Tian, S. Tan, Y. Xu, Y. Yu and Y. Zhang, *Phys. Rev. B*, **47**, 16135-16138 (1993).

[14] Z. Mao, G. Xu, S. Zhang, S. Tan, B. Lu, M. Tian, C. Fan, C. Xu and Y. Zhang, *Phys. Rev. B*, **55**, 9130-9135 (1993).

[15] S. Kaneko, K. Akiyama, H. Funakubo and M. Yoshimoto, *Phys. Rev. B*, **74**, 054503-1-4 (2006).

[16] S. Kaneko, K. Akiyama, T. Ito, Y. Hirabayashi, H. Funakubo and M. Yoshimoto, *Jpn. J. Appl. Phys.*, **47**, 5602-5604 (2008).

[17] D. M. Hwang, T. S. Ravi, R. Ramesh, S. W. Chan, C. Y. Chen, L. Nazar, X. D. Wu, A. Inam and T. Venkatesan, *Appl. Phys. Lett.*, **57**, 1690-1692 (1990).

[18] T. Zheleva, K. Jagannadham and J. Narayan, *J. Appl. Phys.*, **75**, 860-871 (1994).

[19] J. Narayan and B. C. Larson, *J. Appl. Phys.*, **93**, 278-285 (2003).

[20] S. Kaneko, Y. Shimizu and S. Ohya, *Jpn. J. Appl. Phys.*, **40**, 4870-4873 (2001).

[21] T. Zheleva, K. Jagannadham and J. Narayan, *J. Appl. Phys.*, **75**, 860-871 (1994).

[22] S. Kaneko, H. Funakubo, T. Kadowaki, Y. Hirabayashi and K. Akiyama, *Europhys. Lett.*, **81**, 46001-p1-p5 (2008).

(Received December 11, 2008; Accepted September 10, 2009)

Magneto-Resistance Effect in γ' -Fe₄N/CrO₂ Granular System

Ryota Taninoki, Yuya Konishi, Masatomo Uehara and Yoshihide Kimishima

Department of Physics, Faculty of Engineering, Graduate School of Yokohama National University,
Tokiwadai 79-5, Hodogaya, Yokohama 240-8501, Japan
Fax: +81-45-339-4182, e-mail: kimi@ynu.ac.jp

Magnetization and magneto-resistance ratio (*MRR*) were measured for $(\gamma'$ -Fe₄N)_x(CrO₂)_{1-x} granular system between 77 K and 300 K, where *x* is the mole ratio of Fe₄N in the measured samples. The γ' -Fe₄N and CrO₂ are the ferromagnetic half metals with high Curie temperature and relatively high electrical conductivity. Since the spin polarization coefficient *P* of conduction electrons is nearly -1 in Fe₄N and 1 in CrO₂, the various junctions in this system are expected to show the competing tunneling magneto-resistance (TMR) effects. The *MRR* of this system showed the compensated behavior at *x* around 0.2, which is the percolation threshold of connectivity of Fe₄N grains.

Key Words : γ' -Fe₄N, CrO₂, magnetization, magneto-resistance, TMR

1. INTRODUCTION

Perovskite-type γ' -Fe₄N is a ferromagnet with a large magnetic moment below the Curie temperature *T_c* of 761 K [1]. From the calculated electronic structure of this compound [2, 3], it was shown that the spin polarization coefficient *P* was nearly -1 at the Fermi level [4].

On the other hand, rutile-type CrO₂ has been known to be a half-metallic oxide with *P* = 1 and *T_c* = 400 K [5,6].

Since the perfect spin polarization should result in large magneto-resistance (MR), γ' -Fe₄N and CrO₂ can be the candidate materials for the development of spintronics devices such as spin valves and magnetic random access memories (MRAMs).

We studied the TMR effects of the $(\gamma'$ -Fe₄N)_x(CrO₂)_{1-x} mixtures. This system shall be composed of the granular TMR junctions of [γ' -Fe₄N/ γ' -Fe₄N], [CrO₂/CrO₂] and [γ' -Fe₄N/CrO₂], where “/” means the insulating barrier. The [γ' -Fe₄N/ γ' -Fe₄N] and [CrO₂/CrO₂] are the TMR junctions with same sign of *P*, and [γ' -Fe₄N/CrO₂] is those with different sign of *P*. Therefore the competing TMR behaviors are expected in the present system, as in the case of (Fe₃O₄)_x(CrO₂)_{1-x} [7-9].

2. SAMPLE PREPARATION

First, the precursors of Fe₃O₄ nano-particles were prepared from a mixed aqueous solution of FeCl₂·4H₂O and FeCl₃·6H₂O with the mole ratio of 1:2. When an aqueous ammonium solution (NH₄OH) was dripped onto the above mixed solution, Fe₃O₄ nano-particles with a diameter of about 10 nm were precipitated [10-12]. Washed and dried Fe₃O₄ nano-particles were pressed to form pellets with a diameter of 10 mm, and sintered to produce the γ' -Fe₄N in the NH₃+H₂ mixed gases for 12 hours at 673 K. Then the mixtures of prepared γ' -Fe₄N specimen and CrO₂ powder (Aldrich Chemical Company, Inc.) were sintered at 473K for 3 hours in air.

Powder CuK α X-ray diffraction (XRD) patterns of

$(\gamma'$ -Fe₄N)_{0.2}(CrO₂)_{0.8} samples are shown in Fig. 1. The crystal structure of γ' -Fe₄N is a cubic perovskite with the lattice parameter of *a* = 0.379 nm [13], while CrO₂ has a rutile structure with *a* = 0.4419 nm and *c* = 0.29154 nm [14].

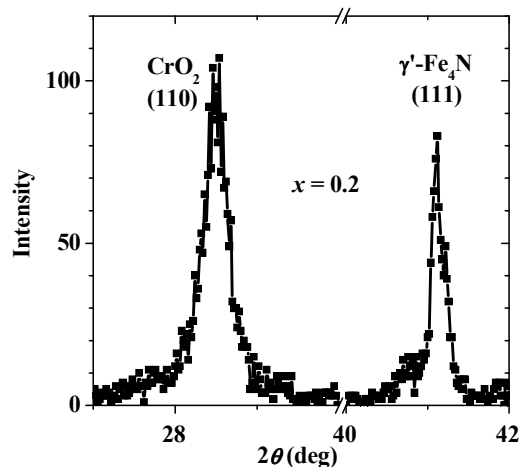


Fig. 1 XRD pattern of $(\gamma'$ -Fe₄N)_{0.2}(CrO₂)_{0.8} sample.

From the half width of each diffraction peak, the mean diameter *d* of γ' -Fe₄N and CrO₂ particles were estimated by Sherrer's formula as about 16 nm and 12 nm, respectively.

3. EXPERIMENTAL RESULTS AND DISCUSSION

3.1 Magnetization

The magnetization *M* was measured by means of a vibrating sample magnetometer (VSM) between 77 K and 300 K. Fig. 2 shows the temperature dependence of *M* at 5 kOe. The magnitude of *M* monotonically increases with the mole ratio *x* of γ' -Fe₄N. Ferromagnetic

transition of CrO₂ is clearly indicated near 400 K. Since the Curie temperature T_c of Fe₄N is known to be 761 K [1] and far above the T_c of CrO₂, the large amount of magnetization due to the Fe₄N remains below 400 K.

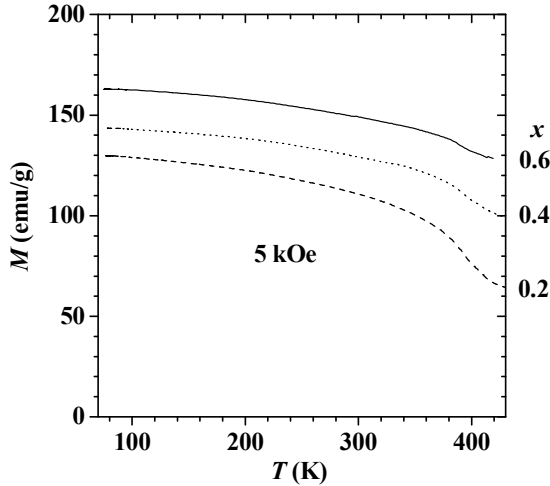


Fig. 2 Temperature dependence of the magnetization at 5 kOe, where x is the mole ratio of γ' -Fe₄N.

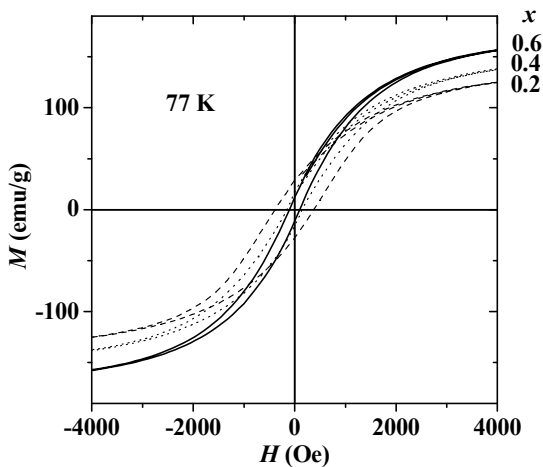


Fig. 3 Field dependence of the magnetization at 77 K, where x is the mole ratio of γ' -Fe₄N.

Field dependences of magnetization M at 77 K are shown in Fig. 3. The M is nearly saturated at 77 K and 10 kOe. The saturation magnetization M_s increases with increasing of x , and the cohesive force H_c decreases with x .

The x -dependence of M_s at 77 K are shown in Fig. 4. The value of M_s increases almost linearly with x . It shows that magnetically non-interactive coexistence of γ' -Fe₄N and CrO₂ phase is realized in this system.

The x -dependence of coercive field H_c at 77 K is

shown in Fig. 5. The behavior of H_c is nonlinear with x . It means that the simple average of $xH_c^{\text{Fe}_4\text{N}} + (1-x)H_c^{\text{CrO}_2}$ does not hold in the present mixed granular system with random anisotropy.

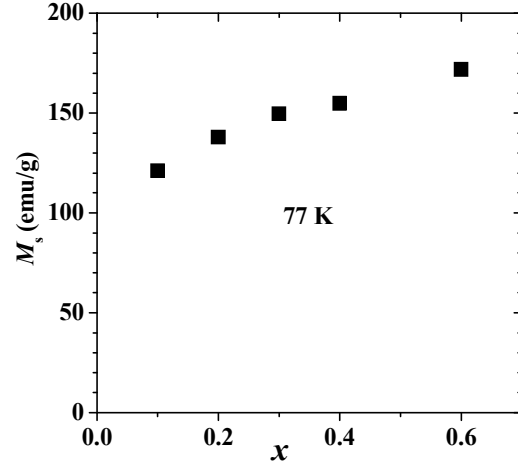


Fig. 4 x -dependence of the saturation magnetization at 77 K.

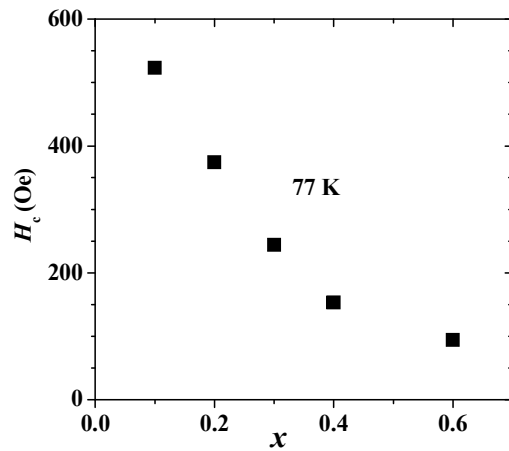


Fig. 5 x -dependence of the cohesive force at 77 K.

3.2 Magneto-resistance

The field dependence of the resistivity $\rho(H)$ was measured between -10 kOe and 10 kOe at 77 K and 300 K, and the experimental results of the magneto-resistance ratio (MRR) are shown in Fig. 6 for $x=0.5$ samples. Here the MRR is defined by

$$\frac{\rho(H) - \rho(H_p)}{\rho(H_p)} \times 100 \quad (1),$$

where H_p is the peak field at which $\rho(H)$ becomes maximum. All of the samples, except for $x=1$ sample, had the TMR like behaviors, as shown in Fig. 6.

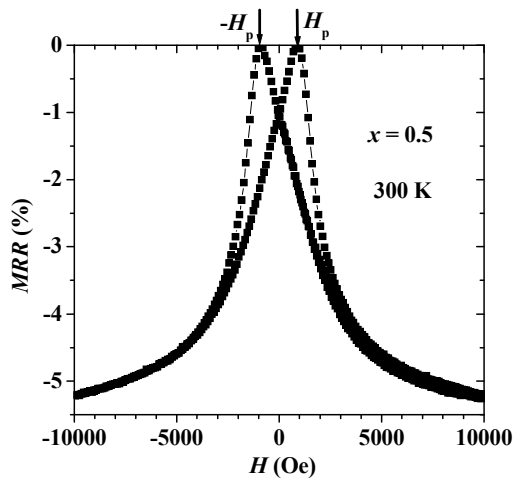


Fig. 6 Field dependence of the magneto-resistance ratio *MRR* at 77 K for $x = 0.5$.

The tunneling magneto-resistance (TMR) theory [15, 16] gives the following expression for the resistivity of a granular system.

$$\rho(H) = \frac{\rho_0}{1 + P^2 m(H)^2} \exp\left(\sqrt{\frac{\Delta}{T}}\right) \quad (2)$$

where ρ_0 and Δ are constants, P is the spin polarization coefficient of conduction electrons, and m is defined by $M(H)/M_s$. The parameter Δ is defined by $8\kappa C$, where $\kappa = \sqrt{2m^*(V - E_F)/\hbar^2}$ and $C = sE_c = \text{const}$. The parameter m^* is the effective mass of electrons, V is the barrier potential, E_F is the Fermi energy, s is the barrier thickness, and E_c is the charging energy. Then the magneto-resistance ratio *MRR* is given by

$$MRR(H) = -\frac{P^2 m(H)^2}{1 + P^2 m(H)^2} \times 100 \quad (3)$$

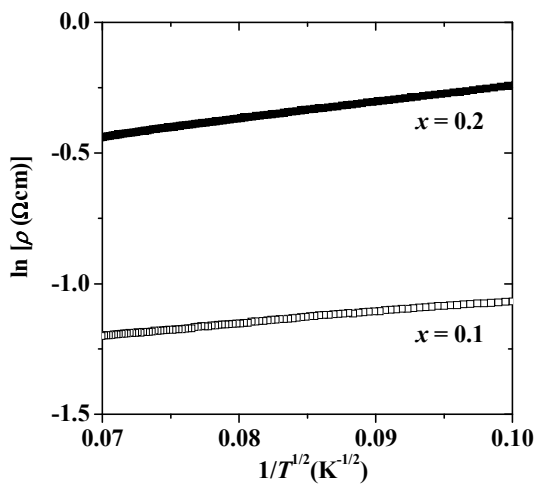


Fig. 7 $\ln \rho$ vs. $1/\sqrt{T}$ plots for $x = 0.1$ and 0.2 samples.

In Fig.7, $\ln \rho$ vs. $1/\sqrt{T}$ plots are shown for $x = 0.1$ and 0.2 samples, where $\ln \rho$ linearly varies with $1/\sqrt{T}$. The Δ/k_B -values, estimated from eq.(2), were 21 K and 45 K for $x=0.1$ and 0.2 sample, respectively. Thus the tunneling energy gap Δ increased with x of Fe_4N amount.

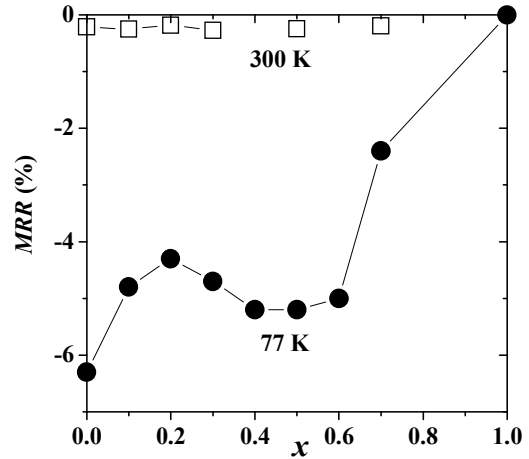


Fig.8 x -dependences of *MRR* at 300 K and 77 K.

The x -dependences of *MRR* at 300 K and 77 K under the field of 10 kOe are shown in Fig.8, where the absolute value of magneto-resistance ratio $|MRR|$ reduces to about 4% at $x = 0.2$. The above result can be explained by the percolation theory and inverse TMR effect, as following.

The present $(\text{Fe}_4\text{N})_x(\text{CrO}_2)_{1-x}$ granular system composed of the granular TMR junctions of $[\gamma\text{-Fe}_4\text{N}/\gamma\text{-Fe}_4\text{N}]$, $[\text{CrO}_2/\text{CrO}_2]$ and $[\gamma\text{-Fe}_4\text{N}/\text{CrO}_2]$. By the percolation theory [17,18], the number of $[\gamma\text{-Fe}_4\text{N}/\text{CrO}_2]$ junctions becomes maximal at the percolation threshold x_c of about 0.2 for the Fe_4N connectivity.

The *MRR* under large magnetic field was presented as

$$MRR = -\frac{P_1 P_2}{1 + P_1 P_2} \times 100 \quad (4)$$

for two kinds of grains with different polarization coefficient of P_1 and P_2 [19]. If P_1 and P_2 have same signs as in the case of $[\gamma\text{-Fe}_4\text{N}/\gamma\text{-Fe}_4\text{N}]$ or $[\text{CrO}_2/\text{CrO}_2]$ junctions, negative *MRR*, namely TMR effect appears. If P_1 and P_2 have opposite signs as in the case of $[\gamma\text{-Fe}_4\text{N}/\text{CrO}_2]$ junctions, positive *MRR*, namely inverse TMR effect, should be observed. Therefore the small $|MRR|$ value at $x \sim x_c \sim 0.2$ is considered to be due to the compensation of $|MRR|$ by the inverse TMR effect in $[\gamma\text{-Fe}_4\text{N}/\text{CrO}_2]$ junctions.

4. CONCLUSION

Magnetization and magneto-resistance ratio (*MRR*) were measured for $(\gamma\text{-Fe}_4\text{N})_x(\text{CrO}_2)_{1-x}$ granular system between 77 K and 300 K. The $\gamma\text{-Fe}_4\text{N}$ and CrO_2 are the ferromagnetic half metals with high Curie temperature and relatively high electrical conductivity. Since the spin

polarization coefficient P of conduction electrons is nearly -1 in Fe₄N and 1 in CrO₂, the [γ -Fe₄N/CrO₂] junctions were expected to show the positive tunneling magneto-resistance (inverse TMR) effects. The $|MRR|$ of this system showed a small value at x around 0.2 . These results can be explained by the percolation theory and inverse TMR effect.

REFERENCES

- [1] C. Guillaud, and H. Creveaux, *Compt. Rend.*, **222**, 1170-72 (1946).
- [2] A. Sakuma, *J. Magn. Magn. Mat.*, **102**, 127-34 (1991).
- [3] A. Sakuma, *J. Phys. Soc. Jpn.*, **60**, 2007-12 (1991).
- [4] S. Kokado, N. Fujima, K. Harigaya, H. Shimizu, and A. Sakuma, *Phys. Rev. B*, **73**, 172410-1-4 (2006).
- [5] K. Schwarz: *J. Phys. F : Met. Phys.*, **16**, L211-215 (1986).
- [6] K.P. Kämper, W. Schmitt, G. Güntherodt, R.J. Gambino, and R. Ruf: *Phys. Rev. Lett.*, **59**, 2788-2791 (1987).
- [7] Y. Kimishima, T. Sasaki, M. Uehara, Y. Satoh, M. Matsuo, *Microelec. Eng.*, **81**, 366-370 (2005).
- [8] Y. Kimishima, T. Sasaki, M. Uehara and Y. Satoh, *Trans. Magn. Soc. Jpn.*, **5**, 5-8 (2005).
- [9] X.Y. Zhang, Y.J. Chen and Z.Y. Li, *Mat. Lett.*, **60**, 1762-1766 (2006).
- [10] Y. Kimishima, M. Uehara, Y. Notani, K. Kobayashi, and W. Yamada, *Trans. Mat. Res. Soc. Jpn.*, **29**, 1543-46 (2004).
- [11] Y. Kimishima, W. Yamada, K. Kobayashi, M. Uehara, T. Asaka, K. Kimoto, and Y. Matsui, *Trans Magn. Soc. Jpn.*, **5**, 73-76 (2005).
- [12] Y. Kimishima, W. Yamada, M. Uehara, T. Asaka, K. Kimoto, and Y. Matsui, *Mat. Sci. Eng. B.*, **138**, 69-73 (2007).
- [13] H. Jacobs, D. Rechenbach, and U. Zachwieja, *J. Alloys Compds.*, **227**, 10-17 (1995).
- [14] J.K. Burdett, G.J. Miller, J.W. Richardson Jr. and J.V. Smith: *J. Am. Chem. Soc.*, **110**, 8064-8071 (1988).
- [15] P. Sheng, B. Abeles, and Y. Arie, *Phys. Rev. Lett.*, **31**, 44-47 (1973).
- [16] J. Inoue, and S. Maekawa, *Phys. Rev. B*, **53**, R11927-29 (1996).
- [17] V. K. Shante, and S. Kirkpatrick, *Adv. Phys.*, **20**, 325-357 (1971).
- [18] J. P. Straley, *Phys. Rev. B*, **15**, 5733-5737 (1977).
- [19] M. Julliere: *Phys. Lett. A*, **54**, 225-226 (1977).

(Received December 12, 2008; Accepted September 10, 2009)

Texture and Formability of Heat-treatable Magnesium Alloy Sheets Processed by Differential Speed Rolling

Xinsheng Huang, Kazutaka Suzuki, Akira Watazu,
Ichinori Shigematsu and Naobumi Saito

Materials Research Institute for Sustainable Development,
National Institute of Advanced Industrial Science and Technology (AIST), Nagoya, Aichi 463-8560, Japan
Fax: 81-52-736-7406, e-mail: huang-xs@aist.go.jp

The differential speed rolling (DSR) process has been carried out on a heat-treatable AZ61 magnesium alloy at different rotation speed ratios (RSR). Compared with the normal symmetrically rolled sheet without an inclination of basal pole, the sheets DSR-processed at the RSRs of 1.17 and 1.36 exhibit the inclination of basal pole toward the rolling direction at about 5° and 10°, respectively, while the microstructures show approximately the same grain size of 7 μm. Increasing the RSR leads to the decreases in 0.2% proof stress (YS) and *r*-value as well as the increases in uniform elongation and *n*-value. For the sheet DSR-processed at the RSR of 1.36, the ultimate tensile strength (UTS), the YS, the fracture elongation (FE) and the Erichsen value (IE) are 313 MPa, 182 MPa, 24.3% and 4.7, respectively. This IE is higher than that (4.1) of the normal-rolled sheet. The improvement of the stretch formability can be attributable to the texture favored for the basal slip during deformation. After aging treatment, the UTS and the YS further increase to 336 MPa and 208 MPa, respectively, accompanied with a decrease in the FE.

Key words: Magnesium alloys; Asymmetric rolling; Texture; Mechanical properties; Formability

1. INTRODUCTION

Magnesium (Mg) wrought alloys have a great potential as light-weight structural materials substituting for steel and aluminum (Al) parts in automotive and electronic industries due to their excellent properties such as low density, high specific strength, good damping characteristics, good electromagnetic shielding capability, easiness of recycling and abundance of resources [1]. However, normal symmetric rolling generally gives rise to a strong basal texture for the Mg alloys [2]. This induces a high normal anisotropy in sheet and increases the difficulty in deformation accompanied with thickness reduction, and consequently leads to a very limited formability at ambient temperatures.

The deformation capability of the Mg alloy sheets is strongly affected by the texture [3,4]. In recent years, differential speed rolling (DSR) has been utilized for enhancing deformation capability of the Mg alloy sheets by microstructure modifications [5-7]. The DSR is a process carried out at different rotation speeds for upper and lower rolls so that intense shear deformation can be introduced throughout the sheet thickness and thus may lead to a weakened basal texture and/or an inclination of basal pole [8,9]. However, the DSR-processed Mg alloy sheets reported in the literature are mainly limited to the AZ31 alloy. In general, the AZ31

alloy exhibits a better ductility but a lower mechanical strength compared with the other AZ series alloys such as AZ61, AZ80 and AZ91 with higher Al contents. This limits the applications as a structural component requiring a high strength. The tensile strength of the AZ61 alloy is comparable to the 5000 and 6000 series Al alloys, which have been applied to auto body panels [10]. In addition, it is possible to improve the mechanical strength of the AZ61 alloy further by subsequent artificial aging treatment, which induces precipitation strengthening due to precipitation of β-phase (Mg₁₇Al₁₂).

In this study, the DSR process was carried out on the AZ61 alloy in order to achieve the Mg alloy sheet with a combination of high strength and superior formability, and the influences of the rotation speed ratio (RSR) on microstructure, texture, mechanical properties and stretch formability were systematically investigated.

2. EXPERIMENTAL PROCEDURE

The starting billets were cut from the commercial hot-extruded AZ61 (Mg-6.9Al-0.5Zn-0.2Mn in wt.%) alloy plates with a thickness of 5 mm. The as-received material consists of equiaxial recrystallized grains with an average grain size of 13 μm. The rolling was conducted at the RSRs of 1 (i.e. normal rolling), 1.17 and 1.36 without lubrication on roll and billet surfaces. The billets were rolled from 5 mm to 1 mm in thickness

by 4 passes with a large thickness reduction per pass of 33% and the total thickness reduction was 80%. The billets for rolling were heated to a high temperature of 703 K in order to avoid the precipitation of $Mg_{17}Al_{12}$ during rolling and both rolls were heated to 573 K using heat elements embedded inside the rolls. The sheet was rotated and reversed after each pass so that the shear strain was introduced unidirectionally throughout the rolling. All as-rolled sheets were subjected to optical microscopic observation, x-ray texture analysis, microhardness measurement, tensile test and Erichsen test at room temperature. Hereafter, RD, TD and ND denote the rolling, transverse and normal directions of sheet, respectively.

The (0002) pole figure was measured at the mid-plane of sheet by the Schulz reflection method. The tensile tests were conducted using an Instron universal testing machine with an extensometer at the angles of 0° (RD), 45° and 90° (TD) between the tensile direction and the RD. The average values of the mechanical properties were given from the values of the three tensile directions by the following expression:

$$\bar{X} = (X_{RD} + 2X_{45^\circ} + X_{TD})/4$$

The circular blanks with a diameter of 50 mm were used for the Erichsen tests for evaluating the stretch formability. The Erichsen tests were conducted using a hemispherical punch with a diameter of 20 mm. The punch speed was set as 5 mm/min and the blank holder force was set as 10 kN. The graphite grease was used as a lubricant for the Erichsen tests. The Erichsen value (IE) was measured as the punch stroke at fracture initiation.

3. RESULTS AND DISCUSSION

The microstructures of the sheets rolled at different RSRs are shown in Fig. 1. The as-rolled sheets exhibit the well-equiaxed grains indicating the occurrence of dynamic recrystallization due to the high rolling temperature. All sheets exhibit approximately the same grain size of $7 \mu\text{m}$, which is smaller than that ($13 \mu\text{m}$) of the as-received hot-extruded plate. Almost no $Mg_{17}Al_{12}$ precipitates can be observed, indicating that most of the Al atoms dissolve in the matrix.

The (0002) pole figures of the sheets rolled at different RSRs are shown in Fig. 2. The basal texture intensities are approximately the same while the distributions of {0001} orientation are different among the sheets. The normal-rolled sheet exhibits the spread of {0001} orientation toward the RD without an inclination of basal pole. In contrast, the basal pole inclines toward the RD for the DSR-processed sheets. The inclination angles of the basal pole are 5° and 10° for the sheets DSR-processed at the RSRs of 1.17 and 1.36, respectively. In addition, the spread of the basal pole in the TD is also slightly wider and tends to exhibit a roughly circle-shaped distribution of {0001} orientation compared with the normal-rolled sheet. The inclination of the basal pole can be attributable to the intense shear deformation throughout the sheet thickness during the DSR process.

The changes in average values of the ultimate tensile strength (UTS), the 0.2% proof stress (YS), the fracture elongation (FE) and the uniform elongation (UE), the Lankford values (r -value), the strain hardening exponent

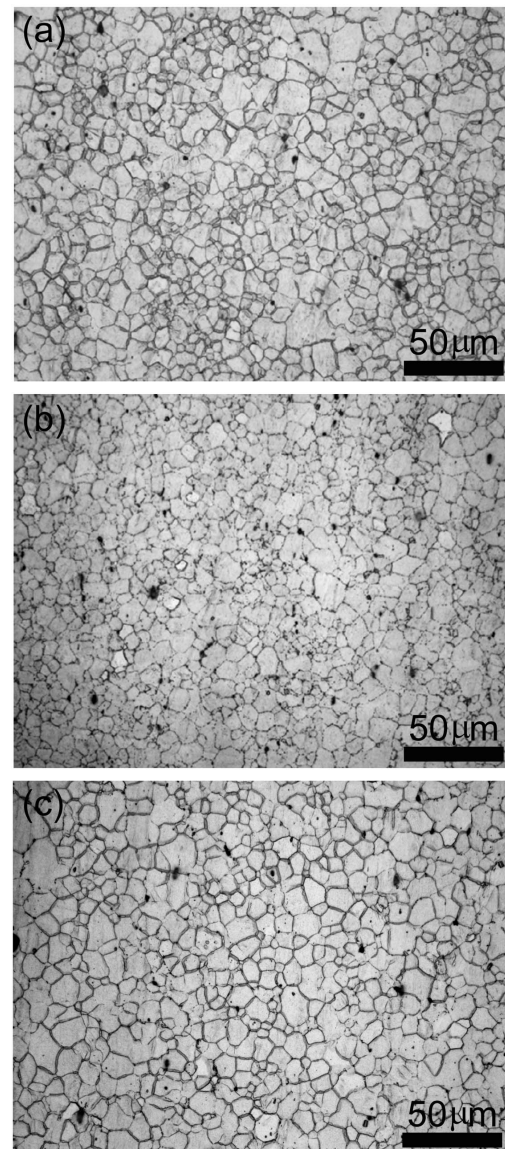


Fig. 1. Optical micrographs taken in the longitudinal sections (RD-ND plane) of the sheets rolled at rotation speed ratios of (a) 1, (b) 1.17 and (c) 1.36.

value (n -value) and the IE as a function of RSR are shown in Fig. 3. All sheets exhibit approximately the same UTS of 313-318 MPa while the YS slightly decreases from 191 MPa to 182 MPa with increasing the RSR from 1 to 1.36. The decrease in the YS can be attributable to the texture effect considering the same grain size. The inclination of basal pole may lead to a larger Schmid factor of the basal slip due to the inclination of the basal planes from the rolling plane and thus exerts an effect on the decrease in the YS. The FE also slightly increases from 23.0% to 24.3% and it is originated from the increase in the UE, which increases from 18.4% to 19.7% with increasing the RSR. The r -value decreases from 2.06 to 1.71 and the n -value increases from 0.239 to 0.256 simultaneously. The IEs are 4.1, 4.4 and 4.7 for the sheets rolled at the RSRs of 1, 1.17 and 1.36, respectively, exhibiting the enhancement

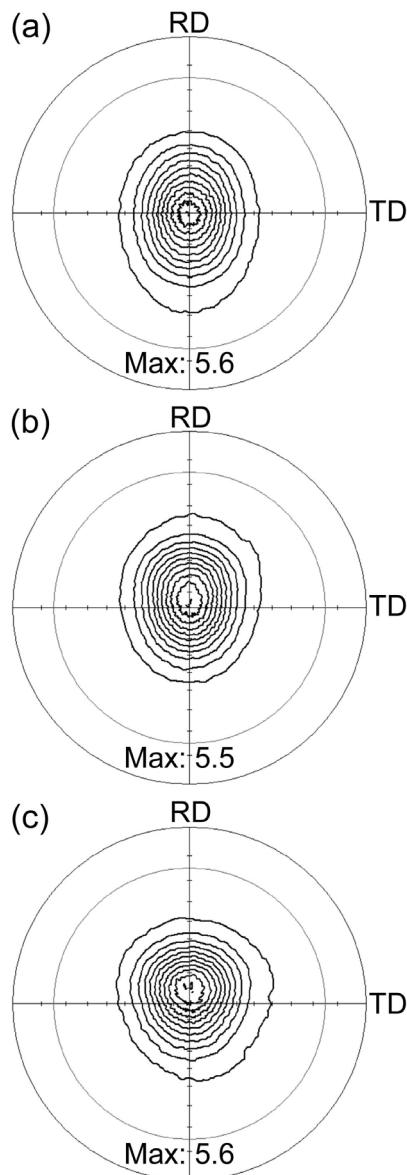


Fig. 2. (0002) pole figures of the sheets rolled at the RSRs of (a) 1, (b) 1.17 and (c) 1.36. Intensity level are 0.5, 1, 1.5, 2...

of the stretch formability with increasing the RSR. Under a biaxial tension stress state of the stretch forming, the thickness strain is most necessary for forming. The enhancement of the stretch formability can be attributed to the decrease in the r -value and the increase in the n -value, which enhances the capability of sheet thinning. It is known that the r -value is strongly related to the texture. The Mg alloy sheet with a very strong basal texture unfavorable for the basal slip during tensile deformation generally exhibits a large r -value, because pyramidal $\langle c+a \rangle$ slip with the largest critical resolved shear stress (CRSS) in the slip systems is needed for generating the thickness strain while the width strain can be generated by prismatic $\langle a \rangle$ slip [11,12]. A tilted basal pole increases the Schmid factor of basal slip with the lowest CRSS and is favored for the basal slip during deformation. This promotes the strain in the thickness

direction and in turn decreases the r -value. In addition, the inclination of the basal pole may also increase the n -value [13]. Therefore, the enhancement of the stretch formability of the DSR-processed sheet is originated from the texture effect. Compared with the hot-rolled AZ31B alloy sheets generally exhibiting the IE of 3-5 and the UTS of 250-260 MPa [3,7,14], the AZ61 alloy sheet DSR-processed at the RSR of 1.36 exhibits a comparable IE of 4.7 but a much higher UTS of 313 MPa. This high strength results from the solid solution strengthening due to the dissolution of Al in the matrix.

The change in Vickers microhardness of the sheet DSR-processed at the RSR of 1.36 during the aging treatment at 448 K is shown in Fig. 4a. The microhardness increases with the aging time and reaches the peak at about 48 h. The Vickers hardnesses for the as-rolled and peak-aged conditions are 71 and 85, respectively. The nominal stress-strain curves of the DSR-processed sheets at the as-rolled and peak-aged conditions in the tensile directions of RD, 45° and TD are shown in Fig. 4b. After aging treatment, the UTS enhances from 313 to 336 MPa and the YS also improves from 182 to 208 MPa by 23 and 26 MPa, respectively, due to the precipitation of $Mg_{17}Al_{12}$. However, the FE, the UE and the n -value decrease from 24.3% to 21.0%, from 19.7% to 15.2%, and from 0.256 to 0.189, respectively, which would result in a deterioration in stretch formability. It is suggested that the precipitates increase the flow stress and thus activate the dynamic recovery during deformation, which results in the decrease in work hardening rate. Therefore, the aging treatment should be conducted after the shape forming. Anyway, a further improvement in mechanical strength can be achieved by the aging treatment for the AZ61 alloy while this effect is weak for the AZ31 alloy.

4. CONCLUSIONS

- (1) The DSR-processed sheets exhibit approximately the same grain size compared with the normal-rolled sheet while the inclination of basal pole enhances with increasing the RSR.
- (2) The sheet DSR-processed at the RSR of 1.36 in the as-rolled condition exhibits a combination of high strength (UTS: 313 MPa) and high ductility (FE: 24.3%). The IE also improves from 4.1 to 4.7 compared with the normal-rolled sheet. The improvement in the stretch formability can be attributed to the favored texture for the basal slip during deformation.
- (3) The aging treatment improves the mechanical strength further while it decreases the work-hardening capability and the tensile elongation.

REFERENCES

- [1] I. J. Polmear, *Mater. Sci. Tech.*, **10**, 1-16 (1994).
- [2] G.S. Rao and Y.V.R.K. Prasad, *Metall. Trans.*, **13A**, 2219-2226 (1982).
- [3] E. Yukutake, J. Kaneko and M. Sugamata, *Mater. Trans.*, **44**, 452-457 (2003).
- [4] K. Iwanaga, H. Tashiro, H. Okamoto and K. Shimizu, *J. Mater. Process. Technol.*, **155-156**, 1313-1316 (2004).
- [5] H. Watanabe, T. Mukai and K. Ishikawa, *J. Mater. Sci.*, **39**, 1477-1480 (2004).

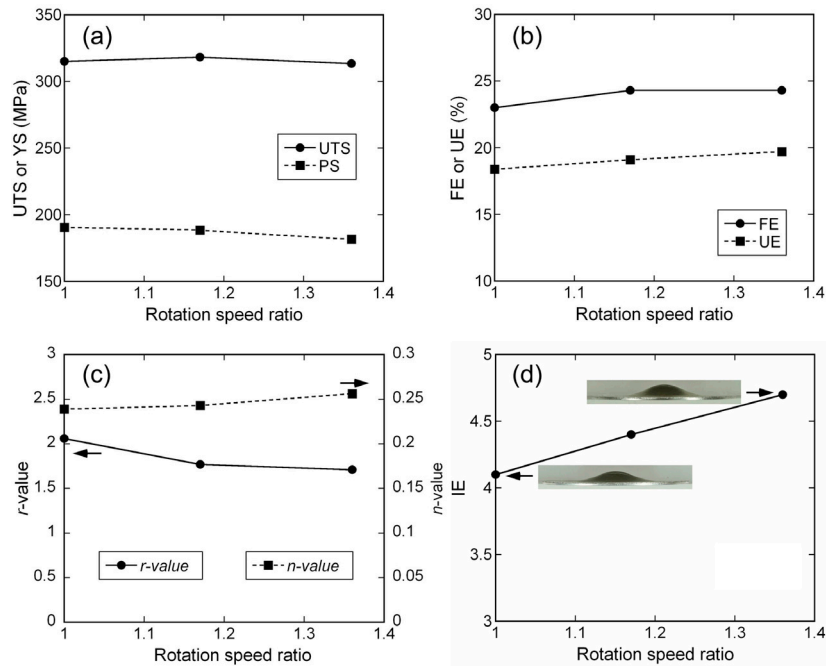


Fig. 3. Changes in average values of (a) the UTS and the YS, (b) the FE and the UE, (c) the r -value and the n -value, and (d) the IE as a function of RSR. The blanks of the normal-rolled sheet and the sheet DSR-processed at the RSR of 1.36 after the Erichsen tests are shown in the inset of (d).

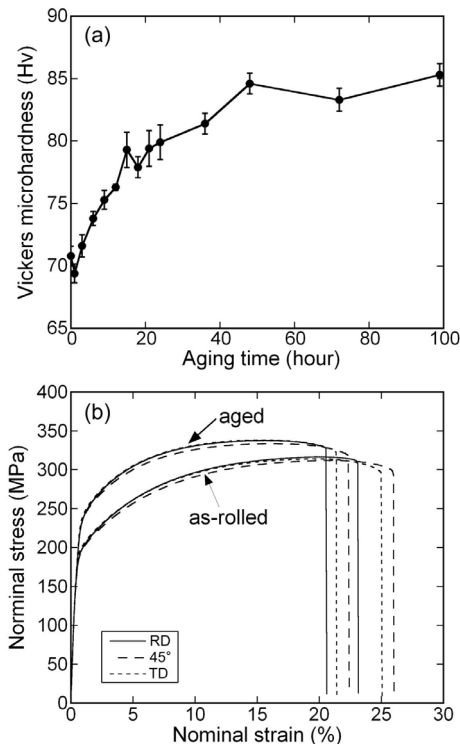


Fig. 4. (a) Vickers microhardness of the sheet DSR-processed at the RSR of 1.36 as a function of aging time at 448 K starting from the as-rolled condition. (b) Nominal stress-strain curves of the DSR-processed sheets in the as-rolled and aged at 448 K for 18 h conditions in the tensile directions of RD, 45° and TD.

- [6] W.J. Kim, J.B. Lee, W.Y. Kim, H.T. Jeong and H.G. Jeong, *Scripta Mater.*, **56**, 309-312 (2007).
 [7] X.S. Huang, K. Suzuki, A. Watazu, I. Shigematsu and N. Saito, *J. Alloy Compd.* **470**, 263-268 (2009).
 [8] S.H. Kim, B.S. You, C.D. Yim and Y.M. Seo, *Mater. Lett.*, **59**, 3876-3880 (2005).
 [9] X.S. Huang, K. Suzuki, A. Watazu, I. Shigematsu and N. Saito, *J. Alloy Compd.*, **457**, 408-412 (2008).
 [10] H. Hayashi and T. Nakagawa, *J. Mater. Process. Technol.*, **46**, 455 (1994).
 [11] S.R. Agnew and O. Duygulu, *Int. J. Plasticity*, **21**, 1161-1193 (2005).
 [12] J. Koike, T. Kobayashi, T. Mukai, H. Watanabe, M. Suzuki, K. Maruyama and K. Higashi, *Acta Mater.*, **51**, 2055-2065 (2003).
 [13] X.S. Huang, K. Suzuki, A. Watazu, I. Shigematsu and N. Saito, *Mater. Sci. Eng. A*, **488**, 214-220 (2008).
 [14] M. Sugamata, J. Kaneko and M. Numa, *J. Jpn. Soc. Technol. Plasticity*, **41**, 233-238 (2000).

(Received December 12, 2008; Accepted November 25, 2009)

Low Temperature Preparation of TiO₂ Films by RF Magnetron Sputtering Method

Masaaki ISAI^{1,2}, Tatsuya ENDO², Yuichi MIZUCHI¹

¹ Faculty of Engineering, Shizuoka University 3-5-1 Johoku, Naka, Hamamatsu, 432-8561 Japan

² Graduate School of Engineering, Shizuoka University 3-5-1 Johoku, Naka, Hamamatsu, 432-8561 Japan

E-mail: ¹temisai@ipc.shizuoka.ac.jp, ²f0730115@ipc.shizuoka.ac.jp

In the conventional preparation processes, a heating substrate should be applied to improve their crystallinity and films are easily peeled from substrates. This research was aimed to prepare TiO₂ films on slide-glass substrates at room temperature by using magnetron sputtering method. TiO₂ powder was used as a target material. Ar gas was used as a sputtering atmosphere. Variations of crystal property and morphology were investigated as a function of substrate temperature. It was found that Anatase-type films could be prepared at room temperature.

Keyword: TiO₂ thin films, RF magnetron sputtering, photocatalyst, low temperature preparation

1. INTRODUCTION

TiO₂ films have been focused as a photocatalyst. They have remarkable properties, for example, to resolve organic pollutant and to give hydrophobicity by irradiating near ultraviolet light. These characteristics are used in the fields of antifouling, antifog, sterilization and self cleaning.¹ The photocatalytic reaction of titanium oxide (TiO₂) films occurs only under the irradiation of ultraviolet light. Therefore, the photocatalytic properties under visible light irradiation have been widely investigated recently. In the future, various applications of photocatalysts will be developed.

To use the TiO₂ films as a photocatalyst, it must be immobilized on a substrate. For this purpose, low temperature preparation methods with large area and strong adhesion have been desired.² The immobilization techniques include wet processes of sol-gel and spray methods, and dry processes of sputtering and ionized cluster beam methods.³ It is possible to prepare large area with strong adhesion by using a sputtering method. Moreover, a RF magnetron sputtering method is possible for low temperature preparation compared with other sputtering methods because the confinement of electrons and the cathode-drop voltage of high-energy charged-particle are low.

TiO₂ has crystal structures of rutile, anatase and brookite. The anatase has the highest photocatalytic activity. This is due to the difference of their band structures. The bandgap of anatase is 3.2 eV, so it is 0.2 eV bigger than that of rutile. The reduction of the oxygen of the anatase is easier than a rutile structure. Also, because the grain size of the anatase structure is smaller than that of rutile, a large area induces higher activity. Therefore, for the photocatalytic reaction, it is possible to say that the anatase type TiO₂ is superior to other structures.⁵

This research was aimed to prepare TiO₂ films on slide-glass substrates at room temperature (R.T.) by using magnetron sputtering method. The crystal structure and optical properties of the films were investigated to obtain an optimum preparation condition. This paper reports some part of the results.

2. EXPERIMENT

Figure 1 shows a schematic of a RF magnetron sputtering apparatus. There are three substrate folders in this apparatus and the substrates can be exchanged without breaking a vacuum. Ar ions bombard the 2-inch TiO₂ targets under the RF power of 13.56 MHz. The distance between substrate and target was 40 mm. The distance between target and shutter was 25 mm. The distance between shutter and substrate was 15 mm. The target material (TiO₂ powder) was put on a duralumin hearth. A halogen lamp for substrate heater was installed back side of the substrate folder.

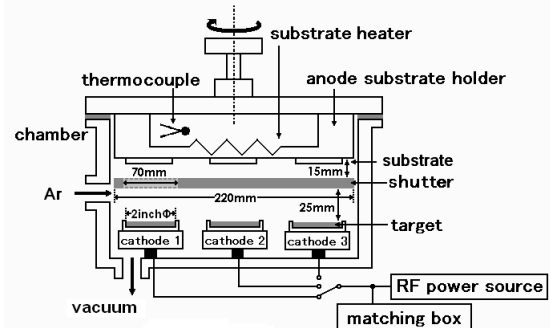


Fig. 1 Schematic of a RF magnetron sputtering apparatus.

Preparation condition is shown in table 1. Slide glass was used as a substrate. TiO₂ powder was used as a target material. The sputtering power was 100, 150 and 200W. The deposition time was 60, 90, 120, 150 and 180 minutes. The films were prepared on non-heated and heated (400°C) substrates. The Ar gas was introduced into a vacuum chamber through a mass flow controller. The Ar flow rate was 4 standard cc/min (sccm) and sputtering gas pressure was maintained at 5 Pa.

An X-ray diffraction, a scanning electron microscope (SEM), a film thickness measurement and an UV-visible spectral photometer were used for evaluation of crystal structure, surface structure, film thickness and optical properties, respectively.

Table 1. A typical film preparation condition

type	value	unit
sputtering target	TiO ₂	
substrate	slide glass	
sputtering power	100, 150, 200	[W]
sputtering time	60,90,120,150,180	[min]
Ar flow	4	[sccm]
substrate temperature	R.T., 400	[°C]
sputtering pressure	4.8~5.4	[Pa]
thickness	505~9937	[Å]
deposition rate	0.14~1.42	[Å /sec]

3. RESULTS AND DISCUSSION

Figure 2 (a) and (b) show the XRD data of films prepared under the substrate temperature (T_{sub}) of 400°C and R.T., respectively. The sputtering power was fixed at 100W. The deposition time was varied from 60 to 180 minutes. The films were crystallized within 120 minutes at T_{sub} of 400°C. The film thickness was increased and the peak intensity became strong as increasing the deposition time. The films prepared at R.T. were crystallized at the deposition time of 180 minutes.

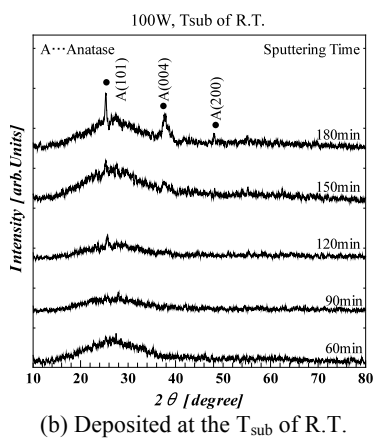
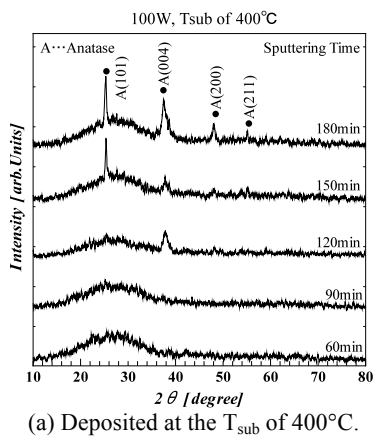


Fig. 2 XRD data as a function of deposition time under the sputtering power of 100W.

Figure 3 shows the dependence of deposition rate on the sputtering time at sputtering power of 100W. The films were deposited under the T_{sub} of R.T. and 400°C. As the deposition time increases, the deposition rate also increases because of incasing surface roughness.

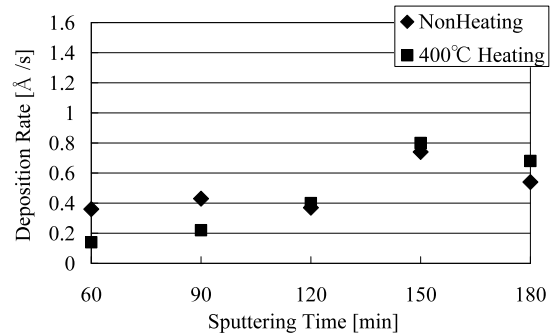


Fig. 3 The dependence of deposition rate on the sputtering time. The parameter is T_{sub}. The sputtering power was fixed at 100W.

Figure 4 (a) and (b) show that the transmittance characteristics of the TiO₂ films as a function of deposition time at the sputtering power of 100W. In the transmittance measurement, the effect of T_{sub} was not observed. The film with about 70 % of transmittance could be made without introducing oxygen gas.

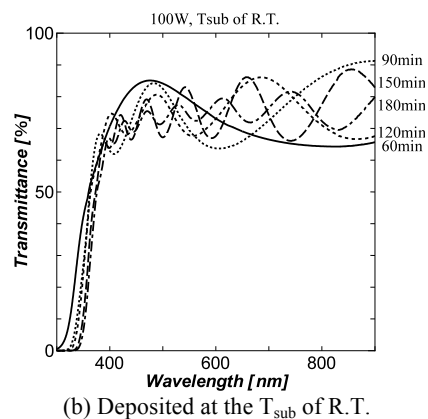
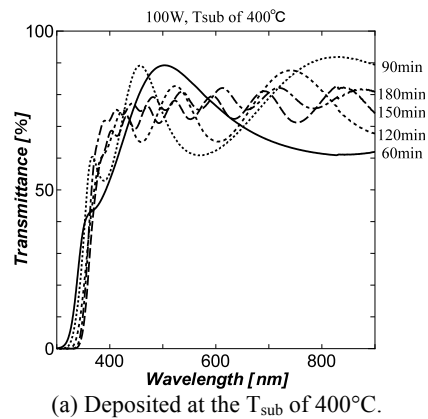


Fig. 4 Transmittance characteristics of the TiO₂ films as a function of deposition time under the

sputtering power of 100W.

Figure 5 (a) and (b) show the graphs of $(\alpha h\nu)^{1/2}$ vs photon energy as a function of deposition time at the sputtering power of 100W. As a result of bandgaps computed from the absorption spectrum, the crystallized films have bandgaps of 3.2 eV.

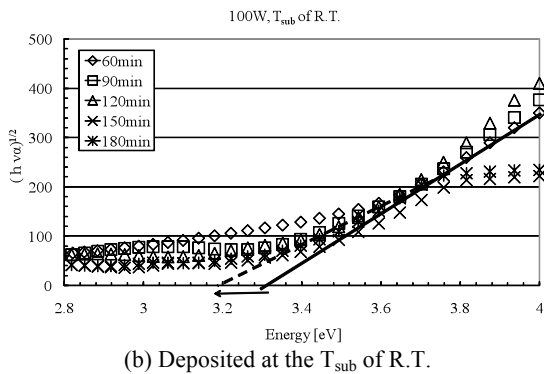
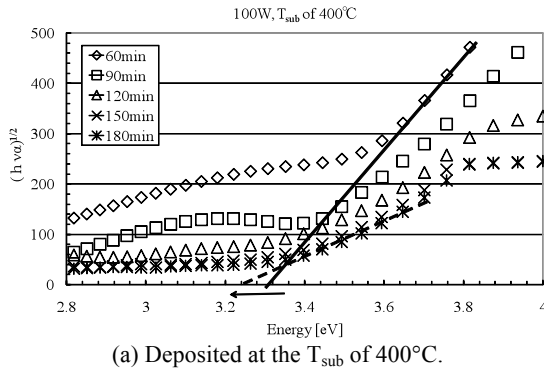
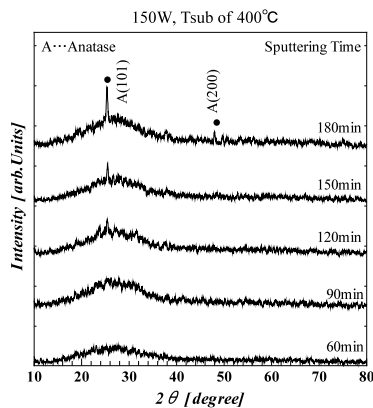


Fig. 5 Figure 5 (a) and (b) show the graphs of $(\alpha h\nu)^{1/2}$ vs photon energy as a function of deposition time at the sputtering power of 100W.

Figure 6 (a) and (b) show the XRD data of the films prepared under T_{sub} of 400°C and R.T., respectively. The sputtering power was fixed at 150W. The deposition time was varied from 60 to 180 minutes. The films could be crystallized until 90 minute-deposition time at T_{sub} of R.T. However, the XRD peak intensity of the films prepared at T_{sub} of 400 °C was decreased.



(a) Deposited at the T_{sub} of 400°C.

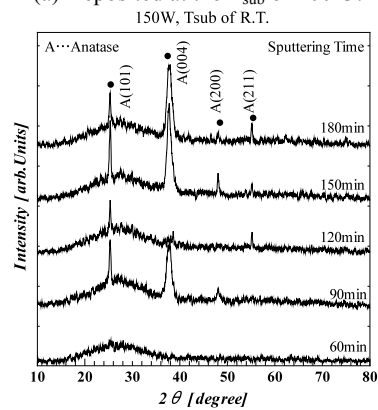


Fig. 6 XRD data as a function of deposition time under the sputtering power of 150W. (a) At the T_{sub} of 400°C. (b) At the T_{sub} of R.T.

In the transmittance measurement, the effect of T_{sub} was not observed. The films which have transmittance values of about 70% could be prepared without introducing oxygen gas. As a result of computing bandgap energy from the absorption spectrum, the crystallized films have bandgap of 3.2 eV.

Figure 7 shows the time dependence of deposition rate at the sputtering power of 150W. The deposition rate was decreased by the substrate heating. This seems to be due to the re-evaporation of deposited film. When high energy Ar particles bomber the film surface at T_{sub} of 400°C, TiO2 compound tend to resolve to Ti and O2 and they can re-evaporate from the film surface.

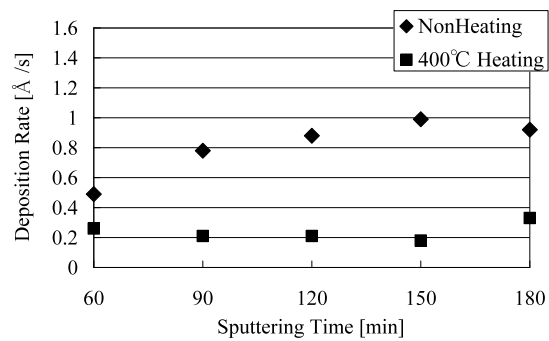
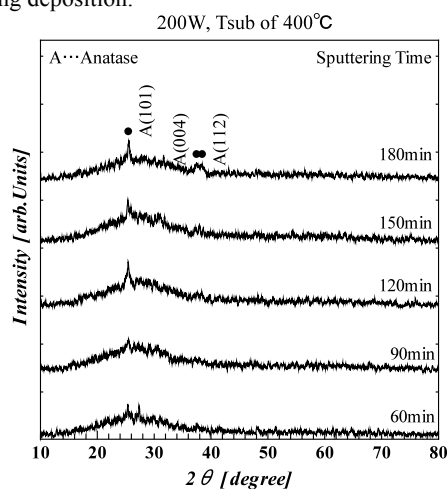


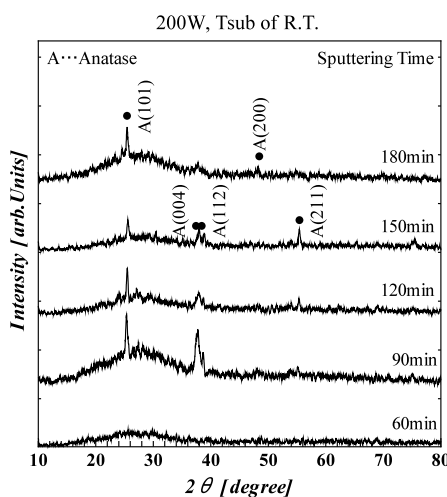
Fig. 7 The dependence of deposition rate on sputtering time. The parameter is T_{sub} . The sputtering power was fixed at 150W.

Figure 8 (a) and (b) show the XRD data of films prepared at T_{sub} of 400°C and R.T., respectively. The sputtering power was fixed at 200W. The deposition time was varied from 60 to 180 minutes. The XRD peak intensity of films prepared at the T_{sub} of R.T. was decreased as compared with those prepared at 150W. It seems that the damage to the films was increased because of high energy sputtering particles. At T_{sub} of 400 °C, the re-evaporation of the films was occurred

during deposition.



(a) Deposited at the T_{sub} of 400°C.



(b) Deposited at the T_{sub} of R.T.

Fig. 8 XRD data as a function of deposition time at the sputtering power of 200W.

In the transmittance measurement, the effect of T_{sub} on the transmittance properties was not observed. The films have transmittance of about 70 % of transmittance could be made without introducing oxygen gas. No change of absorption spectra was observed.

Figure 9 shows sputtering the time dependence of deposition rate at the sputtering power of 200W. The deposition rate was decreased as increasing the T_{sub} . The re-evaporation of films seems to occur in the case of 150 W. At the sputtering power of 200 W, a stable discharge could not last long, the deposition rate has been roughly disordered. The deposition rate was decreased at T_{sub} of 400 °C. It seems that the re-evaporation of films was occurred in a similar way at the deposition power of 150 W. In the case of 180 min-sputtering time at R.T., the position of substrates was misaligned. So the deposition was not properly proceeded. It seems to induce the decrease of the film thickness.

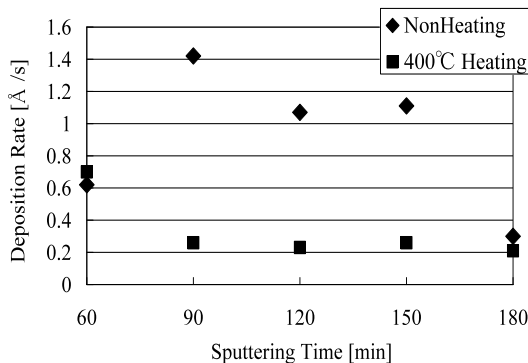


Fig. 9 Dependence of deposition rate on the sputtering time. The parameter is T_{sub} . The sputtering power was fixed at 200W.

4. CONCLUSION

This study was aimed to find an optimum preparation condition of TiO₂ films on a non-heating substrate by RF magnetron sputtering method. As a result, the following results were obtained.

- 1) The TiO₂ films of anatase structure could be prepared at T_{sub} of R.T.
- 2) The films of high transmittance could be prepared with only Ar gas flow.
- 3) At T_{sub} of 400°C and sputtering power more than 150W, the deposition rate was decreased as compared with other conditions. It seems to be due to the re-evaporation of deposited films.
- 4) At the sputtering power of equal to or more than 200 W, the crystal growth was not proceeded by the substrate damage.

ACKNOWLEDGEMENTS

This study was supported by Prof. Y. Hoshi and Ph.D student T. Sakai of Tokyo Polytechnic University.

REFERENCE

1. A. Fujishima and K. Honda, "Electrochemical Photolysis of Water at a Semiconductor Electrode", *Nature* 37 pp.238, 1972.
2. P. Zeman, S. Takabayashi, "Effect of total and oxygen partial pressures on structure of photocatalytic TiO₂ films sputtered on unheated substrate", *Surface and Coatings Technology* 153, pp.93-99, 2002
3. J. Musil, D. Herman and J. Sicha, "Low-temperature sputtering of crystalline TiO₂ films", *Journal of Vacuum Science Technology A* Vol.24 No.3 pp.521-528, 2006.
4. T. Endo, Y. Mizuchi and M. Isai, "Preparation of TiO₂ films by RF magnetron sputtering method", *IEICE Technical Report ED2008-6 CPM2008-14 SDM2008-26* (2008-5), pp.23-28, 2008.
5. T. Yazaki, T. Nagata, T. Takahashi and Y. EMA, "Preparation of N-doped TiO₂ Thin Films by Sputtering Using TiO₂: TiN Mixed Target", *IEICE Technical Report ED2007-27 CPM2007-26 SDM2007-27* (2007-05), pp.97-102, 2007.

(Received December 12, 2008; Accepted September 10, 2009)

Characterization of Si₃N₄-TiN Composites Prepared by Spark Plasma Sintering

Norhayati Ahmad*, Kozo Obara, Soichiro Sameshima, Hidekazu Sueyoshi
Department of Nano-structure and Advanced Materials, Graduate School of Science and Engineering,
Kagoshima University, 1-21-40 Korimoto, Kagoshima, 890-0065 Japan.
Tel./Fax: 81-99-285-7879

*Department of Materials Engineering, Faculty of Mechanical Engineering, Universiti Teknologi Malaysia,
81310 UTM Skudai, Johor, Malaysia.
Email: nhayatie@gmail.com.

Spark plasma sintering (SPS) was applied to produce electroconductive Si₃N₄-20 vol%TiN composites. The sintering mechanism for SPS was a hybrid of dissolution-reprecipitation and viscous flow at 1450 and 1500 °C and viscous flow at 1600 °C. At temperatures higher than 1550 °C, nearly full density (relative density of 98%) was achieved. The Vickers micro-hardness reached a maximum (21.7 GPa) at 1550 °C. Homogeneous distribution without the agglomeration of TiN particles in the Si₃N₄ matrix was achieved by SPS at 1600 °C. The composites prepared by SPS at 1550 and 1600 °C had low electrical resistivity and could be machined by electrical discharge machining.

Key words: Spark Plasma Sintering, Silicon Nitride/Titanium Nitride Composite, Machinability

1. INTRODUCTION

Silicon nitride-based materials have promising high temperature properties such as strength, creep resistance and oxidation resistance. A successful approach for the possibility of mass production at a lower manufacturing cost is to incorporate an electrically conductive reinforcement such as TiN [1]. TiN has a high melting temperature (2950 °C), high hardness (21 GPa), and good electroconductivity ($2.5 \times 10^{-5} \Omega\text{cm}$) [2]. Depending on the amount of TiN particles added and the type of TiN subnetwork formed in the composite, it is possible to make a composite that is sufficiently electroconductive to be machined by electrical discharge machining (EDM), thus avoiding the expensive grinding operation for the final shaping and surface finishing of components [3, 4]. The electrical resistivity of the Si₃N₄/TiN composite is affected by the initial size of the powder, the sintering method and the microstructure formed during sintering. Si₃N₄/TiN composites have been produced by various methods including hot pressing (HP) [3, 4], gas pressure sintering (GPS) [5, 6], in situ processing [7], and self-propagating high temperature synthesis (SHS) [8]. However these methods require a high temperature and a long processing time.

A new rapid sintering method, spark plasma sintering (SPS) has been applied to produce hard sintered materials via the application of a large pulsed current using a graphite mold under a high compressive stress [9]. In SPS, rapid heating due to the large current shortens the densification time, thereby making this process suitable for the sintering of materials. However, there have been few reports on the application of SPS to electroconductive Si₃N₄/TiN composites. The aim of the present study was to evaluate the applicability of SPS to the consolidation of Si₃N₄-TiN nano powders. The

influences of sintering temperature on electrical resistivity were investigated and correlated with the microstructure.

2. EXPERIMENTAL PROCEDURE

The starting materials used for this study were Si₃N₄ containing 5 mass% Y₂O₃ and 2 mass% Al₂O₃ (Wako Co. Ltd.) and TiN powders (Wako Co. Ltd.). Fig.1 shows secondary electron (SE) images of the starting materials. The mean particle size of Si₃N₄ and TiN was approximately 50 nm. The amount of TiN added should be as small as possible because TiN is readily oxidized at 600 °C, leading to the degradation of oxidation resistance [10]. On the other hand, the percolation concentration at which the electrical resistivity of Si₃N₄/TiN composites decreased drastically is nearly 20 vol%TiN [7]. Therefore, Si₃N₄-20 vol%TiN powders were mixed by ultrasonic vibration, followed by planetary ball milling (Pulverisette 6, Fritsch Co. Ltd.) at a rotation speed of 100 rpm for 6 h in ethanol using ZrO₂ balls.

The mixed powders of 2 g were put into a graphite die with an inner diameter of 15 mm. A graphite sheet of 0.25 mm thickness was used to prevent powder/die and powder/punch reactions. The unit was rapidly heated to 1450-1600 °C by SPS (SPS-3.20 MK-4, Sumitomo Coal Co. Ltd.) under a compressive stress of 40 MPa in vacuum (10 Pa). The temperature was monitored and regulated by an infrared ray thermometer focused on the surface of the graphite die. The temperature was increased at a rate of 100 °C/min from 600 °C up to the sintering temperature, followed by holding for 10 min at the sintering temperature.

The density was measured by the Archimedes method (MD-300S, Alfa Mirage Co. Ltd.). The microstructure

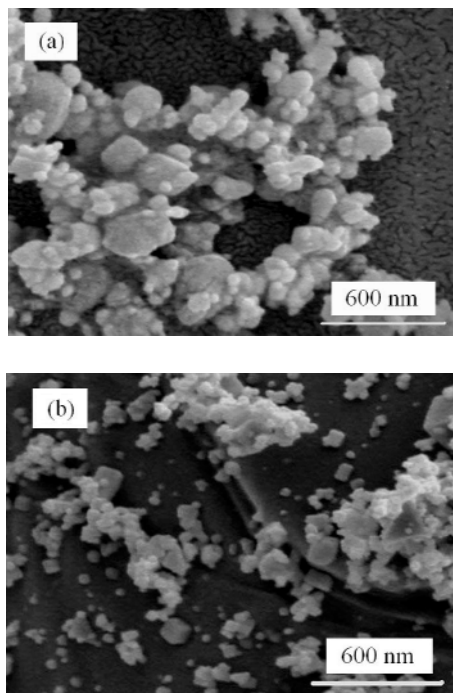


Fig.1 SE images of the as-received powders (a) Si₃N₄ and (b) TiN

of the polished and plasma-etched (Tensec SP10, Horiba Co. Ltd.) specimen was examined using a scanning electron microscope (ESEM XL-30 Series, Philips Co. Ltd.) and an energy dispersive X-ray spectrometer (EDX) installed in the ESEM. The crystalline structure was examined by X-ray diffraction (XRD-6000S, Shimadzu Co. Ltd.), which was performed with Cu K α -ray at a scanning rate of 3 °/min. The Vickers micro-hardness of the composites under a load of 9.807 N was measured using Vickers hardness tester (HVM, Shimadzu Co. Ltd.). The electrical resistivity was measured at room temperature on the polished surface of the specimen (2 × 3 × 14 mm) using a four-point probe method. The machinability of the composites was examined by EDM (Robocut α -OA, Fanuc Co. Ltd.) with 0.25 mm diameter of Cu wire at a speed of 0.2 mm/min

3. RESULTS AND DISCUSSION

Fig.2 shows the relationships between logarithmic shrinkage ($\log \Delta L/L_0$) and holding time ($\log t$) for the composites prepared by SPS at 1450, 1500 and 1600 °C. A dense composite was obtained by SPS at 1600 °C for 80 s but was not achieved at 1450 or 1500 °C, even when the holding time was 10 min. Kingery et al [11, 12] proposed a linear relation between shrinkage and holding time based on a theoretical consideration during the initial stage of sintering. According to the relationships, the slope k is 0.5 for dissolution-precipitation mechanism [11] and the slope k is 1 for viscous flow [12]. From Fig.2, the slopes in the early stage (~ 62 s) of sintering are 0.71, 0.78 and 0.90 at 1450, 1500 and 1600 °C, respectively. This implies that the dominant mechanisms for SPS are a hybrid of dissolution-precipitation and viscous flow at 1450 and 1500 °C and viscous flow at 1600 °C.

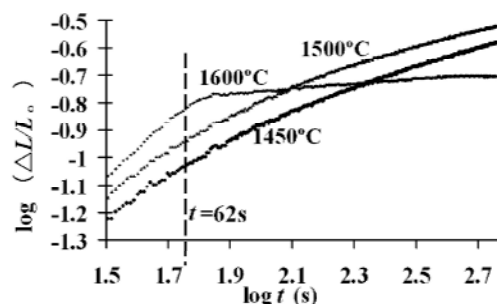


Fig.2 Relationships between log shrinkage and log holding time.

Fig.3 shows back-scattered electron (BSE) images of the Si₃N₄-20vol%TiN composites prepared by SPS and Fig.4 shows the EDX analyses of (a) grey region and (b) white region of composite prepared by SPS at 1600 °C. It is found that the grey region is Si₃N₄ (matrix) and white grains are TiN. It was observed in Figs.3(a) and (b) that a black part are pores. Porosity decreased with the increase in sintering temperature. No pores were found in the composites prepared by SPS at temperatures higher than 1550 °C. As shown in Figs. 3(a) and (b), the agglomeration of TiN particles were observed, although there was less agglomeration at 1550 °C (Fig.3(c)). A homogeneous distribution without the agglomeration of TiN particles was achieved by SPS at 1600 °C, while the grain growth of TiN particles was observed (Fig.3 (d)). This is because the sintering mechanism is governed by viscous flow as shown by $k = 0.9$.

Fig.5 shows the relative density and Vickers micro-hardness of Si₃N₄-20 vol%TiN composites plotted against sintering temperature. The full density was calculated on the basis of the densities of 3.18, 5.44, 4.84 and 3.98 g/cm³ for Si₃N₄, TiN, Y₂O₃ and Al₂O₃, respectively. The relative density increased with increasing sintering temperature up to 1550 °C, reaching 98 % at 1550 and 1600 °C. This result corresponds to the microstructure of the composites (Figs. 3(c) and (d)). These findings are in good agreement with the results of Gao et al [7]; dense Si₃N₄-20 vol%TiN composites were achieved by HP at 1550-1800 °C for 1 h under a compressive stress of 30 MPa. Thus, the total processing time required for SPS was less than that required for HP. This suggests that SPS is an efficient sintering process for consolidating Si₃N₄-20 vol%TiN powders. The maximum hardness (21.7 GPa) was achieved at 1550 °C. This is because porosity decreases with increasing sintering temperature. However, a slight decrease in hardness was found at 1600 °C. It is thought that not only the growth of TiN particles but also the grain growth of the Si₃N₄ matrix may occur at 1600 °C.

Fig.6 shows XRD patterns of the starting powders and composites prepared by SPS at different temperatures. α - and β - Si₃N₄ phases were present in the as-received Si₃N₄ powder and in the composite sintered at 1450 °C. No α -Si₃N₄ peaks were detected in the composites sintered at higher temperatures (1500-1600 °C), only the β -Si₃N₄ was present in these composites. These findings are in good agreement with the results of Hojo [13], who showed that the complete transformation of α -Si₃N₄ to β -

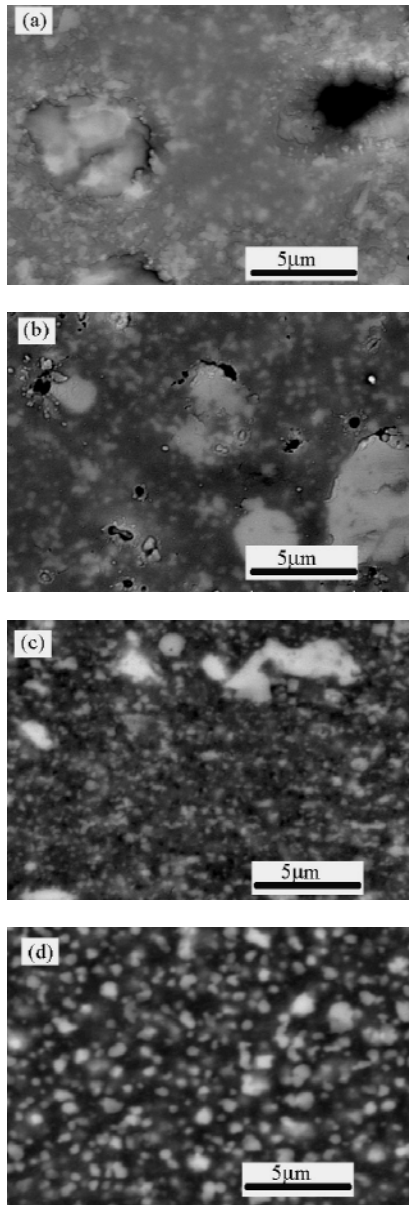


Fig.3 BSE images of Si_3N_4 -20vol%TiN composites prepared by SPS at different temperatures. (a) 1450 °C, (b) 1500 °C, (c) 1550 °C and (d) 1600 °C.

Si_3N_4 occurs during the dissolution-precipitation process at 1600 °C. No rodlike β - Si_3N_4 was observed in the microstructure (Fig. 3). It is thought that the added TiN particles inhibit the formation of rodlike β - Si_3N_4 .

Fig.7 shows the room temperature DC electrical resistivity of composites prepared by SPS. The electrical resistivity of the composites decreased with the increase in sintering temperature. The composite prepared at 1450 °C ($5 \times 10^{13} \Omega\text{cm}$) had the same order of electrical resistivity as that of monolithic Si_3N_4 . Microstructural factors such as the grain shape and size of the matrix, the distribution and size of TiN particles and the porosity influence the electrical resistivity of the composites. Rodlike β - Si_3N_4 improves the fracture toughness of the composite but increases its electrical resistivity [5]. The electrical resistivity decreases with decreasing matrix

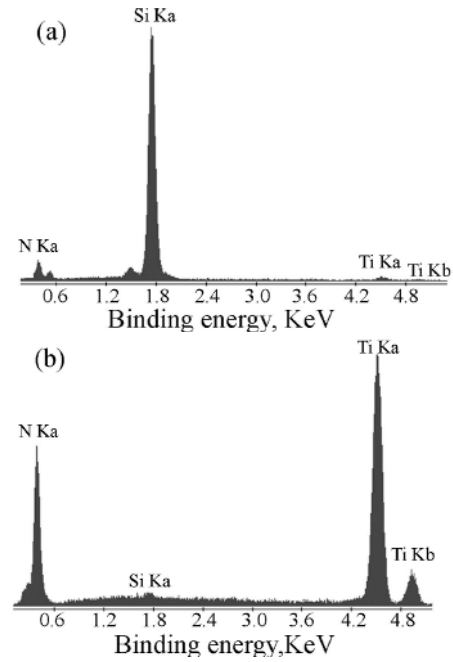


Fig.4 EDX analyses of composite prepared by SPS at 1600 °C. (a) grey region and (b) white region

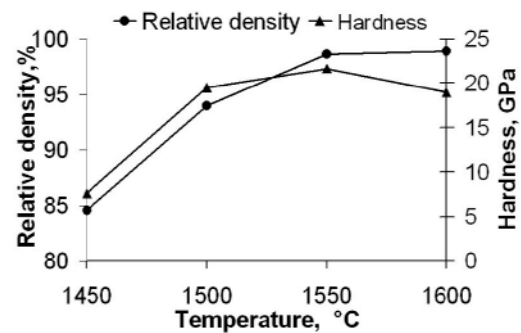


Fig.5 Relative density and Vickers hardness of Si_3N_4 -20 vol%TiN composites versus sintering temperature.

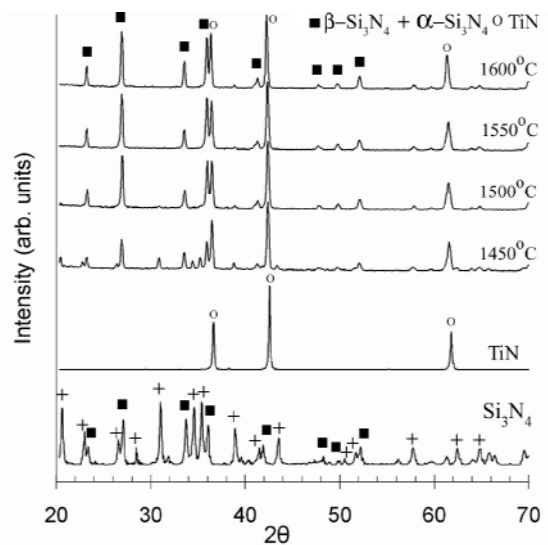


Fig.6 XRD patterns of the starting powders and composites prepared by SPS at different temperatures.

grain size because electrons flow through the grain boundaries containing TiN particles. The porosity increases the electrical resistivity. The composite prepared by SPS at 1450 °C has many pores and a long TiN-to-TiN distance due to the large amount of agglomeration, resulting in high electrical resistivity. The decrease in electrical resistivity at higher SPS temperatures is attributed to both the reduction of porosity (Fig. 5) and the shorter TiN-to-TiN distance due to the decrease in agglomeration. In SPS at 1600 °C, a homogeneous TiN distribution without the agglomeration was achieved (Fig. 3(d)). As a result, the TiN-to-TiN distance decreased and the electrical resistivity was considerably reduced. The value of electrical resistivity (3.46 Ωcm) of the composite prepared by SPS at 1600 °C is small compared with that of composites obtained by HP (10⁹-order Ωcm, 20 vol%TiN, 1850 °C for 1 h) [4] and GPS (10³-order Ωcm, 20 vol%TiN, 1950 °C for 3.5 h) [6], and is equivalent to that of the composite produced by in situ processing (about 2 Ωcm, 20 vol%TiN, in situ direct nitridation + HP at 1650 °C for 1 h) [7].

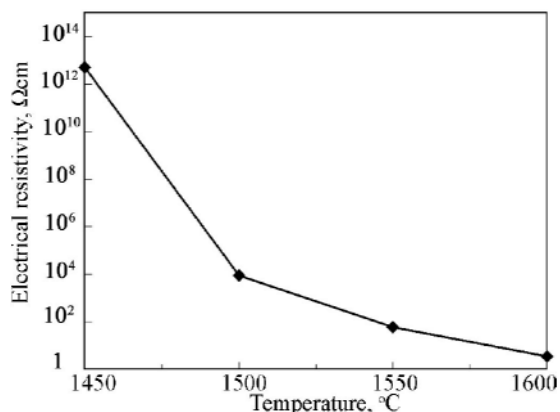


Fig.7 Electrical resistivity versus sintering temperature of Si₃N₄-20 vol%TiN composites.

The composites prepared by SPS at 1450 and 1500 °C could not be machined by EDM, while the composites prepared at 1550 and 1600 °C could be machined by EDM. Fig.8 shows an optical micrograph of the composites prepared by SPS at 1450 °C and at 1600 °C after machined by EDM. Liu [4] reported that TiN content higher than 30 vol% must be added to produce the composites with a low electrical resistivity (approximately 10⁻² Ωcm) to facilitate EDM. In this study, the amount of TiN required for the composite to be machinable by EDM was only 20 vol%. This is because a homogeneous distribution of TiN particles in the matrix was achieved, resulting in a low electrical resistivity

4. CONCLUSIONS

Si₃N₄ with additives (Y₂O₃ and Al₂O₃) and 20 vol%TiN powders were mixed using a planetary ball mill, then subjected to SPS at 1450-1600 °C for 10 min under a compressive stress of 40 MPa. The sintering mechanism for SPS was a hybrid of dissolution-precipitation and viscous flow at 1450 and 1500 °C and viscous flow at 1600 °C. At temperatures higher

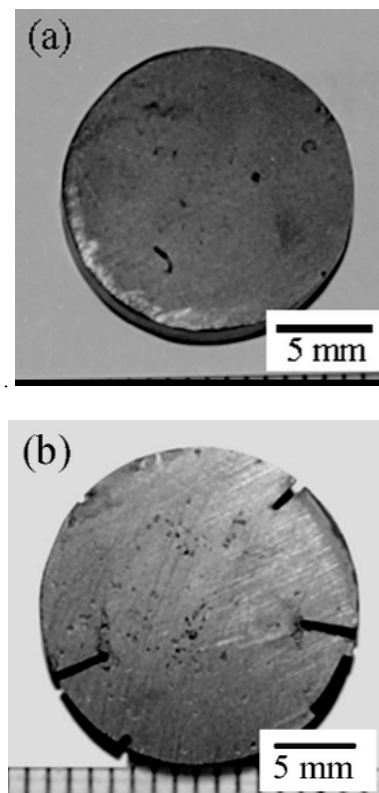


Fig.8 Optical micrograph of the composites prepared by SPS at (a) 1450 and (b) 1600 °C after machined by EDM.

than 1550 °C, nearly full density (relative density of 98%) was achieved. The Vickers micro-hardness reached a maximum (21.7 GPa) at 1550 °C then decreased slightly when the temperature was increased to 1600 °C. The transformation of α-Si₃N₄ to β-Si₃N₄ occurred at temperatures higher than 1500 °C. A homogeneous distribution without the agglomeration of TiN particles in the Si₃N₄ matrix was achieved by SPS at 1600 °C. The electrical resistivity was related to the microstructure of the composites. The composites prepared by SPS at 1550 and 1600 °C had a low electrical resistivity and could be easily machined by EDM

ACKNOWLEDGEMENTS

The authors greatly acknowledge the support of the Hitachi Scholarship Foundation (Tokyo) for the scholarship and to Dr. Y. Kawakami from Ind.Tech. Center of Saga, Japan for using the SPS apparatus.

REFERENCES

- [1] A. Bellosi, S. Guicciardi, A. Tamperi, *J. Eur. Cer. Soc.*, **9**, 83-93 (1992).
- [2] J. Mukerji, S.K. Biswas, *J. Am. Cer. Soc.*, **73**, 142-145 (1990).
- [3] C.C. Liu, J.L. Huang, *Ceramic Inter.*, **29**, 679-687(2003).
- [4] C.C. Liu, *Mater. Sci. Eng.*, **A363**, 221-227 (2003).
- [5] L. Zivkovic, Z. Nikolic, S. Boskovic, M. Miljkovic, *J. Alloys & Comp.*, **373**, 231-236 (2004).

- [6] B.T. Lee, Y.J. Yoon, K.H. Lee, *Mater. Lett.*, **47**, 71-76 (2001).
- [7] L. Gao, J. Li, T. Kusunose, K. Niihara, *J. Eur. Cer. Soc.*, **24**, 381-386 (2004).
- [8] H. Wanbao, Z. Baolin, Z. Hanrui, L. Wenlan, *Ceramic Inter.*, **30**, 2211-2214 (2004).
- [9] D.S. Perera, M. Tokita, S. Moricca, *J. Eur. Cer. Soc.*, **18**, 401-404 (1998).
- [10] Y.G. Gogotsi, F. Porz, *Corros. Sci.*, **33**, 627-640 (1992).
- [11] W.D. Kingery, *J. Appl. Phys.*, **30**, 301-306 (1959).
- [12] W.D. Kingery, M. Berg, *J. Appl. Phys.*, **26**, 1205-1212 (1956).
- [13] J.Hojo, *J. Cer. Soc. Japan*, **112**, s1003-s1008 (2004).

(Received June 9, 2009; Accepted November 25, 2009)

